Ontwikkeling en implementatie van theoretische methodes
voor de berekening van EPR-parameters in periodieke simulaties

Development and Implementation of Theoretical Methods
for the Calculation of EPR Parameters in Periodic Simulations

Reinout Declerck

Promotor: prof. dr. M. Waroquier
Proefschrift ingediend tot het behalen van de graad van
Doctor in de Ingenieurswetenschappen: Toegepaste Natuurkunde

Vakgroep Subatomaire en Stralingsfysica
Voorzitter: prof. dr. D. Ryckbosch
Faculteit Wetenschappen
Academiejaar 2007 - 2008

UNIVERSITEIT
GENT

ISBN 978-90-8578-000-7
NUR 928
Wettelijk depot: D/2008/10.500/43

Dit onderzoekswerk werd uitgevoerd in het Centrum voor Moleculaire Modellering, onder leiding van prof. dr. Michel Waroquier.

The present work marks, at least for the time being, the final stage of eight years of university studies, and new challenges and experiences are waiting around the corner. I am grateful first and foremost to my promotor Michel Waroquier and the steadily growing list of members and former members of the Center for Molecular Modeling, many (if not all) of which have become more than just colleagues.* Secondly, I would like to thank Bart De Sterck, Jürg Hutter, Ewald Pauwels, Maarten Schurmans, Daniel Sebastiani, Dimitri Van Neck, Veronique Van Speybroeck, and Valéry Weber for their invaluable scientific contributions to this work. Finally, I am greatly indebted to my friends and family for their unconditional support.

Reinout Declerck
September 9th 2008

* Diederica Claeys, Hendrik De Cooman, Bart De Sterck, Matthias Degroote, Wim Dewitte, An Ghysels, Karen Hemelsoet, David Lesthaeghe, Emmanuel Baribefe Naziga, Ewald Pauwels, Franky Stevens, Karen Van Cauter, Diederik Van Fleteren, Marc Van Houteghem, Dimitri Van Neck, Veronique Van Speybroeck, Matthias Vandichel, Peter Vansteenkiste, Stijn Verdonck, Brecht Verstichel, and Toon Verstraelen.

Leden van de examencommissie

Voorzitter

prof. dr. ir. Daniël De Zutter (Universiteit Gent, IR05)

Leescommissie

prof. dr. Jürg Hutter (Universität Zürich)

prof. dr. ir. Femke Olyslager (Universiteit Gent, IR05)

dr. Daniel Sebastiani (Max-Planck-Institut für Polymerforschung Mainz)

prof. dr. Dimitri Van Neck (Universiteit Gent, WE05)

prof. dr. ir. Veronique Van Speybroeck (Universiteit Gent, IR17)

Overige leden

prof. dr. Freddy Callens (Universiteit Gent, WE04)

prof. em. dr. Kris Heyde

dr. Ewald Pauwels (Universiteit Gent, WE05)

prof. dr. Sabine Van Doorslaer (Universiteit Antwerpen)

dr. Valéry Weber (Universität Zürich)

prof. dr. Michel Waroquier (Universiteit Gent, WE05), promotor

Contents

Nederlandstalige samenvatting

De bepaling en voorspelling van de eigenschappen van materie op het niveau van de nanoschaal, enkel uitgaande van de fundamentele wetten van de kwantumfysica (*ab initio*), vormt sinds vele jaren een zeer actief en waardevol onderzoeksdomein. Dichtheidsfunctionaaltheorie (*density functional theory*, DFT) is een bijzonder succesvolle ab-initiotechniek, die werd ontwikkeld door Hohenberg en Kohn en in een bruikbaar algoritme geformuleerd door Kohn en Sham. Essentieel stelt het theorema van Hohenberg-Kohn dat de elektronische grondtoestandsgolffunctie van eender welk moleculair systeem eenduidig wordt bepaald door de elektronische grondtoestandsdichtheid. De elektronendichtheid hangt af van slechts drie ruimtelijke variabelen en is daarmee een stuk simpeler te hanteren dan de veeldeeltjesgolffunctie, zowel conceptueel als praktisch.

Elektron-paramagnetische-resonantie (*electron paramagnetic resonance*, EPR), ook wel elektronspinresonantie (*electron spin resonance*, ESR) genoemd, is één van de voornaamste spectroscopische technieken om specimens met één of meerdere ongepaarde elektronen te onderzoeken. De basisgedachte van EPR is analoog aan die van de beter gekende nucleaire magnetische resonantie (*nuclear magnetic resonance*, NMR): in de eerste techniek wordt de spin van de elektronen geëxciteerd, in de laatste de spin van de atoomkernen. De energieniveaus en intensiteiten van de spincentra, die volgen uit een EPR-experiment, kunnen worden gereproduceerd met behulp van een zogeheten effectieve Hamiltoniaan (*effectief* in de zin dat het een zuiver mathematisch object betreft, dat niet uit fundamentele fysische principes volgt). Vaak volstaat een effectieve Hamiltoniaan met de volgende laagste-orde interactietermen: i) de g-tensor die de interactie beschrijft van de netto elektronenspin met een extern aangelegde magnetische veld, ii) de A- of hyperfijntensoren die de interactie beschrijven van de netto elektronenspin met de atoomkernspins,

en iii) in het geval van een netto elektronenspin hoger dan 1/2, de D- of nulveldsplitsingstensor die volgt uit magnetische-dipoolinteracties tussen verschillende ongepaarde elektronen.

De laatste jaren groeide de interesse in de ab-initioberekening van EPR-parameters sterk. Voor de experimentator vormen theoretische berekeningen een krachtig hulpmiddel bij de analyse van de spectra die soms zeer complex kunnen zijn. Door de experimenteel verkregen EPR-parameters te vergelijken met ab-initiobepaalde waarden is het mogelijk om de moleculaire structuur in de omgeving van het spincentrum te identificeren en meer diepgaand te analyseren.

Tot voor kort kon men EPR-parameters enkel berekenen in gasfase-simulaties, waarin de te onderzoeken molecule zich in vacuum bevindt. Heel wat interessante toepassingen van de EPR-techniek vindt men echter terug in de vaste fase, waarbij de spincentra volledig ingebed zitten in materie. Een succesvolle techniek om de vaste fase te simuleren bestaat erin aan een simulatiecel periodieke randvoorwaarden op te leggen. Dit is meestal een correcte benadering, aangezien de vaste fase van veel stoffen een periodieke structuur kent.

De aanpassing van de theoretische methodes voor de berekening van EPR-parameters in periodieke simulaties blijkt echter verre van triviaal, en tot nu toe werden daartoe slechts een beperkt aantal pogingen ondernomen. Elk van deze implementaties kent echter een aantal methodologische en/of praktische beperkingen, en om die reden worden theoretische EPR-parameters van vaste-fase-structuren nog steeds hoofdzakelijk berekend met behulp van cluster-in-vacuomodellen. Bij deze techniek wordt (noodgedwongen) slechts een deel van de moleculaire omgeving in rekening gebracht, een benadering die vaak een gevoelig verlies aan nauwkeurigheid tot gevolg heeft.

Dit doctoraatsonderzoek richt zich op de ontwikkeling, implementatie, validatie en toepassing van DFT-methodes voor de snelle en nauwkeurige berekening van de g- en A-tensoren in periodieke simulaties. Daartoe werden een aantal nieuw-ontwikkelde theoretische methodes geïmplementeerd in CPMD en CP2K, twee populaire simulatiepakketten die gebruik maken van periodieke randvoorwaarden. Vervolgens werden de ontwikkelde theoretische methodes gevalideerd, door de EPR-parameters van een uitgebreide selectie van atomen en kleine molecules in de gasfase te vergelijken met reeds bestaande berekeningsmethodes voor de gasfase (zowel CPMD als CP2K kunnen via speciale technieken ook met de gasfase overweg). Daarna

werden met de nieuwe methode de EPR-parameters van enkele periodieke structuren berekend, en grondig vergeleken met de beschikbare experimentele gegevens en resultaten verkregen met onder andere cluster-in-vacuomodellen. Verschillende ideeën voor de versnelling van de methodes, zoals bijvoorbeeld het gebruik van een gelaagd hybride schema waarin een nauwkeurige alle-elektronenbehandeling voor het radicalaire centrum kan worden gecombineerd met een relatief goedkope pseudopotentiaalbenadering en/of klassieke moleculaire-mechanicatechnieken voor de rest van de simulatiecel, werden uitvoerig getest.

Vervolgens werden een aantal interessante applicaties bestudeerd, zoals bijvoorbeeld de studie van de afhankelijkheid van de moleculaire omgeving van A-tensoren in een reeks van suikerkristalradicalen, de berekening van de A-tensoren van het R2-centrum in β-D-fructose langsheen een compleet moleculaire-dynamicatraject op eindige temperatuur, en de berekening van de g-tensor voor het E_1'-centrum in α-kwarts met behulp van een simulatiecel bestaande uit 15551 atomen en het gelaagd hybride schema.

Waarschijnlijk zal blijken dat de CP2K-methodes, omdat zij breder inzetbaar zijn, beter tegen de tijd bestand zijn dan hun CPMD-tegenhangers. Via de GAPW-voorstelling en de gelaagde aanpak, bieden de CP2K-methodes een zeer aantrekkelijk compromis tussen nauwkeurigheid en computationele kost in vergelijking met het beperkte aantal concurrerende methodes voor periodieke simulaties.

Alle programmacode werd integraal opgenomen in de publieke distributies van beide simulatiepakketten (beschikbaar op de respectievelijke websites).

Nevenprojecten

In de marge van het onderzoek werd de opgedane expertise in het simuleren van vaste stoffen op DFT-niveau ingezet in een samenwerkingsverband met het Fysico-Chemisch Laboratorium van de Katholieke Universiteit Leuven. Er werd gewerkt aan een nieuw semi-empirisch energiemodel voor de studie van oppervlaktefenomenen in metaallegeringen, gefit aan berekeningen op DFT-niveau. Het voorgestelde model werd gebruikt voor de theoretische voorspelling van oppervlaktesegregatie in CuPt-legeringen.

Daarnaast werden, op basis van moleculaire-dynamicasimulaties en metadynamica in een expliciet periodiek solventmodel, de solvatatie- en isomerisatiekarakteristieken van gelithieerde 3-chloro-1-azaallylische anionen in een

tetrahydrofuraanoplossing ontrafeld. De bevindingen werden onafhankelijk bevestigd door ROESY-NMR experimenten,[1] uitgevoerd aan het Departement Organische Chemie van de Universiteit Gent. Een gedetailleerde kennis over de structuur van deze gesolvateerde anionen leidt tot een beter begrip van de chemische reacties (bvb. aldol- of Mannich-typereacties) waarin zij een rol spelen.

Net voor de voltooiing van deze thesis, werd nog een bijkomend onderzoeksproject afgewerkt over silica-templaat-interacties in de beginfase van de zeolietsynthese. Dit project werd uitgevoerd in samenwerking met de Faculteit Scheikundige Technologie van de Technische Universiteit Eindhoven, het Department of Fuels Chemistry and Technology van de Wroclaw University of Technology en het Centrum voor Oppervlaktechemie en Katalyse van de Katholieke Universiteit Leuven.

[1] roterend-assenstelsel-nucleair-overhauser-effectspectroscopie, (*rotational frame nuclear overhauser effect spectroscopy*, ROESY)

English summary

For many years now, the determination and prediction of the properties of matter at the level of the nanoscale, based only on the fundamental laws of quantum physics (*ab initio*), has been a very active and valuable field of research. Density functional theory (DFT) is a particularly successful ab-initio technique, which was developed by Hohenberg and Kohn, and formulated into a useful algorithm by Kohn and Sham. Essentially, the theorem of Hohenberg-Kohn states that the electronic ground-state wave function of any molecular system is uniquely determined by the electronic ground-state density. The latter is a lot easier to handle than the many-body wave function, both conceptually and practically.

Electron paramagnetic resonance (EPR), or electron-spin resonance (ESR), is one of the main spectroscopic techniques for the investigation of specimens featuring one or more unpaired electrons. The basic idea of EPR is analogous to the one of the well-known nuclear magnetic resonance (NMR) technique: in the former, the spin of the electrons is excited, whereas in the latter, the spin of the atomic nuclei is excited. The energy levels and intensities of the spin centra, which follow from an EPR experiment, can be reproduced by employing a so-called effective Hamiltonian (*effective* in the sense that it is a purely mathematical object, which does not follow from fundamental physical principles). Often, an effective Hamiltonian which includes only the lowest-order interaction terms is sufficient: i) the g tensor which describes the interaction of the net electron spin with an external magnetic field, ii) the A or hyperfine tensors which describe the interaction of the net electron spin with the spins of the atomic nuclei, and iii) in the case of a net electron spin higher than 1/2, the D- or zero-field splitting tensor resulting from magnetic-dipole interactions between multiple unpaired electrons.

In recent years, interest in the ab-initio calculation of EPR parameters has grown steadily. Theoretical calculations represent a powerful tool for the experimentalist in the analysis of the spectra which can sometimes be very

complex. Through comparison of the experimentally obtained EPR parameters with theoretically-determined values, it becomes possible to identify and analyze more thoroughly the molecular structure in the surroundings of the spin center.

Until very recently, the calculation of EPR parameters was feasible only in gas-phase simulations, in which the molecule under examination is surrounded by vacuum. However, many interesting applications which would potentially benefit from a theoretical EPR study are found in the solid phase, in which the spin centers are fully embedded in matter. A successful technique for the simulation of the solid phase imposes periodic boundary conditions (PBC) on a simulation cell. This is usually a correct approach, since the solid phase of many substances features a periodic structure.

The adaptation to PBC simulations of the theoretical methods for calculating EPR parameters proves to be far from trivial, and only a limited number of attempts have been made so far. However, all of these implementations share a number of methodological and/or practical limitations, and for this reason, theoretical EPR parameters of solid-phase structures were still mainly calculated using cluster-in-vacuo models. In this technique, only a limited portion of the molecular environment is included, an approximation which in many cases leads to a noticeable loss of accuracy.

This doctoral research focuses on the development, implementation, validation, and application of DFT methods for the fast and accurate calculation of the g and A tensors in PBC simulations. To this end, a number of newly-developed theoretical methods were implemented in CPMD (`http://www.cpmd.org`) and CP2K (`http://cp2k.berlios.de`, two popular program packages that adopt periodic boundary conditions. These theoretical methods were validated by comparing the EPR parameters of a wide range of atoms and small molecules in the gas phase with existing gas-phase methods (through special techniques, both CPMD and CP2K can also simulate the gas phase). Then, using these new methods, the EPR parameters of several periodic structures were calculated and thoroughly compared with available experimental data from literature and results obtained with, amongst others, cluster-in-vacuo models. Several ideas for the acceleration of the methods, such as for example the usage of a three-layered hybrid scheme combining an accurate all-electron treatment for the radical center and a relatively cheap pseudopotential approximation or classical molecular mechanics for the remainder of the simulation cell, have been carefully tested.

Subsequently, a number of exciting applications have been carried out, such as for example the study of the molecular environment dependence of A tensors in a set of sugar crystal radicals, the calculation of the A tensors of the R2 center in β-D-fructose along a complete molecular dynamics trajectory at finite temperature, and the calculation of the g tensor for the E_1' center in α-quartz using a 15551-atom simulation cell and the aforementioned three-layered hybrid scheme.

It is likely that the CP2K methods will last longer than their CPMD counterparts, as they are the most generally applicable. Through the Gaussian and augmented-plane-wave (GAPW) representation and the aforementioned layered approach, the CP2K methods offer a very attractive accuracy/cost trade-off over the few competing methods applicable to PBC simulations.

All source code has been included in the public distributions of the aforementioned program packages (available on the respective websites).

Projects on the side

The acquired expertise in the simulation of solids on the DFT level was used in a collaboration with the Physico-Chemical Laboratory of Catholic University of Leuven. We have been working on a new semi-empirical energy model for the study of surface phenomenae in metallic alloys, fitted to calculations on the DFT level. The proposed model was used in the theoretical prediction of surface segregation in CuPt alloys.

In addition, based on molecular-dynamics simulations and metadynamics in an explicit periodic solvent model, we unraveled the solvation and isomerisation characteristics of lithiated 3-chloro-1-azaallylic anions in a tetrahydrofuran solution. Our findings were independently confirmed by ROESY-NMR experiments,[2] conducted at the Department of Organic Chemistry of Ghent University. A detailed knowledge of the structure of these solvated anions leads to a better understanding of the chemical reactions (e.g. aldol- or Mannich-type reactions) in which they play a key role.

Just as this thesis was nearing completion, a further project on silica-template interactions during the initial stages of zeolite synthesis was finished. This project was carried out in conjunction with the Department of Chemical Engineering and Chemistry of Eindhoven University of Technology, the Department of Fuels Chemistry and Technology of Wroclaw University of Technology,

[2] rotational frame nuclear overhauser effect spectroscopy (ROESY).

and the Centre for Surface Chemistry and Catalysis of Catholic University of Leuven.

List of abbreviations

AE	all-electron
AO	atomic orbital
BZ	Brillouin zone
CGF	contracted Gaussian function
CPGF	contracted periodic Gaussian function
CSGT	continuous set of gauge transformations
DFPT	density functional perturbation theory
DFT	density functional theory
EPR	electron paramagnetic resonance
ESR	electron spin resonance
FFT	fast Fourier transform
GAPW	Gaussian and augmented plane wave
GGA	generalized gradient approximation
GIPAW	gauge-including projector-augmented wave
GPW	Gaussian and plane wave
KS	Kohn-Sham
LCAO	linear combination of atomic orbitals
LDA	local density approximation
LSDA	local spin density approximation
MLWF	maximally localized Wannier function
MM	molecular mechanics
NMR	nuclear magnetic resonance
PAW	projector-augmented wave
PBC	periodic boundary conditions
PSP	pseudopotential
PW	plane wave
Ry	Rydberg

1 Introduction

The determination and prediction of the properties of matter at the level of the nanoscale, based only on the fundamental laws of quantum physics (*ab initio*), has become an indispensable scientific discipline over the last 50 years. This steep rise in popularity is partly due to the ever increasing numerical computing power, but also due to the development of new theoretical concepts which, sometimes only after adopting a number of approximations, drastically reduce the required computation time, which is commonly referred to as the *computational cost*.

In the class of ab-initio methods, a particular place is assumed by density functional theory (DFT), developed by Hohenberg and Kohn, and formulated into a useful algorithm by Kohn and Sham. Essentially, the theorem of Hohenberg-Kohn states that the electronic ground-state wave function of any molecular system is uniquely determined by the electronic ground-state density. The latter is a lot easier to handle than the many-body wave function, both conceptually and practically. The Kohn-Sham formulation of DFT enables, at least formally, the exact solution of this interacting many-body system, provided that the exchange-correlation functional is known. For the time being, however, this is not the case, and therefore we rely on approximative functionals which are (partly) phenomenological. For this reason, DFT cannot be regarded as an ab-initio method *in sensu stricto*. Nonetheless, the current generation of functionals are capable of describing the ground-state density and its derived properties with a satisfactory accuracy in many different situations.

Electron paramagnetic resonance (EPR), or electron-spin resonance (ESR), is

one of the main spectroscopic techniques for the investigation of specimens featuring one or more unpaired electrons. The basic idea of EPR is analogous to the one of the well-known nuclear magnetic resonance (NMR) technique: in the former, the spin of the electrons is excited, whereas in the latter, the spin of the atomic nuclei is excited. Since most stable molecules have a configuration without unpaired electrons, the application domain of EPR is more specific than is the case for NMR. EPR is used in solid-state physics for the identification or quantification of radicals (molecules with one or more unpaired electrons), in chemistry for the identification of reaction chains, as well as in biology and medicine where, amongst others, proteins are marked with spin labels in order to obtain insight in their structure and dynamics.

The energy levels and intensities of the spin centra, which follow from an EPR experiment, can be reproduced by employing a so-called effective Hamiltonian (*effective* in the sense that it is a purely mathematical object, which does not follow from fundamental physical principles). Often, an effective Hamiltonian which includes only the lowest-order interaction terms is sufficient: i) the g tensor which describes the interaction of the net electron spin with an external magnetic field, ii) the A or hyperfine tensors which describe the interaction of the net electron spin with the spins of the atomic nuclei, and iii) in the case of a net electron spin higher than $1/2$, the D- or zero-field splitting tensor resulting from magnetic-dipole interactions between multiple unpaired electrons.

In recent years, interest in the ab-initio calculation of EPR parameters has grown steadily. Theoretical calculations represent a powerful tool for the experimentalist in the analysis of the spectra which can sometimes be very complex. Through comparison of the experimentally obtained EPR parameters with theoretically-determined values, it becomes possible to identify and analyze more thoroughly the molecular structure in the surroundings of the spin center.

Until very recently, the calculation of EPR parameters was feasible only in gas-phase simulations, in which the molecule under examination is surrounded by vacuum. For the g tensor, a rich variety of DFT-based implementations for the gas phase is available. In the first group of one-component methods, the spin-orbit operators are treated perturbatively. Schreckenbach and Ziegler[1] introduced an effective potential to approximate the spin-orbit operators, Malkina *et al.*[2] used the atomic mean-field concept for this purpose and, finally, the so-called scaled spin-orbit approximation was proposed by Neese.[3] In the second group of two-component methods, the g tensor is

evaluated as a first-order property. The spin-orbit interaction is included in the two-component Kohn-Sham equations. In the implementation of van Lenthe *et al*,[4] relativistic effects are incorporated through through the zero-order regular approximation. A similar method in combination with the Douglas-Kroll transformation of the Dirac-Kohn-Sham equations was devised by Neyman *et al*..[5] The most relevant contributions to the A tensor can be evaluated from the ground-state density, and therefore this property is readily available within almost all DFT-based program packages for the gas phase.

However, many interesting applications which would potentially benefit from a theoretical EPR study are found in the solid phase, in which the spin centers are fully embedded in matter. A successful technique for the simulation of the solid phase imposes periodic boundary conditions (PBC) on a simulation cell. This is usually a correct approach, since the solid phase of many substances features a periodic structure. The adaptation to PBC simulations of the theoretical methods for calculating EPR parameters proves to be far from trivial, and only a limited number of attempts have been made so far. To my knowledge, upon the start of this doctoral research back in 2005, only the method of Pickard and Mauri[6] was able to calculate the g tensor in PBC simulations, and for the A tensor, only a handful of methods were available,[7–9] all taking a very similar approach. However, as will be substantiated further in this work, all of the aforementioned methods share a number of methodological and/or practical limitations, and for this reason, theoretical EPR parameters of solid-phase structures are still mainly calculated using cluster-in-vacuo models. In this technique, only a limited portion of the molecular environment is included, an approximation which in many cases leads to a noticeable loss of accuracy.

The main goal of this doctoral research is therefore the development, implementation, validation, and application of DFT methods for the fast and accurate calculation of the g and A tensors in PBC simulations. To this end, a number of newly-developed theoretical methods, or *algorithms*, have been implemented in two program packages which adopt periodic boundary conditions: CPMD (`http://www.cpmd.org`, longstanding, still very popular) and CP2K (`http://cp2k.berlios.de`, new, revolutionary, and quickly gaining popularity). Part of this work was carried out in a collaboration with the research group of Prof. dr. Jürg Hutter of the Physikalisch-Chemisches Institut of Universität Zürich, which coordinates the development of both packages. Both implementations differ greatly one from the other, as each package has its own specific possibilities and limitations.

Subsequently, these theoretical methods were validated by comparing the EPR parameters of a wide range of atoms and small molecules in the gas phase with existing gas-phase methods (through special techniques, both CPMD and CP2K can also simulate the gas phase). Then, using these new methods, the EPR parameters of several periodic structures were calculated and thoroughly compared with available experimental data from literature and results obtained with, amongst others, cluster-in-vacuo models. Several ideas for the acceleration of the methods, such as for example the usage of a three-layered hybrid scheme combining an accurate all-electron treatment for the radical center and a relatively cheap pseudopotential approximation or classical molecular mechanics for the remainder of the simulation cell, have been carefully tested. A number of exciting applications have been carried out, such as for example the study of the molecular environment dependence of A tensors in a set of sugar crystal radicals, the calculation of the A tensors of the R2 center in β-D-fructose along a complete molecular dynamics trajectory at finite temperature, and the calculation of the g tensor for the E_1' center in α-quartz using a 15551-atom simulation cell and the three-layered hybrid scheme.

All source code of the present methods has been included in the public distributions of the aforementioned program packages (available on the respective websites).

Next to this main research activity, the acquired expertise in the simulation of solids on the DFT level was used in a collaboration with the Physico-Chemical Laboratory of Catholic University of Leuven. We have been working on a new semi-empirical energy model for the study of surface phenomenae in metallic alloys, fitted to calculations on the DFT level. The proposed model was used in the theoretical prediction of surface segregation in CuPt alloys.

In addition, based on molecular-dynamics simulations and metadynamics in an explicit periodic solvent model, we unraveled the solvation and isomerisation characteristics of lithiated 3-chloro-1-azaallylic anions in a tetrahydrofuran solution. Our findings were independently confirmed by ROESY-NMR experiments,[1] conducted at the Department of Organic Chemistry of Ghent University. A detailed knowledge of the structure of these solvated anions leads to a better understanding of the chemical reactions (e.g. aldol-

[1] rotational frame nuclear overhauser effect spectroscopy (ROESY).

or Mannich-type reactions) in which they play a key role.

Just as this thesis was nearing completion, a further project on silica-template interactions during the initial stages of zeolite synthesis was finished. This project was carried out in collaboration with the Department of Chemical Engineering and Chemistry of Eindhoven University of Technology, the Department of Fuels Chemistry and Technology of Wroclaw University of Technology, and the Centre for Surface Chemistry and Catalysis of Catholic University of Leuven.

Before outlining the structure of this thesis, I wish to formulate a number of general remarks. The various publications that have appeared in international journals over the past few years, are the actual representation of this doctoral research, and their full (and unaltered) reproductions have been included further in this work. The following text is not a traditional, comprehensive overview of the entire doctoral research, but was (deliberately) limited to a thorough explanation of its main part, the calculation of EPR parameters in PBC simulations. The text addresses an audience with a basic understanding of quantum mechanics and attempts to explain the theoretical and technical aspects of the developed algorithms, which will hopefully facilitate reading the publications. I will especially discuss the CP2K implementation in detail because this implementation is the most innovative and more generally applicable. (Bio-)chemists and/or solid-state physicists will probably appreciate the different applications. These are discussed only in the publications, but are relatively independent of the theory. Although the *projects on the side* described above demanded a significant amount of research time, they have nevertheless been omitted in this text because they essentially belong to a different research domain. For an introduction to these research areas, I recommend the interested reader to consult the references in the introductory section of the respective publications. Finally, for the sake of clarity for the reader, the chronological order of the different research steps that have been taken is not always rigorously respected.

This thesis is structured as follows: chapter 2 contains an in-depth study of the theoretical and technical aspects of the calculation of EPR parameters in PBC simulations, chapters $3-10$ contain the full reproductions of the publications, and in chapter 11, the main conclusions are summarized and a few suggestions for future research are given.

References to publications that resulted from this doctoral research will be

indicated with [Art. 1], in order to distinguish them from publications of others, such as for example [1]. We will always assume a net electron spin equal to $\frac{1}{2}$, although all formulas are easily expandable to greater spins. We will also make use of atomic units, defined by $\hbar = m = e = 4\pi\epsilon = 1$, for which the velocity of light c equals $c = 1/\alpha \approx 137$, with α the fine structure constant.

2 The calculation of EPR parameters in PBC simulations

2.1 The many-body problem and density functional theory

The Schrödinger equation, established in 1925 by Austrian physicist Erwin Schrödinger, is the basic formula for the time-dependent nonrelativistic description of a quantum system:

$$H\left|\Psi(t)\right\rangle = i\hbar\frac{d}{dt}\left|\Psi(t)\right\rangle \ . \tag{2.1}$$

The time-independent Schrödinger equation has the well-known form:

$$H\left|\Psi\right\rangle = E\left|\Psi\right\rangle \ , \tag{2.2}$$

and constitutes an eigenvalue problem.

When applied to a many-body system of n electrons and N atomic nuclei, and projected onto the coordinate space of electron and nuclear positions, we arrive at the spin-independent,[1] $(3n+3N)$-dimensional, time-independent Schrödinger wave equation:

$$H\Psi(\mathbf{r}_1,\ldots,\mathbf{r}_n,\mathbf{R}_1,\ldots,\mathbf{R}_N) = E\Psi(\mathbf{r}_1,\ldots,\mathbf{r}_n,\mathbf{R}_1,\ldots,\mathbf{R}_N) \ , \tag{2.3}$$

[1] This is for the purpose of simplicity. In section 2.1.2, the spin of the electron will be introduced.

with eigenvalues E and eigenfunctions Ψ corresponding to the many-body operator H which, in atomic units, equals:

$$H = \sum_i -\frac{1}{2}\nabla_i^2 + \sum_I -\frac{1}{2M_I}\nabla_I^2 + \frac{1}{2}\sum_{i\neq j}\frac{1}{|\mathbf{r}_i - \mathbf{r}_j|} + \frac{1}{2}\sum_{I\neq J}\frac{Q_I Q_J}{|\mathbf{R}_I - \mathbf{R}_J|} - \sum_{i,I}\frac{Q_I}{|\mathbf{r}_i - \mathbf{R}_I|} \quad . \tag{2.4}$$

$\mathbf{r}_i$ and $\mathbf{R}_I$ denote the position operators which operate on the i-th electron and the I-th atomic nucleus, respectively.[2] M_I and Q_I represent the mass and the charge of the I-th atomic nucleus in atomic units.[3]

2.1.1 The Born-Oppenheimer approximation

The Born-Oppenheimer approximation [10, 11] assumes that the description of electrons and atomic nuclei can be separated. This is plausible: since the mass of an electron is many times smaller than the one of an atomic nucleus, electrons *move* much faster than atomic nuclei do. The total wave function is written as the product of a wave function for the electrons Ψ^{el} and a wave function for the atomic nuclei Ψ^{ion}:

$$\Psi(\mathbf{r}_1, \ldots, \mathbf{r}_n, \mathbf{R}_1, \ldots, \mathbf{R}_N) = \Psi^{\text{el}}_{\mathbf{R}_1,\ldots,\mathbf{R}_N}(\mathbf{r}_1, \ldots, \mathbf{r}_n)\Psi^{\text{ion}}(\mathbf{R}_1, \ldots, \mathbf{R}_N) \; . \tag{2.5}$$

This approximation leads to the separation of the Schrödinger wave equation (2.3) into:

1. A time-independent Schrödinger wave equation for the electrons in the constant potential field of fixed atomic nuclei. The electronic wave functions and energy levels still depend parametrically on the positions of the atomic nuclei.

[2] Throughout this work, indices $i, j, \ldots$ generally refer to electrons (and positrons), whereas indicies $I, J, \ldots$ denote atomic nuclei.

[3] Disambiguation: $\sum_{i\neq j}$ (and similar) indicates a double sum over i and j, but excludes the case where $i = j$.

2. A time-independent Schrödinger wave equation for the atomic nuclei in a potential field derived from the (ground) state of the electronic Schrödinger wave equation. From the total potential energy surface (originating from the attraction and the repulsion of the electron cloud and the atomic nuclei, respectively), the dynamics of the atomic nuclei can then be explored. In practice, classical Newtonian mechanics suffices for this purpose.

The time-independent Schrödinger wave equation for the electrons equals:

$$H^{\text{el}}\Psi^{\text{el}}_{\mathbf{R}_1,\ldots,\mathbf{R}_N}(\mathbf{r}_1,\ldots,\mathbf{r}_n) = E^{\text{el}}_{\mathbf{R}_1,\ldots,\mathbf{R}_N}\Psi^{\text{el}}_{\mathbf{R}_1,\ldots,\mathbf{R}_N}(\mathbf{r}_1,\ldots,\mathbf{r}_n)\ , \tag{2.6}$$

with:

$$H^{\text{el}} = \sum_i -\frac{1}{2}\nabla_i^2 + \frac{1}{2}\sum_{i\neq j}\frac{1}{|\mathbf{r}_i-\mathbf{r}_j|} - \sum_{i,I}\frac{Q_I}{|\mathbf{r}_i-\mathbf{R}_I|} + \frac{1}{2}\sum_{I\neq J}\frac{Q_IQ_J}{|\mathbf{R}_I-\mathbf{R}_J|}\ . \tag{2.7}$$

Here, too, we will treat the atomic nuclei as classical particles, enabling us to replace the position operators of the atomic nuclei by position variables.[4] Consequently, we can replace the interaction term between the atomic nuclei and the electrons in (2.7) by an arbitrary external potential $V_{\text{ext}}(\mathbf{r}_1,...,\mathbf{r}_n) = \sum_i v_{\text{ext}}(\mathbf{r}_i)$:

$$H^{\text{el}} = \sum_i -\frac{1}{2}\nabla_i^2 + \frac{1}{2}\sum_{i\neq j}\frac{1}{|\mathbf{r}_i-\mathbf{r}_j|} + V_{\text{ext}}(\mathbf{r}_1,...,\mathbf{r}_n)\ . \tag{2.8}$$

In general, there is no analytical solution for the electronic Schrödinger wave equation, and hence one must approach it using techniques such as DFT. Because DFT constitutes the basis for the algorithms developed further in this work, this theory will be elaborated thoroughly in the following sections.

From here on, we will work only with electronic Hamiltonians, states, wave functions, and energy levels, so that we can further omit the superscript *el*.

[4] Note that operators and variables use the same notation in this work.

2.1.2 Density functional theory

Hohenberg - Kohn theorems

In the time-independent electronic Schrödinger wave equation in an arbitrary external potential, the Hamiltonian equals:

$$H = \sum_i -\frac{1}{2}\nabla_i^2 + \frac{1}{2}\sum_{i\neq j}\frac{1}{|\mathbf{r}_i - \mathbf{r}_j|} + V_{\text{ext}}(\mathbf{r}_1, ..., \mathbf{r}_n) \ . \tag{2.9}$$

From the above equation, we infer that the Hamiltonian of a system consisting of n electrons (and hence the system itself) is entirely defined as soon as the external potential V_{ext} is defined. Consequently, n and V_{ext} determine *all the properties* of the ground state Ψ_0, as well as of the excited states Ψ.

First, let us recapitulate the **variational principle**:[5]

> The normalized wave function Ψ which minimizes the energy functional $E[\Psi]$ is the ground-state wave function:
>
> $$E[\Psi] \geq E[\Psi_0] = E_0 \ , \tag{2.10}$$
>
> where:
>
> $$E[\Psi] = \langle \Psi | H | \Psi \rangle \ . \tag{2.11}$$
>
> **Proof**
>
> An arbitrary normalized wave function Ψ can be expanded in a linear combination of the orthonormal eigenfunctions Ψ_n of the Hamiltonian H:
>
> $$|\Psi\rangle = \sum_n c_n |\Psi_n\rangle \ . \tag{2.12}$$
>
> The expectation value of H for Ψ then equals:

[5] Note that we *loosely* interchange between $\Psi(\mathbf{r}_1, ..., \mathbf{r}_n)$ and $|\Psi\rangle$. This is allowed as long as the Hamiltonian contains only spatial operators.

$$\begin{aligned} \langle \Psi | H | \Psi \rangle &= \sum_{m,n} c_m^* c_n \langle \Psi_m | H | \Psi_n \rangle \\ &= \sum_n |c_n|^2 E_n \ . \end{aligned} \tag{2.13}$$

The ground-state energy E_0 is by definition the lowest possible energy, $E_n \geq E_0$. Therefore it follows:

$$\langle \Psi | H | \Psi \rangle \geq E_0 \sum_n |c_n|^2 = E_0 \ . \tag{2.14}$$

Now we will prove the following one-to-one relationships for a system of n electrons:

$$V_{\text{ext}}(\mathbf{r}_1, ..., \mathbf{r}_n) \longleftrightarrow \Psi_0(\mathbf{r}_1, ..., \mathbf{r}_n) \ , \tag{2.15}$$

$$\rho(\mathbf{r}) \longleftrightarrow \Psi_0(\mathbf{r}_1, ..., \mathbf{r}_n) \ , \tag{2.16}$$

where ρ represents the ground-state density.

Proof

1. $V_{\text{ext}} \longrightarrow \Psi_0$ has already been made plausible: the external potential V_{ext} determines the Hamiltonian H, and thus the ground state Ψ_0.
2. $\Psi_0 \longrightarrow V_{\text{ext}}$ follows from an indirect demonstration, a *reductio ad absurdum*. Suppose that the ground state Ψ_0 gives rise to two different external potentials V_{ext} and V'_{ext}. These two potentials determine two Hamiltonians H and H' which both feature Ψ_0 as their respective ground state:

$$\begin{aligned} H\Psi_0(\mathbf{r}_1, ..., \mathbf{r}_n) &= E_0 \Psi_0(\mathbf{r}_1, ..., \mathbf{r}_n) \ , \\ H'\Psi_0(\mathbf{r}_1, ..., \mathbf{r}_n) &= E'_0 \Psi_0(\mathbf{r}_1, ..., \mathbf{r}_n) \ . \end{aligned} \tag{2.17}$$

Substracting the above equations one from the other, we obtain:

$$\left(V_{\text{ext}}(\mathbf{r}_1, ..., \mathbf{r}_n) - V'_{\text{ext}}(\mathbf{r}_1, ..., \mathbf{r}_n)\right) \Psi_0(\mathbf{r}_1, ..., \mathbf{r}_n) = (E_0 - E'_0)\Psi_0(\mathbf{r}_1, ..., \mathbf{r}_n) \ . \tag{2.18}$$

It follows immediately that $V_{\text{ext}} = V'_{\text{ext}}$ to within a constant term which, from a physical point of view, is the same.

3. $\Psi_0 \longrightarrow \rho(\mathbf{r})$ is trivial: from the knowledge of the ground-state wave function we obtain the ground-state density through:

$$\rho(\mathbf{r}) = n \int \mathrm{d}\mathbf{r}_2 ... \mathrm{d}\mathbf{r}_n \Psi_0^*(\mathbf{r}, \mathbf{r}_2, ..., \mathbf{r}_n) \Psi_0(\mathbf{r}, \mathbf{r}_2, ..., \mathbf{r}_n) \ . \tag{2.19}$$

4. $\rho(\mathbf{r}) \longrightarrow \Psi_0$ is again a reductio ad absurdum. Suppose that $\rho(\mathbf{r})$ gives rise to two different normalized wave functions which both represent a ground-state. Then, because of the relationschip (2.15), these wave functions uniquely define two different Hamiltonians:

$$\begin{aligned} \rho(\mathbf{r}) &\rightarrow \Psi_0(\mathbf{r}_1, ..., \mathbf{r}_n) \\ &\rightarrow V_{\mathrm{ext}}(\mathbf{r}_1, ..., \mathbf{r}_n) \\ &\rightarrow H = T + V_{2\mathrm{e}} + V_{\mathrm{ext}}(\mathbf{r}_1, ..., \mathbf{r}_n) \ , \\ \rho(\mathbf{r}) &\rightarrow \Psi_0'(\mathbf{r}_1, ..., \mathbf{r}_n) \\ &\rightarrow V_{\mathrm{ext}}'(\mathbf{r}_1, ..., \mathbf{r}_n) \\ &\rightarrow H' = T + V_{2\mathrm{e}} + V_{\mathrm{ext}}'(\mathbf{r}_1, ..., \mathbf{r}_n) \ . \end{aligned} \tag{2.20}$$

T and $V_{2\mathrm{e}}$ are short-hand notation for the kinetic energy and the two-particles interaction term. From the variational principle (2.10) (and assuming moreover that Ψ_0 and Ψ_0' are not a pair of degenerate states), it follows for both cases that:

$$\begin{aligned} E_0 &= \langle \Psi_0 | H | \Psi_0 \rangle < \langle \Psi_0' | H | \Psi_0' \rangle \ , \\ E_0' &= \langle \Psi_0' | H' | \Psi_0' \rangle < \langle \Psi_0 | H' | \Psi_0 \rangle \ . \end{aligned} \tag{2.21}$$

These inequalities result in:[6]

$$\begin{aligned} E_0 &< E_0' + \int \rho(\mathbf{r}) (v_{\mathrm{ext}}(\mathbf{r}) - v_{\mathrm{ext}}'(\mathbf{r})) \mathrm{d}\mathbf{r} \ , \\ E_0' &< E_0 - \int \rho(\mathbf{r}) (v_{\mathrm{ext}}(\mathbf{r}) - v_{\mathrm{ext}}'(\mathbf{r})) \mathrm{d}\mathbf{r} \ , \end{aligned} \tag{2.22}$$

or:

[6] Actually, according to (2.7) we should include in (2.22), next to the integral, also the energy of the Coulombic nuclei-nuclei interaction. This does not alter the validity of (2.23).

$$E_0 + E_0' < E_0 + E_0' \,. \tag{2.23}$$

This relation is conflicting and, taking into account (2.15), it follows that:

$$\Psi_0(\mathbf{r}_1, ..., \mathbf{r}_n) = \Psi_0'(\mathbf{r}_1, ..., \mathbf{r}_n) \,. \tag{2.24}$$

Both relationships (2.15) and (2.16) together determine the **first Hohenberg - Kohn theorem**:[12]

1. The ground-state density $\rho(\mathbf{r})$ uniquely determines the total Hamiltonian, and therefore also V_{ext} (for a nondegenerate ground state).
2. The ground-state energy is a functional of $\rho(\mathbf{r})$:

$$E_0[\rho] = \langle \Psi_0[\rho] | H[\rho] | \Psi_0[\rho] \rangle \,. \tag{2.25}$$

It is important to note that this theorem is not applicable to just any arbitrary density. Only those ground-state densities which originate from a solution Ψ_0 of an electronic Schrödinger wave equation can be linked to the external potential from which they originate. If a density is obtained in this way, this density is called *v-representable*.

The **second Hohenberg-Kohn theorem**[12] is a minimal principle for the density. It is similar to the variational principle (2.10), which was formulated for wave functions, and states:

> The (particular) density, out of all v-representable densities, which minimizes the energy functional for a given external potential, represents the ground-state density.

The proof follows from the variational principle (2.10). The ground-state solution of the Schrödinger wave equation for a given external potential V_{ext} is obtained through minimization of the energy functional by varying the electronic wave function. To all v-representable densities which differ from the ground-state density, a wave function can be assigned that differs from the ground-state wave function. Therefore, the energy functional will not be minimal for each of these wave functions.

An important disadvantage of the second theorem is that it is applicable only to v-representable densities. Not every trial density has the property of being

v-representable, so that through a simple minimization of the energy functional non-physical (i.e. not v-representabele) densities can be obtained.

The problem of v-representability can be circumvented by employing the Levy formalism,[13] in which only the N-representability (which means that the density is derived from an n-particles wave function or from an ensemble of n-particles wave functions) of a trial density is required. A trial density is N-representable if it is non-negative and integrates to the correct number of electrons, and if in addition the following condition is fulfilled:[14]

$$\int \mathrm{d}\mathbf{r} \left| \nabla(\rho(\mathbf{r})^{1/2}) \right|^2 < \infty \,. \tag{2.26}$$

This N-representability is imposed much easier. In practical calculations, v- and N-representability are always assumed to be fulfilled.

The Kohn-Sham equations

The Hohenberg-Kohn theorems only show that it is in principle possible to calculate physical quantities (which normally follow from the ground-state wave function) from the ground-state density. But the problem of effectively finding this density is not yet solved. In order to turn DFT into a practical scheme, Kohn and Sham[15] proposed an indirect treatment of this problem.

Primarily, they introduced a fictitious parallel system of n non-interacting electrons which, by definition, features the same density as the exact solution of the interacting electrons. Let us call $\psi_{\mathrm{ni},i}$ the one-particle wave functions of this independent-electron system. Their kinetic energy and density are then defined as:

$$T_{\mathrm{ni}} = -\frac{1}{2} \sum_i \int \mathrm{d}\mathbf{r} \psi^*_{\mathrm{ni},i}(\mathbf{r}) \nabla^2 \psi_{\mathrm{ni},i}(\mathbf{r}) \,, \tag{2.27}$$

$$\rho(\mathbf{r}) = \sum_i |\psi_{\mathrm{ni},i}(\mathbf{r})|^2 \,. \tag{2.28}$$

Assuming that the v-representable densities corresponding with the interacting system are also v-representable in the non-interacting system, it follows from the first Hohenberg-Kohn theorem that this density uniquely defines the total Hamiltonian H_{ni} and $V_{\mathrm{ni,ext}}$.[7] Since it holds for this non-interacting system

[7] ni = non-interacting.

(due to the absence of two-particle interaction between electrons) that:

$$T_{\mathrm{ni}} = H_{\mathrm{ni}} - V_{\mathrm{ni,ext}} \,, \tag{2.29}$$

the kinetic energy T_{ni} is also a unique functional of the density. This kinetic-energy functional can be used to approximate the kinetic energy of the interacting system.

The density from the non-interacting-electron system by definition equals the density from the interacting-electron system. If we would assume that this density represents a classical charge distribution, its Coulombic interaction energy would equal:

$$E_{\mathrm{H}}[\rho(\mathbf{r})] = \frac{1}{2} \int \mathrm{d}\mathbf{r} \int \mathrm{d}\mathbf{r}' \frac{\rho(\mathbf{r})\rho(\mathbf{r}')}{|\mathbf{r} - \mathbf{r}'|} \,. \tag{2.30}$$

E_{H} is called the Hartree energy of the system. The energy from the external potential is:

$$E_{\mathrm{ext}}[\rho(\mathbf{r})] = \int \mathrm{d}\mathbf{r} v_{\mathrm{ext}}(\mathbf{r})\rho(\mathbf{r}) + \frac{1}{2} \sum_{I \neq J} \frac{Q_I Q_J}{|\mathbf{R}_I - \mathbf{R}_J|} \,. \tag{2.31}$$

The total energy of the interacting system is now expressed as:

$$E_{\mathrm{tot}}[\rho(\mathbf{r})] = T_{\mathrm{ni}}[\rho(\mathbf{r})] + E_H[\rho(\mathbf{r})] + E_{\mathrm{ext}}[\rho(\mathbf{r})] + E_{\mathrm{XC}}[\rho(\mathbf{r})] \,. \tag{2.32}$$

By definition, E_{XC} then contains all the many-body effects, as well as the corrections from the kinetic energy of the interacting-electron system. If the functional form of E_{XC} would be known, we would be able to determine exactly the charge density of the ground state of the many-body system. This is (at present) not the case, and therefore we must resort to approximate functionals for E_{XC} which are often (partly) phenomenological (see below).

The minimization of E_{tot} is a constrained-extremum problem, in which the one-particle wave functions must satisfy the following orthonormality conditions:

$$\int \mathrm{d}\mathbf{r} \psi^*_{\mathrm{ni},i}(\mathbf{r})\psi_{\mathrm{ni},j}(\mathbf{r}) = \delta_{ij} \,. \tag{2.33}$$

Therefore, the stationary conditions of the total Lagrangian,[8] in which ϵ_i denotes the Lagrange multipliers,[9] equal:

$$\frac{\partial \left[E_{\text{tot}}[\rho] - \sum_i \epsilon_i \left(\int \psi^*_{\text{ni},i}(\mathbf{r}) \psi_{\text{ni},i}(\mathbf{r}) \mathrm{d}\mathbf{r} - 1 \right) \right]}{\partial \psi^*_{\text{ni},i}(\mathbf{r})} = 0 \, . \tag{2.34}$$

Elaborating the above equations, we obtain the Kohn-Sham (KS) equations, which represent nothing else than specific solutions of a one-particle Schrödinger wave equation:

$$\left[-\frac{1}{2}\nabla^2 + v_{\text{H}}(\mathbf{r}) + v_{\text{XC}}(\mathbf{r}) + v_{\text{ext}}(\mathbf{r}) \right] \psi_{\text{ni},i}(\mathbf{r}) = \epsilon_i \psi_{\text{ni},i}(\mathbf{r}) \, . \tag{2.35}$$

Indeed, we observe that ϵ_i and $\psi_{\text{ni},i}(\mathbf{r})$ represent eigenvalues (KS energy levels) and eigenfunctions (KS orbitals), respectively, corresponding to the KS Hamiltonian H_{KS}:

$$H_{\text{KS}}(\mathbf{r}) = -\frac{1}{2}\nabla^2 + v_{\text{H}}(\mathbf{r}) + v_{\text{XC}}(\mathbf{r}) + v_{\text{ext}}(\mathbf{r}) \, . \tag{2.36}$$

The n non-interacting electrons will occupy the n lowest KS energy levels. From (2.35), we infer that the sum of the occupied KS energy levels equals:

$$\sum_i \epsilon_i = T_{\text{ni}}[\rho(\mathbf{r})] + \int \mathrm{d}\mathbf{r} \left(v_{\text{H}}(\mathbf{r}) + v_{\text{XC}}(\mathbf{r}) + v_{\text{ext}}(\mathbf{r}) \right) \rho(\mathbf{r}) \, , \tag{2.37}$$

allowing us to express E_{tot} as:

[8] Remark: for $z = z_r + i z_i$ and $f(z)$ it holds that:

$$\left. \frac{\partial f}{\partial z^*} \right|_z = \frac{1}{2} \left(\left. \frac{\partial f}{\partial z_r} \right|_{z_i} + i \left. \frac{\partial f}{\partial z_i} \right|_{z_r} \right) \, .$$

Thus, only one equation is required to find the extrema of $f(z)$ over all possible values of z_r and z_i.

[9] In order to accomodate all the boundary conditions of (2.33), a $(n \times n)$ hermitian matrix ϵ of Lagrange multipliers is required. Under a particular unitary transformation within the space of one-particle wave functions, $\psi' = U\psi$, there always exists a diagonal matrix $U^+ \epsilon U$ of new Lagrange multipliers, which effectively reduces the number of boundary conditions to n. E_{tot} remains invariable under an arbitrary unitary transformation. ϵ_i in (2.35) then denotes the diagonal elements of $U^+ \epsilon U$.

$$E_{\mathrm{tot}}[\rho(\mathbf{r})] = \sum_i \epsilon_i - E_{\mathrm{H}}[\rho(\mathbf{r})] - \int \mathrm{d}\mathbf{r} v_{\mathrm{XC}}(\mathbf{r})\rho(\mathbf{r}) + E_{\mathrm{XC}}[\rho(\mathbf{r})] + \frac{1}{2}\sum_{I\neq J}\frac{Q_I Q_J}{|\mathbf{R}_I - \mathbf{R}_J|} \,. \tag{2.38}$$

The potentials in (2.35) equal the functional derivatives of their corresponding energy functionals to the density:

$$v_{\mathrm{H}}(\mathbf{r}) = \frac{\partial}{\partial\rho(\mathbf{r})}E_{\mathrm{H}}[\rho] = \int \mathrm{d}\mathbf{r}' \frac{\rho(\mathbf{r}')}{|\mathbf{r}-\mathbf{r}'|} \,, \tag{2.39}$$

$$v_{\mathrm{XC}}(\mathbf{r}) = \frac{\partial}{\partial\rho(\mathbf{r})}E_{\mathrm{XC}}[\rho] \,, \tag{2.40}$$

$$v_{\mathrm{ext}}(\mathbf{r}) = \frac{\partial}{\partial\rho(\mathbf{r})}E_{\mathrm{ext}}[\rho] = -\sum_I \frac{Q_I}{|\mathbf{r}-\mathbf{R}_I|} \,, \tag{2.41}$$

where the last identity in (2.41) only holds true if the external interaction consists only of the Coulombic attraction of the atomic nuclei.

Since these potentials still depend on the density, the eigenvalue problem (2.35) needs to be solved self-consistently. The Kohn-Sham-DFT scheme therefore comprises the following steps:

1. Choose a set of arbitrary trial wave functions.[10]
2. Calculate the electronic density (from A.28) and subsequently the potentials.
3. Solve the eigenvalue problem (2.35,2.36) and calculate E_{tot} (2.38).
4. Repeat step 2 and 3 from this procedure until E_{tot} (nearly) doesn't change any more (= convergence).

Upon generalization of the Kohn-Sham theory to spin-polarized systems,[16, 17] the exchange-correlation potential v_{XC} becomes spin dependent:

$$\left[-\frac{1}{2}\nabla^2 + v_{\mathrm{H}}(\mathbf{r}) + v^{\tau}_{\mathrm{XC}}(\mathbf{r}) + v_{\mathrm{ext}}(\mathbf{r})\right]\psi^{\tau}_{\mathrm{ni},i}(\mathbf{r}) = \epsilon_i \psi^{\tau}_{\mathrm{ni},i}(\mathbf{r}) \,, \tag{2.42}$$

[10] Convergence is generally achieved faster when eg. atomic configurations are chosen as trial wave functions.

where $\tau = \alpha, \beta$, and α = spin-up, β = spin-down.

Although the KS orbitals $\psi_{\mathrm{ni},i}(\mathbf{r})$ have in principle no physical interpretation, it is often assumed that they represent one-particle wave functions of the interacting-electron system, which in several cases proves to be a (very) good approximation.[18] The theoretical calculation of EPR parameters in the framework of DFT will partly rely on the adoption of this assumption.

From here on we will – unless stated otherwise – describe mostly KS orbitals, therefore we can further omit the subscript *ni*.

Local (spin) density approximation

In the previous sections we have recast the many-body nature of the Schrödinger wave equation into the exchange-correlation energy E_{XC}. Unfortunately, the functional form of E_{XC} is not known, and therefore we must resort to a suitable approximation. In the local density approximation (LDA), E_{XC} is chosen equal to the exchange-correlation energy from a uniform electron gas with the same density:

$$E_{\mathrm{XC}}^{\mathrm{LDA}}[\rho(\mathbf{r})] = \int \mathrm{d}\mathbf{r}\rho(\mathbf{r})v_{\mathrm{XC}}^{\mathrm{LDA}}[\rho(\mathbf{r})] \,. \tag{2.43}$$

In the spin-polarized variant, the local spin density approximation (LSDA), E_{XC} equals the exchange-correlation energy of a uniform polarized electron gas. E_{XC} becomes functionally dependent on both the α- and the β-spin density.

$$E_{\mathrm{XC}}^{\mathrm{LSDA}}\left[\rho^{\alpha}(\mathbf{r}), \rho^{\beta}(\mathbf{r})\right] = \int \mathrm{d}\mathbf{r}\rho(\mathbf{r})v_{\mathrm{XC}}^{\mathrm{LSDA}}[\rho^{\alpha}(\mathbf{r}), \rho^{\beta}(\mathbf{r})] \,. \tag{2.44}$$

Although this approximation seems rather rough, it delivers surprisingly good results for slowly varying electronic densities (in the limit of an electron system with a uniform density, L(S)DA is even exact). In the course of time, however, several shortcomings have been detected, which gave rise to a (still ongoing) quest for better functionals.

Generalized gradient approximation

Several new approximations emerged rather quickly. In the generalized gradient approximation (GGA), the exchange-correlation energy depends not only on the (spin-)polarized density, but also on its spatial derivatives:

$$E_{\mathrm{XC}}^{\mathrm{GGA}}\left[\rho(\mathbf{r})\right] = \int \mathrm{d}\mathbf{r} f[\rho(\mathbf{r}), \nabla\rho(\mathbf{r})] \,, \tag{2.45}$$

or:

$$E_{\mathrm{XC}}^{\mathrm{GGA}}\left[\rho^{\alpha}(\mathbf{r}), \rho^{\beta}(\mathbf{r})\right] = \int \mathrm{d}\mathbf{r} f[\rho^{\alpha}(\mathbf{r}), \rho^{\beta}(\mathbf{r}), \nabla\rho^{\alpha}(\mathbf{r}), \nabla\rho^{\beta}(\mathbf{r})] \,. \tag{2.46}$$

A further extension (referred to as *Meta-GGA*) involves the (liberal) use of more exotic functions of the density (such as eg. the Laplacian of the density), or even explicit functions of the KS orbitals.

Hybrid functionals

In a hybrid functional the exchange-correlation energy (L(S)DA, GGA, meta-GGA, ...) is mixed with the exact-exchange energy E_{X} from the Hartree-Fock formalism applied to the KS orbitals:[19]

$$E_{\mathrm{X}} = -\frac{1}{2}\sum_{ij}\delta_{\tau_i\tau_j}\int \mathrm{d}\mathbf{r}\int \mathrm{d}\mathbf{r}' \frac{\psi_i^*(\mathbf{r})\psi_j^*(\mathbf{r}')\psi_j(\mathbf{r})\psi_i(\mathbf{r}')}{|\mathbf{r}-\mathbf{r}'|} \,. \tag{2.47}$$

$\delta_{\tau_i\tau_j}$ excludes the terms where the spins τ_i and τ_j corresponding with the KS-orbitals i and j differ.

2.1.3 Basis sets

The KS orbitals can be approximated by a linear combination of a set of fixed functions with coefficients or *weights* still to be determined. A successful basis set is able to describe the KS orbitals with only a limited number of functions and/or offers the possibility to carry out certain calculations very fast (if possible: analytically) .

Atomic orbitals (represented by contracted Gaussian functions)

KS orbitals are often expressed as a linear combination of atomic orbitals ψ^{AO} (LCAO), centered on the position of every atomic nucleus in the molecular system:

$$\psi_i(\mathbf{r}) = \sum_k C_{ki}\psi_k^{\mathrm{AO}}(\mathbf{r}) \ . \tag{2.48}$$

During the self-consistent procedure of the Kohn-Sham-DFT scheme, only the weights C_{ki} will be adjusted. Subsequently, every atomic orbital is approximated by a contracted Gaussian function (CGF), this is a fixed linear combination of (atom-centered) primitive cartesian Gaussian functions χ:

$$\psi_k^{\mathrm{AO}}(\mathbf{r}) = \sum_v D_{vk}\chi_v(\mathbf{r}) \ , \tag{2.49}$$

where χ is generally defined as:

$$\chi(\mathbf{r}) = (x - R_x)^{n_x}(y - R_y)^{n_y}(z - R_z)^{n_z}\mathrm{e}^{-\zeta(\mathbf{r}-\mathbf{R})^2} \ . \tag{2.50}$$

χ is determined by the set of natural numbers (n_x, n_y, n_z), a positive exponent ζ, and the origin of the Gaussian function $\mathbf{R}$, in this case the position of the corresponding atomic nucleus.

The KS orbitals are thus, ultimally, expressed in terms of primitive Gaussian functions, for which several types of frequently-occurring integrals can be evaluated analytically, using known recursion relations.[20]

Primitive Gaussian functions are limited in coordinate space. Periodic Gaussian functions χ^{P} are defined as:

$$\chi^{\mathrm{P}}(\mathbf{r}) = \sum_{\mathbf{a}} \chi(\mathbf{r} - \mathbf{L}_{\mathbf{a}}) \ , \tag{2.51}$$

with the vector of integer numbers $\mathbf{a} = a, b, c$, and $\mathbf{L}_{\mathbf{a}} = a\mathbf{L}_x + b\mathbf{L}_y + c\mathbf{L}_z$ the lattice vectors which build up the periodic images of the simulation cell.[11] A

[11] In this work, for reasons of simplicity of the mathematical formulas, we will always assume an orthogonal simulation cell.

contracted periodic Gaussian function (CPGF) is then nothing more than a logical expansion of (2.49):

$$\psi_k^{\mathrm{AO,P}}(\mathbf{r}) = \sum_v D_{vk}\chi_v^{\mathrm{P}}(\mathbf{r}) \ . \tag{2.52}$$

Plane waves

Alternatively, one can choose to express the KS orbitals as a linear combination of plane waves (PW). Given their periodicity and infinite extent, these functions are naturally suitable for PBC simulations. Moreover, several types of integrals are much easier to evaluate in reciprocal space, and it is possible, using fast Fourier-transformation techniques (FFT), to alternate fairly easily between a real and reciprocal representation of certain quantities. One of the disadvantages of plane waves, however, is that rapid oscillations in coordinate space are not well described, without employing an unfavorably large basis set. There exist several techniques to remedy this, some of them are described below.

The Bloch theorem [21] states that the wave functions $\psi_{m,\mathbf{k}}$ of a one-particle Schrödinger-like wave equation (*in casu:* the Kohn-Sham equation) in a periodic potential equals the product of a structure function $\phi_{m,\mathbf{k}}$, a *Bloch function*, with the wave function of a free electron (i.e. a plane wave):

$$\psi_{m,\mathbf{k}}(\mathbf{r}) = \phi_{m,\mathbf{k}}(\mathbf{r})\mathrm{e}^{i\mathbf{k}.\mathbf{r}} \ , \tag{2.53}$$

where m denotes a band index, and $\mathbf{k}$ a continuous wave vector limited to the first Brillouin zone (BZ) of the reciprocal lattice, which is uniquely defined by the geometry of the simulation cell in coordinate space. $\phi_{m,\mathbf{k}}$ features the periodicity of the lattice in coordinate space:

$$\phi_{m,\mathbf{k}}(\mathbf{r} + \mathbf{L}_\mathbf{a}) = \phi_{m,\mathbf{k}}(\mathbf{r}) \ , \tag{2.54}$$

where $\mathbf{a} = a, b, c$ denotes the vector of integer numbers, and $\mathbf{L}_\mathbf{a} = a\mathbf{L}_x + b\mathbf{L}_y + c\mathbf{L}_z$ the lattice vectors which build up the periodic images of the lattice. We expand this periodic function in a linear combination of plane waves which satisfy the periodicity of the lattice:

$$\phi_{m,\mathbf{k}}(\mathbf{r}) = \frac{1}{\sqrt{\Omega}} \sum_{\mathbf{G}} c_{m,\mathbf{k},\mathbf{G}} \mathrm{e}^{i\mathbf{G}.\mathbf{r}} \,. \tag{2.55}$$

Here, Ω indicates the volume of the simulation cell and $\mathbf{G}$ the vectors of the reciprocal lattice defined by:

$$\frac{1}{2\pi} |\mathbf{G}.\mathbf{R}| \in \mathbb{N} \,. \tag{2.56}$$

Consequently, (2.54) is satisfied automatically. (2.55) is also the discrete Fourier expansion of $\phi_{m,\mathbf{k}}$. The coefficients $c_{m,\mathbf{k},\mathbf{G}}$ are obtained through the inverse transformation:

$$c_{m,\mathbf{k},\mathbf{G}} = \frac{1}{\sqrt{\Omega}} \int \mathrm{d}\mathbf{r}\, \phi_{m,\mathbf{k}}(\mathbf{r}) \mathrm{e}^{-i\mathbf{G}.\mathbf{r}} \,. \tag{2.57}$$

The accuracy of the description of a Bloch function in a plane-wave basis set (and therefore also of the total wave function of the electron) is determined by the amount of plane waves in (2.55), which can be controlled by specifying a maximal value E_c for the kinetic energy of the plane waves.[12] The kinetic energy of an orbital $\psi_{m,\mathbf{k}}$ equals:

$$\begin{aligned} T_{m,\mathbf{k}} &= \langle \psi_{m,\mathbf{k}} | \, \frac{1}{2}\mathbf{p}^2 \, | \psi_{m,\mathbf{k}} \rangle \\ &= \sum_{\mathbf{G}} \frac{1}{2} |\mathbf{k}+\mathbf{G}|^2 |c_{m,\mathbf{k},\mathbf{G}}|^2 \,. \end{aligned} \tag{2.58}$$

Upon specification of E_c, only those plane waves are taken into account which satisfy:

$$\frac{1}{2} |\mathbf{k}+\mathbf{G}|^2 \leq E_\mathrm{c} \,. \tag{2.59}$$

[12] This value is – for historical reasons – still expressed in Rydberg (Ry).

In practice, the first Brillouin zone is discretized, and the solutions for a specific $\mathbf{k}$ within a discrete subsection of the first Brillouin zone are assumed to respresent the solution for that entire subsection. In a large, disorderly, non-metallic simulation cell, it is sufficient to consider only one wave vector $\mathbf{k}$ for the entire first Brillouin zone. We choose $\mathbf{k} = \mathbf{0}$, in other words the origin of reciprocal space. This is the so-called Γ-point approximation.

2.1.4 Pseudopotential approximation

In a one-particle picture of the electron system in a free atom or ion, the electrons can be classified according to their corresponding energy-eigenvalue. Often one distinguishes between deeply-bound electrons (core electrons) and electrons with an energy close to the Fermi level (valence electrons). The spatial extent of the wave functions of the core electrons remains limited mostly to the close surroundings of the atomic nucleus, the *core region*, where the Coulombic interaction from the atomic nucleus and the other core electrons strongly predominates. As a result, these wave functions are practically insensitive for external influences exerted on the atom, such as for example the vicinity of another atom for forming a chemical bond.

The valence electrons are located relatively further away from the atomic nucleus than the core electrons, where the Coulomb potential from the atomic nucleus is screened by the core electrons to an important degree. The wave functions of those electrons are sensitive to changes in the surroundings of the atom, and as a result they will mainly determine the chemical properties of that atom. In order to ensure the orthonormality with the other wave functions, and thus to satisfy the Pauli exclusion principle[13], these wave functions can feature rapid oscillations in the core region. Fortunately, these oscillations are less important for the chemical properties of the atom.

In the PSP approximation, one exploits the fact that the core electrons and the behavior of the valence electron wave functions in the core region are of subordinate importance for many chemical properties of an atom, such as for example chemical bonding. The atomic nucleus and the surrounding core electrons are assumed fixed (frozen core approximation) and grouped into a pseudo core, and the interaction of this pseudo core with its surroundings is modeled by a pseudopotential (PSP). In this work, pseudopotentials are of

[13]Two identical fermions cannot simultaneously occupy the same quantum state.

the non-local, separable, and norm-conserving type, and are constructed as follows (see also Figure 2.1):

1. Choose a reference configuration for an atom type (for example the neutral configuration for Si: $[1s^2 2s^2 2p^6]3s^2 3p^2$).

2. Determine the KS orbitals and eigenfunctions for the atom in the reference configuration. A spherical-symmetrical approximation for the Hartree- and XC-potential is assumed, so that one can separate the KS orbitals (indicated with the quantum numbers n, l, m) into their radial and spherical dependencies:

$$\psi_{nlm}(\mathbf{r}) = R_{nl}(r) Y_{lm}(\theta, \phi) \ , \tag{2.60}$$

   where Y_{lm} represents the spherical harmonics, and R_{nl} the all-electron (AE) solutions (using the nuclear Coulomb potential) of the radial KS equation:

$$\left[-\frac{1}{2}\frac{d^2}{dr^2} + \frac{l(l+1)}{2r^2} - \frac{Q}{r} + V_{\mathrm{H}}[\rho(\mathbf{r})] + V_{\mathrm{XC}}[\rho(\mathbf{r})] \right] r R_{nl}(r) = \epsilon_{nl} r R_{nl}(r) \ . \tag{2.61}$$

   It is strongly recommended to use the very same XC-functional for the generation of the pseudopotential as for the simulation in which the pseudopotential will eventually be used.[22]

3. Split up (in a more or less arbitrary way) the reference configuration in core and valence electrons, define $Q^{\mathrm{eff}} = Q - (\#\text{core electrons})$ as the *effective charge number*, and create radial pseudo wave functions R_{nl}^{PSP} and pseudo energy-eigenvalues $\epsilon_{nl}^{\mathrm{PSP}}$ for the valence electrons, which mutually satisfy the Pauli exclusion principle, and moreover adopt a number of boundary conditions, such as for example the following:

   - Every pair of energy-eigenvalues must correspond:

$$\epsilon_{nl}^{\mathrm{PSP}} = \epsilon_{nl} \ . \tag{2.62}$$

   - Outside a given radius $r_{c,nl}$ the corresponding wave functions agree:

$$R_{nl}^{\mathrm{PSP}}(r) = R_{nl}(r) \qquad \text{for } r > r_{c,nl} \ . \tag{2.63}$$

     Assuming normalized wave functions, it then holds for example that:

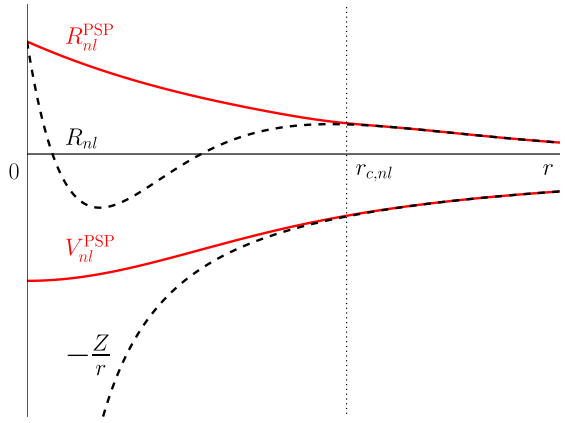

Figure 2.1: Sketch of the pseudopotential approximation in the core region of an atom. Notice how the radial pseudo wave function R_{nl}^{PSP} oscillates less than its all-electron counterpart R_{nl}.

- For $r > r_{c,nl}$ the charge within r must agree for every pair of corresponding wave functions:

$$\int_0^r \mathrm{d}r |R_{nl}^{\mathrm{PSP}}(r)|^2 r^2 = \int_0^r \mathrm{d}r |R_{nl}(r)|^2 r^2 \qquad \text{for } r > r_{c,nl} \,. \quad (2.64)$$

- The logarithmic derivatives[14] of every pair of corresponding wave functions agree for $r > r_{c,nl}$.

If a pseudopotential satisfies the conditions described above, then it is called norm-conserving.[23] A norm-conserving pseudopotential is not fully defined by the above conditions, and this remaining freedom can be exploited for example to ensure that the wave functions generated using this pseudopotential can be described with a relatively small basis set.

4. For every pseudo wave function and pseudo energy-eigenvalue, we can construct from (2.61) a screened (scr) pseudopotential:

$$V_{nl}^{\mathrm{PSP,scr}}(r) = \epsilon_{nl}^{\mathrm{PSP}} - \frac{l(l+1)}{2r^2} + \frac{1}{2rR_{nl}^{PSP}(r)} \frac{d^2}{dr^2} [rR_{nl}^{PSP}(r)] \,. \quad (2.65)$$

[14] i.e.: $\frac{\mathrm{d}}{\mathrm{d}r}(\ln f(r)) = \frac{\frac{\mathrm{d}}{\mathrm{d}r} f(r)}{f(r)}$.

The screening originates from the valence electrons of the atom, and can be removed (*unscreening*) approximately by substracting the Hartree and XC potential of a spherical-symmetric approximation of the pseudo valence density ρ_0^{PSP}, i.e.:

$$\rho_0^{\mathrm{PSP}}(\mathbf{r}) = \frac{1}{4\pi} \sum_{nl} |R_{nl}^{\mathrm{PSP}}(r)|^2 \,, \tag{2.66}$$

from every potential $V_{nl}^{\mathrm{PSP,scr}}(r)$:[15]

$$V_{nl}^{\mathrm{PSP}}(r) = V_{nl}^{\mathrm{PSP,scr}}(r) - V_{\mathrm{H}}[\rho_0^{\mathrm{PSP}}(\mathbf{r})] - V_{\mathrm{XC}}[\rho_0^{\mathrm{PSP}}(\mathbf{r})] \,. \tag{2.67}$$

V_{nl}^{PSP} is an ionic pseudopotential, which now no longer depends on the valence electrons, but still depends on the particular pseudo wave function for which it was constructed. Assuming that the pseudo wave functions $\psi_{nlm}^{\mathrm{PSP}} = R_{nl}^{\mathrm{PSP}} Y_{lm}$ form a complete and orthonormal set in the close region of the atomic nucleus for an arbitrary wave function ψ_i^{PSP} from a simulation in which the pseudopotential is being used,

$$\psi_i^{\mathrm{PSP}}(\mathbf{r}) = \sum_{nlm} C_{nlm,i} \psi_{nlm}^{PSP}(\mathbf{r}) \qquad \text{for } r < \max_{nl}\{r_{c,nl}\} \,, \tag{2.68}$$

we can (in bra-ket notation) offer through projection $\left|\psi_{nlm}^{\mathrm{PSP}}\right\rangle \left\langle p_{nlm}^{\mathrm{PSP}}\right|$ the potential V_{nl}^{PSP} to every component of $\left|\psi_i^{\mathrm{PSP}}\right\rangle$, where p_{nlm}^{PSP} represents a projector function onto $\psi_{nlm}^{\mathrm{PSP}}$. The total pseudopotential in operator notation becomes:

$$V^{\mathrm{PSP}} = \sum_{nlm} V_{nl}^{\mathrm{PSP}}(r) \left|\psi_{nlm}^{\mathrm{PSP}}\right\rangle \left\langle p_{nlm}^{\mathrm{PSP}}\right| \,. \tag{2.69}$$

In the coordinate representation of (2.69) a non-local operator $V^{\mathrm{PSP}}(\mathbf{r}, \mathbf{r}')$ emerges. Mostly, only one projector per orbital quantum number l is chosen.

In a last approximation, all potentials V_{nl}^{PSP} for quantum numbers greater than a specific $(nlm)_{\max}$ are assumed to be equal to a particular V_{nl}^{PSP},

[15] Here, we assume that V_{XC} is linear in ρ, i.e. $V_{\mathrm{XC}}[\rho_{\mathrm{core}}(\mathbf{r}) + \rho_{\mathrm{valencee}}(\mathbf{r})] = V_{\mathrm{XC}}[\rho_{\mathrm{core}}(\mathbf{r})] + V_{\mathrm{XC}}[\rho_{\mathrm{valence}}(\mathbf{r})]$. When this linearity condition is not fulfilled, it may be necessary to treat more electrons as valence electrons, or to include a non-linear core density correction to the XC energy functional and the XC potential in Ref. [24].

further referred to as $V_{\text{loc}}^{\text{PSP}}$. Using the completeness relation for the pseudo wave functions, it follows:

$$V^{\text{PSP}} = V_{\text{loc}}^{\text{PSP}} + \sum_{nlm}^{(nlm)_{\max}} \left(V_{nl}^{\text{PSP}} - V_{\text{loc}}^{\text{PSP}} \right) \left| \psi_{nlm}^{\text{PSP}} \right\rangle \left\langle p_{nlm}^{\text{PSP}} \right| \ . \tag{2.70}$$

A new term E_{PSP} is added to the total energy functional E_{tot} (2.38), which replaces the Coulombic interaction energy between the atomic nuclei and the electrons in E_{ext} for every atomic nucleus for which a PSP approximation is adopted ($I \in \text{PSP}$):

$$E_{\text{PSP}}[\rho(\mathbf{r})] = \sum_{i, I \in \text{PSP}} \langle \psi_i | \, V^{\text{PSP}} \, | \psi_i \rangle \ . \tag{2.71}$$

In addition, Q_I is replaced by Q_I^{eff} for all atomic nuclei $I \in \text{PSP}$ in all previous expressions.

The use of pseudopotentials offers some important advantages:

1. The number of electrons decreases with the number of core electrons per atom for which a pseudopotential approximation is adopted.
2. The size of the basis set can be reduced (especially in the case of a plane-wave basis set).
3. It becomes possible to incorporate (some) relativistic effects into a non-relativistic scheme.

2.1.5 The hybrid Gaussian and plane-wave method

The more recent implementations of the Kohn-Sham-DFT scheme no longer use just one type of basis set functions. In the hybrid Gaussian and plane-wave method (GPW),[25] CPGFs are used as the primary basis set.[16] In addition, an auxiliary basis set of plane waves is maintained, onto which the electronic density (2.28) in CPGFs (with $P_{kl} = \sum_i C_{ki} C_{li}$ the density matrix) is collocated, i.e.

[16] Implicitly, the Γ-point approximation is adopted here. This allows to represent the KS orbitals as real functions.

$$\begin{aligned}\rho(\mathbf{r}) &= \sum_i |\psi_i(\mathbf{r})|^2 \text{ with } \psi_i(\mathbf{r}) = \sum_k C_{ki}\psi_k^{\mathrm{AO,P}}(\mathbf{r}) \\ &= \sum_{kl} P_{kl}\psi_k^{\mathrm{AO,P*}}(\mathbf{r})\psi_l^{\mathrm{AO,P}}(\mathbf{r}) \,, \end{aligned} \tag{2.72}$$

is expressed in plane waves:

$$\tilde{\rho}(\mathbf{r}) = \frac{1}{\Omega} \sum_{\frac{1}{2}|\mathbf{G}|^2 < E_\mathrm{c}} \rho(\mathbf{G}) \mathrm{e}^{i\mathbf{G}.\mathbf{r}} \,. \tag{2.73}$$

This projection[17] allows to evaluate particular components of the energy functional E_{tot} (2.32), the Kohn-Sham matrix,[18] and the forces exerted onto the atomic nuclei,[19] in reciprocal space, where they are much easier to evaluate. Taking into account the fact that the product of two Gaussian functions is again a Gaussian function, there exist two ways to perform the collocation itself: i) the primitive Gaussians functions (multiplied by their corresponding coefficients) are evaluated on the discrete points of the real-space FFT lattice, and after summation over all primitive Gaussian functions, the total values on the lattice points are transformed into reciprocal space, or ii) one exploits the property that the Fourier transform of a Gaussian function is also a Gaussian function (in reciprocal space), which can then then be evaluated (and appropriately summed) on the discrete FFT lattice points in reciprocal space.

In order to reduce the size of the plane-wave basis set, pseudopotentials of Goedecker and co-workers are employed.[26, 27] This pseudopotential type has the following operator form in the coordinate representation:

[17] The tilde in (2.73) indicates that the representation in a plane-wave basis set is only approximative, due to its finite size (only an infinite set of plane waves form a complete set).

[18] The Kohn-Sham-matrix is the matrix representation of the Hamiltonian H_{KS} in the basis of atomic orbitals.

[19] The forces on the atomic nuclei are only calculated in eg. a geometry optimization (and are not needed to determine the electronic ground-state density of a given molecular structure).

$$
\begin{aligned}
V^{\mathrm{PSP}}(\mathbf{r},\mathbf{r}') &= \delta(\mathbf{r}-\mathbf{r}')\left[\frac{Q^{\mathrm{eff}}}{r}\mathrm{erf}\left(\frac{r}{\sqrt{2}r_{\mathrm{loc}}}\right)\right. \\
&- \left.\mathrm{e}^{-\frac{1}{2}\left(\frac{r}{r_{\mathrm{loc}}}\right)^2}\left(C_1+C_2\left(\frac{r}{r_{\mathrm{loc}}}\right)^2+C_3\left(\frac{r}{r_{\mathrm{loc}}}\right)^4+C_4\left(\frac{r}{r_{\mathrm{loc}}}\right)^6\right)\right] \\
&- \sum_l\sum_{i=1}^{3}\sum_{j=1}^{3}\sum_{m=-l}^{l} Y_{lm}(\Omega_{\mathbf{r}})p_i^l(r)h_{ij}^l p_j^l(r')Y_{lm}^*(\Omega_{\mathbf{r}'}) \,, \qquad (2.74)
\end{aligned}
$$

where:

$$
p_i^l(r) = \frac{\sqrt{2}r^{l+2(i-1)}\mathrm{e}^{-\frac{r^2}{2r_l^2}}}{r_l^{l+(4i-1)/2}\sqrt{\Gamma\left(l+\frac{4i-1}{2}\right)}} \,, \qquad (2.75)
$$

$$
\int_0^\infty p_i^l(r)p_i^l(r)r^2\mathrm{d}r = 1 \,, \qquad (2.76)
$$

in which Γ denotes the Gamma function,[20] erf the error function,[21] r_{loc} the range of the Gaussian ionic charge distribution leading to the erf potential, and C_1, C_2, C_3, and C_4 constant real parameters. The advantage of this choice for the pseudopotential is that its matrix elements in the basis of CPGFs can be evaluated analytically. In addition, this pseudopotential type has a closed-form analytical expression in reciprocal space (although in the GPW method, this feature is less important). The local component of (2.74) features a short-range $V_{\mathrm{loc,sr}}^{\mathrm{PSP}}$ and a long-range component $V_{\mathrm{loc,lr}}^{\mathrm{PSP}}$:

$$
V_{\mathrm{loc,sr}}^{\mathrm{PSP}}(\mathbf{r}) = -\mathrm{e}^{-\frac{1}{2}\left(\frac{r}{r_{\mathrm{loc}}}\right)^2}\left(C_1+C_2\left(\frac{r}{r_{\mathrm{loc}}}\right)^2+C_3\left(\frac{r}{r_{\mathrm{loc}}}\right)^4+C_4\left(\frac{r}{r_{\mathrm{loc}}}\right)^6\right) \,, \qquad (2.77)
$$

$$
V_{\mathrm{loc,lr}}^{\mathrm{PSP}}(\mathbf{r}) = \frac{Q^{\mathrm{eff}}}{r}\mathrm{erf}\left(\frac{r}{\sqrt{2}r_{\mathrm{loc}}}\right) \,. \qquad (2.78)
$$

[20] $\Gamma(z) = \int_0^\infty \mathrm{d}t\, t^{z-1}\mathrm{e}^{-t}$, and for $n \in \mathbb{N}$: $\Gamma(n) = (n-1)!$

[21] $\mathrm{erf}(x) = \frac{2}{\sqrt{\pi}}\int_0^x \mathrm{d}t\, \mathrm{e}^{-t^2}$. $\mathrm{erfc}(x) = 1 - \mathrm{erf}(x)$.

In the GPW method, the energy functional E_{tot} has the following form:

$$E_{\text{tot}}[\rho(\mathbf{r})] = T[\rho(\mathbf{r})] + E_{\text{PSP}}[\rho(\mathbf{r})] + E_{\text{H}}[\rho(\mathbf{r})] + E_{\text{ext}}[\rho(\mathbf{r})] + E_{\text{XC}}[\rho(\mathbf{r})] \ , \quad (2.79)$$

with:[22]

$$T[\rho(\mathbf{r})] = \sum_{k_1 k_2} P_{k_1 k_2} \int \mathrm{d}\mathbf{r} \psi_{k_1}^{\text{AO,P}}(\mathbf{r}) \left(-\frac{\nabla^2}{2} \right) \psi_{k_2}^{\text{AO,P}}(\mathbf{r}) \ , \quad (2.80)$$

$$E_{\text{PSP}}[\rho(\mathbf{r})] = \sum_I \sum_{k_1 k_2} P_{k_1 k_2} \int \mathrm{d}\mathbf{r}\mathrm{d}\mathbf{r}' \psi_{k_1}^{\text{AO,P}}(\mathbf{r}) \left(-V_I^{\text{PSP}}(\mathbf{r}, \mathbf{r}') \right) \psi_{k_2}^{\text{AO,P}}(\mathbf{r}') \ , \quad (2.81)$$

$$E_{\text{XC}}[\rho(\mathbf{r})] = \int \mathrm{d}\mathbf{r} f[\tilde{\rho}(\mathbf{r}), \nabla\tilde{\rho}(\mathbf{r}), ...] \ . \quad (2.82)$$

The terms i) E_{H}, ii) the interaction-energy term of the local longe-range component $E_{\text{PSP,loc,lr}}$ of every pseudopotential with the electrons, and iii) E_{ext} (which, when a PSP approximation is adopted for all atomic nuclei, only contains the Coulombic interaction energy among the atomic nuclei themselves) are treated together in PBC simulations, using Ewald summation techniques applied to the electrostatic-energy term E_{ES} of the ensemble of atomic nuclei and electrons:[23]

[22] Note that, in atomic units, a pseudopotential and its corresponding operator term which describes the interaction with the electrons differ by a minus sign.

[23] The electrostatic energy E_{ES} consists of three parts: i) the Hartree energy of the electronic charge distribution, ii) the Coulombic interaction energy of the electrons with the atomic nuclei, and iii) the Coulombic interaction energy between the atomic nuclei:

$$E_{\text{ES}} = \frac{1}{2} \int \mathrm{d}\mathbf{r}\mathrm{d}\mathbf{r}' \frac{\rho(\mathbf{r})\rho(\mathbf{r}')}{|\mathbf{r} - \mathbf{r}'|} - \sum_I \int \mathrm{d}\mathbf{r} V_I^{\text{c}}(\mathbf{r})\rho(\mathbf{r}) + \frac{1}{2} \sum_{I \neq J} \frac{Q_I^{\text{eff}} Q_J^{\text{eff}}}{|\mathbf{R}_I - \mathbf{R}_J|} \ .$$

The shape of the core potential V_I^{c} corresponding with atomic nucleus I can be chosen as the Coulombic potential from a chosen Gaussian charge distribution with total charge Q_I^{eff} and amplitude $r_{\text{loc},I}$ (because the atomic *nucleus* is no longer a point charge, but rather a spread-out *blob* of charge):

$$\rho_I^{\text{c}}(\mathbf{r}) = \frac{Q_I^{\text{eff}}}{(\sqrt{2\pi} r_{\text{loc},I})^3} \mathrm{e}^{-\frac{1}{2}\left(\frac{\mathbf{r} - \mathbf{R}_I}{r_{\text{loc},I}}\right)^2} \ ,$$

$$V_I^{\text{c}}(\mathbf{r}) = \int \mathrm{d}\mathbf{r}' \frac{\rho_I^{\text{c}}(\mathbf{r}')}{|\mathbf{r} - \mathbf{r}'|} = \frac{Q_I^{\text{eff}}}{|\mathbf{r} - \mathbf{R}_I|} \mathrm{erf}\left(\frac{|\mathbf{r} - \mathbf{R}_I|}{\sqrt{2} r_{\text{loc},I}} \right) \ .$$

By definition, it then holds that the local long-range component $V_{\text{loc,lr},I}^{\text{PSP}}$ of a Goedecker PSP equals

$$E_{\mathrm{ES}} = 2\pi\Omega \sum_{\mathbf{G}\neq\mathbf{0}} \frac{\left|\tilde{\rho}^{\mathrm{tot}}(\mathbf{G})\right|^2}{G^2} + \sum_{I\neq J}{}' \sum_{\mathbf{L}} \frac{Q_I^{\mathrm{eff}} Q_J^{\mathrm{eff}}}{\left|\mathbf{R}_I - \mathbf{R}_J - \mathbf{L}\right|} \mathrm{erfc}\left(\frac{\left|\mathbf{R}_I - \mathbf{R}_J - \mathbf{L}\right|}{\sqrt{{r_{\mathrm{loc},I}}^2 + {r_{\mathrm{loc},J}}^2}}\right) - \sum_I \frac{{Q_I^{\mathrm{eff}}}^2}{\sqrt{2\pi} r_{\mathrm{loc},I}} , \tag{2.83}$$

where the accent on the sum indicates that the exclusion of $I = J$ only holds for $\mathbf{L} = \mathbf{0}$. In a hybrid functional, E_{XC} is mixed with E_{X} (2.47), evaluated in the basis set of CPGFs. The evaluation of the Kohn-Sham matrix and the forces on the atomic nuclei are based on the same techniques as sketched above for the energy.

2.1.6 The hybrid Gaussian and augmented-plane-wave method

In the hybrid Gaussian and augmented-plane-wave method (GAPW),[28] the auxiliary basis set of plane waves is augmented with the primitive periodic Gaussian functions from which the CPGFs were constructed. In an arbitrary way, the simulation cell is divided into non-overlapping, localized, spherical regions centered on the atomic nuclei, and the interstitial region. The underlying idea of GAPW is that the electron density in the interstitial region

to V_I^{c}. Using the definitions $\rho^{\mathrm{c}} = \sum_I \rho_I^{\mathrm{c}}$ and $\rho^{\mathrm{tot}} = \rho - \rho^{\mathrm{c}}$ ($-$ due to the sign convention) we can write E_{ES} as:

$$E_{\mathrm{ES}} = \frac{1}{2}\int \mathrm{d}\mathbf{r}\mathrm{d}\mathbf{r}' \frac{\rho^{\mathrm{tot}}(\mathbf{r})\rho^{\mathrm{tot}}(\mathbf{r}')}{|\mathbf{r}-\mathbf{r}'|} + \frac{1}{2}\sum_{I\neq J} \frac{Q_I^{\mathrm{eff}} Q_J^{\mathrm{eff}}}{|\mathbf{R}_I - \mathbf{R}_J|} - \frac{1}{2}\int \mathrm{d}\mathbf{r}\mathrm{d}\mathbf{r}' \frac{\rho^{\mathrm{c}}(\mathbf{r})\rho^{\mathrm{c}}(\mathbf{r}')}{|\mathbf{r}-\mathbf{r}'|} .$$

The second and third term from the above equation can be rewritten as:

$$E_{\mathrm{ES}} = \frac{1}{2}\int \mathrm{d}\mathbf{r}\mathrm{d}\mathbf{r}' \frac{\rho^{\mathrm{tot}}(\mathbf{r})\rho^{\mathrm{tot}}(\mathbf{r}')}{|\mathbf{r}-\mathbf{r}'|} + \frac{1}{2}\sum_{I\neq J} \frac{Q_I^{\mathrm{eff}} Q_J^{\mathrm{eff}}}{|\mathbf{R}_I - \mathbf{R}_J|} \mathrm{erfc}\left(\frac{|\mathbf{R}_I - \mathbf{R}_J|}{\sqrt{r_{\mathrm{loc},I}^2 + r_{\mathrm{loc},J}^2}}\right) - \sum_I \frac{{Q_I^{\mathrm{eff}}}^2}{\sqrt{2\pi} r_{\mathrm{loc},I}} .$$

In a PBC simulation the first term of E_{ES} reduces to a simple sum over reciprocal vectors $\mathbf{G}$:

$$\frac{1}{2}\int \mathrm{d}\mathbf{r}\mathrm{d}\mathbf{r}' \frac{\rho^{\mathrm{tot}}(\mathbf{r})\rho^{\mathrm{tot}}(\mathbf{r}')}{|\mathbf{r}-\mathbf{r}'|} = 2\pi\Omega \sum_{\mathbf{G}\neq\mathbf{0}} \frac{\left|\tilde{\rho}^{\mathrm{tot}}(\mathbf{G})\right|^2}{G^2} .$$

$\rho(\mathbf{0})$ (by definition) corresponds with the total charge in the simulation cell, and either equals zero (charge neutral system) or can be made neutral by adding a uniform background charge, which allows us to omit the divergent term for $\mathbf{G} = \mathbf{0}$ in all cases. After some trivial adaptations, the second and third term from E_{ES} also take into account PBCs.

varies only slowly and can thus be easily represented with a limited number of plane waves, whereas the (heavily) oscillating electron density near the nuclei can be represented more efficiently using localized functions. The GAPW representation of the electron density is a sum of three contributions:

$$\rho(\mathbf{r}) = \tilde{\rho}(\mathbf{r}) + \rho^1(\mathbf{r}) - \tilde{\rho}^1(\mathbf{r}) \,. \tag{2.84}$$

The soft electronic density $\tilde{\rho}$ does not feature the heavy oscillations of the real electron density ρ close to the atomic nuclei, by setting to zero the coefficients in the CPGFs corresponding to the most localized primitive Gaussian functions, thus effectively using only the limited set of less-localized primitive Gaussian functions $\tilde{\chi}^{\mathrm{P}}$. In this way, $\tilde{\rho}$ becomes smoothly varying – hence soft, as compared to a strongly oscillating density which we will call *hard* –, but is still periodically repeated over the entire space, and can thus be represented by a limited number of plane waves:

$$\tilde{\rho}(\mathbf{r}) = \frac{1}{\Omega} \sum_{\frac{1}{2}|\mathbf{G}|^2 < E_c} \tilde{\rho}(\mathbf{G}) \mathrm{e}^{i\mathbf{G}.\mathbf{r}} \,. \tag{2.85}$$

The other densities,

$$\rho^1(\mathbf{r}) = \sum_I \rho_I^1(\mathbf{r}) \,, \qquad \tilde{\rho}^1(\mathbf{r}) = \sum_I \tilde{\rho}_I^1(\mathbf{r}) \,, \tag{2.86}$$

are the sum of local atom-centered densities ρ_I^1 and $\tilde{\rho}_I^1$ which are hard and soft, respectively. ρ_I^1 and $\tilde{\rho}_I^1$ are constructed through a projection of ρ and $\tilde{\rho}$ onto the primitive Gaussian functions χ_I^{P} and $\tilde{\chi}_I^{\mathrm{P}}$, respectively, corresponding with atomic nucleus I.

By construction ρ, $\tilde{\rho}$, ρ_I^1 and $\tilde{\rho}_I^1$ satisfy the following relations:

$$\rho(\mathbf{r}) - \tilde{\rho}(\mathbf{r}) = 0 \qquad \text{for } \mathbf{r} \in U_0 \,, \tag{2.87}$$
$$\rho_I^1(\mathbf{r}) - \tilde{\rho}_I^1(\mathbf{r}) = 0 \qquad \text{for } \mathbf{r} \in U_0 \,, \tag{2.88}$$
$$\tilde{\rho}(\mathbf{r}) - \tilde{\rho}_I^1(\mathbf{r}) = 0 \qquad \text{for } \mathbf{r} \in U_I \,, \tag{2.89}$$
$$\rho(\mathbf{r}) - \rho_I^1(\mathbf{r}) = 0 \qquad \text{for } \mathbf{r} \in U_I \,, \tag{2.90}$$

where U_I denotes a spherical region (with a given radius) around the atomic nucleus I and U_0 the interstitial region outside these atomic regions. In this way, (2.84) is fulfilled in all space (see Figure 2.2).

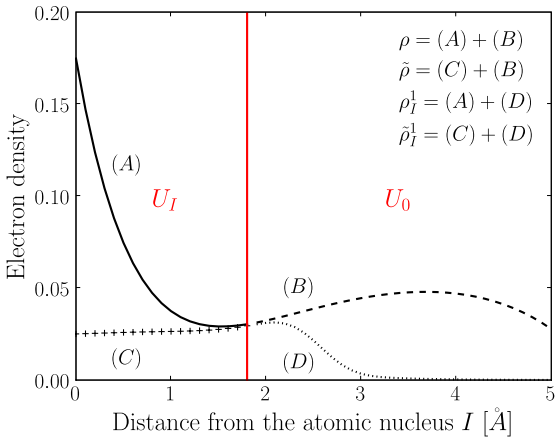

Figure 2.2: The GAPW representation of the electron density near the I-th atomic nucleus.

In the GAPW method, the exchange-correlation energy and the electrostatic energy are evaluated differently, in comparison with the GPW method. In Ref. [29], it is shown that E_{XC} and E_{ES} (using screening densities ρ_I^0) can be separated into independent global and local atom-centered components, enabling a very efficient evaluation of these terms:[24]

[24]The separation for the exchange-correlation energy is rather simple because this term is constructed from (semi-)local contributions only.
The evaluation of the Hartree energy ($E_{\text{H}}[\rho^{\text{tot}}]$) of the total charge distribution ($\rho^{\text{tot}} = \rho + \rho^{\text{c}}$ (which is part of the electrostatic energy) requires the introduction of appropriate localized screening densities in every U_I. The three contributions to $E_{\text{H}}[\rho^{\text{tot}}]$ then become:

$$E_{\text{H}}[\rho^{\text{tot}}(\mathbf{r})] = \tilde{E}_{\text{H}}[\tilde{\rho}(\mathbf{r}) + \rho^0(\mathbf{r})] + E_{\text{H}}^1[\rho^1(\mathbf{r}) + \rho^{\text{c}}(\mathbf{r})] - \tilde{E}_{\text{H}}^1[\tilde{\rho}^1(\mathbf{r}) + \rho^0(\mathbf{r})] \,. \tag{2.91}$$

The screening density $\rho^0 = \sum_I \rho_I^0$ is constructed such that the electrostatic multipole moments of $(\rho_I^1 + \rho_I^{\text{c}}) - (\tilde{\rho}_I^1 + \rho_I^0)$ cancel for every I, and as a result there is no interaction with the charge outside every U_I. In general, a localized charge distribution produces outside its region of localization a potential that depends only on the electrostatic dipole moments, and not on the shape of this charge distribution. The identity in the above equation can be unraveled by adding $(\rho^1 + \rho^{\text{c}}) - (\tilde{\rho}^1 + \rho^0)$ to $\tilde{\rho} + \rho^0$ in $\tilde{E}_{\text{H}}[\tilde{\rho} + \rho^0]$, and to $\tilde{\rho}^1 + \rho^0$ in $\tilde{E}_{\text{H}}^1[\tilde{\rho}^1 + \rho^0]$. The effect of this addition disappears, since i) the quadratic terms in $(\rho^1 + \rho^{\text{c}}) - (\tilde{\rho}^1 + \rho^0)$ originating from $\tilde{E}_{\text{H}}[\tilde{\rho} + \rho^0]$ and $\tilde{E}_{\text{H}}^1[\tilde{\rho}^1 + \rho^0]$ are substracted from each other, and ii) the linear terms in $(\rho_I^1 + \rho_I^{\text{c}}) - (\tilde{\rho}_I^1 + \rho_I^0)$ depend on a) $\tilde{\rho} - \tilde{\rho}^1$, which is zero inside U_I and on b) the potential of $(\rho_I^1 + \rho_I^{\text{c}}) - (\tilde{\rho}_I^1 + \rho_I^0)$, which is zero outside U_I, because the charge distribution is located inside U_I and the multipole moments are zero by construction.
The screening density ρ_I^0 is expanded in the set of primitive Gaussian functions χ_I^{p}:

$$E_{\mathrm{XC}}[\rho(\mathbf{r})] = E_{\mathrm{XC}}[\tilde{\rho}(\mathbf{r})] + \sum_I E_{\mathrm{XC}}[\rho_I^1(\mathbf{r})] - \sum_I E_{\mathrm{XC}}[\tilde{\rho}_I^1(\mathbf{r})] \,. \tag{2.92}$$

$$\begin{aligned} E_{\mathrm{ES}} &= E_{\mathrm{H}}[\tilde{\rho}(\mathbf{r}) + \tilde{\rho}^0(\mathbf{r})] + \sum_I E_{\mathrm{H}}[\rho_I^1(\mathbf{r}) + \rho_I^{\mathrm{c}}(\mathbf{r})] - \sum_I E_{\mathrm{H}}[\tilde{\rho}_I^1(\mathbf{r}) + \rho_I^0(\mathbf{r})] \\ &+ E_{\mathrm{H}}[\rho^0(\mathbf{r})] - E_{\mathrm{H}}[\tilde{\rho}^0(\mathbf{r})] + \int \mathrm{d}\mathbf{r} V_{\mathrm{H}}[\rho^0(\mathbf{r}) - \tilde{\rho}^0(\mathbf{r})]\tilde{\rho}(\mathbf{r}) \\ &+ {\sum_{I\neq J}}' \sum_{\mathbf{L}} \frac{Q_I^{\mathrm{eff}} Q_J^{\mathrm{eff}}}{|\mathbf{R}_I - \mathbf{R}_J - \mathbf{L}|} \mathrm{erfc}\left(\frac{|\mathbf{R}_I - \mathbf{R}_J - \mathbf{L}|}{\sqrt{{r_{\mathrm{loc},I}}^2 - {r_{\mathrm{loc},J}}^2}}\right) \\ &- \sum_I \frac{{Q_I^{\mathrm{eff}}}^2}{\sqrt{2\pi} r_{\mathrm{loc},I}} \,. \end{aligned} \tag{2.93}$$

$$\rho_I^0(\mathbf{r}) = \sum_{lm} Q_I^{lm} \chi_I^{\mathrm{P}} \,.$$

The coefficients Q_I^{lm} are defined as:

$$Q_I^{lm} = N q^{lm}[\rho_I^1(\mathbf{r}) - \tilde{\rho}_I^1(\mathbf{r}) + \rho_I^{\mathrm{c}}(\mathbf{r})] \,,$$

with N a normalization constant and q^{lm} the multipole-moment operator,

$$q^{lm}[\rho(\mathbf{r})] = \frac{4\pi}{2l+1} \int \mathrm{d}\mathbf{r} \rho(\mathbf{r}) r^l S^{lm}(\mathbf{r}) \,,$$

$$S^{l0} = Y^{l0} \,, \qquad S^{lm} = \frac{1}{\sqrt{2}}(Y^{lm} + Y^{l-m}) \,, \qquad S^{l-m} = \frac{1}{i\sqrt{2}}(Y^{lm} - Y^{l-m}) \,.$$

Now we define a second screening density $\rho_I^{0'}$, expanded in the limited set $\tilde{\chi}^{\mathrm{P}}$:

$$\rho_I^{0'}(\mathbf{r}) = \sum_{lm} Q_I^{lm} \tilde{\chi}_I^{\mathrm{P}} \,.$$

Therefore, we can further rewrite $\tilde{E}_{\mathrm{H}}[\tilde{\rho} + \rho^0]$ as:

$$\begin{aligned} \tilde{E}_{\mathrm{H}}[\tilde{\rho}(\mathbf{r}) + \rho^0(\mathbf{r})] &= \tilde{E}_{\mathrm{H}}[\tilde{\rho}(\mathbf{r}) + \rho^{0'}(\mathbf{r})] + \int \mathrm{d}\mathbf{r}\mathrm{d}\mathbf{r}' \tilde{\rho}(\mathbf{r}) v^0(\mathbf{r}) \\ &+ \sum_{IJ} \frac{1}{2} \int \mathrm{d}\mathbf{r}\mathrm{d}\mathbf{r}' \frac{\rho_I^0(\mathbf{r})\rho_J^0(\mathbf{r}') - \rho_I^{0'}(\mathbf{r})\rho_J^{0'}(\mathbf{r}')}{|\mathbf{r} - \mathbf{r}'|} \,, \\ v^0(\mathbf{r}) &= \frac{\rho^0(\mathbf{r}') - \rho^{0'}(\mathbf{r}')}{|\mathbf{r} - \mathbf{r}'|} \end{aligned}$$

The first term in the equation for $\tilde{E}_{\mathrm{H}}[\tilde{\rho} + \rho^0]$ is soft, and can be evaluated in reciprocal space. The second term can also be evaluated exactly in reciprocal space: the possible components with large $|\mathbf{G}|$ in v^0 are zeroed out by the corresponding component in $\tilde{\rho}$. The third term is a double sum over the atomic nuclei of short-range potentials which can be integrated easily in an analytical way.

In most applications, the special case $\rho^0 = \tilde{\rho}^0$ is adopted, and therefore the three terms on the second line of (2.93) cancel.

Because of the construction of the GAPW representation of the density, the required number of plane waves can be strongly reduced.

Now that we can describe the oscillations around the atomic nucleus with relative ease, the use of pseudopotentials is no longer a necessity: the GAPW method can handle all-electron calculations (using the nuclear Coulomb potential) just as well.[30] In order to do this, we must alter in (2.79), for every I for which an all-electron treatment is desired, Q_I^{eff} by Q_I and V_I^{PSP} in E_{PSP} by:

$$\frac{Q_I}{|\mathbf{r}-\mathbf{R}_I|}\text{erfc}\left(\frac{|\mathbf{r}-\mathbf{R}_I|}{\sqrt{2}r_{\text{loc},I}}\right) , \tag{2.94}$$

which, given the identity $\text{erf}(x) + \text{erfc}(x) = 1$ and together with the core potential V_I^c used in the calculation of the electrostatic energy E_{ES} (see section 2.1.5), simplifies back to the Coulomb potentiaal $\frac{Q_I}{|\mathbf{r}-\mathbf{R}_I|}$ for the atomic nucleus I.

2.2 EPR parameters and the Breit-Pauli Hamiltonian

When an electron system is exposed to a set of vectorial perturbations $\mathbf{U}_1, \mathbf{U}_2, ...$, the (possible) change of its energy can be written as a series expansion in the perturbation parameters:

$$E(\mathbf{U}_1, \mathbf{U}_2, ...) = E_0 + \sum_n \mathbf{U}_n.\mathbf{E}_{\mathbf{U}_n} + \frac{1}{2!}\sum_{m,n}\mathbf{U}_m.\mathbf{E}_{\mathbf{U}_n\mathbf{U}_m}.\mathbf{U}_n + \mathcal{O}(\mathbf{U}^3) . \tag{2.95}$$

The coefficients $\mathbf{E}$ define the response of the system to the perturbations and are characteristic for the electron system and its quantum state. For static perturbations, one can calculate the components of the coefficients as follows:

$$E_{\mathbf{U}_n,x} = \left.\frac{\partial E}{\partial U_{n,x}}\right|_{\mathbf{U}_n=\mathbf{0}}, \tag{2.96}$$

$$E_{\mathbf{U}_m\mathbf{U}_n,xy} = \left.\frac{\partial^2 E}{\partial U_{m,x}\partial U_{n,y}}\right|_{\mathbf{U}_m=\mathbf{U}_n=\mathbf{0}}. \tag{2.97}$$

In this way we define the g and the A tensor, the EPR parameters under investigation in this work, as the second-order partial derivatives of the energy of an electron system to the (components of) the net electron spin $\mathbf{S} = \sum_i \mathbf{s}_i$ and a homogeneous external magnetic field $\mathbf{B}$ and the nuclear spin $\mathbf{I}_I$ corresponding with the atomic nucleus I, respectively: [25]

$$g_{xy} = \frac{2}{\alpha}\left.\frac{\partial^2 E}{\partial B_x \partial S_y}\right|_{\mathbf{B}=\mathbf{S}=\mathbf{0}}, \tag{2.98}$$

$$A_{I,xy} = \left.\frac{\partial^2 E}{\partial I_{I,x}\partial S_y}\right|_{\mathbf{I}_I=\mathbf{S}=\mathbf{0}}. \tag{2.99}$$

The electronic energy E is the expectation value of a Hamiltonian H in the electronic ground state Ψ (in the presence of the different perturbations), therefore we can rewrite (2.98) and (2.99) as:

$$g_{xy} = \frac{2}{\alpha}\left.\frac{\partial^2 \langle\Psi| H |\Psi\rangle}{\partial B_x \partial S_y}\right|_{\mathbf{B}=\mathbf{S}=\mathbf{0}}, \tag{2.100}$$

$$A_{I,xy} = \left.\frac{\partial^2 \langle\Psi| H |\Psi\rangle}{\partial I_{I,x}\partial S_y}\right|_{\mathbf{I}_I=\mathbf{S}=\mathbf{0}}. \tag{2.101}$$

From the above equations, it follows that an appropriate Hamiltonian H must be able to describe the coupling of a magnetic field (either external or originating from the magnetic dipole moment of the atomic nuclei) with the electron spin. In the 4-component one-particle Dirac equation, the (special-)relativistic generalization of the 2-component one-particle Schrödinger equation for spin-$\frac{1}{2}$ particles from the previous chapter,[26] this coupling is naturally

[25] x and y assume all three cartesian components in (2.100) and (2.101).

[26] *2-component* denotes the spin-up and spin-down solutions of the spin-polarized Schrödinger equation. The *4-component* solutions can roughly be divided in electronic (positive energy) and positronic (negative energy) solutions, each with two possible spins. This will be explained in more detail below.

included (in the presence of an electromagnetic field). Depending on the chosen particle-particle interaction,[27] the Dirac Hamiltonian can be expanded to the Dirac-Coulomb or the Dirac-Coulomb-Breit Hamiltonian for n electrons in the presence of N atomic nuclei. Using the relativistic analogies of the well-known many-body techniques, such as for example the Dirac-Hartree-Fock or the Dirac-Kohn-Sham methods, one can compute (2.100) and (2.101). The *ratio* of the computational cost between relativistic and non-relativistic calculations [28] is so high in all but the most simple electron systems that, given the aim of applicability to electron systems of considerable magnitude, we chose to treat the relevant terms as a perturbation in a 2-component description of the electron system, more specifically in the framework of DFT. Using for example the Foldy-Wouthuysen or the Douglas-Kroll transformation techniques, we can project out the coupling terms between the electronic and positronic solutions from the 4-component Hamiltonian, up to a given order in the fine structure constant α. In this way, we derive a *quasi-relativistic* 2-component Hamiltonian for both the electrons and the positrons separately, with which (2.100) and (2.101) can be approximated. In this work, the relevant terms are derived from the Foldy-Wouthuysen transformation, this procedure will be elaborated in the next sections.

2.2.1 The Dirac equation

The Dirac equation, formulated in 1928 by British physicist Paul Dirac, is the basic formula for the (special-)relativistic quantum-mechanical description of a spin-$\frac{1}{2}$ particle in space-time:[31, 32]

$$H^{\mathrm{D}}\psi(\mathbf{r},t) = i\hbar\frac{\partial}{\partial t}\psi(\mathbf{r},t)\ . \tag{2.102}$$

In the absence of an electromagnetic field, the Dirac Hamiltonian H^{D} equals:

$$H^{\mathrm{D}} = \boldsymbol{\alpha}.\mathbf{p}c + \beta mc^2\ . \tag{2.103}$$

Note that, for the purpose of clarity of the symbols that are being used, we have not adopted atomic units yet: m and q are the rest mass and the charge of the

[27] The particle-particle interaction consistent with special relativity is formulated in quantum electrodynamics.

[28] We intentionally referred to the ratio of the computational cost. Postulating that relativistic calculations on electron systems of considerable magnitude are not feasible, would (probably) soon make this work look out of date.

spin-$\frac{1}{2}$ particle, and c is the velocity of light. α_i ($i = 1, 2, 3$) and β must be such that the relativistic energy-momentum relation is fulfilled.[29] It follows that $\beta^2 = \mathbf{1}$, $\{\alpha_i, \beta\} = 0$, and $\{\alpha_i, \alpha_j\} = 2\delta_{ij}$. α_i and β represent $(N \times N)$ matrices, and $N = 4$ is the lowest dimension for which solutions can be found (solutions for higher N exist as well), such as for example the Dirac-Pauli representation:

$$\alpha_i = \begin{pmatrix} 0 & \sigma_i \\ \sigma_i & 0 \end{pmatrix} , \qquad \beta = \begin{pmatrix} \mathbf{1}_2 & 0 \\ 0 & -\mathbf{1}_2 \end{pmatrix} , \tag{2.104}$$

with σ_i the Pauli matrices:

$$\sigma_1 = \begin{pmatrix} 0 & 1 \\ 1 & 0 \end{pmatrix} , \qquad \sigma_2 = \begin{pmatrix} 0 & -i \\ i & 0 \end{pmatrix} , \qquad \sigma_3 = \begin{pmatrix} 1 & 0 \\ 0 & -1 \end{pmatrix} . \tag{2.105}$$

The solutions of the Dirac equation in this form are the 4-component Dirac spinors:

$$\psi(\mathbf{r}, t) = \begin{pmatrix} \psi_1(\mathbf{r}, t) \\ \psi_2(\mathbf{r}, t) \\ \psi_3(\mathbf{r}, t) \\ \psi_4(\mathbf{r}, t) \end{pmatrix} . \tag{2.106}$$

The Dirac equation also features solutions with a negative energy, which were interpreted as positrons (the anti-particles of electrons with an opposite charge). Four years after first being postulated by Dirac, these particles were actually discovered.[33] Often, the first two and the last two components of ψ are grouped into ψ_L and ψ_S, which are called large (L) and small (S) components, respectively:

$$\psi(\mathbf{r}, t) = \begin{pmatrix} \psi_\mathrm{L}(\mathbf{r}, t, \tau) \\ \psi_\mathrm{S}(\mathbf{r}, t, \tau) \end{pmatrix} , \tag{2.107}$$

[29] The relativistic energy-momentum relation, $E^2 = (pc)^2 + (mc^2)^2$, must follow from the Dirac equation. In the space-time basis the energy and the momentum operator equal $i\hbar\frac{\partial}{\partial t}$ and $-i\hbar\nabla$, respectively. The conditions for α_i ($i = 1, 2, 3$) and β then follow from the identity of:

$$E^2\psi(\mathbf{r}, t) = -\hbar^2\frac{\partial^2}{\partial t^2}\psi(\mathbf{r}, t) = i\hbar\frac{\partial}{\partial t}(\boldsymbol{\alpha}.\mathbf{p}c + \beta mc^2)\psi(\mathbf{r}, t) = (\boldsymbol{\alpha}.\mathbf{p}c + \beta mc^2)^2\psi(\mathbf{r}, t) ,$$

and:

$$E^2\psi(\mathbf{r}, t) = \left((pc)^2 + (mc^2)^2\right)\psi(\mathbf{r}, t) .$$

and the two components of both ψ_{L} and ψ_{S} are indicated with a spin factor τ. One can prove[30] that for the positive-energy solutions of (2.102) the density $\psi_{\mathrm{L}}^{+}\psi_{\mathrm{L}}$ is often substantially larger than $\psi_{\mathrm{S}}^{+}\psi_{\mathrm{S}}$, whereas the opposite holds true for the negative-energy solutions.

Through the minimal coupling principle, $\mathbf{p} \rightarrow \boldsymbol{\pi} = \mathbf{p} - \frac{q}{c}\mathbf{A}$, where $\mathbf{A}$ denotes the magnetic vector potential and q the charge of the spin-$\frac{1}{2}$ particle, and the addition of the potential energy $V = q\varphi$ of an electric potential φ, we arrive at the Dirac equation for a spin-$\frac{1}{2}$ particle in the presence of an electromagnetic field:

$$\left(\boldsymbol{\alpha}.(\mathbf{p} - \frac{q}{c}\mathbf{A})c + \beta mc^2 + V\right)\psi(\mathbf{r},t) = i\hbar\frac{\partial}{\partial t}\psi(\mathbf{r},t)\ . \tag{2.108}$$

2.2.2 The Dirac-Coulomb(-Breit) Hamiltonian

The extension of the Dirac equation to a many-body system of n spin-$\frac{1}{2}$ particles in the presence of N atomic nuclei is carried out approximatively by adding the Coulombic particle-particle and particle-atomic-nucleus interaction to the sum of n Dirac Hamiltonians H^{D}, (2.102) or (2.108). In this way, the Dirac-Coulomb Hamiltonian arises:

$$H^{\mathrm{DC}} = \sum_i H_i^{\mathrm{D}} + \frac{1}{8\pi\epsilon_0}\sum_{i\neq j}\frac{q_i q_j}{|\mathbf{r}_i - \mathbf{r}_j|} + \frac{1}{4\pi\epsilon_0}\sum_{i,I}\frac{q_i Q_I}{|\mathbf{r}_i - \mathbf{R}_I|}\ . \tag{2.109}$$

[30] The solutions $\psi_p^{\pm}$ of the Dirac equation (2.102) satisfy the general form:

$$\psi_p^{\pm}(\mathbf{r},t) = N_p \mathrm{e}^{i(\mathbf{p}.\mathbf{r}\mp E_p t)}\begin{pmatrix}\chi(\mathbf{r},t,\tau)\\ \eta(\mathbf{r},t,\tau)\end{pmatrix}\ ,$$

where the superscript $\pm$ denotes the solutions with positive $(+)$ or negative energy $(-)$. When a positive-energy solution ψ_p^{+} is inserted in (2.102), it follows that:

$$\eta(\mathbf{r},t,\tau) = \left(\frac{\sigma.\mathbf{p}c}{E_p + mc^2}\right)\chi(\mathbf{r},t,\tau)\ ,$$

whereas for a negative-energy solution ψ_p^{-}:

$$\chi(\mathbf{r},t,\tau) = -\left(\frac{\sigma.\mathbf{p}c}{E_p + mc^2}\right)\eta(\mathbf{r},t,\tau)\ .$$

In the case where E_p^2 is not much larger than $(mc^2)^2$, the square of the rest-mass energy, and using $(\sigma.\mathbf{p})^2 = p^2$, it becomes clear that $\chi^{+}\chi$ will be much more significant than $\eta^{+}\eta$ for the positive-energy solutions, and vice versa for the negative-energy solutions.

Apart from the absence of a relativistic description of the particle-particle interaction, this Dirac-Coulomb equation is also no longer Lorentz covariant, an essential principle of special relativity. An approximative correction for the particle-particle interaction to the Dirac-Coulomb Hamiltonian is the Breit operator,[34] which describes the magnetic interaction (the *Gaunt* term) and the retardation effects due to the finite velocity of light up to order $1/c^2$:

$$H^{\mathrm{B}} = -\frac{1}{16\pi\epsilon_0}\sum_{i\neq j}\frac{q_i q_j}{|\mathbf{r}_i-\mathbf{r}_j|}\left[\boldsymbol{\alpha}_i.\boldsymbol{\alpha}_j + \frac{\left(\boldsymbol{\alpha}_i.(\mathbf{r}_i-\mathbf{r}_j)\right)\left(\boldsymbol{\alpha}_j.(\mathbf{r}_i-\mathbf{r}_j)\right)}{|\mathbf{r}_i-\mathbf{r}_j|^2}\right] . \tag{2.110}$$

The Breit operator, together with the Dirac-Coulomb Hamiltonian, constitute the Dirac-Coulomb-Breit Hamiltonian H^{DCB}:

$$H^{\mathrm{DCB}} = H^{\mathrm{DC}} + H^{\mathrm{B}} . \tag{2.111}$$

2.2.3 The Foldy-Wouthuysen transformation

In section (2.2.1), it was already substantiated why ψ_{L} generally is the most important component for the electronic solutions of the Dirac equation (in absence of an electromagnetic field), whereas for the positronic solutions, this holds true for ψ_{S}. By means of a specific unitary transformation applied to the Dirac Hamiltonian H^{D} (2.103), which is referred to as the Foldy-Wouthuysen transformation[35] for a free spin-$\frac{1}{2}$ particle, we can transform out exactly all the operators which couple the large and small components, causing the electronic and positronic solutions to be entirely determined by a large and a small component, respectively:

$$\begin{pmatrix} \psi'_{\mathrm{L}}(\mathbf{r},t,\tau) \\ 0 \end{pmatrix} = U \begin{pmatrix} \psi_{\mathrm{L}}(\mathbf{r},t,\tau) \\ \psi_{\mathrm{S}}(\mathbf{r},t,\tau) \end{pmatrix} . \tag{2.112}$$

To this effect, we regroup the Dirac Hamiltonian H^{D} for a free spin-$\frac{1}{2}$ particle into so-called *even* operators $\mathcal{E}$ which are not responsible for the coupling between the large and the small components (except for the even operator βmc^2, which we will continue to write separately), and *odd* operators $\mathcal{O}$ which do:[31]

[31] Notice that in the Dirac-Pauli representation, even operators occupy the matrix positions $[1..2,1..2]$ and $[3..4,3..4]$, whereas odd operators $[1..2,3..4]$ and $[3..4,1..2]$.

$$H^{\mathrm{D}} = \beta mc^2 + \mathcal{E} + \mathcal{O} \,, \tag{2.113}$$

with:

$$\mathcal{E} = \mathbf{0} \,, \qquad \mathcal{O} = \boldsymbol{\alpha}.\mathbf{p}c \,. \tag{2.114}$$

We define a unitary transformation $U = \mathrm{e}^{iS}$ generated by a hermitian operator S:

$$\psi'(\mathbf{r},t) = \mathrm{e}^{iS}\psi(\mathbf{r},t) \,, \tag{2.115}$$

which allows us to write (2.102) as:

$$H^{\mathrm{D}'}\psi'(\mathbf{r},t) = \mathrm{e}^{iS}H^{\mathrm{D}}\mathrm{e}^{-iS}\psi'(\mathbf{r},t) = i\hbar\frac{\partial}{\partial t}\psi'(\mathbf{r},t) \,. \tag{2.116}$$

We choose a specific form for S ($S = -i\beta\boldsymbol{\alpha}.\frac{\mathbf{p}}{p}\theta$), and consequently also for U:[32]

$$U = \mathrm{e}^{i(-i\beta\boldsymbol{\alpha}.\frac{\mathbf{p}}{p}\theta)} = \mathbf{1}_4\cos\theta + \beta(\boldsymbol{\alpha}.\frac{\mathbf{p}}{p})\sin\theta \,. \tag{2.117}$$

Therefore, we can write the transformed Hamiltonian $H^{\mathrm{D}'}$ as:

$$\begin{aligned} H^{\mathrm{D}'} &= (\mathbf{1}_4\cos\theta + \beta(\boldsymbol{\alpha}.\frac{\mathbf{p}}{p})\sin\theta)(\boldsymbol{\alpha}.\mathbf{p}c + \beta mc^2)(\mathbf{1}_4\cos\theta - \beta(\boldsymbol{\alpha}.\frac{\mathbf{p}}{p})\sin\theta) \\ &= (\boldsymbol{\alpha}.\mathbf{p}c + \beta mc^2)(\mathbf{1}_4\cos\theta - \beta(\boldsymbol{\alpha}.\frac{\mathbf{p}}{p})\sin\theta)^2 \\ &= (\boldsymbol{\alpha}.\mathbf{p}c + \beta mc^2)\mathrm{e}^{-2\beta\boldsymbol{\alpha}.\frac{\mathbf{p}}{p}\theta} \\ &= \boldsymbol{\alpha}.\mathbf{p}c(\cos 2\theta - \frac{mc}{p}\sin 2\theta) + \beta(m\cos 2\theta + \frac{p}{c}\sin 2\theta)c^2 \,. \end{aligned} \tag{2.118}$$

The odd term $\boldsymbol{\alpha}.\mathbf{p}c$ can be eliminated exactly by choosing $\tan 2\theta = \frac{p}{mc}$, hence reducing $H^{\mathrm{D}'}$ to an even operator:

$$H^{\mathrm{D}'} = \beta\sqrt{(pc)^2 + (mc^2)^2} \,. \tag{2.119}$$

[32] In (2.117), we exploited the identity $(\beta\boldsymbol{\alpha}.\frac{\mathbf{p}}{p})(\beta\boldsymbol{\alpha}.\frac{\mathbf{p}}{p}) = -\mathbf{1}_4$.

In this way, (2.116) is split up in an equation for the large positive-energy components (small components equal to zero), and an equation for the small negative-energy components (large components equal to zero).

For the Dirac Hamiltonian of a spin-$\frac{1}{2}$ particle in an electromagnetic field,

$$H^{\mathrm{D}} = \beta mc^2 + \mathcal{E} + \mathcal{O} \,, \tag{2.120}$$

with:

$$\mathcal{E} = V = q\varphi \,, \qquad \mathcal{O} = \boldsymbol{\alpha}.\left(\mathbf{p} - \frac{q}{c}\mathbf{A}\right)c \,, \tag{2.121}$$

an exact decoupling, such as the one for a free particle, has not been found. However, Foldy and Wouthuysen introduced (also in Ref. [35]) a systematic procedure for the decoupling of the large and small components up to a given order in c^{-1} through repetitive unitary transformations $U = \mathrm{e}^{iS}$ with S equal to:

$$S = -\frac{i\beta\mathcal{O}}{2mc^2} \,. \tag{2.122}$$

For reasons of simplicity, we assume the electromagnetic field to be time-independent, consequently this also holds true for S. After expansion of e^{iS} in a power series in S, assuming that S is *small*, and considering only the terms up to order orde c^{-2}, the transformed Dirac Hamiltonian amounts to:

$$\begin{aligned} H^{\mathrm{D}'} &= \mathrm{e}^{iS} H^{\mathrm{D}} \mathrm{e}^{-iS} \\ &= \left(\sum_{k=0}^{\infty} \frac{(iS)^k}{k!}\right) H^{\mathrm{D}} \left(\sum_{l=0}^{\infty} \frac{(-iS)^l}{l!}\right) \\ &\cong H^{\mathrm{D}} + i\left[S, H^{\mathrm{D}}\right] - \frac{1}{2}\left[S, \left[S, H^{\mathrm{D}}\right]\right] - \frac{i}{6}\left[S, \left[S, \left[S, H^{\mathrm{D}}\right]\right]\right] \\ &+ \frac{1}{24}\left[S, \left[S, \left[S, \left[S, \beta mc^2\right]\right]\right]\right] \,. \end{aligned} \tag{2.123}$$

The commutators in the above equation reduce to:

$$
\begin{aligned}
i\left[S, H^{\mathrm{D}}\right] &= -\mathcal{O} + \frac{\beta\left[\mathcal{O}, \mathcal{E}\right]}{2mc^2} + \frac{\beta\mathcal{O}^2}{mc^2}\,, && (2.124)\\
-\frac{1}{2}\left[S, \left[S, H^{\mathrm{D}}\right]\right] &= -\frac{\beta\mathcal{O}^2}{2mc^2} - \frac{\left[\mathcal{O}, \left[\mathcal{O}, \mathcal{E}\right]\right]}{8(mc^2)^2} - \frac{\mathcal{O}^3}{2(mc^2)^2}\,, && (2.125)\\
-\frac{i}{6}\left[S, \left[S, \left[S, H^{\mathrm{D}}\right]\right]\right] &= \frac{\mathcal{O}^3}{6(mc^2)^2} - \frac{\beta\mathcal{O}^4}{6(mc^2)^3}\,, && (2.126)\\
\frac{1}{24}\left[S, \left[S, \left[S, \left[S, \beta mc^2\right]\right]\right]\right] &= \frac{\beta\mathcal{O}^4}{24(mc^2)^3}\,. && (2.127)
\end{aligned}
$$

$H^{\mathrm{D}'}$ then becomes, up to (and including) second order in c^{-2}:

$$
\begin{aligned}
H^{\mathrm{D}'} &= \beta\left(mc^2 + \frac{\mathcal{O}^2}{2mc^2} - \frac{\mathcal{O}^4}{8(mc^2)^3}\right) + \mathcal{E} - \frac{\left[\mathcal{O}, \left[\mathcal{O}, \mathcal{E}\right]\right]}{8(mc^2)^2}\\
&+ \frac{\beta\left[\mathcal{O}, \mathcal{E}\right]}{2mc^2} - \frac{\mathcal{O}^3}{3(mc^2)^2}\,.
\end{aligned}
\qquad (2.128)
$$

Taking into consideration the properties $\mathcal{E}\times\mathcal{E} = \mathcal{E}$, $\mathcal{E}\times\mathcal{O} = \mathcal{O}$, $\mathcal{O}\times\mathcal{E} = \mathcal{O}$, and $\mathcal{O}\times\mathcal{O} = \mathcal{E}$,[33] it can be readily observed that $H^{\mathrm{D}'}$ is composed of even and odd operators again:

$$
H^{\mathrm{D}'} \equiv \beta mc^2 + \mathcal{E}' + \mathcal{O}'\,. \qquad (2.129)
$$

Upon closer examination of $H^{\mathrm{D}'}$, we notice that the even operators (excluding βmc^2) are of order c^0 and c^{-2}, whereas the odd operators are of order c^{-1} or c^{-2}. Remember that the even and odd operators in H^{D} were of order c^0 and c^1, respectively. In other words, due to the transformation e^{iS}, the order in c of the new odd operator has lowered with 2. We can apply the exact same procedure to (2.129), which is formally identical to (2.120): successive transformations $S = -\frac{i\beta\mathcal{O}'}{2mc^2}$, $S = -\frac{i\beta\mathcal{O}''}{2mc^2}$, ... will lower the order in c of the odd operator even further, and in this way, up to an arbitrary order in c, an even operator is obtained. Again, this results in an equation for the positive-energy

[33] This can be verified simply using the matrix notation.

large components (small components equal to zero), and an equation for the negative-energy small components (large components equal to zero).

The Dirac-Coulomb-Breit Hamiltonian $H^{\mathrm{DCB},n=2}$ for two spin-$\frac{1}{2}$ particles in a time-independent electromagnetic field follows from (2.111):

$$\begin{aligned} H^{\mathrm{DCB},n=2} &= \boldsymbol{\alpha}_1.(\mathbf{p}_1 - \frac{q_1}{c}\mathbf{A}_1)c + \beta_1 m_1 c^2 + q_1\varphi_1 \\ &+ \boldsymbol{\alpha}_2.(\mathbf{p}_2 - \frac{q_2}{c}\mathbf{A}_2)c + \beta_1 m_2 c^2 + q_2\varphi_2 \\ &+ \frac{q_1 q_2}{4\pi\epsilon_0 \left|\mathbf{r}_1 - \mathbf{r}_2\right|} \\ &- \frac{q_1 q_2}{8\pi\epsilon_0 \left|\mathbf{r}_1 - \mathbf{r}_2\right|} \left[\boldsymbol{\alpha}_1.\boldsymbol{\alpha}_2 + \frac{\left(\boldsymbol{\alpha}_1.(\mathbf{r}_1 - \mathbf{r}_2)\right)\left(\boldsymbol{\alpha}_2.(\mathbf{r}_1 - \mathbf{r}_2)\right)}{\left|\mathbf{r}_1 - \mathbf{r}_2\right|^2}\right] . \end{aligned} \tag{2.130}$$

$H^{\mathrm{DCB},n=2}$ can be written as a (16×16) matrix operating on 16-component spinor functions, consisting of 4 combinations of small and large components of two particles, denoted as $\psi_{\mathrm{L}_1\mathrm{L}_2}$, $\psi_{\mathrm{L}_1\mathrm{S}_2}$, $\psi_{\mathrm{S}_1\mathrm{L}_2}$, and $\psi_{\mathrm{S}_1\mathrm{S}_2}$. In a similar way as for (2.113) and (2.120), $H^{\mathrm{DCB},n=2}$ can be regrouped into even-even, even-odd, odd-even, and odd-odd operators:[34]

$$H^{\mathrm{DCB},n=2} = \beta_1 m_1 c^2 + \beta_2 m_2 c^2 + \mathcal{EE} + \mathcal{OE} + \mathcal{EO} + \mathcal{OO} , \tag{2.131}$$

with:

[34]Operators such as for example β_1 and β_2 originate from the direct product (denoted as $\cdot\times$) of two (4×4) matrices:

$$\beta_1 = \beta \cdot \times \mathbf{1}_4 = \begin{pmatrix} \beta & 0 & 0 & 0 \\ 0 & \beta & 0 & 0 \\ 0 & 0 & \beta & 0 \\ 0 & 0 & 0 & \beta \end{pmatrix} , \qquad \beta_2 = \mathbf{1}_4 \cdot \times \beta = \begin{pmatrix} \mathbf{1}_4 & 0 & 0 & 0 \\ 0 & \mathbf{1}_4 & 0 & 0 \\ 0 & 0 & -\mathbf{1}_4 & 0 \\ 0 & 0 & 0 & -\mathbf{1}_4 \end{pmatrix} ,$$

with β and $\mathbf{1}_4$ again the familiar (4×4) matrices.

$$\mathcal{EE} = +q_1\varphi_1 + q_2\varphi_2 + \frac{q_1 q_2}{4\pi\epsilon_0 \left|\mathbf{r}_1 - \mathbf{r}_2\right|} , \tag{2.132}$$

$$\mathcal{OE} = \boldsymbol{\alpha}_1.(\mathbf{p}_1 - \frac{q_1}{c}\mathbf{A}_1)c , \tag{2.133}$$

$$\mathcal{EO} = \boldsymbol{\alpha}_2.(\mathbf{p}_2 - \frac{q_2}{c}\mathbf{A}_2)c , \tag{2.134}$$

$$\mathcal{OO} = -\frac{q_1 q_2}{8\pi\epsilon_0 \left|\mathbf{r}_1 - \mathbf{r}_2\right|} \left[\boldsymbol{\alpha}_1.\boldsymbol{\alpha}_2 + \frac{\left(\boldsymbol{\alpha}_1.(\mathbf{r}_1 - \mathbf{r}_2)\right)\left(\boldsymbol{\alpha}_2.(\mathbf{r}_1 - \mathbf{r}_2)\right)}{\left|\mathbf{r}_1 - \mathbf{r}_2\right|^2}\right] . \tag{2.135}$$

Chaprlyvy[36, 37] generalized the Foldy-Wouthuysen procedure for this two-particle Dirac-Coulomb-Breit Hamiltonian, and showed that the coupling operators between $\psi_{\mathrm{L_1L_2}}$ and the other three possible combinations can be reduced to an arbitrary order in c, through the repetitive application of a unitary transformation $U = \mathrm{e}^{iS}$, where S equals to:

$$S = -\frac{i(\beta_1 + \beta_1\beta_2)}{4m_1c^2}\mathcal{OE} - \frac{i(\beta_2 + \beta_1\beta_2)}{4m_2c^2}\mathcal{EO} - \frac{i(\beta_1 + \beta_2)}{4(m_1 + m_2)c^2}\mathcal{OO} , \tag{2.136}$$

After reduction of the coupling terms up to order c^{-3}, thereby assuming that $m_1 = m_2$, and after projection of $H^{\mathrm{DCB}',N=2}$ onto the space of $\psi_{\mathrm{L_1L_2}}$, we obtain the (4×4) Hamiltonian $H^{\mathrm{DCB}',N=2}_{L_1L_2}$ corresponding with two electronic solutions:[35]

$$\begin{aligned} H^{\mathrm{DCB}',N=2}_{L_1L_2} &= m_1c^2 + m_2c^2 + \mathcal{EE} + \frac{(\mathcal{OE})^2}{2m_1c^2} + \frac{(\mathcal{EO})^2}{2m_2c^2} + \frac{[[\mathcal{OE},\mathcal{EE}],\mathcal{OE}]}{8m_1^2c^4} \\ &+ \frac{[[\mathcal{EO},\mathcal{EE}],\mathcal{EO}]}{8m_2^2c^4} + \frac{\left[[\mathcal{OE},\mathcal{OO}]_+,\mathcal{EO}\right]_+}{4m_1m_2c^4} - \frac{(\mathcal{OE})^4}{8m_1^3c^6} \\ &- \frac{(\mathcal{EO})^4}{8m_2^3c^6} + \frac{(\mathcal{OO})^2}{2(m_1 + m_2)c^2} . \end{aligned} \tag{2.137}$$

[35] This step corresponds to selecting out the upperleft (4×4) matrix in the (16×16)-matrix representation of $H^{\mathrm{DCB}',N=2}$, and also implies the reinterpretation of the Dirac spin matrices α_i as the Pauli matrices σ_i. The derivation is rather tedious, and for this reason it was not included in the text (even Chaprlyvy did not deem necessary its inclusion in Ref. [36] and [37]).

Elaborating the different terms in $H_{L_1L_2}^{\mathrm{DCB}',N=2}$,[36] after insertion of $q_1 = q_2 = -e$ and $m_1 = m_2 = m_e$, after adopting atomic units, and after rearrangement into one-particle and two-particle terms, we obtain:

$$H_{L_1L_2}^{\mathrm{DCB}',N=2} = \sum_{i}^{2} H_{L_1L_2,i}^{\mathrm{DCB}',N=2} + \sum_{i\neq j}^{2} H_{L_1L_2,ij}^{\mathrm{DCB}',N=2} \ , \tag{2.138}$$

with:

[36] We must note that the term in $(\mathcal{OO})^2$ does not appear in a quantum electrodynamic treatment of (2.137). In that respect we note that the Breit operator is only an approximative relativistic correction to the particle-particle interaction. A rigorous explanation falls outside the scope of this work. The remaining terms are easy to develop:

$$(\mathcal{OE})^2 = c^2\left((\mathbf{p}_1 - \frac{q_1}{c}\mathbf{A}_1)^2 - q_1\hbar(\sigma_1.\mathbf{B}_1)\right) \ ,$$
$$(\mathcal{EO})^2 = c^2\left((\mathbf{p}_2 - \frac{q_2}{c}\mathbf{A}_2)^2 - q_2\hbar(\sigma_2.\mathbf{B}_2)\right) \ ,$$
$$(\mathcal{OE})^4 = c^4\left((\mathbf{p}_1 - \frac{q_1}{c}\mathbf{A}_1)^4 - 2q_1\hbar(\sigma_1.\mathbf{B}_1)(\mathbf{p}_1 - \frac{q_1}{c}\mathbf{A}_1)^2 + q_1^2\hbar^2(\sigma_1.\mathbf{B}_1)^2\right) \ ,$$
$$(\mathcal{EO})^4 = c^4\left((\mathbf{p}_2 - \frac{q_2}{c}\mathbf{A}_2)^4 - 2q_2\hbar(\sigma_2.\mathbf{B}_2)(\mathbf{p}_2 - \frac{q_2}{c}\mathbf{A}_2)^2 + q_2^2\hbar^2(\sigma_2.\mathbf{B}_2)^2\right) \ ,$$
$$[[\mathcal{OE},\mathcal{EE}],\mathcal{OE}] = -\frac{q_1q_2c^2}{4\pi\epsilon_0}\left(4\pi\hbar^2\delta(|\mathbf{r}_1-\mathbf{r}_2|) + \frac{2\hbar}{|\mathbf{r}_1-\mathbf{r}_2|^3}\sigma_1.(|\mathbf{r}_1-\mathbf{r}_2|\times(\mathbf{p}_1-\frac{q_1}{c}\mathbf{A}_1))\right)$$
$$-q_1c^2\left(2\hbar\sigma_1.(\mathbf{E}_1\times(\mathbf{p}_1-\frac{q_1}{c}\mathbf{A}_1)) + \hbar^2\nabla_1.\mathbf{E}_1\right) \ ,$$
$$[[\mathcal{EO},\mathcal{EE}],\mathcal{EO}] = -\frac{q_1q_2c^2}{4\pi\epsilon_0}\left(4\pi\hbar^2\delta(|\mathbf{r}_1-\mathbf{r}_2|) + \frac{2\hbar}{|\mathbf{r}_1-\mathbf{r}_2|^3}\sigma_2.(|\mathbf{r}_1-\mathbf{r}_2|\times(\mathbf{p}_2-\frac{q_2}{c}\mathbf{A}_2))\right)$$
$$-q_2c^2\left(2\hbar\sigma_2.(\mathbf{E}_2\times(\mathbf{p}_2-\frac{q_2}{c}\mathbf{A}_2)) + \hbar^2\nabla_2.\mathbf{E}_2\right) \ ,$$
$$\left[[\mathcal{OE},\mathcal{OO}]_+,\mathcal{EO}\right]_+ = \frac{q_1q_2c^2}{4\pi\epsilon_0}\left(\frac{\hbar^2}{|\mathbf{r}_1-\mathbf{r}_2|^3}(\sigma_1.\sigma_2) - \frac{8\pi\hbar^2}{3}\delta(|\mathbf{r}_1-\mathbf{r}_2|)(\sigma_1.\sigma_2)\right.$$
$$-\frac{3\hbar^2}{|\mathbf{r}_1-\mathbf{r}_2|^5}(\sigma_1.|\mathbf{r}_1-\mathbf{r}_2|)(\sigma_2.|\mathbf{r}_1-\mathbf{r}_2|) + \frac{2\hbar}{|\mathbf{r}_1-\mathbf{r}_2|^3}\sigma_1.(|\mathbf{r}_1-\mathbf{r}_2|\times(\mathbf{p}_2-\frac{q_2}{c}\mathbf{A}_2))$$
$$-\frac{2\hbar}{|\mathbf{r}_1-\mathbf{r}_2|^3}\sigma_2.(|\mathbf{r}_1-\mathbf{r}_2|\times(\mathbf{p}_1-\frac{q_1}{c}\mathbf{A}_1)) - \frac{2}{|\mathbf{r}_1-\mathbf{r}_2|}((\mathbf{p}_1-\frac{q_1}{c}\mathbf{A}_1).(\mathbf{p}_2-\frac{q_2}{c}\mathbf{A}_2)$$
$$\left.-\frac{2}{|\mathbf{r}_1-\mathbf{r}_2|^3}((\mathbf{p}_1-\frac{q_1}{c}\mathbf{A}_1).|\mathbf{r}_1-\mathbf{r}_2|)(|\mathbf{r}_1-\mathbf{r}_2|.(\mathbf{p}_2-\frac{q_2}{c}\mathbf{A}_2))\right) \ .$$

$$
\begin{aligned}
H_{L_1L_2,i}^{\mathrm{DCB}',N=2} &= \alpha^{-2} + \frac{(\mathbf{p}_i + \alpha\mathbf{A}_i)^2}{2} - \varphi_i + \frac{\sigma_i.\mathbf{B}_i}{2} - \frac{\alpha^2(\mathbf{p}_i + \alpha\mathbf{A}_i)^4}{8} + \frac{\alpha^2\nabla_i.\mathbf{E}_i}{8} \\
- & \frac{\alpha^2\sigma_i.((\mathbf{p}_i + \alpha\mathbf{A}_i) \times \mathbf{E}_i - \mathbf{E}_i \times (\mathbf{p}_i + \alpha\mathbf{A}_i))}{8} \\
- & \frac{\alpha^2(\sigma_i.\mathbf{B}_i)(\mathbf{p}_i + \alpha\mathbf{A}_i)^2}{4}\,, \qquad (2.139)
\end{aligned}
$$

and:

$$
\begin{aligned}
H_{L_1L_2,ij}^{\mathrm{DCB}',N=2} &= \frac{1}{2\left|\mathbf{r}_1 - \mathbf{r}_2\right|} - \frac{\alpha^2}{4}\left((\mathbf{p}_i + \alpha\mathbf{A}_i)(\mathbf{p}_j + \alpha\mathbf{A}_j)(\frac{1}{\left|\mathbf{r}_i - \mathbf{r}_j\right|})\right. \\
+ & \left.\frac{1}{2\left|\mathbf{r}_i - \mathbf{r}_j\right|^3}((\mathbf{p}_i + \alpha\mathbf{A}_i).\left|\mathbf{r}_i - \mathbf{r}_j\right|)(\left|\mathbf{r}_i - \mathbf{r}_j\right|.(\mathbf{p}_j + \alpha\mathbf{A}_j))\right) \\
+ & \frac{\alpha^2}{4\left|\mathbf{r}_i - \mathbf{r}_j\right|^3}\left(\sigma_i.(\left|\mathbf{r}_i - \mathbf{r}_j\right| \times (\mathbf{p}_j + \alpha\mathbf{A}_j) - \sigma_j.(\left|\mathbf{r}_i - \mathbf{r}_j\right| \times (\mathbf{p}_i + \alpha\mathbf{A}_i))\right) \\
- & \frac{\alpha^2}{8\left|\mathbf{r}_i - \mathbf{r}_j\right|^3}\left(\sigma_i.(\left|\mathbf{r}_i - \mathbf{r}_j\right| \times (\mathbf{p}_i + \alpha\mathbf{A}_i) - \sigma_j.(\left|\mathbf{r}_i - \mathbf{r}_j\right| \times (\mathbf{p}_j + \alpha\mathbf{A}_j))\right) \\
- & \frac{\alpha^2\pi}{2}\delta(\left|\mathbf{r}_i - \mathbf{r}_j\right|) + \frac{\alpha^2}{8}\left(\frac{1}{\left|\mathbf{r}_i - \mathbf{r}_j\right|}\sigma_i.\sigma_j\right. \\
- & \left.\frac{3}{\left|\mathbf{r}_i - \mathbf{r}_j\right|^3}(\sigma_i.\left|\mathbf{r}_i - \mathbf{r}_j\right|)(\sigma_j.\left|\mathbf{r}_i - \mathbf{r}_j\right|) - \frac{8\pi}{3}\delta(\left|\mathbf{r}_i - \mathbf{r}_j\right|)\sigma_i.\sigma_j\right)\,. \qquad (2.140)
\end{aligned}
$$

In the above equations, the following shorthand notations were introduced: $\mathbf{A}_i = \mathbf{A}(\mathbf{r}_i)$, $\varphi_i = \varphi(\mathbf{r}_i)$, $\mathbf{B}_i = \mathbf{B}(\mathbf{r}_i)$, and $\mathbf{E}_i = \mathbf{E}(\mathbf{r}_i)$. $\mathbf{E} = -\nabla\varphi$ and $\mathbf{B} = \nabla \times \mathbf{A}$ represent the electric and the magnetic field, respectively. Since the Dirac-Coulomb-Breit Hamiltonian does not consider interactions between more than two particles, all possible terms should already be present in (2.139) and (2.140) for this simple system. The generalization of this result to n electrons, after deducting the rest-mass energy of n electrons, leads to the quasi-relativistic Breit-Pauli Hamiltonian for n electrons.

Finally, we must specify the electromagnetic field. The scalar potential φ consists of the Coulombic contributions from the charged atomic nuclei:

$$\varphi(\mathbf{r}) = \sum_I \frac{Q_I}{|\mathbf{r} - \mathbf{R}_I|} \ . \tag{2.141}$$

The vector potential $\mathbf{A}$ is composed of $\mathbf{A} = \mathbf{A}_0 + \sum_I \mathbf{A}_I$, where $\mathbf{A}_0$ indicates the vector potential corresponding with the external magnetic field $\mathbf{B}_0$ in the Coulomb gauge, and $\mathbf{A}_I$ the vector potential from the magnetic field generated by the magnetic dipole moment of atomic nucleus I. These vector potentials are given by:

$$\mathbf{A}_0(\mathbf{r}) = \frac{1}{2}\mathbf{B}_0 \times \left(\mathbf{r} - \mathbf{R}_\mathrm{g}\right) \ , \tag{2.142}$$

$$\mathbf{A}_I(\mathbf{r}) = \alpha^2 \gamma_I \frac{\mathbf{I}_I \times (\mathbf{r} - \mathbf{R}_I)}{|\mathbf{r} - \mathbf{R}_I|^3} \ , \tag{2.143}$$

with $\mathbf{R}_\mathrm{g}$ the gauge origin (see section 2.3.5), and γ_I and $\mathbf{I}_I$ the nuclear magnetic ratio and the nuclear spin of atomic nucleus I, respectively.

2.2.4 The g tensor

The g tensor (2.100),

$$g_{xy} = \frac{2}{\alpha} \left. \frac{\partial^2 \langle \Psi | \, H \, | \Psi \rangle}{\partial B_x \partial S_y} \right|_{\mathbf{B}=\mathbf{S}=\mathbf{0}} \ , \tag{2.144}$$

is a second-order property that can be evaluated through double-perturbation theory. The pair of perturbation parameters is composed of the components along the axes of a given coordinate system of a constant external magnetic field B_x and the net electron-spin component S_y. Using the Hellmann-Feynman theorem for double-perturbation theory, we obtain:[37]

$$g_{xy} = \frac{2}{\alpha} \frac{\partial}{\partial B_x} \langle \Psi_{B_x} | \left. \frac{\partial H}{\partial S_y} \right|_{\mathbf{S}=\mathbf{0}} | \Psi_{B_x} \rangle \Bigg|_{\mathbf{B}=\mathbf{0}} \ , \tag{2.145}$$

where Ψ_{B_x} denotes the electronic wave function in the presence of a (unitary) magnetic field coinciding with the x axis. From the above equation, it is apparent that:

[37] For an energy-eigenvalue E corresponding with an eigenstate $|\Psi\rangle$ of a Hamiltonian H, with λ_1

1. we only need to calculate the first-order correction to the electronic wave function for the 3 components of the magnetic field separately,
2. we only have to consider perturbation parameters which:
   (a) depend linearly on the electron-spin operators,
   (b) are of order 0 or 1 in the magnetic field.

A Hamiltonian H^{g} that satisfies these criteria is gathered from the terms in (2.139) and (2.140).[38] H^{g} contains at least the Zeeman term H_Z and the nuclear spin-orbit coupling term $H_{\mathrm{SO(N)}}$ (*nuclear*: The orbital angular momentum originates from the rotation of an electron around a particular atomic nucleus):

$$H_Z = \sum_i h_Z^i = \sum_i \frac{\alpha g_e}{2} \mathbf{s}_i.\mathbf{B} \,, \tag{2.146}$$

$$H_{\mathrm{SO(N)}} = \sum_i h_{\mathrm{SO(N)}}^j = \sum_i \frac{\alpha^2 g'}{4} \sum_I Q_I \mathbf{s}_i . \frac{(\mathbf{r}_i - \mathbf{R}_I) \times \mathbf{p}_i}{|\mathbf{r}_i - \mathbf{R}_I|^3} \,. \tag{2.147}$$

The most important relativistic corrections include the two-electron spin-orbit coupling term $H_{\mathrm{SO(2e)}}$ (*two-electron*: the orbital angular momentum originates from the rotation of an electron around another electron), the two-electron spin-other-orbit coupling term H_{SOO} (*other-orbit*: the spin angular momentum of a particular electron couples with the orbital angular momentum of another electron because of its rotation around that particular electron), and the Zeeman kinetic-energy-correction term (H_{ZKE}):

---

and λ_2 a pair of perturbation parameters, it holds that:

$$\begin{aligned}
&\left.\frac{\partial^2 E}{\partial\lambda_1\partial\lambda_2}\right|_{\lambda_1=\lambda_2=0} = \left.\frac{\partial^2}{\partial\lambda_1\partial\lambda_2}\langle\Psi(\lambda_1,\lambda_2)|H(\lambda_1,\lambda_2)|\Psi(\lambda_1,\lambda_2)\rangle\right|_{\lambda_1=\lambda_2=0} \\
&= \frac{\partial}{\partial\lambda_1}\left(\langle \left.\frac{\partial\Psi(\lambda_1,\lambda_2)}{\partial\lambda_2}\right|_{\lambda_2=0} |H(\lambda_1,0)|\Psi(\lambda_1,0)\rangle + \langle\Psi(\lambda_1,0)|H(\lambda_1,0)| \left.\frac{\partial H(\lambda_1,\lambda_2)}{\partial\lambda_2}\right|_{\lambda_2=0} |\Psi(\lambda_1,0)\rangle \right.\\
&\left. + \langle\Psi(\lambda_1,0)|H(\lambda_1,0)| \left.\frac{\partial\Psi(\lambda_1,\lambda_2)}{\partial\lambda_2}\right|_{\lambda_2=0}\rangle\right)\Bigg|_{\lambda_1=0} \\
&= \frac{\partial}{\partial\lambda_1}\left(E \left.\frac{\partial}{\partial\lambda_2}\langle\Psi(\lambda_1,\lambda_2)|\Psi(\lambda_1,\lambda_2)\rangle\right|_{\lambda_2=0} + \langle\Psi(\lambda_1,0)| \left.\frac{\partial H(\lambda_1,\lambda_2)}{\partial\lambda_2}\right|_{\lambda_2=0} |\Psi(\lambda_1,0)\rangle\right)\Bigg|_{\lambda_1=0} \\
&= \frac{\partial}{\partial\lambda_1}\left(\langle\Psi(\lambda_1,0)| \left.\frac{\partial H(\lambda_1,\lambda_2)}{\partial\lambda_2}\right|_{\lambda_2=0} |\Psi(\lambda_1,0)\rangle\right)\Bigg|_{\lambda_1=0} .
\end{aligned}$$

[38] Note that $\sigma_i = 2\mathbf{s}_i$ and, for a time-independent magnetic field, $\nabla \times \mathbf{E} = 0$.

$$H_{\mathrm{SO(2e)}} = \sum_i \sum_{j\neq i} -\frac{\alpha^2 g'}{4} \mathbf{s}_i . \frac{(\mathbf{r}_i - \mathbf{r}_j) \times \mathbf{p}_i}{|\mathbf{r}_i - \mathbf{r}_j|^3} , \tag{2.148}$$

$$H_{\mathrm{SOO}} = \sum_i \sum_{j\neq i} -\alpha^2 \mathbf{s}_i . \frac{(\mathbf{r}_j - \mathbf{r}_i) \times \mathbf{p}_j}{|\mathbf{r}_j - \mathbf{r}_i|^3} , \tag{2.149}$$

$$H_{\mathrm{ZKE}} = \sum_i -\frac{\alpha^3 g_e}{4} \mathbf{p}_i^2 \mathbf{s}_i . \mathbf{B} . \tag{2.150}$$

Finally, one must also include the *gauge correction* terms. Using the minimal coupling principle ($\mathbf{p} \rightarrow \boldsymbol{\pi} = \mathbf{p} + \alpha \mathbf{A}$), it is easy to notice their analogy with (2.147), (2.148), and (2.149). These terms are also called diamagnetic terms, in accordance with a nomenclature common in NMR:

$$H^{\mathrm{dia}}_{\mathrm{SO(N)}} = \sum_i \frac{\alpha^2 g'}{4} \sum_I Q_I \mathbf{s}_i . \frac{(\mathbf{r}_i - \mathbf{R}_I) \times \alpha \mathbf{A}(\mathbf{r}_i)}{|\mathbf{r}_i - \mathbf{R}_I|^3} , \tag{2.151}$$

$$H^{\mathrm{dia}}_{\mathrm{SO(2e)}} = \sum_i \sum_{j\neq i} -\frac{\alpha^2 g'}{4} \mathbf{s}_i . \frac{(\mathbf{r}_i - \mathbf{r}_j) \times \alpha \mathbf{A}(\mathbf{r}_i)}{|\mathbf{r}_i - \mathbf{r}_j|^3} , \tag{2.152}$$

$$H^{\mathrm{dia}}_{\mathrm{SOO}} = \sum_i \sum_{j\neq i} -\alpha^2 \mathbf{s}_i . \frac{(\mathbf{r}_j - \mathbf{r}_i) \times \alpha \mathbf{A}(\mathbf{r}_j)}{|\mathbf{r}_j - \mathbf{r}_i|^3} . \tag{2.153}$$

$\mathbf{r}_i$, $\mathbf{p}_i$, and $\mathbf{s}_i$ represent the position, the orbital momentum, and the spin operator of electron i, respectively, in the equations (2.146) - (2.153). g_e is the g factor of the free electron ($g_e = 2.0023193043622$),[38] g' is defined as $g' = 2g_e - 2$, $\mathbf{R}_I$ and Q_I represent the position and the charge of the atomic nucleus I in atomic units.[39]

2.2.5 The A tensor

The A tensor (2.101) corresponding with atomic nucleus I,

$$A_{I,xy} = \left. \frac{\partial^2 \langle \Psi | H | \Psi \rangle}{\partial I_{I,x} \partial S_y} \right|_{\mathbf{I}_I = \mathbf{S} = \mathbf{0}} , \tag{2.154}$$

[39] Based on (2.139) and (2.140), g_e and g' would equal 2, but QED corrections cause a (minor) shift.

is also a second-order property which can be evaluated through double-perturbation theory. The pair of perturbation parameters is composed of the components coinciding with the axes of a given coordinate system of a net nuclear-spin component corresponding with the I-th atomic nucleus $I_{I,x}$ and the net electron-spin component S_y. Using the Hellmann-Feynman theorem for double-perturbation theory, we obtain:

$$A_{I,xy} = \frac{\partial}{\partial I_{I,x}} \left\langle \Psi_{I_{I,x}} \right| \left. \frac{\partial H}{\partial S_y} \right|_{\mathbf{S}=\mathbf{0}} \left| \Psi_{I_{I,x}} \right\rangle \Bigg|_{\mathbf{I}_I=\mathbf{0}} . \tag{2.155}$$

From the above equation, it follows that:

1. we only need to calculate the first-order correction to the electronic wave function for the 3 components of the nuclear spin corresponding with the atomic nucleus I,
2. we only have to consider perturbation parameters which:
   (a) depend linearly on the electron-spin operators,
   (b) are of order 0 or 1 in the nuclear-spin operator.

A Hamiltonian H^{A_I} that satisfies these criteria is gathered from the terms in (2.139) and (2.140). The most important terms of H^{A_I} include the isotropic Fermi-contact interaction term $H_{\mathrm{FC},I}$:

$$H_{\mathrm{FC},I} = \frac{2}{3}\mu_0 g_e \mu_e g_I \mu_I \sum_i \delta\left(\mathbf{r}_i - \mathbf{R}_I\right) \mathbf{s}_i . \mathbf{I}_I \, , \tag{2.156}$$

and the anistropic dipole-dipole interaction term $H_{\mathrm{DC},I}$:[40]

$$H_{\mathrm{DC},I} = \frac{1}{4\pi}\mu_0 g_e \mu_e g_I \mu_I \sum_i \mathbf{s}_i . \left[\frac{3\left(\mathbf{r}_i - \mathbf{R}_I\right)^{\mathrm{T}} \left(\mathbf{r}_i - \mathbf{R}_I\right) - \mathbf{1}\left|\mathbf{r}_i - \mathbf{R}_I\right|^2}{\left|\mathbf{r}_i - \mathbf{R}_I\right|^5} \right] . \mathbf{I}_I \, . \tag{2.157}$$

In (2.156) and (2.157), μ_0 represents the permeability of vacuum, μ_e the Bohr magneton, and g_I and μ_I the g value and the nuclear magneton of the atomic

[40] Observe that the term between square brackets represents a (3×3) matrix.

nucleus I, respectively. If we include only the two previous terms into H^{A_I}, which are both linear in the nuclear-spin operator, then (2.155) simplifies to:

$$A_{I,xy} = \langle \Psi | \left. \frac{\partial^2 H^{\mathrm{A}_I}}{\partial I_{I,x} \partial S_y} \right|_{\mathbf{I}_I = \mathbf{S} = \mathbf{0}} | \Psi \rangle \ , \tag{2.158}$$

or, in other words, there is no need for calculating corrections to the electronic wave function.[41]

2.3 Calculation of the g tensor in PBC simulations

2.3.1 The g tensor in DFT

Upon consideration of the terms (2.146) - (2.153) for implementation in DFT, we observe that the expectation value of the four two-particles operators $H_{\mathrm{SO(2e)}}$, H_{SOO}, and their counterparts $H^{\mathrm{dia}}_{\mathrm{SO(2e)}}$ and $H^{\mathrm{dia}}_{\mathrm{SOO}}$, will need to be approximated, since the two-particles density matrix is not available in Kohn-Sham DFT. The development of this theoretical method is mainly the work of Schreckenbach and Ziegler.[1]

[41] We further elaborate on the result of one of the previous footnotes, and assume that $H(\lambda_1, \lambda_2)$ is linear in λ_1:

$$\begin{aligned}
&\left. \frac{\partial^2 E}{\partial \lambda_1 \partial \lambda_2} \right|_{\lambda_1=\lambda_2=0} = \left. \frac{\partial}{\partial \lambda_1} \left(\langle \Psi(\lambda_1,0) | \left. \frac{\partial H(\lambda_1,\lambda_2)}{\partial \lambda_2} \right|_{\lambda_2=0} | \Psi(\lambda_1,0) \rangle \right) \right|_{\lambda_1=0} \\
&= \langle \left. \frac{\partial \Psi(\lambda_1,0)}{\partial \lambda_1} \right|_{\lambda_1=0} | \left. \frac{\partial H(\lambda_1,\lambda_2)}{\partial \lambda_2} \right|_{\lambda_1=\lambda_2=0} | \Psi(0,0) \rangle + \langle \Psi(0,0) | \left. \frac{\partial^2 H(\lambda_1,\lambda_2)}{\partial \lambda_1 \lambda_2} \right|_{\lambda_1=\lambda_2=0} | \Psi(0,0) \rangle \\
&+ \langle \Psi(0,0) | \left. \frac{\partial H(\lambda_1,\lambda_2)}{\partial \lambda_2} \right|_{\lambda_1=\lambda_2=0} | \left. \frac{\partial \Psi(\lambda_1,0)}{\partial \lambda_1} \right|_{\lambda_1=0} \rangle \\
&= \langle \left. \frac{\partial \Psi(\lambda_1,0)}{\partial \lambda_1} \right|_{\lambda_1=0} | 0 | \Psi(0,0) \rangle + \langle \Psi(0,0) | \left. \frac{\partial^2 H(\lambda_1,\lambda_2)}{\partial \lambda_1 \lambda_2} \right|_{\lambda_1=\lambda_2=0} | \Psi(0,0) \rangle \\
&+ \langle \Psi(0,0) | 0 | \left. \frac{\partial \Psi(\lambda_1,0)}{\partial \lambda_1} \right|_{\lambda_1=0} \rangle \\
&= \langle \Psi(0,0) | \left. \frac{\partial^2 H(\lambda_1,\lambda_2)}{\partial \lambda_1 \lambda_2} \right|_{\lambda_1=\lambda_2=0} | \Psi(0,0) \rangle \ .
\end{aligned}$$

The terms obeying a form similar to $\mathbf{r}/r^3$ in $H_{\mathrm{SO(N)}}$ and $H_{\mathrm{SO(2e)}}$ (and in $H^{\mathrm{dia}}_{\mathrm{SO(N)}}$ and $H^{\mathrm{dia}}_{\mathrm{SO(2e)}}$ as well) equal the gradients of the corresponding nuclear and electronic Coulomb potentials which, together, make up the total potential field as experienced by a particular electron. In Kohn-Sham-DFT, it is assumed that the non-interactiong electrons move in an effective KS potential $V_{\mathrm{KS}} = v_{\mathrm{ext}} + v_{\mathrm{H}} + v_{\mathrm{XC}}$ originating from the atomic nucleus and the other electrons. This effective potential attempts to mimic the exact potential field as accurately as possible. Encouraged by the generally satisfying results in determining the (approximate) electronic structure, we will also approximate the total spin-orbit coupling terms by basically using this effective KS potential:[42]

$$H_{\mathrm{SO}} = \frac{\alpha^2 g'}{4} \sum_i \mathbf{s}_i . \left((\nabla V_{\mathrm{KS}}) \times \mathbf{p}_i \right) \ , \tag{2.159}$$

$$H^{\mathrm{dia}}_{\mathrm{SO}} = \frac{\alpha^2 g'}{4} \sum_i \mathbf{s}_i . \left((\nabla V_{\mathrm{KS}}) \times \alpha \mathbf{A}(\mathbf{r}_i) \right) \ . \tag{2.160}$$

For the spin-other-orbit coupling terms, no ready-made solution exists within DFT. We will adopt an approach due to Pickard and Mauri[6] later on, which focuses purely on the physical interpretation of the spin-other-orbit interaction. Fortunately, the chosen approximation proves to be not of vital importance for the g tensor.

We have reduced the relevant quantum-mechanical operators to:

$$H^{\mathrm{g}} = H_{\mathrm{Z}} + H_{\mathrm{ZKE}} + H_{\mathrm{SO}} + H_{\mathrm{SOO}} + H^{\mathrm{dia}}_{\mathrm{SO}} + H^{\mathrm{dia}}_{\mathrm{SOO}} \ . \tag{2.161}$$

We will also make use of a technique called *spin-field reduction*: when the axis of spin quantization coincides with the coordinate axis t, we can recast every one-electron operator $O_t . s_t$, proportional to the t component of the spin operator $\mathbf{s}$, to:

[42] In fact we only need the exchange component of v_{XC}, which corrects for the fact that the Hartree potential v_{H} includes the contribution of all electrons.[10]

$$\begin{aligned}\langle\Psi|\sum_i O_{i,t}.s_{i,t}\,|\Psi\rangle &= \sum_{k,l,m_{\mathbf{s}_k},m_{\mathbf{s}_l}} \langle\phi_k|\,O_t\,|\phi_l\rangle\,\langle m_{\mathbf{s}_k}|\,s_t\,|m_{\mathbf{s}_l}\rangle\,\langle\Psi|\,a^+_{km_{\mathbf{s}_k}}a_{lm_{\mathbf{s}_l}}\,|\Psi\rangle \\ &= \sum_{k,l,m_{\mathbf{s}}} \langle\phi_k|\,O_t\,|\phi_l\rangle\,\langle\Psi|\,a^+_{km_{\mathbf{s}}}a_{lm_{\mathbf{s}}}\,|\Psi\rangle\,\frac{1}{2}(-1)^{1/2-m_{\mathbf{s}}} \\ &= \frac{1}{2}\int_{\mathbf{r}'=\mathbf{r}} \mathrm{d}\mathbf{r}\,O_t(\mathbf{r}')\,(\rho^\alpha(\mathbf{r},\mathbf{r}')-\rho^\beta(\mathbf{r},\mathbf{r}'))\,. \end{aligned} \tag{2.162}$$

In the above equations, we introduced the density matrices for the spin-up and spin-down electrons:

$$\rho^\tau(\mathbf{r},\mathbf{r}') = \sum_i \phi_i^\tau(\mathbf{r})^*\phi_i^\tau(\mathbf{r}')\,, \qquad \tau=\alpha,\beta\,, \tag{2.163}$$

and in addition, we agree to perform the substitution $\mathbf{r}'=\mathbf{r}$ after the operation of $O(\mathbf{r}')$ but before integrating. This way, the operator acts only on the terms in $\mathbf{r}'$, while at the same time we can maintain a concise notation based on the density matrices.

The terms in the Hamiltonian that are linear in the magnetic field and the net electron spin result in a second-order perturbation contribution to the energy matrix of the multiplet which equals to:

$$\begin{aligned}\Delta V_{M_S,M'_S} &= \mathbf{B}.\nabla_{\mathbf{B}}\left(\langle\Psi_{\mathbf{B}}SM_S|\sum_i \mathbf{O}(\mathbf{r}_i).\mathbf{s}_i\,|\Psi_{\mathbf{B}}SM'_S\rangle\right)\Big|_{\mathbf{B}=\mathbf{0}} \\ &= \sum_{xy} B_x G_{xy}\,\langle SM_S|\sum_i s_{i,y}\,|SM'_S\rangle\,. \end{aligned} \tag{2.164}$$

This follows from the Wigner-Eckhart theorem in the spin space:

$$\begin{aligned}&\langle\Psi_{\mathbf{B}}SM_S|\sum_{i\mu}(-1)^\mu O_{-\mu}(\mathbf{r}_i)s_{i\mu}\,|\Psi_{\mathbf{B}}SM'_S\rangle \\ &= \sum_\mu (-1)^\mu(-1)^{S-M_S}\begin{pmatrix} S & 1 & S \\ -M_S & \mu & M'_S\end{pmatrix} \\ &\times\,\langle\Psi_{\mathbf{B}}S||\sum_i(-1)^\mu O_{-\mu}(\mathbf{r}_i)\mathbf{s}_i\,||\Psi_{\mathbf{B}}S\rangle\,, \end{aligned} \tag{2.165}$$

with μ the spherical components of $\mathbf{s}$. It also holds that:

$$\begin{aligned}\langle SM_S|\sum_i s_{i,\mu}\left|SM'_S\right\rangle &= (-1)^{S-M_S}\begin{pmatrix} S & 1 & S \\ -M_S & \mu & M'_S\end{pmatrix} \\ &\quad\times\langle S||\sum_i \mathbf{s}_i||S\rangle\ ,\end{aligned} \tag{2.166}$$

and therefore:

$$\begin{aligned}&\langle\Psi_{\mathbf{B}}SM_S|\sum_{i\mu}(-1)^{\mu}O_{-\mu}(\mathbf{r}_i)s_{i\mu}\left|\Psi_{\mathbf{B}}SM'_S\right\rangle \\ &=\sum_{\mu}(-1)^{\mu}\frac{\langle\Psi_{\mathbf{B}}S||\sum_i O_{-\mu}(\mathbf{r}_i)\mathbf{s}_i||\Psi_{\mathbf{B}}S\rangle}{\langle S||\sum_i \mathbf{s}_i||S\rangle} \\ &\times\langle SM_S|\sum_i s_{i,\mu}\left|SM'_S\right\rangle\ .\end{aligned} \tag{2.167}$$

For $S = M_S = M'_S$, it holds that:

$$\begin{aligned}&\langle\Psi_{\mathbf{B}}SS|\sum_i O_{-\mu}(\mathbf{r}_i)s_{i0}\left|\Psi_{\mathbf{B}}SS\right\rangle \\ &=\begin{pmatrix} S & 1 & S \\ -S & 0 & S\end{pmatrix}\langle\Psi_{\mathbf{B}}S||\sum_i O_{-\mu}(\mathbf{r}_i)\mathbf{s}_i||\Psi_{\mathbf{B}}S\rangle \\ &=\frac{1}{2}\int_{\mathbf{r}'=\mathbf{r}}\mathrm{d}\mathbf{r}\,O_{-\mu}(\mathbf{r}')\,\left(\rho^{\alpha}(\mathbf{B}|\mathbf{r},\mathbf{r}')-\rho^{\beta}(\mathbf{B}|\mathbf{r},\mathbf{r}')\right)\ .\end{aligned} \tag{2.168}$$

Here, the spin-field-reduction technique was applied. The $3j$ symbol from the above equation reduces to:

$$\begin{pmatrix} S & 1 & S \\ -S & 0 & S\end{pmatrix}=\frac{S}{\sqrt{S}\sqrt{S+1}\sqrt{2S+1}}=\frac{S}{\langle S||\,\mathbf{S}\,||S\rangle}\ , \tag{2.169}$$

which allows us to rewrite (2.167) as:

$$\begin{aligned}
&\langle \Psi_{\mathbf{B}} S M_S | \sum_{i\mu} (-1)^{\mu} O_{-\mu}(\mathbf{r}_i) s_{i\mu} \left| \Psi_{\mathbf{B}} S M'_S \right\rangle \\
&= \sum_{\mu} (-1)^{\mu} \frac{\langle S M_S | \, \mathbf{S}_{\mu} \, | S M'_S \rangle}{2S} \int\limits_{\mathbf{r}'=\mathbf{r}} \mathrm{d}\mathbf{r} \; O_{-\mu}(\mathbf{r}') \; (\rho^{\alpha}(\mathbf{B}|\mathbf{r},\mathbf{r}') - \rho^{\beta}(\mathbf{B}|\mathbf{r},\mathbf{r}')) \\
&= \sum_{y} \frac{\langle S M_S | \, \mathbf{S}_{y} \, | S M'_S \rangle}{2S} \int\limits_{\mathbf{r}'=\mathbf{r}} \mathrm{d}\mathbf{r} \; O_{y}(\mathbf{r}') \; (\rho^{\alpha}(\mathbf{B}|\mathbf{r},\mathbf{r}') - \rho^{\beta}(\mathbf{B}|\mathbf{r},\mathbf{r}')) \; . \qquad (2.170)
\end{aligned}$$

Therefore, G_{xy} equals:

$$G_{xy} = \left[\frac{\partial}{\partial B_x} \frac{1}{2S} \int\limits_{\mathbf{r}'=\mathbf{r}} \mathrm{d}\mathbf{r} \left(h_y^{01} + \sum_{s=1}^{3} B_s h_{sy}^{11} \right) (\rho^{\alpha}(\mathbf{B}|\mathbf{r},\mathbf{r}') - \rho^{\beta}(\mathbf{B}|\mathbf{r},\mathbf{r}')) \right] \Bigg|_{\mathbf{B}=0} . \qquad (2.171)$$

From the above discussion, we can rewrite (2.145) into:[43]

$$g_{xy} = \frac{2}{\alpha} \left[\frac{\partial}{\partial B_x} \int\limits_{\mathbf{r}'=\mathbf{r}} \mathrm{d}\mathbf{r} \left(h_y^{01} + \sum_{s=1}^{3} B_s h_{sy}^{11} \right) (\rho^{\alpha}(\mathbf{B}|\mathbf{r},\mathbf{r}') - \rho^{\beta}(\mathbf{B}|\mathbf{r},\mathbf{r}')) \right] \Bigg|_{\mathbf{B}=0} , \qquad (2.172)$$

with h_y^{01} and h_{sy}^{11} given by:

$$\begin{aligned}
h_y^{01} &= h_{\mathrm{SO},y} + h_{\mathrm{SOO},y} \\
&= \frac{\alpha^2 g'}{4} \left((\nabla_{\mathbf{r}'} V_{\mathrm{KS}}) \times \mathbf{p}_{\mathbf{r}'} \right)_y + h_{\mathrm{SOO},y} \; , \qquad (2.173) \\
h_{sy}^{11} &= h_{\mathrm{Z},sy} + h_{\mathrm{ZKE},sy} + h_{\mathrm{SO},sy}^{\mathrm{dia}} + h_{\mathrm{SOO},sy}^{\mathrm{dia}} \\
&= \frac{\alpha}{2} g_e \delta_{sy} - g_e \frac{\alpha^3}{4} p'^2 \delta_{sy} \\
&+ \frac{\alpha^3 g'}{8} \left((\nabla_{\mathbf{r}'} V_{\mathrm{KS}}) . \mathbf{r}' \delta_{sy} - (\nabla_{\mathbf{r}'} V_{\mathrm{KS}})_s r'_y \right) + h_{\mathrm{SOO},sy}^{\mathrm{dia}} \; , \qquad (2.174)
\end{aligned}$$

[43] Note that we assume a net electron spin equal to $\frac{1}{2}$.

with $p'^2 = -\nabla^2_{\mathbf{r}'}$. By expanding the perturbed electron density matrices $\rho(\mathbf{B}_x|\mathbf{r},\mathbf{r}')$ up to first order in B_x, we can carry out the derivation to the magnetic field, and after putting $\mathbf{B} = \mathbf{0}$, we obtain the following expressions for the different contributions to the g tensor (with the exception of the SOO terms):

$$g^{\mathrm{Z}}_{xy} = g_e \delta_{xy} \,, \tag{2.175}$$

$$\Delta g^{\mathrm{ZKE}}_{xy} = -\frac{\alpha^2 g_e}{2} \int\limits_{\mathbf{r}'=\mathbf{r}} \mathrm{d}\mathbf{r}\; p^2 \left[\rho^{\alpha}(\mathbf{r},\mathbf{r}') - \rho^{\beta}(\mathbf{r},\mathbf{r}'))\right] \delta_{xy} \,, \tag{2.176}$$

$$\Delta g^{\mathrm{SO}}_{xy} = \frac{\alpha g'}{2} \left[\int \mathrm{d}\mathbf{r}\; [\mathbf{j}^{\alpha}_{\mathrm{P},\mathbf{B}_x}(\mathbf{r}) - \mathbf{j}^{\beta}_{\mathrm{P},\mathbf{B}_x}(\mathbf{r})] \times \nabla V_{\mathrm{KS}}(\mathbf{r}) \right]_y \,, \tag{2.177}$$

$$\Delta g^{\mathrm{SO,dia}}_{xy} = \frac{\alpha g'}{2} \left[\int \mathrm{d}\mathbf{r}\; [\mathbf{j}^{\alpha}_{\mathrm{D},\mathbf{B}_x}(\mathbf{r}) - \mathbf{j}^{\beta}_{\mathrm{D},\mathbf{B}_x}(\mathbf{r})] \times \nabla V_{\mathrm{KS}}(\mathbf{r}) \right]_y \,, \tag{2.178}$$

where $\mathbf{j}^{\tau}_{\mathrm{D},\mathbf{B}_x}$ and $\mathbf{j}^{\tau}_{\mathrm{P},\mathbf{B}_x}$ denote respectively the diamagnetic (D) and the paramagnetic (P) component of $\mathbf{j}^{\tau}_{\mathbf{B}_x}$, the total induced current density in one spin channel up to first order in the external magnetic field $\mathbf{B}_x$. This will be shown in section 2.3.5. Consequently, the total SO component can be written as:

$$\Delta g^{\mathrm{SO}}_{xy} = \frac{\alpha g'}{2} \left[\int \mathrm{d}\mathbf{r}\; [\mathbf{j}^{\alpha}_{\mathbf{B}_x}(\mathbf{r}) - \mathbf{j}^{\beta}_{\mathbf{B}_x}(\mathbf{r})] \times \nabla V_{\mathrm{KS}}(\mathbf{r}) \right]_y \,. \tag{2.179}$$

Since V_{KS} differs for α and β electrons in the spin-polarized variant of Kohn-Sham-DFT, we can repeat the above discussion, now taking into account this distinction, to obtain:

$$\Delta g^{\mathrm{SO}}_{xy} = \frac{\alpha g'}{2} \left[\int \mathrm{d}\mathbf{r}\; \mathbf{j}^{\alpha}_{\mathbf{B}_x}(\mathbf{r}) \times \nabla V^{\alpha}_{\mathrm{KS}}(\mathbf{r}) - \mathbf{j}^{\beta}_{\mathbf{B}_x}(\mathbf{r}) \times \nabla V^{\beta}_{\mathrm{KS}}(\mathbf{r}) \right]_y \,. \tag{2.180}$$

Until now, we have not yet treated the H_{SOO} and $H^{\mathrm{dia}}_{\mathrm{SOO}}$ terms. The spin-other-orbit coupling term describes the screening of the external field $\mathbf{B}$ by the induced electronic current densities, as experienced by the unpaired electron. An approximative treatment for the SOO contribution was proposed by Pickard and Mauri:[6]

$$\Delta g_{xy}^{\mathrm{SOO}} = 2 \int \mathrm{d}\mathbf{r}\, B_{\mathbf{B}_x,y}(\mathbf{r})[\rho^{\alpha}(\mathbf{r}) - \rho^{\beta}(\mathbf{r})] \,, \tag{2.181}$$

where $\mathbf{B}_{\mathbf{B}_x}$ represents the magnetic field originating from the induced current density, generated by the homogeneous unitary magnetic field coinciding with the x axis:

$$\mathbf{B}_{\mathbf{B}_x}(\mathbf{r}) = \alpha \int \mathrm{d}\mathbf{r}' \, \frac{\mathbf{r}' - \mathbf{r}}{|\mathbf{r}' - \mathbf{r}|^3} \times \left[\left(\mathbf{j}^{\alpha}_{\mathbf{B}_x}(\mathbf{r}') + \mathbf{j}^{\beta}_{\mathbf{B}_x}(\mathbf{r}') \right) - \left(\mathbf{j}^{\alpha}_{\mathbf{B}_x}(\mathbf{r}') - \mathbf{j}^{\beta}_{\mathbf{B}_x}(\mathbf{r}') \right) \right] \,. \tag{2.182}$$

The total induced current density was corrected for self-interaction through substraction of $\mathbf{j}^{\alpha}_{\mathbf{B}_x} - \mathbf{j}^{\beta}_{\mathbf{B}_x}$, which is approximately the contribution to the current density of the unpaired electron.

Eventually, we obtain the following explicit expression for the g tensor:

$$g_{xy} = g^{\mathrm{Z}}_{xy} + \Delta g^{\mathrm{ZKE}}_{xy} + \Delta g^{\mathrm{SO}}_{xy} + \Delta g^{\mathrm{SOO}}_{xy} \,, \tag{2.183}$$

$$g^{\mathrm{Z}}_{xy} = g_e \delta_{xy} \,, \tag{2.184}$$

$$\Delta g^{\mathrm{ZKE}}_{xy} = -\alpha^2 g_e (T^{\alpha} - T^{\beta}) \delta_{xy} \,, \tag{2.185}$$

$$\Delta g^{\mathrm{SO}}_{xy} = \frac{\alpha g'}{2} \int \mathrm{d}\mathbf{r} \left[\mathbf{j}^{\alpha}_{\mathbf{B}_x}(\mathbf{r}) \times \nabla V^{\alpha}_{\mathrm{KS}}(\mathbf{r}) - \mathbf{j}^{\beta}_{\mathbf{B}_x}(\mathbf{r}) \times \nabla V^{\beta}_{\mathrm{KS}}(\mathbf{r}) \right]_y \,, \tag{2.186}$$

$$\Delta g^{\mathrm{SOO}}_{xy} = 2 \int \mathrm{d}\mathbf{r}\, B_{\mathbf{B}_x,y}(\mathbf{r})[\rho^{\alpha}(\mathbf{r}) - \rho^{\beta}(\mathbf{r})] \,, \tag{2.187}$$

where T^{τ} denotes the total unperturbed kinetic energy of the τ electrons:

$$T^{\tau} = -\frac{1}{2} \int_{\mathbf{r}'=\mathbf{r}} \mathrm{d}\mathbf{r} \nabla^2_{\mathbf{r}'} \rho^{\tau}(\mathbf{r}, \mathbf{r}') \,. \tag{2.188}$$

T^{τ}, $\nabla V^{\tau}_{\mathrm{KS}}$, and ρ^{τ} are already known (or can be calculated fairly easy) at the end of the self-consistent procedure of the Kohn-Sham-DFT scheme. The induced current densities $\mathbf{j}^{\tau}_{\mathbf{B}_x}$, and consequently the magnetic fields $\mathbf{B}_{\mathbf{B}_x}$, are a much greater problem. An ingenious approach for calculating these quantities in PBC simulations was elaborated by Sebastiani *et al*,[39, 40] and requires knowledge of the following concepts:

- Density functional perturbation theory, a technique for the determination of the first-order corrections to a set of one-particle orbitals as a result of an external magnetic field (sections 2.3.2 and 2.3.3).
- Wannier functions, an alternative representation of the solutions of a one-particle Schrödinger(-like) equation in a periodic potential (section 2.3.4).

The usefulness of these concepts will become apparent in section 2.3.5, where the method of Sebastiani *et al.* for the calculation of the induced current densities is discussed.

2.3.2 Density functional perturbation theory

The determination of the induced current densities $\mathbf{j}^{\tau}_{\mathbf{B}_x}$ and the induced magnetic fields $\mathbf{B}_{\mathbf{B}_x}$ requires the knowledge of the first-order corrections to a set of one-particle orbitals as a result of an external magnetic field. The Kohn-Sham one-particle orbitals will soon prove unsuitable for calculating these current densities in PBC simulations, which excludes (standard) perturbation theory as a viable option, and therefore we employ density functional perturbation theory (DFPT) [41–43] instead, a flexible variational technique, formulated in its general form by Putrino *et al.*[44]

In order take into account an external perturbation, a perturbation functional is added adiabatically to the energy functional E_{tot} (2.32):

$$E_{\text{tot+p}}\left[\{\psi_i\}\right] = E_{\text{tot}}\left[\{\psi_i\}\right] + \lambda E_{\text{p}}\left[\{\psi_i\}\right] \ . \tag{2.189}$$

Here, λ is a small ($0 \leq \lambda \leq 1$) perturbation parameter which represents the strength of the interaction with the static external field E_{p}. The new energy functional $E_{\text{tot+p}}$ will feature a new minimal value E, which we can expand in a power series of λ around the unperturbed minimal value $E^{(0)}$:

$$E = E^{(0)} + \lambda E^{(1)} + \lambda^2 E^{(2)} + \dots \ . \tag{2.190}$$

The orbitals which minimize $E_{\text{tot+p}}$ can also be expanded in the unperturbed set $\psi_i^{(0)}$:

$$\psi_i(\mathbf{r}) = \psi_i^{(0)}(\mathbf{r}) + \lambda\psi_i^{(1)}(\mathbf{r}) + \lambda^2\psi_i^{(2)}(\mathbf{r}) + \dots . \tag{2.191}$$

Up to first order, the charge density then equals:

$$\rho(\mathbf{r}) = \rho^{(0)}(\mathbf{r}) + \lambda\rho^{(1)}(\mathbf{r}) + \dots , \tag{2.192}$$

with:

$$\rho^{(1)}(\mathbf{r}) = \sum_i \psi_i^{(0)*}(\mathbf{r})\psi_i^{(1)}(\mathbf{r}) + \psi_i^{(1)*}(\mathbf{r})\psi_i^{(0)}(\mathbf{r}) . \tag{2.193}$$

We now formulate the variational (extremal) principle of the **$(2n+1)$ theorem**:[42]

> In general, when perturbation theory is applied to a quantity for which a variational principle holds, there also exists a variatonal principle for the even orders of that quantity in a power series expansion in the perturbation parameter λ.
>
> **Proof**
>
> Because of the minimal variational principle for the functional $X[\Phi]$, a trial wave function Φ which differs from the minimal wave function Φ_0 will always return a functional value higher or equal to X_0, the value of this functional for Φ_0. Moreover, under sufficient conditions of derivability, the difference between both values will be quadratic in the difference between the wave functions, and therefore there exists a fixed real number K for which it holds that:
>
> $$\forall\Phi, \;\; 0 \leq X[\Phi] - X_0 \leq K \left\|\Phi - \Phi_0\right\|^2 . \tag{2.194}$$
>
> Consider now that the functional $X_{(\lambda)}$ depends on a parameter λ. The wave functions which minimize this functional will then of course also depend on this parameter:

$$\forall \Phi, \;\; 0 \leq X_{(\lambda)}[\Phi] - X_0(\lambda) \leq K \left\| \Phi - \Phi_0(\lambda) \right\|^2 \; . \tag{2.195}$$

Then, we expand $\Phi_0(\lambda)$ in an infinite power series of λ around Φ_0:

$$\Phi_0(\lambda) = \sum_{i=0}^{\infty} \lambda^i \Phi_0^{(i)} \; , \tag{2.196}$$

and choose a trial wave function Φ, which already equals to the exact one $\Phi_0(\lambda)$ up to order λ^n,

$$\begin{aligned} \Phi(\lambda) &= \sum_{i=0}^{n} \lambda^i \Phi_0^{(i)} + \lambda^{n+1} \delta\Phi \\ &= \Phi_0(\lambda) - \lambda^{n+1} \left(\sum_{i=n+1}^{\infty} \lambda^{i-n-1} \Phi_0^{(i)} - \delta\Phi \right) \; . \end{aligned} \tag{2.197}$$

Introducing the above expansions of $\Phi_0(\lambda)$ and $\Phi(\lambda)$ in (2.195), we obtain:

$$\begin{aligned} 0 &\leq X_{(\lambda)} \left[\sum_{i=0}^{n} \lambda^i \Phi_0^{(i)} + \lambda^{n+1} \delta\Phi \right] - X_0(\lambda) \\ &\leq K \lambda^{2n+2} \left\| \sum_{i=n+1}^{\infty} \lambda^{i-n-1} \Phi_0^{(i)} - \delta\Phi \right\|^2 \; , \end{aligned} \tag{2.198}$$

an equation that is valid for all $\delta\Phi$. If $\delta\Phi$ is chosen to be equal to zero, the previous expression simplifies to:

$$\begin{aligned} 0 &\leq X_{(\lambda)} \left[\sum_{i=0}^{n} \lambda^i \Phi_0^{(i)} \right] - X_0(\lambda) \\ &\leq K \lambda^{2n+2} \left\| \sum_{i=0}^{\infty} \lambda^i \Phi_0^{(i+n+1)} \right\|^2 \; . \end{aligned} \tag{2.199}$$

Hence, the knowledge of the expansion in a power series of $\Phi_0(\lambda)$ up to order λ^n returns an error in the evalution of the functional of order λ^{2n+2}.

Let's consider (2.198) again, but now only for the terms of order λ^{2n+2}, because we have just shown that the expansion terms up to order λ^{2n+1} vanish anyway. Therefore, we are left with:

$$\begin{aligned} 0 &\leq \left\{ X_{(\lambda)} \left[\sum_{i=0}^{n} \lambda^i \Phi_0^{(i)} + \lambda^{n+1} \delta\Phi \right] \right\}^{2n+2} - X_0^{2n+2}(\lambda) \\ &\leq K \left\| \Phi_0^{(n+1)} - \delta\Phi \right\|^2 . \end{aligned} \tag{2.200}$$

This is the variational principle for the $(2n+2)$th-order term of the functional in λ when the wave function is already known up to order λ^n. Because n is a dummy argument, we can shift n to $n-1$ and write:

$$\begin{aligned} 0 &\leq \left\{ X_{(\lambda)} \left[\sum_{i=0}^{n-1} \lambda^i \Phi_0^{(i)} + \lambda^{n} \delta\Phi \right] \right\}^{(2n)} - X_0^{(2n)}(\lambda) \\ &\leq K \left\| \Phi_0^{(n)} - \delta\Phi \right\|^2 . \end{aligned} \tag{2.201}$$

Thus, at the minimum $\{...\}^{(2n)} \rightarrow X_0^{(2n)}$, the trial nth-order wave function is equal to $\Phi_0^{(n)}$.

In the case of a constrained-extremum problem, i.e. when an energy functional $X[\Phi]$ needs to be minimized under the boundary condition $C[\Phi]$, the Lagrangian equals:

$$Z[\Phi] = X[\Phi] - \Lambda C[\Phi] . \tag{2.202}$$

Using a similar reasoning as before, we obtain:

$$\begin{aligned} 0 &\leq \left\{ Z_{(\lambda)} \left[\sum_{i=0}^{n-1} \lambda^i \Phi_0^{(i)} + \lambda^n \delta\Phi \right] \right\}^{(2n)} - Z_0^{(2n)}(\lambda) \\ &\leq K \left\| \Phi_0^{(n)} - \delta\Phi \right\|^2 . \end{aligned} \tag{2.203}$$

The application of the variational principle of the $(2n+1)$ theorem to the energy functional $E_{\text{tot+p}}$ from (2.189), allows us to compute the first-order corrections $\psi_i^{(1)}$ on the unperturbed orbitals through minimization of the second-order component of $E_{\text{tot+p}}$ in λ:[44]

$$\begin{aligned} E_{\text{tot+p}}^{(2)} &= \frac{1}{2} \int \mathrm{d}\mathbf{r}\mathrm{d}\mathbf{r}' \rho^{(1)}(\mathbf{r}) \frac{\partial (V_{\text{H}}(\mathbf{r}) + V_{\text{xc}}(\mathbf{r}))}{\partial \rho(\mathbf{r}')} \rho^{(1)}(\mathbf{r}') \\ &+ \sum_{i,j} \int \mathrm{d}\mathbf{r} \psi_j^{(1)*}(\mathbf{r}) \left(H_{\text{KS}}(\mathbf{r}) \delta_{ij} - \int \mathrm{d}\mathbf{r}' \psi_i^{(0)*}(\mathbf{r}') H_{\text{KS}}(\mathbf{r}') \psi_j^{(0)}(\mathbf{r}') \right) \psi_i^{(1)}(\mathbf{r}) \\ &+ \sum_j \int \mathrm{d}\mathbf{r} \psi_j^{(1)*}(\mathbf{r}) \frac{\partial E_{\text{p}}}{\partial \psi_j^{(0)*}(\mathbf{r})} + \frac{\partial E_{\text{p}}}{\partial \psi_j^{(0)}(\mathbf{r})} \psi_j^{(1)}(\mathbf{r}) , \end{aligned} \tag{2.204}$$

where it was taken into account that:[45]

$$\frac{\partial \left[E_{\text{tot}} - \sum_i \epsilon_i \left(\int \mathrm{d}\mathbf{r} \psi_i^{(0)*}(\mathbf{r}) \psi_i^{(0)}(\mathbf{r}) - 1 \right) \right]}{\partial \psi_i^{(0)*}(\mathbf{r})} = 0 , \qquad \forall i . \tag{2.205}$$

Up to first order in λ, the orthonormality conditions for the orbitals (2.191) result into:

$$\int \mathrm{d}\mathbf{r} \left(\psi_i^{(0)*}(\mathbf{r}) \psi_j^{(1)}(\mathbf{r}) + \psi_i^{(1)*}(\mathbf{r}) \psi_j^{(0)}(\mathbf{r}) \right) = 0 , \qquad \forall i, j . \tag{2.206}$$

These conditions will be replaced by the following more stringent conditions:

[44] Note that we assume a local KS Hamiltonian H_{KS}. When H_{KS} contains a non-local operator, such as for example when Goedecker pseudopotentials are used), the equations become – at least in the coordinate representation – slightly more complicated.

[45] See (2.34).

$$\int \mathrm{d}\mathbf{r}\psi_i^{(0)*}(\mathbf{r})\psi_j^{(1)}(\mathbf{r}) = 0, \qquad \forall i,j\ , \tag{2.207}$$

which automically impose the conservation of the the total charge q of the system, because the first-order contribution $q^{(1)}$ vanishes:

$$q^{(1)} = \int \mathrm{d}\mathbf{r}\rho^{(1)} = 0\ . \tag{2.208}$$

The conditions (2.207) can be imposed through a Lagrange multiplicator, and the total Lagrangian $\mathcal{L}$ becomes:

$$\mathcal{L} = E^{(2)}_{\mathrm{tot+p}} - \sum_{i,j}\Lambda_{ij}\int \mathrm{d}\mathbf{r}\psi_i^{(0)*}(\mathbf{r})\psi_j^{(1)}(\mathbf{r})\ . \tag{2.209}$$

2.3.3 Magnetic DFPT

A magnetic field is introduced in the Hamiltonian of a system through the minimal coupling principle (see section 2.2.1):

$$\mathbf{p} \rightarrow \boldsymbol{\pi} = \mathbf{p} + \alpha\mathbf{A}(\mathbf{r})\ , \tag{2.210}$$

with $\mathbf{A}$ the vector potential of the magnetic field. The one-electron Hamiltonian in the presence of a potential V becomes:

$$H = \frac{1}{2}\left(\mathbf{p} + \alpha\mathbf{A}(\mathbf{r})\right)^2 + V(\mathbf{r})\ . \tag{2.211}$$

For a constant magnetic field $\mathbf{B}$, $\mathbf{A}$ is linear in $\mathbf{B}$,

$$\mathbf{A}(\mathbf{r}) = -\frac{1}{2}(\mathbf{r} - \mathbf{R}_\mathrm{g}) \times \mathbf{B}\ , \tag{2.212}$$

with $\mathbf{R}_\mathrm{g}$ the gauge origin (see below in section 2.3.5), the above Hamiltonian will have operator terms of first and second order in the magnetic field:

$$H^{(1)} = \frac{\alpha}{2}(\mathbf{p}.\mathbf{A}(\mathbf{r}) + \mathbf{A}(\mathbf{r}).\mathbf{p}) \,, \tag{2.213}$$

$$H^{(2)} = \frac{\alpha^2}{2}\mathbf{A}(\mathbf{r}).\mathbf{A}(\mathbf{r}) \,. \tag{2.214}$$

The second-order term $H^{(2)}$ is not important for the calculation of the g tensor (see the discussion in section 2.2.4). Moreover, we note that the matrix elements of $H^{(1)}$ remain strictly imaginary in the coordinate representation,

$$\langle \mathbf{r}| H^{(1)} |\mathbf{r}'\rangle = \frac{i\alpha}{2}\delta^3(\mathbf{r}-\mathbf{r}') \left((\mathbf{r}-\mathbf{R}_\mathrm{g}) \times \mathbf{B}\right).\nabla \,, \tag{2.215}$$

therefore it follows from i) the (necessarily) real energy functional $E^{(2)}_{\mathrm{tot+p}}$ (2.204) and ii) the choice for real unperturbed obitals,[46] that the first-order corrections $\psi^{(1)}_i$ will be strictly imaginary as well:

$$\Re\psi^{(1)}_i(\mathbf{r}) = 0 \,, \tag{2.216}$$

where $\Re$ selects the real part of $\psi^{(1)}_i$. Consequently, the first-order density $\rho^{(1)}$ from (2.193) and the boundary conditions from (2.209) vanish exactly, and therefore the Lagrangian $\mathcal{L}$ from (2.209) simplifies to:[47]

$$\begin{aligned}\mathcal{L} &= \sum_{i,j}\int \mathrm{d}\mathbf{r}\psi^{(1)*}_j(\mathbf{r}) \left(H_{\mathrm{KS}}(\mathbf{r})\delta_{ij} - \int \mathrm{d}\mathbf{r}'\psi^{(0)*}_i(\mathbf{r}')H_{\mathrm{KS}}(\mathbf{r}')\psi^{(0)}_j(\mathbf{r}')\right)\psi^{(1)}_i(\mathbf{r}) \\ &+ \sum_j\int \mathrm{d}\mathbf{r}\psi^{(1)*}_j(\mathbf{r})H^{(1)}(\mathbf{r})\psi^{(0)}_j(\mathbf{r}') + \sum_j\int \mathrm{d}\mathbf{r}\psi^{(0)*}_j H^{(1)}(\mathbf{r})\psi^{(1)}_j(\mathbf{r}) \,, \end{aligned} \tag{2.217}$$

with $H^{(1)}$ equal to:

[46] This choice is allowed in absence of an external magnetic field and within the Γ-point approximation.

[47] Note that $\psi^{(0)}_i$ do not (necessarily) represent the KS orbitals (see the next section), therefore the matrix A with matrix elements $A_{ij} = \int \mathrm{d}\mathbf{r}'\psi^{(0)*}_i(\mathbf{r}')H_{\mathrm{KS}}(\mathbf{r}')\psi^{(0)}_j(\mathbf{r}')$ is not (necessarily) diagonal.

$$H^{(1)}(\mathbf{r}) = \frac{i\alpha}{2}\left((\mathbf{r}-\mathbf{R}_{\mathrm{g}})\times\mathbf{B}\right).\nabla\ . \tag{2.218}$$

Imposing the stationary conditions,

$$\frac{\partial\mathcal{L}}{\partial\psi_j^{(1)*}(\mathbf{r})} = 0\ , \qquad \forall i\ , \tag{2.219}$$

we obtain an inhomogeneous set of coupled equations for $\psi_i^{(1)}$:

$$-\sum_i\left(H_{\mathrm{KS}}(\mathbf{r})\delta_{ij} - \int \mathrm{d}\mathbf{r}'\psi_i^{(0)*}(\mathbf{r}')H_{\mathrm{KS}}(\mathbf{r}')\psi_j^{(0)}(\mathbf{r}')\right)\psi_i^{(1)}(\mathbf{r}) = H^{(1)}(\mathbf{r})\psi_j^{(0)}(\mathbf{r})\ . \tag{2.220}$$

These equations can be solved using Green's function techniques or directly through minimization of the gradients.

2.3.4 Wannier functions

The solutions of a one-particle Schrödinger equation in a periodic potential can be expressed (see section 2.1.3) as a product of a Bloch function and the wave function of a free electron. Bloch functions feature the same periodicity as this potential, and are infinitely repeated. An alternative representation of these solutions in terms of localized functions, called the *Wannier* functions, was proposed in 1937 by Swiss physicist Gregory Wannier.[45]

The Wannier function $\psi_{m,\mathbf{R}}$ corresponding to the band index m and the particular lattice cell determined by the lattice vector $\mathbf{R}$, is obtained from the solutions $\psi_{m,\mathbf{k}}$ (2.53) by:

$$\psi_{m,\mathbf{R}}(\mathbf{r}) = \frac{V}{(2\pi)^3}\int_{\mathrm{BZ}}\mathrm{d}\mathbf{k}\mathrm{e}^{-i\mathbf{k}.\mathbf{R}}\psi_{m,\mathbf{k}}(\mathbf{r})\ . \tag{2.221}$$

It is straightforward to show that the Wannier functions represent an orthonormal set, and that two Wannier functions $\psi_{m,\mathbf{R}}$ and $\psi_{m,\mathbf{R}'}$ can be transformed

into one another by means of a translation over a lattice vector $\mathbf{R} - \mathbf{R}'$.

Wannier functions are not uniquely defined by (2.221). Within one single band, this is the result of the arbitrariness of the solutions $\psi_{m,\mathbf{k}}$ to within an arbitrary phase $\vartheta_m(\mathbf{k})$. $\vartheta_m(\mathbf{k})$ is periodic in reciprocal space, and is not determined by the Schrödinger equation:

$$\psi_{m,\mathbf{k}}(\mathbf{r}) \rightarrow \mathrm{e}^{i\vartheta_m(\mathbf{k})}\psi_{m,\mathbf{k}}(\mathbf{r}) \ . \tag{2.222}$$

This type of arbitrariness propagates further into the Wannier function.

As a result of the invariance of the energy functional E_{tot} (2.32) under a unitary transformation in the subspace of the n occupied solutions $\psi_{m,\mathbf{k}}$ corresponding with a wave function $\mathbf{k}$, the arbitrariness is even more general:

$$\psi_{m',\mathbf{k}}(\mathbf{r}) \rightarrow \sum_m U^{(\mathbf{k})}_{m'm}\psi_{m,\mathbf{k}}(\mathbf{r}) \ , \tag{2.223}$$

with $U^{(\mathbf{k})}$ a unitary $(n \times n)$ matrix.

We will now exploit (2.223) to define maximally localized Wannier functions (MLWF). MLWFs feature an exponential decay in the case of a non-conductive material,[46] a property which will be used in the next section to tackle the problem of the position operator. The localization of a function can be quantified through the spread functional $\Delta^{(2)}$:

$$\Delta^{(2)} = \langle\psi|\, r^2 \,|\psi\rangle - \langle\psi|\, r \,|\psi\rangle^2 = \left\langle r^2 \right\rangle - \langle r\rangle^2 \ . \tag{2.224}$$

The localization procedure from which the MLWFs are obtained should minimize the spread functional of the entire system:

$$\Delta^{(2)}_{\mathrm{tot}} = \sum_i \left\langle r^2 \right\rangle_i - \langle r\rangle_i^2 \ . \tag{2.225}$$

In the Γ-point approximation (see 2.1.3), the transformation to MLWFs is nothing more than a unitary transformation within the subspace of occupied orbitals $\psi_{m,\mathbf{k}=\mathbf{0}}$.

2.3.5 Calculation of the induced current density

For notational accuracy, we will distinguish (in this section only) between a position operator $\mathbf{r}$ and a position variable $\tilde{\mathbf{r}}$.

In general, the current density is obtained as the expectation value of the current operator in the total electronic state:

$$\mathbf{j}(\tilde{\mathbf{r}}) = -\frac{1}{2} \langle \Psi | \left[\boldsymbol{\pi} | \tilde{\mathbf{r}} \rangle \langle \tilde{\mathbf{r}} | + | \tilde{\mathbf{r}} \rangle \langle \tilde{\mathbf{r}} | \boldsymbol{\pi} \right] | \Psi \rangle \ . \tag{2.226}$$

The current density originating from n (non-interacting) one-electron states ψ_i, such as for example the Kohn-Sham eigenstates, equals the sum of the current densities from each electron separately:

$$\mathbf{j}(\tilde{\mathbf{r}}) = -\frac{1}{2} \sum_i \langle \psi_i | \left[\boldsymbol{\pi} | \tilde{\mathbf{r}} \rangle \langle \tilde{\mathbf{r}} | + | \tilde{\mathbf{r}} \rangle \langle \tilde{\mathbf{r}} | \boldsymbol{\pi} \right] | \psi_i \rangle \ . \tag{2.227}$$

It is now assumed that (2.227) represents a good approximation for (2.226). If we develop the current density in a power series of the magnetic field, then we find the zeroth-order term to be:

$$\begin{aligned} \mathbf{j}^{(0)}(\tilde{\mathbf{r}}) &= -\frac{1}{2} \sum_i \left\langle \psi_i^{(0)} \right| \left[\mathbf{p} | \tilde{\mathbf{r}} \rangle \langle \tilde{\mathbf{r}} | + | \tilde{\mathbf{r}} \rangle \langle \tilde{\mathbf{r}} | \mathbf{p} \right] \left| \psi_i^{(0)} \right\rangle \\ &= -\frac{1}{2} \sum_i \left[\left(i \nabla \psi_i^{(0)*}(\tilde{\mathbf{r}}) \right) \psi_i^{(0)}(\tilde{\mathbf{r}}) + \psi_i^{(0)*}(\tilde{\mathbf{r}}) \left(-i \nabla \psi_i^{(0)}(\tilde{\mathbf{r}}) \right) \right] \\ &= 0 \ . \end{aligned} \tag{2.228}$$

The last identity in the above equation is based on the fact that we have chosen the unperturbed orbitals $\psi^{(0)}$ as real functions (see section 2.3.3).

The first-order component of the current density consists of a diamagnetic and a paramagnetic component:

$$\mathbf{j}^{(1)}(\tilde{\mathbf{r}}) = \mathbf{j}_{\mathrm{D}}^{(1)}(\tilde{\mathbf{r}}) + \mathbf{j}_{\mathrm{P}}^{(1)}(\tilde{\mathbf{r}}) \ , \tag{2.229}$$

with:

$$\mathbf{j}_{\mathrm{D}}^{(1)}(\tilde{\mathbf{r}}) = -\alpha \mathbf{A}(\tilde{\mathbf{r}}) \sum_i \left| \psi_i^{(0)}(\tilde{\mathbf{r}}) \right|^2 , \tag{2.230}$$

$$\begin{aligned} \mathbf{j}_{\mathrm{P}}^{(1)}(\tilde{\mathbf{r}}) &= -\frac{i}{2} \sum_i \left[\left(\nabla \psi_i^{(0)*}(\tilde{\mathbf{r}}) \right) \psi_i^{(1)}(\tilde{\mathbf{r}}) - \psi_i^{(0)*}(\tilde{\mathbf{r}}) \left(\nabla \psi_i^{(1)}(\tilde{\mathbf{r}}) \right) \right. \\ &+ \left. \left(\nabla \psi_i^{(1)*}(\tilde{\mathbf{r}}) \right) \psi_i^{(0)}(\tilde{\mathbf{r}}) - \psi_i^{(1)*}(\tilde{\mathbf{r}}) \left(\nabla \psi_i^{(0)}(\tilde{\mathbf{r}}) \right) \right] . \end{aligned} \tag{2.231}$$

For real $\psi_i^{(0)}$ and imaginary $\psi_i^{(1)}$, we can further simplify $\mathbf{j}^{(1)}$ to:

$$\begin{aligned} \mathbf{j}^{(1)}(\tilde{\mathbf{r}}) &= -\alpha \mathbf{A}(\tilde{\mathbf{r}}) \sum_i \left| \psi_i^{(0)}(\tilde{\mathbf{r}}) \right|^2 \\ &- i \sum_i \left[\left(\nabla \psi_i^{(0)}(\tilde{\mathbf{r}}) \right) \psi_i^{(1)}(\tilde{\mathbf{r}}) - \psi_i^{(0)}(\tilde{\mathbf{r}}) \left(\nabla \psi_i^{(1)}(\tilde{\mathbf{r}}) \right) \right] . \end{aligned} \tag{2.232}$$

Due to (2.228), this current density represents the total current up to first order in the magnetic field. Similar definitions apply for the current densities in each spin channel. The previous elaboration also explains the transition $\mathbf{j}_{\mathbf{B}_x}^{\tau} = \mathbf{j}_{\mathrm{D},\mathbf{B}_x}^{\tau} + \mathbf{j}_{\mathrm{P},\mathbf{B}_x}^{\tau}$ that was made in going from (2.177) and (2.178) to (2.179).

Continuous set of gauge transformations

The vector potential $\mathbf{A}$ corresponding with a magnetic field is only an auxiliary quantity, without a direct physical interpretation. A typical choice for the vector potential $\mathbf{A}$ for a homogeneous magnetic field $\mathbf{B}$ is:

$$\mathbf{A}(\mathbf{r}) = -\frac{1}{2} \mathbf{r} \times \mathbf{B} . \tag{2.233}$$

However, the following vector potential:

$$\mathbf{A}(\mathbf{r}) = -\frac{1}{2} (\mathbf{r} - \mathbf{R}_{\mathrm{g}}) \times \mathbf{B} , \tag{2.234}$$

is also a valid vector potential, since holds in both cases that:

$$\mathbf{B}(\mathbf{r}) = \nabla \times \mathbf{A}(\mathbf{r}) . \tag{2.235}$$

In (2.234), the origin of the coordinate system changes to $\mathbf{R}_\mathrm{g}$. Therefore, $\mathbf{R}_\mathrm{g}$ is also referred to as the *gauge origin* of the vector potential. It is a cyclic variable, a term with which we express that it has no influence on the physicial observables. Thus, the calculation of the current density (2.232) should be independent of the choice for the gauge origin. In practice, the choice for the gauge origin can have a rather significant effect, because of numerical issues: $\mathbf{j}_\mathrm{D}^{(1)}$ and $\mathbf{j}_\mathrm{P}^{(1)}$ both depend on the gauge origin, whereas the total current density $\mathbf{j}^{(1)}$ should be gauge invariant. Since $\mathbf{A}$ is linear in the gauge origin $\mathbf{R}_\mathrm{g}$, this also applies to the diamagnetic current density $\mathbf{j}_\mathrm{D}^{(1)}$ (2.230), and therefore $\mathbf{j}_\mathrm{P}^{(1)}$ should compensate for this in order to satisfy the invariance for the total current density. At large distances $\left|\tilde{\mathbf{r}} - \mathbf{R}_\mathrm{g}\right|$, the total current density $\mathbf{j}^{(1)}$ is then computed from the *small* difference between two large terms. In a computer simulation with a (necessarily) finite basis set, both components will likely feature error flags that are substantial in comparison with the total current density, and hence the invariance will no longer be reproducable.

In order to circumvent this problem, different approaches were proposed. In this work, we will mainly use the continuous set of gauge transformations (CSGT) method,[47] in which the gauge origin depends on the position (in coordinate space) for which the current density must be calculated. For every point $\tilde{\mathbf{r}}$ in coordinate space, the gauge origin $\mathbf{R}_\mathrm{g}$ is set equal to $\tilde{\mathbf{r}}$. This approach assures that the diamagnetic component of the current density vanishes exactly:

$$\mathbf{j}_\mathrm{D}^{(1)}(\tilde{\mathbf{r}}) = 0\,, \tag{2.236}$$

and effectively removes the numerical issues.

Translational freedom for the origin for every individual orbital

The current density in (2.232), which is composed only of a paramagnetic component in the CSGT method, remains invariant under arbitrary orbital-specific translations of the origin of the coordinate system. This will be shown using the Green's function of the inhomogeneous set of coupled equations for $\psi_i^{(1)}$ (2.220):

$$G_{ij}(\tilde{\mathbf{r}},\tilde{\mathbf{r}}') = -\left(H_{\mathrm{KS}}(\mathbf{r})\delta_{ij} - \int \mathrm{d}\tilde{\mathbf{r}}''\psi_i^{(0)*}(\tilde{\mathbf{r}}'')H_{\mathrm{KS}}(\mathbf{r}'')\psi_j^{(0)}(\tilde{\mathbf{r}}'')\right)^{-1} . \quad (2.237)$$

For an arbitrary perturbation operator O, we can formally write the solutions of (2.220) as:

$$\psi_i^{(O)}(\tilde{\mathbf{r}}) = \sum_j \int \mathrm{d}\tilde{\mathbf{r}}' G_{ij}(\tilde{\mathbf{r}},\tilde{\mathbf{r}}')O(\mathbf{r}')\psi_j^{(0)}(\tilde{\mathbf{r}}') . \quad (2.238)$$

From the above formulation, based on linearity considerations, we infer that the solutions of (2.220) for the perturbation operator defined in (2.218) which, for a constant magnetic field, amounts to:

$$H^{(1)} = -\frac{\alpha}{2}\left((\mathbf{r}-\mathbf{R}_{\mathrm{g}})\times\mathbf{p}\right).\mathbf{B} , \quad (2.239)$$

can be computed from the sum of the solutions (2.238) for the perturbation operators $O_1 = -\frac{\alpha}{2}(\mathbf{r}\times\mathbf{p}).\mathbf{B}$ and $O_2 = -\frac{\alpha}{2}\left(\mathbf{R}_{\mathrm{g}}\times\mathbf{p}\right).\mathbf{B}$:

$$\begin{aligned}\psi_i^{(1)}(\tilde{\mathbf{r}}) &= -\frac{\alpha}{2}\sum_j\left(\int \mathrm{d}\tilde{\mathbf{r}}' G_{ij}(\tilde{\mathbf{r}},\tilde{\mathbf{r}}')\left(\mathbf{r}'\times\mathbf{p}'\right)\psi_j^{(0)}(\tilde{\mathbf{r}}')\right. \\ &- \left.\int \mathrm{d}\tilde{\mathbf{r}}' G_{ij}(\tilde{\mathbf{r}},\tilde{\mathbf{r}}')\left(\mathbf{R}_{\mathrm{g}}\times\mathbf{p}'\right)\psi_j^{(0)}(\tilde{\mathbf{r}}')\right).\mathbf{B} . \quad (2.240)\end{aligned}$$

Moreover, it becomes clear that the current density remains invariant under arbitrary orbital-specific translations $\mathbf{d}_j$ of the origin of the position operator $\mathbf{r}$ and the gauge origin $\mathbf{R}_{\mathrm{g}} = \tilde{\mathbf{r}}$:

$$\begin{aligned}\psi_i^{(1)}(\tilde{\mathbf{r}}) &= -\frac{\alpha}{2}\sum_j\left(\int \mathrm{d}\tilde{\mathbf{r}}' G_{ij}(\tilde{\mathbf{r}},\tilde{\mathbf{r}}')\left((\mathbf{r}'-\mathbf{d}_j)\times\mathbf{p}'\right)\psi_j^{(0)}(\tilde{\mathbf{r}}')\right. \\ &- \left.\int \mathrm{d}\tilde{\mathbf{r}}' G_{ij}(\tilde{\mathbf{r}},\tilde{\mathbf{r}}')\left((\tilde{\mathbf{r}}-\mathbf{d}_j)\times\mathbf{p}'\right)\psi_j^{(0)}(\tilde{\mathbf{r}}')\right).\mathbf{B} . \quad (2.241)\end{aligned}$$

The first perturbation operator in (2.241) requires one evaluation of (2.220).[48] The second perturbation operator depends on the position in coordinate

[48] From the solution of (2.220), we obtain the corrections for all i.

space for which the current density is calculated, and consequently requires a solution of (2.220) for every position in coordinate space. The computational cost of one such calculation is of the same order of magnitude as the self-consistent procedure of the Kohn-Sham-DFT scheme (see section 2.1.2) and thus, the evaluation of the second perturbation operator should be performed in a slightly different way. Therefore, the second part of (2.241) is further elaborated into:

$$\begin{aligned} & \frac{\alpha}{2}\sum_j \left(\int \mathrm{d}\tilde{\mathbf{r}}' G_{ij}(\tilde{\mathbf{r}},\tilde{\mathbf{r}}') \left((\tilde{\mathbf{r}} - \mathbf{d}_j) \times \mathbf{p}' \right) \psi_j^{(0)}(\tilde{\mathbf{r}}') \right) .\mathbf{B} \\ = \quad & \frac{\alpha}{2}\sum_j \left((\tilde{\mathbf{r}} - \mathbf{d}_i) \times \int \mathrm{d}\tilde{\mathbf{r}}' G_{ij}(\tilde{\mathbf{r}},\tilde{\mathbf{r}}') \mathbf{p}' \psi_j^{(0)}(\tilde{\mathbf{r}}') \right. \\ + \quad & \left. \int \mathrm{d}\tilde{\mathbf{r}}' G_{ij}(\tilde{\mathbf{r}},\tilde{\mathbf{r}}') \left((\mathbf{d}_i - \mathbf{d}_j) \times \mathbf{p}' \right) \psi_j^{(0)}(\tilde{\mathbf{r}}') \right) .\mathbf{B} \, . \end{aligned} \tag{2.242}$$

The first and second perturbation operator in the above equation require only respectively 1 and n evaluations of (2.220), with n the number of electrons. Moreover, it is possible to facilitate the calculation of the contribution to $\psi_j^{(1)}$ from the second part of (2.242) from the one to $\psi_i^{(1)}$, on the condition that $\mathbf{d}_i \approx \mathbf{d}_j$.[48, 49] If $\mathbf{d}_i = \mathbf{d}_j$, the contribution to $\psi_j^{(1)}$ can even be extracted directly from the one to $\psi_i^{(1)}$, i.e. without an additional evaluation of (2.220).

The problem of the position operator in PBC

The position operator $\mathbf{r}$ operating on a (one-particle) wave function in the coordinate representation $\psi(\tilde{\mathbf{r}})$ results in the multiplication of this wave function with the position variable $\tilde{\mathbf{r}}$. When periodic boundary conditions are imposed, the Hilbert space of the one-particle wave functions $\psi(\tilde{\mathbf{r}})$ is determined by the condition $\psi(\tilde{\mathbf{r}} + \mathbf{L}) = \psi(\tilde{\mathbf{r}})$. A valid operator transforms each vector (in casu: the wave function) of a given Hilbert space to a vector corresponding to the same Hilbert space. The multiplicative position operator clearly is not a valid operator here, since the cartesian components of $\tilde{\mathbf{r}}\psi(\tilde{\mathbf{r}})$ are no longer periodic. This constitutes a problem, since the perturbation operator $(\mathbf{r} - \mathbf{d}_j) \times \mathbf{p}$ from (2.241) contains the position operator.

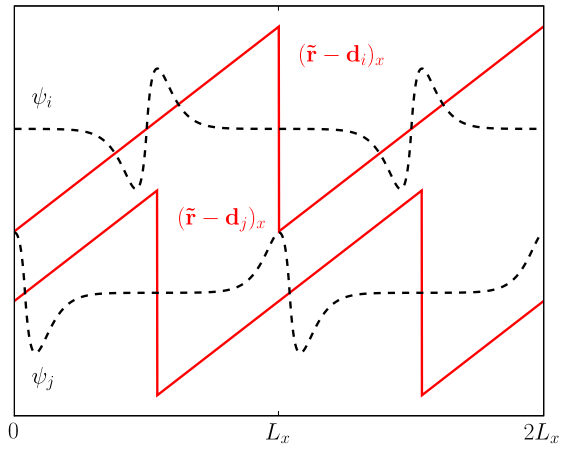

Figure 2.3: Two MLWFs ψ_i and ψ_j with their corresponding position operator expectation values (in one dimension).

The solution for this problem involves a series of procedures, some of these procedures have already been discussed in the previous sections.

First, the KS orbitals are transformed into MLWFs. For a non-conducting material, these functions feature an exponential decay. When the simulation cell is then chosen such that the dimensions remain greater than the decay length, (the density of) each MLWF will only be significant in a limited area of the simulation cell, and will practically cancel anywhere else. This remains true even after the operation of the semi-local operator $\mathbf{p} = -i\nabla$.

The next step consists of assigning to each MLWF an individual virtual cell with the same dimensions $L_x \times L_y \times L_z$ as the simulation cell. This virtual cell is chosen such that the geometrical center coincides with the Wannier center, this is the charge center of the corresponding MLWF. Then we redefine the position operator $\mathbf{r}$ in such a way that its expectation value $\tilde{\mathbf{r}}$ goes linearly from $-L_i/2$ to $+L_i/2$ ($i = x, y, z$) within each virtual cell and in each cartesian component.

In other words, we use the translational freedom (see the preceding section) to set the origin $\mathbf{d}_j$ of the coordinate system at the corresponding Wannier center for every individual MLWF j from (2.241). At the boundaries of each virtual cell the expectation value switches back from $+L_i/2$ to $-L_i/2$, thus

creating (in every cartesian component) a sawtooth-shaped profile. In this way, the position operator obeys the periodic boundary conditions, and becomes a valid operator. The behavior at the boundaries of the virtual cell is of little importance, since the dimensions of the simulation cell were chosen such that (the density of) the MLWF is zero there. This definition of the position operator is illustrated in Figure 2.3.

Here, an important practical limitation for the above technique arises: in some materials, such as metals and other conductors, the decay length of the MLWFs is so large that the dimensions of the simulation cell would far exceed today's computational capabilities.

When the dimensions of the simulation cell are much larger than those of the MLWFs, we can choose just one single origin ($\mathbf{d}_i = \mathbf{d}_j$) for the coordinate system of a group of MLWFs with nearby Wannier centers, which facilitates the computation of the second perturbation operator in (2.242) (see the preceding section). When the dimensions of the MLWFs do not exceed $L_x/2 \times L_y/2 \times L_z/2$,[49] it is straightforward to prove that for an arbitrary distribution of the Wannier centers, no more than 8 calculations of (2.220) are needed to fully determine all the contributions from the second perturbation operator in (2.242). In this case, the scaling behavior lowers by one order.

The problem of the definition of distances in PBC

The definition of $(\mathbf{d}_i - \mathbf{d}_j)$ in (2.242) also requires some attention. In a PBC simulation, distances are only defined up to an arbitrary lattice vector $\mathbf{L_a} = a\mathbf{L}_x + b\mathbf{L}_y + c\mathbf{L}_z$, where $\mathbf{a}$ denotes the vector of integral numbers a, b, c. We choose to retain only the lattice vector $\mathbf{L_a}$ which minimizes the distance $\left|\mathbf{d}_i - \mathbf{d}_j + \mathbf{L_a}\right|$, this is the *minimal image* convention, because:

1. both $(\mathbf{d}_i - \mathbf{d}_j)$ and $\mathbf{p}$ represent (semi-)local operators,
2. the Green's function $G_{ij}(\tilde{\mathbf{r}}, \tilde{\mathbf{r}}')$ is only significant for *nearby* positions $\tilde{\mathbf{r}}$ and $\tilde{\mathbf{r}}'$ in space, while every MLWF is by construction strongly localized around its corresponding Wannier center.

[49] Expressed in a different way: when the simulation cell is chosen such that the dimensions of the MLWFs do not exceed $L_x/2 \times L_y/2 \times L_z/2$.

2.3.6 The g tensor in CPMD: implementation and implications

CPMD employs a pure plane-wave basis set, therefore it requires the use of the PSP approximation. In the PSP approximation, the core electrons are no longer explicitly taken into account in the many-body problem, and the wave functions of the valence electrons have an incorrect shape close to the atomic nuclei. These effects seriously limit the applicability of our method.

In most cases, the missing core electrons only have a subordinate effect on the calculation of the g tensor, since the g tensor is essentially obtained from the substraction of spin-up and spin-down components [see (2.185)-(2.187]. Assuming the polarization of the core electrons to be negligible, the contributions from these core electrons will largely cancel. There exist two main exceptions: first, in the PSP approximation, V_{KS}^{τ} (needed for the $\Delta g_{xy}^{\mathrm{SO}}$ term) is a non-local operator, which we will have to replace by an appropriate local effective potential. Secondly, the induced magnetic field $\mathbf{B}_{\mathbf{B}_x}$ in $\Delta g_{xy}^{\mathrm{SOO}}$ will not contain the contributions of the core electrons, but fortunately $\Delta g_{xy}^{\mathrm{SOO}}$ generally accounts only for a very limited part of the total g tensor.

The most serious artifacts originate from the incorrect shape of the wave functions of the valence electrons in the core regions. Hence, an accurate g tensor prediction will only be possible if the spin polarization is largely contained in those electron orbitals which are still reasonably described in the core region. Generally, this involves the most energetic valence electrons.

The implementation of $\mathbf{j}_{\mathbf{B}_x}^{\tau}$ and $\mathbf{B}_{\mathbf{B}_x}$ in CPMD is mainly the work of Sebastiani *et al.*[39, 40]

The calculation of $\Delta g_{xy}^{\mathrm{ZKE}}$ (2.185) in CPMD

$\Delta g_{xy}^{\mathrm{ZKE}}$ is calculated in a spin-polarized DFT run from the kinetic energy of the KS orbitals obtained in a spin-polarized DFT-run. In reciprocal space, the calculation of the kinetic energy involves a simple sum over the plane waves (2.58).

The calculation of $\Delta g_{xy}^{\mathrm{SO}}$ (2.186) in CPMD

The induced current densities $\mathbf{j}_{\mathbf{B}_x}^{\tau}$ depend on the solutions of the inhomogeneous set of coupled equations (2.220) in reciprocal space for respectively $(\mathbf{r} - \mathbf{d}_j) \times \mathbf{p}$ (the *orbital angular momentum* operator, notation: $\mathbf{L}$), $\mathbf{p}$ (the *momentum*

operator, notation: $\mathbf{p}$), and $(\mathbf{d}_i - \mathbf{d}_j) \times \mathbf{p}$ (the *full correction* operator, notation: $\mathbf{\Delta i}$). The operation of the momentum operator (and hence, the ∇ operator) is easily evaluated in reciprocal space, the operation of the position operator is performed in real space (see the discussion on the position operator in section 2.3.5), and successive FFTs transform the function onto which must be operated to the correct representation. For the position operator, it is important that the transition at the boundaries of the virtual cell is made soft in order to avoid unwanted high-frequency components in the position operator. For the first-order corrections $\psi^{(1)}_{\mathbf{B}_\alpha,i}$ to the MLWFs, we obtain:

$$\psi^{(1)}_{\mathbf{B}_\alpha,i}(\mathbf{r}) = -\frac{i\alpha}{2}\left(\psi_i^{L_\alpha}(\mathbf{r}) - \epsilon_{\alpha\beta\gamma}(\mathbf{r}-\mathbf{d}_i)_\beta \psi_i^{p_\gamma}(\mathbf{r}) - \psi_i^{\Delta i_\alpha}(\mathbf{r})\right) . \tag{2.243}$$

The vector product is concisely written using the total anti-symmetric tensor $\epsilon_{\alpha\beta\gamma}$, i.e. the Levi-Cività symbol, and the indices β and γ follow the Einstein summation rules.[50] Note also that the imaginary nature of $\psi^{(1)}_{\mathbf{B}_\alpha,i}$ has been made explicit, allowing us to work with real functions $\psi_i^{L_\alpha}$, $\psi_i^{p_\gamma}$ and $\psi_i^{\Delta i_\alpha}$. The spin-dependent current density is then calculated according to (2.232):[51]

$$\begin{aligned}
\mathbf{j}^\tau_{\mathbf{B}_\alpha}(\mathbf{r}) &= \sum_i^{n_\tau} \mathbf{j}_{\mathbf{B}_\alpha,i}(\mathbf{r}) \\
&= -i\sum_i^{n_\tau}\left[\left(\nabla\psi_i^{(0)}(\mathbf{r})\right)\psi^{(1)}_{\mathbf{B}_\alpha,i}(\mathbf{r}) - \psi_i^{(0)}(\mathbf{r})\left(\nabla\psi^{(1)}_{\mathbf{B}_\alpha,i}(\mathbf{r})\right)\right] \\
&= -\frac{\alpha}{2}\sum_i^{n_\tau}\Big[\left(\nabla\psi_i^{(0)}(\mathbf{r})\right)\psi_i^{L_\alpha}(\mathbf{r}) - \epsilon_{\alpha\beta\gamma}(\mathbf{r}-\mathbf{d}_i)_\beta\left(\nabla\psi_i^{(0)}(\mathbf{r})\right)\psi_i^{p_\gamma}(\mathbf{r}) \\
&- \left(\nabla\psi_i^{(0)}(\mathbf{r})\right)\psi_i^{\Delta i_\alpha}(\mathbf{r}) - \psi_i^{(0)}(\mathbf{r})\left(\nabla\psi_i^{L_\alpha}(\mathbf{r})\right) \\
&+ \epsilon_{\alpha\beta\gamma}(\mathbf{r}-\mathbf{d}_i)_\beta\psi_i^{(0)}(\mathbf{r})\left(\nabla\psi_i^{p_\gamma}(\mathbf{r})\right) + \psi_i^{(0)}(\mathbf{r})\left(\nabla\psi_i^{\Delta i_\alpha}(\mathbf{r})\right)\Big] .
\end{aligned} \tag{2.244}$$

V^τ_{KS}, the second relevant component of $\Delta g^{\mathrm{SO}}_{xy}$, is computed in reciprocal space from the sum of the local part of the pseudopotentials, the Hartree potential $v_{\mathrm{H},\mathbf{G}\neq\mathbf{0}} = 2\pi\Omega\sum_{\mathbf{G}\neq\mathbf{0}}\frac{|\rho(\mathbf{G})|^2}{G^2}$,[52] and the same exchange-correlation potential as

[50] This means that a summation over all possible values (x, y, z) for β and γ is assumed.
[51] As a reminder: we calculate the current density in the CSGT method.
[52] the component ($\mathbf{G} = \mathbf{0}$) is omitted, because finally we only need its spatial derivatives

the one used in the self-consistent procedure of the Kohn-Sham-DFT scheme. Subsequently, the spatial derivatives of V_{KS}^{τ} are calculated in reciprocal space.

The calculation of $\Delta g_{xy}^{\mathrm{SO}}$ then involves the evalution of:

$$\Delta g_{xy}^{\mathrm{SO}} = \frac{\alpha g'}{2} \int_{\mathrm{FFT}} \mathrm{d}\mathbf{r} \left[\mathbf{j}_{\mathbf{B}_x}^{\alpha}(\mathbf{r}) \times \nabla V_{\mathrm{KS}}^{\alpha}(\mathbf{r}) - \mathbf{j}_{\mathbf{B}_x}^{\beta}(\mathbf{r}) \times \nabla V_{\mathrm{KS}}^{\beta}(\mathbf{r}) \right]_y , \tag{2.245}$$

where the subscript *FFT* indicates that the integration is performed on the discrete points of the FFT lattice.

The calculation of $\Delta g_{xy}^{\mathrm{SOO}}$ (2.187) in CPMD

The magnetic field $\mathbf{B}_{\mathbf{B}_x}$ originating from the induced and self-interaction-corrected current density $\mathbf{j}_{\mathbf{B}_x}^{\mathrm{corr}} = \left(\mathbf{j}_{\mathbf{B}_x}^{\alpha} + \mathbf{j}_{\mathbf{B}_x}^{\beta}\right) - \left(\mathbf{j}_{\mathbf{B}_x}^{\alpha} - \mathbf{j}_{\mathbf{B}_x}^{\beta}\right)$ is computed from (2.182):

$$\begin{aligned} B_{\mathbf{B}_x,\alpha}(\mathbf{r}) &= \alpha \left[\int_{\Omega_{\mathrm{S}}} \mathrm{d}\mathbf{r}' \frac{\mathbf{r}' - \mathbf{r}}{|\mathbf{r}' - \mathbf{r}|^3} \times \mathbf{j}_{\mathbf{B}_x}^{\mathrm{corr}}(\mathbf{r}') \right]_{\alpha} \\ &= \alpha \left[\int_{\Omega_{\mathrm{S}}} \mathrm{d}\mathbf{r}' \left(\frac{\partial}{\partial \mathbf{r}} \frac{1}{|\mathbf{r}' - \mathbf{r}|} \right) \times \mathbf{j}_{\mathbf{B}_x}^{\mathrm{corr}}(\mathbf{r}') \right]_{\alpha} \\ &= \alpha \epsilon_{\alpha\beta\gamma} \frac{\partial}{\partial r_{\beta}} \int_{\Omega_{\mathrm{S}}} \mathrm{d}\mathbf{r}' \frac{1}{|\mathbf{r}' - \mathbf{r}|} j_{\mathbf{B}_x,\gamma}^{\mathrm{corr}}(\mathbf{r}') . \end{aligned} \tag{2.246}$$

The integration in the above equation spans the entire space (Ω_{S}), i.e. not only the simulation cell (Ω). The vector $\mathbf{e}_{\alpha}$ denotes the unity vector in the cartesian direction α. The current density $j_{\mathbf{B}_x,\gamma}^{\mathrm{corr}}$ features the periodicity of the simulation cell, whereas the functions $\frac{\mathbf{r}'-\mathbf{r}}{|\mathbf{r}'-\mathbf{r}|^3}$ and $\frac{1}{|\mathbf{r}'-\mathbf{r}|}$ do not. The integrals over the simulation cell of the current densities of every electron i vanish exactly:

$$\int_{\Omega} \mathrm{d}\mathbf{r} \mathbf{j}_{\mathbf{B}_x,i}(\mathbf{r}) = \mathbf{0} , \tag{2.247}$$

and therefore it also holds that:

$$\int_{\Omega} \mathrm{d}\mathbf{r} \mathbf{j}_{\mathbf{B}_x}^{\mathrm{corr}}(\mathbf{r}) = \mathbf{0} . \tag{2.248}$$

In order to maintain a concise notation, we will discuss the treatment of only one cartesian component of the current density $\mathbf{j}^{\text{corr}}_{\mathbf{B}_x}(\mathbf{r})$ from the integral in (2.246):

$$I^{\text{corr}}_{\mathbf{B}_x,\gamma}(\mathbf{r}) = \int_{\Omega_S} \mathrm{d}\mathbf{r}' \frac{1}{|\mathbf{r}' - \mathbf{r}|} j^{\text{corr}}_{\mathbf{B}_x,\gamma}(\mathbf{r}') \; . \tag{2.249}$$

The property (2.248) holds for every cartesian component, and in reciprocal space this corresponds to:

$$j^{\text{corr}}_{\mathbf{B}_x,\gamma}(\mathbf{G} = \mathbf{0}) = 0 \; . \tag{2.250}$$

Now, we replace $j^{\text{corr}}_{\mathbf{B}_x,\gamma}$ in (2.249) by its reciprocal expression:

$$\begin{aligned} I^{\text{corr}}_{\mathbf{B}_x,\gamma}(\mathbf{r}) &= \int_{\Omega_S} \mathrm{d}\mathbf{r}' \frac{1}{|\mathbf{r}' - \mathbf{r}|} \frac{1}{N_G} \sum_{\mathbf{G}\neq\mathbf{0}} e^{i\mathbf{G}.\mathbf{r}'} j^{\text{corr}}_{\mathbf{B}_x,\gamma}(\mathbf{G}) \\ &= \frac{1}{N_G} \sum_{\mathbf{G}\neq\mathbf{0}} e^{i\mathbf{G}.\mathbf{r}} j^{\text{corr}}_{\mathbf{B}_x,\gamma}(\mathbf{G}) \int_{\Omega_S} \mathrm{d}\mathbf{r}' \frac{1}{|\mathbf{r}' - \mathbf{r}|} e^{i\mathbf{G}.(\mathbf{r}'-\mathbf{r})} \\ &= \frac{1}{N_G} \sum_{\mathbf{G}\neq\mathbf{0}} e^{i\mathbf{G}.\mathbf{r}} j^{\text{corr}}_{\mathbf{B}_x,\gamma}(\mathbf{G}) \int_{\Omega_S} \mathrm{d}\mathbf{s} \frac{1}{s} e^{i\mathbf{G}.\mathbf{s}} \; , \end{aligned} \tag{2.251}$$

where $N_{\mathbf{G}}$ denotes the number of reciprocal lattice vectors. The integral from the above equation is further elaborated through:

$$\begin{aligned} \lim_{a\to 0} \int_{\Omega_S} \mathrm{d}\mathbf{s} \frac{1}{s} e^{-as} e^{i\mathbf{G}\cdot\mathbf{s}} &= \lim_{a\to 0} \int_{\Omega_S} \mathrm{d}\varphi \mathrm{d}(\cos\theta_s) \mathrm{d}s s^2 \frac{1}{s} e^{-as} e^{iGs\cos\theta_s} \\ &= \lim_{a\to 0} \frac{4\pi}{a^2 + G^2} \\ &= \frac{4\pi}{G^2} \; . \end{aligned} \tag{2.252}$$

Notice that this integral diverges for $\mathbf{G} = \mathbf{0}$. Using (2.251) and excluding the $(\mathbf{G} = \mathbf{0})$ component, we can recast (2.246) into:

$$\begin{aligned} B_{\mathbf{B}_x,\mathbf{G}\neq\mathbf{0},\alpha}(\mathbf{r}) &= \alpha \epsilon_{\alpha\beta\gamma} \frac{\partial}{\partial r_\beta} I^{\text{corr}}_{\mathbf{B}_x,\gamma}(\mathbf{r}) \\ &= \frac{1}{N_G} \sum_{\mathbf{G}\neq\mathbf{0}} e^{i\mathbf{G}\cdot\mathbf{r}} \left[i\alpha \epsilon_{\alpha\beta\gamma} G_\beta \frac{4\pi}{G^2} j^{\text{corr}}_{\mathbf{B}_x,\gamma}(\mathbf{G}) \right] \; . \end{aligned} \tag{2.253}$$

Thus, for $\mathbf{G} \neq \mathbf{0}$, the magnetic field in reciprocal space equals the following expression:

$$\begin{aligned} B_{\mathbf{B}_x,\alpha}(\mathbf{G}) &= i\alpha\epsilon_{\alpha\beta\gamma}G_\beta\frac{4\pi}{G^2}j^{\text{corr}}_{\mathbf{B}_x,\gamma}(\mathbf{G}) \\ &= i\alpha\frac{4\pi}{G^2}\left[\mathbf{G}\times\mathbf{j}^{\text{corr}}_{\mathbf{B}_x}(\mathbf{G})\right]_\alpha \ . \end{aligned} \tag{2.254}$$

The $(\mathbf{G} = \mathbf{0})$ component of the induced magnetic field cannot be computed within periodic boundary conditions. An approximative expression for the contribution of this component in real space is presented in Ref. [39]:

$$\mathbf{B}_{\mathbf{B}_x,\mathbf{G}=\mathbf{0}} = \kappa\frac{2\pi\alpha}{\Omega}\int_\Omega \mathrm{d}\mathbf{r}\mathbf{r}\times\mathbf{j}^{\text{corr}}_{\mathbf{B}_x}(\mathbf{r}) \ . \tag{2.255}$$

This contribution depends on the macroscopic shape of the studied material, through a dimensionless form factor κ. For a spherical shape, the above equation is exact and $\kappa = \frac{2}{3}$ (this is also the default value for κ).[53]

$\mathbf{B}_{\mathbf{B}_x,\mathbf{G}=\mathbf{0}}$ contains the position operator again, and must therefore be treated with care. We assume that the localization (i.e. the property of being localized) of each MLWF i is transferable to the corresponding current density. In that case, we can perform the operation of the position operator for each current density i independently, using the same definition for the position variable as in section 2.3.5 (sawtooth-shaped profile + origin identical to the Wannier center of the corresponding MLWF):

$$\begin{aligned} \mathbf{B}_{\mathbf{B}_x,\mathbf{G}=\mathbf{0}} &= \kappa\frac{2\pi\alpha}{\Omega}\sum_i\left(\int_\Omega \mathrm{d}\mathbf{r}(\mathbf{r}-\mathbf{d}_i)\times\mathbf{j}^{\text{corr}}_{\mathbf{B}_x,i}(\mathbf{r})\right. \\ &- \left.\int_\Omega \mathrm{d}\mathbf{r}\mathbf{d}_i\times\mathbf{j}^{\text{corr}}_{\mathbf{B}_x,i}(\mathbf{r})\right) \ . \end{aligned} \tag{2.256}$$

In the above equation, the correction term for every i is multiplied by zero because of (2.247).

[53] Since $\Delta g^{\text{SOO}}_{xy}$ is mostly a relatively small term as compared to $\Delta g^{\text{ZKE}}_{xy}$ and $\Delta g^{\text{SO}}_{xy}$, we chose to neglect the mathematical derivation of (2.255) in this work. The accurate computation of the induced magnetic field is of greater importance for NMR parameters such as the susceptibility and the chemical shift. A detailed elaboration can be found in Ref. [40].

Finally, $\mathbf{B}_{\mathbf{B}_x}(\mathbf{r}) = \mathbf{B}_{\mathbf{B}_x,\mathbf{G}\neq\mathbf{0}}(\mathbf{r}) + \mathbf{B}_{\mathbf{B}_x,\mathbf{G}=\mathbf{0}}$ is multiplied by the spin density $\rho_s = \rho^\alpha - \rho^\beta$, leading to the different components of $\Delta g^{\mathrm{SOO}}_{xy}$:[54]

$$\begin{aligned}\Delta g^{\mathrm{SOO}}_{xy} &= 2\int \mathrm{d}\mathbf{r}\; B_{\mathbf{B}_x,y}(\mathbf{r})\rho_s(\mathbf{r}) \\ &= 2\int_{\mathrm{FFT}} \mathrm{d}\mathbf{r}\left(B_{\mathbf{B}_x,\mathbf{G}\neq\mathbf{0},y}(\mathbf{r}) + B_{\mathbf{B}_x,\mathbf{G}=\mathbf{0},y}\right)\rho_s(\mathbf{r})\;. \end{aligned} \tag{2.257}$$

About the use of a pure plane-wave method for the g tensor

From g tensor calculations on a large number of isolated molecules in Ref. [Art. 1/2], we infer that for radicals consisting only of first- and second-row elements from the periodic table, reliable PSP-g-tensor predictions can be obtained. Heavier elements require more core electrons (than necessary to perform a structural optimization) to be taken up explicitly in the calculation, or require the use of reconstruction techniques, such as for example the (gauge-including) projector-augmented-wave ((GI)PAW) method described in Ref. [6] and section 2.4.2. While such reconstruction techniques remove most of the artifacts, they will still not include the effects of core polarization. Moreover, the (GI)PAW method does not resolve the problems related to the spin-dependent exchange-correlation potential v^τ_{XC} in the PSP approximation, needed for a correct description of the polarization of the valence electrons.[50]

2.3.7 The g tensor in CP2K: implementation and implications

The shortcomings in the calculation of the g tensor within the PSP approximation clearly illustrate the need for a hybrid method which would allow for an AE description[55] of the radical center and a limited region around it, and at the same time leaves open the possibility of a PSP description for the remaining atoms in the simulation cell. Such an approximation will most probably not affect the g tensor, since the g tensor is mainly determined by the electronic structure in a limited region around the radical center. The GAPW method (see section 2.1.6) is ideally suited for this purpose: the method exists in both a PSP and an AE approach, and both can be easily combined within one simulation. Moreover, a GAPW simulation with an AE description for the atoms of interest requires only a relatively small additional computational cost, thanks to the

[54] Note that x denotes the direction of the external magnetic field, and y the cartesian component of $\mathbf{B}_{\mathbf{B}_x}$.

[55] Thus using the nuclear Coulomb potential.

use of Gaussian functions[56]. For example, in a pure plane-wave basis set, the additional computational cost would be manifestly higher.[57]

The calculation of $\Delta g_{xy}^{\mathrm{ZKE}}$ (2.185) in CP2K

$\Delta g_{xy}^{\mathrm{ZKE}}$ is calculated in a spin-polarized DFT run from the kinetic energy of the Kohn-Sham orbitals in the basis set of CPGFs. The matrix elements of the kinetic energy operator $-\frac{\nabla^2}{2}$ can be evaluated analytically in a set of arbitrary cartesian Gaussian functions.[20]

The calculation of $\Delta g_{xy}^{\mathrm{SO}}$ (2.186) in CP2K

The induced current densities $\mathbf{j}_{\mathbf{B}_x}^{\tau}$ are derived fully analytically in a Gaussian representation. In the basis set of CPGFs, the MLWFs are defined similarly as in (2.48):

$$\psi_i^{(0)}(\mathbf{r}) \quad = \quad \sum_k C_{ki}^{(0)} \psi_k^{\mathrm{AO,P}}(\mathbf{r}) \,, \tag{2.258}$$

and the matrix elements of the inhomogeneous set of coupled equations (2.220) become:[58]

$$-\sum_{il} \left(H_{\mathrm{KS},kl}\delta_{ij} - S_{kl} \int \mathrm{d}\mathbf{r} \psi_i^{(0)}(\mathbf{r}) H_{\mathrm{KS}}(\mathbf{r}) \psi_j^{(0)}(\mathbf{r}) \right) i C_{li}^{(1)} = \sum_l H_{kl(j)}^{(1)} C_{lj}^{(0)} \,, \quad \forall k,j \,, \tag{2.259}$$

where S_{kl} denotes the elements of the overlap matrix and $H_{kl}^{(1)}$ the matrix elements of respectively the orbital angular momentum operator $\mathbf{L}$, the momentum operator $\mathbf{p}$) and the full correction operator $\boldsymbol{\Delta i}$. Note also that the imaginary nature of $\psi_i^{(1)}$ has been made explicit, allowing us to work with real expansion coefficients $C_{li}^{(1)}$.

[56] More precisely: contracted periodic Gaussian functions.

[57] Because a basis set with a *huge* amount of plane waves would be required for the correct description of the Coulomb potential and the sharp oscillations of the wave functions in the core regions of the nuclei.

[58] As a reminder (see section 2.3.5): $\psi_i^{(0)}$ and $\psi_i^{(1)}$ represent real and imaginary wave functions, respectively.

The position operator in the orbital angular momentum operator is redefined with respect to the position of the atomic nucleus $\mathbf{R}_l$ corresponding with the atomic orbital $\psi_l^{\mathrm{AO,P}}$:

$$\begin{aligned} H_{klj}^{L_\alpha} &= -i\epsilon_{\alpha\beta\gamma}\int \mathrm{d}\mathbf{r}\psi_k^{\mathrm{AO,P}}(\mathbf{r})\left((\mathbf{r}-\mathbf{d}_j)_\beta\nabla_\gamma\right)\psi_l^{\mathrm{AO,P}}(\mathbf{r}) \\ &= -i\epsilon_{\alpha\beta\gamma}\left(\int \mathrm{d}\mathbf{r}\psi_k^{\mathrm{AO,P}}(\mathbf{r})\left((\mathbf{r}-\mathbf{R}_l)_\beta\nabla_\gamma\right)\psi_l^{\mathrm{AO,P}}(\mathbf{r})\right. \\ &+ \left.(\mathbf{R}_l-\mathbf{d}_j)_\beta\int \mathrm{d}\mathbf{r}\psi_k^{\mathrm{AO,P}}(\mathbf{r})\left(\nabla_\gamma\right)\psi_l^{\mathrm{AO,P}}(\mathbf{r})\right) . \end{aligned} \tag{2.260}$$

This reduces the matrix elements to known integrals over cartesian Gaussian functions.[20] An additional advantage is that these matrix elements only need to be calculated once, instead of for each MLWF separately. The matrix elements of the momentum operator and the full-correction operator are also a function of known integrals:

$$H_{kl}^{p_\alpha} = -i\int \mathrm{d}\mathbf{r}\psi_k^{\mathrm{AO,P}}(\mathbf{r})\left(\nabla_\alpha\right)\psi_l^{\mathrm{AO,P}}(\mathbf{r}) , \tag{2.261}$$

$$\begin{aligned} H_{klj}^{\Delta i_\alpha} &= -i\epsilon_{\alpha\beta\gamma}\int \mathrm{d}\mathbf{r}\psi_k^{\mathrm{AO,P}}(\mathbf{r})\left((\mathbf{d}_i-\mathbf{d}_j)_\beta\nabla_\gamma\right)\psi_l^{\mathrm{AO,P}}(\mathbf{r}) \\ &= -i\epsilon_{\alpha\beta\gamma}(\mathbf{d}_i-\mathbf{d}_j)_\beta\int \mathrm{d}\mathbf{r}\psi_k^{\mathrm{AO,P}}(\mathbf{r})\left(\nabla_\gamma\right)\psi_l^{\mathrm{AO,P}}(\mathbf{r}) . \end{aligned} \tag{2.262}$$

From the solutions of (2.259) for the perturbation operators with matrix elements defined in respectively (2.260), (2.261), and (2.262), we obtain the expansion-coefficients matrices C^{L_α}, C^{p_γ}, and $C^{\Delta i_\alpha}$. This allows us to calculate the first-order corrections $\psi_{\mathbf{B}_\alpha,i}^{(1)}$, including their spatial derivatives $\nabla\psi_{\mathbf{B}_\alpha,i}^{(1)}$:

$$\psi_{\mathbf{B}_\alpha,i}^{(1)}(\mathbf{r}) = -\frac{i\alpha}{2}\sum_k\left(C_{ki}^{L_\alpha}-\epsilon_{\alpha\beta\gamma}(\mathbf{r}-\mathbf{d}_i)_\beta C_{ki}^{p_\gamma}-C_{ki}^{\Delta i_\alpha}\right)\psi_k^{\mathrm{AO,P}}(\mathbf{r}) , \tag{2.263}$$

$$\nabla\psi_{\mathbf{B}_\alpha,i}^{(1)}(\mathbf{r}) = -\frac{i\alpha}{2}\sum_k\left(C_{ki}^{L_\alpha}-\epsilon_{\alpha\beta\gamma}(\mathbf{r}-\mathbf{d}_i)_\beta C_{ki}^{p_\gamma}-C_{ki}^{\Delta i_\alpha}\right)\nabla\psi_k^{\mathrm{AO,P}}(\mathbf{r}) . \tag{2.264}$$

The next step comprises the construction of the current-density matrices. Due to the presence of the term $(\mathbf{r}-\mathbf{d}_i)$ in (2.263) and (2.264), a new current-density matrix would be required for every point in space for which we want to

calculate the current density, if only one current density matrix were to be used for every direction of the external magnetic field. Therefore, we will employ multiple current-density matrices, corresponding to different sets of functions of $\mathbf{r}$. Through an additional substitution $(\mathbf{r}-\mathbf{d}_i) = (\mathbf{r}-\mathbf{R}_l) + (\mathbf{R}_l - \mathbf{d}_i)$, this is done in the most efficient way, since the position variable is separated from the MLWF-dependent Wannier centers:

$$\begin{aligned}
\psi^{(1)}_{\mathbf{B}_\alpha,i}(\mathbf{r}) &= -\frac{i\alpha}{2}\sum_k \left(C^{L_\alpha}_{ki} - \epsilon_{\alpha\beta\gamma}(\mathbf{R}_k-\mathbf{d}_i)_\beta C^{p_\gamma}_{ki} - C^{\Delta i_\alpha}_{ki}\right)\psi^{\mathrm{AO,P}}_k(\mathbf{r}) \\
&+ \frac{i\alpha}{2}\sum_k \epsilon_{\alpha\beta\gamma} C^{p_\gamma}_{ki}\left((\mathbf{r}-\mathbf{R}_k)_\beta \psi^{\mathrm{AO,P}}_k(\mathbf{r})\right) \\
&= -\frac{i\alpha}{2}\sum_k C^{a_\alpha}_{ki}\psi^{\mathrm{AO,P}}_k(\mathbf{r}) \\
&+ \frac{i\alpha}{2}\sum_k \epsilon_{\alpha\beta\gamma} C^{p_\gamma}_{ki}\left((\mathbf{r}-\mathbf{R}_k)_\beta \psi^{\mathrm{AO,P}}_k(\mathbf{r})\right)\ , \qquad (2.265) \\
\nabla\psi^{(1)}_{\mathbf{B}_\alpha,i}(\mathbf{r}) &= -\frac{i\alpha}{2}\sum_k C^{a_\alpha}_{ki}\nabla\psi^{\mathrm{AO,P}}_k(\mathbf{r}) \\
&+ \frac{i\alpha}{2}\sum_k \epsilon_{\alpha\beta\gamma} C^{p_\gamma}_{ki}\left((\mathbf{r}-\mathbf{R}_k)_\beta \nabla\psi^{\mathrm{AO,P}}_k(\mathbf{r})\right)\ . \qquad (2.266)
\end{aligned}$$

Using the above expressions, we calculate the spin-dependent current according to (2.232):[59]

$$\begin{aligned}
\mathbf{j}^\tau_{\mathbf{B}_\alpha}(\mathbf{r}) &= \sum_i^{n_\tau}\mathbf{j}_{\mathbf{B}_\alpha,i}(\mathbf{r}) \\
&= -i\sum_i^{n_\tau}\left[\left(\nabla\psi^{(0)}_i(\mathbf{r})\right)\psi^{(1)}_{\mathbf{B}_\alpha,i}(\mathbf{r}) - \psi^{(0)}_i(\mathbf{r})\left(\nabla\psi^{(1)}_{\mathbf{B}_\alpha,i}(\mathbf{r})\right)\right] \\
&= -\frac{\alpha}{2}\sum_i^{n_\tau}\left[\sum_{kl}\left(C^{(0)}_{ki}C^{a_\alpha}_{li}\right)\left\{\nabla\psi^{\mathrm{AO,P}}_k(\mathbf{r})\psi^{\mathrm{AO,P}}_l(\mathbf{r}) - \psi^{\mathrm{AO,P}}_k(\mathbf{r})\nabla\psi^{\mathrm{AO,P}}_l(\mathbf{r})\right\}\right. \\
&- \epsilon_{\alpha\beta\gamma}\sum_{kl}\left(C^{(0)}_{ki}C^{p_\gamma}_{li}\right)\left\{\nabla\psi^{\mathrm{AO,P}}_k(\mathbf{r})(\mathbf{r}-\mathbf{R}_l)_\beta\psi^{\mathrm{AO,P}}_l(\mathbf{r})\right. \\
&- \left.\left.\psi^{\mathrm{AO,P}}_k(\mathbf{r})(\mathbf{r}-\mathbf{R}_l)_\beta\nabla\psi^{\mathrm{AO,P}}_l(\mathbf{r})\right\}\right]\ . \qquad (2.267)
\end{aligned}$$

[59] As a reminder: we calculate the current density in the CSGT method.

Twelve current-density matrices, i.e.:

$$J_{kl}^{a_\alpha,\tau} = \sum_i^{n_\tau} C_{ki}^{(0)} C_{li}^{a_\alpha} \,, \qquad J_{kl}^{p_\alpha,\tau} = \sum_i^{n_\tau} C_{ki}^{(0)} C_{li}^{p_\alpha} \qquad (\alpha = x,y,z; \tau = \alpha,\beta) \,, \tag{2.268}$$

are needed to describe the spin-dependent current densities originating from an external magnetic field in the 3 cartesian directions, because these current density matrices appear in conjunction with different functions of CPGFs [highlighted with brackets $\{\}$ in (2.267)].

Then, for the computation of $\Delta g_{xy}^{\mathrm{SO}}$, these current densities are collocated onto the auxiliary basis set (plane waves in the GPW method, a combination of plane waves and primitive periodic Gaussian functions in the GAPW method).

In the GAPW method, similar as for the electron density, a GAPW representation for the current density is constructed, this is a separation in global and local components which satisfies the conditions (2.87)-(2.90).

The soft global component is obtained by setting to zero the coefficients in the CPGFs corresponding to the most localized primitive Gaussian functions, thus effectively using only the limited set $\tilde{\chi}^{\mathrm{P}}$. These functions are evaluated, after multiplication with the corresponding coefficient, on the discrete points of the real space FFT lattice, and are then summed up appropriately.

For the local components, through an additional substitution $(\mathbf{r} - \mathbf{R}_k) = (\mathbf{r} - \mathbf{R}_I) + (\mathbf{R}_I - \mathbf{R}_k)$ in (2.265) and (2.266), the position variable is redefined with respect to the position of the atomic nucleus I:

$$
\begin{aligned}
\psi^{(1)}_{\mathbf{B}_\alpha,i}(\mathbf{r}) &= -\frac{i\alpha}{2}\sum_k C^{a_\alpha}_{ki}\psi^{\mathrm{AO,P}}_k(\mathbf{r}) \\
&+ \frac{i\alpha}{2}\sum_k \epsilon_{\alpha\beta\gamma} C^{p_\gamma}_{ki}\left((\mathbf{r}-\mathbf{R}_k)_\beta \psi^{\mathrm{AO,P}}_k(\mathbf{r})\right) \\
&= -\frac{i\alpha}{2}\sum_k C^{a_\alpha}_{ki}\psi^{\mathrm{AO,P}}_k(\mathbf{r}) \\
&+ \frac{i\alpha}{2}\sum_k \epsilon_{\alpha\beta\gamma} C^{p_\gamma}_{ki}\left((\mathbf{R}_I-\mathbf{R}_k)_\beta \psi^{\mathrm{AO,P}}_k(\mathbf{r})\right) \\
&+ \frac{i\alpha}{2}\sum_k \epsilon_{\alpha\beta\gamma} C^{p_\gamma}_{ki}\left((\mathbf{r}-\mathbf{R}_I)_\beta \psi^{\mathrm{AO,P}}_k(\mathbf{r})\right) \\
&= -\frac{i\alpha}{2}\sum_k C^{a'_\alpha}_{ki}\psi^{\mathrm{AO,P}}_k(\mathbf{r}) \\
&+ \frac{i\alpha}{2}\sum_k \epsilon_{\alpha\beta\gamma} C^{p_\gamma}_{ki}\left((\mathbf{r}-\mathbf{R}_I)_\beta \psi^{\mathrm{AO,P}}_k(\mathbf{r})\right) \ . \qquad (2.269)
\end{aligned}
$$

Since the CPGFs are projected onto the primitive Gaussian functions χ^{P}_I and $\tilde{\chi}^{\mathrm{P}}_I$ corresponding to the atomic nucleus I, we can express, because of this additional substitution, the local current density with only a limited number of current density matrices corresponding to different sets of functions of primitive Gaussian functions centered on $\mathbf{R}_I$:

$$
\begin{aligned}
\mathbf{j}^{1,\tau}_{\mathbf{B}_\alpha,I}(\mathbf{r}) &= -\frac{\alpha}{2}\left[\sum_{vw}\sum_{kl} Q^I_{vk} J^{a'_\alpha,\tau}_{kl} Q^I_{wl}\left\{\nabla\chi^{\mathrm{P}}_{I,v}(\mathbf{r})\chi^{\mathrm{P}}_{I,w}(\mathbf{r}) - \chi^{\mathrm{P}}_{I,v}(\mathbf{r})\nabla\chi^{\mathrm{P}}_{I,w}(\mathbf{r})\right\}\right. \\
&- \epsilon_{\alpha\beta\gamma}\sum_{vw}\sum_{kl} Q^I_{vk} J^{p_\alpha,\tau}_{kl} Q^I_{wl}\left\{\nabla\chi^{\mathrm{P}}_{I,v}(\mathbf{r})(\mathbf{r}-\mathbf{R}_I)_\beta\chi^{\mathrm{P}}_{I,w}(\mathbf{r})\right. \\
&- \left.\left.\chi^{\mathrm{P}}_{I,v}(\mathbf{r})(\mathbf{r}-\mathbf{R}_I)_\beta\nabla\chi^{\mathrm{P}}_{I,w}(\mathbf{r})\right\}\right] \ , \qquad (2.270) \\
\tilde{\mathbf{j}}^{1,\tau}_{\mathbf{B}_\alpha,I}(\mathbf{r}) &= -\frac{\alpha}{2}\left[\sum_{vw}\sum_{kl} \tilde{Q}^I_{vk} J^{a'_\alpha,\tau}_{kl} \tilde{Q}^I_{wl}\left\{\nabla\tilde{\chi}^{\mathrm{P}}_{I,v}(\mathbf{r})\tilde{\chi}^{\mathrm{P}}_{I,w}(\mathbf{r}) - \tilde{\chi}^{\mathrm{P}}_{I,v}(\mathbf{r})\nabla\tilde{\chi}^{\mathrm{P}}_{I,w}(\mathbf{r})\right\}\right. \\
&- \epsilon_{\alpha\beta\gamma}\sum_{vw}\sum_{kl} \tilde{Q}^I_{vk} J^{p_\alpha,\tau}_{kl} \tilde{Q}^I_{wl}\left\{\nabla\tilde{\chi}^{\mathrm{P}}_{I,v}(\mathbf{r})(\mathbf{r}-\mathbf{R}_I)_\beta\tilde{\chi}^{\mathrm{P}}_{I,w}(\mathbf{r})\right. \\
&- \left.\left.\tilde{\chi}^{\mathrm{P}}_{I,v}(\mathbf{r})(\mathbf{r}-\mathbf{R}_I)_\beta\nabla\tilde{\chi}^{\mathrm{P}}_{I,w}(\mathbf{r})\right\}\right] \ . \qquad (2.271)
\end{aligned}
$$

The matrix Q^I holds the expansion coefficients of the CPGFs in the primitive Gaussian functions corresponding with the atomic nucleus I.[60]

However, the GAPW representation of the current density, computed in this way, converges only very slowly with respect to the size of the Gaussian basis set. On one hand, this is caused by the use of the CSGT method close to the atomic nuclei. This first issue was solved by fixing the gauge origin to the position of the atomic nucleus I for $\mathbf{j}^{1,\tau}_{\mathbf{B}_\alpha,I}$ within the atom-centered region U_I, i.e. $\mathbf{R}_\mathrm{g} = \mathbf{R}_I$. In this region, the diamagnetic component of the current density (2.232) no longer vanishes. Outside U_I, the CSGT approach $\mathbf{R}_\mathrm{g} = \mathbf{r}$ is maintained,[61] hence assuring that (2.88) is fulfilled. $\mathbf{j}^{1,\tau}_{\mathbf{B}_\alpha,I}$ is still given by (2.270) outside U_I, whereas within U_I it now equals:

$$\begin{aligned}\mathbf{j}^{1,\tau}_{\mathbf{B}_\alpha,I}(\mathbf{r}) &= -\frac{\alpha}{2}\left[\sum_{vw}\sum_{kl} Q^I_{vk} J^{a'_\alpha,\tau}_{kl} Q^I_{wl}\left\{\nabla\chi^\mathrm{P}_{I,v}(\mathbf{r})\chi^\mathrm{P}_{I,w}(\mathbf{r}) - \chi^\mathrm{P}_{I,v}(\mathbf{r})\nabla\chi^\mathrm{P}_{I,w}(\mathbf{r})\right\}\right. \\ &+ \left.\sum_{vw}\sum_{kl} Q^I_{vk} P_{kl} Q^I_{wl}\left\{(\mathbf{B}_\alpha\times\mathbf{r})\,\chi^\mathrm{P}_{I,v}(\mathbf{r})\chi^\mathrm{P}_{I,w}(\mathbf{r})\right\}\right] \\ &\quad \text{for } \mathbf{r}\in U_I\ . \end{aligned} \tag{2.272}$$

A second cause for this slow convergence concerns the use of the expansion coefficients Q^I_{vk} for the spatial derivatives of the CPGFs in the primitive Gaussian functions corresponding to the atomic nucleus I:

$$\nabla\psi^{\mathrm{AO,P}}_k(\mathbf{r}) = \sum_v Q^I_{vk}\nabla\chi^\mathrm{P}_{I,v}(\mathbf{r})\ , \tag{2.273}$$

which proves to be a rather course approximation for smaller Gaussian basis sets. This is solved by computing new expansion coefficients for every spatial derivative of $\psi^{\mathrm{AO,P}}_k$ in the corresponding derivative of every primitive Gaussian function corresponding to the atomic nucleus I:

$$\mathbf{Q}^I_{vk} = \int \mathrm{d}\mathbf{r} p_{\nabla\chi^\mathrm{P}_{I,v}}(\mathbf{r})\nabla\psi^{\mathrm{AO,P}}_k(\mathbf{r})\ , \tag{2.274}$$

with $\mathbf{Q}^I_{vk} = (Q^I_{vk,x}, Q^I_{vk,y}, Q^I_{vk,z})$, and $p_{\nabla\chi^\mathrm{P}_{I,v}}$ the projector corresponding with $\nabla\chi^\mathrm{P}_{I,v}$.

[60] For a CPGF belonging to the atomic nucleus I this expansion of course equals to (2.52).
[61] Of course, the transition at the boundaries of U_I can be smoothed (if necessary).

Now we will discuss the approach taken for evaluating $\nabla V^{\tau}_{\mathrm{KS}}$, the second component of $\Delta g^{\mathrm{SO}}_{xy}$.

For the computation of $\nabla V^{\tau}_{\mathrm{KS}}$, we adopt a fixed choice for the exchange-correlation potential, the X_{α} potential[51]:[62]

$$v^{\tau}_{X_{\alpha}}[\rho(\mathbf{r})] = -\frac{3}{2}\left(\frac{6}{\pi}\right)^{1/3} \alpha \rho^{\tau}(\mathbf{r})^{1/3}\,, \tag{2.275}$$

a choice inspired by the work of Schreckenbach and Ziegler.[1] The variable α is an adjustable real parameter which is, by default, set to $2/3$.

In the GPW method, V^{τ}_{KS} is soft, due to the mandatory use of pseudopotentials. We evaluate this term in reciprocal space and subsequently calculate its spatial derivatives, much in the same way as it was done in CPMD. We thereby exploit the analytical expression for Goedecker-type pseudopotentials in reciprocal space.

In the GAPW method, we attempt to benefit from the presence of plane waves and atom-centered grids. Unfortunately, the construction of a GAPW representation for $\nabla V^{\tau}_{\mathrm{KS}}$ is not feasible. However, just like for the electrostatic energy (see section 2.1.6), we can split up $\nabla V^{\tau}_{\mathrm{KS}}$ in independent global and local, atom-centered components, but generally the GAPW identities Eqs. (2.87)-(2.90) will no longer hold. Nonetheless, the local components are constructed such that they remain limited to a small area around the atomic nuclei. $\nabla V^{\tau}_{\mathrm{KS}}$ is split up in a soft global component $\nabla \tilde{V}^{\tau,\mathrm{PSP}}_{\mathrm{KS}}$ or $\nabla \tilde{V}^{\tau,\mathrm{AE}}_{\mathrm{KS}}$ and local atom-centered components $\nabla V^{\tau,1,\mathrm{PSP}}_{\mathrm{KS},I}$ or $\nabla V^{\tau,1,\mathrm{AE}}_{\mathrm{KS},I}$ (depending on whether a pseudopotential or a nuclear Coulomb potential is used), defined as:

[62] This potential is also referred to as the Dirac/Slater-exchange potential.

$$\begin{aligned}
\nabla\tilde{V}_{\mathrm{KS}}^{\tau,\mathrm{PSP}}(\mathbf{r}) &= \nabla\left(\sum_{I\in\mathrm{PSP}} V_{\mathrm{loc,sr},I}^{\mathrm{PSP}} H(\alpha_{\mathrm{c}} - \frac{1}{2r_{\mathrm{loc},I}^2}) + v_{\mathrm{H}}[\tilde{\rho}(\mathbf{r}) + \rho^0(\mathbf{r})]\right. \\
&+ \left. v_{\mathrm{X}_\alpha}^{\tau}[\tilde{\rho}(\mathbf{r})]\right) , \qquad (2.276) \\
\nabla\tilde{V}_{\mathrm{KS}}^{\tau,\mathrm{AE}}(\mathbf{r}) &= \nabla\left(v_{\mathrm{H}}[\tilde{\rho}(\mathbf{r}) + \rho^0(\mathbf{r})] + v_{\mathrm{X}_\alpha}^{\tau}[\tilde{\rho}(\mathbf{r})]\right) , \qquad (2.277) \\
\nabla V_{\mathrm{KS},I}^{\tau,1,\mathrm{PSP}}(\mathbf{r}) &= \nabla\left(V_{\mathrm{loc,sr},I}^{\mathrm{PSP}}(\mathbf{r}) H'(\alpha_{\mathrm{c}} - \frac{1}{2r_{\mathrm{loc},I}^2}) + v_{\mathrm{H}}[\rho_I^1(\mathbf{r}) + \rho_I^{\mathrm{c}}(\mathbf{r})]\right. \\
&- \left. v_{\mathrm{H}}[\tilde{\rho}_I^1(\mathbf{r}) + \rho_I^0(\mathbf{r})] + v_{\mathrm{X}_\alpha}^{\tau}[\rho_I^1(\mathbf{r})] - v_{\mathrm{X}_\alpha}^{\tau}[\tilde{\rho}_I^1(\mathbf{r})]\right) , \qquad (2.278) \\
\nabla V_{\mathrm{KS},I}^{\tau,1,\mathrm{AE}}(\mathbf{r}) &= \nabla\left(\frac{Q_I}{r}\mathrm{erfc}\left(\frac{r}{\sqrt{2}r_{\mathrm{loc},I}}\right) + v_{\mathrm{H}}[\rho_I^1(\mathbf{r}) + \rho_I^{\mathrm{c}}(\mathbf{r})]\right. \\
&- \left. v_{\mathrm{H}}[\tilde{\rho}_I^1(\mathbf{r}) + \rho_I^0(\mathbf{r})] + v_{\mathrm{X}_\alpha}^{\tau}[\rho_I^1(\mathbf{r})] - v_{\mathrm{X}_\alpha}^{\tau}[\tilde{\rho}_I^1(\mathbf{r})]\right) . \qquad (2.279)
\end{aligned}$$

H is the Heaviside function, and $H' = -(H-1)$, causing $V_{\mathrm{loc,sr},I}^{\mathrm{PSP}}$ to be included either in the global or the appropriate local component, depending on whether the decay of the exponential function in (2.77) is slower or faster than $e^{-\alpha_{\mathrm{c}} r^2}$, with α_{c} an adjustable cutoff parameter. We thus neglect the non-local component of the pseudopotentials, which only operates in the close surroundings of the corresponding atomic nucleus. The long-range behavior of the pseudopotentials remains preserved, and therefore they will still provide the correct contributions in the region of the simulation cell which requires an AE treatment. The soft $\tilde{V}_{\mathrm{KS}}^{\tau}$ is constructed in reciprocal space, and subsequently its spatial derivatives are computed, much like it was done in CPMD. $V_{\mathrm{KS},I}^{\tau,1,\mathrm{PSP}}$ and $V_{\mathrm{KS},I}^{\tau,1,\mathrm{AE}}$ quickly go to zero for large $r = |\mathbf{r}|$, an effect that is even amplified for their spatial derivatives. We will always assume that $\nabla V_{\mathrm{KS},I}^{\tau,1,\mathrm{PSP}}$ and $\nabla V_{\mathrm{KS},I}^{\tau,1,\mathrm{AE}}$ are only significant within U_I.

We now have elaborated all the terms of $\Delta g_{xy}^{\mathrm{SO}}$ in their respective global and local components. The effective calculation of $\Delta g_{xy}^{\mathrm{SO}}$ then involves the evaluation of:

$$
\begin{aligned}
\Delta g_{xy}^{\mathrm{SO}} = \quad & \frac{\alpha g'}{2} \Bigg\{ \int \mathrm{d}\mathbf{r} \left[\tilde{\mathbf{j}}_{\mathbf{B}_x}^{\alpha}(\mathbf{r}) \times \nabla \tilde{V}_{\mathrm{KS}}^{\alpha}(\mathbf{r}) - \tilde{\mathbf{j}}_{\mathbf{B}_x}^{\beta}(\mathbf{r}) \times \nabla \tilde{V}_{\mathrm{KS}}^{\beta}(\mathbf{r}) \right]_y \\
& + \sum_I \int \mathrm{d}\mathbf{r} \left[\tilde{\mathbf{j}}_{\mathbf{B}_x,I}^{\alpha,1}(\mathbf{r}) \times \nabla V_{\mathrm{KS},I}^{\alpha,1}(\mathbf{r}) \right]_y \\
& - \sum_I \int \mathrm{d}\mathbf{r} \left[\tilde{\mathbf{j}}_{\mathbf{B}_x,I}^{\beta,1}(\mathbf{r}) \times \nabla V_{\mathrm{KS},I}^{\beta,1}(\mathbf{r}) \right]_y \\
& + \sum_I \int \mathrm{d}\mathbf{r} \left[\left(\mathbf{j}_{\mathbf{B}_x,I}^{\alpha,1}(\mathbf{r}) - \tilde{\mathbf{j}}_{\mathbf{B}_x,I}^{\alpha,1}(\mathbf{r}) \right) \times \nabla \tilde{V}_{\mathrm{KS}}^{\alpha}(\mathbf{r}) \right]_y \\
& - \sum_I \int \mathrm{d}\mathbf{r} \left[\left(\mathbf{j}_{\mathbf{B}_x,I}^{\beta,1}(\mathbf{r}) - \tilde{\mathbf{j}}_{\mathbf{B}_x,I}^{\beta,1}(\mathbf{r}) \right) \times \nabla \tilde{V}_{\mathrm{KS}}^{\beta}(\mathbf{r}) \right]_y \\
& + \sum_I \int \mathrm{d}\mathbf{r} \left[\left(\mathbf{j}_{\mathbf{B}_x,I}^{\alpha,1}(\mathbf{r}) - \tilde{\mathbf{j}}_{\mathbf{B}_x,I}^{\alpha,1}(\mathbf{r}) \right) \times \nabla V_{\mathrm{KS},I}^{\alpha,1}(\mathbf{r}) \right]_y \\
& - \sum_I \int \mathrm{d}\mathbf{r} \left[\left(\mathbf{j}_{\mathbf{B}_x,I}^{\beta,1}(\mathbf{r}) - \tilde{\mathbf{j}}_{\mathbf{B}_x,I}^{\beta,1}(\mathbf{r}) \right) \times \nabla V_{\mathrm{KS},I}^{\beta,1}(\mathbf{r}) \right]_y \Bigg\} \,, \qquad (2.280)
\end{aligned}
$$

which simplifies to:

$$
\begin{aligned}
\Delta g_{xy}^{\mathrm{SO}} = \quad & \frac{\alpha g'}{2} \Bigg\{ \int_{\mathrm{FFT}} \mathrm{d}\mathbf{r} \left[\tilde{\mathbf{j}}_{\mathbf{B}_x}^{\alpha}(\mathbf{r}) \times \nabla \tilde{V}_{\mathrm{KS}}^{\alpha}(\mathbf{r}) - \tilde{\mathbf{j}}_{\mathbf{B}_x}^{\beta}(\mathbf{r}) \times \nabla \tilde{V}_{\mathrm{KS}}^{\beta}(\mathbf{r}) \right]_y \\
& + \sum_I \int_{\mathrm{LL},U_I} \mathrm{d}\mathbf{r} \left[\left(\mathbf{j}_{\mathbf{B}_x,I}^{\alpha,1}(\mathbf{r}) - \tilde{\mathbf{j}}_{\mathbf{B}_x,I}^{\alpha,1}(\mathbf{r}) \right) \times \nabla \tilde{V}_{\mathrm{KS}}^{\alpha}(\mathbf{r}) \right]_y \\
& - \sum_I \int_{\mathrm{LL},U_I} \mathrm{d}\mathbf{r} \left[\left(\mathbf{j}_{\mathbf{B}_x,I}^{\beta,1}(\mathbf{r}) - \tilde{\mathbf{j}}_{\mathbf{B}_x,I}^{\beta,1}(\mathbf{r}) \right) \times \nabla \tilde{V}_{\mathrm{KS}}^{\beta}(\mathbf{r}) \right]_y \\
& + \sum_I \int_{\mathrm{LL},U_I} \mathrm{d}\mathbf{r} \left[\mathbf{j}_{\mathbf{B}_x,I}^{\alpha,1}(\mathbf{r}) \times \nabla V_{\mathrm{KS},I}^{\alpha,1}(\mathbf{r}) \right]_y \\
& - \sum_I \int_{\mathrm{LL},U_I} \mathrm{d}\mathbf{r} \left[\mathbf{j}_{\mathbf{B}_x,I}^{\beta,1}(\mathbf{r}) \times \nabla V_{\mathrm{KS},I}^{\beta,1}(\mathbf{r}) \right]_y \Bigg\} \,. \qquad (2.281)
\end{aligned}
$$

The subscript LL denotes that the integration is carried out on a spherical grid centered on the position of the atomic nucleus, featuring a logarithmic radial discretization and a Lebedev-type[52–54] angular discretization. U_I indicates that the integration is limited to the spherical region U_I around the atomic nucleus I. The second and third term of the above equation contain the soft components $\nabla \tilde{V}_{\mathrm{KS}}^{\tau}$. These are only available on the FFT grid, but need to

be multiplied with the spin-current densities defined on the LL grids of each atomic nucleus I. This problem is circumvented through a linear interpolation of the values of $\nabla \tilde{V}^{\tau}_{\mathrm{KS}}$ from the FFT-grid to the LL-grid.

The calculation of $\Delta g^{\mathrm{SOO}}_{xy}$ (2.187) in CP2K

The induced magnetic field (2.182) is computed from a non-local operator and the current density. This makes it difficult to generate a GAPW representation for the induced magnetic field from the GAPW representation of the current density. An analytic elaboration through the Gaussian representation of the current density is also far from straightforward. However (this is already mentioned earlier), it generally holds that $\Delta g^{\mathrm{SOO}}_{xy}$ is a relatively small term in comparison with $\Delta g^{\mathrm{ZKE}}_{xy}$ and $\Delta g^{\mathrm{SO}}_{xy}$. For this reason, we chose to neglect the contributions from the atom-centered current densities $\mathbf{j}^{\mathrm{corr},1}_{\mathbf{B}_x} - \tilde{\mathbf{j}}^{\mathrm{corr},1}_{\mathbf{B}_x}$ to the $(\mathbf{G} \neq \mathbf{0})$ components $\tilde{\mathbf{B}}_{\mathbf{B}_x,\mathbf{G}\neq\mathbf{0}}$ of the induced magnetic field. Being computed from the soft current density $\tilde{\mathbf{j}}^{\mathrm{corr}}_{\mathbf{B}_x}$ only through (2.253) on the reciprocal-space FFT-grid, these components will be soft, too (hence the tilde). $\mathbf{B}_{\mathbf{B}_x,\mathbf{G}=\mathbf{0}}$, on the other hand, is computed analytically via (2.256) using the Gaussian representation of the current density (see below). In summary, adopting a concise notation $\rho_{\mathrm{s}} = \rho^{\alpha} - \rho^{\beta}$, $\Delta g^{\mathrm{SOO}}_{xy}$ is evaluated as follows:[63]

$$
\begin{aligned}
\Delta g^{\mathrm{SOO}}_{xy} &= 2 \int \mathrm{d}\mathbf{r}\, B_{\mathbf{B}_x,y}(\mathbf{r}) \rho_{\mathrm{s}}(\mathbf{r}) \\
&\approx 2 \int \mathrm{d}\mathbf{r} \left(\tilde{B}_{\mathbf{B}_x,\mathbf{G}\neq\mathbf{0},y}(\mathbf{r}) + B_{\mathbf{B}_x,\mathbf{G}=\mathbf{0},y} \right) \left(\tilde{\rho}_{\mathrm{s}}(\mathbf{r}) + \rho^1_{\mathrm{s}}(\mathbf{r}) - \tilde{\rho}^1_{\mathrm{s}}(\mathbf{r}) \right) \\
&= 2 \int_{\mathrm{FFT}} \mathrm{d}\mathbf{r} \tilde{B}_{\mathbf{B}_x,\mathbf{G}\neq\mathbf{0},y}(\mathbf{r}) \tilde{\rho}_{\mathrm{s}}(\mathbf{r}) \\
&+ 2 \sum_I \int_{U_I} \mathrm{d}\mathbf{r} \tilde{B}_{\mathbf{B}_x,\mathbf{G}\neq\mathbf{0},y}(\mathbf{r}) \left(\rho^1_{\mathrm{s},I}(\mathbf{r}) - \tilde{\rho}^1_{\mathrm{s},I}(\mathbf{r}) \right) \\
&+ 2 B_{\mathbf{B}_x,\mathbf{G}=\mathbf{0},y} \,. \qquad (2.282)
\end{aligned}
$$

As mentioned earlier, $\mathbf{B}_{\mathbf{B}_x,\mathbf{G}=\mathbf{0}}$ is computed through (2.256).

Omitting the additional substitution that was carried out in order to describe the current density with only a limited number of density matrices, the current density for each electron in a Gaussian representation equals:

[63] As a reminder: we always assume an electron system with net electron spin equal to $\frac{1}{2}$, therefore the integral of the spin density is identically 1, and only the constant term $\mathbf{B}_{\mathbf{B}_x,\mathbf{G}=\mathbf{0}}$ in (2.282) remains.

$$\begin{aligned}\mathbf{j}_{\mathbf{B}_\alpha,i}(\mathbf{r}) &= -\frac{\alpha}{2}\sum_{kl} C_{ki}^{(0)}\left(C_{li}^{L_\alpha} - \epsilon_{\alpha\beta\gamma}(\mathbf{r}-\mathbf{d}_i)_\beta C_{li}^{p_\gamma} - C_{li}^{\Delta i_\alpha}\right) \\ &\quad \left\{\nabla\psi_k^{\mathrm{AO,P}}(\mathbf{r})\psi_l^{\mathrm{AO,P}}(\mathbf{r}) - \psi_k^{\mathrm{AO,P}}(\mathbf{r})\nabla\psi_l^{\mathrm{AO,P}}(\mathbf{r})\right\} . \quad (2.283)\end{aligned}$$

Inserting this current density in (2.256), and taking into account the following identities for $\beta' \neq \gamma'$:

$$\begin{aligned}&\int \mathrm{d}\mathbf{r}\left(\frac{\partial}{\partial\gamma'}\psi_k^{\mathrm{AO,P}}(\mathbf{r})\right)(\mathbf{r}-\mathbf{d}_i)_{\beta'}\psi_l^{\mathrm{AO,P}}(\mathbf{r}) \\ &= -\int \mathrm{d}\mathbf{r}\psi_k^{\mathrm{AO,P}}(\mathbf{r})(\mathbf{r}-\mathbf{d}_i)_{\beta'}\left(\frac{\partial}{\partial\gamma'}\psi_l^{\mathrm{AO,P}}(\mathbf{r})\right) , \quad (2.284)\\ &\int \mathrm{d}\mathbf{r}\left(\frac{\partial}{\partial\gamma'}\psi_k^{\mathrm{AO,P}}(\mathbf{r})\right)(\mathbf{r}-\mathbf{d}_i)_{\beta'}(\mathbf{r}-\mathbf{d}_i)_\alpha\psi_l^{\mathrm{AO,P}}(\mathbf{r}) \\ &= -\int \mathrm{d}\mathbf{r}\psi_k^{\mathrm{AO,P}}(\mathbf{r})(\mathbf{r}-\mathbf{d}_i)_{\beta'}(\mathbf{r}-\mathbf{d}_i)_\alpha\left(\frac{\partial}{\partial\gamma'}\psi_l^{\mathrm{AO,P}}(\mathbf{r})\right) \\ &-\delta_{\alpha,\gamma'}\int \mathrm{d}\mathbf{r}\psi_k^{\mathrm{AO,P}}(\mathbf{r})(\mathbf{r}-\mathbf{d}_i)_{\beta'}(\mathbf{r}-\mathbf{d}_i)_\alpha\psi_l^{\mathrm{AO,P}}(\mathbf{r}) , \quad (2.285)\end{aligned}$$

we obtain for the α' component of $\mathbf{B}_{\mathbf{B}_\alpha,\mathbf{G}=\mathbf{0}}$, with n_β the number of spin-down electrons:

$$
\begin{aligned}
B_{\mathbf{B}_\alpha,\mathbf{G}=\mathbf{0},\alpha'} &= \kappa\frac{2\pi\alpha^2}{\Omega}\sum_i^{n_\beta}\Bigg\{\sum_{kl}C_{ki}^{(0)}\left(C_{li}^{L_\alpha}-C_{li}^{\Delta i_\alpha}\right)\times \\
&\quad\Bigg[2\int \mathrm{d}\mathbf{r}\psi_k^{\mathrm{AO,P}}(\mathbf{r})(\mathbf{r}-\mathbf{d}_i)_{\beta'}\left(\frac{\partial}{\partial\gamma'}\psi_l^{\mathrm{AO,P}}(\mathbf{r})\right) \\
&\quad -2\int \mathrm{d}\mathbf{r}\psi_k^{\mathrm{AO,P}}(\mathbf{r})(\mathbf{r}-\mathbf{d}_i)_{\gamma'}\left(\frac{\partial}{\partial\beta'}\psi_l^{\mathrm{AO,P}}(\mathbf{r})\right) \\
&\quad +2d_{i,\beta'}\int \mathrm{d}\mathbf{r}\psi_k^{\mathrm{AO,P}}(\mathbf{r})\left(\frac{\partial}{\partial\gamma'}\psi_l^{\mathrm{AO,P}}(\mathbf{r})\right) \\
&\quad -2d_{i,\gamma'}\int \mathrm{d}\mathbf{r}\psi_k^{\mathrm{AO,P}}(\mathbf{r})\left(\frac{\partial}{\partial\beta'}\psi_l^{\mathrm{AO,P}}(\mathbf{r})\right)\Bigg] \\
&- \epsilon_{\alpha\beta\gamma}\sum_{kl}C_{ki}^{(0)}C_{li}^{p_\gamma}\times \\
&\quad\Bigg[2\int \mathrm{d}\mathbf{r}\psi_k^{\mathrm{AO,P}}(\mathbf{r})(\mathbf{r}-\mathbf{d}_i)_{\beta'}(\mathbf{r}-\mathbf{d}_i)_{\beta}\left(\frac{\partial}{\partial\gamma'}\psi_l^{\mathrm{AO,P}}(\mathbf{r})\right) \\
&\quad +\delta_{\beta\gamma'}\int \mathrm{d}\mathbf{r}\psi_k^{\mathrm{AO,P}}(\mathbf{r})(\mathbf{r}-\mathbf{d}_i)_{\beta'}\left(\frac{\partial}{\partial\gamma'}\psi_l^{\mathrm{AO,P}}(\mathbf{r})\right) \\
&\quad -2\int \mathrm{d}\mathbf{r}\psi_k^{\mathrm{AO,P}}(\mathbf{r})(\mathbf{r}-\mathbf{d}_i)_{\gamma'}(\mathbf{r}-\mathbf{d}_i)_{\beta}\left(\frac{\partial}{\partial\beta'}\psi_l^{\mathrm{AO,P}}(\mathbf{r})\right) \\
&\quad -\delta_{\beta\beta'}\int \mathrm{d}\mathbf{r}\psi_k^{\mathrm{AO,P}}(\mathbf{r})(\mathbf{r}-\mathbf{d}_i)_{\gamma'}\left(\frac{\partial}{\partial\beta'}\psi_l^{\mathrm{AO,P}}(\mathbf{r})\right) \\
&\quad +2d_{i,\beta'}\int \mathrm{d}\mathbf{r}\psi_k^{\mathrm{AO,P}}(\mathbf{r})(\mathbf{r}-\mathbf{d}_i)_{\beta}\left(\frac{\partial}{\partial\gamma'}\psi_l^{\mathrm{AO,P}}(\mathbf{r})\right) \\
&\quad -2d_{i,\gamma'}\int \mathrm{d}\mathbf{r}\psi_k^{\mathrm{AO,P}}(\mathbf{r})(\mathbf{r}-\mathbf{d}_i)_{\beta}\left(\frac{\partial}{\partial\beta'}\psi_l^{\mathrm{AO,P}}(\mathbf{r})\right)\Bigg]\Bigg\}\ .
\end{aligned}
\tag{2.286}
$$

About the use of the GPW method for the g tensor

The GPW method for the g tensor features more or less the same artifacts as the CPMD implementation (and actually, this method was implemented only for the verification of several routines of the CP2K implementation, before expanding them to the GAPW method).

About the use of the of the GAPW method for the g tensor

In Ref. [Art. 9] the GAPW method for the g tensor is thoroughly tested. The g tensors of an extensive selection of small molecules in the gas phase, computed with the AE implementation of the GAPW method, are in excellent agreement with those obtained with ADF,[55] a program package (exclusively) suitable for gas-phase simulations, which also adopts the LCAO approximation, but uses Slater-type functions to represent the atomic orbitals (for more information, see Ref. [55]). Moreover, it was observed that the hybrid use of an AE approach for the radical center and a PSP approximation (and even a molecular mechanics description) for the remaining atoms in the simulation cell did not significantly affect the g-tensor predictions. We can therefore state that we have obtained both an accurate and at the same time a relatively cheap (in terms of computational cost) method for g-tensor calculations in PBC simulations. We wish to remind, though, that the GAPW method (just like the GPW method) at present assumes the Γ-point approximation, which somewhat restricts the choice for the dimensions of the simulation cell for a material under study, and in turn determines whether this material can be studied in this approximation at a reasonable computational cost.

2.4 Calculation of the A tensor in PBC simulations

2.4.1 The A tensor in DFT

For the computation of the A tensor of the I-th atomic nucleus A_I, defined through (2.158),

$$A_{I,xy} = \langle \Psi | \left. \frac{\partial^2 H^{\mathrm{A}_I}}{\partial I_{I,x} \partial S_y} \right|_{\mathbf{I}_I = \mathbf{S} = \mathbf{0}} | \Psi \rangle \ , \tag{2.287}$$

we make use of the spin-field-reduction technique and the Wigner-Eckhart theorem (see section 2.3.1) applied to the operators $H_{\mathrm{FC},I}$ (2.156) and $H_{\mathrm{DC},I}$ (2.157). In this way, we obtain:[64]

$$A_{I,xy} = \int\limits_{\mathbf{r}'=\mathbf{r}} \mathrm{d}\mathbf{r} \left[\frac{\partial}{\partial I_{I,x}} \left(h_{\mathrm{FC},I,y} + h_{\mathrm{DC},I,y} \right) \right]_{\mathbf{I}_I = \mathbf{0}} \left(\rho^{\alpha}(\mathbf{r}, \mathbf{r}') - \rho^{\beta}(\mathbf{r}, \mathbf{r}') \right) , \tag{2.288}$$

[64] Note that we assume a net electron spin equal to $\frac{1}{2}$.

where $h_{\mathrm{FC},I,y}$ and $h_{\mathrm{DC},I,y}$ denote:

$$h_{\mathrm{FC},I,y} = \frac{2}{3}\mu_0 g_e \mu_e g_I \mu_I \delta\left(\mathbf{r}' - \mathbf{R}_I\right) I_{I,y} \,, \tag{2.289}$$

$$h_{\mathrm{DC},I,y} = \frac{1}{4\pi}\mu_0 g_e \mu_e g_I \mu_I \left[\frac{3\left(\mathbf{r}' - \mathbf{R}_I\right)^{\mathrm{T}}\left(\mathbf{r}' - \mathbf{R}_I\right) - \mathbf{1}\left|\mathbf{r}' - \mathbf{R}_I\right|^2}{\left|\mathbf{r}' - \mathbf{R}_I\right|^5} \cdot \mathbf{I}_I\right]_y . \tag{2.290}$$

In a coordinate system with the origin fixed to the position of the I-th atomic nucleus, and after insertion of the spin density $\rho_{\mathrm{s}} = \rho^{\alpha} - \rho^{\beta}$, (2.288) simplifies to:

$$A_{I,xy} = A^{\mathrm{iso}}_{I,xy}\delta_{xy} + A^{\mathrm{ani}}_{I,xy} \,, \tag{2.291}$$

$$A^{\mathrm{iso}}_{I,xy} = \frac{2}{3}\mu_0 g_e \mu_e g_I \mu_I \rho_{\mathrm{s}}(\mathbf{0}) \,, \tag{2.292}$$

$$A^{\mathrm{ani}}_{I,xy} = \frac{1}{4\pi}\mu_0 g_e \mu_e g_I \mu_I \int \mathrm{d}\mathbf{r}\rho_{\mathrm{s}}(\mathbf{r})\frac{3r_x r_y - \delta_{xy} r^2}{r^5} \,. \tag{2.293}$$

2.4.2 The A tensor in CPMD: implementation and implications

In (2.291)-(2.293), the electron-spin density ρ_{s} is the only quantity needed from the electronic many-body problem. We also observe that the tensor A_I mainly probes the spin density in the close region around the position of the I-th atomic nucleus. It is therefore essential to have an accurate description of the spin density in that region of space.

The almost mandatory use of pseudopotentials in the CPMD code (see section 2.3.6) implies that: i) the PSP-KS orbitals differ from the AE-KS orbitals (which would result from an all-electron simulation) in pre-defined regions centered on the positions of the atomic nuclei, and ii) the possible contributions from core polarization are not included. A popular solution for the former problem is the projector-augmented-wave method (PAW),[56] which involves a reconstruction of the AE-KS orbitals based on the PSP-KS orbitals. The A-tensor implementation in CPMD is an *ex-post* application of the PAW method,[7] since

the reconstruction occurs only after the self-consistent procedure of the PSP-Kohn-Sham-DFT scheme.[65]

The PAW method: basic concepts

Essentially, the PAW method assumes that a PSP-KS orbital ψ_i^{PSP} from a simulation of a molecular configuration is atomic (or atom-like) close to the atomic nucleus I, and therefore this orbital can be expanded locally in a linear combination of the atomic PSP wave functions ϕ_I^{PSP} of this atom in its reference state (see section 2.1.4). The same assumptation is made for the corresponding KS orbital from an all-electron simulation (denoted here with the superscript AE), but the set of atomic AE wave functions is limited to the subset of AE wave functions for which a corresponding PSP wave function is available (again, see section 2.1.4). Moreover, the expansion coefficients corresponding with every pair of atomic AE and PSP wave functions are assumed to be equal.

When we compute the weights of every ϕ_I^{PSP} in ψ_i^{PSP}, using appropriate projectors p_I, the above assumptations allow us to replace every PSP component from ψ_i^{PSP} with a corresponding AE component, a process which effectively reconstructs the AE-KS orbital:[66]

$$\psi_i^{\mathrm{AE}}(\mathbf{r}) = \psi_i^{\mathrm{PSP}}(\mathbf{r}) + \sum_{I\in\mathrm{PSP},nlm} \left(\phi_{I,nlm}^{\mathrm{AE}}(\mathbf{r}) - \phi_{I,nlm}^{\mathrm{PSP}}(\mathbf{r})\right) \int \mathrm{d}\mathbf{r}' p_{I,nlm}^*(\mathbf{r}')\psi_i^{\mathrm{PSP}}(\mathbf{r}') \,, \tag{2.294}$$

where the sum over nlm covers the entire set of atomic PSP wave functions (and therefore also the corresponding AE wave functions) from the reference configuration of the I-th atom. This sum will be concisely denoted with just one index $k \in \{nlm\}$.

The shape of the projectors p_I is determined by the following conditions: i) the projection only occurs in a limited region around the atomic nucleus I, where the wave function is considered atomic, and ii) the overlap integrals with the atomic PSP wave functions ϕ_I^{PSP} satisfy

[65] The PAW method is more commonly applied *within* the self-consistent procedure of the Kohn-Sham-DFT scheme. In this way, effectively, an all-electron description for the valence electons arises, while the core electrons are still considered fixed. For this variant of the PAW method, too, a procedure for the calculation of the A tensor was elaborated.[8]

[66] Note that for every function corresponding to a specific atom, $\mathbf{r}$ is implicitly referenced with respect to the position of the I-th the atomic nucleus.

$$\int \mathrm{d}\mathbf{r} p^*_{I,k'}(\mathbf{r})\phi^{\mathrm{PSP}}_{I,k}(\mathbf{r}) = \delta_{k'k} \; . \tag{2.295}$$

The first condition is fulfilled by including a (spherically symmetric) cutoff function d_I around each atomic nucleus I:

$$p_I(\mathbf{r}) = d_I(r)\tilde{p}_I(\mathbf{r}) \; . \tag{2.296}$$

Under the additional assumption of completeness of the atomic PSP wave functions in the atomic region:

$$\tilde{p}_{I,k'}(\mathbf{r}) = \sum_{k''} \alpha_{k''k'}\phi^{\mathrm{PSP}}_{I,k''}(\mathbf{r}) \; , \tag{2.297}$$

we can express (2.295) as:

$$\int \mathrm{d}\mathbf{r} p^*_{I,k'}(\mathbf{r})\phi^{\mathrm{PSP}}_{I,k}(\mathbf{r}) = \sum_{k''} \alpha^*_{k''k} \int \mathrm{d}\mathbf{r} d^*_I(r)\phi^{*,\mathrm{PSP}}_{I,k''}(\mathbf{r})\phi^{\mathrm{PSP}}_{I,k}(\mathbf{r}) = \delta_{k'k} \; . \tag{2.298}$$

This allows us to determine the expansion coefficients $\alpha_{k''k}$.

Using (2.294), we can calculate the matrix elements of a (semi-)local one-particle operator $O(\mathbf{r})$ in the AE-KS orbitals:

$$\begin{aligned}
&\int \mathrm{d}\mathbf{r}\psi^{*,\mathrm{AE}}_j(\mathbf{r})O(\mathbf{r})\psi^{\mathrm{AE}}_i(\mathbf{r}) = \int \mathrm{d}\mathbf{r}\psi^{*,\mathrm{PSP}}_j(\mathbf{r})O(\mathbf{r})\psi^{\mathrm{PSP}}_i(\mathbf{r}) \\
&+ \sum_{I\in\mathrm{PSP}}\sum_{k'k} \int \mathrm{d}\mathbf{r}\psi^{*,\mathrm{PSP}}_j(\mathbf{r})p_{I,k'}(\mathbf{r}) \left(\int \mathrm{d}\mathbf{r}\phi^{*,\mathrm{AE}}_{I,k'}(\mathbf{r})O(\mathbf{r})\phi^{\mathrm{AE}}_{I,k}(\mathbf{r}) \right. \\
&\left. - \int \mathrm{d}\mathbf{r}\phi^{*,\mathrm{PSP}}_{I,k'}(\mathbf{r})O(\mathbf{r})\phi^{\mathrm{PSP}}_{I,k}(\mathbf{r}) \right) \int \mathrm{d}\mathbf{r} p^*_{I,k}(\mathbf{r})\psi^{\mathrm{PSP}}_i(\mathbf{r}) \; .
\end{aligned} \tag{2.299}$$

Now, a number of (sometimes) drastic approximations are introduced. First, the PSP-KS orbitals are assumed to consist only of one s-type and three p-type (due to the multiplicity $2l+1$ in the energy levels of the orbital angular momentum) atomic PSP wave functions in the different atomic regions. Second, $d_I(r) = 1$ within in the atomic region of the I-th atomic nucleus and $d_I(r) = 0$ outside of that region. Third, the atomic wave functions are redefined: outside their corresponding atomic region, they are put to zero, and the part within the

atomic region is renormalized so as to have a total expectation value of 1. From (2.298), it then follows that the projectors are equal to:

$$p_{I,s}(\mathbf{r}) = \phi^{\mathrm{PSP}}_{I,s}(r)Y_{00}(\Omega)\ , \qquad p_{I,p_m}(\mathbf{r}) = \phi^{\mathrm{PSP}}_{I,p}(r)Y_{1m}(\Omega)\ , \tag{2.300}$$

with Y the spherical harmonics and Ω the solid angle. In this way, we arrive at the simplified PAW method for the A tensor presented in Ref. [7].

The anisotropic component A^{ani} of the A tensor in the simplified PAW method

$A^{\mathrm{ani}}_{I,xy}$ can be expressed as a linear combination of matrix elements of the following type:

$$\int \mathrm{d}\mathbf{r}\psi^{*,\mathrm{AE}}_i(\mathbf{r})\frac{3r_xr_y-\delta_{xy}r^2}{r^5}\psi^{\mathrm{AE}}_i(\mathbf{r})\ , \tag{2.301}$$

with – as always – the origin of $\mathbf{r}$ equal to the position of the atomic nucleus I. The PAW method (2.299) is applied onto these matrix elements. It is assumed that the operator $\frac{3r_xr_y-\delta_{xy}r^2}{r^5}$ is localized to such an extent that the reconstruction is only needed within the atomic region corresponding to the I-th atomic nucleus. After separating the radial and angular components of the operator,[67] we also observe that the angular parts of the integrals $\int \mathrm{d}\mathbf{r}\phi^{*,\mathrm{AE}}_{I,k'}(\mathbf{r})\frac{3r_xr_y-\delta_{xy}r^2}{r^5}\phi^{\mathrm{AE}}_{I,k}(\mathbf{r})$ and $\int \mathrm{d}\mathbf{r}\phi^{*,\mathrm{PSP}}_{I,k'}(\mathbf{r})\frac{3r_xr_y-\delta_{xy}r^2}{r^5}\phi^{\mathrm{PSP}}_{I,k}(\mathbf{r})$ equal zero, unless the atomic wave functions in the integrals are both p-type in the angular component. From (2.299) it follows that:

[67] Using the identities:

$$\begin{aligned}
r_xr_x &= r^2\sin^2(\theta)\cos^2(\phi)\\
r_yr_y &= r^2\sin^2(\theta)\sin^2(\phi)\\
r_zr_z &= r^2\cos^2(\theta)\\
r_xr_y = r_yr_x &= r^2\sin^2(\theta)\cos(\phi)\sin(\phi)\\
r_xr_z = r_zr_x &= r^2\sin(\theta)\cos(\theta)\cos(\phi)\\
r_yr_z = r_zr_y &= r^2\sin(\theta)\cos(\theta)\sin(\phi)
\end{aligned}$$

$$\int \mathrm{d}\mathbf{r}\psi_i^{*,\mathrm{AE}}(\mathbf{r})\frac{3r_xr_y-\delta_{xy}r^2}{r^5}\psi_i^{\mathrm{AE}}(\mathbf{r}) = \int \mathrm{d}\mathbf{r}\psi_i^{*,\mathrm{PSP}}(\mathbf{r})\frac{3r_xr_y-\delta_{xy}r^2}{r^5}\psi_i^{\mathrm{PSP}}(\mathbf{r})$$
$$+\int r^2\mathrm{d}r\frac{r^2}{r^5}\left(|\phi_{I,p}^{\mathrm{AE}}(r)|^2-|\phi_{I,p}^{\mathrm{PSP}}(r)|^2\right)$$
$$\times\sum_{p_{m'},p_m}\mathcal{C}_{p_{m'},p_m,x,y}\int \mathrm{d}\mathbf{r}\psi_i^{*,\mathrm{PSP}}(\mathbf{r})\phi_{I,p_{m'}}^{\mathrm{PSP}}(\mathbf{r})\int \mathrm{d}\mathbf{r}\phi_{I,p_m}^{*,\mathrm{PSP}}(\mathbf{r})\psi_i^{\mathrm{PSP}}(\mathbf{r})\ . \quad (2.302)$$

Here, $\mathcal{C}_{p_{m'},p_m,x,y}$ is the integral in the solid angle of the product of two spherical harmonics $Y_{1m'}^*(\Omega)$ and $Y_{1m}(\Omega)$, and the angular part of $\frac{3r_xr_y-\delta_{xy}r^2}{r^5}$.

Fortunately, we can avoid the computation of $(\sum_{p_{m'},p_m}...)$ in (2.302),[68] by using the completeness relation of the atomic PSP wave functions for the description of the PSP-KS orbitals in the atomic region of the atomic nucleus. In order to indicate this region, we reintroduce the cutoff function $d_I(r)$. The matrix element of the operator $d_I(r)\frac{3r_xr_y-\delta_{xy}r^2}{r^5}$ in the PSP-KS orbitals can then be written as:

$$\int \mathrm{d}\mathbf{r}\psi_i^{*,\mathrm{PSP}}(\mathbf{r})d_I(r)\frac{3r_xr_y-\delta_{xy}r^2}{r^5}\psi_i^{\mathrm{PSP}}(\mathbf{r}) = \int r^2\mathrm{d}r d_I(r)\frac{r^2}{r^5}|\phi_{I,p}^{\mathrm{PSP}}(r)|^2$$
$$\times\sum_{p_{m'},p_m}\mathcal{C}_{p_{m'},p_m,x,y}\int \mathrm{d}\mathbf{r}\psi_i^{*,\mathrm{PSP}}(\mathbf{r})\phi_{I,p_{m'}}^{\mathrm{PSP}}(\mathbf{r})\int \mathrm{d}\mathbf{r}\phi_{I,p_m}^{*,\mathrm{PSP}}(\mathbf{r})\psi_i^{\mathrm{PSP}}(\mathbf{r})\ . \quad (2.303)$$

Using (2.303), we can eliminate the sum $\sum_{p_i,p_j}$ in (2.302). Using an appropriate summation over spin-up and spin-down KS orbitals, we finally obtain the following expression for the anisotropic component A^{ani} of the A tensor:[69]

$$\int \mathrm{d}\mathbf{r}\rho_{\mathrm{s}}^{\mathrm{AE}}(\mathbf{r})\frac{3r_xr_y-\delta_{xy}r^2}{r^5} = \int \mathrm{d}\mathbf{r}\rho_{\mathrm{s}}^{\mathrm{PSP}}(\mathbf{r})\frac{3r_xr_y-\delta_{xy}r^2}{r^5}$$
$$+\frac{\int \mathrm{d}\mathbf{r}d_I(r)\rho_{\mathrm{s}}^{\mathrm{PSP}}(\mathbf{r})\frac{3r_xr_y-\delta_{xy}r^2}{r^5}}{\int r^2\mathrm{d}r d_I(r)\frac{r^2}{r^5}|\phi_{I,p}^{\mathrm{PSP}}(r)|^2}\int r^2\mathrm{d}r\frac{r^2}{r^5}\left(|\phi_{I,p}^{\mathrm{AE}}(r)|^2-|\phi_{I,p}^{\mathrm{PSP}}(r)|^2\right)\ . \quad (2.304)$$

[68] The computation of the integrals $\int \mathrm{d}\mathbf{r}\psi_i^{*,\mathrm{PSP}}(\mathbf{r})\phi_{I,p_{m'}}^{\mathrm{PSP}}(\mathbf{r})$ and $\int \mathrm{d}\mathbf{r}\phi_{I,p_m}^{*,\mathrm{PSP}}(\mathbf{r})\psi_i^{\mathrm{PSP}}(\mathbf{r})$ is a computational burden: ψ_i^{PSP} is defined on an FFT grid determined by the simulation cell, $\phi_{I,p_m}^{\mathrm{PSP}}$ is defined on a spherical grid.

[69] Without the prefactor, see (2.293).

Practically, the integrals containing the spin density are elaborated in reciprocal space, since for an arbitrary periodic function $f(\mathbf{r})$ it holds that:

$$\begin{aligned}&\int \mathrm{d}\mathbf{r} f(\mathbf{r}) \frac{3(r_x - R_{I,x})(r_y - R_{I,y}) - \delta_{xy} \left|\mathbf{r} - \mathbf{R}_I\right|^2}{\left|\mathbf{r} - \mathbf{R}_I\right|^5} \\ &= -4\pi \sum_{\mathbf{G}\neq\mathbf{0}} \frac{G_x G_y - \frac{1}{3} G^2 \delta_{xy}}{G^2} f(\mathbf{G}) \mathrm{e}^{i\mathbf{G}.\mathbf{R}_I} \,, \end{aligned} \tag{2.305}$$

with $\mathbf{R}_I$ the position of the atomic nucleus I. The integrals comprising the atomic wave functions are evaluated in real space using numerical integration techniques. These wave functions are available upon creation of the pseudopotential.

The isotropic component A^{iso} of the A tensor in the simplified PAW method

A similar technique can be applied for the computation of the isotropic hyperfine parameter $A^{\mathrm{iso}}_{I,xy}$ (2.292). In this case, the operator $O(\mathbf{r})$ from (2.299) is equal to $\delta(\mathbf{r})$. Obviously, this operator is strongly localized, therefore the reconstruction only needs to be carried out in the atomic region corresponding with the atomic nucleus I. Since the radial components of the p-type atomic wave functions disappear on the position of the atomic nucleus, whereas those of the s-type do not, it follows from (2.299) that:

$$\begin{aligned}&\int \mathrm{d}\mathbf{r} \psi_i^{*,\mathrm{AE}}(\mathbf{r}) \delta(\mathbf{r}) \psi_i^{\mathrm{AE}}(\mathbf{r}) = \int \mathrm{d}\mathbf{r} \psi_i^{*,\mathrm{PSP}}(\mathbf{r}) \delta(\mathbf{r}) \psi_i^{\mathrm{PSP}}(\mathbf{r}) \\ &+ \left(|\phi_{I,s}^{\mathrm{AE}}(\mathbf{0})|^2 - |\phi_{I,s}^{\mathrm{PSP}}(\mathbf{0})|^2\right) \\ &\times \int \mathrm{d}\mathbf{r} \psi_i^{*,\mathrm{PSP}}(\mathbf{r}) \phi_{I,s}^{\mathrm{PSP}}(\mathbf{r}) \int \mathrm{d}\mathbf{r} \phi_{I,s}^{*,\mathrm{PSP}}(\mathbf{r}) \psi_i^{\mathrm{PSP}}(\mathbf{r}) \,. \end{aligned} \tag{2.306}$$

We can circumvent the computation of the overlap integrals between wave functions that are defined on incompatible grids, by exploiting the completeness relation for the atomic PSP wave functions for the description of the PSP-KS orbitals in the atomic region of the atomic nucleus:

$$\begin{aligned}&\int \mathrm{d}\mathbf{r} \psi_i^{*,\mathrm{PSP}}(\mathbf{r}) \delta(\mathbf{r}) \psi_i^{\mathrm{PSP}}(\mathbf{r}) = |\phi_{I,s}^{\mathrm{PSP}}(\mathbf{0})|^2 \\ &\times \int \mathrm{d}\mathbf{r} \psi_i^{*,\mathrm{PSP}}(\mathbf{r}) \phi_{I,s}^{\mathrm{PSP}}(\mathbf{r}) \int \mathrm{d}\mathbf{r} \phi_{I,s}^{*,\mathrm{PSP}}(\mathbf{r}) \psi_i^{\mathrm{PSP}}(\mathbf{r}) \,. \end{aligned} \tag{2.307}$$

After eliminating the overlap integrals from (2.306) using (2.307), and after an appropriate summation over spin-up and spin-down KS orbitals, we obtain the following expression for the isotropic component A^{iso} of the A tensor:[70]

$$\begin{aligned} \rho_{\text{s}}^{\text{AE}}(\mathbf{0}) &= \rho_{\text{s}}^{\text{PSP}}(\mathbf{0}) + \left(|\phi_{I,s}^{\text{AE}}(\mathbf{0})|^2 - |\phi_{I,s}^{\text{PSP}}(\mathbf{0})|^2\right) \frac{\rho_{\text{s}}^{\text{PSP}}(\mathbf{0})}{|\phi_{I,s}^{\text{PSP}}(\mathbf{0})|^2} \,, \\ &= \rho_{\text{s}}^{\text{PSP}}(\mathbf{0}) \frac{|\phi_{I,s}^{\text{AE}}(\mathbf{0})|^2}{|\phi_{I,s}^{\text{PSP}}(\mathbf{0})|^2} \,. \end{aligned} \tag{2.308}$$

About the use of the simplified PAW method for the A tensor

The simplified PAW method for the A tensor is based on several assumptions, among which the drastic approximation that, in each atomic region, one s-type and three p-type atomic wave functions form a complete set for describing a random PSP-KS orbital. This restricts the use of the simplified PAW method to light elements, because there, the PSP-KS orbitals do not feature significant components with a higher orbital quantum number. For these light elements, the simplified PAW provides good results: although the isotropic component for the A tensor can deviate to some extent, the anisotropic component is mostly quite accurately predicted.[Art. 1-3][50] Naturally, the general PAW method can be applied to higher orbital quantum numbers, but in this way, the effects of the polarization of the core electrons will never be included. Moreover, the PAW method does not correct for the problems related to the spin-dependent exchange-correlation potential v_{XC}^{τ} in the PSP approximation, needed for an accurate description of the polarization of the valence electrons.[50]

2.4.3 The A tensor in CP2K: implementation and implications

The shortcomings related to the calculation of the A tensor in the PSP approximation clearly illustrate the need for a hybrid method which would allow for an AE description[71] of the atomic nuclei of interest (this usually involves the radical center and possibly its surroundings atoms), and at the same time leaves open the possibility of a PSP description of the remaining atoms in the simulation cell. Such an approximation will most probably

[70] Without the prefactor, see (2.292).

[71] Thus using the nuclear Coulomb potential.

not affect the A tensors of interest, since the A tensor is mainly determined by the electronic structure in a limited region around the position of the corresponding atomic nucleus. The GAPW method (see section 2.1.6) is ideally suited for this purpose: the method exists in both a PSP and an AE approach, and both can be easily combined within one simulation. Moreover, a GAPW simulation with an AE description for the atoms of interest requires only a relatively small additional computational cost, thanks to the use of Gaussian functions[72]. In a pure plane-wave basis set for example the additional computational cost would be manifestly higher.[73]

The anisotropic component A^{ani} of the A-tensor in the GAPW method

For the calculation of $A^{\text{ani}}_{I,xy}$, the GAPW representation of the spin density (2.84) is reordered:

$$\rho_s = \tilde{\rho}_s + \rho^1_{s,I} - \tilde{\rho}^1_{s,I} + \sum_{J(J\neq I)} \left(\rho^1_{s,J} - \tilde{\rho}^1_{s,J}\right) \ . \tag{2.309}$$

Inserting this expression into (2.293), and taking into account (2.305) for the soft spin density $\tilde{\rho}_s$, we can calculate $A^{\text{ani}}_{I,xy}$ as follows:

$$\begin{aligned} A^{\text{ani}}_{I,xy} &= \frac{1}{4\pi}\mu_0 g_e \mu_e g_I \mu_I \Bigg(\\ &- 4\pi \sum_{\frac{1}{2}|\mathbf{G}|<E_c, \mathbf{G}\neq\mathbf{0}} \frac{\left(G_x G_y - \frac{1}{3}G^2\delta_{xy}\right)}{G^2} \tilde{\rho}_s(\mathbf{G}) \mathrm{e}^{i\mathbf{G}\cdot\mathbf{R}_I} \\ &+ \int_{U_I} \mathrm{d}\mathbf{r} \left(\rho^1_{s,I}(\mathbf{r}) - \tilde{\rho}^1_{s,I}(\mathbf{r})\right) \frac{3r_x r_y - \delta_{xy} r^2}{r^5} \Bigg) \\ &+ \Delta A^{\text{ani}}_{I,xy} \ . \end{aligned} \tag{2.310}$$

The integration domain of the integration comprising the atom-centered spin densities can be limited to U_I, because of (2.88). $\Delta A^{\text{ani}}_{I,xy}$ denotes the small

[72] More precise: contracted periodic Gaussian functions.

[73] Because a basis set with a *huge* amount of plane waves would be required for the correct description of the Coulomb potential and the sharp oscillations of the wave functions in the close surroundings of the atomic nuclei.

contributions originating from the difference between the real and the soft spin densities $\rho^1_{s,J} - \tilde{\rho}^1_{s,J}$ in neighboring atomic regions U_J:

$$\begin{aligned} \Delta A^{\text{ani}}_{I,xy} &= \frac{1}{4\pi}\mu_0 g_e \mu_e g_I \mu_I \\ &\times \sum_{J(J\neq I, R_{IJ}<R_c)} \int_{U_J} \mathrm{d}\mathbf{r} \left(\rho^1_{s,J}(\mathbf{r}) - \tilde{\rho}^1_{s,J}(\mathbf{r})\right) \\ &\times \frac{3\left(r_x + R_{JI,x}\right)\left(r_y + R_{JI,y}\right) - \delta_{xy}\left|\mathbf{r}+\mathbf{R}_{JI}\right|^2}{\left|\mathbf{r}+\mathbf{R}_{JI}\right|^5} \,. \end{aligned} \tag{2.311}$$

In the above equation, the origin $\mathbf{r}$ always equals the position of the atomic nucleus J, and $\mathbf{R}_{JI} = \mathbf{R}_J - \mathbf{R}_I$ is the vector connecting the atomic nuclei J and I. Only the most nearby atomic regions need to be included in the sum. This can be controlled by choosing a maximum value R_c for $R_{JI} = \left|\mathbf{R}_{JI}\right|$. The effect of including $\Delta A^{\text{ani}}_{I,xy}$ in the total A tensor was studied in Ref. [Art. 3].

The isotropic component A^{iso} of the A tensor in the GAPW method

$A^{\text{iso}}_{I,xy}$ is evaluated from the atom-centered spin density $\rho^1_{s,I}$, which equals to ρ_s in the atom-centered region U_I (2.89):

$$A^{\text{iso}}_{I,xy} = \frac{2}{3}\mu_0 g_e \mu_e g_I \mu_I \rho^1_{s,I}(\mathbf{0}) \,. \tag{2.312}$$

A scalar-relativistic alternative for (2.292) was also implemented. It is defined as:[8, 57][74]

$$A^{\text{iso}}_{I,xy} = \frac{2}{3}\mu_0 g_e \mu_e g_I \mu_I \int_{U_I} \mathrm{d}\mathbf{r}\rho_s(\mathbf{r})\delta_{T,I}(\mathbf{r}) \,, \tag{2.313}$$

where $\delta_{T,I}$ denotes a spread-out δ function, which depends on the atomic number Z corresponding with the I-th atomic nucleus:

$$\delta_{T,I}(\mathbf{r}) \cong \frac{1}{4\pi r^2}\frac{2}{Z_I\alpha^2}\frac{1}{\left(1+\frac{2r}{Z_I\alpha^2}\right)^2} \,. \tag{2.314}$$

[74]The theoretical elaboration will not be discussed here. The interested reader is referred to the aforementioned references.

In the non-relativistic limit, $\delta_{\mathrm{T},I}$ simplifies to the Dirac delta.

Because of this δ function, we can safely restrict the integration in (2.313) to U_I, and employ the atom-centered spin density $\rho^1_{s,I}$ again.

About the use of the of the GAPW method for the A tensor

Very similar statements as with the g tensor can be made about the A tensor. In Ref. [Art. 3], the GAPW method for the A tensor is thoroughly tested. The A tensors of an extensive selection of atoms and small molecules in the gas phase, computed with the AE implementation of the GAPW method, are in excellent agreement with those obtained with GAUSSIAN 03,[58] a program package (exclusively) suitable for gas-phase simulations, which also adopts both the LCAO and the CPGF approximation (see section 2.1.3). Moreover, it was observed that the hybrid use of an AE approach for the radical center and the PSP approximation for the remaining atoms in the simulation cell did not significantly affect the A-tensor predictions in the several crystals defects that were studied (see [Art. 3] and [Art. 4]). We can therefore state that we have obtained both an accurate and at the same time a relatively cheap (in terms of computational cost) method for A-tensor calculations in PBC simulations. We wish to remind, though, that the GAPW method (just like the GPW method) at present assumes the Γ-point approximation, which somewhat restricts the choice for the dimensions of the simulation cell for a material under study, and in turn determines whether this material can be studied in this approximation at a reasonable computational cost.

3 Paper I and II

First-principles calculations of the EPR g tensor in extended periodic systems

R. Declerck, V. Van Speybroeck, and M. Waroquier

1. Physical Review B 73 (11), 115113 (2006)

2. Physicalia Magazine 28 (3), 165-181 (2006)

PHYSICAL REVIEW B **73**, 115113 (2006)

First-principles calculation of the EPR g tensor in extended periodic systems

R. Declerck, V. Van Speybroeck, and M. Waroquier*
Center for Molecular Modeling, Laboratory of Theoretical Physics, Ghent University, Proeftuinstraat 86, B-9000 Gent, Belgium
(Received 12 December 2005; revised manuscript received 13 February 2006; published 20 March 2006)

A method for the *ab initio* prediction of the EPR g tensor for paramagnetic defects in systems under periodic boundary conditions is presented. It is based on density functional theory and the pseudopotential approximation. The formalism is applicable to crystalline and amorphous insulators, as well as to isolated molecules using a supercell technique. The method is validated by comparison with a well-established theoretical approach and experimental data for a series of small isolated molecules. Finally the EPR parameters of an O_3^- defect in a KCl lattice are evaluated following the new procedure, yielding results in good agreement with experiment and at an attractive computational cost.

DOI: 10.1103/PhysRevB.73.115113 PACS number(s): 71.15.−m, 76.30.−v, 61.72.Bb

I. INTRODUCTION

Electron paramagnetic resonance (EPR) is one of the most powerful spectroscopic techniques to identify paramagnetic defects. The *ab initio* quantum mechanical prediction of EPR quantities within density functional theory[1,2] has become possible through the pioneering work by Schreckenbach and Ziegler.[3] Since then, many other DFT-based approaches have been published. A recent overview is given in Ref. 4. These approaches are applicable to isolated systems only. Many useful applications of the EPR technique, however, involve paramagnetic defects embedded in crystals.

Recently, Pickard and Mauri[5] presented an all-electron implementation of the EPR g tensor applicable on extended periodic systems, using their gauge including projector augmented wave (GIPAW) method,[6] which is based on an extension to the projector augmented wave (PAW) method of Blöchl[7] and the method of Mauri *et al.*[8] (MPL). Although the original MPL method neglects the complications inherent within the pseudopotential approximation, it was found to successfully predict the nuclear magnetic resonance (NMR) properties in extended systems for elements up to Ne. The GIPAW method corrects for the deficiencies of the pseudopotentials, and in that sense one could consider it as an all-electron approach. In Ref. 6, the GIPAW method was successfully used for the calculation of all-electron NMR properties.

Almost simultaneously Sebastiani and Parrinello[9] presented a conceptually different approach for the calculation of NMR properties in extended periodic systems (hereafter referred to as the Sebastiani method). The Sebastiani method also lacks corrections for the use of pseudopotentials, and therefore can be best compared with the MPL method. In the prediction of NMR properties, its use is thus also limited to elements up to Ne.

In this paper, we propose an alternative pseudopotential approach for the calculation of the EPR g tensor in extended periodic systems which relies on this Sebastiani method. It was already suggested by Schreckenbach in Ref. 10 that the pseudopotential approximation could also be used for the evaluation of the g tensor, since the g tensor does not depend as crucially on the region near the core as is the case for the NMR shielding tensor. In that region, the pseudopotential approximation does not correctly describe the nodal structure of the electronic wave functions. However, no implementation was available yet that would validate or disprove this assertion. By comparison with experimental data from the literature and calculated results from Schreckenbach and Ziegler, we will investigate for which elements and at what computational cost our pseudopotential-based approach is applicable. Finally, as a typical example of a system under periodic boundary conditions, the proposed method is applied to an ozonide paramagnetic defect (O_3^-) embedded in an alkali halide lattice (KCl).

II. THEORY

The energy levels and intensities derived from EPR experiments can be reproduced using an effective Hamiltonian, expressed in terms of effective spin operators $\mathbf{S}$ (electronic) and $\mathbf{I}_n$ (nuclear). This effective Hamiltonian generally consists of three contributions,

$$H_{\text{eff}} = \sum_n \mathbf{S}\cdot\mathbf{A_n}\cdot\mathbf{I_n} + \frac{\alpha}{2}\mathbf{B}\cdot\mathbf{g}\cdot\mathbf{S} + \mathbf{S}\cdot\mathbf{D}\cdot\mathbf{S}. \quad (1)$$

Here, $\mathbf{A_n}$ is the hyperfine tensor of rank 2 describing the coupling between the electronic $\mathbf{S}$ and the nuclear $\mathbf{I}$ spin at the center of a nucleus n. $\mathbf{g}$ is the g tensor, which describes the coupling between the electronic spin system and a constant external magnetic field $\mathbf{B}$. $\mathbf{D}$ is the zero-field splitting tensor arising from the magnetic dipolar interactions between multiple unpaired electrons in the system. α represents the fine-structure constant and the summation n runs over the nuclei. Atomic units are used throughout this paper. We will consider only systems with net electronic spin 1/2 in the following, although the method can be expanded to higher spin radicals.[11]

The g tensor from EPR spectroscopy is a second-order property and can therefore be evaluated using double perturbation theory. The perturbation parameters are components along the axes of a given coordinate system of a constant external magnetic field, B_x, and the net electronic spin component, S_y,

$$g_{xy} = \frac{2}{\alpha} \left. \frac{\partial^2 \langle \Psi | H_{\text{eff}} | \Psi \rangle}{\partial B_x \partial S_y} \right|_{\boldsymbol{B}=\boldsymbol{S}=\boldsymbol{0}}. \tag{2}$$

Using the Helmann-Feynman theorem of double perturbation theory, which states that molecular orbitals have to be calculated up to first order in one parameter alone, it is sufficient to calculate the magnetic-field perturbed electronic wave function and to consider only perturbing Hamiltonians containing spin operators. In order to obtain a prediction for the g tensor from first principles, we need to equate the expectation value expression of the effective Hamiltonian with the one of a true quantum mechanical (QM) Hamiltonian in the presence of a constant external magnetic field **B**,[12]

$$g_{xy} = \frac{2}{\alpha} \frac{\partial}{\partial B_x} \langle \Psi_{B_x} | \left. \frac{\partial H_{\text{QM}}}{\partial S_y} \right|_{S=0} | \Psi_{B_x} \rangle |_{\boldsymbol{B}=\boldsymbol{0}}. \tag{3}$$

Within the formalism of spin polarized density functional theory, the following expression for the components of the g tensor results:[3,5,12]

$$g_{xy} = g_e \delta_{xy} + \Delta g_{xy}^{\text{ZKE}} + \Delta g_{xy}^{\text{SO}} + \Delta g_{xy}^{\text{SOO}}, \tag{4}$$

where g_e denotes the free electron g value, and

$$\Delta g_{xy}^{\text{ZKE}} = -\alpha^2 g_e (T^\alpha - T^\beta) \delta_{xy} \tag{5}$$

is the electron Zeeman kinetic energy (ZKE) correction, which is a purely kinematic relativistic correction.

A treatment for the spin-orbit (SO) contribution was elaborated by Schreckenbach and Ziegler,[3] and is used in several other implementations,[5,13,14]

$$\Delta g_{xy}^{\text{SO}} = \alpha (g_e - 1) \int d\boldsymbol{r} [\boldsymbol{j}_{\boldsymbol{B}_x}^\alpha(\boldsymbol{r}) \times \nabla V_{\text{eff}}^\alpha(\boldsymbol{r}) - \boldsymbol{j}_{\boldsymbol{B}_x}^\beta(\boldsymbol{r}) \times \nabla V_{\text{eff}}^\beta(\boldsymbol{r})]_y. \tag{6}$$

The spin-other-orbit (SOO) correction describes the screening of the external field **B** by the induced electronic currents, as experienced by the unpaired electron. An ingenious approximate treatment for the SOO contribution, which is often found to be negligible, was suggested by Pickard and Mauri,[5]

$$\Delta g_{xy}^{\text{SOO}} = 2 \int d\boldsymbol{r} B_{y,\boldsymbol{B}_x}(\boldsymbol{r}) [\rho^\alpha(\boldsymbol{r}) - \rho^\beta(\boldsymbol{r})]. \tag{7}$$

In Eqs. (5)–(7), the superscript α denotes the spin-up channel and T^α and ρ^α are the unperturbed kinetic energy and electron probability density of the spin α channel, respectively. $\boldsymbol{j}_{B_x}^\alpha(\boldsymbol{r})$ is the electronic current density of spin α electrons, arising from a unit magnetic field coinciding with the x axis. $V_{\text{eff}}^\alpha(\boldsymbol{r})$ is an effective potential for the spin α channel, defined as

$$V_{\text{eff}}^\alpha = \sum_n \frac{-Z_{\text{ion},n}}{|\boldsymbol{r} - \boldsymbol{R}_n|} \text{erf}\left(\frac{|\boldsymbol{r} - \boldsymbol{R}_n|}{r_{c,n}} \right) + V_H + V_{\text{XC}}^\alpha, \tag{8}$$

where erf denotes the error function, Z_{ion} the ionic charge (i.e., charge of the nucleus minus charge of the core electrons), V_H the Hartree potential, and V_{XC} the exchange correlation potential. r_c gives the range of the Gaussian ionic charge distribution leading to the erf potential.[15] Similar definitions apply to the spin-down channel, denoted with β. Finally, $B_{y,B_x}(\boldsymbol{r})$ is the y component of the magnetic field due to the total induced current $\boldsymbol{j}_{B_x}^\alpha(\boldsymbol{r}) + \boldsymbol{j}_{B_x}^\beta(\boldsymbol{r})$, corrected for self-interaction by removing the contribution from the current of the unpaired electron, $\boldsymbol{j}_{B_x}^\alpha(\boldsymbol{r}) - \boldsymbol{j}_{B_x}^\beta(\boldsymbol{r})$.

A. Evaluation of $\Delta g_{xy}^{\text{ZKE}}$

In a spin-polarized DFT run, one obtains expressions for the KS orbitals and for the effective potential in both spin channels. This easily allows us to evaluate Eq. (5).

B. Evaluation of $\Delta g_{xy}^{\text{SO}}$ and $\Delta g_{xy}^{\text{SOO}}$

In order to evaluate the more elaborate terms of Eqs. (6) and (7), we need to compute the spin-dependent current densities $\boldsymbol{j}_{B_x}^\tau(\boldsymbol{r})$ ($\tau = \alpha, \beta$), and therefore we make use of the techniques proposed by Sebastiani and Parrinello[9] to include these spin-dependent current densities.

The main obstacle to evaluate these current densities is the fact that the magnetic field perturbation Hamiltonian contains the position operator. In a periodic system, this operator is not properly defined. To deal with this problem, the Sebastiani method makes use of maximally localized Wannier (MLW) orbitals,[16] which are obtained from the canonical KS orbitals by means of a unitary transformation in the subspace of occupied states,

$$|\phi_k^{(0)}\rangle = \sum_l U_{kl} |\phi_l^{\text{KS}}\rangle. \tag{9}$$

For an insulator it can be proven that these MLW orbitals decay exponentially,[17] a crucial feature in the approach. Within the continuous set of gauge transformations (CSGT) method,[18] the electronic current density can be written as a sum of three contributions,

$$\boldsymbol{j}^\tau(\boldsymbol{r}') = \sum_k^{n_\tau} \langle \phi_k^{(0)} | \boldsymbol{j}_{\boldsymbol{r}'} [|\phi_k^{(1a)}\rangle - |\phi_k^{(1b)}\rangle + |\phi_k^{(1c)}\rangle], \tag{10}$$

with the current density operator $\boldsymbol{j}_{\boldsymbol{r}'}$, $\tau = \alpha, \beta$, and

$$|\phi_k^{(1a)}\rangle = \sum_l G_{kl}(\boldsymbol{r} - \boldsymbol{d}_l) \times \boldsymbol{p} |\phi_l^{(0)}\rangle \cdot \boldsymbol{B}, \tag{11}$$

$$|\phi_k^{(1b)}\rangle = \sum_l (\boldsymbol{r}' - \boldsymbol{d}_k) \times G_{kl} \boldsymbol{p} |\phi_l^{(0)}\rangle \cdot \boldsymbol{B}, \tag{12}$$

$$|\phi_k^{(1c)}\rangle = \sum_l G_{kl}(\boldsymbol{d}_k - \boldsymbol{d}_l) \times \boldsymbol{p} |\phi_l^{(0)}\rangle \cdot \boldsymbol{B}. \tag{13}$$

Here, G_{kl} denotes the Green's function and $\boldsymbol{d}_k$ is the center of charge of the corresponding MLW orbital. The Green's function is given by

$$G_{kl} = \sum_{o,u} U_{ko}^\dagger \frac{|\phi_u\rangle\langle\phi_u|}{\epsilon_o - \epsilon_u} U_{ol}, \tag{14}$$

where ϵ_o and ϵ_u represent the Kohn-Sham energies of the occupied and unoccupied orbitals, respectively.

Within the CSGT method, the magnetic response is invariant under a translation of the coordinate system for every individual orbital. This allows us to redefine the position operator, thereby exploiting the spatial localization of the MLW orbitals. A sawtooth-shaped position operator is constructed for every orbital featuring the same periodicity as the simulation cell, with its geometric center located at the center of charge of the corresponding orbital. In doing so, the position operator has the required periodicity of the system, although it shows unphysical behavior around the borders. This, however, does not pose a significant problem as these unphysical transitions of the position operator occur in those regions of space where the state on which it is operating vanishes anyway. It is important to note that for a system with completely delocalized orbitals, like a metal, the decay of the MLW orbitals is insufficient, and therefore this approach will likely fail, unless prodigious simulation cell dimensions are adopted. In that case, the MPL method will be more efficient.

The actual calculation of the first-order corrections to the KS orbitals in the magnetic field is not performed using Green's functions. Instead, they are computed by minimization of the energy functional of second order in the magnetic field, for which a variational principle applies,[19] yielding these first-order corrections.

The full evaluation of Eqs. (11) and (12) for all electronic states k at once can be performed at the computational cost of approximately one total energy calculation. On the other hand, the computation of Eq. (13), which often represents a fairly small correction as compared to Eqs. (11) and (12), is much more intensive as it requires one calculation for every electronic state k (although typically at a lower computational cost than one total energy calculation[20,21]). This aspect hinders the practical use of the Sebastiani method. However, we do not always need to evaluate Eq. (13) for every electronic state k, as we will argue in the following. Since the SO [Eq. (6)] term is found to dominate the SOO [Eq. (7)] term by far in most cases, we focus our attention on the former.

The integrandum of $\Delta g_{xy}^{\mathrm{SO}}$ is composed of a substraction of spin α and spin β contributions. Assuming only small differences between the two effective potentials $V_{\mathrm{eff}}^{\alpha}(\boldsymbol{r})$ and $V_{\mathrm{eff}}^{\beta}(\boldsymbol{r})$, it is superfluous to calculate the corrections of Eq. (13) to $\boldsymbol{j}_{B_x}^{\tau}(\boldsymbol{r})$ for pairs of α and β states that remain unaffected by the presence of the unpaired electron (and thus resemble each other), because they are canceled out anyway. This is especially the case for paramagnetic defects embedded in a crystalline environment, for which this theory is intended. In that case the unpaired electron is often localized in one part of the supercell and will affect merely its near vicinity. Other parts of the periodic box such as the lattice environment at a larger distance of the defect will be less affected.

The overlap with the unpaired electron could be used as an indicator that an evaluation of Eq. (13) may be needed for a particular state. However, due to the Wannier localization, the wave function of the unpaired electron is no longer directly available, because it has been mixed up with other states during the unitary transformation. We therefore introduced the root norm of the spin density as an alternative indicator, as follows:

$$\alpha_k = \int d\boldsymbol{r} \sqrt{|\rho_{\mathrm{spin}}(\boldsymbol{r})|} \cdot |\phi_k(\boldsymbol{r})|. \tag{15}$$

Only if an expansion coefficient α_k exceeds a certain threshold is the calculation of $|\phi_k^{(1c)}\rangle$ performed. This approximation allows for a drastic reduction in computation time in the study of paramagnetic defects in a crystalline environment, without compromising the accuracy of the calculations. This reduction is applicable only in the case of g tensor calculations and not, for example, in the case of NMR chemical shielding tensor calculations, where Eq. (13) had to be neglected in order to make the method computationally efficient.

C. Implications of the pseudopotential approach

The method as described here was implemented in the CPMD program package,[22] a frequently used molecular dynamics code based on a plane-wave pseudopotential implementation, resulting in the absence of core electrons as well as in an inaccurate description of the valence orbitals in a spherical region around the core of each element defined during construction of the pseudopotential, hereafter referred to as the core region.

While this method has proven successful in describing chemical bonding, no evidence is available that the use of pseudopotentials could produce equally meaningful results for the EPR g tensor. However, since the g tensor is essentially a valence property[10,23] and depends less critically on the exact behavior of the electronic wave functions near the cores (as compared to the NMR shielding tensor, for which a pseudopotential approach does in fact work[9]), we believed that the g tensor would not suffer too much from the incorrect shape of the orbitals in the core regions.

By careful analysis of Eqs. (5)–(7), we will now argue that most of the errors introduced by the pseudopotentials can be traced back to the incorrect shape of the unpaired electron in the core regions.

(i) In the $\Delta g_{xy}^{\mathrm{ZKE}}$ term, spin α and β kinetic energies are substracted from each other. The shape of the orbitals in the core regions is largely determined by the strong attractive nuclear potentials. For this reason, the faulty contributions within the core regions in the kinetic energies from paired electrons will cancel out. Thus, the main erroneous contribution comes from the kinetic energy part of the unpaired electron in the core regions. The $\Delta g_{xy}^{\mathrm{ZKE}}$ term is isotropic, and these errors will therefore not influence the direction of the principal axes.

(ii) The same considerations apply to the $\Delta g_{xy}^{\mathrm{SO}}$ term, in which the erroneous contributions in the core regions from paired electrons cancel each other out: due to the dominant nuclear potentials, both effective potentials (and hence their gradients) and the current densities from the paired electrons will resemble each other in the core regions. Thus, the major errors originate from the cross product of the current of the unpaired electron and the gradient of the effective potential in the core regions: $[j_{\boldsymbol{B}_x}^{\alpha}(\boldsymbol{r}) - j_{\boldsymbol{B}_x}^{\beta}(\boldsymbol{r})] \times \nabla V_{\mathrm{eff}}(\mathbf{r})$. Unfortunately, the gradient of the effective potential largely favors the current of the unpaired electron near the cores. In addition, the

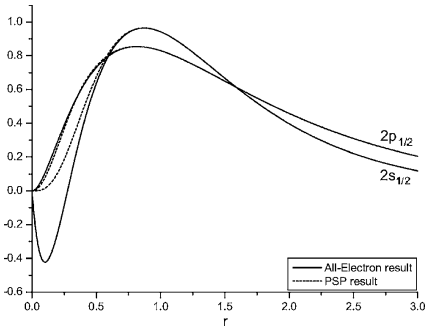

FIG. 1. $2s_{1/2}$ and $2p_{1/2}$ pseudo and all-electron wave functions of the free O atom.

$\Delta g_{xy}^{\mathrm{SO}}$ term is found to be by far the most dominant contribution to the total g tensor.

(iii) In the $\Delta g_{xy}^{\mathrm{SOO}}$ term, the pseudopotential approximation is expected to result in only small errors to the total Δg tensor, because the $\Delta g_{xy}^{\mathrm{SOO}}$ term is found to be very small in comparison with the $\Delta g_{xy}^{\mathrm{SO}}$ term,[5] and because both the induced magnetic field and the spin density do not diverge near the cores.

From this discussion we can conclude that, since $\Delta g_{xy}^{\mathrm{SO}}$ is generally the most important term, a good description of the current of the unpaired electron is the most essential precondition for the success of our pseudopotential method. There are some arguments why this will be the case even when using pseudopotentials. At least for the free atom, the more energetic orbitals do not suffer to the same extent from the use of pseudopotentials in the core region. This is illustrated in Fig. 1 for the $2s_{1/2}$ and $2p_{1/2}$ orbitals of the free O atom. While the $2s_{1/2}$ wave functions completely deviate in the core region, the $2p_{1/2}$ pseudo-wave-function still closely resembles its all-electron counterpart. Close to the core, where a wave function is essentially atomlike (because of the dominating nuclear potential), the unpaired electron wave function will mainly be composed of these more energetic atomic orbitals. In addition, the construction of a pseudopotential for a specific atomic element is not unique. An important degree of freedom is the size of the core region (while acknowledging that the smaller the core region, the higher the computational cost).

III. RESULTS

To validate our pseudopotential approach for the evaluation of the g tensor, we made a comparative study with the all-electron Schreckenbach and Ziegler (SZ) method as well as with experimental data from the literature for a series of small isolated molecules. We also included results from the ZORA approach of Van Lenthe *et al.*,[24] which is based upon a different theoretical approach. We approximated the isolated molecules in the CPMD program package by using large supercells of $(20\ \mathrm{a.u.})^3$. After Wannier localization, we can assume the Wannier orbitals to be so well confined within the supercell that any errors due to the aforementioned nonphysical behavior of the coordinate operator are excluded. The results given are a measure for the accuracy one can expect from a pseudopotential approach without reconstruction techniques for the valence orbitals in the core region. Troullier-Martins[25] (TM) and Goedecker[15] (GO) norm-conserving pseudopotentials were used in this work. Plane-wave cutoff values of 100 Ry (TM) and 150 (GO) were found to yield more than reasonable convergence. These are approximately 30 Ry higher than typically used to describe chemical bonding. Optimized geometries were obtained with the ADF[26–28] package and used throughout. We used PBE[29] gradient corrected functionals in all calculations, and a QZ4P basis set for the nonperiodic calculations. We have also performed the calculations using a BLYP[30,31] functional, but the results have not been reported here, since the choice of the functional only marginally alters the results and does not reveal any additional relevant aspects.

In Table I, the results for radicals composed of lighter elements up to Ne are presented. For both types of pseudopotentials, there is a striking resemblance between our results and those obtained using the SZ method. This accordance could be expected, as both methods are closely related with each other. The deviations that are present should be attributed almost entirely to the effects of pseudopotentials. More insight can be gained from the statistical parameters (see Table II) deduced from the three methods using the data of Table I, whenever experimental results were available. In this statistical study, the predictions of Δg_{zz} for the molecules O_2H and H_2O^+ have been omitted as they perturb completely the statistical parameters for all methods. From Table II, the good agreement between our results and the SZ results becomes particularly clear: the correlation coefficient, the correlation slope, and the standard deviation all agree to within 5% (even within 1% for the GO results), while the SZ method, the ZORA method, and the experimental results deviate on a much larger scale. The good agreement is further confirmed in Table III, where we compare the different contributions to the g tensor for the O_3^- molecule. Summarizing, we believe that it is fair to state that our pseudopotential approach performs equally well as the SZ method in predicting Δg values for lighter elements.

Less accurate results were obtained when studying radicals with heavier elements than Ne, as can be observed from Table IV. Here, the effects of the use of pseudopotentials clearly become apparent, and the available results in Table IV from Ref. 5 show the superior behavior of the GIPAW method for these elements. In many cases, however, the calculated numbers from our method still exhibit at least the right trend. In order to produce better results for these heavier elements, a smaller core region is required. This can be accomplished by including more electrons explicitly in the calculations than required to adequately describe chemical bonding. This will result in a much better description of the electronic wave functions near the core, and as a result, a reduced core region.

To illustrate this, we have plotted the $3s_{1/2}$ and the $3p_{1/2}$ wave functions for the free Si atom in Fig. 2, using the stan-

TABLE I. Calculated Δg values (in ppm) for a series of small isolated molecules composed of elements up to Ne, using the standard Troullier-Martins and Goedecker pseudopotential sets supplied with CPMD, in comparison with experiment and other treatments. For comparison with the SZ results, we omit in this table the SOO contribution to our calculations.

			This method[b]			
Molec.	g value	Expt.[a]	TM	GO	SZ[b,c]	ZORA[b,c]
H_2^+	$\Delta g_\parallel$		−31	−31	−40	−66
	$\Delta g_\perp$		−37	−37	−43	−68
O_2H	Δg_{xx}	−800	−265	−272	−301	−2401
	Δg_{yy}	5580	5692	5905	6322	5072
	Δg_{zz}	39720	28007	27479	30391	90273
H_2O^+	Δg_{xx}	200	−174	−138	−204	−801
	Δg_{yy}	4800	5013	5233	5106	7159
	Δg_{zz}	18800	13048	13489	14416	47268
CO_2^-	Δg_{xx}	−4800	−4814	−4674	−5537	−5312
	Δg_{yy}	−500	−986	−866	−798	−678
	Δg_{zz}	700	569	599	742	1153
O_3^-	Δg_{xx}	200	−503	−507	−512	−441
	Δg_{yy}	10000	8365	9244	10533	12565
	Δg_{zz}	16400	17543	18240	17927	23041
CH_3	$\Delta g_\parallel$		−105	−61	−89	−123
	$\Delta g_\perp$		622	931	821	1147
NH_3^+	$\Delta g_\parallel$		−138	−98	−149	−206
	$\Delta g_\perp$		1834	2385	2195	3190
HCO	Δg_{xx}	−7500	−10108	−10329	−9764	−12372
	Δg_{yy}	0	−136	−192	−263	−194
	Δg_{zz}	1500	2848	2739	2832	3285
H_2CO^+	Δg_{xx}	−800	−1307	−1300	−1408	−1899
	Δg_{yy}	200	145	122	61	−282
	Δg_{zz}	4600	6413	6519	6410	7510
BO	$\Delta g_\parallel$	−800	−70	−77	−71	−118
	$\Delta g_\perp$	−1100	−2975	−2753	−2335	−2487
C_3H_5	Δg_{xx}	0	−106	−91	−110	−118
	Δg_{yy}	400	528	872	704	887
	Δg_{zz}	800	561	926	832	1084
CO_3^-	$\Delta g_\parallel$	4300	4905	4848	3474	3330
	$\Delta g_\perp$	11200	10985	12234	11952	17237
NO_2	Δg_{xx}	−11300	−14204	−14901	−14048	−16419
	Δg_{yy}	−300	−1118	−1029	−768	−734
	Δg_{zz}	3900	2488	3084	4296	5044
CH_4^+	Δg_{xx}	600	−114	−74	−108	−144
	Δg_{yy}	600	556	862	739	988
	Δg_{zz}	600	556	862	739	988
NF_2	Δg_{xx}	−100	−704	−745	−688	−324
	Δg_{yy}	2800	2735	3493	4819	6532
	Δg_{zz}	6200	6908	7752	7836	10866
NF_3^+	$\Delta g_\parallel$	1000	−797	−834	−586	−195
	$\Delta g_\perp$	7000	4782	6011	8045	10356
CO^+	$\Delta g_\parallel$	−3200	−3960	−3918	−3194	−3543
	$\Delta g_\perp$	−1400	−80	−17	−136	−200
CN	$\Delta g_\parallel$	−800	−134	−94	−134	−184
	$\Delta g_\perp$	−2000	−2835	−3223	−2556	−2730
NO_3	$\Delta g_\parallel$	4300	1237	1033	167	−261
	$\Delta g_\perp$	13550	11202	12660	12261	16850

[a]Experimental values are quoted from Refs. 3 and 32. Most experimental measurements were performed in solid matrices, with the exception of O_2H, H_2O^+, NO_2, and NF_2.
[b]Using optimized geometries obtained with ADF (QZ4P basis set, PBE functional).
[c]The g tensor principal values in the SZ and ZORA method were computed in this work, using ADF (QZ4P basis set, PBE functional).

dard Goedecker pseudopotential provided with the CPMD package with $3s^23p^2$ as valence states and a modified Goedecker pseudopotential with $2s^22p^63s^23p^2$ as valence states, and compared it with the all-electron result. The modified pseudopotential manifestly better reproduces the correct oscillating behavior of the all-electron wave functions in the core region, and hence will produce better results for the g tensor. In order to describe these extra nodes correctly, a higher number of plane waves is needed in the basis set, which can be computationally demanding. However, in many cases this harder but more accurate pseudopotential will yield better results at even moderate cutoff energies. We have verified the previous statements for MgF, AlO, and SiH_3 in Table V. We found that an increase of the number of valence electrons results in a better agreement already at 150 Ry, although a higher cutoff was needed to yield fully converged results. In the study of paramagnetic defects embedded in a crystalline environment, we therefore recommend using a modified hard pseudopotential for the heavier atoms of the defect, even at a lower plane-wave energy cutoff.

TABLE II. Statistics of the calculated Δg values (in ppm) in the various methods. All values are taken from Table I, whenever experimental results are available. The linear regression parameters were obtained from a plot of the calculated versus the experimental Δg values.

	This method			
	TM	GO	SZ	ZORA
Correlation coefficient	0.977	0.981	0.980	0.972
Correlation slope	1.034	1.102	1.094	1.365
Standard deviation	1170	1241	1228	2529
Maximum deviation	−3063	−3601	−4133	6641
Mean unsigned error	901	929	890	1804
Mean signed error	−435	−221	−94	528

TABLE III. Deviation from the SZ result of the different contributions to the g values of O_3^-, using Goedecker pseudopotentials.

		abs. error (ppm)	pct. error (%)
Δg^{ZKE}		8	2.2
Δg^{SO}			
	Δg_{xx}^{SO}	3	1.6
	Δg_{yy}^{SO}	1297	11.9
	Δg_{zz}^{SO}	305	1.7

TABLE IV. Calculated Δg values (in ppm) for a series of small isolated molecules with heavier elements than Ne, using the standard Goedecker pseudopotential sets supplied with CPMD, in comparison with experiment and other treatments. For comparison with the SZ results, we omit in this table the SOO contribution to our calculations.

			This method[b]			
Molec.	g value	Expt.[a]	GO	SZ[b,c]	ZORA[b,c]	GIPAW[d]
MgF	$\Delta g_\parallel$	−300	−7	−59	−81	−49
	$\Delta g_\perp$	−1300	−1091	−2156	−1968	−2093
SO_3^-	$\Delta g_\parallel$		−450	−43	162	
	$\Delta g_\perp$		1315	2008	2746	
SO_2^-	Δg_{xx}	−400	−220	−352	−531	
	Δg_{yy}	3400	3796	4881	4901	
	Δg_{zz}	9700	4565	4999	5030	
ClO_3	$\Delta g_\parallel$	5000	801	1133	2091	
	$\Delta g_\perp$	6000	4908	5680	6707	
ClO_2	Δg_{xx}	1300	−241	−487	−666	
	Δg_{yy}	6500	7107	11481	12458	
	Δg_{zz}	16000	9887	13193	15637	
AlO	$\Delta g_\parallel$	−900	−59	−137	−364	−141
	$\Delta g_\perp$	−2600	3543	−2192	1128	−2310
BS	$\Delta g_\parallel$	−700	−21	−81	−471	−80
	$\Delta g_\perp$	−8100	−976	−10123	12276	−9901
KrF	$\Delta g_\parallel$	−2000	−185	−337	−16603	−340
	$\Delta g_\perp$	66000	30916	61668	26471	61676
XeF	$\Delta g_\parallel$	−28000	−173	−334	−67027	−333
	$\Delta g_\perp$	124000	19128	157380	94719	151518
SiH_3	$\Delta g_\parallel$	1000	2	−111	−151	
	$\Delta g_\perp$	5000	128	2570	3779	
GeH_3	$\Delta g_\parallel$	1000	−19	−65	−1675	
	$\Delta g_\perp$	15000	67	18591	24104	
SnH_3	$\Delta g_\parallel$	1000	−21	−248	−11219	
	$\Delta g_\perp$	23000	14	36929	47031	

[a]Experimental values are quoted from Ref. 3. All experimental measurements were performed in solid matrices.
[b]Using optimized geometries obtained with ADF (QZ4P basis set, PBE functional).
[c]The g tensor principal values in the SZ and ZORA method were computed in this work, using ADF (QZ4P basis set, PBE functional).
[d]Results from Pickard and Mauri (Ref. 5).

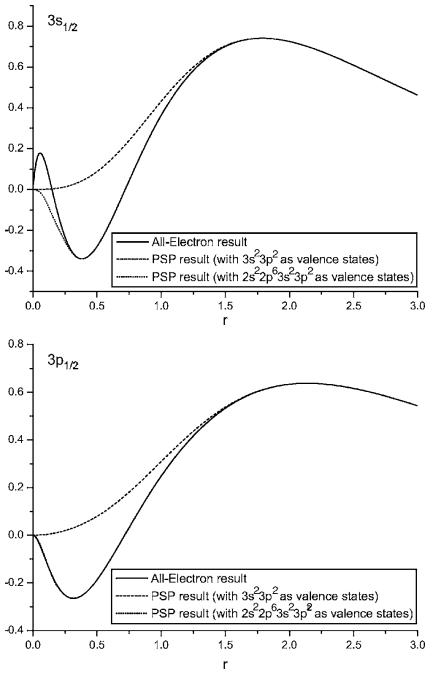

FIG. 2. $3s_{1/2}$ (upper graph) and $3p_{1/2}$ (lower graph) orbitals of the free Si atom using a soft and a hard Goedecker pseudopotential. Note that the hard pseudopotential (PSP) $3p_{1/2}$ orbital corresponds entirely with its all-electron counterpart.

The real application field of the method undoubtedly lies in the prediction of EPR parameters of paramagnetic defects in a crystal environment. Therefore, we further validated our approach by studying the O_3^- radical in a KCl lattice, in which as a function of the tilting angle α with $\langle 110 \rangle$ in the $\{1\bar{1}0\}$ plane, a metastable configuration at α=0° (untilted) and a stable configuration at α=34° (tilted) have been found theoretically,[34] as illustrated in Fig. 3. We modeled the latter with a 66-atom (31 Cl, 32 K, and 3 O) neutrally charged cubic cell, using a Goedecker pseudopotential, a BLYP functional, and a 80 Ry plane-wave cutoff, which is about the lower limit for this type of pseudopotential to obtain good results. In Table VI, the g values, as well as their principal directions, and the hyperfine values (using a method due to Van de Walle and Blöch,[35] which we also implemented in CPMD), are shown. Except for the incorrect prediction of the g_{xx} shift, from which all theoretical methods seem to suffer (see the O_3^- molecule in Table I and Ref. 36), a good agreement with available experimental g values is found, within the error margins of around 1000 ppm as argued by Neese in

TABLE V. Calculated Δg values (in ppm) for some selected molecules from Table IV, using harder pseudopotentials for the heavier elements Mg, Al, and Si. For comparison with the SZ results, we omit in this table the SOO contribution to our calculations.

		This method			
Molec.	g value	150 Ry[a]	150 Ry[b]	200 Ry[b]	SZ
MgF	$\Delta g_\perp$	−1091	−1734	−1813	−2156
	$\Delta g_\parallel$	−7	−17	−17	−59
AlO	$\Delta g_\parallel$	−59	−101	−100	−137
	$\Delta g_\perp$	3543	−634	−1942	−2192
SiH_3	$\Delta g_\parallel$	2	−61	−68	−111
	$\Delta g_\perp$	128	2125	2656	2570

[a]Using standard Goedecker pseudopotentials supplied with CPMD. The following states were explicitly used in the calculations: $3s^2$ for Mg; $3s^23p^1$ for Al; $3s^23p^2$ for Si.
[b]Using modified Goedecker pseudopotentials. The following states were explicitly used in the calculations: $2s^22p^63s^2$ for Mg; $2s^22p^63s^23p^1$ for Al; $2s^22p^63s^23p^2$ for Si.

TABLE VI. Calculated EPR values (Δg values in ppm, hyperfine values in Mhz) for O_3^- in KCl in the tilted configuration ($\alpha = 34°$).

g tensor			Expt.[33]	This method
Δg_{xx}			681	−452
Δg_{yy}			15981	16839
Δg_{zz}			9381	9434
$\alpha = \angle(g_{yy})$ with $\langle 110\rangle$			35°	34.8°
$\angle(g_{yy})$ with $\{1\bar{1}0\}$			0°	0.2°
$\angle(g_{xx})$ with $\langle 1\bar{1}0\rangle$			0°	0.1°
$\angle(g_{xx})$ with $\{001\}$			0°	0.2°
$\angle(g_{zz})$ with $\langle 001\rangle$			35°	34.8°
$\angle(g_{zz})$ with $\{1\bar{1}0\}$			0°	0.7°
Hyperfine tensor	A_{iso}	$A_{ani,xx}$	$A_{ani,yy}$	$A_{ani,zz}$
O_1	−69.61	54.34	53.58	−107.92
O_2	−108.65	71.24	74.56	−145.81
O_3	−68.95	54.17	53.39	−107.57

Ref. 36. The directions of the principal axes are equally well predicted: the theoretical directions do not deviate from experiment by more than 0.7 degrees, and often only 0.2 degrees.

One of the goals of this paper is to present an efficient method for the calculation of the g tensor in extended periodic systems at a reasonable computational cost. In this context, we proposed a selection criterion to pick out those electronic states for which a calculation of the computational expensive $|\phi_k^{(1c)}\rangle$ term [Eq. (13)] is needed to get the required accuracy. Obviously, the lower the threshold value α_{thres}, the more attractive the method becomes due to the reduction of the computational effort. The determination of this threshold value should be submitted to a careful investigation to guarantee sufficient convergence, but the proposed selection criterion turns out to be very efficient, as will be shown now. In Fig. 4, we plot the correlation of the theoretical predictions of Δg with respect to the experiment for the O_3^- radical in a KCl lattice. We considered the two extreme cases (full calculation of $|\phi_k^{(1c)}\rangle$ versus complete neglect of this term) and the intermediate case completely determined by the chosen threshold value α_{thres} (in the figure a value of 0.01 was used). The numerical results of Fig. 4 obviously stress the importance of taking into account the contributions of the $|\phi_k^{(1c)}\rangle$ term, but a full calculation is far from being a prerequisite as the threshold algorithm manifestly predicts the same values. The computational effort of the threshold calculation was only little more than needed for the calculation in which $|\phi_k^{(1c)}\rangle$ was completely neglected.

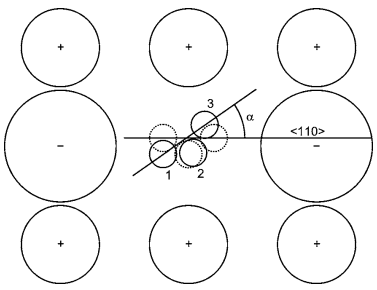

FIG. 3. $\{1\bar{1}0\}$-plane: Configuration of O_3^- in KCl.

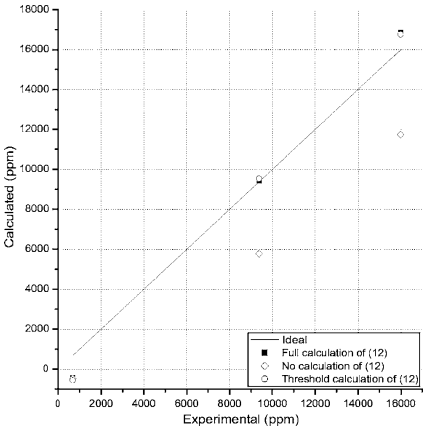

FIG. 4. Calculated Δg values for O_3^- in KCl in the tilted configuration. Comparison of the different methods for the calculation of Eq. (13). $\alpha_{thres}=0.01$ was used in the threshold calculation.

3. Paper I and II :: First-principles calculations of the EPR g tensor in extended periodic systems

IV. CONCLUSION

We have developed an alternative method for the calculation of the EPR g tensor in extended periodic systems, based on a pseudopotential approach without reconstruction techniques and the Sebastiani method. The method has been implemented in the CPMD code.

We have shown that for radicals composed of lighter elements (up to Ne) in the Periodic Table, the prediction of the g tensor is slightly suffering from the use of pseudopotentials, and accuracies similar to the all-electron Schreckenbach and Ziegler calculations were obtained with different types of norm-conserving pseudopotentials. For radicals with heavier elements than Ne, more electrons than strictly required to describe chemical bonding need to be included in the calculation.

The method comes at an attractive computational cost.

Together with the molecular dynamics capabilities of the CPMD package, we plan to use our method for EPR studies at finite temperatures. Calculations on relevant applications are in progress and look promising. We expect the extension of the CPMD code to be of great value in *ab initio* predictions of the EPR g tensor.

ACKNOWLEDGMENTS

This work is supported by the Fund for Scientific Research–Flanders and the Research Board of Ghent University. The authors wish to express their gratitude to J. Hutter, D. Sebastiani, and F. Mauri for discussions and kind support.

*Electronic address: Michel.Waroquier@UGent.be

[1] P. Hohenberg and W. Kohn, Phys. Rev. **136**, B864 (1964).
[2] W. Kohn and L. Sham, Phys. Rev. **140**, A1133 (1965).
[3] G. Schreckenbach and T. Ziegler, J. Phys. Chem. A **101**, 3388 (1997).
[4] M. Kaupp, M. Bühl, and V. G. Malkin, *Calculations of NMR and EPR Parameters: Theory and Applications* (Wiley-VCH, Weinheim, 2004).
[5] C. J. Pickard and F. Mauri, Phys. Rev. Lett. **88**, 086403 (2002).
[6] C. J. Pickard and F. Mauri, Phys. Rev. B **63**, 245101 (2001).
[7] P. E. Blöchl, Phys. Rev. B **50**, 17953 (1994).
[8] F. Mauri, B. G. Pfrommer, and S. G. Louie, Phys. Rev. Lett. **77**, 5300 (1996).
[9] D. Sebastiani and M. Parrinello, J. Phys. Chem. A **105**, 1951 (2001).
[10] G. Schreckenbach, Ph.D. thesis, University of Calgary, Calgary (1996).
[11] S. Patchkovskii and T. Ziegler, J. Phys. Chem. A **105**, 5490 (2001).
[12] J. E. Harriman, *Theoretical Foundations of Electron Spin Resonance* (Academic Press, New York, 1978).
[13] E. van Lenthe, P. E. S. Wormer, and A. van der Avoird, J. Chem. Phys. **107**, 2488 (1997).
[14] O. L. Malkina, J. Vaara, and B. Schimmelpfennig, J. Am. Chem. Soc. **122**, 9206 (2000).
[15] S. Goedecker, M. Teter, and J. Hutter, Phys. Rev. B **54**, 1703 (1996).
[16] G. Wannier, Phys. Rev. **52**, 191 (1937).
[17] W. Kohn, Phys. Rev. **115**, 809 (1959).
[18] T. Keith and R. Bader, Chem. Phys. Lett. **210**, 223 (1993).
[19] A. Putrino, D. Sebastiani, and M. Parrinello, J. Chem. Phys. **113**, 7102 (2000).
[20] D. Sebastiani, G. Goward, I. Schnell, and M. Parrinello, Comput. Phys. Commun. **147**, 707 (2002).
[21] D. Sebastiani, G. Goward, I. Schnell, and H. W. Spiess, J. Mol. Struct. **625**, 283 (2003).
[22] Car-Parrinello Molecular Dynamics, version 3.9.2; Copyright IBM Corp., 1990–2005.
[23] M. Kaupp, *EPR Spectroscopy of Free Radicals in Solids. Trends in Methods and Applications*, edited by A. Lund and M. Shiotani (Kluwer, Dordrecht, 2003).
[24] E. Van Lenthe, A. van der Avoird, W. R. Hagen, and E. J. Reijerse, J. Phys. Chem. A **104**, 2070 (2000).
[25] N. Troullier and J. L. Martins, Phys. Rev. B **43**, 1993 (1991).
[26] G. te Velde, F. M. Bickelhaupt, S. J. A. van Gisbergen, C. Fonseca Guerra, E. J. Baerends, J. G. Snijders, and T. Ziegler, J. Comput. Chem. **22**, 931 (2001).
[27] C. Fonseca Guerra, J. G. Snijders, G. te Velde, and E. J. Baerends, Theor. Chem. Acc. **99**, 391 (1998).
[28] ADF2004.01, SCM, Theoretical Chemistry, Vrije Universiteit, Amsterdam, The Netherlands, http://www.scm.com.
[29] J. P. Perdew, K. Burke, and M. Ernzerhof, Phys. Rev. Lett. **77**, 3865 (1996).
[30] A. D. Becke, Phys. Rev. A **38**, 3098 (1988).
[31] C. Lee, W. Yang, and R. G. Parr, Phys. Rev. B **37**, 785 (1988).
[32] D. Jayatilaka, J. Chem. Phys. **108**, 7587 (1998).
[33] F. Callens, P. Matthys, and E. Boesman, J. Phys. C **21**, 3159 (1988).
[34] V. Van Speybroeck, E. Pauwels, F. Stevens, F. Callens, and M. Waroquier, Int. J. Quantum Chem. **101**, 761 (2005).
[35] C. G. Van de Walle and P. E. Blöchl, Phys. Rev. B **47**, 4244 (1993).
[36] F. Neese, J. Chem. Phys. **115**, 11080 (2001).

4 Paper III

First-principles calculations of hyperfine parameters with the Gaussian and augmented-plane-wave method: Application to radicals embedded in a crystalline environment

R. Declerck, E. Pauwels, V. Van Speybroeck, and M. Waroquier

Physical Review B 74 (24), 245103 (2006)

4. Paper III :: First-principles calculations of hyperfine parameters with the Gaussian and augmented-plane-wave method: Application to radicals embedded in a crystalline environment

PHYSICAL REVIEW B **74**, 245103 (2006)

First-principles calculations of hyperfine parameters with the Gaussian and augmented-plane-wave method: Application to radicals embedded in a crystalline environment

R. Declerck, E. Pauwels, V. Van Speybroeck, and M. Waroquier*
Center for Molecular Modeling, Laboratory of Theoretical Physics, Ghent University, Proeftuinstraat 86, B-9000 Gent, Belgium
(Received 10 August 2006; published 5 December 2006)

A method for the calculation of hyperfine parameters in extended systems under periodic boundary conditions is presented, using the Gaussian and augmented-plane-wave density functional method, and implemented in QUICKSTEP. In order to increase the efficiency in larger systems, a hybrid scheme is proposed, in which an all-electron treatment for the nuclei of interest and a pseudopotential approximation for the remaining atoms in the simulation cell are combined. The method is validated first by comparing the hyperfine parameters for a selection of atoms and small molecules (using a supercell technique) with other theoretical methods and experimental data from literature. As a typical example of a periodic system where our hybrid method can be applied, the hyperfine parameters of the well-characterized *R*2 *L*-α-alanine derived radical are evaluated, yielding results in excellent agreement with the available experimental data.

DOI: 10.1103/PhysRevB.74.245103 PACS number(s): 71.15.−m, 61.72.Bb, 76.30.−v

I. INTRODUCTION

Electron paramagnetic resonance (EPR) is an important spectroscopic tool in the identification of paramagnetic defects. In recent years, there has been a growing interest in the *ab initio* quantum mechanical calculation of these EPR quantities within density functional theory[1,2] (DFT). A recent overview is given in Ref. 3. By comparing the experimental EPR quantities with those computed ab initio from proposed atomic models, it is possible to identify and understand the microscopic structure of these defects.

Three quantities contribute to EPR spectra: (i) the hyperfine parameters (HFP's), (ii) the g tensor, and (iii) the zero-field splitting tensor. In this paper we will focus on the first quantity. The HFP's can be computed from the ground state spin density alone, and they probe the spin density of a region near the nucleus. It is therefore imperative to have an accurate description of the spin density at the nuclei and their near vicinity.

Many useful applications of the EPR technique, however, involve paramagnetic defects embedded in crystals and solvents, or—more generally speaking—in condensed systems. Often, these systems are simulated using the pseudopotential (PSP) approximation and periodic boundary conditions. Unfortunately, difficulties arise when evaluating the HFP's within these periodic PSP schemes: (i) the pseudovalence Kohn-Sham (KS) orbitals differ from their all-electron (AE) counterparts within a (predefined) core region and (ii) the core is frozen and effects due to core spin polarization are not included. A solution to the first problem employs the projector augmented wave (PAW) method of Blöchl,[4] either in an AE (frozen-core) approach,[5] or in the PSP approximation combined with a density reconstruction scheme (post-PSP PAW).[6,7] However, as was argued in Ref. 8, these corrections do not solve the problem of the behavior of the exchange-correlation potential in the vicinity of the nucleus, needed for a correct description of spin-polarization effects on the valence orbitals. A solution to both problems was proposed very recently by Yazyev *et al.*,[8] and uses a reconstruction of the AE orbitals and the frozen valence spin-density approximation to solve the KS equations for the core electrons only. This method yields a non-negligible core spin-polarization correction and cancels the largest part of the error induced by the PSP approximation in the reproduction of the isotropic HFP, corresponding to the Fermi contact interaction.

The previous discussion illustrates the need for a hybrid scheme which can perform an AE HFP calculation (using the AE full potential) on those nuclei of interest (this usually involves the paramagnetic defect center itself and the close region around it), and at the same time leaves open the possibility to use the PSP approximation for the remaining atoms in the simulation cell. Most probably, this approximation will not affect the accuracy of the HFP's of interest, because these are determined mainly by the accurate spin density in a region near the nucleus. For this hybrid AE and PSP scheme, we will make use of the Gaussian and augmented-plane-wave density functional method[9–11] (GAPW method), in which the total density is described in a smooth extended part represented in plane waves (PW's), and parts localized close to the nuclei which are expanded in periodic Gaussian functions. The GAPW method exists in both a PSP (Ref. 10) and an AE (Ref. 11) implementation, and both approaches can be easily combined within one simulation. As an AE approach, the GAPW method solves the problems which are inherent to the PSP approximation. Moreover, due to the fact that the GAPW method employs Gaussians, a simulation with an AE treatment for the nuclei of interest requires only a relatively small extra computational cost, while in a pure PW basis set approach, for example, the computational cost would be manifestly higher.

We will elaborate first on the implementation of the HFP's in the GAPW method. Then we will evaluate its accuracy as an AE method, by comparing with other established DFT HFP methods and experimental data from literature for a number of smaller atoms and molecules. Among these DFT methods, we will benchmark against the very recently proposed all-electron mixed-basis (MB) method,[12] which employs a basis set of confined numerical atomic orbitals supplemented with plane waves. Finally, as an instructive

example of an extended system under periodic boundary conditions, our GAPW implementation will be used to calculate the HFP's of the *R*2 *L*-α-alanine radical, for which ample reference data exist. By comparing with the post-PSP PAW method and the cluster in vacuo approach, we will show that there is an excellent agreement with the available experimental results.

II. THEORY

The energy levels and intensities derived from EPR experiments can be reproduced using an effective Hamiltonian, expressed in terms of effective spin operators. This effective Hamiltonian generally consists of three contributions

$$H_{\text{eff}} = \sum_N \mathbf{S}\cdot\mathbf{A}_N\cdot\mathbf{I}_N + \frac{\alpha}{2}\mathbf{B}\cdot\mathbf{g}\cdot\mathbf{S} + \mathbf{S}\cdot\mathbf{D}\cdot\mathbf{S}. \tag{1}$$

$\mathbf{A}_N$ is the hyperfine tensor of rank 2 describing the coupling between the electronic spin $\mathbf{S}$ and the nuclear spin $\mathbf{I}_N$ of a nucleus N. $\mathbf{g}$ is the g tensor which describes the coupling between the electronic spin system and a constant external magnetic field $\mathbf{B}$. $\mathbf{D}$ is the zero-field splitting tensor arising from the magnetic dipolar interactions between multiple unpaired electrons in the system. α represents the fine structure constant and the summation runs over the nuclei. Atomic units are used throughout this paper.

The components of $\mathbf{A}_N$ can be derived from relativistic many-body quantum mechanics, and the most dominant terms are[13,14]

$$A_{N,ij} = A_{\text{iso},N}\delta_{ij} + A_{\text{ani},N,ij}, \tag{2}$$

where

$$A_{\text{iso},N} = \frac{4\pi}{3}\frac{g_e\mu_e g_N\mu_N}{\langle S_z\rangle}\int d\mathbf{r}\rho_s(\mathbf{r})\delta_T(\mathbf{r}), \tag{3}$$

$$A_{\text{ani},N,ij} = \frac{1}{2}\frac{g_e\mu_e g_N\mu_N}{\langle S_z\rangle}\int d\mathbf{r}\rho_s(\mathbf{r})\frac{3r_ir_j-\delta_{ij}r^2}{r^5}. \tag{4}$$

Here, $\rho_s=\rho^\alpha-\rho^\beta$ represents the net electronic spin density, g_e the free-electron g value, μ_e the Bohr magneton, g_N the nuclear gyromagnetic ratio for the nucleus, μ_N the nuclear magneton, $\langle S_z\rangle$ the expectation value of the z component of the total electronic spin, and the vector $\mathbf{r}$ is taken relative to the position of the nucleus. The isotropic HFP A_{iso} corresponds to the Fermi contact interaction, whereas the anisotropic HFP's $A_{\text{ani},ij}$ result from dipole-dipole interactions. The subscripts i,j refer to Cartesian coordinates x, y, and z. Throughout this work, the gyromagnetic ratio data are taken from Ref. 15.

$\delta_T(\mathbf{r})$ is a smeared out δ function which results from scalar relativistic corrections[5,13]

$$\delta_T(\mathbf{r}) \cong \frac{1}{4\pi r^2}\frac{2}{Z\alpha^2}\frac{1}{\left(1+\frac{2r}{Z\alpha^2}\right)^2}. \tag{5}$$

with Z the atomic number. In the nonrelativistic limit, $\delta_T(\mathbf{r})$ simplifies to a Dirac's delta function.

In the GAPW scheme, the all-electronic density ρ is defined by its expansion in atomic orbitals $\varphi(\mathbf{r})$,

$$\rho(\mathbf{r}) = \sum_{\mu\nu} P_{\mu\nu}\varphi_\mu(\mathbf{r})\varphi_\nu^*(\mathbf{r}), \tag{6}$$

with $P_{\mu\nu}$ the density matrix. The orbitals $\varphi(\mathbf{r})$ can be further expanded in a set of atom-centered contracted Gaussian basis functions

$$\varphi_\mu(\mathbf{r}) = \sum_a C_{a\mu}g_a(\mathbf{r}), \tag{7}$$

where $g_a(\mathbf{r})$ are the primitive Gaussians.

In an arbitrary way, space is now divided into non overlapping localized spherical regions centered at the nuclei, and the interstitial region. The idea behind the GAPW approach is that the interstitial electronic density varies smoothly and is therefore easily representable in a PW basis, while the rapidly varying density close to the nuclei can be represented in terms of localized functions. The GAPW representation of the density is the sum of three contributions

$$\rho = \tilde{\rho} + \rho^1 - \tilde{\rho}^1. \tag{8}$$

In the soft density $\tilde{\rho}$, the rapid variations of ρ close to the nuclei are removed by putting to zero the coefficients of the most localized Gaussian primitives. Thus, $\tilde{\rho}$ becomes smooth—hence *soft*, as opposed to the real density ρ, which is called *hard*—and is distributed over all space, and can be represented by a relatively small auxiliary basis set of PW's

$$\tilde{\rho}(\mathbf{r}) = \frac{1}{\Omega}\sum_{|\mathbf{G}|<G_C}\tilde{\rho}(\mathbf{G})e^{i\mathbf{G}\cdot\mathbf{r}}. \tag{9}$$

The other densities

$$\rho^1 = \sum_N \rho_N^1 \quad \text{and} \quad \tilde{\rho}^1 = \sum_N \tilde{\rho}_N^1 \tag{10}$$

are sums of local atom-centered contributions ρ_N^1 and $\tilde{\rho}_N^1$ which are hard and soft, respectively. ρ_N^1 and $\tilde{\rho}_N^1$ are constructed from an expansion of the density ρ and of the soft density $\tilde{\rho}$, respectively, in the primitive orbital basis functions g_a of atom N.

By construction, ρ, $\tilde{\rho}$, ρ_N^1, and $\tilde{\rho}_N^1$ satisfy the following relations:

$$\rho(\mathbf{r}) - \tilde{\rho}(\mathbf{r}) = 0 \quad \text{for } \mathbf{r}\in I, \tag{11}$$

$$\rho_N^1(\mathbf{r}) - \tilde{\rho}_N^1(\mathbf{r}) = 0 \quad \text{for } \mathbf{r}\in I, \tag{12}$$

$$\tilde{\rho}(\mathbf{r}) - \tilde{\rho}_N^1(\mathbf{r}) = 0 \quad \text{for } \mathbf{r}\in U_N, \tag{13}$$

$$\rho(\mathbf{r}) - \rho_N^1(\mathbf{r}) = 0 \quad \text{for } \mathbf{r}\in U_N, \tag{14}$$

where U_N denotes a spherical region around the nucleus N and I the interstitial region outside these atomic regions. Hence, Eq. (8) is fulfilled in all space.

In a spin-unrestricted DFT run, Eqs. (6)–(9) hold for the density in each spin channel, and hence also for the all-electronic spin density ρ_s. Using the GAPW decomposition of the spin density, we have derived expressions for the

evaluation of the hyperfine parameters as follows.

Due to the presence of the δ_T function, we can safely restrict the integration region of the integral in Eq. (3) to U_N, and evaluate the isotropic HFP using the atom-centered density $\rho^1_{s,N}$, which equals the density ρ_s in a region U_N [Eq. (14)]:

$$A_{\mathrm{iso},N} = \frac{4\pi}{3}\frac{g_e\mu_e g_N\mu_N}{\langle S_z\rangle}\int_{\mathbf{r}<U_N} \mathrm{d}\mathbf{r}\rho^1_{s,N}(\mathbf{r})\delta_T(\mathbf{r}). \quad (15)$$

For the calculation of the anisotropic HFP's of nucleus N, we can reorder the GAPW formulation of the spin density as

$$\rho_s = \tilde{\rho}_s + \rho^1_{s,N} - \tilde{\rho}^1_{s,N} + \sum_{M\neq N}(\rho^1_{s,M} - \tilde{\rho}^1_{s,M}). \quad (16)$$

Inserting this expression, together with the PW expansion of the soft spin density $\tilde{\rho}_s$, in Eq. (4), we can evaluate the anisotropic HFP's as

$$\begin{aligned} A_{\mathrm{ani},N,ij} = {} & \frac{1}{2}\frac{g_e\mu_e g_N\mu_N}{\langle S_z\rangle} \\ & \times\left(-\sum_{|\mathbf{G}|<G_C}\frac{4\pi\left(G_iG_j-\frac{1}{3}G^2\delta_{ij}\right)}{G^2}\tilde{\rho}_s(\mathbf{G})\mathrm{e}^{i\mathbf{G}\cdot\mathbf{R}_N}\right. \\ & \left.+\int_{\mathbf{r}<U_N} d\mathbf{r}\left[\rho^1_{s,N}(\mathbf{r})-\tilde{\rho}^1_{s,N}(\mathbf{r})\right]\frac{3r_ir_j-\delta_{ij}r^2}{r^5}\right) \\ & +\Delta A_{N,\mathrm{ani},ij}. \end{aligned} \quad (17)$$

The integration in the third term can be restricted to U_N because Eq. (12) holds. $\Delta A_{N,\mathrm{ani},ij}$ accounts for the small contributions due to the difference $\rho^1_{s,M}-\tilde{\rho}^1_{s,M}$ from neighboring atomic regions

$$\begin{aligned} \Delta A_{\mathrm{ani},N,ij} = {} & \frac{1}{2}\frac{g_e\mu_e g_N\mu_N}{\langle S_z\rangle} \\ & \times\sum_{M\neq N(R_{MN}<R_C)}\int_{\mathbf{r}<U_M} d\mathbf{r}\left[\rho^1_{s,M}(\mathbf{r})-\tilde{\rho}^1_{s,M}(\mathbf{r})\right] \\ & \times\frac{3(r_i+R_{MN,i})(r_j+R_{MN,j})-\delta_{ij}|\mathbf{r}+\mathbf{R}_{MN}|^2}{|\mathbf{r}+\mathbf{R}_{MN}|^5}. \end{aligned} \quad (18)$$

In this equation, the origin of $\mathbf{r}$ is always the geometric position of each nucleus M, and $\mathbf{R}_{MN}=\mathbf{R}_M-\mathbf{R}_N$ is the vector connecting the nuclei M and N. Only nearest-neighboring atomic regions need to be included. This can be controlled by choosing an appropriate maximum value R_C for $R_{MN}=|\mathbf{R}_{MN}|$.

The effect of including augmentation contributions of neighboring sites [Eq. (18)] was estimated to be small.[5] We will elaborate on the impact of Eq. (18) in the next section.

We have implemented this approach, as outlined in Eqs. (15), (17), and (18), into the existing QUICKSTEP[16] code, which is part of the freely available program package CP2K.[17] Efficient integration can be carried out either numerically using atomic Lebedev grids,[18–20] or analytically using the procedures outlined in Refs. 21 and 5.

III. RESULTS AND DISCUSSION

A. Test calculations

The GAPW method for calculating AE HFP's was validated first by comparing the results for a selection of atoms, ions and small molecules with the results from other DFT-based methods, (i) the MB method and (ii) the method[22–24] employed in the GAUSSIAN 03[25] program package (further referred to as the G03 method), as well as with experimental data from literature. In order to sufficiently assess our method, almost the same set of atoms and molecules as in the MB paper have been chosen. To guarantee a fair comparison with the MB results from literature, the local spin density approximation[26] (LSDA) was adopted in a first batch of test calculations. Subsequent tests include PBE (Ref. 27) and BLYP (Refs. 28 and 29) gradient-corrected functionals.

All the isotropic HFP's have been calculated in the nonrelativistic limit, in accordance with the MB and the G03 method. In our method, all atoms, ions, and isolated molecules were approximated by using large supercells of (25 a.u.)^3 The convergence with respect to the size of the supercell has been verified earlier in Ref. 12. We have used the DZVP (Ref. 30) Gaussian type basis set (GAPW and G03), together with a 200 Ry cutoff for the auxiliary PW grid used to represent the soft density $\tilde{\rho}$ (GAPW only). Furthermore, to examine the basis set dependence, several calculations were carried out using the very extended UGBS2P (Ref. 31) Gaussian type basis set.

In Table I, the calculated isotropic HFP's for a selection of isolated atoms and cations are presented. Reassuringly, using the same Gaussian basis set, the GAPW (LSDA/DZVP/200Ry) and the G03 (LSDA/DZVP) results agree to within less than 2% for all species under study. The use of the much larger UGBS2P basis does not systematically lead to a better experimental agreement, and the results of the MB method are still more accurate [mean percentage error (MPE) compared with experiment: 7.6% (DZVP), 6.2% (UGBS2P), and 3.1% (MB)[39]]. The results for the heavier elements $^{87}Sr^+$ and ^{107}Ag are not as good for all theoretical methods, as could be anticipated from the neglect of relativistic effects.[12] In Ref. 12, the authors attribute the overall success of their MB method to the fact that the method employs numerical atomic orbitals as a basis set to describe the molecular orbitals in the regions close to the cores. These atomic orbitals are better suited than Gaussian basis functions to represent the s wave functions at the nuclei, which often dominate the prediction of the isotropic HFP's. This appears to be confirmed in Table I. However, one should not overestimate the qualitative (dis)agreement with experimental results for all methods presented in Table I as the prediction of the isotropic HFP's heavily relies on the details of the calculation such as the choice of the exchange-correlation (XC) functional.[40] This is shown in Table II, where we have computed the isotropic HFP's for the same set of atoms and cations. Using LSDA, BLYP, and PBE XC functionals, respectively, the predictions for each element vary in a range of as much as 19% (8.9% on average) of the experimental value, and no XC functional is found to be superior to the other.

In Table III, the HFP's of zinc complexes ^{67}ZnX are shown. They provide a more relevant test than atomic calcu-

4. Paper III :: First-principles calculations of hyperfine parameters with the Gaussian and augmented-plane-wave method: Application to radicals embedded in a crystalline environment

TABLE I. Comparison of isotropic HFP's (in MHz) for a selection of isolated atoms and ions.

Atom	G03[a] LSDA/DZVP	GAPW[a] LSDA/DZVP/200Ry	GAPW[a] LSDA/UGBS2P/200Ry	MB[b] LSDA/200Ry	Expt.[c]
^{1}H	1362.6	1353.8	1344.5		1420.4
^{7}Li	382.7	380.0 (400.2[d])	395.6	401.6	401.7
^{25}Na	905.7	891.2	974.3	891.2	885.8
^{25}Mg^{+}	−541.5	−538.0	−619.6	−600.2	±596.2
^{39}K	242.1	236.8	241.5	232.4	230.9
^{43}Ca^{+}		−721.5	−813.8	−812.8	±806.4
^{63}Cu	6000.9	5971.3	5944.8	5935.1	5867
^{87}Sr^{+}	−829.0	−820.1	−899.2	−912.7	990−1000.5
^{107}Ag	−1339.0	−1326.7	−1344.9	−1411.3	−1713

[a]Present work.
[b]MB results from Ref. 12.
[c]Experimental data from Ref. 32 (^{1}H), Ref. 33 (^{7}Li, ^{25}Na, ^{39}K), Ref. 34 (^{63}Cu), Ref. 35 (^{107}Ag), Ref. 36 (^{25}Mg^{+}), Ref. 37 (^{43}Ca^{+}), and Ref. 38 (^{87}Sr^{+}).
[d]Using the *Montreal* variant of the DZVP basis set.

lations, mainly because they also allow us to evaluate the accuracy of the anisotropic HFP results. In Table III, the anisotropy is formulated concisely as $A_{\mathrm{ani}}=A_{\mathrm{ani},\parallel}-A_{\mathrm{ani},\perp}$, the difference between the parallel and the orthogonal principal components of the anisotropic HFP matrix. Due to the absence of reliable experimental data, we benchmarked against the results from two-component scalar relativistic zero-order-regular-approximation (ZORA) calculations.[41] All HFP calculations, including those in the MB method, were performed within the LSDA using the geometries from Ref. 41. We again obtain a good agreement between the GAPW (LSDA/DZVP/200Ry) and the G03 (LSDA/DZVP) results, as should be the case. For the isotropic HFP's, all presented methods perform about equally well, with the exception of ^{107}Ag, where all methods seem to fail due to relativistic effects as mentioned above. For the anisotropic HFP's, however, the MB method performs worse than other methods [MPE from ZORA results: 4.1% (DZVP), 6.8% (UGBS2P), and 26.8% (MB)[43]]. Further investigation is needed to determine exactly why the MB results deviate for this set of zinc complexes.

In order to quantify the effect the inclusion of $\Delta A_{\mathrm{ani},N,ij}$ [Eq. (18)] in the calculation of the anisotropic HFP's using the GAPW method, we have extended the test set to methyl, silyl, and germyl radicals. In these molecules, the unpaired electron is mainly localized around the central ^{13}C/^{29}Si/^{73}Ge nucleus, and therefore it is likely that the prediction of the anisotropic HFP's for the nearby ^{1}H nuclides will suffer from the difference $\rho_s^1-\tilde{\rho}_s^1$ in the C/Si/Ge region $U_{\mathrm{C/Si/Ge}}$. From Table IV, it is clear that the inclusion of Eq. (18) does not affect the anisotropic HFP's for ^{13}C/^{29}Si/^{73}Ge at all [0.0% percentage error from the results with Eq. (18)], as was to be expected, while the ^{1}H anisotropic HFP's differ to a small but pronounced extent [percentage error from the results with Eq. (18): 15.0% max, 4.2% mean].

B. The *R*2 *L*-α-alanine derived radical

The real application field of the GAPW HFP method undoubtedly lies in the prediction of HFP parameters of paramagnetic defects in extended periodic systems, like a crystal. Therefore, we have chosen to calculate the HFP's of the

TABLE II. Dependence of isotropic HFP's from the species of Table I on the XC functional (in MHz).

Atom	GAPW[a,b] LSDA/UGBS2P/200Ry	GAPW[a] BLYP/UGBS2P/200Ry	GAPW[a] PBE/UGBS2P/200Ry	Expt.[b]
^{1}H	1344.5	1495.7	1462.3	1420.4
^{7}Li	395.6	460.4	384.0	401.7
^{25}Na	974.3	1002.5	893.9	885.8
^{25}Mg^{+}	−619.6	−629.0	−593.8	±596.2
^{38}K	241.5	239.1	213.4	230.9
^{43}Ca^{+}	−813.8	−806.7	−762.1	±806.4
^{63}Cu	5944.8	5846.0	5699.0	5867
^{87}Sr^{+}	−899.2	−886.8	−844.3	990−1000.5
^{107}Ag	−1344.9	−1298.0	−1278.0	−1713

[a]Present work.
[b]See Table I.

TABLE III. HFP's (in MHz) for zinc complexes. In this table, $A_{ani}=A_{ani,\parallel}-A_{ani,\perp}$.

		Zn part		*X* part	
Z*nX*	Method	A_{iso}	A_{ani}	A_{iso}	A_{ani}
$^{67}Zn^{107}Ag$	G03 DZVP[a]	315.3	20.7	−988.4	−0.7
	GAPW DZVP[a]	315.1	20.4	−979.2	−0.7
	GAPW UGBS2P[a]	303.0	24.1	−981.1	−0.4
	MB[b]	333.2	26.5	−1051.4	−0.1
	ZORA[c]	357	21	−1297	−1
	Expt.[d]			−1324	0
$^{67}Zn^{1}H$	G03 DZVP[a]	553.7	66.2	540.8	−2.2
	GAPW DZVP[a]	538.3	66.0	551.8	−2.4
	GAPW UGBS2P[a]	547.2	67.2	477.7	−2.0
	MB[b]	549.2	74.1	468.5	−1.3
	ZORA[c]	561	63	543	0
	Expt.[d]			486	−2
$^{67}Zn^{13}CN$	G03 DZVP[a]	1019.0	53.2	277.1	35.1
	GAPW DZVP[a]	1012.9	52.9	281.5	35.1
	GAPW UGBS2P[a]	1003.8	54.8	238.2	36.3
	MB[b]	980.1	64.4	258.4	23.1
	ZORA[c]	1044	53	253	38
	Expt.[d]				
$^{67}Zn^{19}F$	G03 DZVP[a]	1179.9	42.5	353.4	827.1
	GAPW DZVP[a]	1169.8	42.3	363.8	834.2
	GAPW UGBS2P[a]	1188.4	39.7	247.2	774.0
	MB[b]	1151.6	60.5	196.2	822.6
	ZORA[c]	1223	40	235	866
	Expt.[d]			129	816

[a]Present work.
[b]MB results from Ref. 12.
[c]ZORA results from Ref. 41.
[d]Experimental results from Ref. 42.

TABLE IV. Anisotropic HFP's (in MHz) for CH_3, SiH_3, and GeH_3. Calculations were performed in the LSDA, using DZVP basis sets.

Mol.	Nucl.		GAPW w Eq. (18)	GAPW w/o Eq. (18)	pct. error (%)
$^{13}C^{1}H_3$	^{13}C	$A_{ani,\perp}$	−77.2	−77.1	0.0
		$A_{ani,\parallel}$	154.3	154.3	0.0
	^{1}H	$A_{ani,xx}$	−38.0	−37.9	0.2
		$A_{ani,yy}$	−1.6	−1.6	1.4
		$A_{ani,zz}$	39.7	39.5	0.5
$^{29}Si^{1}H_3$	^{29}Si	$A_{ani,\perp}$	86.0	86.0	0.0
		$A_{ani,\parallel}$	−172.0	−172.0	0.0
	^{1}H	$A_{ani,xx}$	−9.9	−9.6	2.8
		$A_{ani,yy}$	1.3	1.5	15.0
		$A_{ani,zz}$	8.7	8.1	6.4
$^{73}Ge^{1}H_3$	^{73}Ge	$A_{ani,\perp}$	41.9	41.9	0.0
		$A_{ani,\parallel}$	−83.9	−83.9	0.0
	^{1}H	$A_{ani,xx}$	−12.1	−11.9	1.7
		$A_{ani,yy}$	4.4	4.6	4.2
		$A_{ani,zz}$	7.7	7.3	5.9

L-α-alanine *R*2 radical (see Fig. 1), which has been well-characterized through experimental and theoretical studies. The amino acid alanine is widely used as a dosimetric system in the solid state, due to a number of valuable radiation dosimetric properties (Refs. 44–46, and references therein). As determined by Sagstuen *et al.*[47] (at room temperature) using a combination of EPR techniques, three radical species are generated within the solid state matrix following irradiation, and two of them are most abundant: *R*1[C$^{\bullet}$H(CH_3)COOH] and *R*2[$N^{+}H_3C^{\bullet}(CH_3)COO^{-}$]. *R*2 is by far the simplest system, as it differs from undamaged alanine only by one hydrogen atom.

Following the experimental characterization of the radiation-induced species in this amino acid, several theoretical studies have been performed with the intent of modeling the radical structures and simulating the corresponding EPR properties. Ban *et al.*[48] and Lahorte *et al.*[49] both used variations of a single molecule approach to calculate the HFP's of alanine radicals. Pauwels *et al.*[50] adopted both cluster in vacuo and periodic approaches to model the alanine *R*2 radical. The explicit incorporation of intermolecular interactions proved essential in the determination of a reliable radical geometry and the subsequent HFP calculations on the single radical.

In this section, we will compare a GAPW periodic HFP calculation on the *R*2 radical with a cluster in vacuo approach and a post-PSP PAW periodic HFP calculation. In the GAPW calculation, we will use an AE treatment for the central *R*2 radical and a PSP treatment for the alanine molecules (denoted as AE+PSP), which is an example of the hybrid AE and PSP scheme mentioned in the Introduction.

In the cluster in vacuo approach, a cluster similar to the one in Ref. 50 was adopted. Radical *R*2 was sur-

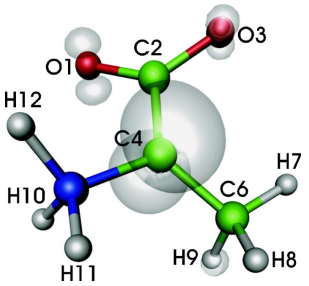

FIG. 1. (Color online) The *R*2 radical geometry, together with an isosurface plot of the spin density (ρ_s=0.01).

4. Paper III :: First-principles calculations of hyperfine parameters with the Gaussian and augmented-plane-wave method: Application to radicals embedded in a crystalline environment

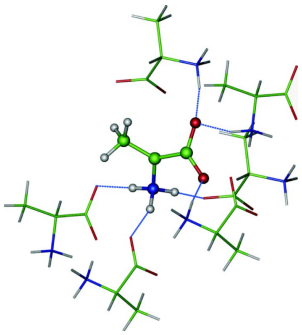

FIG. 2. (Color online) Optimized cluster in vacuo model geometry of the *R*2 radical and its neighboring *L*-α-alanine molecules.

rounded by six alanine molecules in accordance with the space group symmetry of the *L*-α-alanine crystal, which features unit cell constants of a=11.386 a.u., b=23.289 a.u., c=10.928 a.u.[51] This cluster comprises all molecules that are engaged in hydrogen bonds with the central radical. The structure of this hydrogen-bond cluster in vacuo model is shown in Fig. 2. Using GAUSSIAN 03, geometry optimizations were performed on the central radical, while keeping the coordinates of the surrounding alanine molecules fixed in space at the geometry of the crystal structure. Contrary to the original approach by Pauwels *et al.*,[50] the HFP's were calculated using the full cluster, in accordance with the methodology of Ref. 52.

In the periodic boundary model, we doubled the unit cell in the a and c direction, to ensure that neighboring radicals are well separated from each other. The resulting orthorhombic simulation cell contains 15 *L*-α-alanine molecules and a central *R*2 radical, as is shown in Fig. 3. All atoms were free to relax during the geometry optimization, performed with QUICKSTEP.

For the cluster in vacuo model, we employed a TZVP (Ref. 30) basis set for the entire cluster. In the periodic

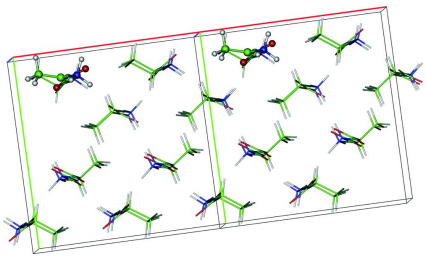

FIG. 3. (Color online) Optimized periodic boundary geometry of the *R*2 radical and its neighboring *L*-α-alanine molecules. The simulation cell and one of its neighboring images are shown.

boundary model, we used the same TZVP basis set for the central radical, and a TZVP-PSP (Ref. 53) basis set and pseudopotentials of Goedecker and co-workers[54,55] for the alanine molecules. A BLYP gradient-corrected functional was used throughout all calculations. The post-PSP PAW[6] HFP calculation was performed with the CPMD program package,[56] using the geometry obtained with QUICKSTEP. In this calculation, we used Troullier-Martins[57] (TM) norm-conserving PSP's at a PW cutoff value of 100 Ry. We have also performed a GAPW HFP calculation using an AE treatment for the entire system, but this did not significantly alter the results obtained using the hybrid AE+PSP GAPW method.

The calculated HFP's of the *R*2 radical are presented in Table V, along with an overview of the available experimental data, measured at room temperature.[47] The numbering of the nuclei is defined in Fig. 1. Since the methyl group is a quasifree rotor at this temperature, only averaged HFP's have been measured. All of our calculations are static though (formally at 0 K) and do not explicitly take into account this rotational averaging. Nevertheless, to allow for comparison, the hyperfine tensors of H7, H8, and H9 have been averaged (denoted as H7-9 in Table V).

Comparing the calculated HFP's with the available experimental data, all three methods are found to perform very well. Isotropic HFP's deviate 5 MHz at most, and the anisotropic HFP's are also quite accurately reproduced. Larger variations among the calculated HFP's are observed for the nuclei O1-C6, but no experimental information is available to assess these results.

The angular differences between experimental and calculated principal directions are denoted between brackets in Table V. For all directions corresponding to the maximum anisotropic HFP, all angles are well below 10°, indicating an excellent agreement with experiment. For the small and intermediate anisotropic interactions, the agreement is somewhat less. The mutual occurrence of rather large angles for both minor anisotropic interactions can be ascribed to the quasidegeneracy of these interactions, rendering them quite sensitive.

Both methods employing periodic boundary conditions are superior to the cluster in vacuo model, which, for instance, shows the largest angular deviations from experiment, and the least accurate anistropic HFP's. This presumably reflects the limited inclusion of the solid-state environment in this model. Furthermore, the cluster in vacuo model necessitates constraints on the molecules surrounding the radical, and cluster size effects can cause errors. Periodic boundary calculations are clearly a more natural way of simulating the solid state.

The hybrid GAPW HFP method introduced in this work edges out the post-PSP PAW method, as the former results in an impressive agreement with the experimental results of Sagstuen *et al.*, both for (an)isotropic HFP's and for the principal directions.

IV. CONCLUSION AND OUTLOOK

We have proposed a method for the calculation of AE HFP's in extended systems under periodic boundary condi-

TABLE V. HFP's for the *R*2 radical. The values between brackets denote the angles (in degrees) between the calculated and the experimental principal directions.

	GAPW AE+PSP[a] BLYP/TZVP/200Ry				post-PSP PAW[a] BLYP/PW/100Ry				G03[a] BLYP/TZVP				Expt.[b]			
	A_{iso}	$A_{ani,xx}$	$A_{ani,yy}$	$A_{ani,zz}$	A_{iso}	$A_{ani,xx}$	$A_{ani,yy}$	$A_{ani,zz}$	A_{iso}	$A_{ani,xx}$	$A_{ani,yy}$	$A_{ani,zz}$	A_{iso}	$A_{ani,xx}$	$A_{ani,yy}$	$A_{ani,zz}$
O1	−5.3	−31.5	14.4	17.1	−20.0	−32.5	14.6	17.9	−12.1	−31.2	14.4	16.8				
C2	−29.2	−2.1	−1.5	3.6	−30.9	−3.1	−1.2	4.2	−23.9	−2.0	−1.0	3.0				
O3	−2.9	−23.2	11.0	12.2	−13.8	−24.1	11.2	12.8	−6.9	−21.7	10.0	11.7				
C4	87.6	−71.9	−70.8	142.8	237.1	−82.0	−80.9	162.9	129.3	−70.5	−69.4	139.9				
N5	−3.6	−1.2	−0.9	2.1	−2.2	−1.3	−1.1	2.4	−3.1	−0.7	−0.6	1.3				
C6	−27.0	−3.0	0.7	2.3	−25.8	−3.1	0.4	2.7	−23.6	−3.4	−0.2	3.6				
H7	129.8	−5.0	−2.8	7.8	120.2	−5.2	−3.4	8.6	81.5	−4.5	−3.0	7.5				
H8	9.2	−4.2	−3.4	7.5	9.0	−4.5	−3.5	8.0	5.0	−3.7	−3.4	7.2				
H9	71.8	−4.8	−3.0	7.8	66.2	−5.2	−3.2	8.5	127.6	−5.7	2.6	8.3				
H7-9	70.2	−2.8	−2.3	5.1	65.1	−2.9	−2.3	5.2	71.4	−2.6	−1.9	4.5	70.8	−2.9	−2.7	5.6
		(5.0°)	(4.5°)	(2.2°)		(5.4°)	(4.9°)	(2.4°)		(47.6°)	(47.9°)	(5.1°)				
H10	87.7	−6.1	−2.5	8.5	81.8	−6.2	−2.9	9.1	84.9	−5.4	−2.9	8.3	86.3	−6.9	−2.7	9.5
		(2.6°)	(1.0°)	(2.5°)		(3.2°)	(3.4°)	(2.8°)		(14.0°)	(15.1°)	(8.3°)				
H11	10.9	−5.0	−4.5	9.5	10.5	−5.4	−4.5	9.9	7.3	−4.5	−4.3	8.8	10.2	−4.9	−4.8	9.7
		(45.6°)	(45.6°)	(0.8°)		(25.6°)	(25.6°)	(0.9°)		(27.3°)	(27.4°)	(4.0°)				
H12	26.0	−5.8	−4.2	10.0	23.9	−6.2	−4.3	10.5	27.4	−5.3	−4.3	8.8	30.2	−6.1	−4.7	10.7
		(0.5°)	(0.3°)	(0.5°)		(8.5°)	(8.5°)	(1.5°)		(8.9°)	(7.4°)	(5.7°)				

[a]Present work.
[b]Experimental results from Ref. 47.

tions, using the GAPW method. We have implemented this method in QUICKSTEP. The method was validated first by comparing the results for a selection of atoms and small molecules (using a supercell technique) with other theoretical and experimental data. Here, we have also quantified the impact of the inclusion of augmentation contributions from neighboring atomic sites. We have proposed a hybrid AE and PSP scheme, a combination of an AE treatment for the nuclei of interest and a PSP approximation for the remaining atoms in the simulation cell. Using the *R*2 *L*-α-alanine derived radical as an example, we then showed that this hybrid scheme results in relatively inexpensive yet highly accurate HFP calculations in an extended periodic system. In combination with the molecular dynamics capabilities of the CP2K program package, we plan to use our method for hyperfine parameter studies at finite temperatures.

ACKNOWLEDGMENTS

This work was supported by the Fund for Scientific Research–Flanders and the Research Board of Ghent University.

*Electronic address: Michel.Waroquier@UGent.be

[1] P. Hohenberg and W. Kohn, Phys. Rev. **136**, B864 (1964).
[2] W. Kohn and L. Sham, Phys. Rev. **140**, A1133 (1965).
[3] M. Kaupp, M. Bühl, and V. G. Malkin, *Calculations of NMR and EPR parameters: Theory and Applications* (Wiley-VCH, Weinheim, 2004).
[4] P. E. Blöchl, Phys. Rev. B **50**, 17953 (1994).
[5] P. E. Blöchl, Phys. Rev. B **62**, 6158 (2000).
[6] C. G. Van de Walle and P. E. Blöchl, Phys. Rev. B **47**, 4244 (1993).
[7] G. Csányi and T. A. Arias, Chem. Phys. Lett. **360**, 552 (2002).
[8] O. V. Yazyev, I. Tavernelli, L. Helm, and U. Röthlisberger, Phys. Rev. B **71**, 115110 (2005).
[9] G. Lippert, J. Hutter, and M. Parrinello, Mol. Phys. **92**, 477 (1997).
[10] G. Lippert, J. Hutter, and M. Parrinello, Theor. Chem. Acc. **103**, 124 (1999).
[11] M. Krack and M. Parrinello, Phys. Chem. Chem. Phys. **2**, 2105 (2000).
[12] M. S. Bahramy, M. H. F. Sluiter, and Y. Kawazoe, Phys. Rev. B **73**, 045111 (2006).
[13] S. Blügel, H. Akai, R. Zeller, and P. H. Dederichs, Phys. Rev. B **35**, 3271 (1987).
[14] J. E. Harriman, *Theoretical Foundations of Electron Spin Resonance* (Academic Press, New York, 1978).
[15] D. M. Granty and R. K. Harris, *Encyclopedia of Nuclear Mag-*

netic Resonance (Wiley, Chichester, UK, 1996), Vol. 5.
[16] J. VandeVondele, M. Krack, F. Mohamed, M. Parrinello, T. Chassaing, and J. Hutter, Comput. Phys. Commun. **167**, 103 (2005).
[17] http://cp2k.berlios.de.
[18] V. I. Lebedev, Zh. Vychisl. Mat. Mat. Fiz. **15**, 48 (1975).
[19] V. I. Lebedev, Zh. Vychisl. Mat. Mat. Fiz. **16**, 293 (1976).
[20] V. I. Lebedev, Sib. Math. J. **15**, 48 (1977).
[21] H. M. Petrilli, P. E. Blöchl, P. Blaha, and K. Schwarz, Phys. Rev. B **57**, 14690 (1998).
[22] R. F. Curl Jr., Mol. Phys. **9**, 585 (1965).
[23] J. Gauss, K. Ruud, and T. Helgaker, J. Chem. Phys. **105**, 2804 (1996).
[24] V. Barone, Chem. Phys. Lett. **262**, 201 (1996).
[25] M. J. Frisch *et al.*, *Gaussian 03, Revision D.01*, Gaussian, Inc., Wallingford, CT, 2004.
[26] J. P. Perdew and A. Zunger, Phys. Rev. B **23**, 5048 (1981).
[27] J. P. Perdew, K. Burke, and M. Ernzerhof, Phys. Rev. Lett. **77**, 3865 (1996).
[28] A. D. Becke, Phys. Rev. A **38**, 3098 (1988).
[29] C. Lee, W. Yang, and R. G. Parr, Phys. Rev. B **37**, 785 (1988).
[30] N. Godbout, D. R. Salahub, J. Andzelm, and E. Wimmer, Can. J. Chem. **70**, 560 (1992).
[31] E. V. R. de Castro and F. E. Jorge, J. Chem. Phys. **108**, 5225 (1998).
[32] L. Wilmer Anderson, F. M. Pipkin, and J. C. Baird, Phys. Rev. **120**, 1279 (1960).
[33] G. H. Fuller and V. W. Cohen, Nucl. Data, Sect. A **5**, 433 (1969).
[34] Y. Ting and H. Lew, Phys. Rev. **105**, 581 (1957).
[35] G. Wessel and H. Lew, Phys. Rev. **92**, 641 (1953).
[36] C. Sur, B. K. Sahoo, R. K. Chaudhuri, B. P. Das, and D. Mukherjee (unpublished).
[37] B. K. Sahoo, R. K. Chaudhuri, B. P. Das, S. Majumder, H. Merlitz, U. S. Mahapatra, and D. Mukherjee, J. Phys. B **36**, 1899 (2003).
[38] A.-M. Mårtensson-Pendrill, J. Phys. B **35**, 917 (2002).
[39] In these figures, the predictions for ^{1}H and ^{87}Sr were omitted.
[40] *Calculation of NMR and EPR parameters: Theory and Applications*, edited by M. Kaupp, M. Bühl, and V. G. Malkin (Wiley-VCH, Weinheim, 2004).
[41] P. Belanzoni, E. van Lenthe, and E. J. Baerends, J. Chem. Phys. **114**, 4421 (2001).
[42] W. Weltner, *Magnetic Atoms and Molecules* (Van Nostrand Reinhold, New York, 1983).
[43] In these figures, the predictions for ^{107}Ag and ^{1}H were omitted.
[44] E. Malinen, M. Z. Heydari, E. Sagstuen, and E. O. Hole, Radiat. Res. **159**, 23 (2003).
[45] D. Regulla, Appl. Radiat. Isot. **52**, 1023 (2000).
[46] V. Gancheva, E. Sagstuen, and N. D. Yordanov, J. Phys. Chem. **75**, 329 (2006).
[47] E. Sagstuen, E. O. Hole, S. R. Haugedal, and W. H. Nelson, J. Phys. Chem. A **101**, 9763 (1997).
[48] F. Ban, S. D. Wetmore, and R. J. Boyd, J. Phys. Chem. A **103**, 4303 (1999).
[49] P. Lahorte, F. De Proft, G. Vanhaelewyn, B. Masschaele, P. Cauwels, F. Callens, P. Geerlings, and W. Mondelaers, J. Phys. Chem. A **103**, 6650 (1999).
[50] E. Pauwels, V. Van Speybroeck, P. Lahorte, and M. Waroquier, J. Phys. Chem. A **105**, 8794 (2001).
[51] M. S. Lehmann, T. F. Koetzle, and W. C. Hamilton, J. Am. Chem. Soc. **94**, 2657 (1972).
[52] E. Pauwels, V. Van Speybroeck, and M. Waroquier, J. Phys. Chem. A **108**, 11321 (2004).
[53] G. Lippert, J. Hütter, P. Ballone, and M. Parrinello, J. Phys. Chem. **100**, 6231 (1996).
[54] S. Goedecker, M. Teter, and J. Hutter, Phys. Rev. B **54**, 1703 (1996).
[55] C. Hartwigsen, S. Goedecker, and J. Hutter, Phys. Rev. B **58**, 3641 (1998).
[56] CPMD, version 3.11.1, Copyright IBM Corp. 1990-2006, Copyright MPI für Festkörperforschung Stuttgart 1997-2001; http://www.cpmd.org
[57] N. Troullier and J. L. Martins, Phys. Rev. B **43**, 1993 (1991).

5 Paper IV

Surface segregation in CuPt alloys by means of an improved modified embedded atom method

M. Schurmans, J. Luyten, C. Creemers, R. Declerck, and M. Waroquier

Physical Review B 76 (17), 174208 (2007)

PHYSICAL REVIEW B **76**, 174208 (2007)

Surface segregation in CuPt alloys by means of an improved modified embedded atom method

M. Schurmans,[1,*] J. Luyten,[1] C. Creemers,[1] R. Declerck,[2] and M. Waroquier[2]
[1]*Department of Chemical Engineering, K.U. Leuven, Willem de Croylaan 46, B-3001 Leuven, Belgium*
[2]*Center for Molecular Modeling, Laboratory of Theoretical Physics, Ghent University, Proeftuinstraat 86, B-9000 Gent, Belgium*
(Received 2 March 2007; revised manuscript received 28 June 2007; published 26 November 2007)

We present a procedure to investigate surface structures in CuPt alloys by combining the modified embedded atom method (MEAM) and the cluster expansion method (CEM). While the MEAM provides structural information for the description of extended anisotropic defects, the CEM improves the ability to correctly reproduce the relevant ground state structures in agreement with *ab initio* data. The procedure is validated with the reproduction of surface energies of pure Cu and Pt, the prediction of T_C for order-disorder transitions, the surface and segregation energies in ordered CuPt alloys, and Monte Carlo (MC) simulations of temperature-dependent surface segregation profiles. A complete MEAM-CEM/MC study of the surface segregation in Cu_3Pt, CuPt, and $CuPt_3$ alloys is presented, engaging only 11 composition- and volume-independent alloy-specific parameters. Results are critically compared with experimental data from literature and with an independent set of *ab initio* periodic density functional theory calculations.

DOI: 10.1103/PhysRevB.76.174208 PACS number(s): 31.15.Ct, 68.35.Dv, 81.30.Hd, 61.66.Dk

I. INTRODUCTION

The physical and chemical behaviors at metal alloy surfaces are crucial for several technological processes. CuPt alloys show interesting catalytic properties, among which is an improved activity and selectivity for CO oxidation and hydrocarbon reactions with respect to pure Pt.[1–3] A detailed knowledge of the energetic interactions at the metallic surfaces, as well as the effect of alloying, is necessary to improve our understanding of these phenomena. In addition to a broad range of experimental techniques that can be used to examine the surface structure, composition, and ordering, several reliable theoretical methods are nowadays also available. The increased computational capacity makes an accurate *ab initio* calculation of the energies of real and hypothetical atomically ordered systems feasible. It has also been shown that a combination of statistical mechanics and parametrized interatomic potentials, e.g., embedded atom method[4] (EAM), modified EAM[5] (MEAM), Bozzolo-Ferrante-Smith[6] (BFS) method, bond order potentials,[7] and cluster expansion method[8,9] (CEM), fitted in a consistent set of *ab initio* data, are able to describe (partly) disordered systems within acceptable time limits. The accuracy that can be expected from calculations using these semi-empirical methods depends on the size and level of theory of the *ab initio* training set data used for fitting the interatomic potentials[10] and even on the predictive power of the potentials[11,12] themselves. The main purpose of this work is to reproduce the equiatomic $L1_1$ CuPt ground state with MEAM so that MEAM calculations are more widely applicable and in better agreement with the first principles benchmarks.

II. METHODOLOGY

The procedure proposed in this work consists of a MEAM description in combination with the flexible parametrization of CEM, thereby making optimal use of the synergism of both methods. This procedure has been validated on CuPt: MEAM introduces structural information, capable of describing extended defects while CEM correctly reproduces the ground state of the equiatomic $L1_1$ CuPt. The surface energy of ordered CuPt alloys as predicted by MEAM-CEM is then assessed by *ab initio* values obtained from periodic density functional theory (DFT) calculations that were not used in the training set. Finally, we will predict the equilibrium surface composition and ordering in the CuPt system with this MEAM-CEM method and Monte Carlo (MC) simulations, and we will compare our estimates with available experimental evidence.

MEAM was originally developed by Baskes,[5] who extended the EAM[4] to account for directional bond characteristics. The interatomic MEAM potentials have been proven to accurately describe a number of properties that explicitly depend on the interatomic distances (e.g., fcc-bcc transition and bulk modulus). This explains its many successful applications in structural calculations,[13] molecular dynamics,[14] surface MC simulations,[15,16] etc. However, the number of interaction parameters in MEAM is limited, and by design, the potential generally maximizes the number of nearest-neighbor bonds between different atomic species. This is a serious drawback in the description of CuPt as the equiatomic alloy orders in the $L1_1$ rather than the $L1_0$ structure. Moreover, in general, CuPt is not an exception by showing non-nearest-neighbor based ground states. Based on extensive *ab initio* investigations,[17,18] complicated ground states in ordered transition metal alloys are nowadays emerging rather as the rule. A CEM correction to MEAM can then also help to take into account the more complicated ground states.

In this paper, we will not present a full CuPt ground state search, but we will illustrate that a combination of MEAM with even a basic version of the CEM substantially improves the validity of the MEAM. The interatomic interaction parameters derived from the CEM generate MEAM-CEM energies, leading to a better reproduction of the heat of formation of a number of atomically ordered alloys. A similar correction has recently been proposed to adjust the nonlinear attractive interactions in the BFS method.[12] In the present paper, we propose an algorithm that is illustrated in Fig. 1.

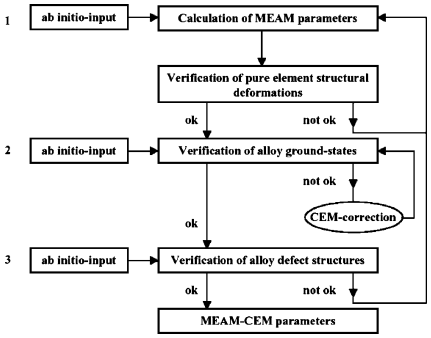

FIG. 1. Scheme for improving MEAM calculations with a CEM correction.

First, we determine MEAM parameters from *ab initio* data (step 1), and then validate them by comparing structural deformations (e.g., bulk distortions, vacancies, and surfaces) and alloy ground state predictions with those predicted by *ab initio* calculations and experiments (step 2). In this process, all the available MEAM parameters are optimized. Step 2 includes the calculation of the heat of formation of bulk alloys as a function of interatomic distance and a number of bulk MC simulations both below and above the critical temperature T_C for an order-disorder transition. If this step reveals the prediction of an incorrect ground state and if this cannot be corrected within the valid boundaries of the MEAM parameters, a number of cluster interactions are selected to correct the MEAM ground state prediction. The ground state is then again verified, and, if necessary, more cluster interactions are added until a completely satisfactory reproduction of the relevant ground state structures is obtained. Finally, in step 3, the resulting MEAM-CEM method is tested by calculating (mainly alloy) structural deformations. In this paper, step 3 includes MC simulations of low index surfaces and energy calculations of ordered CuPt alloy surfaces that are compared to DFT calculations and experiments.

The procedure comprises two completely different sets of DFT calculations. A first type of periodic DFT calculations has been performed on a training set determining the MEAM and CEM parameters. This fitting procedure is tested by calculating surface properties of CuPt alloys (e.g., correct prediction of surface terminations of ordered CuPt alloys) with the MEAM-CEM and comparing them with results from a different DFT study. The two different sets of DFT calculations were performed independently using two different calculation packages in order to obtain maximally unbiased information. DFT-PW91 (Ref. 19) gradient-corrected functional calculations were performed on the training set using the Vienna *ab initio* simulation package (VASP).[20,21] On the other hand, the test set comprises DFT local density approximation (LDA)[22] and DFT-PW91 calculations performed with the QUANTUM-ESPRESSO (QE) package.[23] In this way, the test set helps to understand the surface segregation profiles obtained from MEAM-CEM. The use of two different approaches in the test set strengthens the evidence about the predicted stability of surface terminations of ordered CuPt alloys.

The ground state structures were calculated in VASP and QE while imposing periodic boundary conditions in the three spatial directions. Ultrasoft pseudopotentials[24] are used to describe the electron-ion interaction. The energy of all structures was converged to within 0.001 eV/atom with respect to the plane wave cutoff energy and the number of k points sampling the first Brillouin zone. In a variable cell relaxation, the equilibrium energy and structure of the lattices Cu_3Pt ($L1_2$), CuPt ($L1_0$), CuPt ($L1_1$), and $CuPt_3$ ($L1_2$) were determined. Together with the equilibrium energy per atom of pure Cu (fcc) and Pt (fcc), this allows us to calculate the sublimation energy ΔH^{sub} per atom of each of the constituents and the total heat of formation ΔH^f of the ordered bulk alloys. In the DFT-PW91 (VASP) calculations of CuPt alloys, relaxation effects are constrained so as to maintain the fcc structure enabling a straightforward determination of the MEAM parameters. No such constraint was imposed in the calculation of the test set with QE. This additional degree of freedom only affects the CuPt $L1_0$ lattice, which is subject to a tetragonal distortion that lowers the CuPt $L1_0$ formation energy ΔH^f by 0.018 eV/atom.

The next section provides more details regarding the determination of MEAM parameters. Section III A presents the MEAM parametrization of pure Cu, pure Pt, and CuPt interactions. Section III B gives a brief overview of the description of structural defects with the CEM-formalism. In Sec. IV, an improvement of MEAM ground state predictions is achieved by means of a CEM correction. Finally, the MEAM-CEM algorithm is implemented in order to study and discuss the surface segregation at the three low index single crystal surfaces of CuPt alloys (Secs. V and VI).

III. PARAMETRIZATION OF MEAM AND CEM FOR THE DESCRIPTION OF ALLOY SURFACES

A. Modified embedded atom method description of CuPt alloys

In Ref. 10, Luyten *et al.* described a new and more consistent way of fitting MEAM parameters to DFT calculations and applied the method to describe surface segregation in Cu_3Pt. In that work, all MEAM interactions are restricted to nearest neighbors. Table II in Ref. 10 demonstrates that, even with a limited set of included interactions, MEAM successfully predicts the energies of a wide range of isotropic and anisotropic structural deformations of pure Cu and pure Pt. The bulk heat of formation, the equilibrium lattice parameter, and the bulk modulus of a "reference" structure, Cu_3Pt ($L1_2$) correspond to three MEAM alloy parameters. These material properties of the reference structure are therefore exactly reproduced. A good agreement with the heats of formation of three additional ground state ordered structures, CuPt ($L1_0$), CuPt ($L1_1$), and $CuPt_3$ ($L1_2$), is obtained by including another group of two MEAM parameters. However, despite

TABLE I. MEAM and DFT-PW91 (VASP) predictions for the equilibrium NN distance (R_0) and heat of formation (ΔH^{form}) for various ordered CuPt compounds.

	R_0 (Å)		ΔH^{form} (eV/atom)	
	MEAM	DFT-PW91 (VASP)	MEAM	DFT-PW91 (VASP)
Cu_3Pt ($L1_2$)	2.65	2.65	−0.140	−0.143
CuPt ($L1_0$)	2.71	2.72	−0.219	−0.124
CuPt ($L1_1$)	2.73	2.72	−0.199	−0.153
$CuPt_3$ ($L1_2$)	2.77	2.76	−0.186	−0.118

this additional set, the relative stability of the different ordered structures remains unaltered. Reference 10 lists all the MEAM parameters for the CuPt system determined in this way. The present paper adopts the same numerical values of the MEAM parameters. Predictions of the heat of formation and the equilibrium interatomic distance of a number of CuPt alloys with DFT-PW91 (VASP) and MEAM calculations are presented in Table I.

One of the peculiarities of the CuPt system is the existence of the $L1_1$ structure at the equiatomic composition, with planes of pure Pt and pure Cu alternating in the (111) direction. According to the phase diagram,[25] this $L1_1$ structure is stable up to 1089 K. DFT-PW91 (VASP) calculations at 0 K predict the correct ground state configuration, the $L1_1$ structure being 0.029 eV/atom more stable than the unrelaxed $L1_0$ structure (see Table I). MEAM, on the contrary, predicts a larger stability for CuPt $L1_0$. The latter is favored by eight bonds between unlike nearest neighbors versus only six in the $L1_1$ structure. The larger MEAM stability of CuPt $L1_0$ (Table I) is triggered by the too exothermic interactions between nearest-neighbor CuPt pairs as compared to further ranging interactions. Although $L1_0$ is the most stable equiatomic compound in more binary alloys than $L1_1$,[25] both theoretical and experimental techniques have found a stable $L1_1$ ground state for equiatomic CuPt, and the standard MEAM procedure fails to reproduce this. The energy difference between the two compounds ($L1_1$ versus $L1_0$) may be rather small, but as the MEAM parameters have been determined by a fitting procedure with a training set constructed by DFT-PW91 (VASP) data, one might at least expect that MEAM would reproduce the same ground state configuration. The results of this paper indicate that this has no consequences if MEAM is applied to Cu_3Pt. However, when investigating the equiatomic CuPt alloy, equilibrium MEAM/MC simulations automatically refer to the incorrect $L1_0$ ground state. MEAM/MC simulations of the equiatomic CuPt alloy then evolve to a bulk composition profile oscillating in the (100) direction with alternating layers of pure Cu and pure Pt. Since the $L1_1$ ordered alloy has stoichiometric layers in the (100) direction, one cannot expect to accurately describe segregation in equiatomic CuPt alloys with the current version of MEAM.

B. Cluster expansion method

At this moment, CEM provides the most consistent and versatile framework for including an arbitrary amount of total energy calculations from first principles in the parametrization of a multicomponent system on a lattice structure.[26] CEM[27] calculates the heat of formation of multicomponent lattice systems with the following Ising cluster expansion:

$$\Delta H^f_{CEM} = J_0 + \sum_{sites} J_i \hat{S}_i + \sum_{pairs} J_{ij} \hat{S}_i \hat{S}_j + \sum_{triplets} J_{ijk} \hat{S}_i \hat{S}_j \hat{S}_k + \cdots = \sum_{\alpha} J_\alpha \sigma_\alpha, \quad (3.1)$$

where $\hat{S}_i$ are spin variables with a value of ±1 depending on the occupation of the corresponding sites by an atom A or B. α runs over all symmetry-equivalent figures in the lattice, and the interaction energies J_α are determined[28,29] either via empirical fits, via perturbation theory, via direct inversion, or via a least-squares method. The cluster expansion provides a complete basis,[27] and hence the energy of different configurations can be reproduced with any desired degree of accuracy, provided that enough different symmetry-equivalent figures α are taken into account. A limited number of interactions are usually selected in advance, but, recently, genetic algorithms were used to map *ab initio* results to model Hamiltonians.[30,26]

As far as *local* structural variations and relaxations are concerned, the description in CEM varies from completely neglecting relaxations over determining volume-dependent interaction energies $J_\alpha(V)$ to adding a volume-dependent reference energy E_{ref} [e.g., $E_{ref}=\Omega(V)x(1-x)$]. For the extension to long period superlattices, the concept of constituent strain cluster expansion was developed.[8] Recently, pair potentials dependent on interatomic distances were combined with CEM and have improved ability to model phase stability in bulk alloys.[31] These pair potentials are reported to take into account the effect of local structural variations. To our knowledge, accounting for extended defects such as surfaces has hitherto not been described by structural additions to the CEM.

If, on the other hand, an extended defect is considered as a new degree of freedom, it becomes possible to describe the occupation of the lattice sites in the neighborhood of this defect with a CEM description of that specific structure.[29] The same accuracy can then be obtained as in CEM bulk calculations. However, the parametrization of each additional degree of freedom comes at a computational cost that is similar to an additional ground state search.

As an alternative to the large amount of additional *ab initio* calculations that are needed to describe surfaces with pure CEM only, we propose to combine the ability of MEAM to accurately deal with structural defects in alloys, such as lattice distortions, vacancies, and surfaces, with the versatility of CEM that, by design, is able to predict the bulk alloy ground states with an accuracy comparable to the *ab initio* method by which it was parametrized.

IV. MODIFIED EMBEDDED ATOM METHOD-CLUSTER EXPANSION METHOD

The difference between the heat of formation of a number of relaxed ordered alloy configurations predicted with *ab ini-*

tio methods and with MEAM is expressed by a parameter Δ as follows:

$$\Delta(\text{config}) = \Delta H^{f}_{ab\ initio}(\text{config}) - \Delta H^{f}_{MEAM}(\text{config}). \tag{4.1}$$

By definition, Δ is zero if the configuration was used as the reference structure in the MEAM parametrization. In situations where Δ is of the same order of magnitude as the energy difference between the two most stable configurations, MEAM can predict the wrong alloy structure as the ground state. The competition between the $L1_1$ and $L1_0$ structures for CuPt, described in the previous section, provides a good example of this problem. This is not surprising as the amount of alloying interactions that are included in the standard MEAM is limited. The idea of the method we propose is to calculate Δ for a number K of atomically ordered configurations and to express these Δ's as a correction energy ΔH^{c}_{CE} in an expansion of various cluster interactions,

$$\Delta(\text{config}_k) = \Delta H^{c}_{CE}(\text{config}_k) = \sum_{\alpha} J_{\alpha}\sigma_{\alpha} \quad \text{for } k = 1,2,\ldots,K. \tag{4.2}$$

In order to keep the parametrization effort of the same degree of complexity as in commonly used MEAM versions, the cluster interactions in the expansion described in this paper are all volume independent. Moreover, they are restricted to null (α=0) clusters, point (α=1) clusters, nearest-neighbor (NN) (α=2) and second NN (α=5) pair clusters, and NN triangle (α=3) and NN tetrahedron (α=4) clusters. By construction, the original MEAM parameterization already provides an accurate description of pure Cu, Pt, and $L1_2$ Cu_3Pt. Nevertheless, these structures are also included in the CEM parametrization to ensure that the CEM parameters do not perturb the already established MEAM precision. The inclusion of $L1_0$ and $L1_1$ CuPt leads to a correct ground state description of the equiatomic alloy. For symmetry reasons, $L1_2$ $CuPt_3$ is included as well. The interaction parameters J_{α} are now calculated by matrix inversion[32] and are based on the difference between MEAM and *ab initio* energies for the six ordered configurations. Before introducing the matrix that links the interaction parameters J_{α} with the correction energies $\Delta(\text{config}_k)$, a correlation function $\bar{\Pi}_{\alpha}$ is defined for each class α of symmetry-equivalent figures, expressing the configurational contribution of a specific symmetry-equivalent figure to the formation energy of that configuration,

$$\bar{\Pi}_{\alpha}(\text{config}) = \frac{1}{ND_{\alpha}} \sum_{m=0}^{ND_{\alpha}} \hat{S}_1\hat{S}_2\cdots\hat{S}_{m_{\alpha}}, \tag{4.3}$$

with D_{α} as the number of figures of class α per site and N as the number of sites. $\bar{\Pi}_{\alpha}$ yields a value between −1 and +1. Equation (4.3) can now be rewritten as a function of symmetry-equivalent clusters α and correlation functions $\bar{\Pi}_{\alpha}$,

$$\begin{aligned}\Delta H^{c}_{CE}(\text{config}_k) &= \sum_{\alpha} J_{\alpha}\sigma_{\alpha} \\ &= \sum_{\alpha} J_{\alpha}D_{\alpha}\bar{\Pi}_{\alpha}(\text{config}) \quad \text{for } k = 1 \text{ to } 6,\end{aligned} \tag{4.4}$$

for the six CuPt compounds $A_{4-n}B_n$, with n=0,1,2,2,3,4. The $\bar{\Pi}_{\alpha}(\text{config}_k)$ of each symmetry-equivalent cluster α can easily be calculated for ordered fcc configurations. Rewritten in the vector-matrix notation, Eq. (4.4) results in a 6×6 matrix that expresses the relation between the interaction parameters J_{α} and the correction energies ΔH^{c}_{CE},

$$\begin{pmatrix} \Delta H^{c}_{CE}(\text{fccCu}) \\ \Delta H^{c}_{CE}(L1_2Cu_3Pt) \\ \Delta H^{c}_{CE}(L1_0CuPt) \\ \Delta H^{c}_{CE}(L1_2CuPt_3) \\ \Delta H^{c}_{CE}(\text{fccPt}) \\ \Delta H^{c}_{CE}(L1_1CuPt) \end{pmatrix} = \begin{pmatrix} 1 & 1 & 1 & 1 & 1 & 1 \\ 1 & 1/2 & 0 & -1/2 & -1 & 1 \\ 1 & 0 & -1/3 & 0 & 1 & 1 \\ 1 & -1/2 & 0 & 1/2 & -1 & 1 \\ 1 & -1 & 1 & -1 & 1 & 1 \\ 1 & 0 & 0 & 0 & -1 & -1 \end{pmatrix} \begin{pmatrix} J_0D_0 \\ J_1D_1 \\ J_2D_2 \\ J_3D_3 \\ J_4D_4 \\ J_5D_5 \end{pmatrix}. \tag{4.5}$$

A simple matrix inversion yields J_{α},

$$\begin{pmatrix} J_0D_0 \\ J_1D_1 \\ J_2D_2 \\ J_3D_3 \\ J_4D_4 \\ J_5D_5 \end{pmatrix} = \begin{pmatrix} 0.0625 & 0.0 & 0.375 & 0.0 & 0.0625 & 0.5 \\ 0.25 & 0.5 & 0.0 & -0.5 & -0.25 & 0.0 \\ 0.375 & 0.0 & -0.75 & 0.0 & 0.375 & 0.0 \\ 0.25 & -0.5 & 0.0 & 0.5 & -0.25 & 0.0 \\ 0.0625 & -0.25 & 0.375 & -0.25 & 0.0625 & 0.0 \\ 0.0 & 0.25 & 0.0 & 0.25 & 0.0 & -0.5 \end{pmatrix} \begin{pmatrix} \Delta H^{c}_{CE}(\text{fccCu}) \\ \Delta H^{c}_{CE}(L1_2Cu_3Pt) \\ \Delta H^{c}_{CE}(L1_0CuPt) \\ \Delta H^{c}_{CE}(L1_2CuPt_3) \\ \Delta H^{c}_{CE}(\text{fccPt}) \\ \Delta H^{c}_{CE}(L1_1CuPt) \end{pmatrix}, \tag{4.6}$$

with $D_0=1$, $D_1=1$, $D_2=12$ (i.e., the number of the first NN), $D_3=24$, $D_4=8$, and $D_5=6$ (the number of the second NN).

After having determined all J_α parameters, the energy for every arbitrary configuration is evaluated as

$$\Delta H^f_{MEAM\text{-}CEM} = \Delta H^f_{MEAM} + \Delta H^c_{CEM}. \quad (4.7)$$

The volume-dependent heats of formation of the six ordered CuPt alloys are calculated with this scheme and can then be compared with volume-dependent MEAM and DFT-PW91 (VASP) energies. Figure 2 illustrates the ability of the original MEAM to correctly predict the lattice parameter and the bulk modulus of relaxed ordered alloys. However, Fig. 2 also reveals that the original MEAM fails to quantitatively predict the magnitude of the heat of formation. It thus makes sense to include a limited number of CEM parameters, only to correct the heat of formation of a number of relaxed ordered alloys. The additional CEM parameters do not influence the prediction of the lattice parameter or the bulk modulus.

Then, the energies of these structures and of a number of atomic slabs with single antisite defects are calculated with MEAM-CEM and compared with DFT-PW91 (QE) results. For the $L1_2$ structure, we have considered periodic slabs with six layers and 2×2 atoms per layer and slabs with four layers and 4×4 atoms per layer. For the $L1_1$ structure, periodic atomic slabs were considered with six 2×2 layers and with six 3×3 layers. These slabs were filled according to the $L1_2$ or $L1_1$ symmetry but with one Cu (Pt) atom replaced by a Pt (Cu) atom. Figure 3 illustrates the defect-free $L1_2$, $L1_1$, and $L1_0$ energies and the formation energies of periodic slabs that are based on these structures but with single Pt (Cu) antisite defects. The formation energy ΔH^f_{AS} of an isolated bulk antisite defect in a perfectly ordered stoichiometric atomic slab was calculated as follows:[29]

$$\Delta H^f_{AS} = \Delta H^f_{bulk}(N^A_{bulk}-1, N^B_{bulk}+1) - (N^A_{bulk}+N^B_{bulk})\Delta H^f_{bulk}, \quad (4.8)$$

where N^A_{bulk} (N^B_{bulk}) is the number of A (B) atoms in the bulk and ΔH^f_{bulk} ($N^A_{bulk}-1, N^B_{bulk}+1$) is the formation energy of an atomic slab that refers to the perfectly ordered bulk, but with one B excess atom on an A site. The larger model slabs are necessary for the calculation in order to consider isolated defects. Table II presents a comparison between MEAM, MEAM-CEM, and DFT-PW91 (QE) calculations of formation energies of pairs of antisite defects in stoichiometric ordered CuPt compounds.

The MEAM-CEM features a very satisfying agreement for the prediction of the heat of formation, the bulk modulus, the lattice parameter of relaxed ordered CuPt alloys, and the formation energy of bulk antisite defects. This is achieved by combining the ability of MEAM to accurately describe structural bulk deformations in metallic alloys with the versatility of CEM to include the ground state *ab initio* calculations of an arbitrary number of ordered alloys. It is therefore deemed a considerable improvement over the original MEAM. Moreover, the MEAM-CEM algorithm, elaborated in this paper, has a degree of complexity and parametrization effort that remains comparable to the original MEAM. The extension of MEAM with CEM in this work only induces a small number of additional interaction parameters, but it manifestly gives an added value in view of the closer agreement with the DFT-PW91 benchmarks.

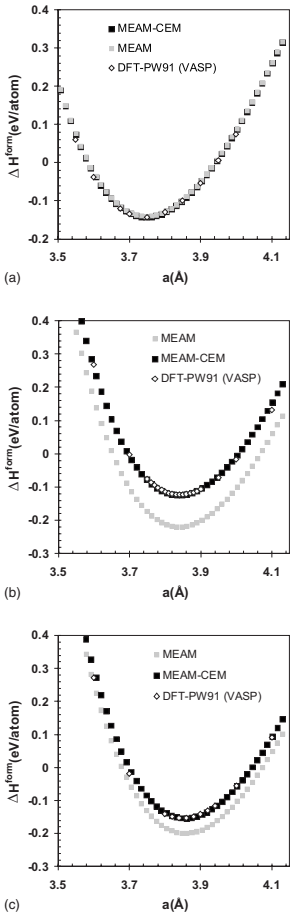

FIG. 2. [(a)–(c)] Volume-dependent heat of formation of $L1_2$ Cu_3Pt, $L1_0$ CuPt, and $L1_1$ CuPt, as calculated with DFT-PW91 (VASP) (◇), MEAM (gray square), and MEAM-CEM (■). (a) corresponds to the MEAM reference structure $L1_2$ Cu_3Pt; the MEAM heat of formation of $L1_0$ CuPt is—erroneously—more exothermic than $L1_1$ CuPt [gray □ in (b) and (c)]. The cluster expansion correction restores the stability of $L1_1$ CuPt, as compared to $L1_0$ CuPt, in agreement with DFT-PW91 (VASP).

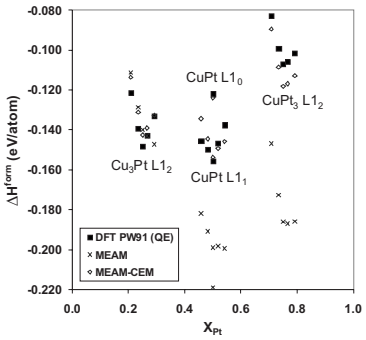

FIG. 3. MEAM, MEAM-CEM, and DFT-PW91 (QE) predictions for the heat of formation of various ordered CuPt compounds with Cu-rich and Pt-rich antisite defects.

Combining the MEAM-CEM with MC simulations allows us to gain information on the short- and long-range orders at equilibrium. Therefore, to confirm the stability of the ordered alloys predicted with MEAM-CEM, the ground state accuracy is tested in a final step by calculating the order-disorder transition temperatures T_C of $L1_2$ Cu_3Pt, $L1_1$ CuPt, and $L1_2$ $CuPt_3$ in a series of MC simulations. In order to determine the order-disorder T_C from MC simulations, virtual crystals are constructed with $24\times24\times24$ lattice sites. Simulations are performed with the Metropolis algorithm,[33] starting with crystals in the ordered state. After 30×10^6 Markov steps, equilibrium can safely be assumed, and from there on, the heat of formation ΔH^f of the simulated crystal, the short-range order (SRO),[34] and the long-range order parameters are sampled every 25 000 additional steps and averaged over another 10×10^6 steps. In order to evaluate the critical order-disorder temperature T_C, a succession of simulations is performed at gradually increasing temperatures (in steps of 50 K). At T_C, the long-range order parameter rather abruptly drops from a value close to 1 to nearly zero. This procedure is performed both with MEAM and MEAM-CEM, and their predictions of T_C are compared with experimental values[25] in Table III. At the three canonical compositions, the MEAM-CEM simulations of CuPt alloys now correspond to the experimentally determined ground states.

TABLE II. Formation energy of pairs of isolated antisite defects in stoichiometrically ordered CuPt compounds.

	Antisite defect energies (eV/antisite)	
Structure	DFT-PW91 (QE)	MEAM-CEM
Cu_3Pt $L1_2$	0.912	0.963
CuPt $L1_1$	0.794	0.730
$CuPt_3$ $L1_2$	0.589	0.692

TABLE III. MEAM and MEAM-CEM predictions of the critical temperature T_C of order-disorder transitions for three CuPt compounds. For the equiatomic CuPt alloy, MEAM predicts an $L1_0$ order; the corresponding T_C is listed for comparison.

	T_C (K)		
	MEAM-CEM	MEAM	Expt.[23]
Cu_3Pt $L1_2$	1225	725	870
CuPt $L1_1$	875 ($L1_1$)	625 ($L1_0$)	1089 ($L1_1$)
$CuPt_3$ $L1_2$	950	1025	850

V. MODIFIED EMBEDDED ATOM METHOD–CLUSTER EXPANSION METHOD DESCRIPTION OF CuPt SURFACES

A. Surface energy of fcc Cu and fcc Pt with modified embedded atom method–cluster expansion method

By construction, the MEAM-CEM prediction for the heat of formation for the bulk materials Cu, Pt, and $L1_2$ Cu_3Pt coincides exactly with the *ab initio* value. In the case of anisotropic defects, however, a number of figures with interaction energy J_α drop out of the MEAM-CEM calculation, and the remaining CEM term no longer vanishes entirely. However, the MEAM parameters are determined in a least-squares fitting scheme to, among other quantities, the pure-element unrelaxed (111) and (100) surface energies. Consequently, CEM parameters disturb the least-squares precision of MEAM for these quantities. A good MEAM description that keeps a CEM correction small is therefore crucial for accurate MEAM-CEM total energy predictions.

An important step in the further validation of the CEM parameters is now to recalculate the pure-element Cu and Pt surface energies of low index orientations with MEAM-CEM and to compare them with MEAM and DFT-PW91 (VASP) results. Provided a lattice film is considered with a sufficient number of atomic layers to eliminate the influence of the surface in the core layers and with periodic boundary conditions in two directions perpendicular to the surface, the surface energy ΔH^{surf} per atom in a pure-element lattice can be calculated as

$$\Delta H^{surf}(k) = \frac{\Delta H^{film}(k,N) - N\Delta H^f_{bulk}}{N^{surf}a^{surf}}. \qquad (5.1)$$

In this expression, ΔH^{film} (k,N) is the formation energy of a metallic film with two surfaces in direction k and N represents the total number of atoms in the film. $N\Delta H^f_{bulk}$ is the formation energy of a bulk metal with N atoms and N^{surf} denotes the number of surface atoms in the film, with a^{surf} as the surface area per atom of the film. In pure materials, ΔH^f_{bulk} equals ΔH^{sub}, with ΔH^{sub} as the sublimation energy per atom of the (fully relaxed) bulk material.

Table IV compares the DFT-PW91 (VASP), MEAM-CEM, and MEAM surface energies of the pure-element fcc Pt and Cu low index surfaces. The DFT-PW91 surface energies were found to have converged with respect to the number of

TABLE IV. MEAM-CEM, MEAM, and DFT-PW91 (VASP) predictions of the unrelaxed surface energy of fcc Cu and fcc Pt at three low index surfaces.

	Cu			Pt		
	MEAM-CEM	MEAM	DFT-PW91 (VASP)	MEAM-CEM	MEAM	DFT-PW91 (VASP)
$\gamma_{(100)}$ (eV/Å^2)	0.087	0.092	0.091	0.123	0.118	0.114
$\gamma_{(111)}$ (eV/Å^2)	0.074	0.080	0.080	0.094	0.091	0.092
$\gamma_{(110)}$ (eV/Å^2)	0.092	0.096	0.097	0.120	0.115	0.121

film layers as a variation between 7, 9, and 11 layers did not result in significant variations of the surface energy. In view of the deviation tolerated for the (110) surface energy, which is part of the MEAM test set, the loss of accuracy of MEAM-CEM was not considered significant enough to start a reiteration of the MEAM and CEM parametrization and to create a closed loop between steps 3 and 1 mentioned in Fig. 1. If the perturbation of the surface energies would be significant, one could either choose a global, simultaneous optimization of the MEAM and the CEM parameters or a correction of the surface interactions through the definition of layer-dependent cluster interactions. Because MEAM describes extended defects with a good accuracy and CEM only restores the stability of the $L1_1$ ground state, no reiteration of this kind was deemed necessary in this work. We will verify this assumption through the calculation of a test set of alloy surface and segregation energies.

B. Surface energy of CuPt alloys

At $T \ll T_C$, the equilibrium surface composition of ordered metallic alloys generally corresponds to a bulk-terminated surface. Ordered alloys display an oscillating bulk composition profile in the (100) and (110) directions of $L1_2$, in the (100) direction of $L1_0$, and in the (111) direction of $L1_1$. At least two distinct surface terminations are then possible. The stability of each possible termination can be described by the surface energy. Starting from free atoms in the gas phase, the surface energy $\Delta H^{surf}(k)$ of an alloy film amounts to[29]

$$\Delta H^{surf}(k) = \frac{\Delta H^{film}(k, N^A_{film}, N^B_{film}) - N^A_{film}\Delta H^{sub}(A) - N^B_{film}\Delta H^{sub}(B) - (N^A_{film} + N^B_{film})\Delta H^f_{bulk}}{N^{surf} a^{surf}}, \tag{5.2}$$

with N^A_{film} (N^B_{film}) as the number of atoms of each atomic species A (B) in the atomic film and with ΔH^f as the total heat of formation of the bulk alloy. Surfaces of ordered alloys with an oscillating bulk profile can have surface terminations with totally different atomic compositions. First, the different surface energies are calculated with MEAM-CEM according to Eq. (5.2) for the surfaces for which the segregation is simulated in Sec. V C. The results, presented in the three leftmost columns of Table V, give a suggestion to identify the relative stability of unreconstructed surface terminations in the ordered CuPt alloys with an oscillating bulk composition profile. These results will help us to discuss segregation and the stability of the different possible surface structures in CuPt. However, the expression of the surface energy as given in Eq. (5.2) is not yet complete. Whenever the stoichiometry of a slab used to compute the surface energy differs from that of the bulk, the energy of this difference has to be accounted for by the chemical potential μ of the excess species,[35,36]

$$\Delta H^{surf}(k) = \frac{1}{N^{surf} a^{surf}}\Bigg(\Delta H^{film}(k, N^A_{film}, N^B_{film}) - N^A_{film}\Delta H^{sub}(A) - N^B_{film} \times \Delta H^{sub}(B) - (N^A_{film} + N^B_{film})\Delta H^f_{bulk} - \mu \sum_{i=1}^{SL} (c_i - c) \Bigg), \tag{5.3}$$

with SL as the number of layers in the surface region, $\{c_i\}$ the concentration profile of some finite surface region, and c the concentration in the bulk. The chemical potential is not fixed but can always vary within a given range depending on the identity of the excess atoms in the bulk. This makes computed surface energies according to Eq. (5.3) not readily interpretable to the stability of surface terminations. We therefore also calculated segregation energies from bulk Cu and Pt antisite defects,[29]

TABLE V. A selection of MEAM-CEM, DFT-LDA (QE), and DFT-PW91 (QE) energies of unreconstructed surface terminations of CuPt compounds [following Eq. (5.2)]. Overall, the MEAM-CEM and the DFT calculations perform equally well in the identification of stable surface terminations.

	$\Delta H^{surf}_{(100)}$ (eV/Å^2) $L1_2$ Cu_3Pt								
	MEAM-CEM			DFT-LDA (QE)			DFT-PW91 (QE)		
Termination	Cu	CuPt	Pt	Cu	CuPt	Pt	Cu	CuPt	Pt
9 layers	0.100	0.109		0.133	0.133		0.104	0.098	
1 layer relaxed	0.098	0.109		0.132	0.133		0.103	0.098	
2 layer relaxed	0.098	0.109		0.132	0.133		0.103	0.097	
11 layers	0.100	0.109		0.133	0.134		0.104	0.098	
Termination	$\Delta H^{surf}_{(110)}$ (eV/Å^2) $L1_2$ Cu_3Pt								
	MEAM-CEM			DFT-LDA (QE)			DFT-PW91 (QE)		
	Cu	CuPt	Pt	Cu	CuPt	Pt	Cu	CuPt	Pt
9 layers	0.104	0.115		0.134	0.146		0.104	0.109	
1 layer relaxed	0.099	0.112		0.129	0.143		0.099	0.107	
2 layer relaxed	0.098	0.111		0.128	0.143		0.099	0.106	
11 layers	0.104	0.115		0.134	0.146		0.104	0.109	
Termination	$\Delta H^{surf}_{(111)}$ (eV/Å^2) $L1_1$ CuPt								
	MEAM-CEM			DFT-LDA (QE)			DFT-PW91 (QE)		
	Cu	CuPt	Pt	Cu	CuPt	Pt	Cu	CuPt	Pt
9 layers	0.101	0.092	0.069	0.140		0.100	0.113	0.105	0.072
1 layer relaxed	0.099	0.092	0.068	0.140		0.100	0.113	0.102	0.071
2 layer relaxed	0.099	0.092	0.068	0.140		0.100	0.113	0.102	0.071
11 layers	0.101	0.092	0.069	0.140		0.100	0.113	0.104	0.071
Termination	$\Delta H^{surf}_{(100)}$ (eV/Å^2) $L1_0$ CuPt								
	MEAM-CEM			DFT-LDA (QE)			DFT-PW91 (QE)		
	Cu	CuPt	Pt	Cu	CuPt	Pt	Cu	CuPt	Pt
9 layers	0.104	0.110	0.107	0.147		0.144	0.102	0.105	0.113
1 layer relaxed	0.100	0.110	0.107	0.147		0.143	0.099	0.104	0.113
2 layer relaxed	0.100	0.110	0.107	0.147		0.143	0.099	0.104	0.113
11 layers	0.104	0.110	0.107	0.147		0.144	0.101	0.105	0.113
Termination	$\Delta H^{surf}_{(100)}$ (eV/Å^2) $L1_2$ $CuPt_3$								
	MEAM-CEM			DFT-LDA (QE)			DFT-PW91 (QE)		
	Cu	CuPt	Pt	Cu	CuPt	Pt	Cu	CuPt	Pt
9 layers		0.120	0.115		0.149	0.145		0.113	0.109
1 layer relaxed		0.118	0.115		0.148	0.144		0.112	0.108
2 layer relaxed		0.118	0.115		0.148	0.144		0.112	0.108
11 layers		0.120	0.115		0.149	0.145		0.113	0.108
Termination	$\Delta H^{surf}_{(110)}$ (eV/Å^2) $L1_2$ $CuPt_3$								
	MEAM-CEM			DFT-LDA (QE)			DFT-PW91 (QE)		
	Cu	CuPt	Pt	Cu	CuPt	Pt	Cu	CuPt	Pt

TABLE V. (*Continued.*)

	$\Delta H^{surf}_{(100)}$ (eV/Å^2) $L1_2$ Cu_3Pt								
	MEAM-CEM			DFT-LDA (QE)			DFT-PW91 (QE)		
Termination	Cu	CuPt	Pt	Cu	CuPt	Pt	Cu	CuPt	Pt
9 layers		0.114	0.124		0.141	0.160		0.108	0.121
1 layer relaxed		0.108	0.121		0.135	0.156		0.102	0.118
2 layer relaxed		0.106	0.119		0.134	0.155		0.101	0.117
11 layers		0.114	0.124		0.141	0.161		0.107	0.121

$$\Delta H^{seg} = \frac{\Delta H^{film}(k, N^A_{film}-2, N^B_{film}+2)}{2} - \frac{\Delta H^{film}(k, N^A_{film}, N^B_{film})}{2} + (N^A_{bulk}+N^B_{bulk})\Delta H^f_{bulk} - \Delta H^f_{bulk}(N^A_{bulk}-1, N^B_{bulk}+1). \quad (5.4)$$

The individual terms in Eq. (5.4) are self-explanatory. For the calculation of segregation energies, atomically ordered films in a rigid lattice with a thickness of nine atomic layers with 2×2 atoms per layer are used. The lattice parameter is set equal to the fully relaxed bulk lattice parameter of the compound under consideration. The (100) and (110) surfaces of the $L1_2$ Cu_3Pt ($CuPt_3$) alloys are considered, both with a pure Cu (Pt) and an equiatomic CuPt (CuPt) bulklike termination, as are the (111) surface of the $L1_1$ CuPt with a pure Cu and a pure Pt bulklike termination. The same calculation is then repeated with an atomic antisite in each top layer of the film. Finally, the bulk antisite defect energy of isolated excess atoms is subtracted [Eq. (4.8)].

Before formulating a full assessment of the stability of CuPt low index surfaces based on surface energies, segregation energies, MC simulations, and the driving forces of surface segregation, the results of the surface and segregation energy calculations are first compared with a number of independent DFT calculations performed with the QE code.

The surface energies at different terminations for three canonical compositions, Cu_3Pt, CuPt, and $CuPt_3$, were computed within the framework of spin-restricted DFT using the QE package.[23] Using each of the fully relaxed Cu_3Pt ($L1_2$), CuPt ($L1_0$), CuPt ($L1_1$), and $CuPt_3$ ($L1_2$) unit structures as a basis, we have built supercells in the direction perpendicular to the surface of interest. This can also be viewed as creating a stack of layers parallel to the surface plane. By separating this stack from its periodic images with empty space, a suitable model was created for a film with a specific termination within three-dimensional periodic boundary conditions. From the energy of this slab, combined with the equilibrium energy per atom of Cu (fcc) and Pt (fcc), we can calculate the formation energy of an alloy film ΔH^{film} (n_i+n_j). Finally, from Eq. (5.2), we obtain the surface energy ΔH^{surf}. The DFT-LDA (QE) and DFT-PW91 (QE) surface energies at different terminations are presented in the middle and right columns of Table V for three canonical compositions, Cu_3Pt, CuPt, and $CuPt_3$.

The convergence of the surface energy with respect to the number of layers in the film and the size of the vacuum in the supercell has been ascertained. It turns out that a vacuum separation of 15 a.u. plus one lattice constant perpendicular to the surface under investigation is largely sufficient to achieve reasonable convergence. The convergent behavior of the surface energy at various film thicknesses is reflected in Table V, where the values are tabulated corresponding to 9 and 11 layers. Also included in Table V are the resulting surface energies where, respectively, one and two layers at both sides of the film were relaxed.

In summary, we would like to stress the good qualitative agreement of the three methods for all terminations and compositions, except for the (100) layer in $L1_2$ Cu_3Pt, for which the DFT-PW91 (QE) method finds a lower surface energy, different from both the DFT-LDA (QE) and the MEAM-CEM method. Quantitatively, we observe that the DFT-LDA (QE) method tends to overestimate the surface energies in comparison with the DFT-PW91 (QE) method. If we consider the difference originating from the use of different functionals as a measure of the error that can be expected in DFT predictions of surface energies, it becomes clear just how close the MEAM-CEM energies coincide with the DFT-PW91 (QE) energies. This is a comforting result: The MEAM-CEM method closely reproduces results from the same DFT functional on which the MEAM-CEM method was initially parametrized, even with another program package.

Table VI presents a comparison between MEAM-CEM and DFT-PW91 (QE) calculations of surface [Eq. (5.2)] and segregation energies [Eq. (5.4)] of antisite defects. For CuPt and $CuPt_3$, we notice a reasonable agreement. It should be stressed that the computational load for the evaluation of segregation energies is heavy. The agreement is less good for Cu_3Pt and this conclusion holds for both surface and segregation energies. Because the surface energies are in reasonably good agreement and because, by definition, the segregation energy describes only the segregating atom in one particular ordered environment,[29] it probably fails to quantitatively describe the segregation profile of (partly) disordered alloys at finite temperatures. It then follows that for alloy surfaces, SRO must be taken into account, which demands a large number of atoms per layer to be considered. This is done in the remaining part of this work, where we focus on surface MC simulations and compare them with experimental results. The segregation energies of Table VI and the differences between MEAM-CEM and DFT-PW91 (QE) will be considered in the interpretation of the MEAM-CEM/MC surface segregation profiles.

TABLE VI. Surface energies of stoichiometrically ordered CuPt compounds with different surface terminations. Bulk terminations are considered with single antisite defects at the surface. In the atomic film, consisting of nine layers and 2×2 atoms per layer, one antisite defect in each surface layer is constructed in order to conserve the symmetry of the atomic slab. Each slab is relaxed according to the equilibrium bulk lattice parameter (Table I).

				Surface energy (eV/atom)		Segregation energy (eV/atom)	
Structure	Surface orientation	Initial termination	Segregating species	DFT-PW91 (QE)	MEAM-CEM	DFT-PW91 (QE)	MEAM-CEM
Cu_3Pt $L1_2$	(100)	CuPt	Cu	0.788	0.838	−0.183	−0.421
	(100)	CuPt	Pt	0.752	0.801	−0.094	−0.062
	(100)	Cu	Pt	0.765	0.768	−0.220	0.042
Cu_3Pt $L1_2$	(110)	CuPt	Cu	1.168	1.169	−0.242	−0.595
	(110)	CuPt	Pt	1.203	1.148	−0.092	0.051
	(110)	Cu	Pt	1.074	1.067	−0.198	−0.045
CuPt $L1_1$	(111)	Cu	Pt	0.754	0.682	−0.407	−0.145
	(111)	Pt	Cu	0.526	0.565	−0.086	−0.028
$CuPt_3$ $L1_2$	(100)	Pt	Cu	0.864	0.889	−0.042	−0.036
	(100)	CuPt	Cu	0.868	0.888	−0.169	−0.203
	(100)	CuPt	Pt	0.962	1.046	−0.221	−0.100
$CuPt_3$ $L1_2$	(110)	Pt	Cu	1.289	1.300	−0.269	−0.222
	(110)	CuPt	Cu	1.173	1.209	−0.170	−0.158
	(110)	CuPt	Pt	1.324	1.310	0.006	−0.282

C. Monte Carlo simulations of surface segregation in CuPt alloys

We have performed canonical MEAM-CEM/MC calculations to investigate the segregation to the three low index surfaces of CuPt, at three stoichiometric "canonical" compositions and at temperatures between 300 and 1900 K. The off-stoichiometric effect was also considered by performing MC simulations with limited excess Cu-rich and excess Pt-rich deviations of the stoichiometric compositions so that, at equilibrium, only a slight ($<\pm1.0\%$) deviation of the bulk stoichiometric composition exists. In this way, the discontinuity of the chemical potential [Eq. (5.3)] at the stoichiometric composition is taken into account.[36,37] The simulations allow for a full discussion on the temperature- and composition-dependent multilayer segregation in CuPt alloys based on one energy model with 10 pure-element and 11 alloy parameters. Exactly the same set of parameters is used to investigate all the considered compositions, surface orientations, and temperatures below and above T_C, illustrating the transferability of these MEAM-CEM parameters. Simulations were performed in the Metropolis algorithm[33] with a simulation slab of 35 atomic layers and 24×24 atoms in each layer. If the segregation of bulk atoms to the surface region has an influence on the bulk concentration in an atomic slab, well below the surface region, a new simulation is started with an additional excess of the segregating species in order to keep the bulk concentration constant with respect to the concentration under study.

I. $L1_2$ Cu_3Pt

The bulk of $L1_2$ Cu_3Pt features oscillating profiles in the (110) and the (100) direction with two possible surface terminations. Surface composition profiles of the $Cu_{3\pm\delta}Pt_{1\mp\delta}$ alloys, obtained from MEAM-CEM/MC simulations, are presented in Fig. 4. Stable and metastable terminations are first considered by initiating the simulations with a Cu-rich and an equiatomic termination. MEAM-CEM/MC simulations find for all $Cu_{3\pm\delta}Pt_{1\mp\delta}$ (100) and (110) surfaces that the lower surface energy of Cu in comparison with Pt (Table VI) is the major factor determining the surface termination and segregation. This results in a pure Cu termination at the (110) and (100) surfaces of the $Cu_{3\pm\delta}Pt_{1\mp\delta}$ alloys at $T<T_C$. The equiatomic CuPt termination is found to be metastable only in Pt-rich $Cu_{3-\delta}Pt_{1+\delta}$ at very low temperatures (<500 K). Above T_C, the atomic layers of the bulk alloy become random and stoichiometric. The surface layer then remains largely enriched with Cu, and the subsurface layers show an oscillating segregation profile damping out to the bulk composition. This profile is typical for disordered alloys with attractive interatomic AB interactions. The oscillations in the segregation profile become attenuated as T increases further above T_C. In stoichiometric $L1_2$ Cu_3Pt and at $T\ll T_C$, MEAM-CEM predicts an ordered (111) surface with the stoichiometric composition. As T approaches T_C, the increased entropy and the lower surface energy of Cu yield a Cu enrichment (to 77.5%), which is almost entirely confined to the very surface layer. The Cu enrichment again gradually di-

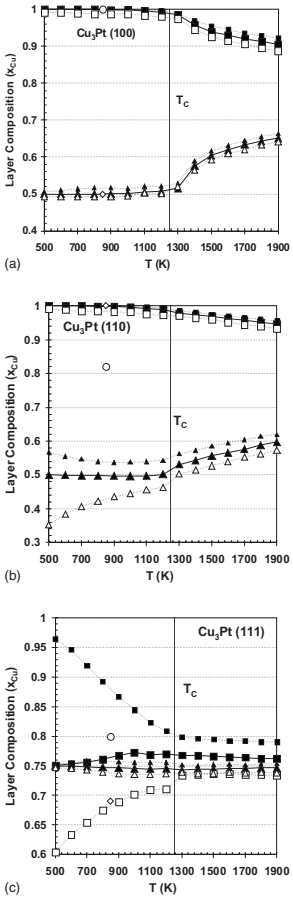

FIG. 4. [(a)–(c)] Composition of the surface (■, ■, □) and subsurface (▲, ▲, △) layers of the low index surfaces in the stoichiometric Cu_3Pt (■, ▲), the Cu-rich $Cu_{3+\delta}Pt_{1-\delta}$ (■, ▲), and the Pt-rich $Cu_{3-\delta}Pt_{1+\delta}$ (□, △) alloys versus temperature. LEIS measurements of the surface (○) and subsurface (◇) composition of Cu_3Pt (100) (Ref. 47), (110) (Ref. 46), and (111) (Refs. 48 and 49) were added to compare the segregation profiles with available experimental evidence.

minishes to the stoichiometric bulk composition when T increases further above T_C. The off-stoichiometric effect leads to a pronounced exothermic Cu (Pt) segregation in $Cu_{3+\delta}Pt_{1-\delta}$ ($Cu_{3-\delta}Pt_{1+\delta}$) that gradually diminishes at increasing temperatures and eventually evolves to the bulk composition far above T_C.

2. $L1_1$ CuPt

In the equiatomic $L1_1$ CuPt alloy, the layer-by-layer bulk composition profiles in the (110) and the (100) direction are stoichiometric. Figure 5 presents the temperature-dependent surface and subsurface concentrations of the equiatomic $Cu_{1\pm\delta}Pt_{1\mp\delta}$ alloys predicted with MEAM-CEM/MC simulations. Well below T_C, the simulations predict a Cu-rich (110) and a somewhat less Cu-rich (100) surface. Over a few layers, the oscillations in the subsurface composition gradually fade to the bulk stoichiometric composition. With an excess Cu concentration in the bulk, both (110) and (100) surfaces become fully enriched with Cu, while with an excess Pt concentration in the bulk, both surfaces have a surface layer with 50% Cu. When T increases to T_C, the Cu concentration in the surfaces of the stoichiometric and the Pt-rich simulation slabs also increases and enhances the subsurface oscillations. In these slabs, the Cu surface concentration reaches a maximum in the neighborhood of T_C, at 800 K, with a (110) [(100)] surface composition varying from 71% (80%) Cu in atomic slabs with excess Pt to 84% (90%) in stoichiometric equiatomic slabs. At temperatures increasing above T_C, the oscillations diminish and the surface concentration evolves to the bulk concentration.

The (111) surface of the ordered $L1_1$ alloy evolves to a pure Pt termination in stoichiometric, Pt-rich, and Cu-rich $Cu_{1\pm\delta}Pt_{1\mp\delta}$ samples below T_C. A metastable Cu (111) surface termination was found at low temperatures only if the simulation was initiated with an atomic slab with a Cu surface. At $T>T_C$, Pt segregates to the surface on top of an oscillating subsurface region. The face-dependent surface composition at the different low index surfaces of the equiatomic CuPt is one of the more striking results of this study. A comparison between MEAM-CEM/MC surface simulations and the DFT and MEAM-CEM calculations in Tables V and VI reveals an excellent agreement supporting the face-dependent segregation in equiatomic CuPt.

3. $L1_2$ $CuPt_3$

MEAM-CEM/MC simulations predict that the strain release of Pt atoms with the larger atomic radius and the ordering effect of the majority Pt atoms at the surface of $Cu_{1\pm\delta}Pt_{3\mp\delta}$ promotes a Pt-rich termination of the (100) surface (Fig. 6). Below T_C, this results in a stable pure Pt termination of the ordered alloy. The (100) surface is also enriched with Pt above T_C, and the subsurface layers oscillate to the stoichiometric composition. The off-stoichiometric Cu-rich $Cu_{1+\delta}Pt_{3-\delta}$ alloy has a metastable equiatomic (100) termination at very low temperature (<600 K). At the (110) surface, the difference between the surface energy of Cu and Pt atoms is larger. The balance of the driving forces for surface segregation then shifts to a Cu-rich termination. Energetically, the (110) surface favors a mixed termination with 50% Pt. However, at the (110) surface, a Pt termination is metastable in the Pt-rich $Cu_{1-\delta}Pt_{3+\delta}$ alloy (<600 K). The Cu concentration in the surface evolves to the bulk composition as T approaches T_C.

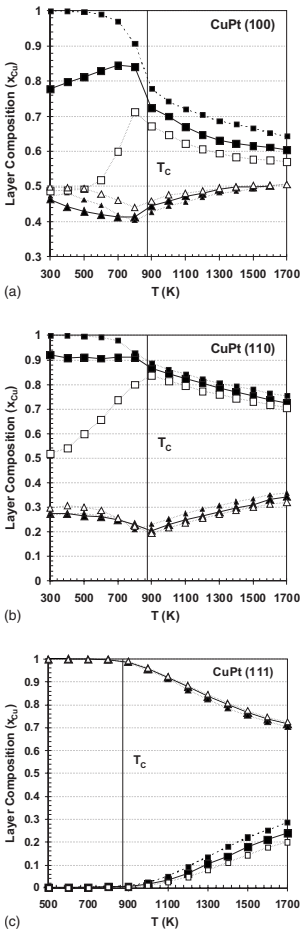

FIG. 5. [(a)–(c)] Composition of the surface (■, ■, □) and subsurface (▲, ▲, △) layers of the low index surfaces in the stoichiometric CuPt (■, ▲), the Cu-rich $Cu_{1+\delta}Pt_{1-\delta}$ (■, ▲), and the Pt-rich $Cu_{1-\delta}Pt_{1+\delta}$ (□, △) alloys versus temperature.

$L1_2$ $CuPt_3$ features stoichiometric layers in the (111) direction of the bulk alloy. Hence, only a small influence of surface segregation would be expected in the stoichiometric alloy. However, a pure Pt (111) surface with a sandwichlike subsurface rearrangement is formed with very pronounced oscillations up to the fourth layer (Fig. 7). A similar profile is found at the (111) surfaces of Cu- and Pt-enriched $L1_2$

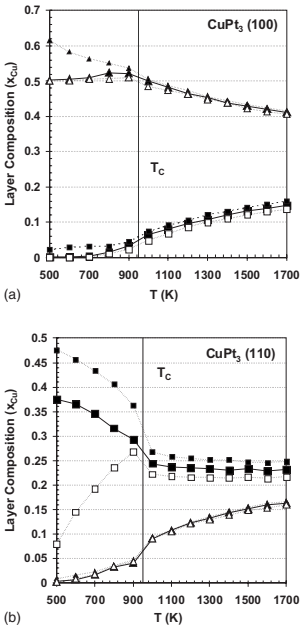

FIG. 6. [(a) and (b)] Composition of the surface (■, ■, □) and subsurface (▲, ▲, △) layers of the low index surfaces in the stoichiometric $CuPt_3$ (■, ▲), the Cu-rich $Cu_{1+\delta}Pt_{3-\delta}$ (■, ▲), and the Pt-rich $Cu_{1-\delta}Pt_{3+\delta}$ (□, △) alloys versus temperature.

$CuPt_3$. At $T > T_C$, the composition oscillates up to the eighth layer and attenuates as T rises further.

VI. DISCUSSION

A. Driving forces for surface segregation in CuPt

In this section, the driving forces for surface segregation in CuPt alloys are first discussed in more detail. Subsequently, in Sec. VI B, the surface terminations and segregation profiles calculated with MEAM-CEM and DFT will be discussed with reference to published experimental and theoretical evidence on surface structures in CuPt.

In the absence of a reactive gaseous atmosphere, three driving forces for segregation have been distinguished:[38,39] the lowering of the surface energy, the lowering of the mixing energy, and the (partial) release of elastic strain energy. Table VII gives an overview of experimental values of the Cu and Pt material properties that are related to these driving forces. The higher ΔH^{sub} of Pt leads to a higher surface energy of Pt as compared to Cu. At alloy surfaces, the atoms occupy surface areas that, ignoring relaxation effects, are

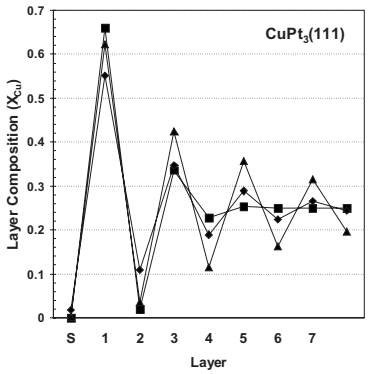

FIG. 7. Surface segregation profiles of stoichiometric $CuPt_3$ at the (111) surface in the ordered state at $T=500$ K (■) and at 1000 K (▲) and in the disordered state at $T=1500$ K (◆) ($T_C^{MEAM\text{-}CEM}=950$ K).

equally large. The surface energy per atom is then more closely related to the driving force for surface segregation than surface energy per unit area. Consequently, the surface energy is a more prominent driving force for segregation at more open surfaces.[45] This is illustrated by Table VIII for the CuPt system. The preference for Cu-rich surfaces at (110) orientations of the CuPt alloys is now easily understood in view of the larger difference in surface energy between Cu and Pt atoms at the (110) surface. From the surface composition profiles in Sec. V C, it appears that a more subtle interplay between elastic strain release and the less pronounced effect of surface energy at the other surface orientations can shift Cu segregation to Pt segregation.

Figure 8 plots the MEAM-CEM (100) surface energies per atom of pure Cu and pure Pt as a function of bulk interatomic distance R. The steep curve of pure Pt arises from strain energy that builds up in the bulk and is relieved at the surface. The surface energies per atom of Cu_3Pt and $CuPt_3$ are plotted in Fig. 9 and illustrate that strain release is more important in the latter. This figure supports the idea that strain release is a driving force for the segregation of the larger Pt atoms in $CuPt_3$ and that it is negligible in Cu_3Pt.

The exothermic mixing energy influences the surface segregation in order to maximize the number of bonds between unlike atomic species. In stoichiometric ordered alloys, this mechanism results in the segregation of the majority component to the surface region. In off-stoichiometric ordered alloys, the segregation of excess atoms is enhanced.

Finally, in stoichiometric systems with exothermic mixing energy, segregation at temperatures below T_C can depend on a combination of bulk entropy (endothermic segregation) and segregation enthalpy (exothermic contribution). In stoichiometric *ordered* systems, the enrichment of the surface can be seen as a two-step process. First, in an endothermic step, a bulk antisite defect is created in the ordered system. In the next step, one of the antisite atoms, generally the one with the lower surface energy, moves from the antisite in the bulk to form an antisite at the surface. In order to provide a driving force for segregation, this second step is exothermic. In equilibrium segregation to surfaces of stoichiometrically ordered systems, the balance between these two steps determines which species segregates and the amount of segregation, which on the whole may be endothermic (e.g.,

TABLE VII. Experimental values of Cu and Pt pure-element properties related to the driving forces for surface segregation. The surface energies in Refs. 43 and 44 correspond to surface free energies calculated from liquid surface tension parameters at the melting temperatures.

	Pt	Cu
Crystal structure	fcc	fcc
Lattice parameter (Å)	3.9158[a]	3.6075[a]
	3.9240[b]	3.6147[b]
Atomic radius (Å)	1.38[b]	1.248[b]
Heat of sublimation (eV/atom)	5.86[c]	3.50[c]
Surface energy (eV/Å^2)	0.138[d]	0.098[d]
	0.155[e]	0.114[e]

[a]Reference 40.
[b]Reference 41.
[c]Reference 42.
[d]Reference 43.
[e]Reference 44.

TABLE VIII. MEAM-CEM, MEAM, and DFT-PW91 (VASP) predictions of the unrelaxed surface energy *per atom* of fcc Cu and fcc Pt at three low index surfaces. At alloy surfaces, the different atoms occupy equal areas. The surface energy per atom is then more closely related to the driving force for surface segregation than surface energy per unit area (Table IV). This table illustrates that, in CuPt, surface energy is a more prominent driving force for surface segregation at more open surfaces.

	Cu			Pt		
	MEAM-CEM	MEAM	DFT-PW91 (VASP)	MEAM-CEM	MEAM	DFT-PW91 (VASP)
$\gamma_{(100)}$ (eV/atom)	0.580	0.612	0.606	0.978	0.938	0.907
$\gamma_{(111)}$ (eV/atom)	0.426	0.461	0.461	0.654	0.627	0.634
$\gamma_{(110)}$ (eV/atom)	0.866	0.904	0.913	1.350	1.293	1.361

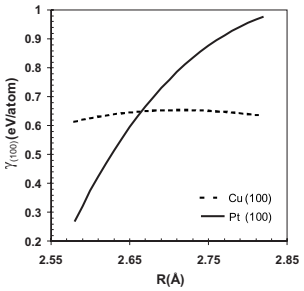

FIG. 8. MEAM-CEM (100) surface energy per atom of pure Cu (--) and pure Pt (—) as a function of bulk interatomic distance R. In this figure, R ranges from the DFT-PW91 (VASP) equilibrium interatomic distance in pure fcc Cu (2.58 Å) to pure fcc Pt (2.82 Å).

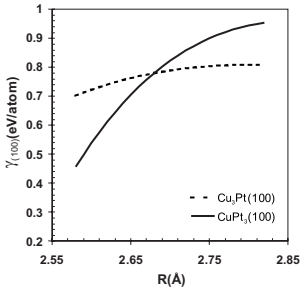

FIG. 9. MEAM-CEM (100) surface energy per atom of CuPt-terminated $L1_2$ Cu_3Pt (--) and CuPt-terminated $L1_2$ $CuPt_3$ (—) as a function of bulk interatomic distance R. In this figure, R ranges from the DFT-PW91 (VASP) equilibrium interatomic distance in pure fcc Cu (2.58 Å) to pure fcc Pt (2.82 Å).

exothermic bulk heat of formation, small difference in surface energy) or exothermic (e.g., small exothermic bulk heat of formation, large difference in surface energy). In systems with endothermic segregation, the amount of segregation is thus governed by the entropy-driven creation of bulk antisite defects. In these systems, two different segregation regimes can be recognized in function of temperature, since in disordered systems at $T > T_C$ segregation is always exothermic. The amount of segregation then reaches a maximum value in the neighborhood of T_C.

Endothermic, entropy-driven segregation can also occur in an *off-stoichiometric ordered* system if the segregation energy of the excess element is less exothermic than the segregation energy of the other element. In that case, segregation of the other element increases with temperature as the number of antisites of the other element grows.

B. Surface segregation in CuPt alloys

1. $L1_2$ Cu_3Pt

For $L1_2$ Cu_3Pt, MEAM-CEM/MC simulations (Fig. 4) and alloy surface energy calculations (Table V) both agree on a Cu termination of the (110) surface. The MEAM-CEM/MC prediction of a Cu termination is further supported by the DFT-PW91 (QE) and the MEAM-CEM segregation energies that exothermically favor segregation of Cu excess atoms to the equiatomic surface. The DFT-PW91 (QE) segregation energy of excess Pt to a pure Cu surface indicates that the (110) surface of $Cu_{3-\delta}Pt_{1+\delta}$ can accommodate more Pt atoms than suggested by the MEAM-CEM/MC simulations. Shen *et al.*[46] investigated the segregation behavior at the Cu_3Pt (110) surface with low energy ion spectroscopy (LEIS) and low energy electron diffraction (LEED). In contrast with the surface energy calculations, they reproducibly found a (110) surface that consists of 82% Cu with a virtually pure Cu second layer. The authors acknowledge that, at present, no quantitative theory seems to be able to reproduce their experimental result and to account for a difference in surface structure and ordering behavior in Cu_3Pt (100) and Cu_3Pt (110). The DFT, MEAM,[10] and MEAM-CEM calculations and simulations in this study cannot explain this phenomenon because a Cu enrichment of the equiatomic CuPt termination always induces segregation of Pt to the second layer. The large difference between the surface energy per atom of pure Cu and pure Pt (110) and the small effect of Pt strain energy in Cu_3Pt further sustain the prediction of a pure Cu (110) surface layer in Cu_3Pt.

At the (100) surface of $L1_2$ ordered Cu_3Pt, the MEAM-CEM/MC simulations also predict a pure Cu layer. DFT-LDA (QE) calculations confirm the Cu termination, but DFT-PW91 (QE) calculations rather give evidence for a CuPt termination (Table V). The segregation energies (Table VI) also point at this discrepancy: MEAM-CEM describes that excess Cu atoms segregate most exothermically to the surface and that Pt atoms do not, while DFT-PW91 (QE) segregation energies suggest that the pure Cu surface can accommodate at least some excess Pt atoms. However, the pure Cu surface termination is in excellent agreement with the LEIS and LEED measurements of Shen *et al.*,[47] who unambiguously measured a (1×1) Cu termination on top of a $c(2\times2)$ Cu-Pt second layer.

Below T_C, MEAM-CEM thus predicts that the low surface energy of Cu leads to a Cu-rich surface at the (100) and (110) surfaces of $L1_2$ Cu_3Pt. Above T_C, also a strong Cu segregation to these surfaces is observed, but the oscillations in the layer-by-layer composition profile are now limited to a few subsurface layers. These oscillations become smaller as T further increases. Such a subsurface profile is typical in alloys with attractive interatomic interactions and a pronounced surface segregation.[39]

For ordered $L1_2$ Cu_3Pt below T_C, the difference between pure Cu and pure Pt (111) surface energies is not sufficient to surpass the chemical interaction energy in the bulk. Segregation to the (111) surface of perfectly stoichiometric Cu_3Pt is then endothermic and thus entropy driven. At $T \ll T_C$, there is no significant surface segregation. As T approaches T_C and

the number of bulk antisite defects rises, the (111) surface evolves to 77.5% Cu and the second layer to 74.5%. For $T > T_C$, the faint and entropy-driven Cu segregation at the ordered (111) surface rapidly attenuates as the bulk order disappears. In stoichiometric Cu_3Pt, two segregation regimes to the (111) surface are thus recognized. Segregation is endothermic at rather low temperatures because the tradeoff between the lowering of the surface energy and the breakdown of the bulk order is endothermic. In this regime, segregation is proportional to the number of bulk antisite defects and increases with temperature. The other regime, at higher temperatures, is the exothermic segregation that lowers the surface energy from a disordered bulk. In off-stoichiometric $Cu_{3\pm\delta}Pt_{1\mp\delta}$, exothermic antisite induced surface segregation causes a substantial segregation of the excess species at low temperatures and diminishes at increasing temperatures. Shen *et al.*[48,49] studied Cu_3Pt (111) with LEIS and LEED and reported a slight enrichment of the surface layer to 80% Cu and a second layer that is depleted in Cu (69%), after annealing for 200 h at a temperature (800 K) close to the bulk order-disorder transition temperature (870 K).

Reference 10 gives a detailed description of the experimental evidence and the MEAM predictions on the surface segregation profile at the low index surfaces of Cu_3Pt. The MEAM results described in that paper are in excellent agreement with the MEAM-CEM results of this work. The prediction of the same segregation behavior illustrates the transferability of the MEAM-CEM formalism to anisotropic defects in alloys.

A recent LEED study[50] of Cu_3Pt (111), however, reports an unusual composition profile: Cu depletion at the surface (to 72%) and a significant Cu enrichment of the second layer (up to 92%). Tight binding Ising model (TBIM) calculations, presented in the same study, need two different sets of alloying pair interactions J_i in order to reproduce the stability of the $L1_1$ CuPt structure, with, on the one hand, $J_5=2J_2$ ($V_2=2V_1$) and, on the other hand, a smaller value of the ratio V_2/V_1 to reproduce the $L1_2$ Cu_3Pt structure. They investigated the segregation profile with the latter parameter set, both below and above T_C. These results are in good agreement with our MEAM-CEM/MC simulations. With the former parameter set, the authors suggest an $L1_1$-type bulk order profile in Cu_3Pt consisting of pure Cu planes and 50% Cu and 50% Pt planes alternating in the (111) direction. Of these two possible surface terminations in this hypothetical structure, according to TBIM, the pure Cu termination is the more stable. However, the corresponding surface profile agrees neither with the LEIS[48,49] profile nor with the LEED[50] results. The alternative, equiatomic termination is found to be only metastable within $45\% C_B < 70\%$ and unstable outside this region. Still, the authors suggested a satisfactory agreement with the LEED measurement. They suggested that the extended stability of this surface structure can be explained by contaminations that are supposed to favor Pt segregation. With the simulation results on surface segregation to the (111) surface of equiatomic CuPt [Fig. 5(c) and the next paragraph], it is now easier to understand the LEED results on (111) Cu_3Pt[50]. The Pt-rich (111) termination of a CuPt $L1_1$ compound can be a stable termination, even in the absence of contaminants.

2. $L1_1$ CuPt

Segregation is very pronounced at the (100) and (110) surfaces of the stoichiometric equiatomic CuPt alloy where the lower surface energy of Cu drives the Cu enrichment at $T < T_C$. The (110) surface of the stoichiometric $L1_1$ CuPt is even more Cu rich (±90% at 500 K) than the (100) surface (±80% at 500 K). This is explained by the larger difference of the surface energy per atom at the more open (110) surface than at the (100) surface. In stoichiometric equiatomic CuPt, this segregation increases as more bulk antisite defects are formed to reach a maximum close to T_C. Antisite induced surface segregation in $Cu_{1+\delta}Pt_{1-\delta}$ results in an exothermic segregation of excess Cu atoms to the (100) and (110) surfaces, resulting in a full Cu enrichment of the surface that decreases monotonously. Cu segregates endothermically at low temperature in $Cu_{1-\delta}Pt_{1+\delta}$. The (100) and (110) surfaces contain 50% Cu at ~300 K, but the number of Cu atoms in the surface rises as more Cu antisite defects are formed in the bulk alloy at increasing temperatures. The Cu concentration in both surfaces reaches a maximum close to T_C.

The stable Pt termination of the closer-packed (111) surface of $L1_1$ CuPt is explained by the release of elastic strain energy that surpasses the difference of the pure Cu and Pt surface energies. MEAM-CEM/MC simulations find the Pt termination stable on both Pt-rich and Cu-rich off-stoichiometric $Cu_{1\pm\delta}Pt_{1\mp\delta}$. Above T_C, Pt segregation to the (111) surface and Cu segregation to the (100) and (110) surfaces are exothermic and attenuate as T further increases.

To our knowledge, only theoretical evidence on the surface segregation in equiatomic CuPt alloys has been published. Khoutami *et al.*[51] and Senhaji *et al.*[52] described a TBIM investigation of the segregation profile. They reported a (90%) Cu termination at the (111) surface at $T > T_C$ and called it a surprising anisotropic effect compared to the (60%) Cu enrichment of the more open (100) surface at the same temperature. This is indeed surprising as one would expect a larger influence of the lower surface energy of Cu at the (100) surface than at the (111) surface. The authors attributed this anisotropy to the alloying effect in $L1_1$ CuPt. Our results on the (100) surface are in good agreement with their findings. This agreement, however, does not extend to the (111) surface. In Table V, both DFT-LDA (QE) and DFT-PW91 (QE) predictions sustain that a Pt termination is more stable than a Cu termination at the (111) surface of an $L1_1$ ordered CuPt alloy. The very exothermic DFT-PW91 (QE) and MEAM-CEM segregation energy of a Pt antisite to a Cu surface (Table VI) also strongly points to a Pt-rich (111) CuPt surface. In a theoretical $L1_0$-type alloy, DFT-LDA (QE) and DFT-PW91 (QE) confirm that a Cu termination is more stable than a Pt termination at the (100) surface, supporting Cu segregation to this surface. Here, a face-dependent segregation reversal is described for surfaces of the equiatomic CuPt alloy.

3. $L1_2$ $CuPt_3$

The lower surface energy of Cu compared to Pt also determines the surface segregation at the (110) surface of $L1_2$ $CuPt_3$ with a Cu-rich surface layer and a 100% Pt second layer. The stoichiometric ordered alloy displays a surface

with 45% Cu at 500 K. MEAM-CEM/MC simulations find that excess Cu (Pt) in the bulk induces exothermic Cu (Pt) segregation to the (110) surface but hardly influences the concentrations in the second layer. The DFT-PW91 (QE) segregation energies of excess Cu and Pt to the equiatomic CuPt surface (Table VI) suggest an even more Cu-rich (110) surface. The larger number of Pt atoms in the bulk $CuPt_3$ alloy leads to an increased influence of the strain energy, resulting in a face-related segregation reversal.

The segregation reversal is now situated between the (110) and (100) surfaces. Thus, at the (100) surface, an almost pure Pt layer terminates the $L1_2$ ordered alloy. Excess Cu atoms do not segregate to the pure Pt (100) surface so that off-stoichiometric $Cu_{1\pm\delta}Pt_{3\mp\delta}$ alloys also have a pure Pt (100) surface layer. This is also confirmed by the low MEAM-CEM and DFT-PW91 (QE) segregation energy of excess Cu to the pure Pt surface (Table VI). In MEAM-CEM/MC simulations, however, excess Cu atoms migrate to the second layer, while excess Pt atoms remain in the deeper layers below the surface.

At the (111) surface of ordered $L1_2$ $CuPt_3$, the release of the elastic strain of the larger Pt atoms and the chemical interactions induce an $L1_1$-like rearrangement of the three outermost surface layers. This results in a pure Pt surface and a sandwichlike subsurface with 66% Cu in the second layer. A surface region is formed, which is similar to the (111) surface of the equiatomic $L1_1$ CuPt alloy. The same surface profile was found at the (111) surface of Cu-rich and Pt-rich $Cu_{1\pm\delta}Pt_{3\mp\delta}$.

No experimental evidence on the surface segregation in $CuPt_3$ has yet been published. However, unpublished measurements[53] of the $CuPt_3$ (111) surface confirm a Pt enrichment of the surface layer. A possible $L1_1$-like surface rearrangement certainly deserves further attention. The segregation reversal between (100) and (110) surfaces is also indicated by the surface and segregation energy calculations of DFT-LDA (QE) and DFT-PW91 (QE): a stable Pt termination of the (100) surface, which is suggested by the low segregation energy of Cu to the pure Pt (100) surface, and a stable equiatomic (110) surface, which is suggested by the exothermic segregation energy of Cu to the pure Pt (110) surface (Table VI).

In conclusion, this discussion has shown that surface segregation in CuPt is mainly driven by the difference in surface energy between Cu and Pt. However, due to the smaller area per atom, this difference in surface energy presents a smaller driving force at the (111) and (100) surfaces, compared to the (110) surface, and the influence of strain energy becomes more important at surfaces of Pt-rich alloys. Both competing effects contribute to a face-dependent shift toward Pt segregation instead of the expected Cu segregation in CuPt between (100) and (111), and in $CuPt_3$ between (110) and (100).

VII. CONCLUSION

DFT parametrized MEAM potentials provide a consistent framework for the description of structural and compositional variations in metals and alloys, but MEAM overestimates the formation energy of ordered structures in which the number of interactions between different atomic species is maximized. This results in, for example, the prediction of an $L1_0$ rather than an $L1_1$ ground state for the equiatomic CuPt alloy.

The principal aim of this paper is to present a framework to further refine DFT-based MEAM calculations. A ground state correction of the MEAM is proposed through the addition of a limited number of cluster interactions as described in CEM. It now becomes possible to calculate the segregation profiles for different compositions, different surface orientations, and different temperatures, with only a small number of interaction parameters.

The main advantage is that the number of cluster interactions can straightforwardly be increased until the desired degree of accuracy for the ground state is achieved. On the other hand, MEAM adds structural information to CEM in order to describe anisotropic defects. A comparison with experimental results and additional DFT calculations of surface and segregation energies validates the results of the MEAM-CEM/MC simulations.

The stability of $L1_1$ in the equiatomic CuPt alloy, the amount of experimental and theoretical information, and the straightforward applicability of MEAM to transition metal alloys make CuPt an ideal alloy system to test the MEAM-CEM procedure. In the equiatomic CuPt alloy, an important correction is required for the MEAM method to adequately account for the greater stability of the $L1_1$ structure compared to $L1_0$. This essential correction could be achieved using a basic version of CEM to maintain the total complexity and parametrization effort comparable to the original MEAM. A large number of additional calculations were carried out to validate the MEAM-CEM parameter set: surface energies of pure Cu and Pt, bulk energies of several CuPt alloys, T_C of order-disorder transitions, surface energies of ordered CuPt alloys, and MC simulations of surface segregation profiles. The results are compared with experimental data from literature and with an independent set of DFT-LDA (QE) and DFT-PW91 (QE) calculations.

Reasoning on the "driving forces of segregation," an explanation is proposed for the observed surface segregation profiles, segregation energies, and surface energies of ordered CuPt alloys. The most remarkable result is the face dependence of the surface segregation in $Cu_{1\pm\delta}Pt_{1\mp\delta}$ and $Cu_{1\pm\delta}Pt_{3\mp\delta}$ alloys, where a subtle interplay of surface energy and release of elastic strain leads to a change in the segregating species. Cu segregates to the more open (100) and (110) surfaces of CuPt and to the (110) surface of $Cu_{3\pm\delta}Pt_{1\mp\delta}$, while Pt enriches the (111) surface of $Cu_{1\pm\delta}Pt_{1\mp\delta}$ and the (100) and (111) surfaces of $Cu_{1\pm\delta}Pt_{3\mp\delta}$. This face dependence was confirmed in this work with *ab initio* calculations.

ACKNOWLEDGMENTS

This work was supported by the Research Board of Katholieke Universiteit Leuven, the Research Foundation – Flanders, and the Research Board of Ghent University.

*Email address: Maarten.Schurmans@eu.umicore.com

[1] H. C. de Jongste and V. Ponec, J. Catal. **63**, 389 (1980).
[2] R. Linke, U. Schneider, H. Busse, C. Becker, U. Schröder, G. R. Castro, and K. Wandelt, Surf. Sci. **307-309**, 407 (1994).
[3] J. T. Kummer, J. Catal. **38**, 166 (1975).
[4] M. S. Daw and M. I. Baskes, Phys. Rev. B **29**, 6443 (1984).
[5] M. I. Baskes, Phys. Rev. B **46**, 2727 (1992).
[6] G. Bozzolo and J. Ferrante, Phys. Rev. B **50**, 5971 (1994).
[7] M. Aoki, Phys. Rev. Lett. **71**, 3842 (1993).
[8] D. B. Laks, L. G. Ferreira, S. F. Froyen, and A. Z. Zunger, Phys. Rev. B **46**, 12587 (1992).
[9] A. van de Walle and G. Ceder, Rev. Mod. Phys. **74**, 11 (2002).
[10] J. Luyten, M. Schurmans, C. Creemers, B. S. Bunnik, and G.-J. Kramer, Surf. Sci. **601**, 2952 (2007).
[11] M. Schurmans, J. Luyten, C. Creemers, and G. Bozzolo, Phys. Rev. B **72**, 064202 (2005).
[12] M. Schurmans, J. Luyten, and C. Creemers, Defect Diffus. Forum **263**, 129 (2007).
[13] J. Schiotz, F. D. Di Tolla, and K. W. Jacobsen, Nature (London) **391**, 561 (1998).
[14] J. G. Swadener, M. I. Baskes, and M. Nastasi, Phys. Rev. Lett. **89**, 085503 (2002).
[15] C. Creemers, P. Deurinck, S. Helfensteyn, and J. Luyten, Appl. Surf. Sci. **219**, 11 (2003).
[16] S. Helfensteyn, J. Luyten, L. Feyaerts, and C. Creemers, Appl. Surf. Sci. **212**, 844 (2003).
[17] S. Curtarolo, D. Morgan, and G. Ceder, CALPHAD: Comput. Coupling Phase Diagrams Thermochem. **29**, 163 (2005).
[18] S. Bärthlein, G. L. W. Hart, A. Zunger and S. Müller, J. Phys.: Condens. Matter **19**, 032201 (2007).
[19] J. P. Perdew, J. A. Chevary, S. H. Vosko, K. A. Jackson, M. R. Pederson, D. J. Singh, and C. Fiolhais, Phys. Rev. B **46**, 6671 (1992).
[20] G. Kresse and J. Furthmüller, Phys. Rev. B **54**, 11169 (1996).
[21] G. Kresse and J. Furthmüller, Comput. Mater. Sci. **6**, 15 (1996).
[22] J. P. Perdew and A. Zunger, Phys. Rev. B **23**, 5048 (1981).
[23] S. Baroni *et al.*, http://www.pwscf.org/
[24] D. Vanderbilt, Phys. Rev. B **41**, 7892 (1990).
[25] P. R. Subramanian and D. E. Laughlin, in *Binary Alloy Phase Diagrams*, 2nd ed., edited by T. B. Massalski (American Society for Metals, Ohio, 1990), Vol. 2.
[26] V. Blum, G. L. W. Hart, M. J. Walorski, and A. Zunger, Phys. Rev. B **72**, 165113 (2005).
[27] J. M. Sanchez, F. Ducastelle, and D. Gratias, Physica A **128**, 334 (1984).
[28] A. Zunger, in *Statics and Dynamics of Alloy Phase Transformations*, NATO Advanced Studies Institute, B: Physics, edited by P. E. A. Turchi and A. Gonis (Plenum, New York, 1994), p. 361.
[29] S. Muller, J. Phys.: Condens. Matter **15**, R1429 (2003).
[30] G. L. W. Hart, V. Blum, M. Walorski, and A. Zunger, Nat. Mater. **4**, 391 (2005).
[31] H. Y. Geng, M. H. F. Sluiter, and N. X. Chen, Phys. Rev. B **73**, 012202 (2006).
[32] J. W. D. Connolly and A. R. Williams, Phys. Rev. B **27**, 5169 (1983).
[33] N. Metropolis, A. W. Rosenbluth, M. N. Rosenbluth, A. H. Teller, and E. Teller, J. Chem. Phys. **21**, 1087 (1953).
[34] J. M. Cowley, Phys. Rev. **77**, 669 (1950).
[35] K. Rapcewicz, B. Chen, B. Yakobson, and J. Bernholc, Phys. Rev. B **57**, 7281 (1998).
[36] A. V. Ruban, Phys. Rev. B **65**, 174201 (2002).
[37] L. V. Pourovskii, A. V. Ruban, B. Johansson, and I. A. Abrikosov, Phys. Rev. Lett. **90**, 026105 (2003).
[38] P. Wynblatt and R. C. Ku, Surf. Sci. **65**, 511 (1977).
[39] C. Creemers, S. Helfensteyn, J. Luyten, and M. Schurmans, in *Applied Computational Materials Modeling: Theory, Experiment, and Simulations*, edited by G. Bozzolo, P. Abel, and R. D. Noebe (Kluwer Academic, New York, 2006).
[40] W. B. Pearson, *A Handbook of Lattice Spacings and Structures of Metals and Alloys* (Pergamon, Oxford, 1958).
[41] J. Emsley, *The Elements* (Clarendon, Oxford, 1991).
[42] *Handbook of Chemistry and Physics*, edited by D. R. Lide (CRC, Boca Raton, FL, 1992).
[43] W. R. Tyson and W. A. Miller, Surf. Sci. **62**, 267 (1977).
[44] F. R. de Boer, R. Boom, W. C. M. Mattens, A. R. Miedema, and A. K. Niessen, in *Cohesion and Structure*, edited by F. R. de Boer and D. G. Pettifor (North-Holland, Amsterdam, 1988), Vol. 1.
[45] F. L. Williams and D. Nason, Surf. Sci. **45**, 377 (1974).
[46] Y. G. Shen, D. J. O'Connor, and K. Wandelt, Surf. Sci. **410**, 1 (1998).
[47] Y. G. Shen, D. J. O'Connor, and K. Wandelt, Surf. Sci. **406**, 23 (1998).
[48] Y. G. Shen, D. J. O'Connor, and R. J. MacDonald, Solid State Commun. **96**, 557 (1995).
[49] Y. G. Shen, D. J. O'Connor, K. Wandelt, and R. J. MacDonald, Surf. Sci. **331-333**, 746 (1995).
[50] Y. Gauthier, A. Senhaji, B. Legrand, G. Tréglia, C. Becker, and K. Wandelt, Surf. Sci. **527**, 71 (2003).
[51] A. Khoutami, B. Legrand, and G. Treglia, Surf. Sci. **287-288**, 851 (1993).
[52] A. Senhaji, G. Treglia, and B. Legrand, Surf. Sci. **307-309**, 440 (1994).
[53] C. Becker, T. Pelster, M. Tanemura, J. Breitbach, and K. Wandelt, Surf. Sci. **427-428**, 403 (1999).

6 Paper V

Evidence for a Grotthuss-Like Mechanism in the Formation of the Rhamnose Alkoxy Radical Based on Periodic DFT Calculations

E. Pauwels, R. Declerck, V. Van Speybroeck, and M. Waroquier

Radiation Research 169 (1), 8-18 (2008)

RADIATION RESEARCH **169**, 8–18 (2008)
0033-7587/08 $15.00

Evidence for a Grotthuss-Like Mechanism in the Formation of the Rhamnose Alkoxy Radical Based on Periodic DFT Calculations

Ewald Pauwels,[1] Reinout Declerck, Veronique Van Speybroeck and Michel Waroquier

Center for Molecular Modeling, Ghent University, Proeftuinstraat 86, B-9000 Gent, Belgium

Pauwels, E., Declerck, R., Van Speybroeck, V. and Waroquier, M. Evidence for a Grotthuss-Like Mechanism in the Formation of the Rhamnose Alkoxy Radical Based on Periodic DFT Calculations. *Radiat. Res.* 169, 8–18 (2008).

Molecular modeling adopting a periodic approach based on density functional theory (DFT) indicates that a Grotthuss-like mechanism is active in the formation of the radiation-induced alkoxy radical in α-L-rhamnose. Starting from an oxidized crystal structure, a hydroxyl proton is transferred along an infinite hydrogen bond chain pervading the entire crystal. The result of this proton shuttling mechanism is a stable radical species dubbed RHop. Only after several reorientations of crystal waters and hydroxyl groups, the more stable radical form RO4 is obtained, which differs in structure from the former by the absence of only one hydrogen bond. Calculations of the energetics associated with the mechanism as well as simulated spectroscopic properties reveal that different variants of the rhamnose alkoxy radical can be observed depending on the temperature of irradiation and consecutive EPR measurement. Cluster calculations on both radical variants provide hyperfine coupling and *g* tensors that are in good agreement with two independent experimental measurements at different temperatures. © 2008 by Radiation Research Society

INTRODUCTION

The radiation chemistry of solid-state sugars has attracted considerable attention, because these highly structured systems can function as model systems to study radiation damage in biomolecules from a general perspective. The involvement of deoxyribose sugar radicals in radiation-induced single-strand breaks of DNA has added to the interest in this subject (*1, 2*), which only recently led to the unambiguous identification and characterization of such radicals in irradiated nucleotides (*3, 4*). However, the exact processes that lead to the formation of radical end products are not known. In an attempt to clarify the initial radiation-induced events, several electron paramagnetic resonance (EPR) studies have been performed on single-crystal sugars at very low temperatures [e.g. ref. (*5*)]. The lack of thermal energy limits the conversion of primary radiation products in secondary reactions, and this allows thorough EPR characterization of the former. One of the archetypal systems in this respect is α-rhamnose, since both oxidation and reduction products have been observed in this sugar. Reduction results in the ''trapping'' of low-energy electrons at intermolecular sites within the crystal matrix, stabilized through the cumulative effect of dipolar molecules or functional groups in the vicinity (*6–8*). Ionization-induced oxidation of rhamnose leads to the formation of an oxygen-centered alkoxy radical (*9, 10*). Several of the secondary radiation-induced radicals have also been characterized in rhamnose and are generally considered to be decay products of the previous primary species under the influence of temperature or light (*7, 8, 11*).

In an earlier theoretical study, we investigated the primary alkoxy and several secondary rhamnose radicals using density functional theory (DFT) calculations (*12*). Adopting a cluster approach, the radical model under scrutiny was surrounded by several intact rhamnose molecules in accordance with crystallography data, and EPR properties were calculated on the optimal conformation of the model. Comparison of calculated *g* and hyperfine tensors and experimental data resulted in the independent identification and corroboration of the radical structures that were proposed in the various EPR experiments. It also led to the assignment of a completely new radical structure to one of the observed species. For the alkoxy radical, however, an unusual discrepancy was encountered. Calculated EPR properties were found to be in accordance with only one of the two EPR measurements on this radical that are available in literature.

In 1980, Samskog and Lund performed a Q-band ESR measurement at 77 K of the alkoxy radical and determined its *g* tensor along with two hyperfine coupling constants (*9*). Five years later, Budzinski and Box used a combination of both ESR and ENDOR to thoroughly characterize this species at 4.2 K (*10*). They succeeded in deriving the *g* tensor and seven hyperfine tensors. An overview of the measured data is given in Table 1, although several likely errors in the data from the original manuscript were corrected (a detailed discussion is given as Supplementary Information). We will refer to the results of these experiments with the notations Alk_{BB} and Alk_{SL}, respectively. From the table, it can easily be seen that the two data sets are very

[1] Address for correspondence: Center for Molecular Modeling, Ghent University, Proeftuinstraat 86, B-9000 Gent, Belgium; e-mail: ewald.pauwels@UGent.be.

TABLE 1
Summary of EPR Measurements and Previous DFT Calculations on Rhamnose Alkoxy Radical

Signal	A_{iso}/g_{iso}	A_{aniso}/g_{aniso}	Direction cosines vs ⟨a*bc⟩		
Alk_{SL} (77 K)[a]					
SL-1	112.1				
SL-2	39.2				
SL-g	2.0184	2.0032	−0.020	−0.982	0.189
		2.0064	−0.698	0.149	0.700
		2.0456	−0.716	−0.118	−0.688
Alk_{BB} (4.2 K)[b]					
BB-1	−3.0	−7.7	0.127	0.003	0.991
		−7.3	0.990	0.056	−0.127
		15.1	−0.056	0.998	0.003
BB-2	5.2	−12.7	−0.136	0.176	0.975
		−0.2	0.787	0.616	−0.001
		12.9	−0.601	0.767	−0.222
BB-3 (xc)	0.1	−5.9	−0.023	0.221	0.974
		−4.9	0.364	0.909	−0.197
		10.8	0.930	−0.351	0.102
BB-4 (xc)	5.2	−7.8	0.259	−0.079	0.962
		−0.1	0.744	0.651	−0.146
		7.9	−0.615	0.754	0.227
BB-5	67.2	−4.0	0.743	−0.481	−0.464
		−0.2	0.409	−0.220	0.884
		4.3	0.528	0.848	−0.033
BB-6	53.9	−7.7	0.219	0.687	0.691
		−2.0	−0.377	−0.594	0.710
		9.7	0.899	−0.417	0.129
BB-7	3.9	−1.9	0.696	−0.607	0.381
		−0.7	0.584	0.789	0.189
		2.6	−0.416	0.091	0.904
BB-g	2.0096	2.0018	−0.339	−0.691	0.637
		2.0068	−0.554	0.694	0.458
		2.0202	−0.759	−0.198	−0.619
RO4 (cluster DFT)[c]					
H2	40.5				
H4	100.4				
g tensor	2.0189	2.0022	−0.251	−0.885	0.392
		2.0090	−0.690	0.448	0.569
		2.0456	−0.679	−0.128	−0.723

Note. Hyperfine couplings are in MHz.
[a] Reference (*9*).
[b] Reference (*10*).
[c] Reference (*12*).

dissimilar, as already noted by Sagstuen *et al.* (*11*). The Alk_{SL} species is characterized by two isotropic splittings (112 and 39 MHz) that cannot be matched with the two largest couplings (67 and 54 MHz) in Alk_{BB}. Furthermore, the maximum anisotropic component of the *g* tensor differs between the two sets: 2.0456 in Alk_{SL} and 2.0202 in Alk_{BB}. In particular, the latter difference is surprising since the corresponding eigenvectors deviate by only a few degrees. Despite these clear distinctions, an identical structure was assigned in both studies, represented in Fig. 1.

Recent theoretical calculations (*12*) on this suggested structure were found to be in complete accordance with the EPR data of Samskog and Lund: hyperfine couplings of 40 and 100 MHz, and a maximum *g*-tensor component of 2.0456 (see calculated **RO4** data in Table 1). Given the temperature difference between the two EPR measurements, it was assumed that Alk_{BB} represents a precursor to the Alk_{SL} structure and differs from the latter mainly because of the closeness of the dissociated H_{O4} hydroxyl proton in the former (see Fig. 1 for atom numbering scheme). In the Alk_{BB} measurements, a hyperfine coupling tensor was determined for this proton, indicating that it is generally situated in the direction of the original O_4–H_{O4} bond.

In the current work, we present the results of new calculations based on a periodic DFT approach in which the origin of this discrepancy is investigated. Starting from the primary radical cation species, generated directly by radiation, proton transfer reactions are considered within the

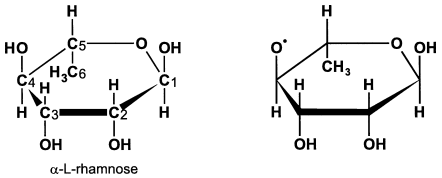

FIG. 1. Atom numbering in α-L-rhamnose and structure of the alkoxy radical. Oxygens and hydrogens are numbered according to the carbon to which they are bound.

solid state. A mechanism is found that likely connects the Alk_{BB} precursor at very low temperature with the Alk_{SL} radical at 77 K. Energetic considerations are corroborated by theoretical EPR calculations on the suggested species, which are in agreement with the experimental EPR data for both the Alk_{SL} and Alk_{BB} species.

COMPUTATIONAL DETAILS

A simulation study of proton transfer reactions between the rhamnose radical and its molecular environment is meaningful only if as little constraint as possible is imposed on the latter. The surrounding molecule(s) in the solid must be able to accommodate the proton that is transferred through atomic relaxation. This requirement seriously limits the use of cluster models in this respect. As adopted in the previous paper (*12*), the smallest rhamnose cluster model that is physically sound already consists of the radical, seven rhamnose molecules, and eight water molecules—those molecules that are involved in hydrogen bonds with the central paramagnetic species. However, only the atoms of the radical were allowed to relax in this model. To enable relaxation of the closest hydrogen-bonded species, it is necessary to expand the cluster with an additional layer: Every hydrogen bond partner of the radical has to be surrounded in a similar fashion by its hydrogen bond partners, all in accordance with the rhamnose crystal symmetry. The resulting supercluster (containing more than 500 atoms) is far too large to be computationally feasible at a reasonable level of theory. The outermost shell of rhamnose/water molecules still has to be constrained because it is at the boundary between the cluster and the vacuum. A more effective and natural way to simulate the radical and its solid-state environment is to perform periodic calculations, thereby exploiting the translational symmetry of the crystalline state. Hence the lattice environment is automatically and fully incorporated, and no constraints are needed on the hydrogen-bonded species.

The unit cell of rhamnose is monoclinic (space group symmetry $P2_1$) and contains two rhamnose and two water molecules. Its cell parameters are a = 7.901 Å, b = 7.922 Å, c = 6.670 Å and β = 95.52° (*13*). To ensure that the radical is well separated from its periodic images, the original unit cell was doubled in all directions. The resulting ⟨2a2b2c⟩ supercell contains 416 atoms. All calculations were performed using the CPMD software package (*14*). The BP86 gradient-corrected density functional (*15, 16*) was used, together with a plane wave basis set (cutoff 25 Ry) and ultrasoft pseudopotentials of the Vanderbilt type to describe the electron-ion interaction (*17*). To corroborate the results obtained with a ⟨2a2b2c⟩ supercell, several simulations were also performed with the ⟨a2bc⟩ and ⟨a3bc⟩ supercells, obtained by respectively doubling and tripling the original unit cell in the *b* direction.

Subsequently, EPR properties were calculated (*18*) on the structures obtained from the periodic ⟨2a2b2c⟩ optimizations. As ascertained in other studies, the environment of a radical has a significant impact on these properties. Hence it is imperative to include this environment also in the EPR calculation, either using a periodic scheme (*19*) or by adopting a cluster approach (*12, 20, 21*). To allow direct comparison with the EPR results in the earlier study of rhamnose (*12*), the latter approach was chosen. After optimization, a cluster was cut out of the periodic system to contain the radical and all the molecules that are hydrogen bound to it (seven rhamnose and eight water molecules). This is the same model space that was used in the previous study, but it was adopted only for the EPR calculation. The benefit of such a hybrid periodic/cluster scheme is that the EPR properties of the radical can be determined consistently with cluster methods, while the structural information obtained from geometry optimization in a periodic approach can still be maintained.

Hyperfine tensors were calculated using the Gaussian03 software suite (*22*), using the B3LYP functional (*23*) and a 6-311G** basis set (*24, 25*) for all atoms within the cluster. However, this level of theory is too expensive from a computational point of view for the calculation of *g* tensors. This difficulty can be overcome either by reducing the model system (taking up fewer molecules in the calculation) or by reducing the level of theory for (part of) the model system. The first approximation was adopted in the previous study (*12*), and only the rhamnose radical itself was considered in the *g*-tensor calculation. Since this is an approach that can essentially provide only gas-phase properties, the second option was preferred in the current work, where intermolecular interactions between radical and environment are at least minimally accounted for in the *g*-tensor calculation. The B3LYP level of theory was maintained for the entire cluster, but now only the atoms of the central radical were described using the 6-311G** basis set, along with those of two nearby water molecules. The other atoms of the cluster were still included in the calculation, but they were considered at the much smaller 3-21G basis set level (*26, 27*). The two water molecules were selected in the high basis set layer, because they are hydrogen bound to oxygen O_4 and effectively make up the immediate environment of the radical center. This mixed basis set scheme offers an affordable way to determine the *g* tensor without neglecting the crucial interactions between the central radical and the molecules in its close environment.

For reference, *g*-tensor properties were also calculated on geometries optimized within a ⟨a2bc⟩ supercell, adopting a consistent periodic approach as described in ref. (*28*). For these calculations, a BLYP functional form (*29, 30*) was used, together with a 100-Ry cutoff plane-wave basis set and Goedecker-type norm-conserving pseudopotentials (*31*). The parameters related to the evaluation of the *g*-tensor contributions in this approach included a threshold value of 0.05 for the magnetic response calculation and an ionic charge potential contribution to the effective potential close to the Coulomb limit [see ref. (*28*) for further information].

RESULTS AND DISCUSSION

Energetic Considerations of Proton Transfer

Following the suggestion in the measurements of Budzinski and Box that the dissociated hydroxyl proton was still in the vicinity of the radical center (O_4), proton transfer from this oxygen was considered. Such a mechanism assumes that the positive charge is (more or less) located on the H_{O4} hydroxyl proton after ionization and that it migrates into the molecular environment, generating the alkoxy species. This migration will follow the path of the original hydrogen bond, which, in the undamaged structure, extends between H_{O4} and the oxygen of a crystal water molecule.

The onset of this reaction is immediately after the ionization event. Hence the system has just been oxidized (an electron has been ejected), leaving the periodic ⟨2a2b2c⟩ supercell positively charged. Within the computational approach, this is compensated by a (nonlocalized) uniform negative charge background to prevent the unphysical sit-

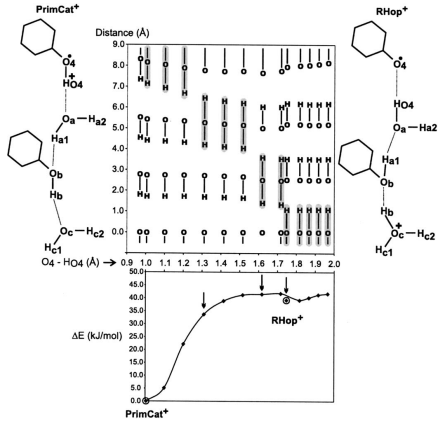

FIG. 2. Overview of energy and structural changes upon elongation of the O_c–H_{O4} bond. ΔE is considered relative to the **PrimCat**$^+$ binding energy (−2222.707 atomic units). Optimized points corresponding to the **PrimCat**$^+$ and **RHop**$^+$ structures are indicated by a circle. Arrows point out proton transfers. For O_c, H_{O4}, O_a, H_{a1}, O_b and H_b, absolute distances are plotted with respect to O_c. The gray highlighted regions indicate the main location of the positive charge.

uation in which the periodic system would get an infinite charge. Starting from the ideal crystal structure, the ionized supercell is optimized without geometric constraints. A symmetrical structure is obtained with the unpaired electron density distributed evenly over (mainly) C_4 and O_4 of all the molecules in the unit cell. The absolute binding energy for the entire cell containing this primary cation structure (labeled **PrimCat**$^+$) is −2222.707 atomic units. Subsequently, the H_{O4}–O_4 bond of one molecule is increased systematically and the system is reoptimized at each point under that constraint. This results in the energy profile presented in the lower half of Fig. 2. The energy difference (in kJ/mol) is considered relative to **PrimCat**$^+$, corresponding to an H_{O4}–O_4 bond distance of about 1.0 Å. The energy of the rhamnose system increases steadily with increasing bond distance until a shallow, local minimum is encountered around 1.85 Å. Along this path, three proton transfers throughout the periodic structure have taken place (at each time indicated by an arrow), although constraints were imposed on only one of the protons. This is illustrated in the top of Fig. 2, where the distances of all atoms involved with respect to O_c are plotted as a function of the constrained H_{O4}–O_4 distance. Gray highlighted regions indicate the main location of the positive charge.

The distances in the undamaged crystal are given for reference at an H_{O4}–O_4 bond length of 0.968 Å. This pattern is not altered much when the entire supercell is ionized. One could visualize the **PrimCat**$^+$ as represented at the left of the plot: Charge and spin density are both still located on the same rhamnose molecule. When the O_4–H_{O4} distance is increased to about 1.3 Å, a first proton transfer occurs. The spin density now becomes firmly localized on O_4, whereas the H_{O4} proton (and hence the charge) is transferred along the hydrogen bond to one of the crystal waters (labeled ''a''). As a result, the alkoxy radical is formed, connected to this $H_3O_a^+$ species with a hydrogen bond. However, this does not correspond to a minimum on the potential energy surface. Only when the O_4–H_{O4} distance is further elongated, thus increasing the distance between the water molecule and the alkoxy radical, is a second minimum eventually found. Between 1.5 and 1.85 Å, two further proton transfers occur. First, the H_{a1} proton of $H_3O_a^+$ is transferred to oxygen O_4 (labeled O_b in the plot) of a rhamnose molecule further away, briefly generating an $R–O_bH_2^+$ cation. Finally, the original H_{O4} proton of this rhamnose (labeled H_b) is in turn transferred to crystal water (O_c), again resulting in an $H_3O_c^+$ species. The stability of the final species resulting from the three proton transfers was verified by reoptimization without constraints (indicated by a circle). This structure, with absolute energy of −2222.692 atomic units, is depicted on the right side of Fig. 2 (referred to as **RHop**$^+$) and has an H_{O4}–O_4 distance of 1.748 Å. In contrast with the **PrimCat**$^+$, the charge is now separated from the main site of the unpaired spin density by almost 8 Å, incidentally comparable to half the length of the ⟨2a2b2c⟩ supercell along the crystallographic *b* axis.

The consecutive proton transfers bear a striking resemblance to the classical Grotthuss mechanism in solutions (*32–35*), where sequential proton ''hops'' between an initial donor and ultimate acceptor are mediated by water molecules or ionizable functional groups, extending along an extensive network. In the case of rhamnose, the three proton hops to go from **PrimCat**$^+$ to **RHop**$^+$ occur along a so-called infinite hydrogen bond chain or ribbon. As illustrated in Fig. 3, this chain extends throughout the crystal along the direction of the *b* axis, alternately connecting the O_4–H_{O4} hydroxyl groups of rhamnose molecules with crystal waters. Hence it is a suitable route for the proton to diffuse through the crystal matrix after ionization at a certain site. Similar proton transfers, or ''multi-proton shuffles'', have been proposed in crystals of nucleic acids, such as cytosine (*36*), adenosine (*37*) or cocrystals of methylcytosine and fluorouracil (*38*).

Attempts were made to initiate further proton jumps along the chain in rhamnose by systematically extending the H_{c1}–O_c bond in **RHop**$^+$. This resulted in a steep uphill potential, indicating that, within this model space, only a structure characterized by three proton jumps constitutes a (local) minimum along this relaxation route. However, the distance between the charged and the spin sites in **RHop**$^+$ (also shown in Fig. 3) is connected to the size of the simulation cell. The ⟨2a2b2c⟩ supercell is 2**b* wide (15.844 Å) in the direction of the *b* axis, implying that the charged site is (roughly) in the middle between the spin site (at a distance $+b$) and its periodic image (at a distance $-b$). This

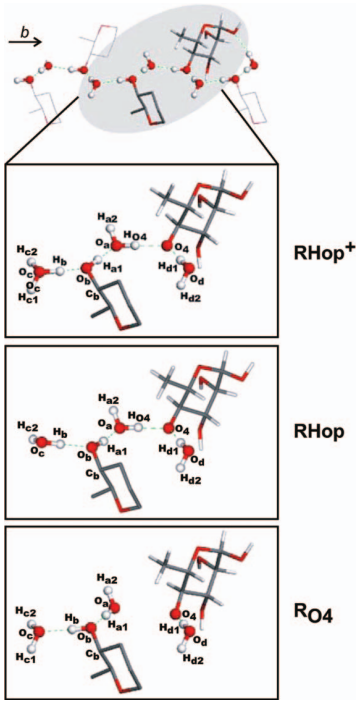

FIG. 3. View of the **RHop**$^+$, **RHop** and **RO4** species along the infinite hydrogen bond chain (*b* axis). A fragment of the intact crystal structure is shown at the top. All H and O atoms that are involved in the hydrogen bond chain are presented as balls.

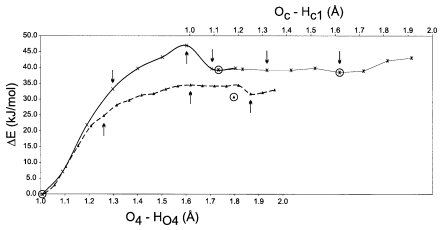

FIG. 4. Energy change upon elongation of the O_4–H_{O4} bond in the ⟨a2bc⟩ (▲) and ⟨a3bc⟩ (×) model space and upon further elongation of the O_c–H_{c1} bond in ⟨a3bc⟩ (*). The energy of the **PrimCat**$^+$ species is taken as reference (respectively −555.686 and −833.520 atomic units). Optimized points are indicated by circles, arrows point out proton transfers.

seems to suggest that the proton is "trapped" between the two spin sites in this model space and that additional proton hops would become possible if the supercell would be further enlarged along *b*.

Additional calculations on ⟨a2bc⟩ and ⟨a3bc⟩ supercells confirm this statement. In Fig. 4, the energy change upon H_{O4}–O_4 elongation in these supercells is plotted, resulting in energy profiles similar to that in Fig. 2. Here also, a minimum is encountered at 1.8 Å for ⟨a2bc⟩ and 1.75 Å for ⟨a3bc⟩, the latter perfectly comparable to the H_{O4}–O_4 distance for **RHop**$^+$ in the ⟨2a2b2c⟩ supercell. Three proton hops occur in the smallest model space (⟨a2bc⟩), yielding a 7.0 Å separation between the charged site (O_c) and the spin site (O_4). However, in the ⟨a3bc⟩ supercell, two further proton jumps along the infinite hydrogen bond chain are energetically favorable when additionally elongating the O_c–H_{c1} bond! Starting from a **PrimCat**$^+$ species, all together, five proton transfers take place in this model space before the charge is finally located on an H_3O^+ species, 10.6 Å away from the O_4 radical center. Since the ⟨a3bc⟩ supercell is 23.766 Å wide along *b*, the charged site is again nicely situated between the spin site (at +3/2 *b*) and its periodic image (at −3/2 *b*). Extrapolating these results, it is clear that the separation between the charge and the unpaired spin density is proportional to the length of the simulation cell along the *b* axis. In reality, of course, an irradiated crystal will not display the perfect supercell periodicity as in the simulations. The ionization sites will be distributed randomly throughout the matrix at relatively long distances from each other. For each such ionization site, the infinite hydrogen bond chain effectively represents something like a conductor channel, along which charge can migrate throughout the crystal matrix.

However, proton migration requires that the initial large energy barrier of about 40 kJ/mol has been crossed. This is not unlikely given that high-energy radiation is applied in these studies [γ rays in ref. (*9*), X rays in ref. (*10*)], often for several minutes. Also, tunneling or excited-state dynamics is likely to be involved in the proton transfer process. Furthermore, it is plausible that the migrating charge will become trapped at some point along the infinite hydrogen bond chain, for instance, when a radiation-induced anion is encountered further on in the crystal matrix. In a study of crystalline nucleic acids (*36*), it is even suggested that the mutual occurrence of both reduction and oxidation products is likely to be observed along this chain. Since the proton can readily move along the channel, it will transfer from the cation site to the anion site, hence irreversibly canceling out the charges and leaving behind two neutral radicals. In rhamnose, such neutralization would effectively prevent back-reaction and recombination with the alkoxy species, driving the system in the direction of **RHop**$^+$ formation. In fact, the mere occurrence (or observation) of a **PrimCat**$^+$ species seems highly unlikely, since it would require that oxidation of the rhamnose crystal would lead to a perfect

TABLE 2
Overview of Calculated *g* and Hyperfine Tensors for the RHop Alkoxy Species, Optimized in a ⟨2a2b2c⟩ Supercell Periodic Approach

	A_{iso}/g_{iso}	A_{aniso}/g_{aniso}	Direction cosines vs ⟨a*bc⟩			Ψ	A_{iso}/g_{iso}	A_{aniso}/g_{aniso}	
H2	61.6	−3.8	0.736	−0.481	−0.476	1	67.2	−4.0	BB−5
		−0.7	0.608	0.160	0.778	26		−0.2	
		4.5	0.297	0.862	−0.410	26		4.3	
H3	1.6	−10.0	−0.117	0.199	0.973	2	5.2	−12.7	BB−2
		−0.8	0.856	0.517	−0.003	7		−0.2	
		10.8	−0.504	0.833	−0.231	7		12.9	
H4	40.7	−5.7	0.219	0.716	0.663	2	53.9	−7.7	BB−6
		−3.9	−0.413	−0.548	0.728	3		−2.0	
		9.6	0.884	−0.433	0.175	3		9.7	
H6a	2.5	−1.9	0.711	−0.625	0.323	4	3.9	−1.9	BB−7
		−0.7	0.634	0.768	0.092	6		−0.7	
		2.5	−0.306	0.139	0.942	7		2.6	
HO3	−5.7	−7.7	−0.546	0.788	0.284	5	−5.2	−7.9	BB−4 (xc)
		−0.5	0.762	0.609	−0.223	5		0.1	
		8.2	0.348	−0.095	0.933	5		7.8	
HO4	−6.6	−11.4	0.608	0.010	0.794	30	−3.0	−7.7	BB−1 (xc)
		−10.3	0.778	0.187	−0.599	31		−7.3	
		21.8	−0.155	0.982	0.106	8		15.1	
Hd1	−0.1	−7.8	0.208	0.575	0.791	27	0.1	−5.9	BB−3 (xc)
		−6.2	0.349	0.712	−0.609	26		−4.9	
		14.0	0.914	−0.403	0.052	4		10.8	
g	2.0112	2.0030	−0.314	−0.704	0.637	2	2.0096	2.0018	BB−g
		2.0087	−0.569	0.676	0.468	1		2.0068	
		2.0220	−0.760	−0.215	−0.613	1		2.0202	
						35	2.0184	2.0032	SL−g
						34		2.0064	
						7		2.0456	

Note. Hyperfine couplings are in MHz, Ψ angle deviations with experiment in degrees.

distribution of the remaining unpaired electron over all molecules. However, multiple ionization and excitation events will be induced by radiation, giving rise to a disorganized and asymmetrical distribution of the spin density.

Of course, when the ejected proton has migrated along the hydrogen bond chain and has possibly recombined at some point with an anionic species, the positive charge is well separated from the alkoxy radical. The (local) geometry of the radical and its direct environment will no longer be influenced by the presence of a positive charge, nor will its EPR properties. To account for this possibility in the simulations, the ⟨2a2b2c⟩ rhamnose supercell was reoptimized after the removal of either the H_{c1} or H_{c2} protons from the **RHop**$^+$ species (see Fig. 3), effectively making the supercell neutral in the calculation. In both cases, this resulted in a significant displacement of the hydrogens and oxygens involved in the infinite hydrogen bond chain, though largely restricted to the locus of the removed proton. The geometry of the alkoxy radical was virtually unaltered. Removal of the H_{c1} proton (absolute energy −2222.004 atomic units) proved to be slightly favored over H_{c2} elimination (−2222.003 atomic units), which makes sense since the latter would disrupt the infinite hydrogen bond chain. With respect to **RHop**$^+$, the energy of the species obtained by removing H_{c1} (dubbed **RHop**) formally increases by more than 0.68 arbitrary units. However, this energy increase does not really constitute a barrier, under the assumption that the proton is not removed altogether from the system but rather migrates at a sufficiently long distance from the alkoxy species. The structure of the **RHop** species is also shown in Fig. 3.

EPR Properties of RHop

The calculated EPR spectroscopy properties of the **RHop** radical are presented in Table 2. Both the hyperfine and *g*-tensor data are separated into an isotropic (A_{iso} or g_{iso}) and an anisotropic part. Diagonalization of the latter matrix produces anisotropic couplings (or principal values A_{aniso}/g_{aniso}) and corresponding eigenvectors (or principal directions), expressed as direction cosines with respect to the orthogonal ⟨*a*bc*⟩ crystal axis reference frame. The Ψ angle (in degrees) reflects the deviation in orientation between the calculated eigenvectors and their experimental counterparts.

Overall, the close match with the Alk_{BB} measurements is remarkable. The calculations predict two main proton hyperfine couplings for this radical (61.6 and 40.7 MHz) that are significantly closer to the Alk_{BB} than to the Alk_{SL} results. What is more, the *g* tensor is in perfect agreement with the measurement of Budzinski and Box: *g*-tensor components agree closely, and the calculated eigenvectors deviate by less than 2° from the measured eigenvectors! The

assignment is further corroborated by several smaller hyperfine coupling tensors, many of which were detected in the EPR experiment. Since the isotropic coupling for these proton tensors is close to zero, their anisotropy is perhaps the most characteristic feature. Based on the correspondence between the calculated EPR properties for the **RHop** model and the Alk_{BB} data, several incorrect assignments were identified in the latter. In the following, this comparison is discussed briefly for each proton hyperfine tensor.

H_2. The calculated isotropic coupling for this proton is very close to the measured value of 67.2 MHz for the BB-5 signal. Interestingly, Budzinski and Box attributed this signal to a δ coupling: from one of the methyl protons on C_6. In the **RHop** model, the unpaired electron density on O_4 interacts with an equally distant proton on the other side of the pyranose sugar ring (H_2).

H_3. As Budzinski and Box mentioned with respect to their BB-2 signal, this tensor indeed "has the characteristics of a strongly coupled γ proton." However, this signal does not correspond to H_5 as was suggested but rather to the other γ coupling, H_3. The agreement between the measured data and the calculations is very good for isotropic and anisotropic couplings as well as for the eigenvectors.

H_4. The calculated tensor for this proton is attributed to the BB-6 signal, despite the 13 MHz difference in isotropic coupling. However, as has been demonstrated on many occasions (*18, 39*), the isotropic coupling is rather sensitive to the level of theory. Thus the reported difference is not uncommon. The anisotropic couplings and eigenvectors, on the other hand, agree very well between theory and experiment.

H_{6a}. The BB-7 signal, originally attributed to the H_3 γ coupling, is found to be in excellent agreement with the calculated EPR hyperfine tensor of H_{6a}, one of the methyl group protons. The level of agreement for this remote δ proton is of rare quality, with almost perfectly reproduced isotropic and anisotropic couplings and Ψ deviations well below 10°.

H_{O3}. Among the Alk_{BB} hyperfine tensors, three of them were found to be exchangeable upon deuteration (BB-1, BB-3 and BB-4). The calculations corroborate the assignment of BB-4 to the H_{O3} hydroxyl proton. In Table 2, comparison is made with the measured tensor with negative isotropic hyperfine coupling, reversing the order of the anisotropic couplings. Absolute determination of the sign of a hyperfine constant is difficult from the experimental point of view, justifying the modification.

H_{O4}. Again, the calculated tensor for this proton affirms the experimental assignment to the dissociated H_{O4} proton, 1.681 Å from the O_4 center in model **RHop**. Calculated hyperfine couplings are in excellent agreement with their experimental counterparts, but a Ψ correspondence lower than 10° is obtained only for the eigenvector with maximum principal component. This effect has been encountered in other studies (*19, 20*) and indicates the quasi-degeneracy for both minor anisotropic interactions, as conveyed by the mutual occurrence of virtually identical but rather large angles for these interactions.

H_{d1}. The last of the exchangeable couplings (BB-3) can be attributed to H_{d1}, which is one of the protons in the crystal water on the other side of the dissociated H_{O4}. The position and orientation of this water molecule are most easily seen in Fig. 3. Comparison between theory and experiment is similar to the case for H_{O4} and overall is very good.

Despite the few incorrect assignments, the accuracy and detail of the original Alk_{BB} EPR measurements are stunning. Furthermore, their accordance with the calculated spectroscopy data, which is both qualitative and quantitative in nature, leaves little doubt that the proposed **RHop** model is valid. Hence, in their 4.2 K measurement on irradiated rhamnose crystals, Budzinski and Box have effectively observed an alkoxy radical precursor obtained by proton transfer along an infinite hydrogen bond chain.

Energetic Considerations of Rearrangement

After consecutive proton hops, a Grotthuss mechanism would also involve a rearrangement of the water molecules to restore the hydrogen bonding network in its initial state. Hence it is sometimes referred to as a "hop-and-turn" process because the water molecules have to reorient. This field has been studied exhaustively [for a review, see ref. (*40*)], spurred by its importance in, for example, conducting proteins like gramicidin [e.g. ref. (*41*)]. In rhamnose single crystals, such a reorientation step can provide the link between the individual observations of apparently different types of alkoxy radicals at different temperatures.

In an earlier theoretical study (*12*), a structure was determined for the alkoxy radical as measured by Samskog and Lund. This **RO4** radical is obtained by removing the H_{O4} hydrogen from the model space. To allow comparison with the results in the current work, the geometry for this radical was reoptimized within a ⟨2a2b2c⟩ supercell approach. The resulting geometry (partially shown in Fig. 3) has an absolute energy of −2222.016 atomic units, which is some 30 kJ/mol lower than that of **RHop**! When the structure of the molecules in the vicinity of the **RHop** and **RO4** radicals is compared (shown in Fig. 3), it is apparent that the main difference lies in the orientation of hydroxyl groups and water molecules. Similar to the Grotthuss mechanism, three rearrangements would suffice to transform **RHop** into **RO4**:

1. rotation of H_b about the O_c–H_{c2} bond over 94° (clockwise),
2. rotation of H_{a1} about the O_b–C_b bond over 134° (counter clockwise), and
3. rotation of H_{O4} about the O_a–H_{a2} bond over 104° (counter clockwise).

In Fig. 5, the energy of the ⟨2a2b2c⟩ system (relative to that of **RHop**) is plotted as a function of these three rotation angles. The encircled points on the graph indicate fully optimized structures; all other points were obtained from constrained geometry optimizations. Apart from the constraint

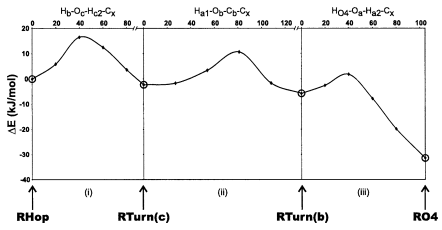

FIG. 5. Energy change upon sequential hydrogen bond rearrangement, relative to **RHop** (−2222.004 atomic units). All dihedral angles (in degrees) are referred to distant carbon atoms C_x further on in the crystal lattice. Circles indicate points that were obtained by full optimization (without constraints).

on the rotation angle, the Cartesian coordinates of the O_c and O_a oxygen atoms were also restrained in space for (1) and (3). The latter restrictions were imposed to prevent translation of the water molecules within the crystal matrix as much as possible. For clarity, only the change in the dihedral angles is reported, relative to its value in the optimized geometry from which the rotation was initiated.

The figure shows that two stable, local minima are encountered when consecutively rearranging the hydroxyl groups in the order (1)-(2)-(3). The structures **RTurn(c)** and **RTurn(b)** were obtained through unrestricted geometry optimizations and are slightly more stable than the **RHop** radical. When H_{O4} finally is rotated about the O_a–H_{a2} bond, the energy has dropped by 30 kJ/mol, indicating that **RO4** is significantly more stable than **RHop**. The energy barriers that have to be crossed are not exceedingly large, although they still amount to 10–15 kJ/mol. Even though this is inevitably a slight overestimation of the true barrier, because of the imposed constraints, the mere presence of these barriers is enough to prevent the transformation of **RHop** into **RO4** at temperatures as low as 4.2 K. Hence the rearrangement barriers allow the separate isolation and identification of an **RHop** species in the measurements of Budzinski and Box. At a temperature of 77 K, the system might just have acquired enough thermal energy to attain the more stable **RO4** species, as measured by Samskog and Lund. Thus it appears that in the radiation-induced alkoxy radical formation in rhamnose, hydrogen bond rearrangement is the slowest step. Comparable conclusions have been reached in computational studies of proton conduction in the ''water wire'' of the gramicidin protein (*42*). Although the hydroxyl group rearrangements were conducted consecutively in the order (1)-(2)-(3), it is doubtful that this exact sequence is followed in a real irradiated rhamnose crystal. First, many more than three proton hops will occur in rhamnose crystals, as argued above, which necessitates the rearrangement of multiple hydroxyl groups to attain the **RO4** species. Second, it is not clear whether these rearrangements occur consecutively or rather simultaneously.

EPR Properties of RO4

Using the ⟨2a2b2c⟩ supercell optimized **RO4** geometry, the EPR properties for this radical were calculated in accordance with the computational protocol adopted in the current work (Table 3a). To enable comparison with the EPR results for the **RHop** species, all proton tensors have been reported except for H_{O4}, which is not present in this system. It is immediately clear that the current results deviate to a larger extent from experiment than the results of previous calculations (as reported in Table 1). Most dramatically, the maximum anisotropic *g*-tensor component has dropped from an excellent 2.0456 to 2.0263. Based solely on this parameter, the **RO4** radical would be in better agreement with the measurement of Budzinski and Box than with that of Samskog and Lund. However, the H_2 and H_4 isotropic hyperfine couplings are still in significantly better agreement with the latter experimental data, even though the quantitative accordance is somewhat less. These discrepancies between current and previous calculations have two origins:

1. The geometries for which the EPR properties were calculated are not identical, because they were obtained with different methodologies. In ref. (*12*), a cluster approach was adopted under the constraint that the molecular environment of the radical remained identical to the crystal structure. In the current work, none of these constraints apply.
2. As mentioned in above, the *g* tensor in the previous work was calculated on the basis of a single molecule approach, i.e., without any of the neighboring molecules present in the model space (not even the water molecules). This is in sharp contrast to the current computational protocol, in which the environment is taken into account for the *g*-tensor calculation.

To quantify the effect of the latter, the current computational procedure for *g*-tensor calculation was applied on the cluster-optimized geometry from the previous work (Table 3b). Compared to the original calculated data for **RO4** in Table 1, the maximum anisotropic *g*-tensor component is already significantly smaller (2.0303)! As regards the first factor, the **RO4** cluster geometry from the previous work and the present geometry are very similar, with a root mean square deviation of only 0.19 Å. Yet even such slight conformational changes seem to have a significant impact on the *g* tensor, as is exemplified in Table 3b. The maximum anisotropy changes from 2.0263 to 2.0303, which is indisputably related to the small difference in both geometries since the same computational protocol was used for both calculations.

To further distinguish the *g* tensors between **RHop** and **RO4**, additional calculations were performed using a periodic formalism as described in ref. (*28*). Since the

TABLE 3
Calculated *g* and Hyperfine Tensors for the RO4 Alkoxy Species Calculated on the Radical Geometry as Optimized in a ⟨2a2b2c⟩ Supercell Periodic Approach and on the Radical Geometry as Obtained from Previous Work (*12*)

	A_{iso}/g_{iso}	A_{aniso}/g_{aniso}	Direction cosines vs ⟨a*bc⟩			Ψ	A_{iso}/g_{iso}	A_{aniso}/g_{aniso}	
a. on radical geometry from ⟨2a2b2c⟩ periodic optimization									
H2	50.4	−3.5	0.692	−0.528	−0.492		39.2		SL−2
		−0.3	0.579	−0.001	0.815				
		3.8	0.431	0.849	−0.305				
H3	−1.7	−10.3	−0.160	0.150	0.976				
		−0.3	0.943	0.316	0.106				
		10.6	−0.293	0.937	−0.192				
H4	87.1	−5.9	0.443	0.881	0.163		112.1		SL−1
		−4.6	−0.209	−0.075	0.975				
		10.5	0.872	−0.466	0.151				
H6a	1.1	−1.5	0.705	−0.672	0.226				
		−0.8	0.654	0.740	0.156				
		2.4	−0.272	0.038	0.961				
HO3	−4.0	−6.6	−0.460	0.865	0.202				
		0.9	0.881	0.474	−0.024				
		5.7	0.116	−0.167	0.979				
Hdl	−0.3	−11.1	0.175	0.385	0.906				
		−8.0	0.278	0.864	−0.420				
		19.1	0.944	−0.325	−0.045				
g	2.0125	2.0023	−0.316	−0.839	0.443	14	2.0096	2.0018	BB−g
		2.0087	−0.547	0.542	0.637	13		2.0068	
		2.0263	−0.775	−0.041	−0.631	9		2.0202	
						24	2.0184	2.0032	SL−g
						25		2.0064	
						6		2.0456	
b. on radical geometry from cluster optimization									
g cluster	2.0138	2.0023	−0.294	−0.870	0.396	17	2.0096	2.0018	BB−g
		2.0087	−0.626	0.488	0.608	15		2.0068	
		2.0303	−0.722	−0.069	−0.688	9		2.0202	
						21	2.0184	2.0032	SL−g
						21		2.0064	
						3		2.0456	

Note. Hyperfine couplings are in MHz, Ψ angle deviations with experiment in degrees.

⟨2a2b2c⟩ supercell approach proved too demanding computationally for this scheme, analogous **RHop** and **RO4** optimized geometries were taken from the ⟨a2bc⟩ supercell calculations. The results are presented in Table 4. Concentrating on the variation in the maximum anisotropic *g*-tensor component, the periodic approach yields results that are consistent with the mixed basis approach of Tables 2 and 3. Both computational approaches rigorously take into account the molecular environment of the radical and succeed in qualitatively reproducing the dissimilarity between the experimental Alk_{SL} and Alk_{BB} *g* tensors. The origin of the residual difference with respect to experiment is unclear and calls for further investigation.

Comparison of the RHop and RO4 Alkoxy Radicals

Probably the most striking feature in both the **RHop** and **RO4** variations of the rhamnose alkoxy radical is the occurrence of the large H_2 δ couplings. Although this proton is located about 4.56 Å, respectively 4.49 Å from the radical center, the unpaired electron density at this site is still sufficiently large to result in couplings of 61.6 or 50.4 Mhz. δ couplings of this magnitude are quite rare, and their occurrence in rhamnose can be understood by considering the unpaired spin density plots in Fig. 6a. Contrary to what would be expected *a priori*, the unpaired electron density is not just simply localized on oxygen O_4, but rather it is notably delocalized over several nuclei in the radical. The plots further exemplify that considerable spin density is present in between C_4 and C_3 in both **RHop** and **RO4**. This is indicative of resonance states that contribute to the calculated density, as illustrated in Fig. 6b. The resonance structure on the left represents the classical view of the alkoxy radical, with the unpaired electron localized mainly on oxygen O_4. In the second resonance conformer, the spin density is concentrated on C_3, O_4 is involved in a double bond with C_4, and the C_3–C_4 bond has been broken. The contribution of this resonance structure is attested by a reduced O_4–C_4 bond length (1.34 Å in both **RHop** and **RO4** compared to 1.42 Å in undamaged rhamnose) and an increased C_3–C_4 bond length (1.67/1.65 Å in **RHop/RO4**

TABLE 4
Results of *g*-Tensor Calculations Adopting a Consistent Periodic Approach as Described in Ref. (*28*)

	g_{iso}	g_{aniso}	Direction cosines vs ⟨a*bc⟩			Ψ(BB)	Ψ(SL)
RHop	2.0128	2.0048	−0.196	−0.810	0.553	12	25
		2.0110	−0.623	0.538	0.568	12	24
		2.0226	−0.758	−0.233	−0.610	2	8
RO4	2.0128	2.0027	−0.269	−0.915	0.302	24	16
		2.0106	−0.569	0.404	0.716	22	16
		2.0252	−0.777	0.021	−0.629	13	9

Note. Calculations were performed on **RHop** and **RO4** geometries optimized within an ⟨a2bc⟩ supercell.

compared to 1.52 Å in undamaged rhamnose). In the second resonance state, H_2 is no longer in a δ position with respect to the unpaired electron but instead has become a β coupling, which accounts for the size of its hyperfine splitting. A similar resonance mechanism was already suggested by Budzinski and Box, albeit not in rhamnose (*43*).

The differences between **RHop** and **RO4** can be understood in terms of this resonance. Due to the extra hydrogen bond in the former radical between O_4 and crystal water H_2O_a, the delocalization mechanism is extended to include this water, indicated by a non-zero spin density on it (Fig. 6a). Conversely, the larger *g*-tensor anisotropy in radical **RO4** is due to reduced delocalization (spin concentration) since it no longer disposes of this hydrogen bond with the crystal water. Since both variations of the alkoxy radical have similar structures, it is clear that they differ mainly in electronic configuration. Hence it is the molecular environment that discriminates the two variants and causes the marked differences in *g* and hyperfine tensors.

CONCLUSIONS

A Grotthuss-like mechanism is shown to be active in the radiation-induced formation of rhamnose alkoxy radicals.

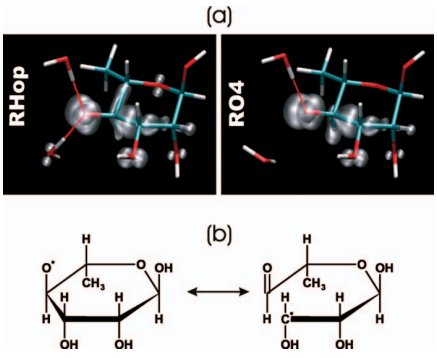

FIG. 6. Panel a: Unpaired spin density in the **RHop** and **RO4** radical species (at an iso value of 0.005). Panel b: Resonance structures contributing to spin density in C_3–C_4 bond give rise to large δ couplings.

Starting from an adiabatically oxidized crystal structure, hydroxyl proton H_{O4} is transferred along an infinite hydrogen bond chain in the crystallographic ⟨b⟩ direction, likely toward a reduction site further on where the proton recombines. The resulting **RHop** radical species can then transform in a more stable radical form, dubbed **RO4**, through a number of (slow) water and hydroxy-group reorientations. Although only low barriers (∼15 kJ/mol) separate the two structures, it is put forward that they are sufficient for the former species to be isolated and observed at very low temperatures. Calculation of EPR properties and comparison with experimental data in the literature shows that the **RHop** radical is in very good agreement with the species observed by Budzinski and Box in EPR experiments at 4.2 K. Similar measurements at 77 K by Samskog and Lund reveal spectroscopic properties that are consistent with the calculated EPR parameters of the **RO4** species.

Hence calculations of the energetics associated with the mechanism as well as simulated spectroscopic properties support the assumption that different variants of the rhamnose alkoxy radical can be observed depending on the temperature of irradiation and consecutive EPR measurement. Both species differ only in their local molecular environment, where **RHop** is involved in an extra hydrogen bond interaction with crystal water compared to the more stable **RO4**. Due to the absence of this additional interaction, the spin density is more concentrated in the latter species, giving rise to typical variations in EPR properties, such as the maximum anisotropic *g*-tensor component (2.0456 compared to 2.0202) or the isotropic hyperfine couplings. The existence of rather large δ-type hyperfine couplings in both species was traced back to resonance contribution of a radical structure in which the pyranose sugar ring was broken. As a result, the unpaired spin density is delocalized over a large part of the rhamnose radical.

ACKNOWLEDGMENTS

This work is supported by the Fund for Scientific Research – Flanders (FWO) and the Research Board of the Ghent University.

Received: March 22, 2007; accepted: September 4, 2007

REFERENCES

1. D. M. Close, Where are the sugar radicals in irradiated DNA? *Radiat. Res.* **147**, 663–673 (1997).

2. L. I. Shukla, R. Pazdro, D. Becker and M. D. Sevilla, Sugar radicals in DNA: Isolation of neutral radicals in gamma-irradiated DNA by hole and electron scavenging. *Radiat. Res.* **163**, 591–602 (2005).
3. A. Adhikary, A. Y. S. Malkhasian, S. Collins, J. Koppen, D. Becker and M. D. Sevilla, UVA-visible photo-excitation of guanine radical cations produces sugar radicals in DNA and model structures. *Nucleic Acids Res.* **33**, 5553–5564 (2005).
4. A. Adhikary, D. Becker, S. Collins, J. Koppen and M. D. Sevilla, C5′- and C3′-sugar radicals produced via photo-excitation of one-electron oxidized adenine in 2′-deoxyadenonsine and its derivatives. *Nucleic Acids Res.* **34**, 1501–1511 (2006).
5. E. E. Budzinski, W. R. Potter and H. C. Box, Radiation effects in X-irradiated hydroxy compounds. *J. Chem. Phys.* **72**, 972–975 (1980).
6. H. C. Box, E. E. Budzinski and H. G. Freund, Studies of electrons trapped in X-irradiated rhamnose crystals. *Radiat. Res.* **121**, 262–266 (1990).
7. P. O. Samskog, A. Lund, G. Nilsson and M. C. R. Symons, Primary reactions of localized electrons in rhamnose crystals studied by pulse-radiolysis and ESR spectroscopy. *J. Chem. Phys.* **73**, 4862–4866 (1980).
8. P. O. Samskog, L. D. Kispert and A. Lund, Geometric model of trapped electrons in X-ray-irradiated single-crystals of rhamnose. *J. Chem. Phys.* **79**, 635–638 (1983).
9. P. O. Samskog and A. Lund, The alkoxy radical RCHO formed in irradiated single crystals of rhamnose. *Chem. Phys. Lett.* **75**, 525–527 (1980).
10. E. E. Budzinski and H. C. Box, Alkoxy radicals—delta-proton hyperfine couplings. *J. Chem. Phys.* **82**, 3487–3490 (1985).
11. E. Sagstuen, M. Lindgren and A. Lund, Electron trapping and reactions in rhamnose by ESR and ENDOR. *Radiat. Res.* **128**, 235–242 (1991).
12. E. Pauwels, V. Van Speybroeck and M. Waroquier, Study of rhamnose radicals in the solid state adopting a density functional theory cluster approach. *J. Phys. Chem. A* **110**, 6504–6513 (2006).
13. S. Takagi and G. A. Jeffrey, Neutron-diffraction refinement of crystal structure of alpha-l-rhamnose monohydrate. *Acta Cryst. B* **34**, 2551–2555 (1978).
14. CPMD V3.11. ©IBM Corp. 1996–2006, ©MPI für Festkörperforschung Stuttgart 1997–2001.
15. J. P. Perdew, Density-functional approximation for the correlation energy of the inhomogeneous electron gas. *Phys. Rev. B* **33**, 8822–8824 (1986).
16. A. D. Becke, Density-functional thermochemistry 1: the effect of the exchange-only gradient correction. *J. Chem. Phys.* **96**, 2155–2160 (1992).
17. D. Vanderbilt, Soft self-consistent pseudopotentials in a generalized eigenvalue formalism. *Phys. Rev. B* **41**, 7892–7895 (1990).
18. M. Kaupp, M. Bühl and V. G. Malkin, *Calculation of NMR and EPR Parameters: Theory and Applications.* Wiley-VCH, Weinheim, 2004.
19. R. Declerck, E. Pauwels, V. Van Speybroeck and M. Waroquier, First-principles calculations of hyperfine parameters with the Gaussian and augmented-plane-wave method: Application to radicals embedded in a crystalline environment. *Phys. Rev. B* **74**, 245103 (2006).
20. E. Pauwels, V. Van Speybroeck and M. Waroquier, Evaluation of different model space approaches based on DFT to examine the EPR parameters of a radiation-induced radical in solid-state alpha glycine. *J. Phys. Chem. A* **108**, 11321–11332 (2004).
21. E. Pauwels, V. Van Speybroeck and M. Waroquier, Radiation-induced radicals in alpha-D-glucose: Comparing DFT cluster calculations with magnetic resonance experiments. *Spectrochim. Acta A* **63**, 795–801 (2006).
22. M. J. Frisch, G. W. Trucks, H. B. Schlegel, G. E. Scuseria, M. A. Robb, J. R. Cheeseman, J. A. Montgomery, Jr., T. Vreven, K. N. Kudin and J. A. Pople, Gaussian 03, Revision B.03. Gaussian, Inc., Wallingford, CT, 2004.
23. A. D. Becke, Density-functional thermochemistry 4: a new dynamical correlation functional and implications for exact-exchange mixing. *J. Chem. Phys.* **104**, 1040–1046 (1996).
24. R. Krishnan, J. S. Binkley, R. Seeger and J. A. Pople, Self-consistent molecular-orbital methods 20: basis set for correlated wave-functions. *J. Chem. Phys.* **72**, 650–654 (1980).
25. A. D. McLean and G. S. Chandler, Contracted Gaussian-basis sets for molecular calculations 1: 2nd row atoms, z = 11–18. *J. Chem. Phys.* **72**, 5639–5648 (1980).
26. J. S. Binkley, J. A. Pople and W. J. Hehre, Self-consistent molecular-orbital methods 21: small split-valence basis sets for 1st-row elements. *J. Am. Chem. Soc.* **102**, 939–947 (1980).
27. M. S. Gordon, J. S. Binkley, J. A. Pople, W. J. Pietro and W. J. Hehre, Self-consistent molecular-orbital methods 22: small split-valence basis sets for 2nd-row elements *J. Am. Chem. Soc.* **104**, 2797–2803 (1982).
28. R. Declerck, V. Van Speybroeck and M. Waroquier, First-principles calculation of the EPR *g* tensor in extended periodic systems. *Phys. Rev. B* **73**, 115113 (2006).
29. A. D. Becke, Density-functional exchange-energy approximation with correct asymptotic behavior. *Phys. Rev. A* **38**, 3098–3100 (1988).
30. C. T. Lee, W. T. Yang and R. G. Parr, Development of the Colle-Salvetti correlation-energy formula into a functional of the electron density. *Phys. Rev. B* **37**, 785–789 (1988).
31. S. Goedecker, M. Teter and J. Hutter, Separable dual-space Gaussian pseudopotentials. *Phys. Rev. B* **54**, 1703–1710 (1996).
32. C. J. T. de Grotthuss, Mémoire sur la décomposition de l'eau et des corps qu'elle tient en dissolution à l'aide de l'électricité galvanique. *Ann. Chim.* **58**, 54–74 (1806).
33. C. J. T. de Grotthuss, Memoir on the decomposition of water and of the bodies that it holds in solution by means of galvanic electricity. *Biochim. Biophys. Acta* **1757**, 871–875 (2006). [English translation by R. Pomès]
34. N. Agmon, The Grotthuss mechanism. *Chem. Phys. Lett.* **244**, 456–462 (1995).
35. P. Adelröth, Special issue on proton transfer in biological systems—Preface. *Biochim. Biophys. Acta* **1757**, 867–870 (2006).
36. W. A. Bernhard, J. Barnes, K. R. Mercer and N. Mroczka, The influence of packing on free radical yields in crystalline nucleic acids—the pyrimidine bases. *Radiat. Res.* **140**, 199–214 (1994).
37. W. H. Nelson, E. Sagstuen, E. O. Hole and D. M. Close, Electron spin resonance and electron nuclear double resonance study of X-irradiated deoxyadenosine: Proton transfer behavior of primary ionic radicals. *Radiat. Res.* **149**, 75–86 (1998).
38. D. M. Close, L. A. Eriksson, E. O. Hole, E. Sagstuen and W. H. Nelson, Experimental and theoretical investigation of the mechanism of radiation-induced radical formation in hydrogen-bonded cocrystals of 1-methylcytosine and 5-fluorouracil. *J. Phys. Chem. B* **104**, 9343–9350 (2000).
39. V. Barone, Structure, magnetic properties and reactivities of open-shell species from density functional and self-consistent hybrid methods. In *Recent Advances in Density Functional Methods, Part I* (D. P. Chong, Ed.), pp. 287–334. World Scientific, Singapore, 1995.
40. S. Cukierman, Et tu, Grotthuss! and other unfinished stories. *Biochim. Biophys. Acta* **1757**, 876–885 (2006).
41. R. Pomès and B. Roux, Molecular mechanism of H^+ conduction in the single-file water chain of the gramicidin channel. *Biophys. J.* **82**, 2304–2316 (2002).
42. R. Pomès and B. Roux, Free energy profiles for H^+ conduction along hydrogen-bonded chains of water molecules. *Biophys. J.* **75**, 33–40 (1998).
43. H. C. Box and E. E. Budzinski, A variation of the alkoxy radical. *J. Chem. Phys.* **79**, 4142–4145 (1983).

7 Paper VI

Molecular Environment and Temperature Dependence of Hyperfine Interactions in Sugar Crystal Radicals from First Principles

R. Declerck, E. Pauwels, V. Van Speybroeck, and M. Waroquier

Journal of Physical Chemistry B 112 (5), 1508-1514 (2008)

7. Paper VI :: Molecular Environment and Temperature Dependence of Hyperfine Interactions in Sugar Crystal Radicals from First Principles

Molecular Environment and Temperature Dependence of Hyperfine Interactions in Sugar Crystal Radicals from First Principles

R. Declerck, E. Pauwels, V. Van Speybroeck, and M. Waroquier*

Center for Molecular Modeling, Ghent University, Proeftuinstraat 86, B-9000 Gent, Belgium

Received: August 15, 2007; In Final Form: October 16, 2007

The effect of the molecular environment and the temperature dependence of hyperfine parameters in first principles calculations in α-D-glucose and β-D-fructose crystal radicals have been investigated. More specifically, we show how static (0 K) cluster in vacuo hyperfine calculations, commonly used today, deviate from more advanced molecular dynamics calculations at the experimental temperature using periodic boundary conditions. From the latter approach, more useful information can be extracted, allowing us to ascertain the validity of proposed molecular models.

1. Introduction

Over the past few decades, radiation-induced radicals in solid-state sugars have received considerable attention.[1−3] These carbohydrates are extremely abundant in plants and animals and play an essential role in several biological processes. A prominent technique to detect such radical defects is electron paramagnetic resonance (EPR) spectroscopy. In recent years, there has been a growing interest in the ab initio quantum mechanical calculation of these EPR quantities within density functional theory (DFT).[4,5] A comprehensive overview is given in ref 6. By comparing the experimental EPR quantities with those computed from proposed molecular models, it is possible to identify and understand the microscopic structure of these defects.

The energy levels and intensities derived from EPR experiments can be reproduced using an effective Hamiltonian which, in the case of these radicals, involves three principal quantities: (i) the hyperfine parameters (HFPs), (ii) the **g** tensor, and (iii) the zero-field splitting tensor. In this paper, we will focus on the first quantity. The HFPs can be computed from the ground state spin density alone, and they probe the spin density of a region near the nucleus.

A recurring problem in the calculation of theoretical HFPs (see, for example, refs 7−9) concerns the inclusion of the molecular environment (ME) in these sugar crystal radicals. One of the most commonly used ME models is the cluster in vacuo approach. Conceptually, this approach is based on the assumption that the embedding of the radical molecule in a sufficiently large cluster mimics the electronic confinement of the radical in the crystalline lattice: a central radical structure is surrounded by molecules fixed in space at the geometry of the crystal structure, and the HFPs can then be readily calculated using the available gas-phase methods.

However, a more natural and more accurate way to simulate crystalline lattices is to perform periodic boundary calculations, thereby exploiting the translational symmetry of the crystalline state. The first purpose of this work is to assess the accuracy of HFPs calculated using different cluster in vacuo approximations found in the literature by comparing them with a reference set of HFPs calculated from periodic boundary simulations. Several methods have been described in the literature to calculate HFPs from such simulations.[10−14] In this work, we will make use of the efficient hybrid HFP scheme recently proposed by the authors in ref 15 and reiterated here briefly in the next section.

Previous HFP calculations by the authors on these sugar crystal radicals were all static (at 0 K) and did not account for the effects that may occur at the finite experimental temperature. The second purpose of this work is to investigate, using the hybrid HFP scheme, the effects of temperature on the HFPs by averaging the HFPs calculated at every step along a Born−Oppenheimer molecular dynamics trajectory equilibrated at the experimental temperature. Some similar work has been done in the past, such as the investigation of temperature effects on nuclear magnetic resonance chemical shifts[16,17] and nuclear quadrupole coupling constants.[18]

2. Theory and Computational Details

The components of the hyperfine tensor $\mathbf{A}_N$ of a nucleus N can be derived from relativistic many-body quantum mechanics, and the most dominant terms are[19,20]

$$A_{N,ij} = A_{\mathrm{iso},N}\delta_{ij} + A_{\mathrm{ani},N,ij} \tag{1}$$

where

$$A_{\mathrm{iso},N} = \frac{1}{3}\frac{g_e\mu_e g_N\mu_N}{\langle S_z\rangle}\int \mathrm{d}\mathbf{r}\ \rho_s(\mathbf{r})\delta_T(\mathbf{r}) \tag{2}$$

$$A_{\mathrm{ani},N,ij} = \frac{1}{8\pi}\frac{g_e\mu_e g_N\mu_N}{\langle S_z\rangle}\int \mathrm{d}\mathbf{r}\ \rho_s(\mathbf{r})\frac{3r_ir_j - \delta_{ij}r^2}{r^5} \tag{3}$$

Here, $\rho_s = \rho^\alpha - \rho^\beta$ represents the net electronic spin density, g_e is the free-electron g value, μ_e is the Bohr magneton, g_N is the nuclear gyromagnetic ratio for the nucleus, μ_N is the nuclear magneton, $\langle S_z\rangle$ is the expectation value of the z-component of the total electronic spin, and the vector $\mathbf{r}$ is taken relative to the position of the nucleus. The isotropic HFP A_{iso} corresponds to the Fermi contact interaction, whereas the anisotropic HFPs $A_{\mathrm{ani},ij}$ results from dipole−dipole interactions. $\delta_T(\mathbf{r})$ is a smeared out δ function that results from scalar relativistic corrections.[10,19] The subscripts i and j refer to Cartesian coordinates x, y, and z. The gyromagnetic ratio data used in this paper originate from ref 21.

10.1021/jp076571w CCC: $40.75
Published on Web 01/12/2008

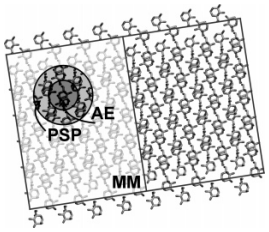

Figure 1. Sketch of the hybrid AE + PSP GAPW scheme, extended with a third MM layer. The simulation cell and one of its neighboring images are shown.

In ref 15, we introduced a method for the calculation of hyperfine parameters in extended systems under periodic boundary conditions using the Gaussian and augmented-plane-wave (GAPW) density functional method. The HFP method was implemented in the Quickstep[22] code, which is part of the freely available program package CP2K.[23] In the GAPW method, the total density is described in a smooth, extended part represented in plane waves and parts localized close to the nuclei that are expanded in periodic Gaussian functions. The GAPW method exists in both a pseudopotential (PSP)[24] and an all-electron (AE)[25] implementation, and both approaches can be easily combined within one simulation. Using a supercell technique to approximate the gas phase, we have shown for a variety of atomic and molecular species that the AE GAPW method reproduces the HFPs calculated from pure gas-phase calculations to within less than 2%. We have also introduced an efficient hybrid HFP calculation scheme, in which an AE treatment for the nuclei of interest and a PSP approximation for the remaining atoms in the simulation cell are combined. It has been shown that the use of this hybrid AE + PSP GAPW scheme does not significantly alter the results obtained with an AE treatment for the entire simulation cell and, hence, makes HFP predictions in large systems computationally more affordable. The scheme could even be extended easily to a three-layer scheme including a classical molecular mechanics (MM) layer, as sketched in Figure 1, allowing for the study of HFPs in even larger molecular systems.

The HFP calculations within the different cluster in vacuo approximations were performed using the Gaussian 03[26] program package. However, whenever possible, they were independently corroborated with the Quickstep HFP code using the aforementioned supercell technique.

3. Effect of the Molecular Environment

Since the hybrid AE + PSP GAPW scheme allows the calculation of HFPs in extended systems under periodic boundary conditions with the AE accuracy that for long has been accessible only to simple gas-phase systems, it can be used as a reference method to evaluate different cluster in vacuo methods for HFP calculations described in the literature. In this comparison, we will consider low-temperature (77 K) radiation-induced radical structures in α-D-glucose and β-D-fructose (see Figure 2), further referred to as Gluc/R1, Gluc/R2, Fruc/R1, and Fruc/R2. These radical structures were proposed in earlier publications.[9,29,30]

It was derived from neutron diffraction studies[31,32] that both the α-D-glucose and the β-D-fructose crystals are orthorhombic, with the former featuring unit cell constants of $a = 19.59$ au, $b = 28.06$ au, and $c = 9.40$ au and the latter, unit cell constants

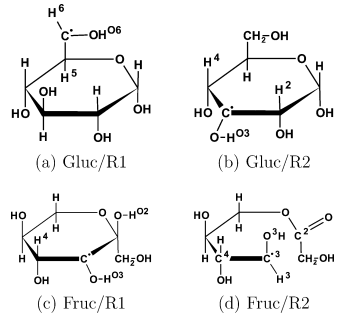

Figure 2. Radical structures in α-D-glucose (a and b) and β-D-fructose (c and d). Some atoms are labeled in superscript for further reference.

of $a = 17.37$ au, $b = 18.98$ au, and $c = 15.30$ au. In the periodic boundary simulations, we doubled the unit cell in the c direction for α-D-glucose (denoted as ab2c) and in the a and c directions for β-D-fructose (2ab2c) to ensure that radicals from neighboring periodic images remain well-separated from each other. The cluster in vacuo models comprised all molecules that are engaged in hydrogen bonds with the central radical in accordance with the crystal structure. This choice for the cluster size corresponds to earlier work, in which it was argued that the intermolecular interactions in crystalline sugars are predominantly governed by hydrogen bonds. Geometry optimizations were performed on the central radical while keeping the coordinates of the surrounding molecules fixed in space at the geometry of the crystal structure.

For a reliable assessment, all calculation details not related to the different ME models have been kept as uniform as possible. A BLYP gradient-corrected exchange-correlation (XC) functional[33,34] was used throughout all calculations. In the periodic boundary model, we used a TZVP-AE[35] basis set and an AE description for the radical and a TZVP-PSP[36] basis set and pseudopotentials of Goedecker and co-workers[37,38] for the undamaged molecules in the simulation cell. Geometry relaxations using this scheme showed that Gluc/R1 was more stable than Gluc/R2 by 3.3 au (8.7 kJ/mol), whereas Fruc/R1 was more stable than Fruc/R2 by 8.0 au (21.0 kJ/mol). In the cluster in vacuo models, the TZVP-AE basis set was consistently employed for the central radical, and the surrounding molecules were treated using various techniques: (i) at the same level of theory as the central radical (full cluster), (ii) at the semiempirical PM3[39,40] level using an Oniom[41−45] technique (Oniom cluster), or (iii) not including the molecular environment at all (radical molecule).

In Table 1, the calculated HFPs are classified according to the ME model (periodic, full cluster, Oniom cluster, or radical molecule) used for relaxing the geometry as well as for the subsequent HFP calculation. As can be observed, the applied ME models can be different for the two steps in the simulation because of the fact that the geometry relaxation often poses a much larger computational burden. The first set of HFPs (denoted as periodic/periodic) were calculated using the reference hybrid AE + PSP GAPW scheme. The other sets of theoretical HFPs are arranged according to the decreasing size of the ME models. The values between brackets denote the angles (in degrees) of the principal directions with respect to the corresponding reference principal directions. The experimental HFPs (and their angular deviations with respect to the

TABLE 1: Proton ^{1}H HFPs (in MHz) for the Gluc/R1 and Gluc/R2 Radicals in α-D-Glucose, and the Fruc/R1 and Fruc/R2 Radicals in β-D-Fructose, Using Various Periodic and Cluster in Vacuo Methods, Classified Both by the ME Model Used to Relax the Geometry and by the Model Used for the Subsequent HFP Calculation Based on This Relaxed Geometry[a]

geometry relaxation HFP calculation		periodic[b] periodic[b]				periodic[b] full cluster[c]				full cluster[c] full cluster[c]			
		A_{iso}	$A_{ani,xx}$	$A_{ani,yy}$	$A_{ani,zz}$	A_{iso}	$A_{ani,xx}$	$A_{ani,yy}$	$A_{ani,zz}$	A_{iso}	$A_{ani,xx}$	$A_{ani,yy}$	$A_{ani,zz}$
						α-D-Glucose							
Gluc/R1	H6	−49.9	−33.4	−1.6	35.0	−49.7	−33.3 (0.3°)	−1.4 (0.0°)	34.7 (0.8°)	−50.9	−33.7 (3.8°)	−1.0 (6.5°)	34.7 (5.4°)
	H5	26.9	−6.3	−3.2	9.4	26.4	−6.2 (1.4°)	−3.2 (1.0°)	9.4 (0.7°)	37.0	−6.2 (3.6°)	−3.0 (3.4°)	9.2 (2.4°)
	HO6	6.4	−11.2	−8.3	19.5	6.1	−11.3 (1.6°)	−8.6 (1.5°)	19.9 (0.0°)	3.9	−11.5 (15.4°)	−8.8 (15.4°)	20.2 (0.7°)
Gluc/R2	H2	95.4	−5.0	−1.4	6.5	90.5	−4.8 (6.3°)	−2.0 (6.6°)	6.8 (2.1°)	93.0	−4.6 (11.2°)	−2.1 (11.3°)	6.6 (1.3°)
	H4	87.3	−5.1	−2.0	7.1	84.9	−4.9 (1.9°)	−2.4 (2.7°)	7.3 (2.1°)	88.2	−4.8 (5.4°)	−2.5 (5.5°)	7.3 (2.0°)
	HO3	6.6	−10.8	−8.5	19.3	6.6	−11.0 (1.1°)	−8.9 (1.0°)	19.9 (0.8°)	1.9	−11.4 (3.3°)	−8.7 (2.2°)	20.1 (3.0°)
						β-D-Fructose							
Fruc/R1	H4	98.9	−5.2	−1.6	6.8	99.9	−5.1 (1.2°)	−1.7 (1.1°)	6.8 (0.0°)	98.6	−5.1 (0.9°)	−1.7 (1.8°)	6.9 (1.5°)
	HO2	17.9	−3.8	−1.9	5.7	18.2	−3.5 (4.4°)	−2.1 (4.4°)	5.5 (0.4°)	19.1	−3.5 (3.1°)	−2.1 (2.7°)	5.5 (1.5°)
	HO3	8.8	−11.3	−8.8	20.0	8.9	−11.2 (4.3°)	−8.9 (4.4°)	20.1 (0.3°)	8.7	−11.2 (7.8°)	−8.9 (7.8°)	20.1 (1.9°)
Fruc/R2	H3	−27.4	−30.4	−1.5	31.9	−28.5	−30.7 (0.4°)	−1.5 (0.7°)	32.2 (0.8°)	−46.8	−34.1 (4.5°)	−1.0 (4.8°)	35.2 (2.5°)

geometry relaxation HFP calculation		oniom cluster[d] full cluster[c]				oniom cluster[d] radical molecule[c]				experiment[e]			
		A_{iso}	$A_{ani,xx}$	$A_{ani,yy}$	$A_{ani,zz}$	A_{iso}	$A_{ani,xx}$	$A_{ani,yy}$	$A_{ani,zz}$	A_{iso}	$A_{ani,xx}$	$A_{ani,yy}$	$A_{ani,zz}$
						α-D-Glucose							
Gluc/R1	H6	−37.0	−32.2 (3.8°)	−2.3 (13.3°)	34.5 (12.9°)	−30.5	−32.1 (4.1°)	−2.1 (11.1°)	34.3 (10.4°)	±57.8	±34.8 (1.2°)	∓2.2 (5.4°)	∓31.4 (5.5°)
	H5	13.2	−6.2 (5.1°)	−3.6 (5.0°)	9.8 (2.0°)	14.0	−6.1 (5.9°)	−3.7 (5.7°)	9.7 (2.1°)	19.3	−5.7 (24.0°)	−4.2 (23.5°)	10.0 (2.5°)
	HO6	−9.5	−12.7 (18.6°)	−7.7 (30.2°)	20.4 (27.0°)	−11.5	−13.8 (15.3°)	−8.5 (29.0°)	22.2 (27.6°)	±9.0			
Gluc/R2	H2	95.1	−4.6 (9.1°)	−2.1 (9.4°)	6.7 (5.1°)	87.2	−4.5 (10.4°)	−1.9 (11.0°)	6.5 (5.2°)	95.3	−4.8 (7.8°)	−2.0 (9.3°)	6.7 (4.9°)
	H4	87.2	−4.9 (2.1°)	−2.4 (2.6°)	7.2 (2.4°)	82.6	−4.8 (7.4°)	−2.4 (8.7°)	7.2 (4.9°)	89.4	−5.1 (9.6°)	−1.6 (9.6°)	7.1 (6.2°)
	HO3	1.5	−11.1 (13.1°)	−8.9 (11.3°)	20.0 (8.1°)	1.6	−11.7 (8.6°)	−8.8 (5.6°)	20.5 (8.9°)	5.6/28.0			
						β-D-Fructose							
Fruc/R1	H4	102.3	−5.2 (1.7°)	−1.8 (1.6°)	6.9 (1.1°)	97.1	−4.9 (7.6°)	−2.4 (8.8°)	7.3 (4.4°)	99.41	−5.01 (2.0°)	−1.99 (3.8°)	7.00 (3.4°)
										98.58	−5.08 (5.5°)	−1.87 (6.9°)	6.95 (4.3°)
	HO2	14.8	−3.8 (17.7°)	−1.9 (16.7°)	5.7 (6.8°)	19.9	−3.4 (18.8°)	−1.8 (18.7°)	5.2 (6.7°)	17.63	−3.57 (1.7°)	−2.29 (1.8°)	5.86 (0.7°)
	HO3	12.8	−11.0 (16.2°)	−9.2 (16.3°)	20.2 (3.0°)	14.4	−11.3 (5.7°)	−9.1 (6.6°)	20.4 (4.5°)				
Fruc/R2	H3	−46.8	−33.4 (5.7°)	−1.0 (6.8°)	34.4 (3.9°)	−45.3	−32.5 (5.8°)	−1.3 (6.7°)	33.8 (3.7°)	−45.59	−34.60 (2.1°)	1.66 (1.6°)	32.94 (1.7°)
										−38.88	−32.65 (5.4°)	3.63 (7.1°)	29.03 (7.7°)

[a] The values in parentheses denote the angles (in degrees) of the principal directions with the corresponding reference hybrid AE + PSP GAPW principal directions. The experimental HFPs are also given. [b] GAPW AE+PSP BLYP/TZVP/200Ry. [c] G03 AE BLYP/TZVP. [d] G03/ONIOM AE+PM3 BLYP/TZVP. [e] Experimental data from refs 27 and 28 (Gluc/R1 and Gluc/R2) and ref 29 (Fruc/R1 and Fruc/R2).

reference results) are also given; in some cases, no unique experimental signal could be attributed to the theoretical HFP prediction. Only the couplings for which experimental values from literature were available are taken up in Table 1. These couplings all involve protons, as they are generally more affordable to detect in EPR experiments than carbons or oxygens. Even when looking only at protons, an all-electron treatment is required, because the hydrogen PSP has a non-Coulombic shape near the core site, which affects the electronic spin density there and, hence, the corresponding HFPs, and thus, even in the simple case of protons, a HFP reconstruction procedure such as the one proposed in ref 46 would be necessary to correct for this deficiency. A HFP calculation using only PSPs on the optimized geometry of (for example) Gluc/R2 illustrates this: the isotropic HFPs of Gluc/R2/H2, Gluc/R2/H4, and Gluc/R2/HO3 become 78.9, 72.3, and 5.7 MHz. The ^{13}C HFPs of the C3 carbon in the radical center of Fruc/R2 (denoted as Fruc/R2/C3) will be discussed later on, even though no experimental

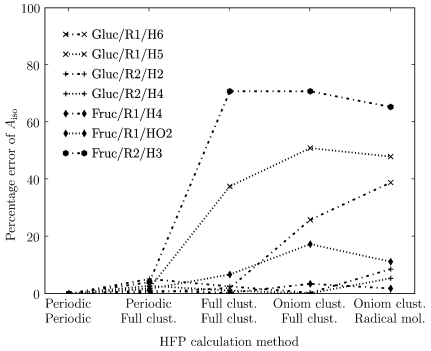

Figure 3. Percentage error of a selection[47] of isotropic HFPs with respect to the reference hybrid AE + PSP GAPW calculations for different cluster in vacuo methods (for notation, see Table 1).

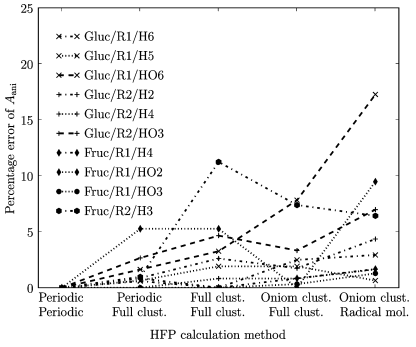

Figure 4. Percentage error of the anisotropy with respect to the reference hybrid AE + PSP GAPW calculations for different cluster in vacuo methods (for notation, see Table 1).

data is available for this coupling. The full list of calculated HFPs is available as Supporting Information.

Inspection of Table 1 shows that the agreement with the reference hybrid AE + PSP GAPW calculations diminishes when a less accurate description of the ME is employed. This effect is particularly pronounced for the isotropic HFPs: in Gluc/R1/H6, Gluc/R1/H5, Gluc/R1/HO6, and Fruc/R2/H3, these couplings can fluctuate by up to around 20 MHz from their reference value. The percentage errors for a selection[47] of isotropic HFPs with the reference calculations are shown in Figure 3 to illustrate the relative degradation of each particular isotropic HFP. From this figure, it becomes clear that the periodic/full cluster and the reference HFPs differ only marginally. The same accounts for the Oniom cluster/full cluster and the Oniom cluster/radical molecule combinations, especially when taking into account the oversimplification of the model in the evaluation of the HFPs, retaining only the radical in the complete absence of its molecular environment. Apparently, the ME model used in the geometry relaxation is the determining factor in the reproduction of the isotropic HFPs.

In the case of the isotropic HFP of Fruc/R2/H3, all methods featuring a cluster geometry relaxation deviate some 20 MHz from their reference value, and surprisingly, enough reproduce almost exactly one of the corresponding experimental values. The origin of this phenomenon can be attributed to the size of the cluster used for the geometry relaxation of the radical. The hydrogen-bonded undamaged molecules do not adequately embed the central radical and fail to impose the constraints imposed by the lattice structure. As a result, the disrupted bond in the radical is overestimated by 0.51 au (full cluster) and by 0.55 au (Oniom cluster) with respect to the periodic prediction of 4.77 au. The enlargement of the disrupted bond causes the electronic configuration in the C3 carbon of Fruc/R2 (for notation, see Figure 2d) to shift from sp to sp hybridization, the unpaired electron becomes more localized on this C3 carbon and influences the HFPs of the radical center due to their dependence on the spin density (eq 2). Similar effects were reported previously by Barone et al.[48−50] A comparison of the different C3 carbon HFP predictions in Table 2 supports this proposition: there exists a quite distinct difference between the HFPs that were obtained using a periodic geometry and those using a cluster geometry. Table 2 even reveals the dissimilarity between full cluster and Oniom cluster geometry HFP predictions. By doubling the number of neighbors in the cluster (from 8 to 16), the shortcomings of the cluster model disappear: after geometry relaxation of the central radical in the enlarged cluster model, its geometry matches perfectly with the periodic geometry. For example, the disrupted bond agrees to within <0.002 au. The isotropic HFPs for Fruc/R2/H3 and Fruc/R2/C3 become −31.5 and 95.6 MHz, respectively, which is in both cases closer to the corresponding periodic/periodic values. Hence, this proves that the initial good agreement with experimental results was only coincidental and that the actual deviation, obtained with an accurate incorporation of the ME, amounts to 11.5−18.2 MHz.

TABLE 2: Carbon ^{13}C HFPs (in MHz) for Fruc/R2/C3, Using Various Periodic and Cluster in Vacuo Methods[a]

type	A_{iso}	$A_{ani,xx}$	$A_{ani,yy}$	$A_{ani,zz}$
periodic/periodic	89.7	−65.2	−64.2	129.4
periodic/full cluster	92.2	−66.1 (1.0°)	−65.1 (1.0°)	131.2 (0.0°)
full cluster/full cluster	79.5	−73.4 (7.8°)	−72.1 (6.5°)	145.5 (4.3°)
Oniom cluster/full cluster	76.1	−70.7 (39.8°)	−71.9 (24.4°)	142.6 (34.4°)
Oniom cluster/radical molecule	74.3	−69.1 (41.6°)	−70.0 (27.6°)	139.0 (34.4°)

[a] For notation, see Table 1. The values between brackets denote the angles (in degrees) of the principal directions with the corresponding reference hybrid AE + PSP GAPW principal directions.

The changes in the anisotropic HFPs are more subtle. These fluctuations can be quantified by the anisotropy A_{ani}, defined as the difference between the maximum and the minimum anisotropic HFPs. Throughout Table 1, the disagreement with the reference data did not exceed 7 MHz. The percentage errors of the anisotropy with respect to the reference hybrid AE + PSP GAPW calculations are plotted in Figure 4. They remain lower than 20%, affirming the less pronounced sensitivity of A_{ani} on the ME description. Their corresponding principal directions vary a bit more and can deviate up to around 30° from the reference calculations. The arithmetic means of the angular deviations of each hyperfine coupling are plotted in Figure 5.

In conclusion, the cluster in vacuo methods used here were all able to reproduce the reference HFPs reasonably well. The largest fluctuations were found in the isotropic HFPs. In a few cases, the cluster size was found to be too small to closely

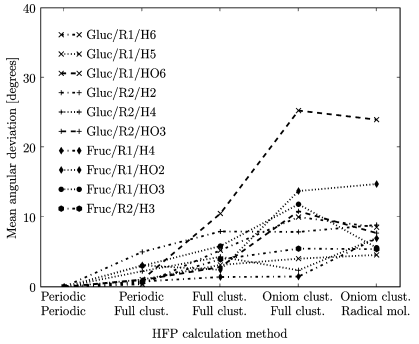

Figure 5. Mean angular deviation of the principal directions from the reference hybrid AE + PSP GAPW calculations for different cluster in vacuo methods (for notation, see Table 1).

reproduce the reference isotropic HFPs. All methods resulted in a good qualitative agreement with experimental data.

4. Effect of the Finite Temperature

The experimental HFPs from Table 1 were all obtained at the experimental temperature of 77 K. Thermally induced vibrations that involve inversion at the radical center are known to affect the HFPs.[48] This can occur due to shifts in the average bond lengths, bond angles, or dihedral angles from their static (0 K) value, which result from anharmonicities in their respective potentials, or are due to nonlinear dependencies that may exist between the HFPs and these geometric parameters. To include these temperature effects in HFP predictions, HFPs were calculated at every step along a Born−Oppenheimer molecular dynamics trajectory equilibrated at the experimental temperature and were subsequently averaged. These calculations were performed on the Fruc/R2 radical, because they may help to unravel the remaining discrepancy between the experimental and the static theoretical isotropic HFPs of Fruc/R2/H3 (see the discussion in the previous section).

Although the hybrid AE + PSP GAPW scheme heavily facilitates the instantaneous evalution of the HFPs, the Fruc/R2/H3 radical was simulated using only the unit cell (abc) as the simulation cell in order to further alleviate the computational burden. The system was sampled at the experimental temperature of 77 K using chains of Nosé−Hoover thermostats[51] attached to the nuclear degrees of freedom. After equilibration of the structure for 1.0 ps, its HFPs were computed on the fly during a production run of another 3.0 ps of canonical MD.

In Figure 6, the time evolution of the Fruc/R2/H3 isotropic HFP is plotted, together with some determining geometrical parameters of the radical center. As apparent, the isotropic coupling varies considerably, from 0 to −52 MHz, and comprises both reported experimental values. Averaging these values (see Table 3) results in an isotropic HFP which is a mere 1.7 MHz closer to the experimental values than the static (0 K) value obtained using the same (abc) simulation cell. Note that the latter result slightly differs from the result reported in Table 1 because of the use of a smaller simulation cell, resulting in a higher interaction with neighboring radicals: the radical from the smaller simulation cell is 4.4 au (11.4 kJ/mol) less stable than the radical from the larger (2ab2c) simulation cell and has geometric features, such as a lower improper dihedral C4−O3−H3−C3 (by 0.3°), that can be related to the Fruc/R2/H3 isotropic HFP prediction (see below). The cumulative averages of the isotropic HFPs at every 100 fs are also taken up in Figure 6 and illustrate the well-converged behavior of this value. The set of anisotropic HFPs and their principal directions comprise both experimental values, as well, but their averages are essentially not different from the static (0 K) values, and the averaged principal directions retain the excellent agreement with

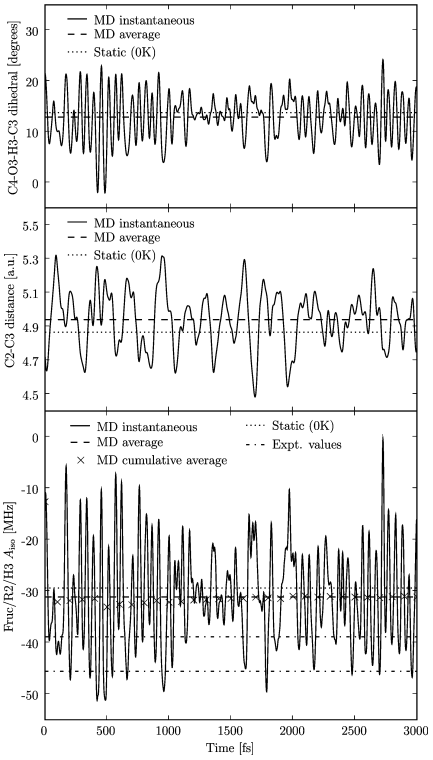

Figure 6. C4−O3−H3−C3 dihedral angle, C2−C3 bond length, and isotropic HFP for Fruc/R2/H3, calculated at every step of a 3 ps MD run (MD instantaneous). The average from all time steps (MD average), the static (0 K) value, and (in the case of the isotropic HFP) the cumulative average at every 100 fs (MD cumulative average) and both experimental values are also shown.

TABLE 3: Proton ^{1}H HFPs (in MHz) for Fruc/R2/H3, Averaged from HFP Calculations at Every Step in the MD or Calculated from the Static Geometry (at 0 K)[a]

type	A_{iso}	$A_{ani,xx}$	$A_{ani,yy}$	$A_{ani,zz}$
77 K	−31.1	−30.5 (1.4°)	−0.8 (1.5°)	31.6 (3.0°)
0 K	−29.4	−30.5 (1.7°)	−1.5 (2.1°)	32.0 (2.5°)
exptl	−45.59	−34.6	1.7	33.0

[a] The values in parentheses denote the angles (in degrees) of the principal directions with the corresponding principal directions of one of the experimental couplings (taken from Table 1).

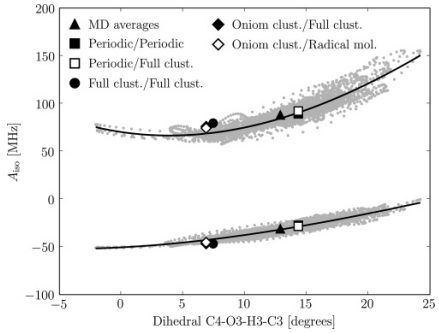

Figure 7. Correlation of the isotropic HFPs of both Fruc/R2/H3 and Fruc/R2/C3 and the C4−O3−H3−C3 dihedral angle. The solid lines represent a best fit of a third-order polynomial to the respective data sets, and the triangle symbols show the intersection point of the averaged values on the *x*- and *y*-axes. For the purpose of reference, results from static HFP calculation methods have also been included (for notation, see Table 1).

one of the experimental couplings. Thus, in this case, temperature effects account for only some, but far from all, of the discrepancies between the theoretical and experimental HFPs of Fruc/R2/H3.

To determine the origin of the large fluctuations in the isotropic HFP of Fruc/R2/H3, it is instructive to derive from the MD simulation some characteristic geometric features that may influence A_{iso}. Two relevant geometric parameters are the C2−C3 broken bond distance and the improper dihedral C4−O3−H3−C3, which represents a measure for the planarity of the radical center (for notation, see Figure 2d). Together, they reflect the continuous variation in the simulation of the electronic configuration in the C3 carbon of Fruc/R2 from sp^3 to sp^2 hybridization. Both parameters are plotted in Figure 6 along the MD trajectory. Averaging these parameters over the simulation period results in small but significant changes: the separation between C2 and C3 is enlarged by 0.1 au, and the radical center becomes more planar by 0.9°. Hence, the potential energy is asymmetric with respect to the planarity and tends to favor a more planar radical center. This is important, because the planarity of a radical center is known to have a significant influence on the isotropic HFP of α-protons, such as Fruc/R2/H3.[52] Figure 7 shows that there is a strong correlation between the isotropic HFP of Fruc/R2/H3 and the planarity. This feature is also present for the Fruc/R2/C3 isotropic HFP, which was also evaluated along the MD trajectory. The plots in Figure 7 clearly reveal the nonlinear dependency of both isotropic HFPs with respect to the planarity. As the radical center switches from sp^3 to sp^2 hybridization in the temperature simulation, the Fruc/R2/H3 isotropic HFP covers a wide range of over 50 MHz. This actually has the same effect as the mechanism causing the discrepancy between the cluster and periodic isotropic HFPs for Fruc/R2/H3 (see the previous section): the unpaired electron density on the C3 carbon fluctuates and influences the HFPs near the radical center due to their dependence on the spin density. Here, the added value of the MD simulation becomes clearly visible: the strong relationship between the planarity and the HFPs of Fruc/R2/H3 shows that the discrepancies between the theoretical and experimental HFPs of Fruc/R2/H3 are due to rather minor geometrical changes, thus, to some degree strengthening the validity of the theoretical model for the Fruc/R2 radical. Similar dependencies were derived earlier in theoretical studies of a glycine radical[48] and the methyl radical,[53] but employing a perturbational approach to account for finite temperature effects on the HFPs.

However, the MD simulation does not reveal the real origin of the observed discrepancies; neither does it explain the occurrence of two alike HFPs in the experimental spectra. In fact, it does not even rule out completely the existence of another structure representing the actual radical. Several factors other than temperature may play an important role. The use of a different XC functional, the PBE[54] functional, in both the geometry relaxation and the HFP calculation gave rise to a shift in the isotropic HFP of Fruc/R2/H3 of a mere 1.6 MHz, but in the opposite direction of both experimental values. Averaging over the zero-point motion[55,56] of the Fruc/R2/H3 proton will also affect the HFP predictions. The incorporation of the quantum nature of the nuclei can be included by performing path integral molecular-dynamics simulations,[57] which have not been considered here. There are also some known issues with DFT-based MD simulations,[58] such as nonergodic behavior at lower temperatures; however, the problems discussed in ref 58 primarily relate to condensed aqueous systems. One phenomenon that could deal with the two aforementioned problems at once involves the occurrence of proton transfer along the infinite hydrogen bond chains pervading throughout the entire crystal. The existence of stable structures featuring different types of proton transfer may alter the geometrical parameters that influence the HFPs of Fruc/R2/H3 in a different way; hence, resulting in multiple theoretical HFPs that essentially originate from the same radical structure. This mechanism was suggested in a previous study on α-L-rhamnose alkoxy radicals[59] and is currently under investigation for Fruc/R2.

5. Conclusion and Outlook

In the first part of this work, the effect of the molecular environment on first principles cluster in vacuo HFP calculations has been assessed in a series of sugar crystal radicals. This was done through a comparison with a reference set of HFPs calculated from periodic boundary simulations. It was shown that the cluster in vacuo models used in this study were able to reproduce the reference HFPs reasonably well in almost all cases, and all resulted in a good qualitative agreement with experimental data. In only a few cases, the cluster size was found to be too small to closely reproduce the reference isotropic HFPs. One example is the isotropic HFP of Fruc/R2/H3: although initial HFP calculations in a small cluster model resulted in a good agreement with one of the experimental values, additional calculations in an extended cluster model closely reproduced the reference result and, hence, proved that the earlier agreement was only coincidental.

A profound investigation of this residual discrepancy was performed by calculating the Fruc/R2/H3 isotropic HFP at every step along a Born−Oppenheimer molecular dynamics trajectory equilibrated at the experimental temperature using the hybrid AE + PSP GAPW scheme. Throughout this trajectory, the isotropic coupling fluctuated heavily, spanning a range of over 50 MHz, and comprised both reported experimental values. Although the average of these values did not bridge the gap between theoretical and experimental HFPs, the MD simulation did show that specific minor geometrical changes in the radical structure would bring the theoretical prediction much closer to the experimental HFPs. Although this study to some degree strengthened the validity of the proposed radical structure, several questions are still unanswered. One suggested phenom-

enon that could resolve the remaining problems assumes the existence of proton transfer along hydrogen bond chains across the entire crystal. This mechanism will be the subject of future work.

Acknowledgment. This work was supported by the Fund for Scientific Research−Flanders and the Research Board of Ghent University.

Supporting Information Available: Additional information as noted in text. This material is available free of charge via the Internet at http://pubs.acs.org.

References and Notes

(1) Debije, M. G.; Bernhard, W. A. *Radiat. Res.* **2001**, *155*, 687.
(2) Sagstuen, E.; Lund, A.; Awadelkarim, O.; Lindgren, M.; Westerling, J. *J. Phys. Chem.* **1986**, *90*, 5584.
(3) Vanhaelewyn, G.; Sadlo, J.; Callens, F.; Mondelaers, W.; De Frenne, D.; Matthys, P. *Appl. Radiat. Isot.* **2000**, *52*, 1221.
(4) Hohenberg, P.; Kohn, W. *Phys. Rev.* **1964**, *136*, B864.
(5) Kohn, W.; Sham, L. *Phys. Rev.* **1965**, *140*, A1133.
(6) Kaupp, M.; Bühl, M.; Malkin, V. G. *Calculations of NMR and EPR parameters: Theory and Applications*; Wiley-VCH: Weinheim, 2004.
(7) Pauwels, E.; Van Speybroeck, V.; Lahorte, P.; Waroquier, M. *J. Phys. Chem. A* **2001**, *105*, 8794.
(8) Pauwels, E.; Van Speybroeck, V.; Waroquier, M. *J. Phys. Chem. A* **2004**, *108*, 11321.
(9) Pauwels, E.; Van Speybroeck, V.; Waroquier, M. *Spectrochim. Acta, A* **2006**, *63*, 795.
(10) Blöchl, P. E. *Phys. Rev. B: Condens. Matter Mater. Phys.* **2000**, *62*, 6158.
(11) Van de Walle, C. G.; Blöchl, P. E. *Phys. Rev. B: Condens. Matter Mater. Phys.* **1993**, *47*, 4244.
(12) Csányi, G.; Arias, T. A. *Chem. Phys. Lett.* **2002**, *360*, 552.
(13) Yazyev, O. V.; Tavernelli, I.; Helm, L.; Röthlisberger, U. *Phys. Rev. B: Condens. Matter Mater. Phys.* **2005**, *71*, 115110.
(14) Bahramy, M. S.; Sluiter, M. H. F.; Kawazoe, Y. *Phys. Rev. B: Condens. Matter Mater. Phys.* **2006**, *73*, 045111.
(15) Declerck, R.; Pauwels, E.; Van Speybroeck, V.; Waroquier, M. *Phys. Rev. B: Condens. Matter Mater. Phys.* **2006**, *74*, 245103.
(16) Bühl, M.; Parrinello, M. *Chem.−Eur. J.* **2001**, *7*, 4487.
(17) Murakhtina, T.; Heuft, J.; Meijer, E. J.; Sebastiani, D. *Chem. Phys. Chem.* **2006**, *7*, 2578.
(18) Schmidt, J.; Sebastiani, D. *J. Chem. Phys.* **2005**, *123*, 074501.
(19) Blügel, S.; Akai, H.; Zeller, R.; Dederichs, P. H. *Phys. Rev. B: Condens. Matter Mater. Phys.* **1987**, *35*, 3271.
(20) Harriman, J. E. *Theoretical Foundations of Electron Spin Resonance*; Academic Press: New York, 1978.
(21) Granty, D. M.; Harris, K. M. *Encyclopedia of Nuclear Magnetic Resonance*; Wiley: Chicester, UK, 1996; Vol. 5.
(22) VandeVondele, J.; Krack, M.; Mohamed, F.; Parrinello, M.; Chassaing, T.; Hutter, J. *Comput. Phys. Commun.* **2005**, *167*, 103.
(23) http://cp2k.berlios.de (accessed June 1, 2007).
(24) Lippert, G.; Hutter, J.; Parrinello, M. *Theor. Chem. Acc.* **1999**, *103*, 124.
(25) Krack, M.; Parrinello, M. *Phys. Chem. Chem. Phys.* **2000**, *2*, 2105.
(26) Frisch, M. J.; Trucks, G. W.; Schlegel, H. B.; Scuseria, G. E.; Robb, M. A.; Cheeseman, J. R.; Montgomery, J. A., Jr.; Vreven, T.; Kudin, K. N.; Burant, J. C.; Millam, J. M.; Iyengar, S. S.; Tomasi, J.; Barone, V.; Mennucci, B.; Cossi, M.; Scalmani, G.; Rega, N.; Petersson, G. A.; Nakatsuji, H.; Hada, M.; Ehara, M.; Toyota, K.; Fukuda, R.; Hasegawa, J.; Ishida, M.; Nakajima, T.; Honda, Y.; Kitao, O.; Nakai, H.; Klene, M.; Li, X.; Knox, J. E.; Hratchian, H. P.; Cross, J. B.; Bakken, V.; Adamo, C.; Jaramillo, J.; Gomperts, R.; Stratmann, R. E.; Yazyev, O.; Austin, A. J.; Cammi, R.; Pomelli, C.; Ochterski, J. W.; Ayala, P. Y.; Morokuma, K.; Voth, G. A.; Salvador, P.; Dannenberg, J. J.; Zakrzewski, V. G.; Dapprich, S.; Daniels, A. D.; Strain, M. C.; Farkas, O.; Malick, D. K.; Rabuck, A. D.; Raghavachari, K.; Foresman, J. B.; Ortiz, J. V.; Cui, Q.; Baboul, A. G.; Clifford, S.; Cioslowski, J.; Stefanov, B. B.; Liu, G.; Liashenko, A.; Piskorz, P.; Komaromi, I.; Martin, R. L.; Fox, D. J.; Keith, T.; Al-Laham, M. A.; Peng, C. Y.; Nanayakkara, A.; Challacombe, M.; Gill, P. M. W.; Johnson, B.; Chen, W.; Wong, M. W.; Gonzalez, C.; Pople, J. A. *Gaussian 03*, Revision 05; gaussian, Inc.: Wallingford, CT, 2004.
(27) Madden, K. P.; Bernard, W. A. *J. Phys. Chem.* **1979**, *83*, 2643.
(28) Madden, K. P.; Bernard, W. A. *J. Phys. Chem.* **1982**, *86*, 4033.
(29) Vanhaelewyn, G. C. A. M.; Pauwels, E.; Callens, F. J.; Waroquier, M.; Sagstuen, E.; Matthys, P. F. A. E. *J. Phys. Chem. A* **2006**, *110*, 2147.
(30) Pauwels, E.; Van Speybroeck, V.; Vanhaelewyn, G.; Callens, F.; Waroquier, M. *Int. J. Quant. Chem.* **2004**, *99*, 102.
(31) Brown, G. M.; Levy, H. A. *Acta Crystallogr., B* **1979**, *35*, 656.
(32) Takagi, S.; Jeffrey, G. A. *Acta Crystallogr., B* **1997**, *33*, 3510.
(33) Becke, A. D. *Phys. Rev. A: At., Mol., Opt. Phys.* **1988**, *38*, 3098.
(34) Lee, C.; Yang, W.; Parr, R. G. *Phys. Rev. B: Condens. Matter Mater. Phys.* **1988**, *37*, 785.
(35) Godbout, N.; Salahub, D. R.; Andzelm, J.; Wimmer, E. *Can. J. Chem.* **1992**, *70*, 560.
(36) Lippert, G.; Hütter, J.; Ballone, P.; Parrinello, M. *J. Phys. Chem.* **1996**, *100*, 6231.
(37) Goedecker, S.; Teter, M.; Hutter, J. *Phys. Rev. B: Condens. Matter Mater. Phys.* **1996**, *54*, 1703.
(38) Hartwigsen, C.; Goedecker, S.; Hutter, J. *Phys. Rev. B: Condens. Matter Mater. Phys.* **1998**, *58*, 3641.
(39) Stewart, J. J. P. *J. Comp. Chem.* **1989**, *10*, 209.
(40) Stewart, J. J. P. *J. Comp. Chem.* **1989**, *10*, 221.
(41) Maseras, F.; Morokuma, K. *J. Comp. Chem.* **1995**, *16*, 1170.
(42) Svensson, M.; Humbel, S.; Froese, R. D. J.; Matsubara, T.; Sieber, S.; Morokuma, K. *J. Phys. Chem.* **1996**, *100*, 19357.
(43) Humbel, S.; Sieber, S.; Morokuma, K. *J. Chem. Phys.* **1996**, *105*, 1959.
(44) Matsubara, T.; Sieber, S.; Morokuma, K. *Int. J. Quantum Chem.* **1996**, *60*, 1101.
(45) Dapprich, S.; Komaromi, I.; Byun, K. S.; Morokuma, K.; Frisch, M. J. *J. Mol. Struct. (THEOCHEM)* **1999**, *461*, 1.
(46) Van, de Walle, C. G.; Blöchl, P. *Phys. Rev. B: Condens. Matter Mater. Phys.* **1993**, *47*, 4244.
(47) The isotropic HFPs of Gluc/R1/HO6, Gluc/R2/HO3, and Fruc/R1/HO3 were not taken up in this selection because their reference isotropic HFPs are too small (in absolute value) and disturb the relative fluctuations to an unrealistic extent.
(48) Barone, V.; Adamo, C.; Grand, A.; Subra, R. *Chem. Phys. Lett.* **1995**, *242*, 351.
(49) Barone, V.; Minichino, C.; Grand, A.; Subra, R. *J. Chem. Phys.* **1993**, *99*, 6787.
(50) Barone, V.; Grand, A.; Minichino, C.; Subra, R. *J. Phys. Chem.* **1993**, *97*, 6355.
(51) Martyna, G. J.; Klein, M. L.; Tuckerman, M. *J. Chem. Phys.* **1992**, *97*, 2635.
(52) Erling, P. A.; Nelson, W. H. *J. Phys. Chem. A* **2004**, *108*, 7591.
(53) Improta, R.; Barone, V. *Chem. Rev.* **2004**, *104*, 1231.
(54) Perdew, J. P.; Burke, K.; Ernzerhof, M. *Phys. Rev. Lett.* **1996**, *77*, 3865.
(55) Luchsinger, R. H.; Zhou, Y.; Meier, P. F. *Phys. Rev. B: Condens. Matter Mater. Phys.* **1997**, *55*, 6927.
(56) Porter, A. R.; Towler, M. D.; Needs, R. J. *Phys. Rev. B: Condens. Matter Mater. Phys.* **1999**, *60*, 13534.
(57) Marx, D.; Parrinello, M. *J. Chem. Phys.* **1996**, *104*, 4077.
(58) VandeVondele, J.; Mohamed, F.; Krack, M.; Hutter, J.; Sprik, M.; Parrinello, M. *J. Chem. Phys.* **2005**, *122*, 014515.
(59) Pauwels, E.; Declerck, R.; Van Speybroeck, V.; Waroquier, M. *Radiat. Res.*, in press.

8 Paper VII

Insight into the solvation and isomerization properties of 3-halo-1-azaallylic anions from ab initio metadynamics calculations and NMR experiments

R. Declerck, B. De Sterck, T. Verstraelen, G. Verniest, S. Mangelinckx, J. Jacobs, N. De Kimpe, M. Waroquier, and V. Van Speybroeck

Submitted to Chemistry A European Journal (June 2008), in revision

CHEMISTRY
A EUROPEAN JOURNAL

COMMUNICATION

DOI: 10.1002/chem.200((will be filled in by the editorial staff))

Insight into the solvation and isomerization of 3-halo-1-azaallylic anions from ab initio metadynamics calcualtions and NMR experiments

Reinout Declerck,[a] Bart De Sterck,[a] Toon Verstraelen,[a] Guido Verniest,[b] Sven Mangelinckx,[b] Jan Jacobs,[b] Norbert De Kimpe,*[b] Michel Waroquier[a] and Veronique Van Speybroeck*[a]

In organic synthesis, it is observed experimentally that the nature of the solvent can influence tremendously the reactivity and overall product selectivity. In this communication, we report on the E/Z isomerization of a typical solvated species, i.e. the stable lithiated 3-chloro-3-methyl-1-azaallylic anion readily accessible from the N-isopropylimine of α-chloropropiophenone, from a theoretical and a subsequent NMR study. It will be shown that the investigated species is a particular example in which the inclusion of the solvent in the modeling study, is of the utmost importance to determine the proper chemical behavior.

The 3-chloro-3-methyl-1-azaallylic anion was chosen as a model compound to obtain a deeper insight into the structural features of 3-halo-1-azaallylic anions and to get a better understanding, and eventually a better control, of the stereochemical outcome of the reactions in which these anions are involved. Since their first use in the early 1960s,[1-3] 1-azaallylic anions have gained a predominant role in organic synthesis due to their ability to form new C-C bonds with a lack of side products.[4] The chemistry of 1-azaallylic anions leads to basic heterocyclic systems such as aziridines, azetidines, pyrrolidines, pyrroles, piperidines, oxiranes, oxolanes,… and higher functionalized ring systems, currently of interest for the pharmaceutical chemistry and agrochemistry. The application of certain halogenated counterparts, i.e. the 3-chloro-3-methyl-1-azaallylic anions, in sensu stricto by the group of De Kimpe and in sensu largo by the group of Florio, which incorporated the 3-chloro-3-methyl-1-azaallylic moiety into heterocyclic structures, has led to the synthesis of various important classes of compounds such as cyclopropanes,[5] tetrahydrofurans,[6] tetrahydropyrans,[6c] oxiranes,[7] aziridines,[7b,d,8]

[a] Ir. R. Declerck, Ir. B. De Sterck, Ir. T. Verstraelen, Prof. Dr. M. Waroquier, Prof. Dr. Ir. V. Van Speybroeck
Center for Molecular Modeling
Ghent University, Proeftuinstraat 86, B-9000 Gent, Belgium
Fax: (+32) 9 264 66 97
E-mail: Veronique.VanSpeybroeck@UGent.be

[b] Dr. Ir. G. Verniest, Dr. Ir. S. Mangelinckx, Ir. J. Jacobs, Prof. Dr. Ir. N. De Kimpe
Department of Organic Chemistry, Faculty of Bioscience Engineering, Ghent University,Coupure links 653, B-9000 Gent, Belgium
E-mail: Norbert.DeKimpe@UGent.be

Supporting information for this article is available on the WWW under http://www.chemeurj.org/ or from the author.

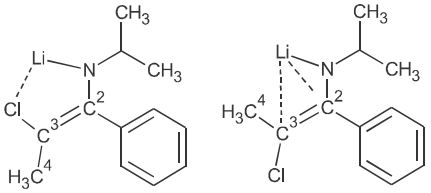

Figure 1. Z isomer 1 and E isomer 2 of the lithiated (2-chloro-1-phenylprop-1-en-1-yl)isopropylamide anion.

chloroimines,[9] pyrroles and pyridines,[10] steroids,[11] alkenylheterocycles,[12] and oxazetidines.[13] As mentioned, 3-chloro-3-methyl-1-azaallylic anions can be used for the synthesis of functionalized oxiranes and aziridines since the former anions behave as nucleophiles in Darzens- and aza-Darzens-type reactions with carbonyl compounds and imines.[7,8] One of the determining factors in the stereochemical outcome of these Darzens-type reactions is the E/Z-stereochemistry of the starting 1-azaallylic anion.[14] Therefore, it is important to know and understand the configurational properties of 3-chloro-3-methyl-1-azaallylic anions in order to perform aldol- and Mannich-type reactions with these intermediates in a stereocontrolled manner. NMR investigation and semiemperical calculations on the stereochemistry of (2-(α-chloroethyl)benzothiazolyl)lithium and (4,4-dimethyl-2-(α-chloroethyl)oxazolinyl)lithium have demonstrated that internal coordination between lithium and chlorine stabilizes the corresponding isomer with nitrogen and chlorine at the same side of the C-C-double bond.[15] The lack of such structural investigations on 3-chloro-3-methyl-1-azaallylic anions in sensu stricto urged us to study their stereochemical properties.

The E/Z isomerism for non-halogenated 1-azaallylic anions has been observed and investigated quite frequently. The facile carbon-carbon bond rotation in simple lithiated 1-azaallylic anions was investigated using 1H NMR.[16] The rotational activation free energy was found to be 74.1 ± 1.3 kJ/mol at 313 K. E/Z isomerization was also observed upon deprotonation of ketimines of 2-butanone at room temperature.[17] For closely related non-chlorinated analogues of the species 1-2 in Figure 1, i.e. the lithiated anion derived

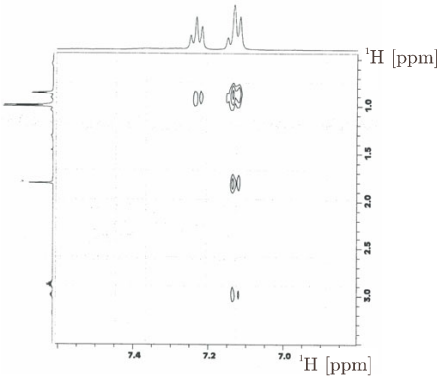

Figure 2. Detail of the Off-resonance ROESY spectrum of the Z isomer 1 of the lithiated 3-chloro-1-azaallylic anion ([D]$_8$THF). The resonance signals at 0.96 ppm (doublet) and 2.84 ppm (septet) are from diisopropylamine formed upon protonation of LDA.

from the N-phenylimine of propiophenone, isomerization from the kinetically favored E isomer with the methyl group and the phenyl group at the same side of the C2-C3-double bond (like in Z isomer 1) to the thermodynamically most stable Z isomer with the methyl group and nitrogen at the same side of the C2-C3-double bond (like in E isomer 2), was observed.[18] Therefore, it was assumed that the lithiated 3-chloro-1-azaallylic anions of the present work could also undergo a similar type of isomerization.

At first instance, the lithiated 3-chloro-3-methyl-1-azaallylic anion was generated by deprotonation of N-(2-chloro-1-phenylpropylidene)isopropylamine with lithium diisopropylamide (LDA) in [D]8THF at 273 K and analyzed by 1H and 13C NMR. The α-chloropropiophenone imine was deprotonated under these conditions to a single stereoisomer as demonstrated by the presence of a single set of characteristic 1H NMR chemical shifts of the methyl group on the double bond (s, 1.77 ppm), methine function (septet, 2.96 ppm) and isopropyl methyl groups (d, 0.83 ppm). Also a single set of characteristic 13C NMR chemical shifts of the lithiated 3-chloro-1-azaallylic anion were observed (see supporting information). The stereochemistry of the Z anion 1 was determined by Off-resonance ROESY spectroscopy showing ROE effects between the methyl group and the ortho-protons of the phenyl ring positioned at the same side of the carbon-carbon double bond (Figure 2). Furthermore, the observed ROE effects between the N-isopropyl substituent and the phenyl group support the anti stereochemistry of the 3-chloro-1-azaallylic anion, i.e. the N-isopropyl group is oriented anti with respect to the C2-C3 double bond. In contrast to the non-chlorinated species,[18] the aforementioned NMR experiments indicate that in THF only the Z/anti isomer 1 occurs and that both amide and C-C double bond rotations are inhibited. This particular behavior of chlorinated 1-azaallylic anions demanded a theoretical interpretation.

Despite the huge amount of theoretical studies that appeared the last years, modeling of complex phenomena such as chemistry in liquids remains a challenge as standard optimization techniques and ab initio molecular dynamics methods are often not suitable.[19,20] The first set of methods is routinely performed nowadays, but for our systems in which the solvent participates actively, a single optimized structure

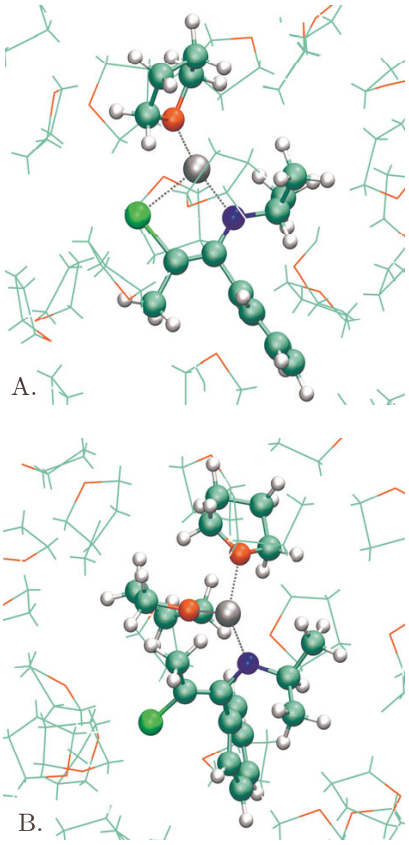

Figure 3. Characteristic snapshot of the MD simulation of the (A) Z isomer **1** and (B) the E isomer **2** solvated in THF.

does not resemble the configurational distribution at finite temperature. First-principles molecular dynamics simulations are often restricted by short simulation times. As such, interesting regions of phase space are often so high in free energy that their sampling during a standard MD simulation is a rare event. Enhanced sampling techniques have become an active research domain.[20] The relatively new metadynamics method has particularly attracted our attention. It was first proposed by Laio and Parrinello and enables an enhanced sampling of separated regions in phase space, simultaneously mapping the underlying free energylandscape as a function of a limited number of collective variables.[21]

Prior to the modeling of the azaallylic anions, we modeled the liquid structure of pure THF by using first-principles molecular dynamics calculations. The liquid structure of THF was recently assessed via hydrogen/deuterium isotopic

substitution neutron diffraction techniques by Bowron, Finney and Soper.[22] A periodic cubic simulation cell was filled with 64 THF molecules. This choice is the result of extensive testing, and represents an optimal compromise between computational cost and accuracy. The simulation cell size was chosen to correspond with the experimental density of 0.88 kg/dm3.[23] The performance of the THF model was validated by calculating the radial distribution function (RDF) of the molecular centers, which was found to be in excellent agreement with the benchmark RDF reported in reference [22] (see Supporting Information). Moreover, the MD simulations yielded a conformational distribution of 59% twisted and 41% oxygen envelope, indicating a thorough sampling of the system. [22]

The THF model being successfully assessed, it was applied to study the degree of coordination of the 3-chloro-1-azaallylic anions in solution. The coordination number for lithium enolates in ethereal solvents is rather difficult to establish but four-coordinate lithium cations have been clearly recognized in NMR studies of solvent separated ion pairs.[24] For contact ion pairs, coordination is expected less important because of the electrostatic effect of the counter ion. Theoretically the structures of a variety of organic lithium compounds were determined in the gas phase and in solvation using microsolvation with explicit ethereal ligands and/or continuum models.[25] For the 1-azaallylic anions as encountered here which are subject to large steric crowding, the degree of coordination is not a priori clear and can not be deduced straightforwardly from the experimental data. Isothermal-isobaric (NPT) molecular dynamics simulations during a period of 2.5 ps show that the Z isomer 1 is monocoordinated whereas the E isomer 2 features a two-fold coordination with THF (illustrated in figure 3). In the E-isomer 2 the halogen-lithium coordination is not present which allows a second THF molecule to coordinate with the counter ion.

In order to obtain insight into the occurrence of only one stereoisomer in case of 3-chloro-3-methyl-1-azaallylic anions 1 and 2, we decided to construct the free energy landscape connecting the basins of the two isomers. To this end we applied the metadynamics method in which the dihedral angles Cl-C3-C2-N and C4-C3-C2-N were chosen as collective variables. This choice guarantees the independent movement of the methyl and chlorine substituents. The resulting free energy landscape as a function of the two dihedral angles is displayed in Figure 4. The Gibbs free energy barriers for E-to-Z and Z-to-E isomerization amount to 107.1 ± 12.1 kJ/mol and 128.6 ± 12.1 kJ/mol, respectively.[26] These barriers are high, preventing isomerization at the experimental temperature. The Z isomer 1 is more stable than the E isomer 2 by ΔGZ-E = 21.5 ± 12.1 kJ/mol, which indicates that the experimentally observed Z isomer 1 is thermodynamically favored. Within a static cluster approach using a combined explicit/implicit solvent model we were unable to determine the transition state for E/Z isomerization as the coordination number varies during the chemical transformation. Moreover the stability of the Z isomer 1 with respect to the E isomer 2 was 20 kJ/mol too high compared to the metadynamics calculations. Finally, reflecting the sp2 to sp3 hybridization transition of the C3 carbon atom upon rotation, the saddle point, denoted as (E-Z)‡, does not lie on the linear pathway connecting both isomers, which confirms a posteriori the importance of capturing the independent movement of both dihedral angles.

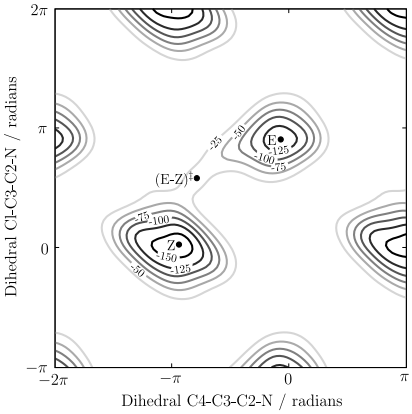

Figure 4. Gibbs free energy profile (in kJ/mol) governing the E-Z isomerization of the lithiated 3-chloro-1-azaallylic anion in THF. The positions of both stable isomers E (**2**) and Z (**1**) and the saddle point (E-Z)‡ are added. Note that the two collective variables feature a 2π-periodicity.

Finally, we conclude that the stereochemistry of 3-chloro-3-methyl-1-azaallylic anions is manifestly different compared to their non-chlorinated counterparts. For the non-chlorinated species, isomerization between the Z and E configuration occurs readily whereas, for the lithiated 3-chloro-3-methyl-1-azaallylic anions, only one configuration is present, as observed in NMR experiments. The contact between the metal and the halogen determines the stereochemistry of the azaenolate and degree of coordination. First-principles metadynamics simulations were able to unravel these effects. In case of the Z configured 3-chloro-3-methyl-1-azaallylic anion, only one THF molecule coordinates with the metal cation. In the transition between the two isomers the coordination number changes as the lithium-chlorine coordination is broken. The interaction between the counter ion and the halogen, an effect that is not present in the non-halogenated azaenolates, stabilizes the Z isomer by about 20 kJ/mol. This configurational stability of 3-chloro-3-methyl-1-azallylic anions should be beneficial during their synthetic use as functionalized intermediates in stereoselective reactions.

Experimental Section

All molecular dynamics calculations were performed within the cp2k/quickstep code,[27] employing the Gaussian and plane-wave (GPW) density functional method and periodic boundary conditions. A BLYP[28] gradient-corrected functional was used throughout, together with a TZVP-PSP[29] basis set, a 400 Ry cutoff for the auxiliary plane wave grid, and pseudopotentials developed by Goedecker and co-workers.[30] Isothermal-isobaric (NPT) MD simulations of both isomers were conducted. The species were properly embedded in the THF solvent model by determining, using atomic Pauling radii, the volume associated with their solvent accessible surface.[31] As the volume of THF is 2.96 times smaller compared to the volume of the 3-chloro-1-azaallylic anion, three THF molecules in the simulation cell were replaced by the 3-chloro-1-azaallylic species. An equilibration time of 2.5 ps has been respected to allow the solvent to accommodate to the presence of the solute and vice versa, followed by a 40 ps metadynamics run. Accurate metadynamics parameter values were determined from Gibbs free energy barrier predictions of the lithiated 3-chloro-1-azaallylic anion in the gas phase (using a supercell approach), including only one THF molecule to impose the limited freedom of the lithium cation. The set of parameter values w = 2.0 kJ/mol, s = 0.33 rad and G = 50 fs (Notation: see Ref. [21]) yielded an energy barrier within 1.0 kJ/mol of the convergence limit. According to Ref. [26], the estimated error using these parameters is ε = 6.1 kJ/mol.

Synthesis of the lithiated 3-chloro-1-azaallylic anion 1: To a stirred solution of diisopropylamine (0.056 g, 0.55 mmol) in [D]8THF (1 mL), nBuLi (0.22 mL, 0.55 mmol, 2.5 N in hexanes) was added slowly at 273 K. After 30 minutes of stirring at 273 K, the solution was evaporated in vacuo to dryness, after which, [D]8THF (0.5 mL) was added and a solution of N-(2-chloro-1-phenylpropylidene)isopropylamine

(0.11 g, 0.5 mmol) in 0.5 mL of [D]8THF was dropped to the LDA solution at 273 K and stirring was continued for 1 h. Subsequently, the reaction mixture was allowed to reach room temperature during 15 min. 1H NMR (300 MHz) and 13C NMR (75 MHz) spectra were taken from the prepared 3-chloro-1-azaallylic anion 1 at room temperature. 1H NMR ([D]8THF, 300 MHz): δ 0.83 (d, 6H, J = 6.33 Hz, (CH3)2CH), 1.77 (s, 3H, CH3), 2.96 (septet, 1H, J = 6.1 Hz, (CH3)2CH), 7.08-7.14 (m, 3H, o-CHar and p-CHar), 7.18-7.24 (m, 2H, m-CHar). 13C NMR ([D]8THF, 75 MHz): □22.3, 28.1, 48.6, 83.6, 125.9, 127.6, 130.0, 144.0, 155.0.

Keywords: isomerization – molecular dynamics- solvent effects- NMR spectroscopy – azo compounds – metadynamics – tetrahydrofuran

[1] G. Stork, S. R. Dowd, *J. Am. Chem. Soc.* **1963**, 85, 2178-2180.

[2] G. Wittig, H. D. Fommeld, P. Suchanek, Angew. Chem. **1963**, 75, 978-979.

[3] G. Wittig, H. Reiff, Angew. *Chem., Int. Ed. Engl.* **1968**, **7**, 7-14.

[4] S. Mangelinckx, N. Giubellina, N. De Kimpe, *Chem. Rev.* **2004**, 104, 2353-2400 and references therein.

[5] a) N. De Kimpe, P. Brunet, R. Verhé, N. Schamp, J. Chem. Soc., *Chem. Commun.* **1988**, 825-827; b) W. Aelterman, K. Abbaspour Tehrani, W. Coppens, T. Huybrechts, N. De Kimpe, D. Tourwé, J.-P. Declercq, *Eur. J. Org. Chem.* **1999**, 239-250; c) V. Capriati, S. Florio, R. Luisi, M. T. Rocchetti, *J. Org. Chem.* 2002, **67**, 759-763; d) S. Florio, F. M. Perna, R. Luisi, J. Barluenga, F. Rodríguez, F. J. Fañanás, *J. Org. Chem.* **2004**, 69, 5480-5482.

[6] a) N. De Kimpe, E. Stanoeva, N. Schamp, *Tetrahedron Lett.* 1988, **29**, 589-592; b) N. De Kimpe, W. Aelterman, K. De Geyter, J.-P. Declercq, *J. Org. Chem.* **1997**, 62, 5138-5143; c) W. Aelterman, N. Giubellina, E. Stanoeva, K. De Geyter, N. De Kimpe, *Tetrahedron Lett.* **2004**, 45, 441-444.

[7] a) P. Sulmon, N. De Kimpe, N. Schamp, J.-P. Declercq, B. Tinant, *J. Org. Chem.* **1988**, 53, 4457-4462; b) V. Capriati, L. Degennaro, S. Florio, R. Luisi, C. Tralli, L. Troisi, *Synthesis* **2001**, 2299-2306; c) F. M. Perna, V. Capriati, S. Florio, R. Luisi, *J. Org. Chem.* **2002**, 67, 8351-8359; d) F. Bona, L. De Vitis, S. Florio, L. Ronzini, L. Troisi, *Tetrahedron* **2003**, 59, 1381-1387; e) L. Troisi, L. De Vitis, C. Granito, P. Metrangolo, T. Pilati, L. Ronzini, *ARKIVOC* **2004**, xiv, 61-73.

[8] a) R. Luisi, V. Capriati, S. Florio, R. Ranaldo, Tetrahedron Lett. **2003**, 44, 2677-2681; b) L. De Vitis, S. Florio, C. Granito, L. Ronzini, L. Troisi, V. Capriati, R. Luisi, T. Pilati, *Tetrahedron* **2004**, 60, 1175-1182; c) R. Luisi, V. Capriati, S. Florio, P. Di Cunto, B. Musio, Tetrahedron **2005**, 61, 3251-3260; d) L. Troisi, C. Granito, C. Carlucci, F. Bona, S. Florio, *Eur. J. Org. Chem.* **2006**, 775-781.

[9] P. Sulmon, N. De Kimpe, N. Schamp, *Synthesis* **1989**, 8-12.

[10] W. Aelterman, N. De Kimpe, V. Tyvorskii, O. Kulinkovich, *J. Org. Chem.* **2001**, 66, 53-58.

[11] L. Troisi, S. Florio, C. Granito, *Steroids* **2002**, 67, 687-693.

[12] V. Capriati, L. Degennaro, S. Florio, R. Luisi, *Eur. J. Org. Chem.* **2002**, 2961-2969.

[13] R. Luisi, V. Capriati, S. Florio, E. Piccolo, *J. Org. Chem.* **2003**, 68, 10187-10190.

[14] V. K. Aggarwal, D. M. Badine, V. A. Moorthie in *Aziridines and Epoxides in Organic Synthesis* (Ed.: A. K. Yudin), Wiley-VCH, Weinheim, **2006**, pp. 1–35.

[15] A. Abbotto, S. Bradamante, S. Florio, V. Capriati, *J. Org. Chem.* **1997**, 62, 8937-8940.

[16] J. Y. Lee, T. J. Lynch, D. T. Mao, D. E. Bergbreiter, M. Newcomb, *J. Am. Chem. Soc.* **1981**, 103, 6215-6217.

[17] J. K. Smith, D. E. Bergbreiter, M. Newcomb, J. Org. Chem. **1981**, 46, 3157-3158.

[18] R. Knorr, P. Low, *J. Am. Chem. Soc.* **1980**, 102, 3241-3242.

[19] a) A. V. Marenich, R. M. Olson, A. C. Chamberlin, C. J. Cramer, D. G. Truhlar, *J. Chem. Theory Comput.* **2007**, 3, 2055-2067. b) C. P. Kelly, C. J. Cramer, D. G. Truhlar, *J. Chem. Theory Comput.* **2005**, 1, 1133-1152. c) J. Tomasi, M. Persico, *Chem. Rev.* **1994**, 94, 2027-2094.

[20] B. Ensing, M. De Vivo, Z. Liu, P. Moore, M. L. Klein, *Acc. Chem. Res.* **2006**, 39, 73-81.

[21] A. Laio, M. Parrinello, *Proc. Natl. Acad. Sci. U.S.A.* **2002**, 99, 12562-12566.

[22] a) D. T. Bowron, J. L. Finney, A. K . Soper, J. Am. Chem. Soc. **2006**, 128, 5119-5126; b) M. Strajbl, J. Florian., *Theor. Chem.* Acc. **1998**, 99, 166-170; c) V. M. Rayon, J. A. Sordo, *J. Chem. Phys.* **2005**, 122, 204303.

[23] a) D. R. Lide in CRC Handbook of Chemistry and Physics, 84th edition (Eds: Crc Press Llc), Wiley, Chicester, **2003**; b) C. Carvajal, K. J. Tölle, J. Smid, M. Szwarc, *J. Am. Chem. Soc.* **1965**, 87, 5548–5553.

[24] a) L. M. Pratt, N. Văn Nguyên, B. Ramachandran, *J. Org. Chem.* **2005**, 70, 4279-4283; b) L. M. Pratt, B. Ramachandran, J. D. Xidos, C. J. Cramer, D. G. Truhlar, *J. Org. Chem.* **2002**, 67, 7607-7612. c) P. L. Fast, M. L. Sanchez, D. G. Truhlar, *Chem. Phys. Lett.* **1999**, 306, 407-410. d) J. A. Pople, M. Head-Gordon, K. Raghavachari, *J. Chem. Phys.* **1987**, 87, 5968-5975.

[25] a) L. M. Pratt, A. Streitwieser, *J. Org. Chem.* 2003, **68**, 2830-2838. b) V. Van Speybroeck, K. Moonen, K. Hemelsoet, C. V. Stevens, M. Waroquier, *J. Am. Chem. Soc.* **2006**, 128, 8468-8478.

[26] A. Laio, A. Rodriguez-Fortea, F. L. Gervasio, M. Ceccarelli, M. Parrinello. *J. Phys. Chem. B* **2005**, 109, 6714–6721.

[27] http://cp2k.berlios.de

[28] a) A. D. Becke, *Phys. Rev. A* **1988**, 38, 3098-3100; b) C. Lee, W. Yang, R. G. Parr, *Phys. Rev. B* **1988**, 37, 785-789.

[29] G. Lippert, J. Hutter, P. Ballone, M. Parrinello, *J. Phys.Chem.* **1996**, 100, 6231-6235.

[30] a) S. Goedecker, M. Teter, J. Hutter, *Phys. Rev. B* **1996**, 54, 1703-1710; b) C. Hartwigsen, S. Goedecker, J. Hutter, *Phys. Rev. B* **1998**, 58, 3641-3662.

[31] a) J. Tomasi, B. Mennucci, R. Cammi, *Chem. Rev.* **2005**, 105, 2999–3093; b) Y. Takano, K. N. Houk, J. Chem. Theory Comput. **2005**, 1, 70–77.

Received: ((will be filled in by the editorial staff))
Revised: ((will be filled in by the editorial staff))
Published online: ((will be filled in by the editorial staff))

9 Paper VIII

Magnetic linear response properties calculations with the Gaussian and augmented-plane-wave method

V. Weber, R. Declerck, M. Iannuzzi, M. Waroquier, J. Hutter, ...

First draft (June 2008)

APS/123-QED

Magnetic linear response properties calculations with the Gaussian and augmented-plane-wave method

V. Weber, J. Hutter, and ...*
Univ Zurich, Inst Phys Chem, Winterthurerstr 190, CH-8057 Zurich, Switzerland

R. Declerck, M. Waroquier, and ...†
Center for Molecular Modeling, Ghent University, Proeftuinstraat 86, B-9000 Gent, Belgium

M. Iannuzzi and ...‡
Paul Scherrer Inst, CH-5232 Villigen, Switzerland
(Dated: September 2, 2008)

...

PACS numbers: XX.XX.XX, XX.XX.XX

I. INTRODUCTION

Nuclear magnetic resonance (NMR) and electron paramagnetic resonance (EPR) are two of the most powerful spectroscopic techniques, providing invaluable insights in the atomic structure of materials across a broad range of scientific disciplines. In recent years, there has been a growing interest in the ab-initio quantum mechanical calculation of the quantities extracted from NMR/EPR spectra within density functional theory[1,2] (DFT). A comprehensive overview of the various approaches in this field is given in Ref. 3. By comparing the experimental NMR/EPR quantities with those computed from proposed molecular models, it is possible to identify and understand the molecular structure. In particular, the possibility to derive structure/spectroscopic correlations from eg. molecular dynamics provides a basis for determining numerous aspects of the molecular structure and its related properties, such as for example chemical bonding and consequently chemical reactions, which are not readily accessible from experiment.

However, many interesting scientific problems that would potentially benefit from a theoretical NMR/EPR study involve simulations that easily require many thousands of atoms, such as nanostructures, interfaces, molecular liquids, and complex biomolecules in their natural environment. Only recently have systems of such size become accessible to a quantum mechanical description, due to the combined benefits of increased computing power and algorithmic developments. One of the efforts in the latter field is the development of the freely available CP2K program package,[4] which provides state-of-the-art methods for the simulation of these systems, employing quantum mechanical – mainly DFT – methods (QM), classical molecular mechanics (MM), or a combination of both (QM/MM).

In CP2K, DFT calculations employing periodic boundary conditions (PBCs) are carried out by the Quickstep[5] module. One of the strongest features of this module is the Gaussian and augmented-plane-wave (GAPW) density functional method, which extends the Gaussian and plane-wave (GPW) variant. In the GAPW representation, the total electron density is the sum of a smooth, extended part represented in plane waves (PWs) and parts localized close to the nuclei that are expanded in periodic primitive Gaussian functions. The GAPW scheme exists in both a pseudopotential[6] (PSP) (using Goedecker-type[7,8] pseudopotentials) and an all-electron[9] (AE) implementation, and both approaches can be easily combined within one simulation.

In this paper, we introduce a GAPW method for the AE calculation of the NMR chemical shifts, the NMR magnetic susceptibility, and the EPR g tensor in PBC simulations. The approach is based on the Sebastiani method[10] which, next to the calculation of the chemical shifts and the magnetic susceptibility, was used also for the calculation of the g tensor.[11] The approach further extends the concepts of the GAPW representation to the electronic current densities induced by the external magnetic field, needed in the calculation of all of the aforementioned quantities. Through the use of a GAPW scheme, the mandatory usage of the pseudopotential approximation, one of the main obstacles in the original Sebastiani implementation, is finally lifted. To our knowledge, the GIPAW method[12,13] is the only other AE method (using a frozen-core approach) currently able to calculate these quantities in PBC simulations.

The structure of this paper is as follows: first, we will elaborate extensively on the theoretical aspects of our method. Then, using a supercell technique, the accuracy of the different quantities calculated with the present method will be evaluated, by comparison with established gas-phase methods for a wide range of atoms and small molecules in the gas phase. Finally, we will present two examplary applications for our method, one involving the calculation of the chemical shifts and the susceptibility in a large biomolecule, the other the calculation of the g tensor for the E_1' center in α-quartz using a 15551-atom simulation cell and a three-layered AE/PSP/MM approach.

II. THEORY

(Note that atomic units will be adopted throughout this paper.)

The components of the three quantities under consideration in this work, the chemical shift tensor σ corresponding with nucleus I, the susceptibility χ, and the g tensor (for systems with net electronic spin 1/2), can be evaluated through the following expressions:

$$\sigma_{I,xy} = \alpha \int_{\Omega_S} \mathrm{d}\mathbf{r} \left[\frac{\mathbf{r}-\mathbf{R}_I}{|\mathbf{r}-\mathbf{R}_I|^3} \times \mathbf{j}_{\mathbf{B}_x}(\mathbf{r}) \right]_y , \quad (1)$$

$$\chi_{xy} = \frac{2\pi\alpha}{\Omega} \int \mathrm{d}\mathbf{r} \left[\mathbf{r} \times \mathbf{j}_{\mathbf{B}_x}(\mathbf{r}) \right]_y , \quad (2)$$

$$g_{xy} = g^{\mathrm{Z}}_{xy} + \Delta g^{\mathrm{ZKE}}_{xy} + \Delta g^{\mathrm{SO}}_{xy} + \Delta g^{\mathrm{SOO}}_{xy} , \quad (3)$$

where:

$$g^{\mathrm{Z}}_{xy} = g_{\mathrm{e}} \delta_{xy} , \quad (4)$$

$$\Delta g^{\mathrm{ZKE}}_{xy} = -\alpha^2 g_{\mathrm{e}} (T^\alpha - T^\beta) \delta_{xy} , \quad (5)$$

$$\Delta g^{\mathrm{SO}}_{xy} = \alpha (g_{\mathrm{e}} - 1) \int \mathrm{d}\mathbf{r} \left[\mathbf{j}^\alpha_{\mathbf{B}_x}(\mathbf{r}) \times \nabla V^\alpha_{\mathrm{eff}}(\mathbf{r}) - \mathbf{j}^\beta_{\mathbf{B}_x}(\mathbf{r}) \times \nabla V^\beta_{\mathrm{eff}}(\mathbf{r}) \right]_y , \quad (6)$$

$$\Delta g^{\mathrm{SOO}}_{xy} = 2 \int \mathrm{d}\mathbf{r}\, B^{\mathrm{corr}}_{\mathbf{B}_x,y}(\mathbf{r}) [\rho^\alpha(\mathbf{r}) - \rho^\beta(\mathbf{r})] . \quad (7)$$

In Eqs. 1-7, α represents the fine-structure constant, $\mathbf{R}_I$ the position of the I-th nucleus, $\mathbf{j}_{\mathbf{B}_x}$ the current density induced from a unitary external magnetic field coinciding with the x axis (up to the terms linear in that external magnetic field), and Ω the volume of the integration domain. g_{e} denotes the free-electron g value, the superscript α the spin-up channel and T^α, $\mathbf{j}^\alpha_{\mathbf{B}_x}$, and ρ^α are the unperturbed kinetic energy, the induced current density, and the electron density of the spin-up channel, respectively. V^α_{eff} is an effective potential in which the spin-up electrons are thought to move, and will be defined below. Similar definitions apply to the spin-down channel, denoted with the superscript β. The integrals with subscript Ω_S span the entire space, the ones without just one simulation cell. The subscripts x and y iterate over all three Cartesian directions. $\mathbf{B}^{\mathrm{corr}}_{\mathbf{B}_x}$ respresents the magnetic field originating from the corresponding total induced current density $\mathbf{j}_{\mathbf{B}_x}$, which was corrected for self-interaction through substraction of $\mathbf{j}^\alpha_{\mathbf{B}_x} - \mathbf{j}^\beta_{\mathbf{B}_x}$:

$$\mathbf{B}^{\mathrm{corr}}_{\mathbf{B}_x}(\mathbf{r}) = \alpha \int_{\Omega_S} \mathrm{d}\mathbf{r}' \frac{\mathbf{r}'-\mathbf{r}}{|\mathbf{r}'-\mathbf{r}|^3} \times \left[\left(\mathbf{j}^\alpha_{\mathbf{B}_x}(\mathbf{r}') + \mathbf{j}^\beta_{\mathbf{B}_x}(\mathbf{r}') \right) - \left(\mathbf{j}^\alpha_{\mathbf{B}_x}(\mathbf{r}') - \mathbf{j}^\beta_{\mathbf{B}_x}(\mathbf{r}') \right) \right] . \quad (8)$$

It is readily apparent from Eqs. 1-8 that the induced current densities are a key ingredient in all of the three quantities. After a brief recapitulation of the essential ideas of the GAPW representation, we will therefore focus first on the determination of these current densities, before turning our attention to the actual evaluation of the involved quantities.

A. The GAPW representation

In the GAPW density functional method,[6,9] the electron density ρ is defined by its expansion in periodic atomic orbitals $\psi^{\mathrm{AO,P}}(\mathbf{r})$,

$$\rho(\mathbf{r}) = \sum_{kl} P_{kl} \psi^{\mathrm{AO,P}*}_k(\mathbf{r}) \psi^{\mathrm{AO,P}}_l(\mathbf{r}) , \quad (9)$$

with P_{kl} the density matrix. Each atomic orbital is a contracted periodic Gaussian function (CPGF), i.e. a fixed linear combination of (atom-centered) primitive Cartesian Gaussian functions χ^{P}_I.

In an arbitrary way, the simulation cell is now divided into non-overlapping, localized, spherical regions centered on the atomic nuclei, and the interstitial region. The underlying idea in GAPW is that the electron density varies smoothly in the interstitial region and is therefore easily representable in a PW basis, whereas the (heavily) oscillating electron density near the nuclei can be represented more efficiently in terms of localized functions. The GAPW representation of the electron density is the sum of three contributions:

$$\rho(\mathbf{r}) = \tilde{\rho}(\mathbf{r}) + \rho^1(\mathbf{r}) - \tilde{\rho}^1(\mathbf{r}) . \quad (10)$$

In the soft density $\tilde{\rho}$, the rapid variations of ρ close to the nuclei are removed by putting to zero the coefficients of the most localized Gaussian primitives, thus effectively using only a limited set $\tilde{\chi}^{\mathrm{P}}$, which consists of the primitives $\tilde{\chi}^{\mathrm{P}}_I$ corresponding with each nucleus I. $\tilde{\rho}$ becomes smooth — hence *soft*, as opposed to the real density ρ, which is called *hard* — and is distributed over all space, and can thus be represented by a relatively small auxiliary basis set of PWs:

$$\tilde{\rho}(\mathbf{r}) = \frac{1}{\Omega} \sum_{\frac{1}{2}|\mathbf{G}|^2 < E_{\mathrm{c}}} \tilde{\rho}(\mathbf{G}) \mathrm{e}^{i\mathbf{G}.\mathbf{r}} . \quad (11)$$

The other densities,

$$\rho^1(\mathbf{r}) = \sum_I \rho^1_I(\mathbf{r}) , \qquad \tilde{\rho}^1(\mathbf{r}) = \sum_I \tilde{\rho}^1_I(\mathbf{r}) , \quad (12)$$

are the sum of local atom-centered densities ρ^1_I and $\tilde{\rho}^1_I$ which are hard and soft, respectively. ρ^1_I and $\tilde{\rho}^1_I$ are constructed through a projection of ρ and $\tilde{\rho}$ onto the primitive Gaussian functions χ^{P}_I and $\tilde{\chi}^{\mathrm{P}}_I$, respectively, corresponding with atomic nucleus I.

By construction ρ, $\tilde{\rho}$, ρ_I^1 and $\tilde{\rho}_I^1$ satisfy the following relations:

$$\rho(\mathbf{r}) - \tilde{\rho}(\mathbf{r}) = 0 \qquad \text{for } \mathbf{r} \in U_0 \,, \tag{13}$$
$$\rho_I^1(\mathbf{r}) - \tilde{\rho}_I^1(\mathbf{r}) = 0 \qquad \text{for } \mathbf{r} \in U_0 \,, \tag{14}$$
$$\tilde{\rho}(\mathbf{r}) - \tilde{\rho}_I^1(\mathbf{r}) = 0 \qquad \text{for } \mathbf{r} \in U_I \,, \tag{15}$$
$$\rho(\mathbf{r}) - \rho_I^1(\mathbf{r}) = 0 \qquad \text{for } \mathbf{r} \in U_I \,, \tag{16}$$

where U_I denotes the spherical region (with a specified radius) around each atomic nucleus I, and U_0 the interstitial region outside these atomic regions. In this way, Eq. 10 is fulfilled in the entire space.

B. Calculation of the induced current densities

(For notational accuracy, we will distinguish (in this section only) between a position operator $\mathbf{r}$ and a position variable $\tilde{\mathbf{r}}$.)

In general, the current density is obtained as the expectation value of the current operator in the total electronic state:

$$\mathbf{j}(\tilde{\mathbf{r}}) = -\frac{1}{2} \langle \Psi | \left[\boldsymbol{\pi} | \tilde{\mathbf{r}} \rangle \langle \tilde{\mathbf{r}} | + | \tilde{\mathbf{r}} \rangle \langle \tilde{\mathbf{r}} | \boldsymbol{\pi} \right] | \Psi \rangle \,, \tag{17}$$

where:

$$\boldsymbol{\pi} = \mathbf{p} + \alpha \mathbf{A}(\mathbf{r}) \,, \tag{18}$$

with $\mathbf{A}$ the vector potential of the magnetic field $\mathbf{B}$. The vector potential for a constant magnetic field equals:

$$\mathbf{A}(\mathbf{r}) = -\frac{1}{2}(\mathbf{r} - \mathbf{R}_\mathrm{g}) \times \mathbf{B} \,, \tag{19}$$

with $\mathbf{R}_\mathrm{g}$ the gauge origin of the vector potential.

The current density originating from n (non-interacting) one-electron states ψ_i, such as for example the Kohn-Sham eigenstates, is obtained from the sum of the current densities from each electron separately:

$$\mathbf{j}(\tilde{\mathbf{r}}) = -\frac{1}{2} \sum_i \langle \psi_i | \left[\boldsymbol{\pi} | \tilde{\mathbf{r}} \rangle \langle \tilde{\mathbf{r}} | + | \tilde{\mathbf{r}} \rangle \langle \tilde{\mathbf{r}} | \boldsymbol{\pi} \right] | \psi_i \rangle \,. \tag{20}$$

It is assumed henceforth that Eq. 20 represents a good approximation for Eq. 17. The one-electron orbitals can be expanded in a power series of the magnetic field:

$$\psi_i(\mathbf{r}) = \psi_i^{(0)}(\mathbf{r}) + B\psi_i^{(1)}(\mathbf{r}) + B^2\psi_i^{(2)}(\mathbf{r}) + \ldots \,. \tag{21}$$

Within the Γ-point approximation (in which only one wave vector, $\mathbf{k} = \mathbf{0}$, is approximated to represent the entire first Brillouin zone), and with a perturbation originating from a unitary external magnetic field, it is possible to choose $\psi_i^{(0)}$ and $\psi_i^{(1)}$ as purely real and imaginary, respectively. If we then develop the current density in a power series of the magnetic field, we find that the current density up to first order in the magnetic field consists of a diamagnetic (D) and a paramagnetic (P) component:

$$\mathbf{j}(\tilde{\mathbf{r}}) = \mathbf{j}_\mathrm{D}(\tilde{\mathbf{r}}) + \mathbf{j}_\mathrm{P}(\tilde{\mathbf{r}}) \,, \tag{22}$$

with:

$$\mathbf{j}_\mathrm{D}(\tilde{\mathbf{r}}) = -\alpha \mathbf{A}(\tilde{\mathbf{r}}) \sum_i \left| \psi_i^{(0)}(\tilde{\mathbf{r}}) \right|^2 \,, \tag{23}$$

$$\mathbf{j}_\mathrm{P}(\tilde{\mathbf{r}}) = -i \sum_i \left[\left(\nabla \psi_i^{(0)}(\tilde{\mathbf{r}}) \right) \psi_i^{(1)}(\tilde{\mathbf{r}}) - \psi_i^{(0)}(\tilde{\mathbf{r}}) \left(\nabla \psi_i^{(1)}(\tilde{\mathbf{r}}) \right) \right] \,. \tag{24}$$

From the above equations, it is apparent that the determination of the induced current densities requires the knowledge of the first-order corrections to the one-particle orbitals due to the presence of an external magnetic field. The Kohn-Sham one-particle orbitals will soon prove unsuitable for calculating these current densities in PBC simulations, which excludes (standard) perturbation theory as a viable option, and therefore we employ density functional perturbation theory (DFPT) instead, a flexible variational technique, formulated in its general form by Putrino *et al.*[14] In magnetic DFPT, these first-order corrections are obtained through the solution of the following inhomogeneous set of coupled equations for $\psi_i^{(1)}$:

$$-\sum_i \left(H_\mathrm{KS}(\mathbf{r})\delta_{ij} - \int \mathrm{d}\mathbf{r}' \psi_i^{(0)*}(\mathbf{r}') H_\mathrm{KS}(\mathbf{r}') \psi_j^{(0)}(\mathbf{r}') \right) \psi_i^{(1)}(\mathbf{r}) = H^{(1)}(\mathbf{r}) \psi_j^{(0)}(\mathbf{r}) \,, \tag{25}$$

in which H_KS denotes the Kohn-Sham Hamiltonian used to obtain the KS orbitals, and $H^{(1)}$ the perturbation operator which, for a constant magnetic field, equals to:

$$H^{(1)}(\mathbf{r}) = -\frac{\alpha}{2}\left((\mathbf{r}-\mathbf{R}_\mathrm{g})\times\mathbf{p}\right).\mathbf{B}\,. \tag{26}$$

Eq. 25 can be solved using Green's function techniques or directly through minimization of the gradients.

The gauge origin $\mathbf{R}_\mathrm{g}$ is a cyclic variable, i.e. it has no influence on the physicial observables. In our approach, we primarily adopt the continuous set of gauge transformations (CSGT) method:[15] for every point $\tilde{\mathbf{r}}$ in coordinate space, $\mathbf{R}_\mathrm{g}$ is set equal to $\tilde{\mathbf{r}}$. This approach assures that the diamagnetic component of the current density cancels exactly:

$$\mathbf{j}_\mathrm{D}(\tilde{\mathbf{r}}) = 0\,, \tag{27}$$

and removes the numerical issues associated with a fixed choice for the gauge origin at large distances $|\tilde{\mathbf{r}}-\mathbf{R}_\mathrm{g}|$.

The current density (Eq. 22), which is composed only of a paramagnetic component in the CSGT method, remains invariant under arbitrary orbital-specific translations of the origin of the coordinate system. This will be shown using the Green's function of the inhomogeneous set of coupled equations for $\psi_i^{(1)}$ (Eq. 25):

$$\begin{aligned} G_{ij}(\tilde{\mathbf{r}},\tilde{\mathbf{r}}') \;=\; & -\left(H_\mathrm{KS}(\mathbf{r})\delta_{ij}\right. \\ & \left. -\int \mathrm{d}\tilde{\mathbf{r}}''\psi_i^{(0)*}(\tilde{\mathbf{r}}'')H_\mathrm{KS}(\mathbf{r}'')\psi_j^{(0)}(\tilde{\mathbf{r}}'')\right)^{-1} \end{aligned} \tag{28}$$

For an arbitrary perturbation operator O, we can formally write the solutions of Eq. 25 as:

$$\psi_i^{(O)}(\tilde{\mathbf{r}}) = \sum_j \int \mathrm{d}\tilde{\mathbf{r}}' G_{ij}(\tilde{\mathbf{r}},\tilde{\mathbf{r}}')O(\mathbf{r}')\psi_j^{(0)}(\tilde{\mathbf{r}}')\,. \tag{29}$$

From the above formulation, based on linearity considerations, we infer that the solutions of Eq. 25 for the perturbation operator defined in Eq. 26 can be computed from the sum of the solutions Eq. 29 for the perturbation operators $O_1 = -\frac{\alpha}{2}\left(\mathbf{r}\times\mathbf{p}\right).\mathbf{B}$ and $O_2 = -\frac{\alpha}{2}\left(\mathbf{R}_\mathrm{g}\times\mathbf{p}\right).\mathbf{B}$:

$$\begin{aligned} \psi_i^{(1)}(\tilde{\mathbf{r}}) \;=\; & -\frac{\alpha}{2}\sum_j\left(\int \mathrm{d}\tilde{\mathbf{r}}' G_{ij}(\tilde{\mathbf{r}},\tilde{\mathbf{r}}')\left(\mathbf{r}'\times\mathbf{p}'\right)\psi_j^{(0)}(\tilde{\mathbf{r}}')\right. \\ & \left. -\int \mathrm{d}\tilde{\mathbf{r}}' G_{ij}(\tilde{\mathbf{r}},\tilde{\mathbf{r}}')\left(\mathbf{R}_\mathrm{g}\times\mathbf{p}'\right)\psi_j^{(0)}(\tilde{\mathbf{r}}')\right).\mathbf{B}\,. \end{aligned} \tag{30}$$

Moreover, it becomes clear that the current density remains invariant under arbitrary orbital-specific translations $\mathbf{d}_j$ of the origin of the position operator $\mathbf{r}$ and the gauge origin $\mathbf{R}_\mathrm{g} = \tilde{\mathbf{r}}$:

$$\psi_i^{(1)}(\tilde{\mathbf{r}}) \;=\; -\frac{\alpha}{2}\sum_j\left(\int \mathrm{d}\tilde{\mathbf{r}}' G_{ij}(\tilde{\mathbf{r}},\tilde{\mathbf{r}}')\left((\mathbf{r}'-\mathbf{d}_j)\times\mathbf{p}'\right)\psi_j^{(0)}(\tilde{\mathbf{r}}') - \int \mathrm{d}\tilde{\mathbf{r}}' G_{ij}(\tilde{\mathbf{r}},\tilde{\mathbf{r}}')\left((\tilde{\mathbf{r}}-\mathbf{d}_j)\times\mathbf{p}'\right)\psi_j^{(0)}(\tilde{\mathbf{r}}')\right).\mathbf{B}\,. \tag{31}$$

The first perturbation contribution in Eq. 31 requires one single solution of Eq. 25. The second perturbation operator depends on the position in coordinate space for which the current density is calculated, and consequently requires a solution of Eq. 25 for every position in coordinate space. The computational cost of one such calculation is of the same order of magnitude as the self-consistent procedure of the Kohn-Sham-DFT scheme and thus, the evaluation of the second perturbation operator should be performed in a slightly different way. Therefore, the second part of Eq. 31 is further elaborated into:

$$\begin{aligned} & \frac{\alpha}{2}\sum_j\left(\int \mathrm{d}\tilde{\mathbf{r}}' G_{ij}(\tilde{\mathbf{r}},\tilde{\mathbf{r}}')\left((\tilde{\mathbf{r}}-\mathbf{d}_j)\times\mathbf{p}'\right)\psi_j^{(0)}(\tilde{\mathbf{r}}')\right).\mathbf{B} \\ = \; & \frac{\alpha}{2}\sum_j\left((\tilde{\mathbf{r}}-\mathbf{d}_i)\times\int \mathrm{d}\tilde{\mathbf{r}}' G_{ij}(\tilde{\mathbf{r}},\tilde{\mathbf{r}}')\mathbf{p}'\psi_j^{(0)}(\tilde{\mathbf{r}}')\right. \\ + \; & \left.\int \mathrm{d}\tilde{\mathbf{r}}' G_{ij}(\tilde{\mathbf{r}},\tilde{\mathbf{r}}')\left((\mathbf{d}_i-\mathbf{d}_j)\times\mathbf{p}'\right)\psi_j^{(0)}(\tilde{\mathbf{r}}')\right).\mathbf{B}\,. \end{aligned} \tag{32}$$

The first and second perturbation operator in the above equation require only respectively 1 and n evaluations of Eq. 25, with n the number of electrons. Moreover, it is possible to facilitate the calculation of the contribution to $\psi_j^{(1)}$ from the second part of Eq. 32 from the one to $\psi_i^{(1)}$, on the condition that $\mathbf{d}_i \approx \mathbf{d}_j$.[16,17] Such techniques will be further explored below (*to be added*). If $\mathbf{d}_i = \mathbf{d}_j$, the contribution to $\psi_j^{(1)}$ can even be extracted directly from the one to $\psi_i^{(1)}$, i.e. without an additional

evaluation of Eq. 25.

1. The position operator in PBC

The position operator $\mathbf{r}$ operating on a (one-particle) wave function in the coodinate representation $\psi(\tilde{\mathbf{r}})$ results in the multiplication of this wave function with the position variable $\tilde{\mathbf{r}}$. When periodic boundary conditions are imposed, the Hilbert space of the one-particle wave functions $\psi(\tilde{\mathbf{r}})$ is determined by the condition $\psi(\tilde{\mathbf{r}} + \mathbf{L}) = \psi(\tilde{\mathbf{r}})$. A valid operator transforms each vector (in casu: the wave function) of a given Hilbert space to a vector corresponding to the same Hilbert space. The multiplicative position operator clearly is not a valid operator here, since the Cartesian components of $\tilde{\mathbf{r}}\psi(\tilde{\mathbf{r}})$ are no longer periodic. This constitutes a problem, since the perturbation operator $(\mathbf{r}' - \mathbf{d}_j) \times \mathbf{p}'$ from Eq. 31 contains the position operator. This problem is solved as follows:

First, the KS orbitals are transformed into maximally localized Wannier functions (MLWFs).[18] For a non-conducting material, these functions feature an exponential decay. When the simulation cell is then chosen such that the dimensions remain greater than the decay length, (the density of) each MLWF will only be significant in a limited area of the simulation cell, and will practically cancel anywhere else. This remains true even after the operation of the semi-local operator $\mathbf{p} = -i\nabla$.

The next step consists of assigning to each MLWF an individual virtual cell with the same dimensions $L_x \times L_y \times L_z$ as the simulation cell. This virtual cell is chosen such that the geometrical center coincides with the Wannier center, this is the charge center of the corresponding MLWF. Then, we redefine the position operator $\mathbf{r}$ in such a way that its expectation value $\tilde{\mathbf{r}}$ goes linearly from $-L_i/2$ to $+L_i/2$ ($i = x, y, z$) within each virtual cell and in each Cartesian component.

In other words, we use the translational freedom (see the preceding section) to set the origin $\mathbf{d}_j$ of the coordinate system at the corresponding Wannier center for every individual MLWF j from Eq. 31. At the boundaries of each virtual cell the expectation value switches back from $+L_i/2$ to $-L_i/2$, thus creating (in every Cartesian component) a sawtooth-shaped profile. In this way, the position operator obeys the periodic boundary conditions, and becomes a valid operator. The behavior at the boundaries of the virtual cell is of little importance, since the dimensions of the simulation cell were chosen such that the (the density of) MLWF is zero there.

Here, an important practical limitation for the above technique arises: in some materials, such as metals and other conductors, the decay length of the MLWFs is so large that prohibitive dimensions for the simulation would be required.

2. The definition of distances in PBC

The definition of $(\mathbf{d}_i - \mathbf{d}_j)$ in Eq. 32 also requires some attention. In a periodic simulation, distances are only defined up to an arbitrary lattice vector $\mathbf{L_a} = a\mathbf{L}_x + b\mathbf{L}_y + c\mathbf{L}_z$, where $\mathbf{a}$ denotes the vector of integral numbers a, b, c. We choose to retain only the lattice vector $\mathbf{L_a}$ which minimizes the distance $|\mathbf{d}_i - \mathbf{d}_j + \mathbf{L_a}|$, this is the *minimal image* convention, because (i) both $(\mathbf{d}_i - \mathbf{d}_j)$ and $\mathbf{p}$ represent (semi-)local operators, and (ii) the Green's function $G_{ij}(\tilde{\mathbf{r}}, \tilde{\mathbf{r}}')$ is only significant for *nearby* positions $\tilde{\mathbf{r}}$ and $\tilde{\mathbf{r}}'$ in space, while every MLWF is by construction strongly localized around its corresponding Wannier center.

3. GAPW representation of the induced current densities

The induced current densities $\mathbf{j}_{\mathbf{B}_z}$ are derived fully analytically in a Gaussian representation. Expanding the MLWFs and their first-order corrections $\psi_i^{(1)}$ in periodic atomic orbitals $\psi^{\mathrm{AO,P}}(\mathbf{r})$, with expansion coefficients $C^{(0)}$ and $C^{(1)}$, respectively, we obtain for the matrix elements of the inhomogeneous set of coupled equations Eq. 25:

$$-\sum_{il}\left(H_{\mathrm{KS},kl}\delta_{ij} - S_{kl}\int \mathrm{d}\mathbf{r}\psi_i^{(0)}(\mathbf{r})H_{\mathrm{KS}}(\mathbf{r})\psi_j^{(0)}(\mathbf{r})\right) iC_{li}^{(1)} = \sum_l H_{kl(j)}^{(1)}C_{lj}^{(0)}\,, \qquad \forall k, j\,, \tag{33}$$

where S_{kl} denotes the elements of the overlap matrix and $H_{kl}^{(1)}$ the matrix elements of $(\mathbf{r} - \mathbf{d}_j) \times \mathbf{p}$ (the *orbital angular momentum* operator, notation: $\mathbf{L}$), $\mathbf{p}$ (the *momentum* operator, notation: $\mathbf{p}$), and $(\mathbf{d}_i - \mathbf{d}_j) \times \mathbf{p}$ (the *full correction* operator, notation: $\boldsymbol{\Delta i}$). Note also that the imaginary nature of $\psi_i^{(1)}$ has been made explicit, allowing us to work with real expansion coefficients $C_{li}^{(1)}$.

The position operator in the orbital angular momentum operator is redefined with respect to the position of the atomic nucleus $\mathbf{R}_l$ corresponding with the atomic orbital $\psi_l^{\mathrm{AO,P}}$:

$$\begin{aligned} H^{L_\alpha}_{klj} &= -i\epsilon_{\alpha\beta\gamma}\int \mathrm{d}\mathbf{r}\psi^{\mathrm{AO,P}}_k(\mathbf{r})\left((\mathbf{r}-\mathbf{d}_j)_\beta\nabla_\gamma\right)\psi^{\mathrm{AO,P}}_l(\mathbf{r}) \\ &= -i\epsilon_{\alpha\beta\gamma}\left(\int \mathrm{d}\mathbf{r}\psi^{\mathrm{AO,P}}_k(\mathbf{r})\left((\mathbf{r}-\mathbf{R}_l)_\beta\nabla_\gamma\right)\psi^{\mathrm{AO,P}}_l(\mathbf{r})\right. \\ &+ \left.(\mathbf{R}_l-\mathbf{d}_j)_\beta\int \mathrm{d}\mathbf{r}\psi^{\mathrm{AO,P}}_k(\mathbf{r})\left(\nabla_\gamma\right)\psi^{\mathrm{AO,P}}_l(\mathbf{r})\right) . \quad (34) \end{aligned}$$

where the vector product is concisely written using the total anti-symmetric tensor $\epsilon_{\alpha\beta\gamma}$, i.e. the Levi-Cività symbol, and the indices β and γ follow the Einstein summation rules. This step reduces the matrix elements to known integrals over Cartesian Gaussian functions.[19] An additional advantage is that these matrix elements only need to be calculated once, instead of for each MLWF separately. The matrix elements of the momentum operator and the full-correction operator are also a function of known integrals:

$$H^{p_\alpha}_{kl} = -i\int \mathrm{d}\mathbf{r}\psi^{\mathrm{AO,P}}_k(\mathbf{r})\left(\nabla_\alpha\right)\psi^{\mathrm{AO,P}}_l(\mathbf{r}) , \quad (35)$$

$$\begin{aligned} H^{\Delta i_\alpha}_{klj} &= -i\epsilon_{\alpha\beta\gamma}\int \mathrm{d}\mathbf{r}\psi^{\mathrm{AO,P}}_k(\mathbf{r})\left((\mathbf{d}_i-\mathbf{d}_j)_\beta\nabla_\gamma\right)\psi^{\mathrm{AO,P}}_l(\mathbf{r}) \\ &= -i\epsilon_{\alpha\beta\gamma}(\mathbf{d}_i-\mathbf{d}_j)_\beta\int \mathrm{d}\mathbf{r}\psi^{\mathrm{AO,P}}_k(\mathbf{r})\left(\nabla_\gamma\right)\psi^{\mathrm{AO,P}}_l(\mathbf{r}) . \end{aligned} \quad (36)$$

From the solutions of Eq. 33 for the perturbation operators with matrix elements defined in respectively Eq. 34, Eq. 35, and Eq. 36, we obtain the expansion coefficients matrices C^{L_α}, C^{p_γ}, and $C^{\Delta i_\alpha}$. This allows us to calculate the first-order corrections $\psi^{(1)}_{\mathbf{B}_\alpha,i}$, including their spatial derivatives $\nabla\psi^{(1)}_{\mathbf{B}_\alpha,i}$:

$$\psi^{(1)}_{\mathbf{B}_\alpha,i}(\mathbf{r}) = -\frac{i\alpha}{2}\sum_k\left(C^{L_\alpha}_{ki}-\epsilon_{\alpha\beta\gamma}(\mathbf{r}-\mathbf{d}_i)_\beta C^{p_\gamma}_{ki}-C^{\Delta i_\alpha}_{ki}\right)\psi^{\mathrm{AO,P}}_k(\mathbf{r}) , \quad (37)$$

$$\nabla\psi^{(1)}_{\mathbf{B}_\alpha,i}(\mathbf{r}) = -\frac{i\alpha}{2}\sum_k\left(C^{L_\alpha}_{ki}-\epsilon_{\alpha\beta\gamma}(\mathbf{r}-\mathbf{d}_i)_\beta C^{p_\gamma}_{ki}-C^{\Delta i_\alpha}_{ki}\right)\nabla\psi^{\mathrm{AO,P}}_k(\mathbf{r}) . \quad (38)$$

The next step comprises the construction of the current-density matrices. Due to the presence of the term $(\mathbf{r}-\mathbf{d}_i)$ in Eqs. 37 and 38, a new current-density matrix would be required for every point in space for which we want to calculate the current density, if only one current density matrix were to be used for every direction of the external magnetic field. Therefore, we will employ multiple current-density matrices, corresponding to different sets of functions of $\mathbf{r}$. Through an additional substitution $(\mathbf{r}-\mathbf{d}_i)=(\mathbf{r}-\mathbf{R}_l)+(\mathbf{R}_l-\mathbf{d}_i)$, this is done in the most efficient way, since the position variable is separated from the MLWF-dependent Wannier centers:

$$\begin{aligned} \psi^{(1)}_{\mathbf{B}_\alpha,i}(\mathbf{r}) &= -\frac{i\alpha}{2}\sum_k\left(C^{L_\alpha}_{ki}-\epsilon_{\alpha\beta\gamma}(\mathbf{R}_k-\mathbf{d}_i)_\beta C^{p_\gamma}_{ki}-C^{\Delta i_\alpha}_{ki}\right)\psi^{\mathrm{AO,P}}_k(\mathbf{r})+\frac{i\alpha}{2}\sum_k\epsilon_{\alpha\beta\gamma}C^{p_\gamma}_{ki}\left((\mathbf{r}-\mathbf{R}_k)_\beta\psi^{\mathrm{AO,P}}_k(\mathbf{r})\right) \\ &= -\frac{i\alpha}{2}\sum_k C^{a_\alpha}_{ki}\psi^{\mathrm{AO,P}}_k(\mathbf{r})+\frac{i\alpha}{2}\sum_k\epsilon_{\alpha\beta\gamma}C^{p_\gamma}_{ki}\left((\mathbf{r}-\mathbf{R}_k)_\beta\psi^{\mathrm{AO,P}}_k(\mathbf{r})\right) , \end{aligned} \quad (39)$$

$$\nabla\psi^{(1)}_{\mathbf{B}_\alpha,i}(\mathbf{r}) = -\frac{i\alpha}{2}\sum_k C^{a_\alpha}_{ki}\nabla\psi^{\mathrm{AO,P}}_k(\mathbf{r})+\frac{i\alpha}{2}\sum_k\epsilon_{\alpha\beta\gamma}C^{p_\gamma}_{ki}\left((\mathbf{r}-\mathbf{R}_k)_\beta\nabla\psi^{\mathrm{AO,P}}_k(\mathbf{r})\right) . \quad (40)$$

Using the above expressions, we calculate the induced current density according to Eq. 22:

$$\begin{aligned}
\mathbf{j}_{\mathbf{B}_\alpha}(\mathbf{r}) &= \sum_i \mathbf{j}_{\mathbf{B}_\alpha,i}(\mathbf{r}) \\
&= -i\sum_i \left[\left(\nabla\psi_i^{(0)}(\mathbf{r})\right)\psi^{(1)}_{\mathbf{B}_\alpha,i}(\mathbf{r}) - \psi_i^{(0)}(\mathbf{r})\left(\nabla\psi^{(1)}_{\mathbf{B}_\alpha,i}(\mathbf{r})\right)\right] \\
&= -\frac{\alpha}{2}\sum_i \left[\sum_{kl}\left(C_{ki}^{(0)}C_{li}^{a_\alpha}\right)\left\{\nabla\psi_k^{\mathrm{AO,P}}(\mathbf{r})\psi_l^{\mathrm{AO,P}}(\mathbf{r}) - \psi_k^{\mathrm{AO,P}}(\mathbf{r})\nabla\psi_l^{\mathrm{AO,P}}(\mathbf{r})\right\}\right. \\
&- \left.\epsilon_{\alpha\beta\gamma}\sum_{kl}\left(C_{ki}^{(0)}C_{li}^{p_\gamma}\right)\left\{\nabla\psi_k^{\mathrm{AO,P}}(\mathbf{r})(\mathbf{r}-\mathbf{R}_I)_\beta\psi_l^{\mathrm{AO,P}}(\mathbf{r}) - \psi_k^{\mathrm{AO,P}}(\mathbf{r})(\mathbf{r}-\mathbf{R}_I)_\beta\nabla\psi_l^{\mathrm{AO,P}}(\mathbf{r})\right\}\right] . \qquad (41)
\end{aligned}$$

Thus, six current-density matrices, i.e.:

$$J_{kl}^{a_\alpha} = \sum_i C_{ki}^{(0)}C_{li}^{a_\alpha} , \qquad J_{kl}^{p_\alpha} = \sum_i C_{ki}^{(0)}C_{li}^{p_\alpha} , \quad (\alpha = x,y,z) \qquad (42)$$

are needed to describe the current densities originating from an external magnetic field in the three Cartesian directions.

From Eq. 41, a GAPW representation for these induced current densities is now constructed.

The soft global component is obtained by setting to zero the coefficients in the CPGFs corresponding to the most localized primitive Gaussian functions, thus effectively using only the limited set $\tilde{\chi}^{\mathrm{P}}$. These functions are evaluated, after multiplication with their corresponding coefficient, on the discrete points of the real space FFT lattice, and are then summed up appropriately.

For the local components, through an additional substitution $(\mathbf{r}-\mathbf{R}_k) = (\mathbf{r}-\mathbf{R}_I)+(\mathbf{R}_I-\mathbf{R}_k)$ in Eqs. 39 and 40, the position variable is redefined with respect to the position of the atomic nucleus I:

$$\begin{aligned}
\psi^{(1)}_{\mathbf{B}_\alpha,i}(\mathbf{r}) &= -\frac{i\alpha}{2}\sum_k C_{ki}^{a_\alpha}\psi_k^{\mathrm{AO,P}}(\mathbf{r}) + \frac{i\alpha}{2}\sum_k \epsilon_{\alpha\beta\gamma}C_{ki}^{p_\gamma}\left((\mathbf{r}-\mathbf{R}_k)_\beta\psi_k^{\mathrm{AO,P}}(\mathbf{r})\right) \\
&= -\frac{i\alpha}{2}\sum_k C_{ki}^{a_\alpha}\psi_k^{\mathrm{AO,P}}(\mathbf{r}) + \frac{i\alpha}{2}\sum_k \epsilon_{\alpha\beta\gamma}C_{ki}^{p_\gamma}\left((\mathbf{R}_I-\mathbf{R}_k)_\beta\psi_k^{\mathrm{AO,P}}(\mathbf{r})\right) + \frac{i\alpha}{2}\sum_k \epsilon_{\alpha\beta\gamma}C_{ki}^{p_\gamma}\left((\mathbf{r}-\mathbf{R}_I)_\beta\psi_k^{\mathrm{AO,P}}(\mathbf{r})\right) \\
&= -\frac{i\alpha}{2}\sum_k C_{ki}^{a'_\alpha}\psi_k^{\mathrm{AO,P}}(\mathbf{r}) + \frac{i\alpha}{2}\sum_k \epsilon_{\alpha\beta\gamma}C_{ki}^{p_\gamma}\left((\mathbf{r}-\mathbf{R}_I)_\beta\psi_k^{\mathrm{AO,P}}(\mathbf{r})\right) . \qquad (43)
\end{aligned}$$

Since the CPGFs are projected onto the primitive Gaussian functions χ_I^{P} and $\tilde{\chi}_I^{\mathrm{P}}$ corresponding to the atomic nucleus I, we can express, because of this additional substitution, the local current density with only a limited number of current density matrices corresponding to different sets of functions of primitive Gaussian functions centered on $\mathbf{R}_I$:

$$\mathbf{j}^1_{\mathbf{B}_\alpha,I}(\mathbf{r}) = -\frac{\alpha}{2}\left[\sum_{vw}\sum_{kl} Q^I_{vk} J^{a'_\alpha}_{kl} Q^I_{wl} \left\{\nabla\chi^{\mathrm{P}}_{I,v}(\mathbf{r})\chi^{\mathrm{P}}_{I,w}(\mathbf{r}) - \chi^{\mathrm{P}}_{I,v}(\mathbf{r})\nabla\chi^{\mathrm{P}}_{I,w}(\mathbf{r})\right\}\right.$$
$$\left. - \epsilon_{\alpha\beta\gamma}\sum_{vw}\sum_{kl} Q^I_{vk} J^{p_\alpha}_{kl} Q^I_{wl} \left\{\nabla\chi^{\mathrm{P}}_{I,v}(\mathbf{r})(\mathbf{r}-\mathbf{R}_I)_\beta\chi^{\mathrm{P}}_{I,w}(\mathbf{r}) - \chi^{\mathrm{P}}_{I,v}(\mathbf{r})(\mathbf{r}-\mathbf{R}_I)_\beta\nabla\chi^{\mathrm{P}}_{I,w}(\mathbf{r})\right\}\right] , \quad (44)$$

$$\tilde{\mathbf{j}}^1_{\mathbf{B}_\alpha,I}(\mathbf{r}) = -\frac{\alpha}{2}\left[\sum_{vw}\sum_{kl} \tilde{Q}^I_{vk} J^{a'_\alpha}_{kl} \tilde{Q}^I_{wl} \left\{\nabla\tilde{\chi}^{\mathrm{P}}_{I,v}(\mathbf{r})\tilde{\chi}^{\mathrm{P}}_{I,w}(\mathbf{r}) - \tilde{\chi}^{\mathrm{P}}_{I,v}(\mathbf{r})\nabla\tilde{\chi}^{\mathrm{P}}_{I,w}(\mathbf{r})\right\}\right.$$
$$\left. - \epsilon_{\alpha\beta\gamma}\sum_{vw}\sum_{kl} \tilde{Q}^I_{vk} J^{p_\alpha}_{kl} \tilde{Q}^I_{wl} \left\{\nabla\tilde{\chi}^{\mathrm{P}}_{I,v}(\mathbf{r})(\mathbf{r}-\mathbf{R}_I)_\beta\tilde{\chi}^{\mathrm{P}}_{I,w}(\mathbf{r}) - \tilde{\chi}^{\mathrm{P}}_{I,v}(\mathbf{r})(\mathbf{r}-\mathbf{R}_I)_\beta\nabla\tilde{\chi}^{\mathrm{P}}_{I,w}(\mathbf{r})\right\}\right] . \quad (45)$$

The matrix Q^I contains the expansion coefficients of the CPGFs in the primitive Gaussian functions corresponding with the atomic nucleus I.

However, the GAPW representation of the current density, computed in this way converges only very slowly with respect to the size of the Gaussian basis set. On one hand, this is caused by the use of the CSGT method close to the atomic nuclei. This first issue was solved by fixing the gauge origin to the position of the atomic nucleus I for $\mathbf{j}^1_{\mathbf{B}_\alpha,I}$ within the atom-centered region U_I, i.e. $\mathbf{R}_\mathrm{g} = \mathbf{R}_I$. In this region, the diamagnetic component of the current density (Eq. 22) no longer vanishes. Outside U_I, the CSGT approach $\mathbf{R}_\mathrm{g} = \mathbf{r}$ is maintained, hence assuring that the condition in Eq. 14 remains fulfilled. The current density $\mathbf{j}^1_{\mathbf{B}_\alpha,I}$ is still defined by Eq. 44 outside the region U_I, within U_I it is now calculated through:

$$\mathbf{j}^1_{\mathbf{B}_\alpha,I}(\mathbf{r}) = -\frac{\alpha}{2}\left[\sum_{vw}\sum_{kl} Q^I_{vk} J^{a'_\alpha}_{kl} Q^I_{wl} \left\{\nabla\chi^{\mathrm{P}}_{I,v}(\mathbf{r})\chi^{\mathrm{P}}_{I,w}(\mathbf{r}) - \chi^{\mathrm{P}}_{I,v}(\mathbf{r})\nabla\chi^{\mathrm{P}}_{I,w}(\mathbf{r})\right\}\right.$$
$$\left. + \sum_{vw}\sum_{kl} Q^I_{vk} P_{kl} Q^I_{wl} \left\{(\mathbf{B}_\alpha\times\mathbf{r})\,\chi^{\mathrm{P}}_{I,v}(\mathbf{r})\chi^{\mathrm{P}}_{I,w}(\mathbf{r})\right\}\right]$$
$$\text{for } \mathbf{r}\in U_I \, . \quad (46)$$

A second cause for this slow convergence concerns the use of the expansion coefficients Q^I_{vk} for the spatial derivatives of the CPGFs in the primitive Gaussian functions corresponding to the atomic nucleus I:

$$\nabla\psi^{\mathrm{AO,P}}_k(\mathbf{r}) = \sum_v Q^I_{vk}\nabla\chi^{\mathrm{P}}_{I,v}(\mathbf{r}) \, , \quad (47)$$

which proves to be a rather rough approximation for smaller Gaussian basis sets. This is solved by computing new expansion coefficients for every spatial derivative of $\psi^{\mathrm{AO,P}}_k$ in the corresponding derivative of every primitive Gaussian function corresponding to the atomic nucleus I:

$$\mathbf{Q}^I_{vk} = \int \mathrm{d}\mathbf{r} p_{\nabla\chi^{\mathrm{P}}_{I,v}}(\mathbf{r})\nabla\psi^{\mathrm{AO,P}}_k(\mathbf{r}) \, , \quad (48)$$

with $\mathbf{Q}^I_{vk} = (Q^I_{vk,x}, Q^I_{vk,y}, Q^I_{vk,z})$, and $p_{\nabla\chi^{\mathrm{P}}_{I,v}}$ the projector corresponding with $\nabla\chi^{\mathrm{P}}_{I,v}$.

C. Calculation of the chemical shift tensor

Essentially, the computation of the chemical shift tensor requires the knowledge of the induced magnetic field, i.e.

$$\mathbf{B}_{\mathbf{B}_x}(\mathbf{r}) = \alpha\int \mathrm{d}\mathbf{r}' \, \frac{\mathbf{r}'-\mathbf{r}}{|\mathbf{r}'-\mathbf{r}|^3}\times\mathbf{j}_{\mathbf{B}_x}(\mathbf{r}') \, , \quad (49)$$

on the positions of the atomic nuclei of interest. This is efficiently done using the GAPW representation of the current density.

For the global soft current density, we can re-use the techniques elaborated in Ref. 10. This means that we distinguish between the ($\mathbf{G}\neq\mathbf{0}$) components and the ($\mathbf{G}=\mathbf{0}$) component of the induced magnetic field, where $\mathbf{G}$ denotes the reciprocal space FFT-grid points. The former is evaluated in reciprocal space from:

$$\tilde{\mathbf{B}}_{\mathbf{B}_x,\mathbf{G}\neq\mathbf{0}}(\mathbf{r}) = \frac{1}{N_\mathbf{G}}\sum_{\mathbf{G}\neq\mathbf{0}} e^{i\mathbf{G}\cdot\mathbf{r}}\left[i4\pi\alpha\frac{\mathbf{G}\times\tilde{\mathbf{j}}_{\mathbf{B}_x}(\mathbf{G})}{G^2}\right] , \quad (50)$$

whereas the latter cannot be computed within periodic boundary conditions. An approximative expression for the contribution of this component in real space (where it is a constant term) is elaborated in Ref. 10:

$$\tilde{\mathbf{B}}_{\mathbf{B}_x,\mathbf{G}=\mathbf{0}} = \kappa\frac{2\pi\alpha}{\Omega}\int \mathrm{d}\mathbf{r}\ \mathbf{r}\times\tilde{\mathbf{j}}_{\mathbf{B}_x}(\mathbf{r})\ . \tag{51}$$

This contribution depends on the macroscopic shape of the studied material, through a dimensionless form factor κ. For a spherical shape, the above expression is exact and $\kappa = \frac{2}{3}$ (this is also the default value for κ). We also observe that the expression is almost the same as the one for the magnetic susceptibility (Eq. 2), with the exception of the form factor, and the fact that in the latter case, the hard current is being used.

The integral in Eq. 51 contains the position operator again, and must therefore be treated with care. We assume that the localization (i.e. the property of being localized) of each MLWF i is transferable to the corresponding current density. In that case, we can perform the operation of the position operator for each current density i independently, using the same definition for the position variable as in section II B 1 (sawtooth-shaped profile + origin identical to the Wannier center of the corresponding MLWF):

$$\begin{aligned}\tilde{\mathbf{B}}_{\mathbf{B}_x,\mathbf{G}=\mathbf{0}} &= \kappa\frac{2\pi\alpha}{\Omega}\sum_i\left(\int \mathrm{d}\mathbf{r}(\mathbf{r}-\mathbf{d}_i)\times\mathbf{j}_{\mathbf{B}_x,i}(\mathbf{r})\right.\\ &- \left.\int_\Omega \mathrm{d}\mathbf{r}\ \mathbf{d}_i\times\mathbf{j}_{\mathbf{B}_x,i}(\mathbf{r})\right)\ .\end{aligned} \tag{52}$$

For the magnetic susceptibility, the correction term for every i vanishes, because the integral over the simulation cell of the total current from each electron amounts to zero.

Omitting the additional substitution that was carried out in order to describe the current density with only a limited number of density matrices, the current density for each electron in a Gaussian representation equals:

$$\begin{aligned}\mathbf{j}_{\mathbf{B}_\alpha,i}(\mathbf{r}) &= -\frac{\alpha}{2}\sum_{kl}C_{ki}^{(0)}\left(C_{li}^{L_\alpha}-\epsilon_{\alpha\beta\gamma}(\mathbf{r}-\mathbf{d}_i)_\beta C_{li}^{p_\gamma}-C_{li}^{\Delta i_\alpha}\right)\\ &\left\{\nabla\psi_k^{\mathrm{AO,P}}(\mathbf{r})\psi_l^{\mathrm{AO,P}}(\mathbf{r})-\psi_k^{\mathrm{AO,P}}(\mathbf{r})\nabla\psi_l^{\mathrm{AO,P}}(\mathbf{r})\right\}\ .\end{aligned} \tag{53}$$

Inserting this current density in Eq. 52, we obtain for the α' component of $\tilde{\mathbf{B}}_{\mathbf{B}_\alpha,\mathbf{G}=\mathbf{0}}$ $(\alpha,\alpha'=x,y,z)$:

$$\begin{aligned}\tilde{B}_{\mathbf{B}_\alpha,\mathbf{G}=\mathbf{0},\alpha'} &= \kappa\frac{2\pi\alpha^2}{\Omega}\sum_i\left\{\sum_{kl}C_{ki}^{(0)}\left(C_{li}^{L_\alpha}-C_{li}^{\Delta i_\alpha}\right)\times\right.\\ &\left[2\int \mathrm{d}\mathbf{r}\psi_k^{\mathrm{AO,P}}(\mathbf{r})(\mathbf{r}-\mathbf{d}_i)_{\beta'}\left(\frac{\partial}{\partial\gamma'}\psi_l^{\mathrm{AO,P}}(\mathbf{r})\right)-2\int \mathrm{d}\mathbf{r}\psi_k^{\mathrm{AO,P}}(\mathbf{r})(\mathbf{r}-\mathbf{d}_i)_{\gamma'}\left(\frac{\partial}{\partial\beta'}\psi_l^{\mathrm{AO,P}}(\mathbf{r})\right)\right.\\ &\left.+2d_{i,\beta'}\int \mathrm{d}\mathbf{r}\psi_k^{\mathrm{AO,P}}(\mathbf{r})\left(\frac{\partial}{\partial\gamma'}\psi_l^{\mathrm{AO,P}}(\mathbf{r})\right)-2d_{i,\gamma'}\int \mathrm{d}\mathbf{r}\psi_k^{\mathrm{AO,P}}(\mathbf{r})\left(\frac{\partial}{\partial\beta'}\psi_l^{\mathrm{AO,P}}(\mathbf{r})\right)\right]\\ &- \epsilon_{\alpha\beta\gamma}\sum_{kl}C_{ki}^{(0)}C_{li}^{p_\gamma}\times\\ &\left[2\int \mathrm{d}\mathbf{r}\psi_k^{\mathrm{AO,P}}(\mathbf{r})(\mathbf{r}-\mathbf{d}_i)_{\beta'}(\mathbf{r}-\mathbf{d}_i)_\beta\left(\frac{\partial}{\partial\gamma'}\psi_l^{\mathrm{AO,P}}(\mathbf{r})\right)+\delta_{\beta\gamma'}\int \mathrm{d}\mathbf{r}\psi_k^{\mathrm{AO,P}}(\mathbf{r})(\mathbf{r}-\mathbf{d}_i)_{\beta'}\left(\frac{\partial}{\partial\gamma'}\psi_l^{\mathrm{AO,P}}(\mathbf{r})\right)\right.\\ &-2\int \mathrm{d}\mathbf{r}\psi_k^{\mathrm{AO,P}}(\mathbf{r})(\mathbf{r}-\mathbf{d}_i)_{\gamma'}(\mathbf{r}-\mathbf{d}_i)_\beta\left(\frac{\partial}{\partial\beta'}\psi_l^{\mathrm{AO,P}}(\mathbf{r})\right)-\delta_{\beta\beta'}\int \mathrm{d}\mathbf{r}\psi_k^{\mathrm{AO,P}}(\mathbf{r})(\mathbf{r}-\mathbf{d}_i)_{\gamma'}\left(\frac{\partial}{\partial\beta'}\psi_l^{\mathrm{AO,P}}(\mathbf{r})\right)\\ &\left.\left.+2d_{i,\beta'}\int \mathrm{d}\mathbf{r}\psi_k^{\mathrm{AO,P}}(\mathbf{r})(\mathbf{r}-\mathbf{d}_i)_\beta\left(\frac{\partial}{\partial\gamma'}\psi_l^{\mathrm{AO,P}}(\mathbf{r})\right)-2d_{i,\gamma'}\int \mathrm{d}\mathbf{r}\psi_k^{\mathrm{AO,P}}(\mathbf{r})(\mathbf{r}-\mathbf{d}_i)_\beta\left(\frac{\partial}{\partial\beta'}\psi_l^{\mathrm{AO,P}}(\mathbf{r})\right)\right]\right\}\ .\end{aligned} \tag{54}$$

The contributions to the magnetic field on the position of the I-th nucleus from the local atom-centered current

densities are evaluated as follows:

$$\mathbf{B}_{\mathbf{B}_x}(\mathbf{R}_I) = \alpha \sum_{J,R_{IJ}<R_C} \int_{\mathrm{LL},U_J} \mathrm{d}\mathbf{r}\, \frac{\mathbf{r}-\mathbf{R}_I}{|\mathbf{r}-\mathbf{R}_I|^3} \times \left(\mathbf{j}^1_{\mathbf{B}_x,J}(\mathbf{r}) - \tilde{\mathbf{j}}^1_{\mathbf{B}_x,J}(\mathbf{r})\right) . \quad (55)$$

The subscript LL denotes that the integration is carried out on a spherical grid centered on the position of the atomic nucleus, featuring a logarithmic radial discretization and a Lebedev-type[20–22] angular discretisation. U_J indicates that the integration is limited to the spherical region U_J around the atomic nucleus J. In the above equation, the origin of $\mathbf{r}$ is always the geometric position of each nucleus J, and $\mathbf{R}_{JI} = \mathbf{R}_J - \mathbf{R}_I$ is the vector connecting the nuclei J and I. Only nearest-neighboring atomic regions need to be included. This can be controlled by choosing an appropriate maximum value R_C for $R_{JI} = |\mathbf{R}_{JI}|$.

D. Calculation of the g tensor

1. The $\Delta g^{\mathrm{ZKE}}_{xy}$ term (Eq. 5)

$\Delta g^{\mathrm{ZKE}}_{xy}$ is calculated in a spin-polarized DFT run from the kinetic energy of the Kohn-Sham orbitals in the basis set of CPGFs. The matrix elements of the kinetic energy operator $-\frac{\nabla^2}{2}$ can be evaluated analytically in a set of arbitrary Cartesian Gaussian functions.[19]

2. The $\Delta g^{\mathrm{SO}}_{xy}$ term (Eq. 6)

$\Delta g^{\mathrm{SO}}_{xy}$ is obtained essentially from integrating multiple products of an induced current density with the gradient of an effective potential over the simulation cell. The calculation of the former has already been elaborated in section II B. Note that the current for each spin channel separately is computed in a similar way. The effective potential V^τ_{eff} ($\tau = \alpha, \beta$) is defined as:[23]

$$V^\tau_{\mathrm{eff}}(\mathbf{r}) = v_{\mathrm{ext}}(\mathbf{r}) + v_{\mathrm{H}}(\mathbf{r}) + v^\tau_{X_\alpha}(\mathbf{r}) , \quad (56)$$

where v_{ext} denotes the Coulombic potential from the nuclei, v_{H} the Hartree potential, and $v^\tau_{X_\alpha}$ the X_α potential, which is also referred to as the Dirac/Slater-exchange potential:[24]

$$v^\tau_{X_\alpha}(\mathbf{r}) = -\frac{3}{2}\left(\frac{6}{\pi}\right)^{1/3} \alpha \rho^\tau(\mathbf{r})^{1/3} . \quad (57)$$

The variable α is an adjustable real parameter which, by default, is set to 2/3.

In the GAPW method, we attempt to benefit from the presence of plane waves and atom-centered grids. Unfortunately, the construction of a GAPW representation for $\nabla V^\tau_{\mathrm{KS}}$ is not feasible. However, using a technique elaborated in Ref. 25, we can split up $\nabla V^\tau_{\mathrm{eff}}$ in independent global and local atom-centered components, but the GAPW identities Eqs. 13-16 will no longer hold. Nonetheless, the local components are constructed such that they remain limited to a small area around the atomic nuclei, using appropriate screening densities ρ^0, ρ^0_I, and ρ^c_I constructed in Ref. 25. $\nabla V^\tau_{\mathrm{eff}}$ is split up in a soft global component $\nabla \tilde{V}^{\tau,\mathrm{PSP}}_{\mathrm{eff}}$ or $\nabla \tilde{V}^{\tau,\mathrm{AE}}_{\mathrm{eff}}$ and local atom-centered components $\nabla V^{\tau,1,\mathrm{PSP}}_{\mathrm{eff},I}$ or $\nabla V^{\tau,1,\mathrm{AE}}_{\mathrm{eff},I}$ (depending on whether a pseudopotential or a nuclear Coulomb potential is used), defined as:

$$\nabla \tilde{V}^{\tau,\mathrm{PSP}}_{\mathrm{eff}}(\mathbf{r}) = \nabla\left(\sum_{I\in\mathrm{PSP}} V^{\mathrm{PSP}}_{\mathrm{loc,sr},I} H(\alpha_{\mathrm{c}} - \frac{1}{2r^2_{\mathrm{loc},I}}) + v_{\mathrm{H}}[\tilde{\rho}(\mathbf{r}) + \rho^0(\mathbf{r})] + v^\tau_{X_\alpha}[\tilde{\rho}(\mathbf{r})]\right) , \quad (58)$$

$$\nabla \tilde{V}^{\tau,\mathrm{AE}}_{\mathrm{eff}}(\mathbf{r}) = \nabla\left(v_{\mathrm{H}}[\tilde{\rho}(\mathbf{r}) + \rho^0(\mathbf{r})] + v^\tau_{X_\alpha}[\tilde{\rho}(\mathbf{r})]\right) , \quad (59)$$

$$\nabla V^{\tau,1,\mathrm{PSP}}_{\mathrm{eff},I}(\mathbf{r}) = \nabla\left(V^{\mathrm{PSP}}_{\mathrm{loc,sr},I}(\mathbf{r}) H'(\alpha_{\mathrm{c}} - \frac{1}{2r^2_{\mathrm{loc},I}}) + v_{\mathrm{H}}[\rho^1_I(\mathbf{r}) + \rho^c_I(\mathbf{r})] - v_{\mathrm{H}}[\tilde{\rho}^1_I(\mathbf{r}) + \rho^0_I(\mathbf{r})] + v^\tau_{X_\alpha}[\rho^1_I(\mathbf{r})] - v^\tau_{X_\alpha}[\tilde{\rho}^1_I(\mathbf{r})]\right) , \quad (60)$$

$$\nabla V^{\tau,1,\mathrm{AE}}_{\mathrm{eff},I}(\mathbf{r}) = \nabla\left(\frac{Q_I}{r}\mathrm{erfc}\left(\frac{r}{\sqrt{2}r_{\mathrm{loc},I}}\right) + v_{\mathrm{H}}[\rho^1_I(\mathbf{r}) + \rho^c_I(\mathbf{r})] - v_{\mathrm{H}}[\tilde{\rho}^1_I(\mathbf{r}) + \rho^0_I(\mathbf{r})] + v^\tau_{X_\alpha}[\rho^1_I(\mathbf{r})] - v^\tau_{X_\alpha}[\tilde{\rho}^1_I(\mathbf{r})]\right) \quad (61)$$

H is the Heaviside function, and $H' = -(H-1)$, causing $V^{\mathrm{PSP}}_{\mathrm{loc,sr},I}$, the short-range part of the pseudopotential for the I-th nucleus, to be included either in the global or the appropriate local component, depending on

whether the decay of the exponential factor in $V^{\mathrm{PSP}}_{\mathrm{loc,sr},I}$ is slower or faster than $e^{-\alpha_c r^2}$, with α_c an adjustable cutoff parameter. We thus neglect the non-local component of the pseudopotentials, which only operates in the close surroundings of the corresponding atomic nucleus. The long-range behaviour of the pseudopotentials remains preserved, and therefore they will still provide the correct contributions in the region of the simulation cell which requires an AE treatment. The soft $\tilde{V}^{\tau}_{\mathrm{eff}}$ is constructed in reciprocal space, and subsequently its spatial derivatives are computed. $V^{\tau,1,\mathrm{PSP}}_{\mathrm{eff},I}$ and $V^{\tau,1,\mathrm{AE}}_{\mathrm{eff},I}$ quickly go to zero for large $r = |\mathbf{r}|$, an effect that is even amplified for their spatial derivatives. We will therefore assume that $\nabla V^{\tau,1,\mathrm{PSP}}_{\mathrm{eff},I}$ and $\nabla V^{\tau,1,\mathrm{AE}}_{\mathrm{eff},I}$ are only significant within U_I.

We now have elaborated all terms of $\Delta g^{\mathrm{SO}}_{xy}$ in their respective global and local components. The effective calculation of $\Delta g^{\mathrm{SO}}_{xy}$ then involves the evaluation of:

$$\begin{aligned}\Delta g^{\mathrm{SO}}_{xy} = \quad & \frac{\alpha g'}{2}\left\{\int_{\mathrm{FFT}} \mathrm{d}\mathbf{r}\left[\tilde{\mathbf{j}}^{\alpha}_{\mathbf{B}_x}(\mathbf{r})\times\nabla\tilde{V}^{\alpha}_{\mathrm{eff}}(\mathbf{r}) - \tilde{\mathbf{j}}^{\beta}_{\mathbf{B}_x}(\mathbf{r})\times\nabla\tilde{V}^{\beta}_{\mathrm{eff}}(\mathbf{r})\right]_y\right.\\ & + \sum_I \int_{\mathrm{LL},U_I} \mathrm{d}\mathbf{r}\left[\left(\mathbf{j}^{\alpha,1}_{\mathbf{B}_x,I}(\mathbf{r}) - \tilde{\mathbf{j}}^{\alpha,1}_{\mathbf{B}_x,I}(\mathbf{r})\right)\times\nabla\tilde{V}^{\alpha}_{\mathrm{eff}}(\mathbf{r}) - \left(\mathbf{j}^{\beta,1}_{\mathbf{B}_x,I}(\mathbf{r}) - \tilde{\mathbf{j}}^{\beta,1}_{\mathbf{B}_x,I}(\mathbf{r})\right)\times\nabla\tilde{V}^{\beta}_{\mathrm{eff}}(\mathbf{r})\right]_y\\ & \left. + \sum_I \int_{\mathrm{LL},U_I} \mathrm{d}\mathbf{r}\left[\mathbf{j}^{\alpha,1}_{\mathbf{B}_x,I}(\mathbf{r})\times\nabla V^{\alpha,1}_{\mathrm{eff},I}(\mathbf{r}) - \mathbf{j}^{\beta,1}_{\mathbf{B}_x,I}(\mathbf{r})\times\nabla V^{\beta,1}_{\mathrm{eff},I}(\mathbf{r})\right]_y\right\}. \end{aligned} \tag{62}$$

The second integral of the above equation contains the soft components $\nabla\tilde{V}^{\tau}_{\mathrm{eff}}$. These are only available on the FFT grid, but need to be multiplied with the spin-current densities defined on the LL grids of each atomic nucleus I. This problem is circumvented through a linear interpolation of the values of $\nabla\tilde{V}^{\tau}_{\mathrm{eff}}$ from the FFT-grid to the LL-grid.

3. *The $\Delta g^{\mathrm{SOO}}_{xy}$ term (Eq. 7)*

The computation of the induced magnetic field $\mathbf{B}^{\mathrm{corr}}_{\mathbf{B}_x}$ (Eq. 8) employs many of the techniques already used in the calculation of the chemical shift tensor. For the chemical shift tensor, only the positions of the atomic nuclei are of interest, whereas here, the induced magnetic field must be known in entire space. Unfortunately, due to the presence of a non-local operator, i.e. $\frac{\mathbf{r}'-\mathbf{r}}{|\mathbf{r}'-\mathbf{r}|^3}$, the creation of a GAPW representation for the induced magnetic field is not straightforward. In addition, the analytic elaboration through the Gaussian representation of the current density is also far from trivial. However, it generally holds that $\Delta g^{\mathrm{SOO}}_{xy}$ is a relatively small term in comparison with $\Delta g^{\mathrm{ZKE}}_{xy}$ and $\Delta g^{\mathrm{SO}}_{xy}$. For this reason, we choose to neglect the contributions from the atom-centered current densities $\mathbf{j}^{\mathrm{corr},1}_{\mathbf{B}_x} - \tilde{\mathbf{j}}^{\mathrm{corr},1}_{\mathbf{B}_x}$ to the ($\mathbf{G} \neq \mathbf{0}$) components $\tilde{\mathbf{B}}^{\mathrm{corr}}_{\mathbf{B}_x,\mathbf{G}\neq\mathbf{0}}$ of the induced magnetic field. Being computed from the soft current density $\tilde{\mathbf{j}}^{\mathrm{corr}}_{\mathbf{B}_x}$ only, through Eq. 50 on the reciprocal-space FFT-grid, these components will be soft, too (hence the tilde). $\mathbf{B}^{\mathrm{corr}}_{\mathbf{B}_x,\mathbf{G}=\mathbf{0}}$, on the other hand, will be computed analytically via Eq. 52, using the Gaussian representation of the current density. In summary, adopting a concise notation $\rho_{\mathrm{s}} = \rho^{\alpha} - \rho^{\beta}$, $\Delta g^{\mathrm{SOO}}_{xy}$ is evaluated as follows:

$$\begin{aligned}\Delta g^{\mathrm{SOO}}_{xy} &= 2\int \mathrm{d}\mathbf{r}\; B^{\mathrm{corr}}_{\mathbf{B}_x,y}(\mathbf{r})\rho_{\mathrm{s}}(\mathbf{r})\\ &\approx 2\int \mathrm{d}\mathbf{r}\left(\tilde{B}^{\mathrm{corr}}_{\mathbf{B}_x,\mathbf{G}\neq\mathbf{0},y}(\mathbf{r}) + B^{\mathrm{corr}}_{\mathbf{B}_x,\mathbf{G}=\mathbf{0},y}\right)\times\\ &\quad\left(\tilde{\rho}_{\mathrm{s}}(\mathbf{r}) + \rho^1_{\mathrm{s}}(\mathbf{r}) - \tilde{\rho}^1_{\mathrm{s}}(\mathbf{r})\right)\\ &= 2\int_{\mathrm{FFT}} \mathrm{d}\mathbf{r}\tilde{B}^{\mathrm{corr}}_{\mathbf{B}_x,\mathbf{G}\neq\mathbf{0},y}(\mathbf{r})\tilde{\rho}_{\mathrm{s}}(\mathbf{r})\\ &+ 2\sum_I\int_{U_I}\mathrm{d}\mathbf{r}\tilde{B}^{\mathrm{corr}}_{\mathbf{B}_x,\mathbf{G}\neq\mathbf{0},y}(\mathbf{r})\left(\rho^1_{\mathrm{s},I}(\mathbf{r}) - \tilde{\rho}^1_{\mathrm{s},I}(\mathbf{r})\right)\\ &+ 2B^{\mathrm{corr}}_{\mathbf{B}_x,\mathbf{G}=\mathbf{0},y}. \end{aligned} \tag{63}$$

III. RESULTS AND DISCUSSION

A. Test calculations

The GAPW method for the AE calculation of the NMR chemical shifts, the NMR magnetic susceptibility, and the EPR g tensor was validated by comparison for a series of small isolated molecules with the results from conceptually similar gas-phase methods, (i) the NMR routines as implemented in the GAUSSIAN03 program package (further referred to as the G03 method), and (ii) the g tensor method of Schreckenbach and Ziegler[23] as implemented in the ADF[26] program package. In our method, all isolated molecules were approximated by using large supercells of $(20\mathring{A})^3$. We have used a 300Ry cutoff for the auxiliary PW grid and a BLYP[27,28] gradient-corrected exchange-correlation functional.

Since both the GAPW and the G03 method essentially use Gaussian basis sets, a side-by-side comparison of the

NMR quantities obtained with different Gaussian basis set types is possible. Three basis set types have been used: aug-cc-pVDZ, aug-cc-pVTZ, aug-cc-pVQZ.[29–32] A comparison between the G03 and our GAPW method for the isotropic (mean of the three principal values) and the anisotropic (highest minus lowest principal value) chemical shifts of a comprehensive set of molecules is shown in Figure 1. The chemical shifts are expressed in parts per million (ppm). (discussion *to be added*).

For the g tensor, a true side-by-side comparison is not feasible, since ADF employs Slater-type basis set functions. Nevertheless, we calculated the g tensors in ADF employing the very large ET-pVQZ basis set, and chose to regard this a fully converged set. In Figure 2, we compared with this reference set for three different Gaussian basis sets, i.e. 6-311++G(3df,3pd), aug-cc-pVTZ, and aug-cc-pVQZ. The same geometry (optimized using ADF/ET-pVQZ) was used throughout. A comparison between the ADF method and our GAPW method for the isotropic (mean of the three principal values) and the anisotropic (highest minus lowest principal value) g values of a comprehensive set of molecules is shown in Figure 2. Just as was the case for the chemical shifts, the g values are expressed in parts per million (ppm). Using the 6-311++G(3df,3pd) basis set, most g values agree to within just a few percent, an excellent result, especially when taking into account the fact that very different basis sets have been used. For both the aug-cc-pVTZ and the aug-cc-pVQZ basis set, the agreement is worse: while most of the g values still agree to within less than ten percent with the ADF results (which appears to be possible, given the fact that different basis sets have been used), larger deviations (up to 30%) are obtained for ClO_3, SO_2^-, and SO_3^-. Presumably, the origin of this deviation lies in the fact that some of the default settings of the GAPW method are no longer applicable to these heavier elements. (further discussion *to be added*).

B. Chemical shift and magnetic susceptibility for a large biomolecule

to be added.

C. g tensor of the E_1' center in α-quartz

To further validate our method for the calculation of the g tensor and to apply it in a PBC simulation, we have calculated the g tensor of the positively charged oxygen vacancy E_1' center in α-quartz. Being one of the most abundant point defects in silica and due to its importance in the degradation of the performance of the gate oxide in transistors, the E_1' center has been the subject of a large number of calculations (an excellent overview can be found in Ref. 33). To our knowledge, the g tensor of this defect has been calculated only once,[13] using the GIPAW g-tensor method. However, the (periodic) simulation cell that was used included only 71 atoms (24 silicon atoms and 47 oxygen atoms), while the real E_1' center in nature has quite a long (up to 4-5 SiO_2 shells) defect geometry propagation, causing the structure to be somewhat biased by the periodic replica. Moreover, the interaction range of the +1 positive charge of the E_1' center is even much larger than 4-5 SiO_2 shells, since the quite well ordered structure does not help in screening the bare charge.

For the present calculation, we have used a QM/MM scheme previously tuned and tested on α-quartz.[33–35] The MM α-quartz crystal is made of 15552 atoms in an orthorhombic cell with lattice constants of 49.94, 57.66, and 63.49$\AA$ is described using the van Beest-Kramer-van Santen (BKS) potential.[36] After removal of an oxygen atom, a portion of 159 QM atoms was chosen in order to surround the oxygen vacancy defect. The geometry was relaxed using the GPW method, using a PSP approximation for the entire QM subsystem. For the GAPW g-tensor calculation on the relaxed structure, 17 QM atoms are described with AE treatment (using the full nuclear potential), while the remaining 142 QM atoms are still described within the PSP approximation. The different subsystems of this approach, which will be referred to as AE/PSP/MM, are shown in Figure 3. We have also performed a calculation using an AE treatment for the entire QM subsystem, this approach will be referred to as AE/MM. A PBE[37] gradient-corrected functional was used (in correspondance with the GIPAW calculation), together with a TZV2P-PSP[38] basis set for the PSP atoms and a 6-311G** basis set for the AE atoms, and a 320 Ry cutoff for the auxiliary plane wave grid.

The QM/MM potential is efficiently computed by the recently proposed scheme[39] based on a Gaussian Expansion of the Electrostatic Potential (GEEP). The long-range electrostatic term in the QM/MM coupling scheme is essential to properly describe the quantum properties of the QM subsystem in ordered structures such as α-quartz.[35] The proper treatment of the long-range electrostatic effects, between the QM and the MM subsystems, is achieved introducing a reciprocal space term of the MM electrostatic potential through a modified Ewald scheme.[35] Moreover, the QM subsystem is coupled to its own periodic images using the same scheme proposed to decouple periodic images in PW-based QM calculations.[40]

The calculated Δg tensors are presented in Table I, together with the corresponding experimental (Ref. 41) and theoretical (using the GIPAW method) data from literature. Comparing the calculated Δg tensors with the available experimental data, all three methods — GAPW AE/PSP/MM, GAPW AE/MM, and GIPAW — are found to perform very well. While the principal values in the GIPAW approach are overestimated to some extent, the GIPAW approach does not feature the quasidegeneracy of the Δg_{yy} and Δg_{zz} principal values found in both GAPW approaches, which also affects the predictions for the corresponding principal directions.

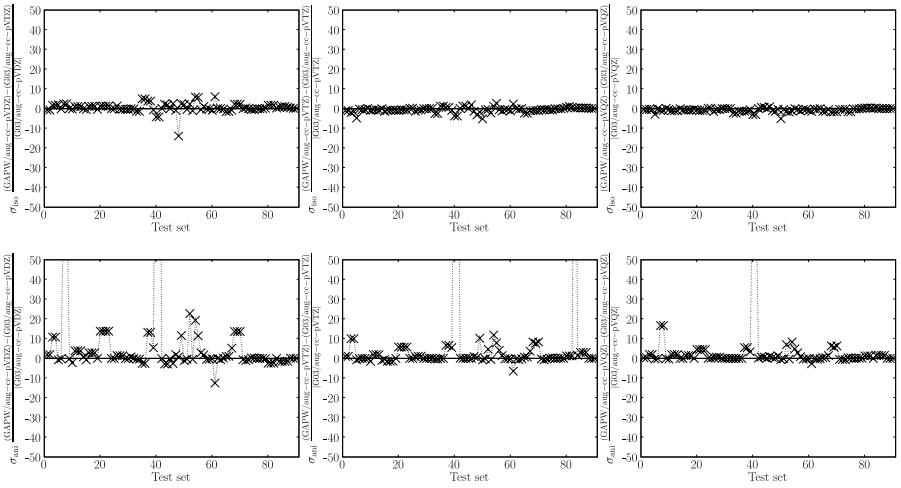

FIG. 1: Percentage deviation of our GAPW method from the G03 method for the isotropic ($\sigma_{\rm iso}$) and anisotropic ($\sigma_{\rm ani}$) chemical shifts (in ppm) calculated on the following set of small isolated molecules: C_2H_2, CH_2O, CH_3Cl, CH_3F, CH_4, Cl_2, CO_2, F_2, FCl, H_2O_2, H_2O, H_2, H_2S, HCl, HCN, HCO_2H, HF, HNO_3, N_2O, N_2, NH_3, NO_2, O_2, O_3, PH_3, SiH_4, SO_2.

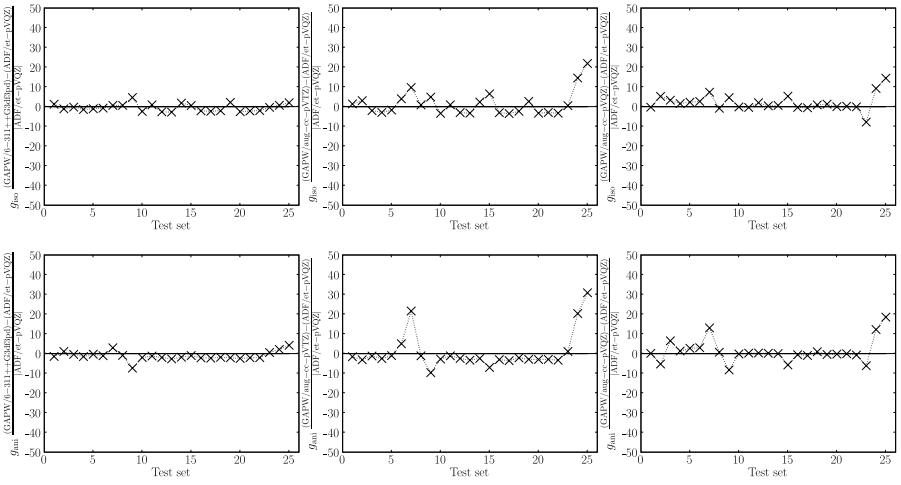

FIG. 2: Percentage deviation of our GAPW method from the ADF method for the isotropic ($g_{\rm iso}$) and anisotropic ($g_{\rm ani}$) g values (in ppm) calculated on the following set of small isolated molecules: BO, BS, C_3H_5, CH_3, CH_4^+, ClO_2, ClO_3, CN, CO_2^-, CO_3^-, CO_+, H_2CO^+, H_2O^+, COH, MgF, NF_2, NF_3^+, NH_3^+, NO_2, NO_3, O_2H, O_3^-, SiH_3, SO_2^-, SO_3^-.

The use of the PSP approximation does not affect the results by much, as the GAPW AE/PSP/MM and the GAPW AE/MM results agree really well, especially taking into account the much lower computational cost. Of course, a better agreement (at an elevated computational cost) is always possible, by adopting an AE treatment for additional atoms.

IV. CONCLUSION

We have introduced a method for the AE calculation of the NMR chemical shifts, the NMR magnetic susceptibility, and the EPR g tensor in PBC simulations, using the GAPW method. Through the use of a GAPW scheme, the mandatory usage of the pseudopotential approximation, one of the main obstacles in the original Sebastiani implementation, is finally lifted. We have implemented this method in QUICKSTEP. The method was validated first by comparison with other theoretical methods for a selection of atoms and small molecules (using a supercell technique). Then, two exemplary applications of the method have been presented, one involving the calculation of the chemical shifts and the susceptibility in a large biomolecule, the other the calculation of the g tensor for the E_1' center in α-quartz using a 15551-atom simulation cell and a three-layered AE/PSP/MM approach. These two examples are indicative for the application field in which we hope our method to be of great value.

V. ACKNOWLEDGEMENTS

This work was supported by the Fund for Scientific Research-Flanders and the Research Board of Ghent University.

* Electronic address: hutter@pci.uzh.ch
† Electronic address: Michel.Waroquier@UGent.be
‡ Electronic address: marcella.iannuzzi-mauri@psi.ch

[1] P. Hohenberg and W. Kohn, Phys. Rev. **136**, B864 (1964).
[2] W. Kohn and L. J. Sham, Phys. Rev. **140**, A1133 (1965).
[3] M. Kaupp, M. Bühl, and V. G. Malkin, *Calculations of NMR and EPR parameters: Theory and Applications* (Wiley-VCH, Weinheim, 2004).
[4] Http://cp2k.berlios.de.
[5] J. VandeVondele, M. Krack, F. Mohamed, M. Parrinello, T. Chassaing, and J. Hutter, Comput. Phys. Commun. **167**, 103 (2005).
[6] G. Lippert, J. Hutter, and M. Parrinello, Theor. Chem. Acc. **103**, 124 (1999).
[7] S. Goedecker, M. Teter, and J. Hutter, Phys. Rev. B **54**, 1703 (1996).
[8] C. Hartwigsen, S. Goedecker, and J. Hutter, Phys. Rev. B **58**, 3641 (1998).
[9] M. Krack and M. Parrinello, Phys. Chem. Chem. Phys. **2**, 2105 (2000).
[10] D. Sebastiani and M. Parrinello, J. Phys. Chem. A **105**, 1951 (2001).
[11] R. Declerck, V. Van Speybroeck, and M. Waroquier, Phys. Rev. B **73**, 115113 (2006).
[12] F. Mauri, B. G. Pfrommer, and S. G. Louie, Phys. Rev. Lett. **77**, 5300 (1996).
[13] C. Pickard and F. Mauri, Phys. Rev. Lett. **88**, 086403 (2002).
[14] A. Putrino, D. Sebastiani, and M. Parrinello, J. Chem. Phys. **113**, 7102 (2000).
[15] T. A. Keith and R. F. W. Bader, Chem. Phys. Lett. **210**, 223 (1993).
[16] D. Sebastiani, G. Goward, I. Schnell, and M. Parrinello, Comput. Phys. Commun. **147**, 707 (2002).
[17] D. Sebastiani, G. Goward, I. Schnell, and H. W. Spiess, J. Mol. Struct. **625**, 283 (2003).
[18] G. H. Wannier, Phys. Rev. **52**, 191 (1937).
[19] S. Obara and A. Saika, J. Chem. Phys. **84**, 3963 (1986).
[20] Lebedev VI (1975) Zh Vychisl Mat Mat Fiz 15: 48.
[21] Lebedev VI (1976) Zh Vychisl Mat Mat Fiz 16: 293.
[22] Lebedev VI (1977) Sib Math 15: 48.
[23] G. Schreckenbach and T. Ziegler, J. Phys. Chem. A **101**, 3388 (1997).
[24] J. C. Slater, Phys. Rev. 81 **81**, 385 (1951).
[25] P. E. Blöchl, Phys. Rev. B **50**, 17953 (1994).
[26] ADF2007.01, SCM, Theoretical Chemistry, Vrije Universiteit, Amsterdam, The Netherlands, http://www.scm.com.
[27] A. D. Becke, Phys. Rev. A **38**, 3098 (1988).
[28] C. Lee, W. Yang, and R. G. Parr, Phys. Rev. B **37**, 785 (1988).
[29] T. H. Dunning, J. Chem. Phys. **90**, 1007 (1989).
[30] D. E. Woon and T. H. Dunning, J. Chem. Phys. **100**, 2975 (1994).
[31] R. A. Kendall, T. H. Dunning, and R. J. Harrison, J. Chem. Phys. **96**, 6796 (1992).
[32] D. E. Woon and T. H. Dunning, J. Chem. Phys. **98**, 1358 (1993).
[33] T. Laino, D. Donadio, and I. W. Kuo, Phys. Rev. B **76**, 195210 (2007).
[34] F. Zipoli, T. Laino, A. Laio, M. Bernasconi, and M. Parrinello, J. Chem. Phys. **124**, 154707 (2006).
[35] T. Laino, A. Mohamed, and M. Parrinello, J. Chem. Theory Comput. **2**, 1370 (2006).
[36] W. H. van Beest, G. J. Kramer, and R. A. van Santen, Phys. Rev. Lett. **64**, 1955 (1990).
[37] J. P. Perdew, K. Burke, and M. Ernzerhof, Phys. Rev. Lett. **77**, 3865 (1996).
[38] G. Lippert, J. Hütter, P. Ballone, and M. Parrinello, J. Phys. Chem. **100**, 6231 (1996).
[39] F. Laino, A. Mohamed, and M. Parrinello, J. Chem. Theory Comput. **1**, 1176 (2005).
[40] P. E. Blöchl, J. Chem. Phys. **103**, 7422 (1995).
[41] M. G. Jani, R. B. Bossoli, and L. E. Halliburton, Phys. Rev. B **27**, 2285 (1983).

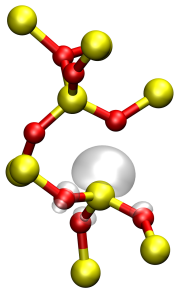

(a) The AE fragment, together with an isosurface plot of the spin density ($\rho_s = 0.01$).

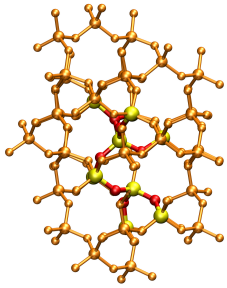

(b) The AE fragment, embedded in the PSP layer (orange).

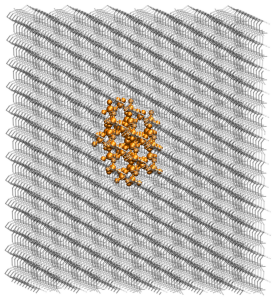

(c) The QM (AE and PSP) fragment (orange), embedded in the MM layer (grey).

FIG. 3: The hybrid AE/PSP/MM scheme used to describe the E_1' center in α-quartz. The periodically repeated simulation cell has a total of 15551 atoms, 142 of those are described within the PSP approximation, and another 17 with an AE treatment (i.e. using the full nuclear potential).

TABLE I: Principal values and principal directions of the calculated Δg tensors for the E_1' center in α-quartz, and corresponding experimental (Ref. 41) and theoretical (using the GIPAW method) data from literature. Principal values are expressed in parts per million (ppm), principal directions in degrees.

	Principal values				Principal directions							
		GAPW	GAPW				GAPW		GAPW			
	Expt.	AE/PSP/MM	AE/MM	GIPAW	Expt.		AE/PSP/MM		AE/MM		GIPAW	
	Δg_{ii}	Δg_{ii}	Δg_{ii}	Δg_{ii}	θ	φ	θ	φ	θ	φ	θ	φ
Δg_{xx}	-530	-561	-593	-651	114.5°	227.7°	108.3°	229.6°	108.3°	230.1°	110.0°	223.5°
Δg_{yy}	-1790	-1830	-1870	-2255	134.5°	344.4°	157.6°	372.8°	149.0°	353.6°	142.3°	341.6°
Δg_{zz}	-2020	-1898	-1901	-2481	125.4°	118.7°	102.5°	135.4°	114.1°	131.5°	120.4°	121.1°

10 Paper IX

Multi-level modeling of silica-template interactions during initial stages of zeolite synthesis

T. Verstraelen, B. M. Szyja, D. Lesthaeghe, R. Declerck, V. Van Speybroeck, M. Waroquier, A. P. J. Jansen, A. Aerts, L. R. A. Follens, J. A. Martens, C. E. A. Kirschhock, and R. A. van Santen

Submitted to Journal of the American Chemical Society (July 2008)

Multi-level modeling of silica-template interactions during initial stages of zeolite synthesis

Toon Verstraelen,[1] *Bartłomiej M. Szyja,*[2,3] *David Lesthaeghe,*[1] *Reinout Declerck,*[1]

Veronique Van Speybroeck,[1,*] *Michel Waroquier,*[1] *Antonius P. J. Jansen,*[2]

Alexander Aerts,[4] *Lana R. A. Follens,*[4]

Johan A. Martens,[4] *Christine E. A. Kirschhock,*[4] *Rutger A. van Santen*[2,*]

[1] Ghent University, Center for Molecular Modeling, Proeftuinstraat 86, 9000 Gent, Belgium

[2] Eindhoven University of Technology, Department of Chemical Engineering and Chemistry, Den Dolech 2, 5612 AZ Eindhoven, The Netherlands

[3] Wrocław University of Technology, Faculty of Chemistry, Department of Fuels Chemistry and Technology, Gdańska 7/9, 50-344 Wrocław, Poland

[4] K. U. Leuven, Centre for Surface Chemistry and Catalysis, Kasteelpark Arenberg 23, 3001 Leuven, Belgium

veronique.vanspeybroeck@ugent.be, r.a.v.santen@tue.nl

RECEIVED DATE

Abstract

Zeolite synthesis is driven by structure-directing agents, such as tetrapropyl ammonium ions (TPA^+) for Silicalite-1 and ZSM-5. However, the guiding role of these organic templates in the complex assembly to highly ordered frameworks remains unclear, limiting the prospects for advanced material synthesis. In this work, both static ab initio and dynamic classical modeling techniques are employed to provide insight into the interactions between TPA^+ and Silicalite-1 precursors, Key variables, such as charge compensation, temperature and solvation, are monitored with multiple methods. Our simulations reveal that, as soon as the typical straight 10-ring channel of Silicalite-1 or ZSM-5 is formed from smaller oligomers, the TPA^+ template is partially squeezed out of the resulting cavity. They also show that partial retention of the template in the cavity is, however, indispensable to prevent collapse of the channel and subsequent hydrolysis. After this initial transition, the position of the template hints at a supramolecular organization of precursors to larger aggregates, suggesting that template molecules provide a variety of functions during the initial stages of zeolite synthesis.

KEYWORDS Zeolites, TPA template, structure-directing agent, ZSM-5, Silicalite-1, precursors, nucleation, molecular dynamics, density functional theory

BRIEFS Silica-water-template interactions during the initial stages of zeolite synthesis

10. Paper IX :: Multi-level modeling of silica-template interactions during initial stages of zeolite synthesis

Introduction

This study aims to unravel the elementary interactions and driving forces behind Silicalite-1 formation, whose aluminosilicate counterpart ZSM-5 is a commonly used catalyst in the petrochemical industry.[1] Silicalite-1 provides a textbook case study: it has been the object of countless investigations on zeolite formation and is formed through the best understood zeolite synthesis procedure to date.[2-26] Colloidal Silicalite–1 is synthesized from 'clear solutions', from which it is obtained by hydrolysis of tetraethylorthosilicate (TEOS) as a monomeric silica source in aqueous tetrapropylammonium hydroxide (TPAOH) at room temperature. The 'clear solution' is actually a clear suspension of subcolloidal nanoparticles smaller than 10 nm that forms spontaneously upon mixing the reagents at ambient temperature. The nature of these nanoparticles and their role in the nucleation and growth process is currently subject to considerable discussion. Some believe that the silica nanoparticles do not participate in nucleation directly, but dissolve and serve as nutrients during crystallization.[8,27,28] Others assume the direct incorporation of formed nanoparticles into the growing crystals. This could be accomplished via an aggregation mechanism[5,16,23,29-32] in which these nanoparticles either already resemble the MFI structure[29-31] or exhibit a different silicon connectivity beforehand.[16,21-23] For the particular case of Silicalite-1 formation in presence of tetrapropylammonium cations (TPA^+), evidence in favor of the aggregation type mechanisms is growing.[16,22,23,33]

The exact role of organic cations like TPA^+ as structure-directing agents (SDAs) for zeolite synthesis is also still controversial. It is not clear whether they act as true templates shaping silica around them,[4,34,35] whether they act as external 'scaffolds', organizing the solvent and stabilizing the hetero-network of oligomers,[36-38] or whether they form a shell around the silica-rich, negatively charged core of the nanoparticles.[21,40] The first function implies direct silicate organization by the template inside the nanoparticles on a molecular level,[39] while the second and third hypotheses assume supramolecular organization, during which silica nanoparticles are shielded from excessive hydrolysis.

This study will focus on these early stages of zeolite formation from a modeling perspective. We focus particularly on aggregation type mechanisms, given the growing evidence for their role as mentioned above. In an aggregation type mechanism, silica-template interactions convert smaller oligomers into nano-sized precursor species.[41-43] Many such species have been identified in the synthesis mixture. Our analysis is based primarily on the Si_{33} precursor species (constructed from three Si_{11} undecamers). This precursor with MFI-like connectivity has been proposed to participate actively in Silicalite-1 formation as it strongly resembles a fragment of the future crystal.[41-43] This study aims to reveal how the interactions between such a silica precursor species and TPA^+ templates in aqueous solution evolve during the zeolitization process. Recently, comparison between simulated and experimental IR patterns has illustrated how the silica enclosed in the colloidal nanoparticles evolves in time, leading from small five-ring oligomers towards successively more condensed 5-ring species.[44] We will, therefore, not only focus on the Si_{33} precursor, but also on possibly preceding Si_{22} intermediates (formed from two Si_{11} undecamers), which are the smallest oligomers able to create an initial section of the straight 10-ring channels that are present in the final Silicalite-1 structure. The Si_{11} undecamer units, based on 5-membered rings, are the elementary building blocks for the simulated species. For these S_{11} units, Kirschhock et al. have proposed three possible structures: the capped double five ring, the tetracyclic undecamer and the tricyclic undecamer,[41,42] for which only the latter can be combined to a Si_{22} nanoparticle. As observed from the splitting of the chromatographic peak corresponding to the Si_{22} species,[43] such a construction can proceed via two routes, for which only one forms the 10-ring channel. Addition of a third Si_{11} unit to either of these double units can lead to the formation of the proposed Si_{33} precursor, as shown in Figure 1.[43]

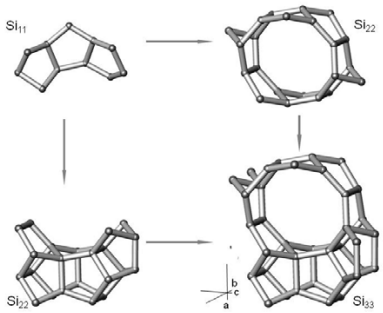

Figure 1. Assembly of Si_{11} units to Si_{22} and Si_{33} precursor nanoparticles.

For such a complex system, many different variables need to be addressed and many different techniques can be used, which is why theoretical modeling of zeolite synthesis has proven to be a challenging task.[45-47] Nevertheless, several attempts have already been made, using both quantum chemical and classical molecular mechanics techniques.[48] Major contributions have been given by Catlow and co-workers using a variety of different modeling techniques including both static and dynamic approaches.[49-53] From classical molecular dynamics simulations of silica precursors and a structure-directing agent, they found long range electrostatic interactions to be of crucial importance, since without these interactions the investigated complexes tended to dissociate rather than agglomerate. Rao and Gelb,[54] on the other hand, studied earlier stages of silica polymerization using the reactive forcefield developed by Feuston and Garofalini.[55] They observed that at time scales shorter than 0.5 ns four-membered rings will be most common, while at time scales longer than 1 ns five-membered rings will dominate. Very recently, Mora-Fonz, Catlow and Lewis have shown the importance of solvent and pH to control specific oligomerization and cyclization processes in the nucleation of microporous silicas.[56-57]

The major drawback for theoretical simulations is the fact that there are many different variables which, each to a specific yet unknown extent, might all influence the interaction between silica and template molecules. In this paper, we have tried to address this shortcoming through a multi-level approach. Among the most crucial parameters that can be varied are the many ways solvent can be treated, from polarizable continuum methods to the explicit treatment of individual molecules. The silica-template interaction can furthermore be described by many different levels of theory, ranging from fast yet approximate force fields to highly accurate but extremely time-demanding *ab initio* methods. To reduce the enormous task of performing many different simulations tailored to each individual parameter, while at the same time maximizing the benefits of various approaches, we have performed just two sets of calculations that complement each other well, one static and one dynamic. Within these two sets of simulations, we have accommodated as many different variables as possible: an overview of the major differences between the two sets is given in Table 1. A more detailed discussion of the various contributions will be given in the following section.

Table 1. Comparison of the treatment of crucial variables for the two complementary sets of calculations.

	Static approach	Dynamic approach
Level of theory	Hartree-Fock	Universal Forcefield (UFF)
	Density Functional Theory (DFT)	
Solvent treatment	dielectric continuum model (COSMO)	explicit molecules
Solvent type	no solvent	water + additional TPA+
	water	
	ethanol	
Charge on silica nanoparticle	neutral	SiO-
	Al defect	
Total charge on nanoparticle	0	-1 on Si_{33}
	-1	-3 on Si_{11}
		-6 on Si_{22}
Nanoparticle size	Si_{33}	Si_{11}
		Si_{22}
		Si_{33}

Theoretical basis

Ab initio static calculations

In our first type of calculations, the system was treated using static ab initio calculations with the GAUSSIAN03 and CP2K/QUICKSTEP packages.[58-59] We used the 33T precursor as proposed by Kirschhock et al.,[41] which was also modeled in previous work.[44,60] With GAUSSIAN03, the silica cluster and the template were optimized at the ab initio HF/3-21g level of theory, after which HF/6-31+g(d) and density functional theory (DFT) B3LYP/6-31+g(d) single-point energies were calculated.[61-62] Throughout the manuscript, these two level methods will be designated as HF/6-31+g(d)//HF/3-21g and B3LYP/6-31+g(d)//HF/3-21g respectively. All initial optimizations were performed in the gas-phase, while the solvent was taken into account by using the COSMO model as implemented in GAUSSIAN03.[63-64] Both water and ethanol solvents were considered, as these are typical solvents for a clear solution synthesis procedure. We further corroborated these results with a full DFT treatment (i.e. also for the geometry relaxation), by employing the Gaussian and plane-wave (GPW) density functional method with periodic boundary conditions, as implemented in the CP2K/QUICKSTEP program package.[59] A PBE gradient-corrected functional was used throughout,[65] together with a TZ2VP-PSP basis set,[66] a 320 Ry cutoff for the auxiliary plane wave grid, and pseudopotentials developed by Goedecker *et al.*[67-68] This method is further referenced in the paper by GPW/PBE/TZ2VP-PSP.

A single tetrapropylammonium (TPA^+) template molecule was considered for each precursor species. Since the TPA^+ molecule is positively charged, the entire system's charge neutrality was maintained by incorporating an Al atom substituting a Si atom, thus creating a net negative charge on the Si_{33} precursor. In addition, similar calculations with a neutral precursor were performed as well by treating the entire system (precursor + TPA^+) as net positively charged to evaluate the effect of the electrostatic interactions. In the remainder of this article, the following nomenclature is used for the precursor-template structures : Si_{33}-TPA^+ and $Si_{32}Al^-$-TPA^+ for the net positively charged and the neutral system, $Si_{32}Al^-$-TPA^+ /water and $Si_{32}Al^-$-TPA^+ /ethanol for the neutral system that is additionally embedded in a dielectric medium that characterizes water and ethanol. Initial structures for all complexes were generated with the in house developed software

package ZEOBUILDER, which is specifically designed for building molecular architectures starting from elementary building blocks.[69]

Classical molecular dynamics calculations

In our second type of calculations, the system was simulated using classical molecular dynamics (MD) with periodic boundary conditions. The unit cell was cubic in shape with an edge length of 25 Å. The content of the unit cell was varied to capture different stages during synthesis. A first set of simulations was performed on a unit cell containing 3 Si_{11} oligomers, two of which were connected to form the Si_{22} structure (shown in Figure 2). While the third Si_{11} oligomer was also present, it remained a spectator species during the entire simulation. In addition, the environment contained 9 TPA^+ molecules and 250 explicit water molecules. To study the influence of charged configurations on the system, we applied the following classical approach: all nitrogen atoms belonging to TPA^+ were assigned a positive charge (+1). Formation of a Si-O-Si bridge requires some of the oxygen atoms to be ionized, which is illustrated by the high pH required for condensation reactions to occur.[56,70] Therefore, three oxygen atoms in each of the silica oligomers were deprotonated, and charged negatively (-1) to counter-balance the TPA^+ ions. Since the total number of positive and negative charges was kept equal, the whole system could be treated as electrostatically neutral. This approach still requires a dielectric constant correction to properly account for bulk solvent effects.[71] This relative dielectric constant was set to 60, which corresponds to the dielectric constant of water under simulation conditions.

In a subsequent set of calculations, the unit cell contained the fully formed Si_{33} precursor with only one positively charged TPA template and 333 water molecules. As before, the nitrogen of the TPA^+ ion was assigned a positive charge (+1), while the precursor was deprotonated at one oxygen to maintain charge neutrality in the simulated box. As noted above, the dielectric constant was set to the value of 60. These simulations with explicit water molecules serve as an ideal comparative set to the static simulations.

The MD simulations were carried out in the NVT ensemble. The total time was set to 1000 ps with a timestep of 1 fs, while the temperature was set to 350 K, controlled by the temperature damping thermostat described by Berendsen et al.[72]

The selection of an adequate potential is crucial for every classical molecular simulation. There are many reactive and non-reactive forcefields optimized for zeolitic systems available: Feuston-Garofalini,[55,73] ReaxFF,[74-77] BKS,[78] CVFF[79] or the Catlow library-collection of potentials.[80-81] All of them suffer from important disadvantages related to the system described here. Both reactive forcefields (Feuston-Garofalini and ReaxFF) allow creation or breaking of chemical bonds during simulation, but they do not include interactions between the silica oligomers and TPA. Similarly, the BKS forcefield, which is limited only to the atom types Si, Al, P and O, also fails to do so. Among the aforementioned forcefields, only CVFF could provide the required parameters for the MD simulation. However, the quality of the results obtained with CVFF were well below expectations: even for long time-scale simulations we only observed minor thermal vibrations, and the system did not significantly evolve during the simulation.

Therefore, the Universal Forcefield (UFF) was applied in the present work, despite the absence of a hydrogen bonding term.[82] Results obtained using this forcefield are qualitatively consistent with the quantum chemical calculations.

The molecular dynamics runs were analysed using the in house developed software package TRACKS, allowing efficient analysis of molecular dynamics and Monte Carlo runs and generation of physical properties such as radial distribution functions along the run.[83]

Models used in simulations

Due to the fact that a non-reactive forcefield was applied in the classical simulations, it was necessary to manually create the bonds connecting two Si_{11} oligomers before starting new simulations. We created four different models of Si_{22} oligomers, and carried out Molecular Dynamics simulations for each of them. These models differ in number of connections (oxygen bridges) between two Si_{11} oligomers. The most flexible structure is the model with only one connection between the Si_{11} units, as shown in Fig. 2(a). The Si_{22} structure with 4 connections, representing a segment of the straight channel in an MFI type zeolite, 2(d), is the most rigid.

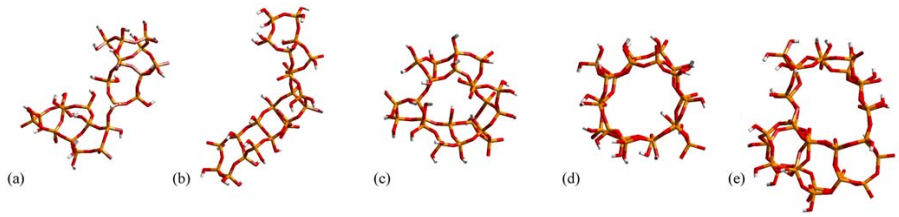

Figure 2. Five silica models used in simulations. (a) Si_{22} with one connection (oxygen bridge) between two Si_{11} oligomers; (b) Si_{22} with 2 connections; (c) Si_{22} with 3 connections; (d) Si_{22} with 4 connections (fully formed channel); (e) Si_{33} precursor

The MD simulations represent two stages in the formation of Si_{22} – models (a) and (b) represent the initial stage, where only one end of the Si_{22} structure is connected, while models (c) , (d) and (e) represent the final stage where a silicalite channel fragment is formed. For the computationally more demanding ab initio calculations only one model was used: the Si_{33} precursor, as shown in figure 1(e), which is obtained when an additional Si_{11} structure is added. This structure fully corresponds to the Silicalite-1 precursor species proposed in literature.[41]

Results and discussion

In this section, the stability of the Si_{33} precursor structure and its interaction with the template is discussed first, after which the positioning of the template with the preceding Si_{22} species will be investigated. Finally, a possible scenario for subsequent aggregation to a full crystal is put forward.

Ab initio static calculations: precursor-template interaction

An initial important observation applies to the neutral Si_{33} cluster without a TPA^+ molecule interacting with it. When optimizing this structure to a global minimum, the channel of this silica precursor collapses completely, as shown in figure 3. This observation is in accordance with earlier results by Lewis et al.:[53] a template prevents the decrease in surface area of the open-structured fragment. Absence of this stabilization will lead to reduction of the surface area, increasing the likelihood of subsequent hydrolysis. Without TPA^+, the precursor structure is not favored nor can it lead to a fully crystalline zeolite.

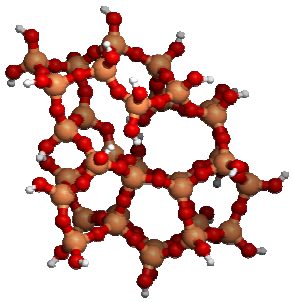

Figure 3: Structure of the optimized neutral Silica cluster Si_{33} without a TPA^+ at the B3LYP/6-31+g(d) level of theory.

In presence of the organic template, however, the neutral precursor does not fully collapse. In agreement with earlier results of Magusin et al.,[60] encapsulation of the TPA cation within the 10-ring of the Si_{33} precursor corresponds to a stable minimum on the potential energy surface (Si_{33}-TPA^+ is similar in structure to $Si_{32}Al$-TPA^+, which is labeled as structure B in Figure 4). However, two additional stable structures were located (their aluminosilica counterparts are labeled as structures A and C in Figure 4), for which TPA^+ is adsorbed slightly off-centre to the precursor. These 'half in- half out' structures are considerably more stable than structure B, where TPA is fully located inside the precursor: up to 205 and 164 kJ/mol at the GPW/PBE/TZ2VP-PSP level of theory, depending on the side along which the

TPA template molecule moves out of the precursor. The relative energies of these calculated structures at various levels of theory are given in Table 2.

Table 2. Relative energies [kJ/mol] for the precursor and a single TPA^+ molecule.

	Level of theory	structure A[a]	structure B[a]	structure C[a]	Solvation energy
Si_{33}-TPA^+	HF/3-21g//HF-3-21g	-188.4	0.0	-180.1	
	GPW/PBE/TZ2VP-PSP.	-205.2	0.0	-163.6	
$Si_{32}Al^-$-TPA^+	HF/3-21g // HF-3-21g	-407.8	0.0	-279.2	
	HF/3-21g//HF/6-31+g(d)	-464.2	0.0	-346.8	
	HF/3-21g//B3LYP/6-31+g(d)	-413.1	0.0	-293.6	
	GPW/PBE/TZ2VP-PSP.	-411.3	0.0	-258.4	
$Si_{32}Al^-$-TPA^+/water	HF/3-21g//B3LYP/6-31+g(d)	-353.4	0.0	-278.2	-216.0
$Si_{32}Al^-$-TPA^+ /ethanol	HF/3-21g//B3LYP/6-31+g(d)	-373.8	0.0	-282.4	-321.9

[a] In structure A the TPA cation is fully encapsulated within the 10-ring of the 33T precursor, in structures B and C the TPA cation is positioned off-centre of the precursor as shown in figure 4. [b] The solvation energy is defined as the energy difference between gas phase energies and the energies obtained by including a continuous dielectric medium.

As long as TPA^+ fully resides within the cavity, it prevents any collapse of the structure. In this configuration Coulombic interactions between template and framework are of considerable importance[53] and the positively charged template will mostly interact with the diffuse electron cloud of the surrounding framework oxygen atoms.[84-85] For the structures in which TPA is 'half in- half out', this interaction is reduced and the silicate structure is allowed to slightly relax, yet without collapsing completely. The interaction between the propyl 'arms' of the template and the hydrophobic inner surface of the precursor channel remains strong enough to stabilize an open precursor structure.

When the Si_{33} precursor is negatively charged with an Al defect to compensate for the charged template ($Si_{32}Al^-$-TPA^+), the qualitative picture remains identical, while the energy differences between the various structures in Figure 4 are more pronounced. For the GPW/PBE/TZ2VP-PSP level of theory this amounts to 411 kJ/mol and 258 kJ/mol (Table 2), depending not only on the side along which the TPA template molecule moves out of the precursor, but also on the position of the Al defect. Structure A, for which the positively charged TPA is located closest to the negative Al defect, is substantially more favored over structure C, where the template is on the opposite side of the Al substitution. In both cases there is a significant reduction in energy with the template positioned 'half in - half out' of the precursor. The precursor is partially relaxed along one side (i.e. on the side facing away from the template) to account for this energy difference.

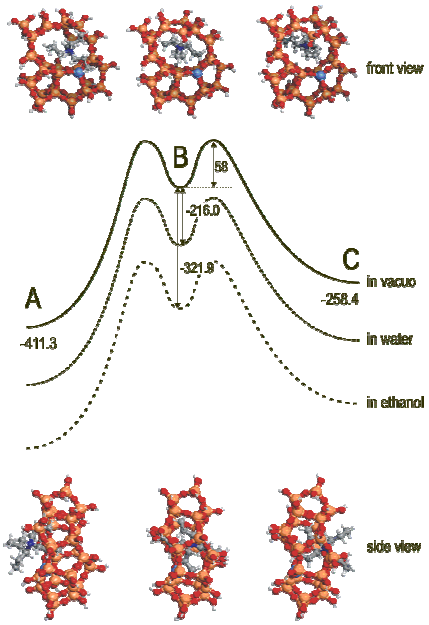

Figure 4. Relative energies in kJ/mol between the three stable structures ($Si_{32}Al^-$ precursor + TPA^+) at the GPW/PBE/TZ2VP-PSP level of theory.

To assess the barrier between these various structures, an energy profile was constructed along a pathway during which TPA moves out of the precursor. The energy profile resembles a possible transition path connecting structure B to structure A.[86] The barrier for escape of the TPA from the precursor was estimated at 58 kJ/mol, which should be considered as an upper limit since other, more preferable, escape paths might exist. This value is relatively small, indicating that such a transition should easily occur.

In a next step, the influence of solvation was investigated by applying the COSMO model in Gaussian03, since this methodology has already been validated for this type of systems by Mora-Fonz *et al.*[56] Solvation leads to an increased stability of the $Si_{32}Al^-$-TPA^+ complex by 216 and 322 kJ/mol for water and ethanol respectively. The solvation energy as shown in Table 2 originates from enclosing the complex in a cavity within a dielectric medium and is often referred to as the dielectric solvation energy (DSE).[71,87-88] The DSE values are larger for ethanol than for water, in accordance with experimental observations by Kirschhock et al.,[41,43] stating that the precursor species are long-lived in ethanol, or at least more so than in water. The qualitative picture on the relative stability of the various structures remains unaltered by including the solvent, while the energy difference between structures A and C is slightly reduced.

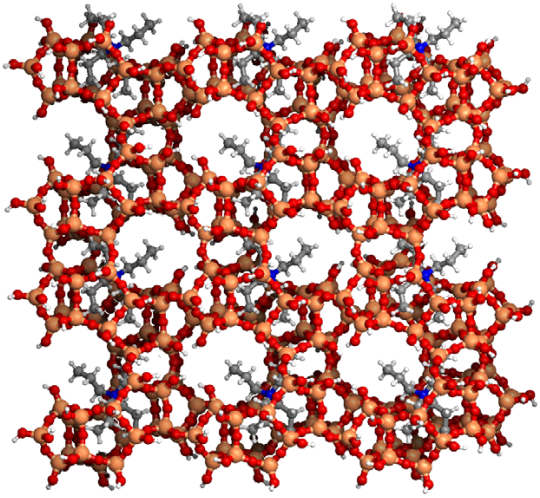

Figure 5. MFI-type nano-crystal containing 12 aggregated Si_{33} precursors, constructed from stable structures A and C from Figure 4.

The structures for which the template is positioned partially out of the 10-ring fragment hint at a supramolecular structure-directing role of TPA. The template is responsible for stabilizing tiny segments of the straight MFI channel, and one could speculate about the tendency of supramolecular precursor-TPA complexes to organize into larger aggregates. At first instance, we only investigated this possibility from a purely geometrical point of view, by using our optimized precursor-TPA complexes to construct nano-crystalline structures as proposed earlier in literature.[33,41-43] This was achieved by using our in-house developed software ZEOBUILDER, which allows construction of complex molecular architectures starting from elementary building blocks,[69] similar to building toy structures with Lego® blocks. The program uses a condensation algorithm that searches for optimal connections between sets of oxygen pairs in order to form new oxygen bridges. The procedure employed here, was based purely on geometrical constraints and the obtained structures were not further optimized. If serious geometrical obstacles would be encountered via this procedure, this would mean that the proposed structures can definitely not organize into larger subunits. However, by combining both A and C structures from Figure 4, it was possible to generate a small nano-crystallite in which the template resides close to the channel intersections (as shown in Figure 5). The template molecule is expected to move more or less freely into the relatively larger space available, but additional molecular dynamics simulations of TPA in the channel intersections would be necessary to further support this proposal, by investigating the flexibility of the template in the channel intersections. To date, this type of calculation at a solid level of theory is beyond current computer capabilities. Even ab initio geometry optimizations of the illustrated nano-crystal (containing approximately 2200 atoms) are beyond what is feasible today. For such an optimized structure, there would be approximately 9 TPA molecules inside a 12-block nano-crystal.[30]

From the quantum chemical results, it seems that only the hydrophobic interaction between the alkyl groups of the template and the inner pore surface of the precursor are of crucial importance for the stabilization of an MFI precursor on a molecular level. Together with the exceptional lattice stability of the MFI topology,[89] the partial role of TPA in a 'half in – half out' structure indicates why, next to TPA, also many other template molecules are capable of creating MFI-like structures.

Classical molecular dynamics calculations: template positioning at elevated temperatures

In the previous section, the static ab initio calculations showed the template to partially exit the straight channel fragment in the precursor. In this section, molecular dynamics calculations using a classical force field are presented to complement these findings and to provide additional insight into the position of the template during the preceding stages of precursor synthesis. Therefore, various Si_{22} intermediates are taken into consideration, where the number of bonds is gradually increased to mimic the

initial assembly of silica into a local MFI connectivity, culminating in the formation of a rigid fragment of the straight 10-ring channel.

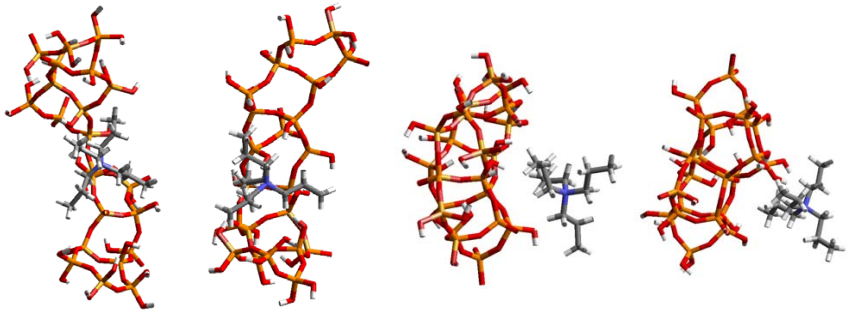

(a) (b) (c) (d)

Figure 6. Position of TPA molecules relative to Si_{22} oligomers with 1 bond (a), 2 bonds (b), 3 bonds (c) and 4 bonds (d). These representative snapshots from the simulations demonstrate how the template molecule can be initially enclosed by the Si_{22} structure, but will be pushed out as the channel is formed.

Figure 6 shows representative snapshots during the molecular dynamics runs for the various Si_{22} oligomers. The structures shown in (a) and (b), in which the channel is not yet formed, offer a wide enough gap between the Si_{11} parts to fit a TPA^+ ion. This is confirmed by geometry analysis which shows that the template molecule is located in between separate ends of the silica oligomer during the entire molecular dynamics run. The template's position changes when additional oxygen bridges are formed to obtain structures (c) and (d). Although the TPA^+ ion might be able to fit inside the channel of system (c), its preferred position is outside the channel. The same holds for the fully formed 10-ring (d). Just as in the static calculations, the template moves out of the channel fragment into the direction of the later to be formed channel cross-section in MFI.

As opposed to the continuum solvent model used in the static ab initio calculations, the current simulations provide insight in explicit silica-water interactions. The closest water molecules are arranged in a single layer around the silica species, while the template shields the inner hydrophobic region from the water layer, which is in accordance with simulations of Catlow et al.[53] Since temperature is also accounted for in the MD simulations, the template can move further apart from the nano-particle compared to the static calculations. Despite the template exiting, the six negative charges on the oxygen atoms of the Si_{22} structure induce strong electrostatic repulsive interactions, which prevents further collapse of the 10-membered ring. It needs to be pointed out that under experimental conditions the charge of the silica species decreases with increasing condensation due to release of hydroxyls. In order to assess the dependence of the results on the assigned charges, we repeated the simulations for the investigated systems, where only 2 or 4 out of total 6 negative charges were present on the Si_{22} cluster and the other charges were transferred to hydroxide anions in solution. During these simulations, the repulsive interactions between closely positioned oxygen atoms on the silica nanocluster are reduced, but the qualitative picture on the relative position of TPA with respect to the Si_{22} cluster is maintained.

In order to assess the effect of explicit solvation and temperature on the position of the template with respect to the Si_{33} precursor, molecular dynamics calculations were also performed on a single Si_{33} unit (only once deprotonated) and one TPA^+ cation further surrounded by 333 water molecules. A representative snapshot taken during the simulation is shown in Figure 7. Just as in the static calculations, the template moves out of the 10-ring into the direction of the future channel cross-section.

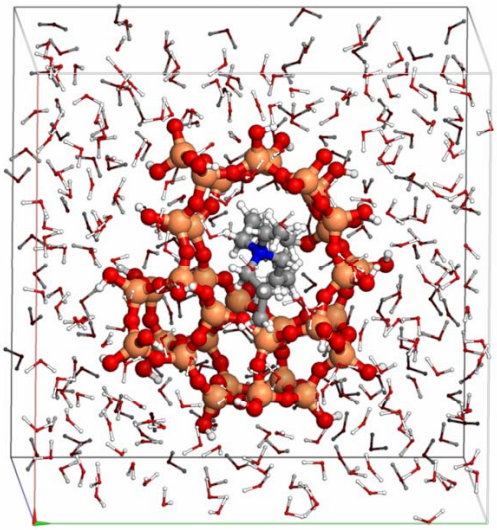

Figure 7: Snapshot from the classical molecular dynamics run of the Si_{33} precursor with one TPA cation, solvated by 333 explicit water molecules.

Further insight into the position of the template with respect to the silica precursor is obtained by analyzing a variety of distances along the trajectory and by calculating a histogram of the nitrogen-oxygen distances from the canonical (NVT) molecular dynamics calculations. This histogram, as shown in Figure 8, describes the frequency with which various distances were observed during the molecular dynamics run. Distinctions between the deprotonated oxygen (circle in figure 8 (a)), the oxygens in the hydrophobic 10-membered rings (which are highlighted in figure 8 (a)), and the other oxygens are made. The distance between the deprotonated oxygen atom and the TPA nitrogen atom remains at an average value of about 3.5 Å during the entire molecular dynamics run (figure 8 (b)).

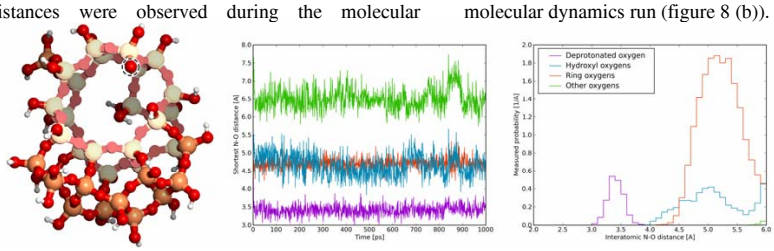

Figure 8 : (a) Labeling of various oxygen atoms in the precursor (b) Oxygen-nitrogen distances during the molecular dynamics run (c) Histogram of the oxygen-nitrogen distances calculated from the canonical (NVT) molecular dynamics calculations

According to the histogram for the oxygen-nitrogen distance, a first probability peak is situated around 3.5 Å, which corresponds to the contact between TPA^+ and the deprotonated oxygen atom, primarily governed by electrostatic Coulomb interactions. A second broader peak around 4.5 Å, originates from coordination of the TPA to the oxygen bridges of the 10-membered rings forming the inner hydrophobic layer. This interaction works independently from the oxygen charge defect, and is similar to what was observed in the ab initio simulations, where the diffuse electron cloud of the oxygen atoms provided additional stabilization of the TPA cation.

The molecular dynamics calculations, allowing elevated temperatures and presence of explicit water molecules, fully corroborate the static ab initio calculations. TPA^+ is pushed out of the straight channel but remains coordinated with the Si_{33} precursor, despite inclusion of temperature effects.

Conclusions

Structure directing agents or templates are the key components in zeolite synthesis as they steer the system to a certain framework topology, yet their specific function on a molecular level remains vague. For Silicalite-1 (whose aluminosilicate counterpart is ZSM-5) a clear solution synthesis technique is based on tetrapropyl ammonium ions (TPA^+) as templates. To gain more insight into the interactions between TPA^+ and possible Silicalite-1 precursors, we have performed two complementary sets of calculations. Both static and dynamic simulations were performed which allowed the investigation of a variety of parameters, such as temperature, charge compensation, implicit/explicit solvation models, and quantum mechanical versus classical force field treatment of the system. All our simulations reveal that, as soon as the typical straight 10-ring channel of Silicalite-1 is formed from smaller oligomers, the TPA^+ template is partially squeezed out of the resulting cavity. This result is found for charged as well as neutral silicate species, indicating that the interaction between the template molecule and a precursor with local zeolite connectivity is not purely based on electrostatic contributions with a localized negative charge. Partial retention of the template is, however, indispensable to prevent collapse of the channel and subsequent hydrolysis. In solvation, the template will also shield the hydrophobic inner region of the channel: without an organic template, open framework-like building blocks would succumb under the influence of water. The 'half in – half out' adsorption of the template shows that only the hydrophobic appendages are necessary to prevent collapse of the precursor nano-particle. This contribution not necessarily needs to be given by TPA^+, but might be provided by a whole range of organic molecules, which may explain why the MFI structure is observed for many other templates as well.

After this initial phase, the final 'half in – half out' position of the template hints at the possibility of a supramolecular organization of precursors to larger aggregates and maybe even the final crystalline product. The template has already shifted closer to what should be its final position at the channel intersections, which suggests that it could take on a different role, this time in supramolecular organization. Such a hypothesis would fit nicely in the gap between the three major theories regarding the role of the organic cations. This would result in two different functions for TPA^+: the hydrophobic appendages are vital to stabilize any kind of 10-ring containing precursor species, while the structure of TPA^+ exactly fits the channel intersections during and after aggregation. The mobility of TPA^+ during these various stages holds the key to a fundamental understanding of this synthesis process.

ACKNOWLEDGMENT

Calculations have been carried out in the Wrocław Centre of Networking and Supercomputing (PWr), in the Department of Chemical Engineering and Chemistry (TU/e) and at the Center for Molecular Modeling (UGent). Software used for simulations was Cerius2, Materials Studio, Gaussian03, Zeobuilder, CP2K and TRACKS [31]. DL, RD, MW, VVS, JAM and CEAK acknowledge support from the Fund for Scientific Research Flanders (FWO-Vlaanderen), ESA and the Belgian Prodex office. TV also acknowledge the Institute for the Promotion of Innovation through Science and Technology in Flanders (IWT-Vlaanderen) for funding this strategic basic research (SBO).

References

1. Corma A. *Chem. Rev.* **1997,** *97,* 2373-2420.

2. Persson, A. E.; Schoeman, B. J.; Sterte, J.; Otterstedt, J. E. *Zeolites* **1994,** *14,* 557-567.

3. Twomey, T. A. M.; Mackey, M.; Kuipers, H. P. C. E.; Thompson, R. W. *Zeolites* **1994,** *14,* 162-168.

4. Burkett, S. L.; Davis, M. E. *Chem. Mater.* **1995,** *7,* 920-928.

5. Dokter, W. H.; Van Garderen, H. F.; Beelen, T. P. M.; van Santen R. A.; Bras, W. *Angew. Chem. Int. Ed.* **1995,** *34,* 73-75.

6. Corkery, R. W.; Ninham, B. W. *Zeolites*, **1997,** *18,* 379-386.

7. Gougeon, R.; Delmotte, L.; Reinheimer, P.; Meurer, B.; Chezeau, J. M. *Mag. Res. Chem.* **1998,** *36,* 415-421.

8. Schoeman, B. J. *Microporous Mesoporous Mater.* **1998,** *22,* 9-22.

9. Tsay, C. S.; Chiang, A. S. T. *Microporous Mesoporous Mater.* **1998,** *26,* 89-99.

10. Watson, J. N.; Brown, A. S.; Iton, L. E.; White, J. W. *J. Chem. Soc. Faraday Trans.* **1998,** *94,* 2181-2186.

11. de Moor, P. P. E. A.; Beelen, T. P. M.; Van Santen, R. A.; Beck, L. W.; Davis, M. E. *J. Phys. Chem. B* **2000,** *104,* 7600-7611.

12. Li, Q.; Mihailova, B.; Creaser, D.; Sterte, J. *Microporous Mesoporous Mater.* **2001,** *43,* 51-59.

13. Mintova, S.; Olson, N. H.; Senker, J.; Bein, T. *Angew. Chem. Int. Ed.* **2002,** *41,* 2558-2561.

14. Yang, S.; Navrotsky, A. *Chem. Mater.* **2004,** *16,* 3682-3687.

15. Cheng, C. H.; Shantz, D. F. *J. Phys. Chem. B* **2006,** *110,* 313-318.

16. Davis, T. M.; Drews, T. O.; Ramanan, H.; He, C.; Dong, J.; Schnablegger, H.; Katsoulakis, M. A.; Kokkoli, E., McCormick, A. V.; Penn, L. R.; Tsapatsis, M. *Nat. Mater.* **2006,** *5,* 400-408.

17. Haouas M.; Taulelle, F. *J. Phys. Chem. B* **2006,** *110,* 3007-3014.

18. Knight, C. T. G.; Wang, J.; Kinrade, S. D. *Phys. Chem. Chem. Phys.* **2006,** *8,* 3099-3103.

19. Rimer, J. D.; Fedeyko, J. M.; Vlachos, D. G.; Lobo, R. F. *Chem. Eur. J.* **2006,** *12,* 2926-2934.

20. van Santen, R. A. *Nature* **2006,** *444,* 46-47.

21. Aerts, A.; Follens, L. R. A.; Haouas, M.; Caremans, T. P.; Delsuc, M. A.; Loppinet, B.; Vermant, J.; Goderis, B.; Taulelle, F.; Martens, J. A.; Kirschhock, C. E. A. *Chem. Mater.* **2007,** *19,* 3448-3454.

22. Kirschhock, C. E. A.; Aerts, A.; Martens, J. A. *Stud. Surf. Sci. Catal.* **2007,** *170,* 1473-1478.

23. Kumar, S.; Davis, T. M.; Ramanan, H.; Penn, R. L.; Tsapatsis, M. *J. Phys. Chem. B* **2007,** *111,* 3398-3403.

24. Pelster, S. A.; Kalamajka, R.; Schrader, W.; Schüth, F. *Angew. Chem. Int. Ed.* **2007,** *46,* 2299-2302.

25. Patis, A.; Dracopoulos, V.; Nikolakis, V. *J. Phys. Chem. C* **2007,** *111,* 17478-17484.

26. Fyfe, C. A.; Darton, R. J.; Schneider, C.; Scheffler, F. *J. Phys. Chem. C* **2008,** *112,* 80-88.

27. Cundy, C. S.; Henty, M.; Plaisted, R. *Zeolites* **1995,** *15,* 353-372.

28. Cundy, C. S.; Cox, P. A. *Microporous Mesoporous Mater.* **2005,** *82,* 1-78.

29. Watson, J. N.; Iton, L. E.; Keir, R. I.; Thomas, J. C.; Dowling, T. L.; White, J. W. *J. Phys. Chem. B* **1997,** *101,* 10094-10104.

30. Kirschhock, C. E. A.; Ravishankar, R.; Jacobs, P. A.; Martens, J. A. *J. Phys. Chem. B* **1999,** *103,* 11021-11027.

31. Houssin, C. J. Y.; Kirschhock, C. E. A.; Magusin, P. C. M. M.; Mojet, B. L.; Grobet, P. J.; Jacobs, P. A.; Martens, J. A.; van Santen, R. A. *Phys. Chem. Chem. Phys.* **2003,** *5,* 3518-3524.

32. de Moor, P.-P. E. A.; Beelen, T. P. M.; Komanschek, B. U.; Beck, L. W.; Wagner, P.; Davis, M. E.; van Santen, R. A. *Chem. Eur. J.* **1999,** *5,* 2083-2088.

33. Liang, D.; Follens, L. R. A.; Aerts, A.; Martens, J. A.; VanTendeloo, G.; Kirschhock, C. E. A. *J. Phys. Chem. C* **2007,** *111,* 14283-14285.

34. Burkett, S. L.; Davis, M. E. *Chem. Mater.* **1995,** *7,* 1453-1463.

35. Lewis, D.; Willock, D.; Catlow, C.; Thomas, J. M.; Hutchings, G. *Nature* **1996,** *382,* 604-606.

36. Kinrade, S. D.; Knight, C. T. G.; Pole, D. L.; Syvitski, R. T. *Inorg. Chem.* **1998,** *37,* 4272-4277.

37. Caratzoulas, S.; Vlachos, D. G. *J. Phys. Chem. B* **2008,** *112,* 7-10.

38. Caratzoulas, S.; Vlachos, D. G.; Tsapatsis, M. *J. Am. Chem. Soc.* **2006,** *128,* 16138-16147.

39. Kirschhock, C. E. A.; Kremer, S. P. B.; Grobet, P. J.; Jacobs, P. A.; Martens, J. A. *J. Phys. Chem. B* **2002,** *106,* 4897-4900.

40. Fedeyko, J. M.; Rimer, J. D.; Lobo, R. F.; Vlachos, D. G. *J. Phys. Chem. B* **2004,** *108,* 12271-12275.

41. Kirschhock, C. E. A.; Ravishankar, R.; Verspeurt, F.; Grobet, P. J.; Jacobs, P. A.; Martens, J. A. *J. Phys. Chem. B* **1999,** *103,* 4965-4971.

42. Ravishankar, R.; Kirschhock, C. E. A.; Knops-Gerrits, P. P.; Feijen, E. J. P.; Grobet, P. J.; Vanoppen, P.; De Schryver, F. C.; Miehe, G.; Fuess, H.; Schoeman, B. J.; Jacobs, P. A., Martens, J. A. *J. Phys. Chem. B* **1999,** *103*, 4960-4964.

43. Kirschhock, C. E. A.; Ravishankar, R.; Looveren, L. V.; Jacobs, P. A.; Martens, J. A. *J. Phys. Chem. B* **1999,** *103,* 4972-4978.

44. Lesthaeghe, D.; Vansteenkiste, P.; Verstraelen, T.; Ghysels, A.; Kirschhock, C. E. A.;

Martens, J. A.; Speybroeck, V. V.; Waroquier, M. *J. Phys. Chem. C* **2008,** *112,* 9186-9191.

45. *New Trends in Materials Chemistry;* Catlow, C. R. A.; Cheetham A. K., Eds.; NATO Scientific Affairs Division; Kluwer Academic: London; 1997.

46. *Computer Modelling of Microporous Materials*; Catlow, C. R. A.; van Santen R. A., Eds; Academic Press: London; 2004.

47. *Handbook of materials modeling;* Yip, S., Ed; Springer: London; 2005.

48. Auerbach, S. M.; Ford, M. H.; Monson, P. A. *Curr. Opin. Colloid Interface Sci.* **2005,** *10,* 220-225.

49. Catlow, C. R. A.; Coombes, D. S.; Lewis, D. W.; Pereira, J. C. G.; *Chem. Mater.* **1998,** *10,* 3249-3265.

50. Pereira, J. C. G.; Catlow, C. R. A; Price, G. D. *J. Phys. Chem. A* **1999,** *103,* 3252-3267

51. Pereira, J. C. G; Catlow, C. R. A; Price, G. D. *J. Phys. Chem. A* **1999,** *103,* 3268-3284

52. Pereira, J. C. G.; Catlow, C. R. A; Price, G. D. *J. Phys.Chem. A* **2002,** *106,* 130-148

53. Lewis, D. W.; Catlow, C. R. A.; Thomas, J. M. *Faraday Discuss.* **1997,** *106,* 451-471.

54. Rao, N. D.; Gelb, L. D. *J. Phys. Chem. B* **2004,** *108,* 12418-12428.

55. Feuston, B. P.; Garofalini, S. H. *J. Phys. Chem.* **1990,** *94,* 5351-5356.

56. Mora-Fonz, M. J.; Catlow, C. R. A.; Lewis, D. W. *Angew. Chem. Int. Ed.* **2005,** *44,* 3082-3086.

57. Mora-Fonz, M. J.; Hamad, S.; Catlow, C. R. A. *Molecular Physics,* **2007,** *105,* 177-187.

58. *Gaussian 03, Revision C.02;* Frisch, M. J. et al.; Gaussian, Inc.: Wallingford CT; 2004.

59. http://cp2k.berlios.de

60. Magusin, P. C. M. M.; Zorin, V. E.; Aerts, A.; Houssin, C. J. Y.; Yakovlev, A. L.; Kirschhock, C. E. A.; Martens, J. A.; van Santen, R. A. *J. Phys. Chem. B* **2005,** *109,* 22767-22774.

61. Becke, A. D. *J. Chem. Phys.* **1993,** *98*, 5648-5652.

62. Zygmunt, S. A.; Mueller, R. M.; Curtiss, L. A.; Iton, L. E. *J. Mol. Struct.* **1998,** *430,* 9-16.

63. Barone V.; Cossi, M. *J. Phys. Chem. A* **1998,** *102,* 1995-2001.

64. Cossi, M.; Rega, N.; Scalmani, G.; Barone, V. *J. Comp. Chem.* **2003,** *24,* 669-681.

65. Perdew, J. P.; Burke, K.; Ernzerhof, M. *Phys. Rev. Lett.* **1996,** *77,* 3865-3868.

66. Lippert, G.; Hutter, J.; Ballone, P.; Parrinello, M. *J. Phys. Chem.* **1996,** *100,* 6231-6235.

67. Goedecker, S.; Teter, M.; Hutter, J. *Phys. Rev. B* **1996,** *54,* 1703-1710.

68. Hartwigsen, C.; Goedecker, S.; Hutter, J. *Phys. Rev. B* **1998,** *58,* 3641-3662.

69. Verstraelen, T.; Van Speybroeck, V.; Waroquier, M. *J. Chem. Inf. Model.* **2008,** *48,* published online. The Zeobuilder program can be freely accessed at https://molmod22.UGent.be/zeobuilder/wiki

70. Trinh, T. T.; Jansen, A. P. J.; van Santen, R. A. *J. Phys. Chem. B* **2006,** *110,* 23099-23106

71. Van Speybroeck, V.; Moonen, K.; Hemelsoet, K.; Stevens, C. V.; Waroquier, M. *J. Am. Chem. Soc.* **2006,** *128,* 8468-8478.

72. Berendsen, H. J. C.; Postma, J. P. M.; van Gunsteren, W. F.; DiNola, A.; Haak, J. R. *J. Chem. Phys.* **1984,** *81,* 3684-3690.

73. Garofalini, S. H.; Martin, G. *J. Phys. Chem.* **1994,** *98,* 1311-1316.

74. van Duin, A. C. T.; Dasgupta, S.; Lorant, F.; Goddard III, W. A. *J. Phys. Chem. A* **2001,** *105,* 9396-9409.

75. Nielson, K. D.; van Duin, A. C. T.; Oxgaard, J.; Deng, W.-Q. Goddard III, W. A. *J. Phys. Chem. A* **2005,** *109,* 493-499.

76. Strachan, A.; Kober, E. M.; van Duin, A. C. T.; Oxgaard, J.; Goddard III, W. A. *J. Chem. Phys.* **2005,** *122,* 54501-54510.

77. Strachan, A.; van Duin, A. C. T.; Chakraborty, D.; Dasgupta, S.; Goddard III, W. A. *Phys. Rev. Lett.* **2003,** *91,* 98301-98304.

78. van Beest, B. W. H.; Kramer, G. J.; van Santen, R. A. *Phys. Rev. Lett.* **1990,** *64,* 1955-1958.

79. Dauber-Osguthorpe, P.; Roberts, V. A.; Osguthorpe, D. J.; Wolff, J.; Genest Hagler, M. *Proteins: Structure, Function and Genetics* **1988,** *4,* 31-47.

80. Schroder, K. P. ; Sauer, J.; Leslie, M.; Catlow, C. R. A.; Thomas, J. M. *Chem. Phys. Lett.* **1992,** *188,* 320-325.

81. Gale, J. D.; Henson, N. J. *J. Chem. Soc. Faraday Trans.* **1994,** *90,* 3175-3179.

82. Rappe, A. K.; Casewit, C. J.; Colwell, K. S.; Goddard III, W. A.; Skiff. W. M. *J. Am. Chem. Soc.* **1992,** *114,* 10024-10035.

83. Verstraelen, T.; Van Speybroeck, V.; Waroquier, M. *J. Chem. Inf. Model.* **2008,** submitted.

84. Fricke, R.; Kosslick, H.; Lischke, G.; Richter, M. *Chem. Rev.* **2000,** *100,* 2303-2405.

85. Lesthaeghe, D.; De Sterck, B.; Van Speybroeck, V.; Marin, G. B.; Waroquier, M. *Angew. Chem. Int. Ed.* **2007,** *46,* 1311-1314.

86. This trajectory was approximated roughly by applying harmonic restraints [i.e. adding E=1/2 k (x - x_0)² to the total energy term, with k = 46.9 kJ/(mol Å²)] on equidistant points of a collective variable. This collective variable was defined as the component in channel direction of the vector between the geometric centers of the framework and the template.

87. Kelly, C. P.; Cramer, C. J.; Truhlar, D. G. *J. Chem. Theory Comput.* **2005,** *1,* 1133-1152.

88. Pratt, L. M.; Streitwieser, A. *J. Org. Chem.* **2003,** *68,* 2830-2838.

89. Navrotsky, A.; Current Opinion in Colloid & Interface Science **2005,** *10*, 195– 202

11 Conclusions

This doctoral research focused on the development, implementation, validation, and application of DFT methods for the fast and accurate calculation of the g and A tensors in PBC simulations. To this end, a number of newly-developed theoretical methods were implemented in CPMD and CP2K, two popular program packages that adopt periodic boundary conditions. These theoretical methods were validated by comparing the EPR parameters of a wide range of atoms and small molecules in the gas phase with existing gas-phase methods (through special techniques, both CPMD and CP2K can also simulate the gas phase). Then, using these new methods, the EPR parameters of several periodic structures were calculated and thoroughly compared with available experimental data from literature and results obtained with, amongst others, cluster-in-vacuo models. Several ideas for the acceleration of the methods, such as for example the usage of a three-layered hybrid AE/PSP/MM approach, have been carefully tested.

Most likely, the CP2K methods will last longer than their CPMD counterparts, as they are the most generally applicable. Through the GAPW representation and the layered approach, the CP2K methods offer a very attractive accuracy/cost trade-off over the few competing methods applicable to PBC simulations, as they enable a full AE treatment (without the need for reconstruction techniques such as PAW, which is known not to correct for all the problems inherent to the PSP approximation) of the radical center at a relatively small additional cost, and a relatively cheap PSP approximation or MM techniques for the remainder of the simulation cell.

A number of exciting applications have already been carried out, such as for

example the study of the molecular environment dependence of A tensors in a set of sugar crystal radicals [Art. 7], the calculation of the A tensors of the R2 center in β-D-fructose along a complete molecular dynamics trajectory at finite temperature [Art. 7], and the calculation of the g tensor for the E_1' center in α-quartz using a 15551-atom simulation cell and the three-layered AE/PSP/MM approach [Art. 8]. Further applications are in progress.

There remain still a number of opportunities for improvement. Future research should concentrate first on the following three issues: i) the improvement of the scalability in the calculation of the first-order wave functions $\psi_i^{(1)}$, as discussed in section 2.3.5, ii) the possibility to use hybrid functionals, and iii) the inclusion of (additional) relativistic effects, which (inter alia) should enable a more precise calculation of EPR parameters in structures with heavy elements.

A Nederlandstalige tekst: de berekening van EPR-parameters in PBC-simulaties

A.1 Inleiding

In de laatste 50 jaar is de bepaling en voorspelling van de eigenschappen van materie op het niveau van de nanoschaal, enkel uitgaande van de fundamentele wetten van de kwantumfysica (*ab initio*), uitgegroeid tot een onmisbare wetenschappelijke discipline. De steile opmars is enerzijds te danken aan de steeds toenemende numerieke rekenkracht van computers, maar anderzijds ook aan de ontwikkeling van nieuwe theoretische concepten die, al dan niet via enkele benaderingen, de benodigde rekentijd drastisch reduceren.

In de klasse van ab-initio-methodes neemt de dichtheidsfunctionaaltheorie (*density functional theory*, DFT), ontwikkeld door Hohenberg en Kohn en in een bruikbaar algoritme geformuleerd door Kohn en Sham, een bijzondere plaats in. Essentieel stelt het theorema van Hohenberg-Kohn dat de elektronische grondtoestandsgolffunctie van eender welk moleculair systeem eenduidig wordt bepaald door de elektronische grondtoestandsdichtheid. De elektronendichtheid hangt af van slechts drie ruimtelijke variabelen en is daarmee een stuk simpeler te hanteren dan de veeldeeltjesgolffunctie, zowel conceptueel als praktisch. De Kohn-Shamformulering van DFT biedt, althans formeel, een exacte oplossing voor dit interagerend veeldeeltjessysteem, op voorwaarde dat men de uitwisselings-correlatiefunctionaal exact zou kennen. Dit is echter (voorlopig) niet het geval, en daarom is men aangewezen op benaderende

functionalen die deels fenomenologisch van aard zijn. Om die reden is DFT eigenlijk geen ab-initiomethode in de strikte zin van het woord. Toch kan de huidige generatie functionalen in vele diverse situaties de elektronische grondtoestandsdichtheid en de hieruit afleidbare eigenschappen goed tot zeer goed beschrijven.

Elektron-paramagnetische-resonantie (*electron paramagnetic resonance*, EPR), ook wel elektronspinresonantie (*electron spin resonance*, ESR) genoemd, is één van de voornaamste spectroscopische technieken om specimens met één of meerdere ongepaarde elektronen te onderzoeken. De basisgedachte van EPR is analoog aan die van de beter gekende nucleaire magnetische resonantie (*nuclear magnetic resonance*, NMR): in de eerste techniek wordt de spin van de elektronen geëxciteerd, in de laatste de spin van de atoomkernen. Aangezien de meeste stabiele moleculen een configuratie hebben zonder ongepaarde elektronen, kent de techniek specifiekere toepassingen dan NMR. EPR wordt in de vaste-stoffysica gebruikt voor de identificatie of kwantificatie van radicalen (moleculen met één of meerdere ongepaarde elektronen), in de chemie om reactieketens te identificeren, alsook in de biologie en de geneeskunde waar onder andere eiwitten van zogenaamde spinlabels worden voorzien om inzicht in hun structuur en dynamiek te verkrijgen.

De energieniveaus en intensiteiten van de spincentra, die volgen uit een EPR-experiment, kunnen worden gereproduceerd met behulp van een zogeheten effectieve Hamiltoniaan (*effectief* in de zin dat het een zuiver mathematisch object betreft, dat niet uit fundamentele fysische principes volgt). Vaak volstaat een effectieve Hamiltoniaan met de volgende laagste-orde interactietermen: i) de g-tensor die de interactie beschrijft van de netto elektronenspin met een extern aangelegde magnetische veld, ii) de A- of hyperfijntensoren die de interactie beschrijven van de netto elektronenspin met de atoomkernspins, en iii) in het geval van een netto elektronenspin hoger dan $1/2$, de D- of nulveldsplitsingstensor die volgt uit magnetische-dipoolinteracties tussen verschillende ongepaarde elektronen.

De laatste jaren groeide de interesse in de ab-initioberekening van EPR-parameters sterk. Voor de experimentator vormen theoretische berekeningen een krachtig hulpmiddel bij de analyse van de spectra die soms zeer complex kunnen zijn. Door de experimenteel verkregen EPR-parameters te vergelijken met ab-initiobepaalde waarden is het mogelijk om de moleculaire structuur in de omgeving van het spincentrum te identificeren en meer diepgaand te analyseren.

Tot voor kort kon men EPR-parameters enkel berekenen in gasfase-simulaties, waarin de te onderzoeken molecule zich in vacuum bevindt. Voor de g-tensor is een rijke waaier aan DFT-implementaties voor de gasfase beschikbaar. In de eerste groep van één-component-methodes worden de spin-baanoperatoren perturbatief in rekening gebracht. Schreckenbach en Ziegler[1] introduceerden een effectieve potentiaal om de spin-baanoperatoren te benaderen, Malkina *et al.*[2] gebruikten het atomaire gemiddelde-veldconcept voor dit doel, en Neese[3] stelde de zogeheten geschaalde spin-baanbenadering voor. In de tweede groep van twee-componenten-methodes wordt de g-tensor berekend als een eerste-orde eigenschap. De spin-baaninteractie is opgenomen in de twee-componenten-Kohn-Sham-vergelijkingen. In de implementatie van van Lenthe *et al.*[4] werden de relativistische effecten opgenomen via de nulde-orde reguliere benadering. Een soorgelijke methode in combinatie met de Douglas-Kroll-transformatie toegepast op de Dirac-Kohn-Sham-vergelijkingen werd opgesteld door Neyman *et al.*[5]. De meest relevante bijdragen tot de A-tensor kunnen worden afgeleid uit de grondtoestandsdichtheid, en daarom is deze grootheid vrijwel vanzelf beschikbaar in bijna alle DFT-gebaseerde simulatiepakketten voor de gasfase.

Heel wat interessante toepassingen van de EPR-techniek vindt men echter terug in de vaste fase, waarbij de spincentra volledig ingebed zitten in materie. Een succesvolle techniek om de vaste fase te simuleren bestaat erin aan een simulatiecel periodieke randvoorwaarden (*periodic boundary conditions*, PBC) op te leggen. Dit is meestal een correcte benadering, aangezien de vaste fase van veel stoffen een periodieke structuur kent. De aanpassing van de theoretische methodes voor de berekening van EPR-parameters in PBC-simulaties blijkt echter verre van triviaal, en tot nu toe werden daartoe slechts een beperkt aantal pogingen ondernomen. Aan het begin van dit doctoraatsonderzoek was, voor zover ik weet, enkel de methode van Pickard en Mauri[6] in staat om de g-tensor in PBC-simulaties te berekenen, en voor de A-tensor waren slechts een handvol methodes beschikbaar,[7–9] allen gebaseerd op een zeer vergelijkbare aanpak. Echter, zoals zal worden onderbouwd verderop in dit werk, hebben alle van de bovengenoemde methodes een aantal methodologische en/of praktische beperkingen, en om die reden worden theoretische EPR-parameters van vaste-fase-structuren nog steeds hoofdzakelijk berekend met behulp van cluster-in-vacuomodellen. Bij deze techniek wordt (noodgedwongen) slechts een deel van de moleculaire omgeving in rekening gebracht, een benadering die vaak een gevoelig verlies aan nauwkeurigheid tot gevolg heeft.

Het belangrijkste doel van dit doctoraatsonderzoek is daarom de ontwikkeling, implementatie, validatie en toepassing van DFT-methodes voor de snelle en nauwkeurige berekening van de g- en A-tensoren in PBC-simulaties. Daartoe werden een aantal nieuw-ontwikkelde theoretische methodes, of *algoritmen*, geïmplementeerd in twee simulatiepakketten die gebruik maken van periodieke randvoorwaarden: CPMD (`http://www.cpmd.org`, vrij oud, maar nog steeds zeer populair) en CP2K (`http://cp2k.berlios.de`, nieuw, revolutionair, en sterk aan populariteit winnend). Hiervoor werd onder andere samengewerkt met de onderzoeksgroep van prof. dr. Jürg Hutter van het Physikalisch-Chemisches Institut van de Universität Zürich, die de ontwikkeling van beide pakketten coördineert. Beide implementaties verschillen sterk van elkaar, aangezien beide pakketten specifieke mogelijkheden en beperkingen kennen.

Vervolgens hebben we deze theoretische methodes gevalideerd, door de EPR-parameters van een uitgebreide selectie van atomen en kleine molecules in de gasfase te vergelijken met reeds bestaande berekeningsmethodes voor de gasfase (zowel CPMD als CP2K kunnen via speciale technieken ook met de gasfase overweg). Daarna werden met de nieuwe methodes de EPR-parameters van enkele periodieke structuren berekend, en grondig vergeleken met de beschikbare experimentele gegevens en resultaten verkregen met onder andere cluster-in-vacuomodellen. Verschillende ideeën voor de versnelling van de methodes, zoals bijvoorbeeld het gebruik van een gelaagd hybride schema waarin een nauwkeurige alle-elektronenbehandeling voor het radicalaire centrum kan worden gecombineerd met een relatief goedkope pseudopotentiaalbenadering en/of klassieke moleculaire-mechanicatechnieken voor de rest van de simulatiecel, werden uitvoerig getest. Daarop werden een aantal interessante applicaties bestudeerd, zoals bijvoorbeeld de studie van de afhankelijkheid van de moleculaire omgeving van A-tensoren in een reeks van suikerkristalradicalen, de berekening van de A-tensoren van het R2-centrum in β-D-fructose langsheen een compleet moleculaire-dynamicatraject op eindige temperatuur, en de berekening van de g-tensor voor het E_1'-centrum in α-kwarts met behulp van een simulatiecel bestaande uit 15551 atomen en het gelaagd hybride schema.

Alle programmacode werd opgenomen in de publieke distributies van beide simulatiepakketten (beschikbaar op de respectievelijke websites).

In de marge van het onderzoek werd de opgedane expertise in het simuleren

van vaste stoffen op DFT-niveau ingezet in een samenwerkingsverband met het Fysico-Chemisch Laboratorium van de Katholieke Universiteit Leuven. Er werd gewerkt aan een nieuw semi-empirisch energiemodel voor de studie van oppervlaktefenomenen in metaallegeringen, gefit aan berekeningen op DFT-niveau. Het voorgestelde model werd gebruikt voor de theoretische voorspelling van oppervlaktesegregatie in CuPt-legeringen.

Daarnaast werden, op basis van moleculaire-dynamicasimulaties en metadynamica in een expliciet periodiek solventmodel, de solvatatie- en isomerisatiekarakteristieken van gelithieerde 3-chloro-1-azaallylische anionen in een tetrahydrofuraanoplossing ontrafeld. De bevindingen werden onafhankelijk bevestigd door ROESY-NMR experimenten,[1] uitgevoerd aan het Departement Organische Chemie van de Universiteit Gent. Een gedetailleerde kennis over de structuur van deze gesolvateerde anionen leidt tot een beter begrip van de chemische reacties (bvb. aldol- of Mannich-typereacties) waarin zij een rol spelen. De voorgestelde methode is bovendien generiek, en kan dus bijdragen tot het oplossen van soortgelijke vraagstukken.

Net voor de voltooiing van deze thesis, werd nog een bijkomend onderzoeksproject afgewerkt over silica-templaat-interacties in de beginfase van de zeolietsynthese. Dit project werd uitgevoerd in samenwerking met de Faculteit Scheikundige Technologie van de Technische Universiteit Eindhoven, het Department of Fuels Chemistry and Technology van de Wroclaw University of Technology en het Centrum voor Oppervlaktechemie en Katalyse van de Katholieke Universiteit Leuven.

Vooraleer we de structuur van deze thesis schetsen, formuleren we nog een aantal algemene opmerkingen. De verschillende publicaties die de voorbije jaren in internationale vakbladen zijn verschenen, vormen de feitelijke neerslag van dit doctoraatsonderzoek, en werden verderop in deze thesis integraal opgenomen. De hierna volgende tekst is dan ook geen traditionele, alomvattende weergave van het doctoraatsonderzoek, maar werd (bewust) beperkt tot een grondige uiteenzetting van haar belangrijkste onderdeel: de berekening van EPR-parameters in PBC-simulaties. De tekst beoogt een publiek met een elementaire kennis van de kwantummechanica in te wijden in de theoretische en technische aspecten van de ontwikkelde algoritmen, wat het doornemen van de publicaties zal vereenvoudigen. We zullen vooral de implementatie in CP2K in detail bespreken, omdat deze innovatiever en breder inzetbaar is. (Bio-)chemici zullen vermoedelijk vooral de verschillende toepassingen

[1] roterend-assenstelsel-nucleair-overhauser-effectspectroscopie, (*rotational frame nuclear overhauser effect spectroscopy*, ROESY)

waarderen. Deze worden uitsluitend behandeld in de publicaties, maar staan relatief los van de theorie. Hoewel de eerder beschreven *nevenprojecten* in de marge een aanzienlijk deel van het onderzoek opeisten, blijven ook deze onbesproken in deze tekst, omdat zij in essentie behoren tot een ander onderzoeksgebied. Om zich in te werken, wordt de geïnteresseerde lezer aangeraden de referenties uit de inleiding van de betreffende publicaties te raadplegen. Tenslotte wordt, omwille van de duidelijkheid voor de lezer, de chronologische volgorde van het onderzoek niet altijd rigoureus gerespecteerd.

Deze thesis is als volgt opgebouwd: hoofdstuk 2 bevat de grondige studie van de theoretische en technische aspecten van de berekening van EPR-parameters in periodieke systemen, daarna volgen in hoofdstukken $3-10$ de integrale reproducties van de publicaties, en in hoofdstuk 11 worden de belangrijkste conclusies samengevat en enkele aanwijzingen gegeven voor toekomstig onderzoek.

Verwijzingen naar de eigen publicaties zullen we met [Art. 1] aanduiden, om hen van deze naar publicaties van anderen in de bibliografie, bijvoorbeeld [1], te onderscheiden. We zullen steeds uitgaan van een netto elektronenspin gelijk aan $\frac{1}{2}$, maar alle formules zijn eenvoudig uitbreidbaar tot grotere spins. We zullen verder gebruik maken van atomaire eenheden, gedefinieerd door $\hbar = m = e = 4\pi\epsilon = 1$, waarvoor $c = 1/\alpha \approx 137$, met α de fijnstructuurconstante.

A.2 Het veeldeeltjesprobleem en dichtheidsfunctionaaltheorie

De Schrödingervergelijking, in 1925 opgesteld door de Oostenrijkse natuurkundige Erwin Schrödinger, vormt de basisformule voor de tijdsafhankelijke niet-relativistische beschrijving van een kwantumsysteem:

$$H\left|\Psi(t)\right\rangle = i\hbar\frac{d}{dt}\left|\Psi(t)\right\rangle \ . \tag{A.1}$$

De tijdsonafhankelijke Schrödingervergelijking heeft de welbekende vorm:

$$H\left|\Psi\right\rangle = E\left|\Psi\right\rangle \ , \tag{A.2}$$

en vormt een eigenwaardeprobleem.

Toegepast op een veeldeeltjessysteem van n elektronen en N atoomkernen, en geprojecteerd op de coördinatenruimte van elektronische en nucleaire posities volgt hieruit de spinonafhankelijke,[2] $(3n+3N)$-dimensionele, tijdsonafhankelijke Schrödingergolfvergelijking:

$$H\Psi(\mathbf{r}_1,\ldots,\mathbf{r}_n,\mathbf{R}_1,\ldots,\mathbf{R}_N) = E\Psi(\mathbf{r}_1,\ldots,\mathbf{r}_n,\mathbf{R}_1,\ldots,\mathbf{R}_N) \ , \tag{A.3}$$

met eigenwaarden E en eigenfuncties Ψ behorend bij de veeldeeltjesoperator H die, in atomaire eenheden, gegeven wordt door:

$$\begin{aligned} H = \sum_i -\frac{1}{2}\nabla_i^2 + \sum_I -\frac{1}{2M_I}\nabla_I^2 + \frac{1}{2}\sum_{i\neq j}\frac{1}{|\mathbf{r}_i-\mathbf{r}_j|} \\ + \frac{1}{2}\sum_{I\neq J}\frac{Q_I Q_J}{|\mathbf{R}_I-\mathbf{R}_J|} - \sum_{i,I}\frac{Q_I}{|\mathbf{r}_i-\mathbf{R}_I|} \quad . \end{aligned} \tag{A.4}$$

Met $\mathbf{r}_i$ en $\mathbf{R}_I$ duiden we de positie-operatoren aan die inwerken op respectievelijk elektron i en atoomkern I.[3] M_I en Q_I stellen de massa en lading voor van atoomkern I in atomaire eenheden.[4]

[2] Spinonafhankelijk ten behoeve van de eenvoud, vanaf paragraaf A.2.2 wordt de spin van het elektron ingevoerd.

[3] Doorheen dit werk zullen de indices $i, j, \ldots$ elektronen (en positronen) aanduiden, terwijl de indices $I, J, \ldots$ refereren naar atoomkernen.

[4] Voor de goede orde: $\sum_{i\neq j}$ (en dergelijke) staat voor een dubbele som over i en j, waarbij het geval $i = j$ wordt uitgesloten.

A.2.1 De Born-Oppenheimerbenadering

In de Born-Oppenheimerbenadering [10, 11] veronderstelt men dat (de beschrijving van) de beweging van elektronen en atoomkernen van elkaar kunnen worden gescheiden: de elektronen bewegen veel sneller dan de atoomkernen. Dit is plausibel, aangezien de massa van elektronen vele malen kleiner is dan die van atoomkernen. De totale golffunctie wordt geschreven als het produkt van een golffunctie voor de elektronen Ψ^{el} en een golffunctie voor de atoomkernen Ψ^{ion}:

$$\Psi(\mathbf{r}_1, \ldots, \mathbf{r}_n, \mathbf{R}_1, \ldots, \mathbf{R}_N) = \Psi^{\text{el}}_{\mathbf{R}_1,\ldots,\mathbf{R}_N}(\mathbf{r}_1, \ldots, \mathbf{r}_n)\Psi^{\text{ion}}(\mathbf{R}_1, \ldots, \mathbf{R}_N) \; . \tag{A.5}$$

Deze benadering leidt tot de opsplitsing van de Schrödingergolfvergelijking (A.3) in:

1. Een tijdsonafhankelijke Schrödingergolfvergelijking voor de elektronen in het constante potentiaalveld van vaste atoomkernen. De elektronische golffuncties en energieniveaus hangen wel nog parametrisch af van de posities van de atoomkernen.
2. Een tijdsonafhankelijke Schrödingergolfvergelijking voor de atoomkernen in een potentiaalveld afgeleid uit de oplossing van de elektronische Schrödingergolfvergelijking. Uitgaande van het totale potentiële-energie-oppervlak (aantrekking en repulsie van de respectievelijk elektronenwolk en de atoomkernen) kan de beweging van de atoomkernen dan worden berekend. In de praktijk volstaat hiervoor de klassieke Newtoniaanse mechanica.

De tijdsonafhankelijke Schrödingergolfvergelijking voor de elektronen wordt gegeven door:

$$H^{\text{el}}\Psi^{\text{el}}_{\mathbf{R}_1,\ldots,\mathbf{R}_N}(\mathbf{r}_1, \ldots, \mathbf{r}_n) = E^{\text{el}}_{\mathbf{R}_1,\ldots,\mathbf{R}_N}\Psi^{\text{el}}_{\mathbf{R}_1,\ldots,\mathbf{R}_N}(\mathbf{r}_1, \ldots, \mathbf{r}_n) \; , \tag{A.6}$$

met:

$$H^{\text{el}} = \sum_i -\frac{1}{2}\nabla_i^2 + \frac{1}{2}\sum_{i\neq j}\frac{1}{|\mathbf{r}_i - \mathbf{r}_j|} - \sum_{i,I}\frac{Q_I}{|\mathbf{r}_i - \mathbf{R}_I|} + \frac{1}{2}\sum_{I\neq J}\frac{Q_I Q_J}{|\mathbf{R}_I - \mathbf{R}_J|} \; . \tag{A.7}$$

Ook hier zullen we de atoomkernen als klassieke deeltjes behandelen, zodat we de positie-operatoren van de atoomkernen kunnen vervangen door positievariabelen.[5] Dit laat ons toe de interactieterm tussen de atoomkernen en de elektronen in (A.7) te veralgemenen tot een willekeurige externe potentiaal $V_{\text{ext}}(\mathbf{r}_1, ..., \mathbf{r}_n) = \sum_i v_{\text{ext}}(\mathbf{r}_i)$:

$$H^{\text{el}} = \sum_i -\frac{1}{2}\nabla_i^2 + \frac{1}{2}\sum_{i \neq j} \frac{1}{|\mathbf{r}_i - \mathbf{r}_j|} + V_{\text{ext}}(\mathbf{r}_1, ..., \mathbf{r}_n) \; . \tag{A.8}$$

In het algemeen is er geen analytische oplossing voor de elektronische Schrödingervergelijking, en dient men benaderende technieken zoals DFT te gebruiken. Omdat DFT de basis vormt voor de ontwikkelde algoritmen verder in dit werk, zal deze theorie in extenso behandeld worden in de volgende paragrafen.

Vanaf hier werken we enkel nog met de elektronische Hamiltoniaan, toestanden, golffuncties en energieniveaus, zodat we het superscript *el* voortaan achterwege kunnen laten.

A.2.2 Dichtheidsfunctionaaltheorie

Theorema's van Hohenberg - Kohn

Het uitgangspunt voor de kwantummechanische beschrijving van de elektronische structuur in een algemene externe potentiaal is een tijdsonafhankelijke Schrödingergolfvergelijking met de volgende Hamiltoniaan:

$$H = \sum_i -\frac{1}{2}\nabla_i^2 + \frac{1}{2}\sum_{i \neq j} \frac{1}{|\mathbf{r}_i - \mathbf{r}_j|} + V_{\text{ext}}(\mathbf{r}_1, ..., \mathbf{r}_n) \; . \tag{A.9}$$

We merken op dat de Hamiltoniaan van een systeem met n elektronen (en dus ook het systeem zelf) volledig is gedefinieerd als de externe potentiaal V_{ext} gekend is. n en V_{ext} bepalen bijgevolg *alle eigenschappen* van de grondtoestand Ψ_0, en ook van alle geëxciteerde toestanden Ψ.

We formuleren eerst het **variationeel principe**:[6]

[5] Merk op: operatoren en variabelen worden op dezelfde manier genoteerd.

[6] Bemerk dat we hier $\Psi(\mathbf{r}_1, ..., \mathbf{r}_n)$ en $|\Psi\rangle$ losweg door elkaar gebruiken. Dit is toegestaan zolang de Hamiltoniaan enkel ruimtelijke operatoren bevat.

De genormaliseerde golffunctie Ψ die de energie-functionaal $E[\Psi]$ minimaliseert is de grondtoestandsgolffunctie:

$$E[\Psi] \geq E[\Psi_0] = E_0 \,, \tag{A.10}$$

waarbij:

$$E[\Psi] = \langle \Psi | H | \Psi \rangle \,. \tag{A.11}$$

Bewijs

Een willekeurige genormaliseerde golffunctie Ψ kan worden geschreven als een lineaire combinatie van de orthonormale eigenfuncties Ψ_n van de Hamiltoniaan H:

$$|\Psi\rangle = \sum_n c_n \, |\Psi_n\rangle \;. \tag{A.12}$$

Dan volgt voor de verwachtingswaarde van H voor Ψ:

$$\begin{aligned} \langle \Psi | \, H \, | \Psi \rangle &= \sum_{m,n} c_m^* c_n \, \langle \Psi_m | \, H \, | \Psi_n \rangle \\ &= \sum_n |c_n|^2 \, E_n \,. \end{aligned} \tag{A.13}$$

De grondtoestandsenergie E_0 is bij definitie de laagst mogelijke energie, $E_n \geq E_0$. Daarom volgt er:

$$\langle \Psi | \, H \, | \Psi \rangle \geq E_0 \sum_n |c_n|^2 = E_0 \,. \tag{A.14}$$

Nu gaan we de volgende één-op-één-relaties bewijzen voor een systeem met n elektronen:

$$V_{\text{ext}}(\mathbf{r}_1, ..., \mathbf{r}_n) \quad \longleftrightarrow \quad \Psi_0(\mathbf{r}_1, ..., \mathbf{r}_n) \,, \tag{A.15}$$

$$\rho(\mathbf{r}) \quad \longleftrightarrow \quad \Psi_0(\mathbf{r}_1, ..., \mathbf{r}_n) \,. \tag{A.16}$$

Met ρ stellen we de grondtoestandsdichtheid voor.

Bewijs

1. $V_{\text{ext}} \longrightarrow \Psi_0$ hebben we daarnet reeds aannemelijk gemaakt: de externe potentiaal V_{ext} bepaalt de Hamiltoniaan H, en aldus de grondtoestand Ψ_0.

2. $\Psi_0 \longrightarrow V_{\text{ext}}$ volgt uit het ongerijmde. Veronderstel dat de grondtoestand Ψ_0 aanleiding geeft tot twee verschillende externe potentialen V_{ext} en V'_{ext}. Deze twee potentialen bepalen twee Hamiltonianen H en H' die beide Ψ_0 als grondtoestand hebben:

$$\begin{aligned} H\Psi_0(\mathbf{r}_1, ..., \mathbf{r}_n) &= E_0\Psi_0(\mathbf{r}_1, ..., \mathbf{r}_n) \,, \\ H'\Psi_0(\mathbf{r}_1, ..., \mathbf{r}_n) &= E'_0\Psi_0(\mathbf{r}_1, ..., \mathbf{r}_n) \,, \end{aligned} \tag{A.17}$$

   waaruit:

$$\left(V_{\text{ext}}(\mathbf{r}_1, ..., \mathbf{r}_n) - V'_{\text{ext}}(\mathbf{r}_1, ..., \mathbf{r}_n)\right) \Psi_0(\mathbf{r}_1, ..., \mathbf{r}_n) = (E_0 - E'_0)\Psi_0(\mathbf{r}_1, ..., \mathbf{r}_n) \,. \tag{A.18}$$

   Hieruit volgt onmiddellijk dat $V_{\text{ext}} = V'_{\text{ext}}$ op een constante na, wat fysisch geen verschil uitmaakt.

3. $\Psi_0 \longrightarrow \rho(\mathbf{r})$ is triviaal: kennis van de grondtoestandsgolffunctie leidt tot de grondtoestandsdichtheid via:

$$\rho(\mathbf{r}) = n \int \mathrm{d}\mathbf{r}_2 ... \mathrm{d}\mathbf{r}_n \Psi_0^*(\mathbf{r}, \mathbf{r}_2, ..., \mathbf{r}_n)\Psi_0(\mathbf{r}, \mathbf{r}_2, ..., \mathbf{r}_n) \,. \tag{A.19}$$

4. $\rho(\mathbf{r}) \longrightarrow \Psi_0$ wordt opgenieuw aangetoond uit het ongerijmde. Onderstel dat $\rho(\mathbf{r})$ leidt tot twee verschillende genormeerde golffuncties die beiden een grondtoestand voorstellen. Dan definiëren deze golffuncties via de correspondentie (A.15) op unieke wijze twee verschillende Hamiltonianen:

$$\begin{aligned} \rho(\mathbf{r}) &\rightarrow \Psi_0(\mathbf{r}_1, ..., \mathbf{r}_n) \\ &\rightarrow V_{\text{ext}}(\mathbf{r}_1, ..., \mathbf{r}_n) \\ &\rightarrow H = T + V_{2\text{e}} + V_{\text{ext}}(\mathbf{r}_1, ..., \mathbf{r}_n) \,, \\ \rho(\mathbf{r}) &\rightarrow \Psi'_0(\mathbf{r}_1, ..., \mathbf{r}_n) \\ &\rightarrow V'_{\text{ext}}(\mathbf{r}_1, ..., \mathbf{r}_n) \\ &\rightarrow H' = T + V_{2\text{e}} + V'_{\text{ext}}(\mathbf{r}_1, ..., \mathbf{r}_n) \,, \end{aligned} \tag{A.20}$$

waarbij V_{2e} de tweedeeltjesinteractieterm aanduidt. Nu geldt in de beide gevallen, steunend op het variationele principe (A.10) (en bovendien veronderstellend dat Ψ_0 en Ψ_0' geen stel ontaarde toestanden vormen):

$$\begin{aligned} E_0 &= \langle \Psi_0 | H | \Psi_0 \rangle < \langle \Psi_0' | H | \Psi_0' \rangle \ , \\ E_0' &= \langle \Psi_0' | H' | \Psi_0' \rangle < \langle \Psi_0 | H' | \Psi_0 \rangle \ . \end{aligned} \tag{A.21}$$

Deze ongelijkheden leiden tot:[7]

$$\begin{aligned} E_0 &< E_0' + \int \rho(\mathbf{r})(v_{\text{ext}}(\mathbf{r}) - v_{\text{ext}}'(\mathbf{r}))\mathrm{d}\mathbf{r} \ , \\ E_0' &< E_0 - \int \rho(\mathbf{r})(v_{\text{ext}}(\mathbf{r}) - v_{\text{ext}}'(\mathbf{r}))\mathrm{d}\mathbf{r} \ , \end{aligned} \tag{A.22}$$

ofwel:

$$E_0 + E_0' < E_0 + E_0' \ . \tag{A.23}$$

Deze relatie is strijdig, en rekening houdend met de correspondentie (A.15) volgt hieruit:

$$\Psi_0(\mathbf{r}_1, ..., \mathbf{r}_n) = \Psi_0'(\mathbf{r}_1, ..., \mathbf{r}_n) \ . \tag{A.24}$$

Beide correspondenties (A.15) en (A.16) bepalen het **eerste theorema van Hohenberg - Kohn**:[12]

1. (Voor een niet-ontaarde grondtoestand) bepaalt de grondtoestandsdichtheid $\rho(\mathbf{r})$ op unieke wijze de totale Hamiltoniaan, en dus ook V_{ext}.
2. De grondtoestandsenergie is een functionaal van $\rho(\mathbf{r})$:

$$E_0[\rho] = \langle \Psi_0[\rho] | H[\rho] | \Psi_0[\rho] \rangle \ . \tag{A.25}$$

[7] $v_{\text{ext}}(\mathbf{r})$ is de externe potentiaal op positie $\mathbf{r}$, en wordt verderop gedefinieerd. In feite moet volgens (A.7) in (A.22) behalve de integraal ook de energie van de Coulombse atoomkern-atoomkerninteractie staan. Dit verandert echter niets aan (A.23).

Het is belangrijk op te merken dat dit theorema niet toepasbaar is op elke willekeurige dichtheid. Enkel die grondtoestandsdichtheden die volgen uit een Ψ_0 die oplossing is van een elektronische Schrödingergolfvergelijking kunnen worden gelinkt aan de externe potentiaal waaruit deze voorkomt. Als een dichtheid op die manier werd bekomen, dan noemt men deze *v-representabel*.

Het **tweede theorema van Hohenberg-Kohn**[12] is een minimumprincipe voor de dichtheid. Vergelijkbaar met het variationele principe uit (A.10), dat geformuleerd werd voor golffuncties, luidt het:

> Van alle v-representabele dichtheden, is de grondtoestandsdichtheid die dichtheid die de energie-functionaal bij een gegeven externe potentiaal minimaliseert.

Het bewijs volgt direct uit het variationele principe (A.10). Bij een gegeven externe potentiaal V_{ext} wordt de grondtoestandsoplossing van de Schrödingervergelijking verkregen door minimalisatie van de energiefunctionaal bij variatie van de elektronische golffunctie. Aan alle v-representabele dichtheden die verschillen van de grondtoestandsdichtheid kan een golffunctie worden gelinkt die verschilt van de grondtoestandsgolffunctie. Dus is de energiefunctionaal niet minimaal voor elk van hen.

Een belangrijk nadeel van dit tweede theorema is dat het enkel geldt voor v-representabele dichtheden. Niet elke testdichtheid heeft de eigenschap v-representabel te zijn, zodat bij simpele minimalisatie van de energiefunctionaal niet-fysische (niet v-representabele) dichthed kunnen worden gevonden.

Het probleem van de v-representabiliteit wordt omzeild door gebruik van het formalisme van Levy,[13] waarin enkel de N-representabiliteit (dit betekent dat de dichtheid afgeleid is van een n-deeltjesgolffunctie of van een ensemble van n-deeltjesgolffuncties) van een testdichtheid wordt geëist. Een testdichtheid is N-representabel als deze nergens negatief wordt en integratie over de ruimte het correcte aantal elektronen oplevert, en als bovendien wordt voldaan aan de volgende voorwaarde:[14]

$$\int \mathrm{d}\mathbf{r} \left| \nabla(\rho(\mathbf{r})^{1/2}) \right|^2 < \infty \,. \tag{A.26}$$

Deze N-representabiliteit is veel gemakkelijker op te leggen. In de praktische berekeningen gaat men ervan uit dat v- en N-representabiliteit steeds zijn voldaan.

De Kohn-Shamvergelijkingen

De Hohenberg-Kohn theorema's tonen enkel aan dat het in principe mogelijk is om fysische grootheden (die normaal uit de grondtoestandsgolffunctie volgen) uit de elektronische grondtoestandsdichtheid te berekenen. Daarmee is het probleem om deze dichtheid ook effectief te vinden nog niet opgelost. Om van DFT ook een praktisch schema te maken voor echte berekeningen, stelden Kohn en Sham[15] een indirecte aanpak voor van het probleem.

Om te beginnen stelden ze een fictief parallel systeem van n niet-interagerende elektronen voor, dat bij definitie dezelfde dichtheid als de exacte oplossing van de interagerende elektronen heeft. Noem $\psi_{\mathrm{ni},i}(\mathbf{r})$ de ééndeeltjegolffuncties van dit onafhankelijke-elektronensysteem. De kinetische energie en de dichtheid van dat systeem zijn dan gedefinieerd als:

$$T_{\mathrm{ni}} = -\frac{1}{2}\sum_i \int \mathrm{d}\mathbf{r}\psi^*_{\mathrm{ni},i}(\mathbf{r})\nabla^2\psi_{\mathrm{ni},i}(\mathbf{r}) \ , \tag{A.27}$$

$$\rho(\mathbf{r}) = \sum_i |\psi_{\mathrm{ni},i}(\mathbf{r})|^2 \ . \tag{A.28}$$

Als we aannemen dat de v-representabele dichtheden behorend tot het interagerend systeem ook v-representabel zijn in het niet-interagerend systeem, dan volgt uit het eerste theorema van Hohenberg-Kohn dat deze dichtheid op unieke wijze de totale Hamiltoniaan H_{ni} en V_{ext} bepaalt.[8] Aangezien in dit niet-interagerende systeem (wegens geen tweedeeltjesinteractie tussen de elektronen) geldt dat:

$$T_{\mathrm{ni}} = H_{\mathrm{ni}} - V_{\mathrm{ext}} \ , \tag{A.29}$$

is ook de kinetische energie T_{ni} een unieke functionaal van de dichtheid. Deze kinetische-energiefunctionaal kan worden gebruikt om de kinetische energie van het interagerende systeem te benaderen.

De dichtheid van het niet-interagerende-elektronensysteem is bij definitie gelijk aan de dichtheid van het interagerende-elektronensysteem. Als we veronderstellen dat deze dichtheid een klassieke ladingsdistributie voorstelt, dan is de Coulombse interactie-energie gelijk aan:

[8] ni = niet-interagerend.

$$E_{\mathrm{H}}[\rho(\mathbf{r})] = \frac{1}{2}\int \mathrm{d}\mathbf{r}\int \mathrm{d}\mathbf{r}'\frac{\rho(\mathbf{r})\rho(\mathbf{r}')}{|\mathbf{r}-\mathbf{r}'|}\ . \tag{A.30}$$

E_{H} noemt men de Hartree-energie van het systeem. De energie afkomstig van de externe potentiaal is:

$$E_{\mathrm{ext}}[\rho(\mathbf{r})] = \int \mathrm{d}\mathbf{r} v_{\mathrm{ext}}(\mathbf{r})\rho(\mathbf{r}) + \frac{1}{2}\sum_{I\neq J}\frac{Q_I Q_J}{|\mathbf{R}_I-\mathbf{R}_J|}\ . \tag{A.31}$$

De totale energie van het interagerende-elektronensysteem schrijft men nu als:

$$E_{\mathrm{tot}}[\rho(\mathbf{r})] = T_{\mathrm{ni}}[\rho(\mathbf{r})] + E_H[\rho(\mathbf{r})] + E_{\mathrm{ext}}[\rho(\mathbf{r})] + E_{\mathrm{XC}}[\rho(\mathbf{r})]\ . \tag{A.32}$$

Per definitie bevat E_{XC} dan alle veeldeeltjeseffecten alsook de correcties op de kinetische energie van het interagerende-elektronsysteem. Als we de functionele vorm van E_{XC} exact kenden, zouden we in staat zijn de ladingsdichtheid van de grondtoestand van het veeldeeltjessysteem exact te bepalen. Dit is echter (voorlopig) niet het geval, en dus is men aangewezen op benaderende functionalen voor E_{XC} die dikwijls fenomenologisch van aard zijn (zie verder).

De minimalisatie van E_{tot} is een gebonden-extremumprobleem, waarbij de ééndeeltjegolffuncties aan de volgende orthonormaliteitsrelaties dienen te voldoen:

$$\int \mathrm{d}\mathbf{r}\psi^*_{\mathrm{ni},i}(\mathbf{r})\psi_{\mathrm{ni},j}(\mathbf{r}) = \delta_{ij}\ , \tag{A.33}$$

zodat de stationariteitsvoorwaarden van de totale Lagrangiaan,[9] met ϵ_i de Lagrangemultiplicatoren,[10] er als volgt uitzien:

[9] Merk op: voor $z = z_r + iz_i$ en $f(z)$ geldt:

$$\left.\frac{\partial f}{\partial z^*}\right|_z = \frac{1}{2}\left(\left.\frac{\partial f}{\partial z_r}\right|_{z_i} + i\left.\frac{\partial f}{\partial z_i}\right|_{z_r}\right)\ .$$

Er is dus slechts één vergelijking nodig om $f(z)$ te extremeren over alle mogelijke waarden van z_r en z_i.

[10] Voor de randvoorwaarden uit (A.33) is een $(n\times n)$ hermitische matrix ϵ van Lagrangemultiplicatoren nodig. Onder invloed van een unitaire transformatie binnen de ruimte van ééndeeltjegolffuncties, $\psi' = U\psi$, kan steeds een diagonaalmatrix $U^+\epsilon U$ van nieuwe Lagrangemultiplicatoren worden gevonden, waardoor het aantal randvoorwaarden effectief tot n reduceert. E_{tot} is steeds invariabel onder een willekeurige unitaire transformatie. ϵ_i in (A.35) zijn de diagonaalelementen van $U^+\epsilon U$.

$$\frac{\partial \left[E_{\mathrm{tot}}[\rho] - \sum_i \epsilon_i \left(\int \psi^*_{\mathrm{ni},i}(\mathbf{r}) \psi_{\mathrm{ni},i}(\mathbf{r}) \mathrm{d}\mathbf{r} - 1 \right) \right]}{\partial \psi^*_{\mathrm{ni},i}(\mathbf{r})} = 0 \,. \tag{A.34}$$

Uitwerking hiervan geeft de Kohn-Sham-vergelijkingen (KS), die niets anders voorstellen dan specifieke oplossingen van een ééndeeltje-Schrödingervergelijking:

$$\left[-\frac{1}{2}\nabla^2 + v_{\mathrm{H}}(\mathbf{r}) + v_{\mathrm{XC}}(\mathbf{r}) + v_{\mathrm{ext}}(\mathbf{r}) \right] \psi_{\mathrm{ni},i}(\mathbf{r}) = \epsilon_i \psi_{\mathrm{ni},i}(\mathbf{r}) \,. \tag{A.35}$$

Inderdaad, we stellen vast dat ϵ_i en $\psi_{\mathrm{ni},i}(\mathbf{r})$ respectievelijk de eigenwaarden (KS-energieniveaus) en eigenfuncties (KS-orbitalen) vormen van de KS-Hamiltoniaan H_{KS}:

$$H_{\mathrm{KS}}(\mathbf{r}) = -\frac{1}{2}\nabla^2 + v_{\mathrm{H}}(\mathbf{r}) + v_{\mathrm{XC}}(\mathbf{r}) + v_{\mathrm{ext}}(\mathbf{r}) \,. \tag{A.36}$$

De n niet-interagerende elektronen zullen de n laagste KS-energieniveaus bezetten. Gebruik makend van (A.35) leren we dat voor de som van de bezette KS-energieniveaus geldt:

$$\sum_i \epsilon_i = T_{\mathrm{ni}}[\rho(\mathbf{r})] + \int \mathrm{d}\mathbf{r} \left(v_{\mathrm{H}}(\mathbf{r}) + v_{\mathrm{XC}}(\mathbf{r}) + v_{\mathrm{ext}}(\mathbf{r}) \right) \rho(\mathbf{r}) \,, \tag{A.37}$$

waardoor E_{tot} kan worden uitgedrukt als:

$$E_{\mathrm{tot}}[\rho(\mathbf{r})] = \sum_i \epsilon_i - E_{\mathrm{H}}[\rho(\mathbf{r})] - \int \mathrm{d}\mathbf{r} v_{\mathrm{XC}}(\mathbf{r}) \rho(\mathbf{r}) + E_{\mathrm{XC}}[\rho(\mathbf{r})] + \frac{1}{2} \sum_{I \neq J} \frac{Q_I Q_J}{|\mathbf{R}_I - \mathbf{R}_J|} \,. \tag{A.38}$$

De potentialen in (A.35) zijn gelijk aan de functionele afgeleiden van de corresponderende energiefunctionalen naar de dichtheid:

$$v_{\mathrm{H}}(\mathbf{r}) = \frac{\partial}{\partial \rho(\mathbf{r})} E_{\mathrm{H}}[\rho] = \int \mathrm{d}\mathbf{r}' \frac{\rho(\mathbf{r}')}{|\mathbf{r} - \mathbf{r}'|} \,, \tag{A.39}$$

$$v_{\mathrm{XC}}(\mathbf{r}) = \frac{\partial}{\partial \rho(\mathbf{r})} E_{\mathrm{XC}}[\rho] \,, \tag{A.40}$$

$$v_{\mathrm{ext}}(\mathbf{r}) = \frac{\partial}{\partial \rho(\mathbf{r})} E_{\mathrm{ext}}[\rho] = -\sum_I \frac{Q_I}{|\mathbf{r} - \mathbf{R}_I|} \,, \tag{A.41}$$

waarbij de laatste gelijkheid in (A.41) natuurlijk enkel opgaat als de externe invloed enkel bestaat uit de Coulombse aantrekking van de atoomkernen.

Aangezien deze potentialen nog steeds afhangen van de dichtheid, moet het eigenwaardeprobleem (A.35) op zelfconsistente wijze worden opgelost. Het Kohn-Sham-DFT-schema ziet er dus als volgt uit:

1. Kies een set van willekeurige testgolffuncties.[11]
2. Bereken de elektronendichtheid (volgens A.28) en daaruit de potentialen.
3. Los het eigenwaardeprobleem (A.35,A.36) op en bereken E_{tot} (A.38).
4. Herhaal stap 2 en 3 uit deze procedure totdat (quasi) geen wijzingen meer optreden in E_{tot} (= convergentie).

In de veralgemening van de Kohn-Shamtheorie naar spingepolariseerde systemen[16, 17] wordt de uitwisselings-correlatiepotentiaal v_{XC} spinafhankelijk:

$$\left[-\frac{1}{2}\nabla^2 + v_{\text{H}}(\mathbf{r}) + v^{\tau}_{\text{XC}}(\mathbf{r}) + v_{\text{ext}}(\mathbf{r})\right] \psi^{\tau}_{\text{ni},i}(\mathbf{r}) = \epsilon_i \psi^{\tau}_{\text{ni},i}(\mathbf{r}) \ , \tag{A.42}$$

met $\tau = \alpha, \beta$, en α = spin-op, β = spin-neer.

Hoewel de KS-orbitalen $\psi_{\text{ni},i}(\mathbf{r})$ in principe geen fysische interpretatie hebben, gaat men er toch vaak van uit dat zij ééndeeltjegolffuncties voorstellen van het interagerende elektronisch systeem, wat in verschillende gevallen een goede tot zelfs zeer goede benadering blijkt.[18] Ook de theoretische berekening van EPR-grootheden in het raamwerk van DFT zal ten dele uitgaan van deze aanname.

Vanaf hier zullen we – tenzij anders vermeld – voornamelijk nog met KS-orbitalen werken, zodat we voortaan het subscript *ni* achterwege kunnen laten.

[11] Meestal wordt convergentie sneller bereikt wanneer bijvoorbeeld de atomaire configuraties als testgolffuncties worden gekozen.

Lokale-(spin)dichtheidsbenadering

In de vorige paragrafen hebben we de veeldeeltjesnatuur van de Schrödingervergelijking geherformuleerd in de uitwisselings-correlatie-energie E_{XC}. Helaas kennen we de functionele vorm van E_{XC} niet, en moeten we op zoek gaan naar een gepaste benadering. Binnen de lokale-dichtheidsbenadering (*local density approximation*, LDA) kiest men de uitwisselings-correlatie-energie gelijk aan die van een uniform elektronengas met dezelfde dichtheid:

$$E_{\mathrm{XC}}^{\mathrm{LDA}}[\rho(\mathbf{r})] = \int \mathrm{d}\mathbf{r}\rho(\mathbf{r}) v_{\mathrm{XC}}^{\mathrm{LDA}}[\rho(\mathbf{r})] \,. \tag{A.43}$$

In de spingepolariseerde variant, de lokale-spindichtheidsbenadering (*local spin density approximation*, LSDA) stelt men de uitwisselings-correlatie-energie gelijk aan deze voor een uniform gepolariseerd elektronengas. De uitwisselings-correlatie-energie wordt dan functioneel afhankelijk van zowel de α- als de β-spindichtheid.

$$E_{\mathrm{XC}}^{\mathrm{LSDA}}\left[\rho^{\alpha}(\mathbf{r}), \rho^{\beta}(\mathbf{r})\right] = \int \mathrm{d}\mathbf{r}\rho(\mathbf{r}) v_{\mathrm{XC}}^{\mathrm{LSDA}}[\rho^{\alpha}(\mathbf{r}), \rho^{\beta}(\mathbf{r})] \,. \tag{A.44}$$

Alhoewel deze benadering vrij ruw lijkt, levert ze toch verrassend goede resultaten op voor traag variërende elektronische dichtheden (in de limiet, voor een systeem met een uniforme dichtheid, is L(S)DA zelfs exact). In de loop der tijd werden echter diverse tekortkomingen vastgesteld, die de aanzet vormden voor de zoektocht naar betere functionalen.

Veralgemeende-gradiëntbenadering

Al snel werden verschillende nieuwe benaderingen geïntroduceerd. In de veralgemeende-gradiëntbenadering (*generalized gradient approximation*, GGA) hangt de uitwisselings-correlatie-energie niet enkel af van de (spingepolariseerde) dichtheid, maar ook van de ruimtelijke afgeleiden van de (spingepolariseerde) dichtheid:

$$E_{\mathrm{XC}}^{\mathrm{GGA}}\left[\rho(\mathbf{r})\right] = \int \mathrm{d}\mathbf{r} f[\rho(\mathbf{r}), \nabla\rho(\mathbf{r})] \,, \tag{A.45}$$

of:

$$E_{\mathrm{XC}}^{\mathrm{GGA}}\left[\rho^{\alpha}(\mathbf{r}),\rho^{\beta}(\mathbf{r})\right]=\int \mathrm{d}\mathbf{r} f[\rho^{\alpha}(\mathbf{r}),\rho^{\beta}(\mathbf{r}),\nabla\rho^{\alpha}(\mathbf{r}),\nabla\rho^{\beta}(\mathbf{r})]\ . \tag{A.46}$$

In een verdere uitbreiding (*Meta-GGA*) worden meer exotische functies van de dichtheid (vrijelijk) toegelaten (zoals bijvoorbeeld de Laplaciaan van de dichtheid), of zelfs expliciete functies van de KS-orbitalen.

Hybride functionalen

In een hybride functionaal (*hybrid functional*) wordt de uitwisselings-correlatie-energie (L(S)DA, GGA, meta-GGA, ...) opgemengd met de exacte-uitwisselingsenergie E_X (*exact exchange*) uit het Hartree-Fockformalisme toegepast op de KS-orbitalen:[19]

$$E_X=-\frac{1}{2}\sum_{ij}\delta_{\tau_i\tau_j}\int \mathrm{d}\mathbf{r}\int \mathrm{d}\mathbf{r}'\,\frac{\psi_i^*(\mathbf{r})\psi_j^*(\mathbf{r}')\psi_j(\mathbf{r})\psi_i(\mathbf{r}')}{|\mathbf{r}-\mathbf{r}'|}\ . \tag{A.47}$$

$\delta_{\tau_i\tau_j}$ weerhoudt enkel de termen met gelijke spins τ_i en τ_j behorend bij de KS-orbitalen i en j.

A.2.3 Basissets

De KS-orbitalen kunnen worden benaderd als een lineaire combinatie van een set van vaste functies met nader te bepalen coëfficiënten of *gewichten*. Een succesvolle basisset is in staat om met een beperkt aantal functies de KS-orbitalen correct te beschrijven en/of biedt de mogelijkheid om bepaalde rekenkundige bewerkingen heel snel (eventueel analytisch) uit te voeren.

Atomaire orbitalen (voorgesteld door gecontraheerde Gaussische functies)

Vaak worden de KS-orbitalen uitgedrukt als een lineaire combinatie van atomaire orbitalen ψ^{AO} (*lineair combination of atomic orbitals*, LCAO), gecentreerd op de positie van elke atoomkern die deel uitmaakt van het molecular systeem:

$$\psi_i(\mathbf{r})=\sum_k C_{ki}\psi_k^{\mathrm{AO}}(\mathbf{r})\ . \tag{A.48}$$

Tijdens de zelfconsistente procedure van het Kohn-Sham-DFT-schema zullen dus enkel de gewichten C_{ki} worden aangepast. Vervolgens wordt elke atomaire orbitaal nog benaderd door een gecontraheerde Gaussische functie (*contracted Gaussian function*, CGF), dit is een vaste lineaire combinatie van (atoomgecentreerde) primitieve cartesische Gaussische functies χ:

$$\psi_k^{\mathrm{AO}}(\mathbf{r}) = \sum_v D_{vk}\chi_v(\mathbf{r}) \,, \tag{A.49}$$

waarbij χ algemeen wordt geschreven als:

$$\chi(\mathbf{r}) = (x - R_x)^{n_x}(y - R_y)^{n_y}(z - R_z)^{n_z}\mathrm{e}^{-\zeta(\mathbf{r}-\mathbf{R})^2} \,. \tag{A.50}$$

χ wordt bepaald door het set van natuurlijke getallen (n_x, n_y, n_z), een positieve exponent ζ, en $\mathbf{R}$, de oorsprong van de Gaussische functie, in dit geval de positie van de betreffende atoomkern.

De KS-orbitalen worden dus uiteindelijk uitgedrukt in primitieve Gaussische functies, waarvoor verschillende types van vaak-voorkomende integralen analytisch kunnen worden opgelost, met behulp van gekende recursiebetrekkingen.[20]

Primitieve Gaussische functies zijn beperkt in de coördinatenruimte. Periodieke primitieve Gaussische functies χ^{P} worden gedefinieerd als:

$$\chi^{\mathrm{P}}(\mathbf{r}) = \sum_{\mathbf{a}} \chi(\mathbf{r} - \mathbf{L}_{\mathbf{a}}) \,, \tag{A.51}$$

met de vector van gehele getallen $\mathbf{a} = a, b, c$, en $\mathbf{L}_{\mathbf{a}} = a\mathbf{L}_x + b\mathbf{L}_y + c\mathbf{L}_z$ de roostervectoren die de periodieke beelden van de simulatiecel opbouwen.[12] Een gecontraheerde periodieke Gaussische functie (*contracted periodic Gaussian function*, CPGF) is dan niet meer dan een logische uitbreiding van (A.49):

$$\psi_k^{\mathrm{AO,P}}(\mathbf{r}) = \sum_v D_{vk}\chi_v^{\mathrm{P}}(\mathbf{r}) \,. \tag{A.52}$$

[12]Merk op dat we in dit werk voor de eenvoud van de wiskundige formules uitgaan van een orthogonale simulatiecel.

Vlakke golven

Het is evengoed mogelijk om de KS-orbitalen uit te drukken als een lineaire combinatie van vlakke golven (*plane waves*, PW). Gezien de periodiciteit en oneindige uitgestrektheid van vlakke golven, lenen deze functies zich uitstekend tot PBC-simulaties. Bovendien zijn verschillende types integralen veel eenvoudiger in de reciproque ruimte te evalueren, en kan er heel snel tussen een reële en een reciproque voorstelling van grootheden worden gewisseld via snelle Fouriertransformatietechnieken (*fast Fourier transform*, FFT). Eén van de nadelen van vlakke golven is wel dat snelle variaties in de ruimte niet goed worden beschreven, tenzij de dimensie van de basisset onhandelbaar groot wordt gemaakt. Er bestaan echter verschillende technieken om dit te verhelpen, enkele daarvan worden verderop beschreven.

Het theorema van Bloch [21] stelt dat de golffuncties $\psi_{m,\mathbf{k}}$ van een ééndeeltje-Schrödingervergelijking (*in casu:* de Kohn-Sham-vergelijking) in een periodieke potentiaal kunnen worden geschreven als het product van een structuurfunctie $\phi_{m,\mathbf{k}}$, de *Bloch-functies*, met de golffunctie van een vrij elektron (een vlakke golf):

$$\psi_{m,\mathbf{k}}(\mathbf{r}) = \phi_{m,\mathbf{k}}(\mathbf{r})\mathrm{e}^{i\mathbf{k}.\mathbf{r}} \,, \tag{A.53}$$

aangeduid met bandindex m en een continue golfvector $\mathbf{k}$ beperkt tot de eerste Brillouinzone (*Brillouin zone*, BZ) van het reciproque rooster, die eenduidig wordt bepaald door de simulatiecel in de coördinatieruimte. De functie $\phi_{m,\mathbf{k}}$ heeft de periodiciteit van het rooster in de coördinatenruimte:

$$\phi_{m,\mathbf{k}}(\mathbf{r} + \mathbf{L}_\mathbf{a}) = \phi_{m,\mathbf{k}}(\mathbf{r}) \,, \tag{A.54}$$

met de vector van gehele getallen $\mathbf{a} = a, b, c$, en $\mathbf{L}_\mathbf{a} = a\mathbf{L}_x + b\mathbf{L}_y + c\mathbf{L}_z$ de roostervectoren die de periodieke beelden van het rooster opbouwen.. Deze periodieke functie drukken we uit als een lineaire combinatie van vlakke golven die aan de periodiciteit van het rooster voldoen:

$$\phi_{m,\mathbf{k}}(\mathbf{r}) = \frac{1}{\sqrt{\Omega}} \sum_{\mathbf{G}} c_{m,\mathbf{k},\mathbf{G}} \mathrm{e}^{i\mathbf{G}.\mathbf{r}} \,. \tag{A.55}$$

Hier is Ω het volume van de simulatiecel en zijn $\mathbf{G}$ de vectoren van het reciproque rooster gedefinieerd door:

$$\frac{1}{2\pi}|\mathbf{G}.\mathbf{R}| \in \mathbb{N} \, . \tag{A.56}$$

Op die manier is automatisch voldaan aan (A.54). (A.55) is eveneens de discrete Fourierontwikkeling van $\phi_{m,\mathbf{k}}$. De coëfficiënten $c_{m,\mathbf{k},\mathbf{G}}$ worden bekomen door de inverse transformatie:

$$c_{m,\mathbf{k},\mathbf{G}} = \frac{1}{\sqrt{\Omega}} \int \mathrm{d}\mathbf{r}\, \phi_{m,\mathbf{k}}(\mathbf{r}) \mathrm{e}^{-i\mathbf{G}.\mathbf{r}} \, . \tag{A.57}$$

De nauwkeurigheid van de beschrijving van een Bloch-functie in een PW-basisset, en bij uitbreiding de totale golffunctie van het elektron, wordt dus bepaald door de grootte van het set vlakke golven in (A.55). In praktijk wordt de gewenste nauwkeurigheid opgelegd door een maximumwaarde E_c op te leggen voor de kinetische-energiebijdrage van een vlakke golf.[13] De kinetische energie van een orbitaal $\psi_{m,\mathbf{k}}$ is gelijk aan:

$$\begin{aligned} T_{m,\mathbf{k}} &= \langle \psi_{m,\mathbf{k}} | \, \frac{1}{2}\mathbf{p}^2 \, | \psi_{m,\mathbf{k}} \rangle \\ &= \sum_{\mathbf{G}} \frac{1}{2} |\mathbf{k}+\mathbf{G}|^2 |c_{m,\mathbf{k},\mathbf{G}}|^2 \, . \end{aligned} \tag{A.58}$$

Bij opgave van E_c worden enkel die vlakke golven in de PW-basisset opgenomen die voldoen aan:

$$\frac{1}{2}|\mathbf{k}+\mathbf{G}|^2 \leq E_\mathrm{c} \, . \tag{A.59}$$

In de praktijk wordt de eerste Brillouinzone gediscretiseerd, en staan de oplossingen voor een specifieke $\mathbf{k}$ model voor een discreet stuk van de eerste Brillouinzone. In een grote, wanordelijke, niet-metallische simulatiecel is het zelfs voldoende om met één enkele golfvector $\mathbf{k}$ te werken voor de volledige eerste Brillouinzone. We kiezen $\mathbf{k} = \mathbf{0}$, met andere woorden de oorsprong van de reciproque ruimte. Dit is de zogeheten Γ-puntbenadering.

[13] Deze waarde wordt om historische redenen nog steeds uitgedrukt in Rydberg (Ry).

A.2.4 Pseudopotentiaalbenadering

In een ééndeeltjesbeeld (*one-particle picture*) van het elektronisch systeem in een vrij atoom of ion kunnen de elektronen (de deeltjes) worden geclassificeerd volgens de energie-eigenwaarde corresponderend met hun golffunctie. Dikwijls wordt er onderscheid gemaakt tussen diepgebonden elektronen en elektronen met een energie dicht bij het Ferminiveau, en men noemt deze respectievelijk kern- (*core*) en valentie-elektronen (*valence electrons*). De ruimtelijke uitgebreidheid van de golffuncties van de kernelektronen blijft beperkt tot de nabije omgeving van de atoomkern, de kernregio (*core region*), waar de Coulombinteractie van de atoomkern en van de andere kernelektronen sterk overheersen. Deze golffuncties zijn daardoor praktisch ongevoelig voor externe invloeden op het atoom, zoals bijvoorbeeld de nabijheid van een ander atoom voor het aangaan van een chemische binding.

De valentie-elektronen bevinden zich relatief verder van de atoomkern dan de kernelektronen, waar de Coulombpotentiaal van de atoomkern in belangrijke mate wordt afgeschermd door de kernelektronen. Het zijn de golffuncties van deze elektronen die belangrijke wijzigingen zullen ondergaan wanneer de externe omgeving van het atoom wijzigt, en daardoor onder andere grotendeels de chemische eigenschappen van het atoom bepalen. Om de orthonormaliteit met de andere golffuncties te verzekeren, en zo aan het Pauliverbod[14] te voldoen, kunnen de golffuncties van de valentie-elektronen snelle oscillaties hebben in de kernregio. Deze oscillaties zijn echter minder belangrijk voor bijvoorbeeld de chemische eigenschappen van het atoom.

In de pseudopotentiaalbenadering maakt men handig gebruik van het feit dat de kernelektronen en het gedrag van de valentie-elektronen in de kernregio van ondergeschikt belang zijn voor vele chemische eigenschappen van een atoom, zoals bijvoorbeeld de bindingseigenschappen. De atoomkern en de omringende kernelektronen worden vast verondersteld (*frozen core approximation*) en gegroepeerd tot een pseudokern (*pseudo core*), en de interactie van deze pseudokern met zijn omgeving wordt gemodelleerd door een pseudopotentiaal (*pseudopotential*, PSP). De in dit werk gebruikte pseudopotentialen zijn van het niet-lokale, scheidbare, en normbehoudende type (*non-local separable norm-conserving*), en worden als volgt geconstrueerd (zie ook Figuur A.1):

1. Kies een referentieconfiguratie voor een atoomtype (bijvoorbeeld de neutrale configuratie voor Si: $[1s^2 2s^2 2p^6]3s^2 3p^2$).

[14] Twee identieke fermionen mogen niet gelijktijdig dezelfde kwantumtoestand bezetten.

2. Bepaal de KS-orbitalen en KS-eigenfuncties van het atoom in de referentieconfiguratie. Hierbij wordt van een sferisch-symmetrische benadering van de Hartree- en XC-potentiaal uitgegaan, zodat men de radiale en sferische afhankelijkheden van de KS-orbitalen (aangeduid met de kwantumgetallen n,l en m) kan scheiden:

$$\psi_{nlm}(\mathbf{r}) = R_{nl}(r)Y_{lm}(\theta,\phi) \ , \tag{A.60}$$

waarbij Y_{lm} de sferische harmonieken voorstellen, en R_{nl} de alle-elektronen-oplossingen (*all-electron*, AE) van de radiale Kohn-Sham-vergelijking (met de volledige nucleaire Coulombpotentiaal):

$$\left[-\frac{1}{2}\frac{d^2}{dr^2} + \frac{l(l+1)}{2r^2} - \frac{Q}{r} + V_{\mathrm{H}}[\rho(\mathbf{r})] + V_{\mathrm{XC}}[\rho(\mathbf{r})]\right] rR_{nl}(r) = \epsilon_{nl} rR_{nl}(r) \ . \tag{A.61}$$

Het is hierbij sterk aan te raden om dezelfde XC-functionaal te gebruiken voor de aanmaak van de pseudopotentiaal als voor de simulatie waarin de pseudopotentiaal zal worden gebruikt.[22]

3. Splits de referentieconfiguratie (arbitrair) op in kern- en valentie-elektronen, definieer $Q^{\mathrm{eff}} = Q - (\#\text{kernelektronen})$ als het *effectieve ladingsgetal*, en creëer voor de valentie-elektronen radiale pseudogolffuncties R_{nl}^{PSP} en pseudo-energie-eigenwaarden $\epsilon_{nl}^{\mathrm{PSP}}$, die onderling aan het Pauliverbod voldoen, en daarnaast rekening houden met enkele (in zekere mate zelf in te vullen) randvoorwaarden, zoals bijvoorbeeld de volgende:

   - Elk paar eigenwaarden moet overeenstemmen:

$$\epsilon_{nl}^{\mathrm{PSP}} = \epsilon_{nl} \ . \tag{A.62}$$

   - Voorbij een bepaalde straal $r_{c,nl}$ valt het paar corresponderende golffuncties samen:

$$R_{nl}^{\mathrm{PSP}}(r) = R_{nl}(r) \qquad \text{voor } r > r_{c,nl} \ . \tag{A.63}$$

     Wanneer we genormeerde golffuncties veronderstellen geldt dan onder meer dat:

     – Voor elke $r > r_{c,nl}$ moet de lading binnen r gelijk zijn voor elk paar corresponderende golffuncties:

$$\int_0^r \mathrm{d}r |R_{nl}^{\mathrm{PSP}}(r)|^2 r^2 = \int_0^r \mathrm{d}r |R_{nl}(r)|^2 r^2 \qquad \text{voor } r > r_{c,nl} \ . \tag{A.64}$$

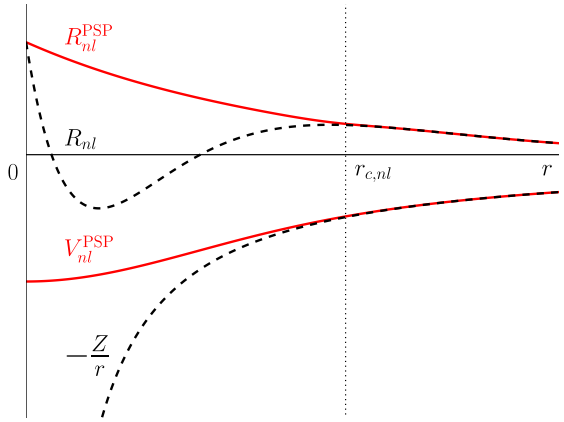

Figuur A.1: Schets van de pseudopotentiaalbenadering. Bemerk hoe de radiale pseudo-golffunctie R_{nl}^{PSP} minder oscilleert dan de overeenkomstige alle-elektronengolffunctie R_{nl}.

- De logaritmische afgeleiden[15] van elk paar corresponderende golffuncties gelijk zijn voor $r > r_{c,nl}$.

Als een pseudopotentiaal aan de hierboven beschreven voorwaarden voldoet, dan wordt deze normbehoudend genoemd.[23] Dit type wordt door bovenstaande voorwaarden duidelijk niet uniek bepaald, en deze vrijheid kan men bijvoorbeeld benutten om er voor te zorgen dat de golffuncties gegenereerd bij gebruik van deze pseudopotentiaal met een relatief kleine basisset kunnen worden beschreven.

4. Voor elke pseudogolffunctie en pseudo-energie-eigenwaarde apart kan men uit (A.61) een afgeschermde (*screened*, scr) pseudopotentiaal berekenen:

$$V_{nl}^{\mathrm{PSP,scr}}(r) = \epsilon_{nl}^{\mathrm{PSP}} - \frac{l(l+1)}{2r^2} + \frac{1}{2rR_{nl}^{PSP}(r)} \frac{d^2}{dr^2}\left[rR_{nl}^{PSP}(r)\right] . \qquad \text{(A.65)}$$

De afscherming is afkomstig van de valentie-elektronen van het atoom, en deze kan in goede benadering worden verwijderd (*unscreening*) door de Hartree- en XC-potentiaal afkomstig van een sferisch-symmetrische benadering van de pseudovalentiedichtheid ρ_0^{PSP},

[15] dit is: $\frac{\mathrm{d}}{\mathrm{d}r}(\ln f(r)) = \frac{\frac{\mathrm{d}}{\mathrm{d}r} f(r)}{f(r)}$.

$$\rho_0^{\mathrm{PSP}}(\mathbf{r}) = \frac{1}{4\pi}\sum_{nl}|R_{nl}^{\mathrm{PSP}}(r)|^2 \,, \tag{A.66}$$

van elke potentiaal af te trekken:[16]

$$V_{nl}^{\mathrm{PSP}}(r) = V_{nl}^{\mathrm{PSP,scr}}(r) - V_{\mathrm{H}}[\rho_0^{\mathrm{PSP}}(\mathbf{r})] - V_{\mathrm{XC}}[\rho_0^{\mathrm{PSP}}(\mathbf{r})] \,. \tag{A.67}$$

V_{nl}^{PSP} is een ionaire pseudopotentiaal die niet meer afhangt van zijn atomaire elektronische omgeving, maar wel nog afhangt van de pseudogolffunctie waarvoor deze werd geconstrueerd. Wanneer we er nu van uitgaan dat de pseudogolffuncties $\psi_{nlm}^{\mathrm{PSP}} = R_{nl}^{\mathrm{PSP}}Y_{lm}$ in de buurt van de atoomkern een complete en orthonormale set vormen voor een willekeurige golffunctie ψ_i^{PSP} uit een simulatie waarin de pseudopotentiaal wordt gebruikt,

$$\psi_i^{\mathrm{PSP}}(\mathbf{r}) = \sum_{nlm} C_{nlm,i}\psi_{nlm}^{PSP}(\mathbf{r}) \qquad \text{voor } r < \max_{nl}\{r_{c,nl}\} \,, \tag{A.68}$$

dan kunnen we (in bra-ketnotatie) via projectie $\left|\psi_{nlm}^{\mathrm{PSP}}\right\rangle\left\langle p_{nlm}^{\mathrm{PSP}}\right|$, waarbij p_{nlm}^{PSP} een projectiefunctie op $\psi_{nlm}^{\mathrm{PSP}}$ voorstelt, aan elke component van $\left|\psi_i^{\mathrm{PSP}}\right\rangle$ de potentiaal V_{nl}^{PSP} aanbieden. De totale pseudopotentiaal in operatorvorm wordt dan:

$$V^{\mathrm{PSP}} = \sum_{nlm} V_{nl}^{\mathrm{PSP}}(r)\left|\psi_{nlm}^{\mathrm{PSP}}\right\rangle\left\langle p_{nlm}^{\mathrm{PSP}}\right| \,. \tag{A.69}$$

In de coördinatenrepresentatie van (A.69) ontstaat een niet-lokale operator $V^{\mathrm{PSP}}(\mathbf{r},\mathbf{r}')$. Meestal is er slechts één projector per baankwantumgetal l.

In een laatste benadering worden alle V_{nl}^{PSP} met kwantumgetallen voorbij een zekere $(nlm)_{\max}$ gelijk gesteld aan een bepaalde V_{nl}^{PSP}, voortaan aangeduid als $V_{\mathrm{loc}}^{\mathrm{PSP}}$. Gebruik makend van de compleetheidsrelatie voor de pseudogolffuncties volgt er:

[16] Hierbij veronderstelt men dat V_{XC} lineair is in ρ, zodat $V_{\mathrm{XC}}[\rho_{\mathrm{kern}}(\mathbf{r}) + \rho_{\mathrm{valentie}}(\mathbf{r})] = V_{\mathrm{XC}}[\rho_{\mathrm{kern}}(\mathbf{r})] + V_{\mathrm{XC}}[\rho_{\mathrm{valentie}}(\mathbf{r})]$. Wanneer de veronderstelde lineariteit niet opgaat, kan men dit (soms) oplossen door meer elektronen als valentie-elektronen te beschouwen, ofwel door in de uiteindelijke simulatie waarin de pseudopotentiaal wordt gebruikt een niet-lineaire correctie van de kerndichtheid (*non-linear core correction*) toe te voegen in de XC-energiefunctionaal en XC-potentiaal.[24]

$$V^{\mathrm{PSP}} = V_{\mathrm{loc}}^{\mathrm{PSP}} + \sum_{nlm}^{(nlm)_{\max}} \left(V_{nl}^{\mathrm{PSP}} - V_{\mathrm{loc}}^{\mathrm{PSP}} \right) \left| \psi_{nlm}^{\mathrm{PSP}} \right\rangle \left\langle p_{nlm}^{\mathrm{PSP}} \right| \ . \tag{A.70}$$

Aan de totale energiefunctionaal E_{tot} (A.38) wordt een nieuwe term E_{PSP} toegevoegd, die de Coulombse interactie-energieterm tussen de atoomkernen en de elektronen in E_{ext} vervangt voor elke atoomkern waarvoor een PSP-benadering werd aangenomen ($I \in \mathrm{PSP}$):

$$E_{\mathrm{PSP}}[\rho(\mathbf{r})] = \sum_{i, I \in \mathrm{PSP}} \langle \psi_i | \, V^{\mathrm{PSP}} \, | \psi_i \rangle \ . \tag{A.71}$$

Daarnaast wordt voor alle atoomkernen $I \in \mathrm{PSP}$ in alle voorgaande uitdrukkingen Q_I vervangen door Q_I^{eff}.

Het gebruik van pseudopotentialen biedt enkele belangrijke voordelen:

1. Het aantal elektronen daalt met het aantal kernelektronen per atoom waarvoor een pseudopotentiaal wordt gebruikt.
2. De grootte van de basisset kan beperkt worden.
3. Men kan ten dele relativistische effecten opnemen in een niet-relativistisch schema.

A.2.5 De hybride Gaussische en vlakke-golfmethode

De recentere implementaties van het Kohn-Sham-DFT-schema maken niet langer gebruik van één type basissetfuncties. In de hybride Gaussische en vlakke-golfmethode (*Gaussian and plane-wave method*, GPW) [25] worden CPGF's als primaire basisset gebruikt.[17] Daarnaast wordt een hulpbasisset van vlakke golven aangehouden om de elektronendichtheid (A.28) in CPGF's (met $P_{kl} = \sum_i C_{ki} C_{li}$ de dichtheidsmatrix):

$$\begin{aligned} \rho(\mathbf{r}) &= \sum_i |\psi_i(\mathbf{r})|^2 \ \text{met} \ \psi_i(\mathbf{r}) = \sum_k C_{ki} \psi_k^{\mathrm{AO,P}}(\mathbf{r}) \\ &= \sum_{kl} P_{kl} \psi_k^{\mathrm{AO,P},*}(\mathbf{r}) \psi_l^{\mathrm{AO,P}}(\mathbf{r}) \ , \end{aligned} \tag{A.72}$$

[17] Impliciet wordt hier de Γ-puntbenadering ingevoerd. Dit laat toe de KS-orbitalen als reële functies te veronderstellen.

in op te spannen:

$$\tilde{\rho}(\mathbf{r}) = \frac{1}{\Omega} \sum_{\frac{1}{2}|\mathbf{G}|^2 < E_c} \rho(\mathbf{G}) e^{i\mathbf{G}.\mathbf{r}} \,. \tag{A.73}$$

Deze projectie[18] laat toe om bepaalde termen uit de energiefunctionaal E_{tot} (A.32), de Kohn-Sham-matrix[19] en de berekening van de krachten op de atoomkernen,[20] die sterk vereenvoudigen bij Fouriertransformatie naar de reciproque ruimte, veel sneller uit te rekenen. Rekening houdend met de eigenschap dat het product van twee Gaussische functies opnieuw een Gaussische functie is, bestaan er voor de uitwerking van de projectie zelf twee mogelijkheden: ofwel worden de primitieve Gaussische functies, na vermenigvuldiging met de bijpassende coefficiënt, geëvalueerd op de discrete punten van het FFT-raster in de reële ruimte, en na sommatie over alle primitieve Gaussische functies worden de totale waarden op die rasterpunten via FFT naar de reciproque ruimte omgezet, ofwel wordt gebruik gemaakt van de eigenschap dat de Fourier-getransformeerde van een Gaussische functie opnieuw een Gaussische functie is (in de reciproque ruimte), die dan rechtstreeks kan worden geëvalueerd en bijgeteld op de discrete punten van het FFT-raster in de reciproque ruimte.

Om de grootte van de vlakke-golfbasisset te beperken, worden pseudopotentialen gebruikt, opgesteld door Goedecker *et al.*[26, 27] Dit type pseudopotentiaal heeft de volgende operatorvorm in de coördinatenrepresentatie:

$$\begin{aligned} V^{\text{PSP}}(\mathbf{r},\mathbf{r}') &= \delta(\mathbf{r}-\mathbf{r}') \left[\frac{Q^{\text{eff}}}{r} \text{erf}\left(\frac{r}{\sqrt{2}r_{\text{loc}}}\right) \right. \\ &- \left. e^{-\frac{1}{2}\left(\frac{r}{r_{\text{loc}}}\right)^2} \left(C_1 + C_2 \left(\frac{r}{r_{\text{loc}}}\right)^2 + C_3 \left(\frac{r}{r_{\text{loc}}}\right)^4 + C_4 \left(\frac{r}{r_{\text{loc}}}\right)^6 \right) \right] \\ &- \sum_l \sum_{i=1}^{3} \sum_{j=1}^{3} \sum_{m=-l}^{l} Y_{lm}(\Omega_{\mathbf{r}}) p_i^l(r) h_{ij}^l p_j^l(r') Y_{lm}^*(\Omega_{\mathbf{r}'}) \,, \end{aligned} \tag{A.74}$$

[18] De tilde in (A.73) duidt erop dat de opspanning in vlakke golven, als gevolg van het eindige set van vlakke golven, steeds een benadering betreft (enkel een oneindig set van vlakke golven vormt een compleet set).

[19] De Kohn-Sham-matrix is de matrixvoorstelling van de Hamiltoniaan H_{KS} in de basis van atomaire orbitalen.

[20] De krachten op de atoomkernen worden slechts berekend in bijvoorbeeld een geometrie-optimalisatie (en zijn niet nodig voor de bepaling van de elektronische grondtoestandsdichtheid van een gegeven moleculaire structuur).

met:

$$p_i^l(r) = \frac{\sqrt{2} r^{l+2(i-1)} \mathrm{e}^{-\frac{r^2}{2r_l^2}}}{r_l^{l+(4i-1)/2} \sqrt{\Gamma\left(l+\frac{4i-1}{2}\right)}} \,, \tag{A.75}$$

$$\int_0^\infty p_i^l(r) p_i^l(r) r^2 \mathrm{d}r = 1 \,, \tag{A.76}$$

waarbij Γ de gammafunctie[21] en erf de foutfunctie[22] aanduidt, r_{loc} de reikwijdte van de Gaussische ladingsdistributie afkomstig van de atoomkern die tot de erf-potentiaal leidt, en C_1, C_2, C_3 en C_4 constante reële parameters. Het grote voordeel van deze keuze voor de pseudopotentiaal is dat de matrixelementen in de basis van CPGF analytisch kunnen worden berekend. Bovendien, maar niet van belang in de GPW-methode, heeft deze pseudopotentiaal ook een analytische uitdrukking in gesloten vorm in de reciproque ruimte. Merk op dat de lokale component van (A.74) een korte- en een lange-drachtscomponent heeft, respectievelijk $V_{\mathrm{loc,sr}}^{\mathrm{PSP}}$ en $V_{\mathrm{loc,lr}}^{\mathrm{PSP}}$ genoemd:

$$V_{\mathrm{loc,sr}}^{\mathrm{PSP}}(\mathbf{r}) = -\mathrm{e}^{-\frac{1}{2}\left(\frac{r}{r_{\mathrm{loc}}}\right)^2} \left(C_1 + C_2 \left(\frac{r}{r_{\mathrm{loc}}}\right)^2 + C_3 \left(\frac{r}{r_{\mathrm{loc}}}\right)^4 + C_4 \left(\frac{r}{r_{\mathrm{loc}}}\right)^6 \right) \,, \tag{A.77}$$

$$V_{\mathrm{loc,lr}}^{\mathrm{PSP}}(\mathbf{r}) = \frac{Q^{\mathrm{eff}}}{r} \mathrm{erf}\left(\frac{r}{\sqrt{2} r_{\mathrm{loc}}}\right) \,. \tag{A.78}$$

De energiefunctionaal E_{tot} ziet er in de GPW-methode als volgt uit:

$$E_{\mathrm{tot}}[\rho(\mathbf{r})] = T[\rho(\mathbf{r})] + E_{\mathrm{PSP}}[\rho(\mathbf{r})] + E_{\mathrm{H}}[\rho(\mathbf{r})] + E_{\mathrm{ext}}[\rho(\mathbf{r})] + E_{\mathrm{XC}}[\rho(\mathbf{r})] \,, \tag{A.79}$$

met:[23]

[21] $\Gamma(z) = \int_0^\infty \mathrm{d}t\, t^{z-1} \mathrm{e}^{-t}$, en voor $n \in \mathbb{N}$: $\Gamma(n) = (n-1)!$

[22] $\mathrm{erf}(x) = \frac{2}{\sqrt{\pi}} \int_0^x \mathrm{d}t\, \mathrm{e}^{-t^2}$. $\mathrm{erfc}(x) = 1 - \mathrm{erf}(x)$.

[23] Merk op dat een pseudopotentiaal en de corresponderende operatorterm die de interactie met de elektronen beschrijft in atomaire eenheden nog steeds verschillen met een minteken.

$$T[\rho(\mathbf{r})] = \sum_{k_1 k_2} P_{k_1 k_2} \int \mathrm{d}\mathbf{r} \psi_{k_1}^{\mathrm{AO,P}}(\mathbf{r}) \left(-\frac{\nabla^2}{2} \right) \psi_{k_2}^{\mathrm{AO,P}}(\mathbf{r}) \,, \quad \text{(A.80)}$$

$$E_{\mathrm{PSP}}[\rho(\mathbf{r})] = \sum_I \sum_{k_1 k_2} P_{k_1 k_2} \int \mathrm{d}\mathbf{r}\mathrm{d}\mathbf{r}' \psi_{k_1}^{\mathrm{AO,P}}(\mathbf{r}) \left(-V_I^{\mathrm{PSP}}(\mathbf{r}, \mathbf{r}') \right) \psi_{k_2}^{\mathrm{AO,P}}(\mathbf{r}') \,, \quad \text{(A.81)}$$

$$E_{\mathrm{XC}}[\rho(\mathbf{r})] = \int \mathrm{d}\mathbf{r} f[\tilde{\rho}(\mathbf{r}), \nabla\tilde{\rho}(\mathbf{r}), ...] \,. \quad \text{(A.82)}$$

i) E_{H}, ii) de interactie-energieterm van de lokale lange-drachtscomponent $E_{\mathrm{PSP,loc,lr}}$ van elke pseudopotentiaal met de elektronen en iii) E_{ext} (die, wanneer voor alle atoomkernen een PSP-benadering werd aangenomen, enkel nog de Coulombse interactie-energie tussen de atoomkernen onderling bevat) worden in PBC-simulaties via de Ewald-somtechniek samen berekend in de elektrostatische-energieterm E_{ES} van het geheel van atoomkernen en elektronen:[24]

[24] De elektrostatische energie E_{ES} bestaat uit drie delen, de Hartree-energie van de elektronische ladingsdistributie, de Coulombse interactie-energie van de elektronen met de atoomkernen en de Coulombse interactie-energie tussen de atoomkernen onderling:

$$E_{\mathrm{ES}} = \frac{1}{2} \int \mathrm{d}\mathbf{r}\mathrm{d}\mathbf{r}' \frac{\rho(\mathbf{r})\rho(\mathbf{r}')}{|\mathbf{r} - \mathbf{r}'|} - \sum_I \int \mathrm{d}\mathbf{r} V_I^{\mathrm{c}}(\mathbf{r})\rho(\mathbf{r}) + \frac{1}{2} \sum_{I \neq J} \frac{Q_I^{\mathrm{eff}} Q_J^{\mathrm{eff}}}{|\mathbf{R}_I - \mathbf{R}_J|} \,.$$

De vorm van de kernpotentiaal V_I^{c} behorend bij atoomkern I kan bij het gebruik van een pseudopotentiaal als de Coulombse potentiaal van een Gaussische ladingsdistributie met totale lading Q_I^{eff} en breedte $r_{\mathrm{loc},I}$ worden gekozen (want de atoom*kern* is niet langer een puntlading, maar eerder een uitgesmeerde vlek van lading):

$$\rho_I^{\mathrm{c}}(\mathbf{r}) = \frac{Q_I^{\mathrm{eff}}}{(\sqrt{2\pi} r_{\mathrm{loc},I})^3} \mathrm{e}^{-\frac{1}{2}\left(\frac{\mathbf{r}-\mathbf{R}_I}{r_{\mathrm{loc},I}}\right)^2} \,,$$

$$V_I^{\mathrm{c}}(\mathbf{r}) = \int \mathrm{d}\mathbf{r}' \frac{\rho_I^{\mathrm{c}}(\mathbf{r}')}{|\mathbf{r} - \mathbf{r}'|} = \frac{Q_I^{\mathrm{eff}}}{|\mathbf{r} - \mathbf{R}_I|} \mathrm{erf}\left(\frac{|\mathbf{r} - \mathbf{R}_I|}{\sqrt{2} r_{\mathrm{loc},I}} \right) \,.$$

Per definitie is de lokale lange-drachtscomponent $V_{\mathrm{loc,lr},I}^{\mathrm{PSP}}$ van een Goedecker-pseudopotentiaal dan gelijk aan V_I^{c}. Met de definities $\rho^{\mathrm{c}} = \sum_I \rho_I^{\mathrm{c}}$ en $\rho^{\mathrm{tot}} = \rho - \rho^{\mathrm{c}}$ ($-$ wegens tekenconventie) kunnen we E_{ES} herschrijven als:

$$E_{\mathrm{ES}} = \frac{1}{2} \int \mathrm{d}\mathbf{r}\mathrm{d}\mathbf{r}' \frac{\rho^{\mathrm{tot}}(\mathbf{r})\rho^{\mathrm{tot}}(\mathbf{r}')}{|\mathbf{r} - \mathbf{r}'|} + \frac{1}{2} \sum_{I \neq J} \frac{Q_I^{\mathrm{eff}} Q_J^{\mathrm{eff}}}{|\mathbf{R}_I - \mathbf{R}_J|} - \frac{1}{2} \int \mathrm{d}\mathbf{r}\mathrm{d}\mathbf{r}' \frac{\rho^{\mathrm{c}}(\mathbf{r})\rho^{\mathrm{c}}(\mathbf{r}')}{|\mathbf{r} - \mathbf{r}'|} \,.$$

De tweede en derde term uit bovenstaande vergelijking kunnen worden herschreven tot:

$$E_{\mathrm{ES}} = \frac{1}{2} \int \mathrm{d}\mathbf{r}\mathrm{d}\mathbf{r}' \frac{\rho^{\mathrm{tot}}(\mathbf{r})\rho^{\mathrm{tot}}(\mathbf{r}')}{|\mathbf{r} - \mathbf{r}'|} + \frac{1}{2} \sum_{I \neq J} \frac{Q_I^{\mathrm{eff}} Q_J^{\mathrm{eff}}}{|\mathbf{R}_I - \mathbf{R}_J|} \mathrm{erfc}\left(\frac{|\mathbf{R}_I - \mathbf{R}_J|}{\sqrt{r_{\mathrm{loc},I}^2 + r_{\mathrm{loc},J}^2}} \right) - \sum_I \frac{{Q_I^{\mathrm{eff}}}^2}{\sqrt{2\pi} r_{\mathrm{loc},I}} \,.$$

$$E_{\mathrm{ES}} = 2\pi\Omega \sum_{\mathbf{G}\neq\mathbf{0}} \frac{\left|\tilde{\rho}^{\mathrm{tot}}(\mathbf{G})\right|^2}{G^2} + \sum_{I\neq J}{}' \sum_{\mathbf{L}} \frac{Q_I^{\mathrm{eff}} Q_J^{\mathrm{eff}}}{\left|\mathbf{R}_I - \mathbf{R}_J - \mathbf{L}\right|} \mathrm{erfc}\left(\frac{\left|\mathbf{R}_I - \mathbf{R}_J - \mathbf{L}\right|}{\sqrt{{r_{\mathrm{loc},I}}^2 + {r_{\mathrm{loc},J}}^2}}\right) - \sum_I \frac{{Q_I^{\mathrm{eff}}}^2}{\sqrt{2\pi} r_{\mathrm{loc},I}} , \tag{A.83}$$

waarbij het accent boven de som aanduidt dat $I \neq J$ enkel geldt voor $\mathbf{L} = \mathbf{0}$. In een hybride functionaal wordt E_{XC} aangevuld met E_{X} (A.47), uitgewerkt in de basisset van CPGF. De berekening van de Kohn-Sham-matrix en de krachten op de atoomkernen is gebaseerd op dezelfde technieken als hierboven geschetst voor de energie.

A.2.6 De hybride Gaussische en uitgebreide-vlakke-golfmethode

In de hybride Gaussische en uitgebreide-vlakke-golfmethode (*Gaussian and augmented-plane-wave method*, GAPW) [28] wordt de hulpbasisset van vlakke golven aangevuld met de primitieve periodieke Gaussische functies waaruit de CPGF werden opgebouwd. Op arbitraire wijze wordt de simulatiecel opgedeeld in niet-overlappende, gelokaliseerde, sferische regio's gecentreerd op de atoomkernen, en de tussenliggende ruimte (*interstitial region*). De onderliggende gedachte in GAPW is dat de elektronendichtheid in de tussenliggende ruimte slechts traag varieert en dus reeds goed opspanbaar is in een beperkte set van vlakke golven, terwijl de sneller variërende elektronendichtheid dicht bij de atoomkernen efficiënter met behulp van gelokaliseerde functies kan worden beschreven. De GAPW-voorstelling van de elektronendichtheid is een som van drie bijdragen:

$$\rho(\mathbf{r}) = \tilde{\rho}(\mathbf{r}) + \rho^1(\mathbf{r}) - \tilde{\rho}^1(\mathbf{r}) . \tag{A.84}$$

In een simulatie met periodieke randvoorwaarden herleidt de eerste term uit E_{ES} zich in de reciproque ruimte tot een eenvoudige som over de vectoren $\mathbf{G}$:

$$\frac{1}{2}\int \mathrm{d}\mathbf{r}\mathrm{d}\mathbf{r}' \frac{\rho^{\mathrm{tot}}(\mathbf{r})\rho^{\mathrm{tot}}(\mathbf{r}')}{|\mathbf{r}-\mathbf{r}'|} = 2\pi\Omega \sum_{\mathbf{G}\neq\mathbf{0}} \frac{\left|\tilde{\rho}^{\mathrm{tot}}(\mathbf{G})\right|^2}{G^2} .$$

$\rho(\mathbf{0})$ komt (per definitie) overeen met de totale lading in de simulatiecel, en is ofwel nul (neutraal systeem) of kan neutraal worden gemaakt door het invoeren van een uniforme achtergrondlading, zodat we de divergente term voor $\mathbf{G} = \mathbf{0}$ steeds achterwege kunnen laten. Mits enkele triviale aanpassingen houden de tweede en derde termp uit E_{ES} ook rekening met de periodieke randvoorwaarden.

In de zachte (*soft*) elektronendichtheid $\tilde{\rho}$ worden de snelle variaties van de echte elektronendichtheid ρ dicht bij de atoomkernen geëlimineerd door in de CPGF de coëfficiënten behorend bij de sterkst gelokaliseerde primitieve Gaussische functies op nul te stellen, zodat effectief slechts de beperkte set van minder-gelokaliseerde primitieve Gaussische functies $\tilde{\chi}^{\mathrm{P}}$ wordt gebruikt. Daardoor varieert $\tilde{\rho}$ traag – vandaar zacht, tegenover een sterk oscillerende dichtheid die we hard (*hard*) zullen noemen –, maar wordt nog steeds periodiek herhaald over de volledige ruimte, en kan dus worden voorgesteld door een relatief beperkte set van vlakke golven:

$$\tilde{\rho}(\mathbf{r}) = \frac{1}{\Omega} \sum_{\frac{1}{2}|\mathbf{G}|^2 < E_c} \tilde{\rho}(\mathbf{G}) \mathrm{e}^{i\mathbf{G}.\mathbf{r}} \,. \tag{A.85}$$

De andere dichtheden,

$$\rho^1(\mathbf{r}) = \sum_I \rho_I^1(\mathbf{r}) \,, \qquad \tilde{\rho}^1(\mathbf{r}) = \sum_I \tilde{\rho}_I^1(\mathbf{r}) \,, \tag{A.86}$$

zijn de som van lokale atoomgecentreerde dichtheden ρ_I^1 en $\tilde{\rho}_I^1$ die respectievelijk hard en zacht zijn. ρ_I^1 en $\tilde{\rho}_I^1$ worden geconstrueerd via een projectie van ρ en $\tilde{\rho}$ op respectievelijk de primitieve Gaussische functies χ_I^{P} en $\tilde{\chi}_I^{\mathrm{P}}$ behorend bij atoomkern I.

Bij constructie voldoen ρ, $\tilde{\rho}$, ρ_I^1 en $\tilde{\rho}_I^1$ aan de volgende relaties:

$$\rho(\mathbf{r}) - \tilde{\rho}(\mathbf{r}) = 0 \qquad \text{voor } \mathbf{r} \in U_0 \,, \tag{A.87}$$

$$\rho_I^1(\mathbf{r}) - \tilde{\rho}_I^1(\mathbf{r}) = 0 \qquad \text{voor } \mathbf{r} \in U_0 \,, \tag{A.88}$$

$$\tilde{\rho}(\mathbf{r}) - \tilde{\rho}_I^1(\mathbf{r}) = 0 \qquad \text{voor } \mathbf{r} \in U_I \,, \tag{A.89}$$

$$\rho(\mathbf{r}) - \rho_I^1(\mathbf{r}) = 0 \qquad \text{voor } \mathbf{r} \in U_I \,, \tag{A.90}$$

waarbij U_I een sferische regio aanduidt (met een zelf te kiezen straal) rond atoomkern I en U_0 de tussenliggende ruimte buiten deze atomaire regio's. Op die manier is voldaan aan (A.84) in de volledige ruimte (zie Figuur A.2).

In vergelijking met de GPW-methode wordt de uitwisselings-correlatie-energie en de elektrostatische energie op een andere manier berekend. In Ref. [29] wordt aangetoond dat E_{XC} en E_{ES} (gebruik makend van afschermingsdichtheden ρ_I^0) opgegeplitst kunnen worden in onafhankelijke globale en lokale,

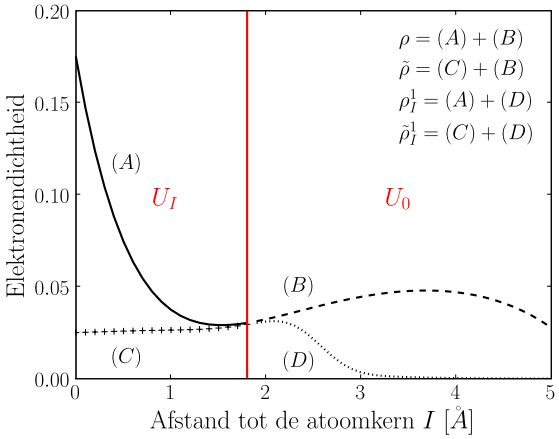

Figuur A.2: De GAPW-voorstelling van de elektronendichtheid in de omgeving van atoomkern I.

rond de atoomkern gecentreerde componenten, waardoor een zeer efficiënte berekening van deze termen mogelijk wordt:[25]

[25]De opsplitsing voor de uitwisselings-correlatie-energie is vrij eenvoudig omdat deze enkel uit (semi-)lokale bijdragen is opgebouwd. Voor de berekening van de Hartree-energie $E_{\mathrm{H}}[\rho^{\mathrm{tot}}]$ van de totale ladingsdistributie ($\rho^{\mathrm{tot}} = \rho + \rho^{\mathrm{c}}$) tot de elektrostatische energie moeten gepaste gelokaliseerde afschermingsdichtheden in elke U_I worden ingevoerd. De drie bijdragen tot $E_{\mathrm{H}}[\rho^{\mathrm{tot}}]$ zijn dan:

$$E_{\mathrm{H}}[\rho^{\mathrm{tot}}(\mathbf{r})] = \tilde{E}_{\mathrm{H}}[\tilde{\rho}(\mathbf{r}) + \rho^0(\mathbf{r})] + E^1_{\mathrm{H}}[\rho^1(\mathbf{r}) + \rho^{\mathrm{c}}(\mathbf{r})] - \tilde{E}^1_{\mathrm{H}}[\tilde{\rho}^1(\mathbf{r}) + \rho^0(\mathbf{r})] \,. \tag{A.91}$$

De afschermingsdichtheid $\rho^0 = \sum_I \rho_I^0$ wordt zodanig geconstrueerd dat de elektrostatische multipoolmomenten van elke $(\rho_I^1 + \rho_I^{\mathrm{c}}) - (\tilde{\rho}_I^1 + \rho_I^0)$ nul worden, waardoor er geen interactie meer optreedt met de lading buiten elke U_I. Een gelokaliseerde ladingsdistributie produceert buiten deze regio een potentiaal die enkel afhangt van de elektrostatische dipoolmomenten, en niet van de vorm van deze ladingsdistributie. De gelijkheid van bovenstaande vergelijking kan worden verklaard door $(\rho^1 + \rho^{\mathrm{c}}) - (\tilde{\rho}^1 + \rho^0)$ toe te voegen aan $\tilde{\rho} + \rho^0$ in $\tilde{E}_{\mathrm{H}}[\tilde{\rho} + \rho^0]$, en aan $\tilde{\rho}^1 + \rho^0$ in $\tilde{E}^1_{\mathrm{H}}[\tilde{\rho}^1 + \rho^0]$. Het effect van deze toevoeging verdwijnt, aangezien i) de kwadratische termen in $(\rho^1 + \rho^{\mathrm{c}}) - (\tilde{\rho}^1 + \rho^0)$ afkomstig van $\tilde{E}_{\mathrm{H}}[\tilde{\rho} + \rho^0]$ en $\tilde{E}^1_{\mathrm{H}}[\tilde{\rho}^1 + \rho^0]$ van elkaar worden afgetrokken, en ii) de lineaire termen in $(\rho_I^1 + \rho_I^{\mathrm{c}}) - (\tilde{\rho}_I^1 + \rho_I^0)$ afhangen van a) $\tilde{\rho} - \tilde{\rho}^1$, wat nul is binnen U_I en van b) de potentiaal van $(\rho_I^1 + \rho_I^{\mathrm{c}}) - (\tilde{\rho}_I^1 + \rho_I^0)$, die nul is buiten U_I, omdat de ladingsdistributie zich binnen U_I bevindt en de multipoolmomenten bij constructie gelijk aan nul worden gesteld.
De afschermingsdichtheid ρ_I^0 wordt opgespannen in het set van primitieve Gaussische functies χ_I^{p}:

$$\rho_I^0(\mathbf{r}) = \sum_{lm} Q_I^{lm} \chi_I^{\mathrm{p}} \,.$$

De coëfficiënten Q_I^{lm} zijn gedefinieerd als:

$$E_{\mathrm{XC}}[\rho(\mathbf{r})] = E_{\mathrm{XC}}[\tilde{\rho}(\mathbf{r})] + \sum_I E_{\mathrm{XC}}[\rho_I^1(\mathbf{r})] - \sum_I E_{\mathrm{XC}}[\tilde{\rho}_I^1(\mathbf{r})] \,. \tag{A.92}$$

$$\begin{aligned} E_{\mathrm{ES}} &= E_{\mathrm{H}}[\tilde{\rho}(\mathbf{r}) + \tilde{\rho}^0(\mathbf{r})] + \sum_I E_{\mathrm{H}}[\rho_I^1(\mathbf{r}) + \rho_I^{\mathrm{c}}(\mathbf{r})] - \sum_I E_{\mathrm{H}}[\tilde{\rho}_I^1(\mathbf{r}) + \rho_I^0(\mathbf{r})] \\ &+ E_{\mathrm{H}}[\rho^0(\mathbf{r})] - E_{\mathrm{H}}[\tilde{\rho}^0(\mathbf{r})] + \int \mathrm{d}\mathbf{r} V_{\mathrm{H}}[\rho^0(\mathbf{r}) - \tilde{\rho}^0(\mathbf{r})]\tilde{\rho}(\mathbf{r}) \\ &+ \sum_{I\neq J}{}' \sum_{\mathbf{L}} \frac{Q_I^{\mathrm{eff}} Q_J^{\mathrm{eff}}}{|\mathbf{R}_I - \mathbf{R}_J - \mathbf{L}|} \mathrm{erfc}\left(\frac{|\mathbf{R}_I - \mathbf{R}_J - \mathbf{L}|}{\sqrt{{r_{\mathrm{loc},I}}^2 - {r_{\mathrm{loc},J}}^2}} \right) \\ &- \sum_I \frac{{Q_I^{\mathrm{eff}}}^2}{\sqrt{2\pi} r_{\mathrm{loc},I}} \,. \end{aligned} \tag{A.93}$$

In de meeste gevallen wordt aangenomen dat $\rho^0 = \tilde{\rho^0}$, zodat de drie termen in

$$Q_I^{lm} = N q^{lm}[\rho_I^1(\mathbf{r}) - \tilde{\rho}_I^1(\mathbf{r}) + \rho_I^{\mathrm{c}}(\mathbf{r})] \,,$$

met N een normalisatieconstante en q^{lm} de multipoolmomentoperator,

$$q^{lm}[\rho(\mathbf{r})] = \frac{4\pi}{2l+1} \int \mathrm{d}\mathbf{r} \rho(\mathbf{r}) r^l S^{lm}(\mathbf{r}) \,,$$

$$S^{l0} = Y^{l0} \,, \qquad S^{lm} = \frac{1}{\sqrt{2}}(Y^{lm} + Y^{l-m}) \,, \qquad S^{l-m} = \frac{1}{i\sqrt{2}}(Y^{lm} - Y^{l-m}) \,.$$

Nu definiëren we een tweede afschermingsdichtheid $\rho_I^{0'}$ opgespannen in de beperkte set $\tilde{\chi}^{\mathrm{P}}$:

$$\rho_I^{0'}(\mathbf{r}) = \sum_{lm} Q_I^{lm} \tilde{\chi}_I^{\mathrm{P}} \,,$$

zodat we $\tilde{E}_{\mathrm{H}}[\tilde{\rho} + \rho^0]$ verder kunnen uitsplitsen tot:

$$\begin{aligned} \tilde{E}_{\mathrm{H}}[\tilde{\rho}(\mathbf{r}) + \rho^0(\mathbf{r})] &= \tilde{E}_{\mathrm{H}}[\tilde{\rho}(\mathbf{r}) + \rho^{0'}(\mathbf{r})] + \int \mathrm{d}\mathbf{r}\mathrm{d}\mathbf{r}' \tilde{\rho}(\mathbf{r}) v^0(\mathbf{r}) \\ &+ \sum_{IJ} \frac{1}{2} \int \mathrm{d}\mathbf{r}\mathrm{d}\mathbf{r}' \frac{\rho_I^0(\mathbf{r})\rho_J^0(\mathbf{r}') - \rho_I^{0'}(\mathbf{r})\rho_J^{0'}(\mathbf{r}')}{|\mathbf{r} - \mathbf{r}'|} \,, \\ v^0(\mathbf{r}) &= \frac{\rho^0(\mathbf{r}') - \rho^{0'}(\mathbf{r}')}{|\mathbf{r} - \mathbf{r}'|} \end{aligned}$$

De eerste term in de vergelijking voor $\tilde{E}_{\mathrm{H}}[\tilde{\rho} + \rho^0]$ is zacht, en kan in de reciproque ruimte worden uitgewerkt. Ook de tweede term is in de reciproque ruimte exact op te lossen: voor de eventuele componenten met grote $|\mathbf{G}|$ in v^0 zijn die componenten in $\tilde{\rho}$ bij constructie nul. De derde term is een dubbele som over de atoomkernen van korte-drachtpotentialen die analytisch kan worden uitgewerkt.

de tweede regel van (A.93) wegvallen.

Dankzij de constructie van de GAPW-dichtheid kunnen we het benodigde aantal vlakke golven sterk laten dalen. Nu we de oscillaties rond de atoomkern met relatief gemak kunnen beschrijven, is ook het gebruik van pseudopotentialen niet langer noodzakelijk: de GAPW-methode is evengoed in staat om alle-elektronenberekeningen met de volledige nucleaire Coulombpotentiaal te doen.[30] Hiervoor moeten we in (A.79 voor elke I waarvoor we een alle-elektronenbehandeling wensen Q_I^{eff} vervangen door Q_I en V_I^{PSP} in E_{PSP} vervangen door:

$$\frac{Q_I}{|\mathbf{r}-\mathbf{R}_I|}\text{erfc}\left(\frac{|\mathbf{r}-\mathbf{R}_I|}{\sqrt{2}r_{\text{loc},I}}\right) , \tag{A.94}$$

wat, gezien de identiteit $\text{erf}(x)+\text{erfc}(x)=1$, samen met de kernpotentiaal V_I^c gebruikt voor de berekening van de elektrostatische energie E_{ES} (zie paragraaf A.2.5), terug de Coulomb-potentiaal $\frac{Q_I}{|\mathbf{r}-\mathbf{R}_I|}$ voor de atoomkern I geeft.

A.3 EPR-parameters en de Breit-Pauli-Hamiltoniaan

Wanneer een elektronisch systeem wordt blootgesteld aan een set vectoriële perturbaties $\mathbf{U}_1, \mathbf{U}_2, ...$, dan kan de (eventuele) wijziging van de energie worden voorgesteld als een reeksontwikkeling in de perturbatieparameters:

$$E(\mathbf{U}_1, \mathbf{U}_2, ...) = E_0 + \sum_n \mathbf{U}_n.\mathbf{E}_{\mathbf{U}_n} + \frac{1}{2!}\sum_{m,n}\mathbf{U}_m.\mathbf{E}_{\mathbf{U}_n\mathbf{U}_m}.\mathbf{U}_n + \mathcal{O}(\mathbf{U}^3) . \tag{A.95}$$

De coëfficiënten $\mathbf{E}$ definiëren de respons van het systeem op de perturbaties en zijn karakteristiek voor het elektronische systeem en de kwantumtoestand waarin dit systeem zich bevindt. In het geval van statische perturbaties kan men de componenten van de coëfficiënten als volgt berekenen:

$$E_{\mathbf{U}_n,x} = \left.\frac{\partial E}{\partial U_{n,x}}\right|_{\mathbf{U}_n=\mathbf{0}} , \tag{A.96}$$

$$E_{\mathbf{U}_m\mathbf{U}_n,xy} = \left.\frac{\partial^2 E}{\partial U_{m,x}\partial U_{n,y}}\right|_{\mathbf{U}_m=\mathbf{U}_n=\mathbf{0}} . \tag{A.97}$$

Op deze manier definiëren we de g- en de A-tensor, de EPR-parameters die het onderwerp van dit doctoraat uitmaken, als de tweede-orde partiële afgeleiden van de energie van een elektronisch systeem naar de (componenten van) de netto elektronische spin $\mathbf{S} = \sum_i \mathbf{s}_i$ en respectievelijk een homogeen extern magnetisch veld $\mathbf{B}$ en de nucleaire spin $\mathbf{I}_I$ behorend bij de atoomkern I:

$$g_{xy} = \frac{2}{\alpha} \left. \frac{\partial^2 E}{\partial B_x \partial S_y} \right|_{\mathbf{B}=\mathbf{S}=\mathbf{0}} , \tag{A.98}$$

$$A_{I,xy} = \left. \frac{\partial^2 E}{\partial I_{I,x} \partial S_y} \right|_{\mathbf{I}_I=\mathbf{S}=\mathbf{0}} . \tag{A.99}$$

Nu is de elektronische energie E de verwachtingswaarde van een Hamiltoniaan H in de elektronische grondtoestand Ψ (in aanwezigheid van de verschillende perturbaties), zodat we (A.98) en (A.99) kunnen herschrijven als:[26]

$$g_{xy} = \frac{2}{\alpha} \left. \frac{\partial^2 \langle \Psi | H | \Psi \rangle}{\partial B_x \partial S_y} \right|_{\mathbf{B}=\mathbf{S}=\mathbf{0}} , \tag{A.100}$$

$$A_{I,xy} = \left. \frac{\partial^2 \langle \Psi | H | \Psi \rangle}{\partial I_{I,x} \partial S_y} \right|_{\mathbf{I}_I=\mathbf{S}=\mathbf{0}} . \tag{A.101}$$

Uit de bovenstaande vergelijkingen volgt dat de Hamiltoniaan H de koppeling van een magnetisch veld (ofwel extern ofwel afkomstig van het magnetisch dipoolmoment van de atoomkernen) met de spin van de elektronen correct zal moeten beschrijven. In de 4-componenten-ééndeeltjes-Diracvergelijking, de (speciaal-)relativistische veralgemening van de 2-componenten-ééndeeltjes-Schrödingervergelijking voor spin-$\frac{1}{2}$-deeltjes uit het vorige hoofdstuk,[27] in aanwezigheid van een elektromagnetisch veld, is deze koppeling van nature aanwezig. De Dirac-Hamiltoniaan kan, al naar gelang de gekozen benadering voor de deeltje-deeltje-interactie,[28] worden uitgebreid naar de Dirac-Coulomb- of de Dirac-Coulomb-Breit-Hamiltoniaan voor n elektronen

[26] x en y in (A.100) en (A.101) nemen alle drie cartesische componenten aan.

[27] 2-componenten slaat op spin-op- en spin-neeroplossingen van de spingepolariseerde Schrödingervergelijking. De 4-componentenoplossingen kan men (grosso modo) opdelen in elektronische (met positieve energie) en positronische (met negatieve energie) oplossingen, telkens met twee mogelijke spins. Eén en ander wordt verderop verduidelijkt.

[28] De deeltje-deeltje-interactie die consistent is met de speciale relativiteit wordt in de kwantumelektrodynamica opgesteld.

in aanwezigheid van N atoomkernen. Via de relativistische analoga van gekende veeldeeltjestechnieken, zoals bijvoorbeeld de Dirac-Hartree-Fock- of de Dirac-Kohn-Sham-methode, kunnen (A.100) en (A.101) dan worden berekend. De verhouding van de computationele kost van relativistische tot die van niet-relativistische berekeningen [29] is in alle behalve de meest eenvoudige elektronische systemen zodanig groot, dat we er, in het licht van de toepasbaarheid op elektronische systemen van enige omvang, voor kiezen om de relevante termen als een perturbatie te behandelen in een 2-componentenbeschrijving van het elektronisch systeem, meer bepaald in het raamwerk van DFT. Via bijvoorbeeld de Foldy-Wouthuysen- of de Douglas-Krolltechniek kunnen we de koppelingstermen tussen de elektronische en de positronische oplossingen tot op een zekere orde in de fijnstructuurconstante α uit de 4-componenten-Hamiltoniaan transformeren. Op die manier leiden we een *quasi-relativistische* 2-componenten-Hamiltoniaan af voor zowel de elektronen als de positronen apart, waarmee (A.100) en (A.101) in goede benadering kunnen worden opgelost. In dit werk worden de relevante termen via de Foldy-Wouthuysentechniek afgeleid. Deze werkwijze wordt in de volgende paragrafen uitgewerkt.

A.3.1 De Diracvergelijking

De Diracvergelijking, in 1928 opgesteld door de Britse natuurkundige Paul Dirac, vormt de basisformule voor de (speciaal-)relativistische kwantummechanische beschrijving van een vrij spin-$\frac{1}{2}$-deeltje in de ruimte-tijd:[31, 32]

$$H^{\mathrm{D}}\psi(\mathbf{r},t) = i\hbar\frac{\partial}{\partial t}\psi(\mathbf{r},t)\ , \tag{A.102}$$

met de Dirac-Hamiltoniaan H^{D}, in afwezigheid van een elektromagnetisch veld,

$$H^{\mathrm{D}} = \boldsymbol{\alpha}.\mathbf{p}c + \beta mc^2\ , \tag{A.103}$$

waarbij we, ten behoeve van de duidelijkheid van de symbolen, tot nader order niet in atomaire eenheden werken: m en q zijn de rustmassa en de lading van het spin-$\frac{1}{2}$-deeltje, en c is de lichtsnelheid. α_i ($i = 1,2,3$) en β moeten zodanig zijn dat aan de relativistische energie-impulsvergelijking is

[29] We spreken met opzet over de verhouding van de computationele kost. Stellen dat relativistische berekeningen op elektronische systemen van enige omvang *ondoenbaar* zijn, zou dit werk binnen afzienbare tijd waarschijnlijk hopeloos achterhaald doen lijken.

voldaan.[30] Hieruit volgt dat $\beta^2 = \mathbf{1}$, $\{\alpha_i, \beta\} = 0$, en $\{\alpha_i, \alpha_j\} = 2\delta_{ij}$. α_i en β stellen $(N \times N)$-matrices voor, en $N = 4$ is de laagste dimensie waarvoor oplossingen kunnen gevonden worden (oplossingen voor hogere N bestaan eveneens), zoals bijvoorbeeld de Dirac-Paulivoorstelling:

$$\alpha_i = \begin{pmatrix} 0 & \sigma_i \\ \sigma_i & 0 \end{pmatrix} , \qquad \beta = \begin{pmatrix} \mathbf{1}_2 & 0 \\ 0 & -\mathbf{1}_2 \end{pmatrix} , \tag{A.104}$$

met σ_i de Paulimatrices:

$$\sigma_1 = \begin{pmatrix} 0 & 1 \\ 1 & 0 \end{pmatrix} , \qquad \sigma_2 = \begin{pmatrix} 0 & -i \\ i & 0 \end{pmatrix} , \qquad \sigma_3 = \begin{pmatrix} 1 & 0 \\ 0 & -1 \end{pmatrix} . \tag{A.105}$$

De oplossingen van de Diracvergelijking in deze vorm zijn de Diracspinoren met vier componenten:

$$\psi(\mathbf{r}, t) = \begin{pmatrix} \psi_1(\mathbf{r}, t) \\ \psi_2(\mathbf{r}, t) \\ \psi_3(\mathbf{r}, t) \\ \psi_4(\mathbf{r}, t) \end{pmatrix} . \tag{A.106}$$

De Diracvergelijking heeft ook oplossingen met een negatieve energie, die men interpreteerde als positronen (de antideeltjes van elektronen met een tegengestelde lading), en vier jaar later ook experimenteel kon waarnemen.[33] Vaak worden de eerste twee en de laatste twee componenten van ψ gegroepeerd tot respectievelijk ψ_L en ψ_S, grote (*large*, L) en kleine (*small*, S) componenten genoemd:

$$\psi(\mathbf{r}, t) = \begin{pmatrix} \psi_\mathrm{L}(\mathbf{r}, t, \tau) \\ \psi_\mathrm{S}(\mathbf{r}, t, \tau) \end{pmatrix} , \tag{A.107}$$

[30] De relativistische energie-impulsvergelijking, $E^2 = (pc)^2 + (mc^2)^2$, moet uit de Diracvergelijking volgen. In de ruimte-tijdbasis zijn de energie-operator en de impulsoperator gelijk aan respectievelijk $i\hbar\frac{\partial}{\partial t}$ en $-i\hbar\nabla$. De voorwaarden voor α_i $(i = 1, 2, 3)$ en β volgen dan uit de gelijkheid van:

$$E^2\psi(\mathbf{r}, t) = -\hbar^2\frac{\partial^2}{\partial t^2}\psi(\mathbf{r}, t) = i\hbar\frac{\partial}{\partial t}(\boldsymbol{\alpha}.\mathbf{p}c + \beta mc^2)\psi(\mathbf{r}, t) = (\boldsymbol{\alpha}.\mathbf{p}c + \beta mc^2)^2\psi(\mathbf{r}, t) ,$$

en:

$$E^2\psi(\mathbf{r}, t) = \left((pc)^2 + (mc^2)^2\right)\psi(\mathbf{r}, t) .$$

en worden de twee componenten van zowel ψ_{L} als ψ_{S} terug aangeduid met een spinfactor τ. Men kan bewijzen[31] dat voor de oplossingen van (A.102) met positieve energie de dichtheid $\psi_{\mathrm{L}}^{+}\psi_{\mathrm{L}}$ veelal aanzienlijk groter is dan $\psi_{\mathrm{S}}^{+}\psi_{\mathrm{S}}$, terwijl het omgekeerde geldt voor de oplossingen met een negatieve energie.

Via het principe van de minimale koppeling, $\mathbf{p} \rightarrow \boldsymbol{\pi} = \mathbf{p} - \frac{q}{c}\mathbf{A}$ met $\mathbf{A}$ de magnetische vectorpotentiaal en q de lading van het spin-$\frac{1}{2}$-deeltje, en toevoeging van de potentiële energie $V = q\varphi$ van een elektrische potentiaal φ, ontstaat de Diracvergelijking voor een spin-$\frac{1}{2}$-deeltje in aanwezigheid van een elektromagnetisch veld:

$$\left(\boldsymbol{\alpha}.(\mathbf{p} - \frac{q}{c}\mathbf{A})c + \beta mc^2 + V\right)\psi(\mathbf{r},t) = i\hbar\frac{\partial}{\partial t}\psi(\mathbf{r},t)\ . \tag{A.108}$$

A.3.2 De Dirac-Coulomb(-Breit)-Hamiltoniaan

De uitbreiding van de Diracvergelijking naar een veeldeeltjessysteem van n spin-$\frac{1}{2}$-deeltjes in aanwezigheid van N atoomkernen gebeurt in eerste benadering door de Coulombse deeltje-deeltje- en deeltje-atoomkerninteracties aan de som van n Dirac-Hamiltonianen H^{D} (A.102 of A.108) toe te voegen. Zo onstaat de Dirac-Coulomb-Hamiltoniaan:

$$H^{\mathrm{DC}} = \sum_i H_i^{\mathrm{D}} + \frac{1}{8\pi\epsilon_0}\sum_{i\neq j}\frac{q_i q_j}{|\mathbf{r}_i - \mathbf{r}_j|} + \frac{1}{4\pi\epsilon_0}\sum_{i,I}\frac{q_i Q_I}{|\mathbf{r}_i - \mathbf{R}_I|}\ . \tag{A.109}$$

[31] De oplossingen $\psi_p^{\pm}$ van de Diracvergelijking (A.102) zijn van de algemene vorm:

$$\psi_p^{\pm}(\mathbf{r},t) = N_p \mathrm{e}^{i(\mathbf{p}.\mathbf{r}\mp E_p t)}\begin{pmatrix}\chi(\mathbf{r},t,\tau)\\ \eta(\mathbf{r},t,\tau)\end{pmatrix}\ ,$$

waarbij het superscript $\pm$ de oplossingen met positieve $(+)$ of negatieve $(-)$ energie aanduidt. Wanneer we een oplossing met positieve energie, ψ_p^{+}, invullen in (A.102), dan leiden we daaruit af dat:

$$\eta(\mathbf{r},t,\tau) = \left(\frac{\sigma.\mathbf{p}c}{E_p + mc^2}\right)\chi(\mathbf{r},t,\tau)\ ,$$

en voor de oplossingen met negatieve energie, ψ_p^{-}:

$$\chi(\mathbf{r},t,\tau) = -\left(\frac{\sigma.\mathbf{p}c}{E_p + mc^2}\right)\eta(\mathbf{r},t,\tau)\ .$$

Wanneer E_p^2 niet veel groter is dan $(mc^2)^2$, het kwadraat van de rustmassa-energie, en gebruik makend van $(\sigma.\mathbf{p})^2 = p^2$, dan wordt het duidelijk dat $\chi^{+}\chi$ veel beduidender zal zijn dan $\eta^{+}\eta$ voor de oplossingen met positieve energie, en vice versa voor de oplossingen met negatieve energie.

Behalve de afwezigheid van een relativistische beschrijving van de deeltje-deeltje-interactie, is de Dirac-Coulombvergelijking ook niet langer Lorentzcovariant, een essentieel principe in de speciale relativiteit. Een benaderende correctie voor de deeltje-deeltje-interactie op de Dirac-Coulomb-Hamiltoniaan is de Breit-operator,[34] die de magnetische interactie (de *Gaunt*-term) en de vertragingseffecten als gevolg van de eindige snelheid van het licht beschrijft tot op orde $1/c^2$:

$$H^{\mathrm{B}} = -\frac{1}{16\pi\epsilon_0}\sum_{i\neq j}\frac{q_i q_j}{|\mathbf{r}_i-\mathbf{r}_j|}\left[\boldsymbol{\alpha}_i.\boldsymbol{\alpha}_j + \frac{\left(\boldsymbol{\alpha}_i.(\mathbf{r}_i-\mathbf{r}_j)\right)\left(\boldsymbol{\alpha}_j.(\mathbf{r}_i-\mathbf{r}_j)\right)}{|\mathbf{r}_i-\mathbf{r}_j|^2}\right] . \tag{A.110}$$

De Breit-operator, samen met de Dirac-Coulomb-Hamiltoniaan, vormt de Dirac-Coulomb-Breit-Hamiltoniaan H^{DCB}:

$$H^{\mathrm{DCB}} = H^{\mathrm{DC}} + H^{\mathrm{B}} . \tag{A.111}$$

A.3.3 De Foldy-Wouthuysen transformatie

In paragraaf (A.3.1) werd al beargumenteerd waarom ψ_{L} meestal de belangrijkste component vormt bij de elektronische oplossingen van de Diracvergelijking (in afwezigheid van een elektromagnetisch veld), terwijl ψ_{S} dat is voor de positronische oplossingen. Via een specifieke unitaire transformatie, de Foldy-Wouthuysentransformatie[35] voor een vrij spin-$\frac{1}{2}$-deeltje, toegepast op de Dirac-Hamiltoniaan H^{D} (A.103) kunnen we zelfs exact alle operatoren wegtransformeren die de grote en de kleine componenten koppelen, zodat de elektronische en positronische oplossingen volledig door respectievelijk een grote en een kleine component worden bepaald:

$$\begin{pmatrix} \psi'_{\mathrm{L}}(\mathbf{r},t,\tau) \\ 0 \end{pmatrix} = U \begin{pmatrix} \psi_{\mathrm{L}}(\mathbf{r},t,\tau) \\ \psi_{\mathrm{S}}(\mathbf{r},t,\tau) \end{pmatrix} . \tag{A.112}$$

We kunnen de Dirac-Hamiltoniaan H^{D} voor een vrij spin-$\frac{1}{2}$-deeltje opsplitsen in zogenaamde *even* operatoren $\mathcal{E}$ die niet verantwoordelijk zijn voor koppeling tussen de grote en de kleine componenten (op de even operator βmc^2 na, die men apart blijft schrijven), en *oneven* operatoren $\mathcal{O}$ die dat wel zijn:[32]

[32]Ter verduidelijking, in de Dirac-Paulivoorstelling bezetten even operatoren de posities $[1..2,1..2]$ en $[3..4,3..4]$, en oneven operatoren de posities $[1..2,3..4]$ en $[3..4,1..2]$.

$$H^{\mathrm{D}} = \beta mc^2 + \mathcal{E} + \mathcal{O} \,, \tag{A.113}$$

met:

$$\mathcal{E} = \mathbf{0} \,, \qquad \mathcal{O} = \boldsymbol{\alpha}.\mathbf{p}c \,. \tag{A.114}$$

We definiëren een unitaire transformatie $U = \mathrm{e}^{iS}$ gegenereerd door een hermitische operator S:

$$\psi'(\mathbf{r},t) = \mathrm{e}^{iS}\psi(\mathbf{r},t) \,, \tag{A.115}$$

waardoor we (A.102) kunnen herschrijven als:

$$H^{\mathrm{D}'}\psi'(\mathbf{r},t) = \mathrm{e}^{iS}H^{\mathrm{D}}\mathrm{e}^{-iS}\psi'(\mathbf{r},t) = i\hbar\frac{\partial}{\partial t}\psi'(\mathbf{r},t) \,. \tag{A.116}$$

We kiezen een specifieke vorm voor S ($S = -i\beta\boldsymbol{\alpha}.\frac{\mathbf{p}}{p}\theta$), en dus voor U:[33]

$$U = \mathrm{e}^{i(-i\beta\boldsymbol{\alpha}.\frac{\mathbf{p}}{p}\theta)} = \mathbf{1}_4\cos\theta + \beta(\boldsymbol{\alpha}.\frac{\mathbf{p}}{p})\sin\theta \,, \tag{A.117}$$

zodat we de getransformeerde Dirac-Hamiltoniaan $H^{\mathrm{D}'}$ kunnen herschrijven als:

$$\begin{aligned} H^{\mathrm{D}'} &= (\mathbf{1}_4\cos\theta + \beta(\boldsymbol{\alpha}.\frac{\mathbf{p}}{p})\sin\theta)(\boldsymbol{\alpha}.\mathbf{p}c + \beta mc^2)(\mathbf{1}_4\cos\theta - \beta(\boldsymbol{\alpha}.\frac{\mathbf{p}}{p})\sin\theta) \\ &= (\boldsymbol{\alpha}.\mathbf{p}c + \beta mc^2)(\mathbf{1}_4\cos\theta - \beta(\boldsymbol{\alpha}.\frac{\mathbf{p}}{p})\sin\theta)^2 \\ &= (\boldsymbol{\alpha}.\mathbf{p}c + \beta mc^2)\mathrm{e}^{-2\beta\boldsymbol{\alpha}.\frac{\mathbf{p}}{p}\theta} \\ &= \boldsymbol{\alpha}.\mathbf{p}c(\cos 2\theta - \frac{mc}{p}\sin 2\theta) + \beta(m\cos 2\theta + \frac{p}{c}\sin 2\theta)c^2 \,. \end{aligned} \tag{A.118}$$

We kunnen de oneven term $\boldsymbol{\alpha}.\mathbf{p}c$ exact elimineren door $\tan 2\theta = \frac{p}{mc}$ te kiezen, waardoor $H^{\mathrm{D}'}$ reduceert tot een even operator:

[33] In (A.117) werd gebruik gemaakt van $(\beta\boldsymbol{\alpha}.\frac{\mathbf{p}}{p})(\beta\boldsymbol{\alpha}.\frac{\mathbf{p}}{p}) = -\mathbf{1}_4$.

$$H^{\mathrm{D}'} = \beta\sqrt{(pc)^2 + (mc^2)^2}\,. \tag{A.119}$$

Op die manier splitst (A.116) op in een vergelijking voor de grote componenten met positieve energie (kleine componenten gelijk aan nul), en een vergelijking voor de kleine componenten met negatieve energie (grote componenten gelijk aan nul).

Voor een spin-$\frac{1}{2}$-deeltje in een elektromagnetisch veld,

$$H^{\mathrm{D}} = \beta mc^2 + \mathcal{E} + \mathcal{O}\,, \tag{A.120}$$

waarbij:

$$\mathcal{E} = V = q\varphi\,, \qquad \mathcal{O} = \boldsymbol{\alpha}.\left(\mathbf{p} - \frac{q}{c}\mathbf{A}\right)c\,, \tag{A.121}$$

werd een exacte ontkoppeling zoals bij het vrije deeltje niet gevonden. Foldy en Wouthuysen introduceerden wel (eveneens in Ref. [35]) een systematische procedure voor de ontkoppeling van de grote en de kleine componenten tot op een willekeurige orde in c^{-1} door het achtereenvolgens uitvoeren van unitaire transformaties $U = \mathrm{e}^{iS}$ met S:

$$S = -\frac{i\beta\mathcal{O}}{2mc^2}\,. \tag{A.122}$$

Voor de eenvoud nemen we aan dat het elektromagnetisch veld tijdsonafhankelijk is, zodat S dit ook zeker is. De getransformeerde Dirac-Hamiltoniaan geeft na ontwikkeling van e^{iS} in een machtsreeks, aangenomen dat S *klein* is, en weerhouden van de termen tot en met orde c^{-2}:

$$\begin{aligned} H^{\mathrm{D}'} &= \mathrm{e}^{iS}H^{\mathrm{D}}\mathrm{e}^{-iS} \\ &= \left(\sum_{k=0}^{\infty}\frac{(iS)^k}{k!}\right)H^{\mathrm{D}}\left(\sum_{l=0}^{\infty}\frac{(-iS)^l}{l!}\right) \\ &\cong H^{\mathrm{D}} + i\left[S, H^{\mathrm{D}}\right] - \frac{1}{2}\left[S,\left[S, H^{\mathrm{D}}\right]\right] - \frac{i}{6}\left[S,\left[S,\left[S, H^{\mathrm{D}}\right]\right]\right] \\ &+ \frac{1}{24}\left[S,\left[S,\left[S,\left[S,\beta mc^2\right]\right]\right]\right]\,. \end{aligned} \tag{A.123}$$

De commutatoren in de bovenstaande vergelijking reduceren na wat rekenwerk tot:

$$
\begin{aligned}
i\left[S,H^{\mathrm{D}}\right] &= -\mathcal{O}+\frac{\beta\left[\mathcal{O},\mathcal{E}\right]}{2mc^2}+\frac{\beta\mathcal{O}^2}{mc^2}\,, && \text{(A.124)}\\
-\frac{1}{2}\left[S,\left[S,H^{\mathrm{D}}\right]\right] &= -\frac{\beta\mathcal{O}^2}{2mc^2}-\frac{\left[\mathcal{O},\left[\mathcal{O},\mathcal{E}\right]\right]}{8(mc^2)^2}-\frac{\mathcal{O}^3}{2(mc^2)^2}\,, && \text{(A.125)}\\
-\frac{i}{6}\left[S,\left[S,\left[S,H^{\mathrm{D}}\right]\right]\right] &= \frac{\mathcal{O}^3}{6(mc^2)^2}-\frac{\beta\mathcal{O}^4}{6(mc^2)^3}\,, && \text{(A.126)}\\
\frac{1}{24}\left[S,\left[S,\left[S,\left[S,\beta mc^2\right]\right]\right]\right] &= \frac{\beta\mathcal{O}^4}{24(mc^2)^3}\,. && \text{(A.127)}
\end{aligned}
$$

$H^{\mathrm{D}'}$, correct tot en met tweede orde in c^{-2} is dan gelijk aan:

$$
\begin{aligned}
H^{\mathrm{D}'} &= \beta\left(mc^2+\frac{\mathcal{O}^2}{2mc^2}-\frac{\mathcal{O}^4}{8(mc^2)^3}\right)+\mathcal{E}-\frac{\left[\mathcal{O},\left[\mathcal{O},\mathcal{E}\right]\right]}{8(mc^2)^2}\\
&+ \frac{\beta\left[\mathcal{O},\mathcal{E}\right]}{2mc^2}-\frac{\mathcal{O}^3}{3(mc^2)^2}\,,
\end{aligned}
\qquad \text{(A.128)}
$$

en, rekening houdend met de rekenregels $\mathcal{E}\times\mathcal{E}=\mathcal{E}$, $\mathcal{E}\times\mathcal{O}=\mathcal{O}$, $\mathcal{O}\times\mathcal{E}=\mathcal{O}$, en $\mathcal{O}\times\mathcal{O}=\mathcal{E}$,[34] zien we dat $H^{\mathrm{D}'}$ opnieuw uit even en oneven operatoren bestaat:

$$
H^{\mathrm{D}'} \equiv \beta mc^2+\mathcal{E}'+\mathcal{O}'\,. \qquad \text{(A.129)}
$$

Bij nader onderzoek van $H^{\mathrm{D}'}$ zien we dat de even operatoren (exclusief βmc^2) van de orde c^0 en c^{-2} zijn, en de oneven operatoren van de orde c^{-1} of c^{-2}. De even en oneven operator in H^{D} waren respectievelijk van de orde c^0 en c^1. Met andere woorden, dankzij de transformatie e^{iS} is de orde in c van de nieuwe oneven operator met 2 gedaald. We kunnen exact dezelfde procedure toepassen op (A.129), die vormelijk identiek is aan (A.120): opeenvolgende transformaties van het type $S=-\frac{i\beta\mathcal{O}'}{2mc^2}$, $S=-\frac{i\beta\mathcal{O}''}{2mc^2}$, ... zullen de orde in c van

[34] Dit is eenvoudig te verifiëren aan de hand van de matrixnotatie.

de oneven operator verder verlagen, zodat tot op een willekeurige orde in c een even operator overblijft. Hierdoor ontstaat opnieuw een vergelijking voor de grote componenten met positieve energie (kleine componenten gelijk aan nul), en een vergelijking voor de kleine componenten met negatieve energie (grote componenten gelijk aan nul).

De Dirac-Coulomb-Breit-Hamiltoniaan $H^{\mathrm{DCB},n=2}$ voor twee spin-$\frac{1}{2}$-deeltjes in een tijdsonafhankelijk elektromagnetisch veld volgt uit (A.111):

$$\begin{aligned} H^{\mathrm{DCB},n=2} &= \boldsymbol{\alpha}_1.(\mathbf{p}_1 - \frac{q_1}{c}\mathbf{A}_1)c + \beta_1 m_1 c^2 + q_1\varphi_1 \\ &+ \boldsymbol{\alpha}_2.(\mathbf{p}_2 - \frac{q_2}{c}\mathbf{A}_2)c + \beta_1 m_2 c^2 + q_2\varphi_2 \\ &+ \frac{q_1 q_2}{4\pi\epsilon_0 \left|\mathbf{r}_1 - \mathbf{r}_2\right|} \\ &- \frac{q_1 q_2}{8\pi\epsilon_0 \left|\mathbf{r}_1 - \mathbf{r}_2\right|}\left[\boldsymbol{\alpha}_1.\boldsymbol{\alpha}_2 + \frac{\left(\boldsymbol{\alpha}_1.(\mathbf{r}_1 - \mathbf{r}_2)\right)\left(\boldsymbol{\alpha}_2.(\mathbf{r}_1 - \mathbf{r}_2)\right)}{\left|\mathbf{r}_1 - \mathbf{r}_2\right|^2}\right] . \end{aligned} \tag{A.130}$$

$H^{\mathrm{DCB},n=2}$ kan worden geschreven als een (16×16)-matrix die inwerkt op spinorfuncties met 16 componenten, onder te verdelen in 4 combinaties van grote en kleine componenten van de twee deeltjes, genoteerd als $\psi_{\mathrm{L_1L_2}}$, $\psi_{\mathrm{L_1S_2}}$, $\psi_{\mathrm{S_1L_2}}$ en $\psi_{\mathrm{S_1S_2}}$. $H^{\mathrm{DCB},n=2}$ kan, analoog aan (A.113) en (A.120), geschreven worden in even-even, even-oneven, oneven-even en oneven-oneven operatoren:[35]

$$H^{\mathrm{DCB},n=2} = \beta_1 m_1 c^2 + \beta_2 m_2 c^2 + \mathcal{EE} + \mathcal{OE} + \mathcal{EO} + \mathcal{OO} \, , \tag{A.131}$$

met:

[35] Operatoren zoals bijvoorbeeld β_1 en β_2 ontstaan uit het direct product (genoteerd met $\cdot\times$) van twee (4×4)-matrices:

$$\beta_1 = \beta \cdot \times \mathbf{1}_4 = \begin{pmatrix} \beta & 0 & 0 & 0 \\ 0 & \beta & 0 & 0 \\ 0 & 0 & \beta & 0 \\ 0 & 0 & 0 & \beta \end{pmatrix} , \qquad \beta_2 = \mathbf{1}_4 \cdot \times \beta = \begin{pmatrix} \mathbf{1}_4 & 0 & 0 & 0 \\ 0 & \mathbf{1}_4 & 0 & 0 \\ 0 & 0 & -\mathbf{1}_4 & 0 \\ 0 & 0 & 0 & -\mathbf{1}_4 \end{pmatrix} ,$$

met β en $\mathbf{1}_4$ terug de gekende (4×4)-matrices.

$$\mathcal{EE} = +q_1\varphi_1 + q_2\varphi_2 + \frac{q_1 q_2}{4\pi\epsilon_0 \left|\mathbf{r}_1 - \mathbf{r}_2\right|} \,, \tag{A.132}$$

$$\mathcal{OE} = \boldsymbol{\alpha}_1.(\mathbf{p}_1 - \frac{q_1}{c}\mathbf{A}_1)c \,, \tag{A.133}$$

$$\mathcal{EO} = \boldsymbol{\alpha}_2.(\mathbf{p}_2 - \frac{q_2}{c}\mathbf{A}_2)c \,, \tag{A.134}$$

$$\mathcal{OO} = -\frac{q_1 q_2}{8\pi\epsilon_0 \left|\mathbf{r}_1 - \mathbf{r}_2\right|} \left[\boldsymbol{\alpha}_1.\boldsymbol{\alpha}_2 + \frac{\left(\boldsymbol{\alpha}_1.(\mathbf{r}_1 - \mathbf{r}_2)\right)\left(\boldsymbol{\alpha}_2.(\mathbf{r}_1 - \mathbf{r}_2)\right)}{\left|\mathbf{r}_1 - \mathbf{r}_2\right|^2}\right] . \tag{A.135}$$

Chaprlyvy[36, 37] veralgemeende de Foldy-Wouthuysenprocedure voor deze tweedeeltjes-Dirac-Coulomb-Breit-Hamiltoniaan, en toonde aan dat door het herhaaldelijk toepassen van een unitaire transformatie $U = \mathrm{e}^{iS}$ met S van de volgende vorm:

$$S = -\frac{i(\beta_1 + \beta_1\beta_2)}{4m_1c^2}\mathcal{OE} - \frac{i(\beta_2 + \beta_1\beta_2)}{4m_2c^2}\mathcal{EO} - \frac{i(\beta_1 + \beta_2)}{4(m_1 + m_2)c^2}\mathcal{OO} \,, \tag{A.136}$$

de koppelingsoperatoren tussen $\psi_{\mathrm{L_1L_2}}$ en de andere drie combinaties tot een willekeurige orde in c kunnen worden gereduceerd. Na reductie van deze koppelingsoperatoren tot orde c^{-3}, daarbij aangenomen dat $m_1 = m_2$, en na projectie van de $H^{\mathrm{DCB}',N=2}$ op de $\psi_{\mathrm{L_1L_2}}$-ruimte, krijgen we de (4×4)-Hamiltoniaan $H^{\mathrm{DCB}',N=2}_{L_1L_2}$ behorend bij twee elektronische oplossingen:[36]

$$\begin{aligned} H^{\mathrm{DCB}',N=2}_{L_1L_2} &= m_1c^2 + m_2c^2 + \mathcal{EE} + \frac{(\mathcal{OE})^2}{2m_1c^2} + \frac{(\mathcal{EO})^2}{2m_2c^2} + \frac{[[\mathcal{OE},\mathcal{EE}],\mathcal{OE}]}{8m_1^2c^4} \\ &+ \frac{[[\mathcal{EO},\mathcal{EE}],\mathcal{EO}]}{8m_2^2c^4} + \frac{\left[[\mathcal{OE},\mathcal{OO}]_+,\mathcal{EO}\right]_+}{4m_1m_2c^4} - \frac{(\mathcal{OE})^4}{8m_1^3c^6} \\ &- \frac{(\mathcal{EO})^4}{8m_2^3c^6} + \frac{(\mathcal{OO})^2}{2(m_1 + m_2)c^2} \,. \end{aligned} \tag{A.137}$$

[36] Deze stap komt overeen met het uitselecteren van de (4×4)-matrix linksbovenaan in de (16×16)-matrixvoorstelling van $H^{\mathrm{DCB}',N=2}$, en impliceert eveneens de herinterpretatie van de Dirac-spinmatrices α_i als de Paulimatrices σ_i. De afleiding is verder langdradig, en werd om die reden niet opgenomen (zelfs Chaprlyvy vond het niet nodig de verschillende stappen in de afleiding op te nemen in Ref. [36] en [37]).

Uitwerking van de verschillende termen[37] in $H_{L_1L_2}^{\mathrm{DCB}',N=2}$ geeft, na het invullen van $q_1 = q_2 = -e$ en $m_1 = m_2 = m_e$, na overgang terug op atomaire eenheden, en na opsplitsing in ééndeeltjes- en tweedeeltjestermen:

$$H_{L_1L_2}^{\mathrm{DCB}',N=2} = \sum_{i}^{2} H_{L_1L_2,i}^{\mathrm{DCB}',N=2} + \sum_{i\neq j}^{2} H_{L_1L_2,ij}^{\mathrm{DCB}',N=2} \ , \tag{A.138}$$

met:

[37] We moeten opmerken dat de term in $(\mathcal{OO})^2$ niet opduikt in een kwantumelektrodynamische afleiding van (A.137). In dat verband merken we op dat de Breit-operator slechts een benaderende relativistische correctie voor de deeltje-deeltje-interactie. Een rigoureuze verklaring valt echter buiten het bereik van deze uiteenzetting. De overige termen zijn eenvoudig uit te werken:

$$(\mathcal{OE})^2 = c^2\left((\mathbf{p}_1 - \frac{q_1}{c}\mathbf{A}_1)^2 - q_1\hbar(\sigma_1.\mathbf{B}_1)\right) \ ,$$
$$(\mathcal{EO})^2 = c^2\left((\mathbf{p}_2 - \frac{q_2}{c}\mathbf{A}_2)^2 - q_2\hbar(\sigma_2.\mathbf{B}_2)\right) \ ,$$
$$(\mathcal{OE})^4 = c^4\left((\mathbf{p}_1 - \frac{q_1}{c}\mathbf{A}_1)^4 - 2q_1\hbar(\sigma_1.\mathbf{B}_1)(\mathbf{p}_1 - \frac{q_1}{c}\mathbf{A}_1)^2 + q_1^2\hbar^2(\sigma_1.\mathbf{B}_1)^2\right) \ ,$$
$$(\mathcal{EO})^4 = c^4\left((\mathbf{p}_2 - \frac{q_2}{c}\mathbf{A}_2)^4 - 2q_2\hbar(\sigma_2.\mathbf{B}_2)(\mathbf{p}_2 - \frac{q_2}{c}\mathbf{A}_2)^2 + q_2^2\hbar^2(\sigma_2.\mathbf{B}_2)^2\right) \ ,$$
$$[[\mathcal{OE},\mathcal{EE}],\mathcal{OE}] = -\frac{q_1q_2c^2}{4\pi\epsilon_0}\left(4\pi\hbar^2\delta(|\mathbf{r}_1-\mathbf{r}_2|) + \frac{2\hbar}{|\mathbf{r}_1-\mathbf{r}_2|^3}\sigma_1.(|\mathbf{r}_1-\mathbf{r}_2|\times(\mathbf{p}_1-\frac{q_1}{c}\mathbf{A}_1))\right)$$
$$-q_1c^2\left(2\hbar\sigma_1.(\mathbf{E}_1\times(\mathbf{p}_1-\frac{q_1}{c}\mathbf{A}_1)) + \hbar^2\nabla_1.\mathbf{E}_1\right) \ ,$$
$$[[\mathcal{EO},\mathcal{EE}],\mathcal{EO}] = -\frac{q_1q_2c^2}{4\pi\epsilon_0}\left(4\pi\hbar^2\delta(|\mathbf{r}_1-\mathbf{r}_2|) + \frac{2\hbar}{|\mathbf{r}_1-\mathbf{r}_2|^3}\sigma_2.(|\mathbf{r}_1-\mathbf{r}_2|\times(\mathbf{p}_2-\frac{q_2}{c}\mathbf{A}_2))\right)$$
$$-q_2c^2\left(2\hbar\sigma_2.(\mathbf{E}_2\times(\mathbf{p}_2-\frac{q_2}{c}\mathbf{A}_2)) + \hbar^2\nabla_2.\mathbf{E}_2\right) \ ,$$
$$\left[[\mathcal{OE},\mathcal{OO}]_+,\mathcal{EO}\right]_+ = \frac{q_1q_2c^2}{4\pi\epsilon_0}\left(\frac{\hbar^2}{|\mathbf{r}_1-\mathbf{r}_2|^3}(\sigma_1.\sigma_2) - \frac{8\pi\hbar^2}{3}\delta(|\mathbf{r}_1-\mathbf{r}_2|)(\sigma_1.\sigma_2)\right.$$
$$-\frac{3\hbar^2}{|\mathbf{r}_1-\mathbf{r}_2|^5}(\sigma_1.|\mathbf{r}_1-\mathbf{r}_2|)(\sigma_2.|\mathbf{r}_1-\mathbf{r}_2|) + \frac{2\hbar}{|\mathbf{r}_1-\mathbf{r}_2|^3}\sigma_1.(|\mathbf{r}_1-\mathbf{r}_2|\times(\mathbf{p}_2-\frac{q_2}{c}\mathbf{A}_2))$$
$$-\frac{2\hbar}{|\mathbf{r}_1-\mathbf{r}_2|^3}\sigma_2.(|\mathbf{r}_1-\mathbf{r}_2|\times(\mathbf{p}_1-\frac{q_1}{c}\mathbf{A}_1)) - \frac{2}{|\mathbf{r}_1-\mathbf{r}_2|}((\mathbf{p}_1-\frac{q_1}{c}\mathbf{A}_1).(\mathbf{p}_2-\frac{q_2}{c}\mathbf{A}_2)$$
$$\left.-\frac{2}{|\mathbf{r}_1-\mathbf{r}_2|^3}((\mathbf{p}_1-\frac{q_1}{c}\mathbf{A}_1).|\mathbf{r}_1-\mathbf{r}_2|)(|\mathbf{r}_1-\mathbf{r}_2|.(\mathbf{p}_2-\frac{q_2}{c}\mathbf{A}_2))\right) \ .$$

$$
\begin{aligned}
H_{L_1L_2,i}^{\mathrm{DCB}',N=2} &= \alpha^{-2} + \frac{(\mathbf{p}_i + \alpha\mathbf{A}_i)^2}{2} - \varphi_i + \frac{\sigma_i.\mathbf{B}_i}{2} - \frac{\alpha^2(\mathbf{p}_i + \alpha\mathbf{A}_i)^4}{8} + \frac{\alpha^2\nabla_i.\mathbf{E}_i}{8} \\
- & \frac{\alpha^2\sigma_i.((\mathbf{p}_i + \alpha\mathbf{A}_i) \times \mathbf{E}_i - \mathbf{E}_i \times (\mathbf{p}_i + \alpha\mathbf{A}_i))}{8} \\
- & \frac{\alpha^2(\sigma_i.\mathbf{B}_i)(\mathbf{p}_i + \alpha\mathbf{A}_i)^2}{4}\,, \qquad \text{(A.139)}
\end{aligned}
$$

$$
\begin{aligned}
H_{L_1L_2,ij}^{\mathrm{DCB}',N=2} &= \frac{1}{2\left|\mathbf{r}_1 - \mathbf{r}_2\right|} - \frac{\alpha^2}{4}\left((\mathbf{p}_i + \alpha\mathbf{A}_i)(\mathbf{p}_j + \alpha\mathbf{A}_j)(\frac{1}{\left|\mathbf{r}_i - \mathbf{r}_j\right|})\right. \\
+ & \left.\frac{1}{2\left|\mathbf{r}_i - \mathbf{r}_j\right|^3}((\mathbf{p}_i + \alpha\mathbf{A}_i).\left|\mathbf{r}_i - \mathbf{r}_j\right|)(\left|\mathbf{r}_i - \mathbf{r}_j\right|.(\mathbf{p}_j + \alpha\mathbf{A}_j))\right) \\
+ & \frac{\alpha^2}{4\left|\mathbf{r}_i - \mathbf{r}_j\right|^3}\left(\sigma_i.(\left|\mathbf{r}_i - \mathbf{r}_j\right| \times (\mathbf{p}_j + \alpha\mathbf{A}_j) - \sigma_j.(\left|\mathbf{r}_i - \mathbf{r}_j\right| \times (\mathbf{p}_i + \alpha\mathbf{A}_i))\right) \\
- & \frac{\alpha^2}{8\left|\mathbf{r}_i - \mathbf{r}_j\right|^3}\left(\sigma_i.(\left|\mathbf{r}_i - \mathbf{r}_j\right| \times (\mathbf{p}_i + \alpha\mathbf{A}_i) - \sigma_j.(\left|\mathbf{r}_i - \mathbf{r}_j\right| \times (\mathbf{p}_j + \alpha\mathbf{A}_j))\right) \\
- & \frac{\alpha^2\pi}{2}\delta(\left|\mathbf{r}_i - \mathbf{r}_j\right|) + \frac{\alpha^2}{8}\left(\frac{1}{\left|\mathbf{r}_i - \mathbf{r}_j\right|}\sigma_i.\sigma_j\right. \\
- & \left.\frac{3}{\left|\mathbf{r}_i - \mathbf{r}_j\right|^3}(\sigma_i.\left|\mathbf{r}_i - \mathbf{r}_j\right|)(\sigma_j.\left|\mathbf{r}_i - \mathbf{r}_j\right|) - \frac{8\pi}{3}\delta(\left|\mathbf{r}_i - \mathbf{r}_j\right|)\sigma_i.\sigma_j\right)\,. \qquad \text{(A.140)}
\end{aligned}
$$

In de bovenstaande vergelijkingen werden de volgende bondige notaties geïntroduceerd: $\mathbf{A}_i = \mathbf{A}(\mathbf{r}_i)$, $\varphi_i = \varphi(\mathbf{r}_i)$, $\mathbf{B}_i = \mathbf{B}(\mathbf{r}_i)$ en $\mathbf{E}_i = \mathbf{E}(\mathbf{r}_i)$. $\mathbf{E} = -\nabla\varphi$ is het elektrische en $\mathbf{B} = \nabla \times \mathbf{A}$ het magnetische veld. Aangezien in de Dirac-Coulomb-Breit-Hamiltoniaan geen interactie plaatsvindt tussen meer dan twee deeltjes, zouden alle mogelijke termen reeds voor dit eenvoudige systeem in (A.139) en (A.140) moeten aanwezig zijn. De veralgemening van dit resultaat tot n elektronen is dan vanzelfsprekend, en na aftrek van de rustmassa-energieën van n elektronen onstaat de quasi-relativistische Breit-Pauli-Hamiltoniaan voor n elektronen.

Nu rest er ons enkel nog het elektromagnetisch veld te specifiëren. De scalaire potentiaal φ bestaat uit de Coulombse bijdragen afkomstig van de geladen atoomkernen:

$$\varphi(\mathbf{r}) = \sum_I \frac{Q_I}{|\mathbf{r} - \mathbf{R}_I|} \ . \tag{A.141}$$

De vectorpotentiaal $\mathbf{A}$ is opgebouwd als $\mathbf{A} = \mathbf{A}_0 + \sum_I \mathbf{A}_I$, waarbij met $\mathbf{A}_0$ de vectorpotentiaal aangeduid wordt behorend bij het extern aangelegde magnetisch veld $\mathbf{B}_0$ in de Coulomb-ijk, en met $\mathbf{A}_I$ de vectorpotentiaal behorend bij het magnetisch veld gegeneerd door het magnetische dipoolmoment van atoomkern I. Deze vectorpotentialen worden gegeven door:

$$\mathbf{A}_0(\mathbf{r}) = \frac{1}{2}\mathbf{B}_0 \times \left(\mathbf{r} - \mathbf{R}_\mathrm{g}\right) \ , \tag{A.142}$$

$$\mathbf{A}_I(\mathbf{r}) = \alpha^2 \gamma_I \frac{\mathbf{I}_I \times (\mathbf{r} - \mathbf{R}_I)}{|\mathbf{r} - \mathbf{R}_I|^3} \ , \tag{A.143}$$

met $\mathbf{R}_\mathrm{g}$ de ijk-oorsprong (zie verder in hoofdstuk A.4.5), en γ_I en $\mathbf{I}_I$ respectievelijk de nucleaire magnetische verhouding en de nucleaire spin van atoomkern I.

A.3.4 De g-tensor

De g-tensor (A.100),

$$g_{xy} = \frac{2}{\alpha} \left. \frac{\partial^2 \langle \Psi | \, H \, | \Psi \rangle}{\partial B_x \partial S_y} \right|_{\mathbf{B}=\mathbf{S}=\mathbf{0}} \ , \tag{A.144}$$

is een tweede-orde eigenschap die men kan evalueren via dubbele-storingstheorie. Het stel storingsparameters wordt gevormd door de componenten langs de assen van een gegeven coördinatensysteem van een constant extern magnetisch veld, B_x, en de netto elektronische-spincomponent, S_y. Gebruik makend van het Hellmann-Feynmantheorema voor dubbele-storingstheorie krijgen we:[38]

$$g_{xy} = \frac{2}{\alpha} \frac{\partial}{\partial B_x} \langle \Psi_{B_x} | \left. \frac{\partial H}{\partial S_y} \right|_{\mathbf{S}=\mathbf{0}} | \Psi_{B_x} \rangle \Bigg|_{\mathbf{B}=\mathbf{0}} \ , \tag{A.145}$$

waarbij Ψ_{B_x} de elektronische golffunctie aanduidt in aanwezigheid van een (eenheids)magnetisch veld parallel met de x-as. Hieruit blijkt dus dat we

[38] Voor een energie-eigenwaarde E corresponderend met een eigentoestand $|\Psi\rangle$ van een

1. slechts de eerste-ordecorrectie op de elektronische golffunctie van de 3 componenten van het magnetische veld afzonderlijk moeten berekenen,
2. enkel storingsoperatoren moeten bekijken die:
   (a) lineair afhankelijk zijn van de elektronische-spinoperatoren,
   (b) van de orde 0 of 1 zijn in het magnetische veld.

Een Hamiltoniaan H^{g} die beantwoordt aan deze criteria wordt samengesteld uitgaande van de termen die voorkomen in (A.139) en (A.140).[39] H^{g} bevat minimaal de Zeemanterm H_{Z} en de nucleaire spin-baankoppelingsterm $H_{\mathrm{SO(N)}}$ (*nucleair*: het baanimpulsmoment is afkomstig van de rotatie van een elektron rond een bepaalde atoomkern):

$$H_{\mathrm{Z}} = \sum_i h^i_{\mathrm{Z}} = \sum_i \frac{\alpha g_e}{2} \mathbf{s}_i.\mathbf{B} \,, \tag{A.146}$$

$$H_{\mathrm{SO(N)}} = \sum_i h^j_{\mathrm{SO(N)}} = \sum_i \frac{\alpha^2 g'}{4} \sum_I Q_I \mathbf{s}_i.\frac{(\mathbf{r}_i - \mathbf{R}_I) \times \mathbf{p}_i}{|\mathbf{r}_i - \mathbf{R}_I|^3} \,. \tag{A.147}$$

Tot de belangrijkste relativistische correcties behoren de twee-elektron spin-baankoppelingsterm $H_{\mathrm{SO(2e)}}$ (*twee-elektron*: het baanimpulsmoment is afkomstig van de rotatie van het elektron rond een ander elektron), de twee-elektron spin-andere-baankoppelingsterm H_{SOO} (*andere-baan*: het spinimpulsmoment van een bepaald elektron koppelt met het baanimpulsmoment van een ander

Hamiltoniaan H, met λ_1 en λ_2 een stel storingsparameters, geldt:

$$\begin{aligned}
&\frac{\partial^2 E}{\partial\lambda_1\partial\lambda_2}\bigg|_{\lambda_1=\lambda_2=0} = \frac{\partial^2}{\partial\lambda_1\partial\lambda_2}\langle\Psi(\lambda_1,\lambda_2)|H(\lambda_1,\lambda_2)|\Psi(\lambda_1,\lambda_2)\rangle\bigg|_{\lambda_1=\lambda_2=0} \\
&= \frac{\partial}{\partial\lambda_1}\left(\langle\,\frac{\partial\Psi(\lambda_1,\lambda_2)}{\partial\lambda_2}\bigg|_{\lambda_2=0}|H(\lambda_1,0)|\Psi(\lambda_1,0)\rangle + \langle\Psi(\lambda_1,0)|\,\frac{\partial H(\lambda_1,\lambda_2)}{\partial\lambda_2}\bigg|_{\lambda_2=0}|\Psi(\lambda_1,0)\rangle\right. \\
&+ \left.\langle\Psi(\lambda_1,0)|H(\lambda_1,0)|\,\frac{\partial\Psi(\lambda_1,\lambda_2)}{\partial\lambda_2}\bigg|_{\lambda_2=0}\rangle\right)\bigg|_{\lambda_1=0} \\
&= \frac{\partial}{\partial\lambda_1}\left(E\,\frac{\partial}{\partial\lambda_2}\langle\Psi(\lambda_1,\lambda_2)|\Psi(\lambda_1,\lambda_2)\rangle\bigg|_{\lambda_2=0} + \langle\Psi(\lambda_1,0)|\,\frac{\partial H(\lambda_1,\lambda_2)}{\partial\lambda_2}\bigg|_{\lambda_2=0}|\Psi(\lambda_1,0)\rangle\right)\bigg|_{\lambda_1=0} \\
&= \frac{\partial}{\partial\lambda_1}\left(\langle\Psi(\lambda_1,0)|\,\frac{\partial H(\lambda_1,\lambda_2)}{\partial\lambda_2}\bigg|_{\lambda_2=0}|\Psi(\lambda_1,0)\rangle\right)\bigg|_{\lambda_1=0} .
\end{aligned}$$

[39] Merk op dat $\sigma_i = 2\mathbf{s}_i$ en, voor een tijdsonafhankelijk magnetisch veld, $\nabla \times \mathbf{E} = 0$.

elektron afkomstig van de rotatie rond dat ene elektron) en de Zeeman-kinetische-energie-correctieterm (H_{ZKE}):

$$H_{\mathrm{SO(2e)}} = \sum_i \sum_{j\neq i} -\frac{\alpha^2 g'}{4} \mathbf{s}_i . \frac{(\mathbf{r}_i - \mathbf{r}_j) \times \mathbf{p}_i}{|\mathbf{r}_i - \mathbf{r}_j|^3} , \tag{A.148}$$

$$H_{\mathrm{SOO}} = \sum_i \sum_{j\neq i} -\alpha^2 \mathbf{s}_i . \frac{(\mathbf{r}_j - \mathbf{r}_i) \times \mathbf{p}_j}{|\mathbf{r}_j - \mathbf{r}_i|^3} , \tag{A.149}$$

$$H_{\mathrm{ZKE}} = \sum_i -\frac{\alpha^3 g_e}{4} \mathbf{p}_i^2 \mathbf{s}_i . \mathbf{B} . \tag{A.150}$$

Tenslotte dient men ook de *ijk-correctietermen* op te nemen. Vanuit het principe van de minimale koppeling ($\mathbf{p} \rightarrow \boldsymbol{\pi} = \mathbf{p} + \alpha\mathbf{A}$) is de analogie met (A.147), (A.148) en (A.149) heel eenvoudig te zien. Men noemt deze termen ook diamagnetische termen, overeenkomstig de nomenclatuur in NMR:

$$H^{\mathrm{dia}}_{\mathrm{SO(N)}} = \sum_i \frac{\alpha^2 g'}{4} \sum_I Q_I \mathbf{s}_i . \frac{(\mathbf{r}_i - \mathbf{R}_I) \times \alpha\mathbf{A}(\mathbf{r}_i)}{|\mathbf{r}_i - \mathbf{R}_I|^3} , \tag{A.151}$$

$$H^{\mathrm{dia}}_{\mathrm{SO(2e)}} = \sum_i \sum_{j\neq i} -\frac{\alpha^2 g'}{4} \mathbf{s}_i . \frac{(\mathbf{r}_i - \mathbf{r}_j) \times \alpha\mathbf{A}(\mathbf{r}_i)}{|\mathbf{r}_i - \mathbf{r}_j|^3} , \tag{A.152}$$

$$H^{\mathrm{dia}}_{\mathrm{SOO}} = \sum_i \sum_{j\neq i} -\alpha^2 \mathbf{s}_i . \frac{(\mathbf{r}_j - \mathbf{r}_i) \times \alpha\mathbf{A}(\mathbf{r}_j)}{|\mathbf{r}_j - \mathbf{r}_i|^3} . \tag{A.153}$$

In vergelijkingen (A.146) - (A.153) stellen $\mathbf{r}_i$, $\mathbf{p}_i$, en $\mathbf{s}_i$ respectievelijk de positie-, de impuls-, de baanmoment- en de spinoperator voor van elektron i. g_e is de g-factor van het vrije elektron ($g_e = 2.0023193043622$),[38] g' definieert men als $g' = 2g_e - 2$, $\mathbf{R}_I$ en Q_I stellen de positie en de lading in atomaire eenheden voor van een atoomkern I.[40]

A.3.5 De A-tensor

De A-tensor (A.101) behorend bij atoomkern I,

[40] Op basis van (A.139) en (A.140) geldt $g_e = g' = 2$, maar QED-correcties zorgen voor een (geringe) afwijking.

$$A_{I,xy} = \left. \frac{\partial^2 \langle \Psi | H | \Psi \rangle}{\partial I_{I,x} \partial S_y} \right|_{\mathbf{I}_I = \mathbf{S} = \mathbf{0}} , \tag{A.154}$$

is eveneens een tweede orde eigenschap die men kan evalueren via dubbele perturbatietheorie. Het stel storingsparameters wordt gevormd door de componenten langs de assen van een gegeven coördinatensysteem van een netto nucleaire-spincomponent behorend bij atoomkern I, $I_{I,x}$, en de netto elektronische-spincomponent, S_y. Opnieuw gebruik makend van het Hellmann-Feynmantheorema voor dubbele-storingstheorie krijgen we:

$$A_{I,xy} = \frac{\partial}{\partial I_{I,x}} \left\langle \Psi_{I_{I,x}} \right| \left. \frac{\partial H}{\partial S_y} \right|_{\mathbf{S}=\mathbf{0}} \left| \Psi_{I_{I,x}} \right\rangle \Bigg|_{\mathbf{I}_I = \mathbf{0}} . \tag{A.155}$$

Hieruit blijkt dus dat we

1. slechts de eerste-ordecorrectie op de elektronische golffunctie van de 3 componenten van de nucleaire spin behorend bij atoomkern I afzonderlijk moeten kennen,
2. enkel storingsoperatoren moeten bekijken die:
   (a) lineair afhankelijk zijn van de elektronische-spinoperatoren,
   (b) van de orde 0 of 1 zijn in de nucleaire-spinoperator.

Een Hamiltoniaan H^{A_I} die beantwoordt aan deze criteria wordt samengesteld uitgaande van de termen die voorkomen in (A.139) en (A.140). Tot de belangrijkste termen van H^{A_I} behoren de isotrope Fermi-contactinteractieterm $H_{\mathrm{FC},I}$:

$$H_{\mathrm{FC},I} = \frac{2}{3} \mu_0 g_e \mu_e g_I \mu_I \sum_i \delta \left(\mathbf{r}_i - \mathbf{R}_I \right) \mathbf{s}_i . \mathbf{I}_I , \tag{A.156}$$

en de anisotrope dipool-dipoolinteractieterm $H_{\mathrm{DC},I}$:[41]

$$H_{\mathrm{DC},I} = \frac{1}{4\pi} \mu_0 g_e \mu_e g_I \mu_I \sum_i \mathbf{s}_i . \left[\frac{3 \left(\mathbf{r}_i - \mathbf{R}_I \right)^{\mathrm{T}} \left(\mathbf{r}_i - \mathbf{R}_I \right) - \mathbf{1} \left| \mathbf{r}_i - \mathbf{R}_I \right|^2}{\left| \mathbf{r}_i - \mathbf{R}_I \right|^5} \right] . \mathbf{I}_I . \tag{A.157}$$

[41] Voor alle duidelijkheid: de term tussen vierkante haken stelt een (3×3)-matrix voor.

In (A.156) en (A.157) stelt μ_0 de permeabiliteit van het vacuum voor, μ_e het Bohr-magneton, en g_I en μ_I respectievelijk de g-waarde en het nucleair magneton van de atoomkern I. Wanneer we H^{A_I} beperken tot de twee voorgaande termen, die allebei lineair zijn in de nucleaire-spinoperator, dan vereenvoudigt (A.155) tot:

$$A_{I,xy} = \langle \Psi | \left. \frac{\partial^2 H^{\mathrm{A}_I}}{\partial I_{I,x} \partial S_y} \right|_{\mathbf{I}_I = \mathbf{S} = \mathbf{0}} | \Psi \rangle \ , \tag{A.158}$$

of met andere woorden, er hoeven geen correcties op de elektronische golffunctie te worden berekend.[42]

A.4 Berekening van de g-tensor in PBC-simulaties

A.4.1 De g-tensor in DFT

Wanneer we (A.146) - (A.153) opnieuw bekijken met het oog op de implementatie in DFT, zien we dat de verwachtingswaarde van de vier tweedeeltjesoperatoren $H_{\mathrm{SO(2e)}}$, H_{SOO} en hun tegenhangers $H^{\mathrm{dia}}_{\mathrm{SO(2e)}}$, $H^{\mathrm{dia}}_{\mathrm{SOO}}$ zullen moeten worden benaderd, aangezien in Kohn-Sham-DFT de tweedeeltjesdichtheidsmatrix niet beschikbaar is. De opstelling van deze theorische methode is grotendeels

[42] We bouwen verder op het resultaat van één van de vorige voetnoten, en nemen aan dat $H(\lambda_1, \lambda_2)$ lineair is in λ_1:

$$\begin{aligned}
&\left. \frac{\partial^2 E}{\partial \lambda_1 \partial \lambda_2} \right|_{\lambda_1=\lambda_2=0} = \left. \frac{\partial}{\partial \lambda_1} \left(\langle \Psi(\lambda_1,0)| \left. \frac{\partial H(\lambda_1,\lambda_2)}{\partial \lambda_2} \right|_{\lambda_2=0} |\Psi(\lambda_1,0)\rangle \right) \right|_{\lambda_1=0} \\
&= \langle \left. \frac{\partial \Psi(\lambda_1,0)}{\partial \lambda_1} \right|_{\lambda_1=0} | \left. \frac{\partial H(\lambda_1,\lambda_2)}{\partial \lambda_2} \right|_{\lambda_1=\lambda_2=0} |\Psi(0,0)\rangle + \langle \Psi(0,0)| \left. \frac{\partial^2 H(\lambda_1,\lambda_2)}{\partial \lambda_1 \lambda_2} \right|_{\lambda_1=\lambda_2=0} |\Psi(0,0)\rangle \\
&+ \langle \Psi(0,0)| \left. \frac{\partial H(\lambda_1,\lambda_2)}{\partial \lambda_2} \right|_{\lambda_1=\lambda_2=0} | \left. \frac{\partial \Psi(\lambda_1,0)}{\partial \lambda_1} \right|_{\lambda_1=0} \rangle \\
&= \langle \left. \frac{\partial \Psi(\lambda_1,0)}{\partial \lambda_1} \right|_{\lambda_1=0} |0| \Psi(0,0)\rangle + \langle \Psi(0,0)| \left. \frac{\partial^2 H(\lambda_1,\lambda_2)}{\partial \lambda_1 \lambda_2} \right|_{\lambda_1=\lambda_2=0} |\Psi(0,0)\rangle \\
&+ \langle \Psi(0,0)|0| \left. \frac{\partial \Psi(\lambda_1,0)}{\partial \lambda_1} \right|_{\lambda_1=0} \rangle \\
&= \langle \Psi(0,0)| \left. \frac{\partial^2 H(\lambda_1,\lambda_2)}{\partial \lambda_1 \lambda_2} \right|_{\lambda_1=\lambda_2=0} |\Psi(0,0)\rangle \ .
\end{aligned}$$

het werk van Schreckenbach en Ziegler.[1]

We merken op dat de termen van het type $\mathbf{r}/r^3$ in $H_{\mathrm{SO(N)}}$ en $H_{\mathrm{SO(2e)}}$ (en evenzo in $H^{\mathrm{dia}}_{\mathrm{SO(N)}}$ en $H^{\mathrm{dia}}_{\mathrm{SO(2e)}}$) gelijk zijn aan de gradiënten van de corresponderende nucleaire en elektronische Coulombpotentialen, die samen het totale potentiaalveld vormen zoals dat door één bepaald elektron wordt gevoeld. In Kohn-Sham-DFT veronderstelt men dat de niet-interagerende elektronen bewegen in een effectieve KS-potentiaal $V_{\mathrm{KS}} = v_{\mathrm{ext}} + v_{\mathrm{H}} + v_{\mathrm{XC}}$ afkomstig van de atoomkernen en de andere elektronen. Deze effectieve potentiaal probeert dus het exacte potentiaalveld zo goed mogelijk te reproduceren. Aangemoedigd door de vaak goede resultaten in de bepaling van de (benaderende) elektronische structuur, zullen we de totale spin-baankoppelingstermen benaderen met behulp van deze effectieve KS-potentiaal:[43]

$$H_{\mathrm{SO}} = \frac{\alpha^2 g'}{4} \sum_i \mathbf{s}_i . \left((\nabla V_{\mathrm{KS}}) \times \mathbf{p}_i \right) \ , \tag{A.159}$$

$$H^{\mathrm{dia}}_{\mathrm{SO}} = \frac{\alpha^2 g'}{4} \sum_i \mathbf{s}_i . \left((\nabla V_{\mathrm{KS}}) \times \alpha \mathbf{A}(\mathbf{r}_i) \right) \ . \tag{A.160}$$

Voor de spin-andere-baankoppelingstermen biedt zich geen kant-en-klare oplossing aan binnen DFT. We zullen later een benadering overnemen opgesteld door Pickard en Mauri [6], die zich louter baseert op de fysische betekenis van de spin-andere-baaninteractie. De gekozen benadering zal gelukkig van weinig cruciaal belang blijken voor de g-tensor.

Voorlopig hebben we de relevante kwantummechanische operatoren gereduceerd tot:

$$H^{\mathrm{g}} = H_{\mathrm{Z}} + H_{\mathrm{ZKE}} + H_{\mathrm{SO}} + H_{\mathrm{SOO}} + H^{\mathrm{dia}}_{\mathrm{SO}} + H^{\mathrm{dia}}_{\mathrm{SOO}} \ . \tag{A.161}$$

We zullen ook gebruik maken van spinveldreductie (*spin-field reduction*): wanneer we de as van spin-kwantisatie laten samenvallen met de coördinaat-as t, kunnen we elke één-elektron operator $O_t . s_t$, evenredig met de t-component van de spinoperator $\mathbf{s}$, uitschrijven als:

[43] In feite hebben we enkel de uitwisselingscomponent van v_{XC} nodig, die corrigeert voor het feit dat de Hartree-potentiaal v_{H} de potentiaal is afkomstig van alle elektronen.[10]

$$\begin{aligned}
\langle\Psi|\sum_i O_{i,t}.s_{i,t}\,|\Psi\rangle &= \sum_{k,l,m_{\mathbf{s}_k},m_{\mathbf{s}_l}} \langle\phi_k|\,O_t\,|\phi_l\rangle\,\langle m_{\mathbf{s}_k}|\,s_t\,|m_{\mathbf{s}_l}\rangle\,\langle\Psi|\,a^+_{km_{\mathbf{s}_k}}a_{lm_{\mathbf{s}_l}}\,|\Psi\rangle \\
&= \sum_{k,l,m_{\mathbf{s}}} \langle\phi_k|\,O_t\,|\phi_l\rangle\,\langle\Psi|\,a^+_{km_{\mathbf{s}}}a_{lm_{\mathbf{s}}}\,|\Psi\rangle\,\frac{1}{2}(-1)^{1/2-m_{\mathbf{s}}} \\
&= \frac{1}{2}\int_{\mathbf{r}'=\mathbf{r}} \mathrm{d}\mathbf{r}\,O_t(\mathbf{r}')\,(\rho^\alpha(\mathbf{r},\mathbf{r}')-\rho^\beta(\mathbf{r},\mathbf{r}'))\,, \qquad \text{(A.162)}
\end{aligned}$$

waarbij we de dichtheidsmatrices voor de spin-op- en spin-neer-elektronen invoerden:

$$\rho^\tau(\mathbf{r},\mathbf{r}') = \sum_i \phi_i^\tau(\mathbf{r})^*\phi_i^\tau(\mathbf{r}')\,, \qquad \tau=\alpha,\beta\,. \qquad \text{(A.163)}$$

Hierbij stellen we bij conventie $\mathbf{r}' = \mathbf{r}$ na het inwerken van $O(\mathbf{r}')$ maar vóór het integreren. Op die manier werkt de operator enkel in op de termen in $\mathbf{r}'$, terwijl we toch een beknopte schrijfwijze behouden op basis van de dichtheid.

De termen in de elektronische Hamiltoniaan lineair in het magnetisch veld en de netto elektronenspin geven een tweede-ordestoringsbijdrage tot de energiematrix van het multiplet gelijk aan:

$$\begin{aligned}
\Delta V_{M_S,M'_S} &= \mathbf{B}.\nabla_{\mathbf{B}}\left(\langle\Psi_{\mathbf{B}}SM_S|\sum_i \mathbf{O}(\mathbf{r}_i).\mathbf{s}_i\,|\Psi_{\mathbf{B}}SM'_S\rangle\right)\Big|_{\mathbf{B}=\mathbf{0}} \\
&= \sum_{xy} B_x G_{xy}\,\langle SM_S|\sum_i s_{i,y}\,|SM'_S\rangle\,. \qquad \text{(A.164)}
\end{aligned}$$

Dit is een gevolg van het Wigner-Eckhart theorema in de spinruimte:

$$\begin{aligned}
&\langle\Psi_{\mathbf{B}}SM_S|\sum_{i\mu}(-1)^\mu O_{-\mu}(\mathbf{r}_i)s_{i\mu}\,|\Psi_{\mathbf{B}}SM'_S\rangle \\
&= \sum_\mu (-1)^\mu(-1)^{S-M_S}\begin{pmatrix} S & 1 & S \\ -M_S & \mu & M'_S\end{pmatrix} \\
&\times\,\langle\Psi_{\mathbf{B}}S||\sum_i(-1)^\mu O_{-\mu}(\mathbf{r}_i)\mathbf{s}_i\,||\Psi_{\mathbf{B}}S\rangle\,, \qquad \text{(A.165)}
\end{aligned}$$

waarbij μ de sferische componenten van $\mathbf{s}$ aanduidt. Daarnaast geldt ook dat:

$$\begin{aligned}\langle SM_S|\sum_i s_{i,\mu}\left|SM'_S\right\rangle &= (-1)^{S-M_S}\begin{pmatrix} S & 1 & S \\ -M_S & \mu & M'_S\end{pmatrix} \\ &\quad\times\langle S||\sum_i \mathbf{s}_i\,||S\rangle\ ,\end{aligned} \tag{A.166}$$

zodat:

$$\begin{aligned}&\langle\Psi_{\mathbf{B}}SM_S|\sum_{i\mu}(-1)^{\mu}O_{-\mu}(\mathbf{r}_i)s_{i\mu}\left|\Psi_{\mathbf{B}}SM'_S\right\rangle \\ &=\sum_{\mu}(-1)^{\mu}\frac{\langle\Psi_{\mathbf{B}}S||\sum_i O_{-\mu}(\mathbf{r}_i)\mathbf{s}_i\,||\Psi_{\mathbf{B}}S\rangle}{\langle S||\sum_i \mathbf{s}_i\,||S\rangle} \\ &\times\langle SM_S|\sum_i s_{i,\mu}\left|SM'_S\right\rangle\ .\end{aligned} \tag{A.167}$$

Voor $S = M_S = M'_S$ geldt:

$$\begin{aligned}&\langle\Psi_{\mathbf{B}}SS|\sum_i O_{-\mu}(\mathbf{r}_i)s_{i0}\left|\Psi_{\mathbf{B}}SS\right\rangle \\ &=\begin{pmatrix} S & 1 & S \\ -S & 0 & S\end{pmatrix}\langle\Psi_{\mathbf{B}}S||\sum_i O_{-\mu}(\mathbf{r}_i)\mathbf{s}_i\,||\Psi_{\mathbf{B}}S\rangle \\ &=\frac{1}{2}\int_{\mathbf{r}'=\mathbf{r}}\mathrm{d}\mathbf{r}\,O_{-\mu}(\mathbf{r}')\,\left(\rho^{\alpha}(\mathbf{B}|\mathbf{r},\mathbf{r}')-\rho^{\beta}(\mathbf{B}|\mathbf{r},\mathbf{r}')\right)\ .\end{aligned} \tag{A.168}$$

In de laatste gelijkheid werd spinveldreductie toegepast. Het $3j$-symbool uit bovenstaande vergelijking reduceert tot:

$$\begin{pmatrix} S & 1 & S \\ -S & 0 & S\end{pmatrix}=\frac{S}{\sqrt{S}\sqrt{S+1}\sqrt{2S+1}}=\frac{S}{\langle S||\,\mathbf{S}\,||S\rangle}\ , \tag{A.169}$$

waardoor (A.167) herleidt tot:

$$\begin{aligned}
&\langle \Psi_{\mathbf{B}} S M_S | \sum_{i\mu} (-1)^{\mu} O_{-\mu}(\mathbf{r}_i) s_{i\mu} \left| \Psi_{\mathbf{B}} S M'_S \right\rangle \\
&= \sum_{\mu} (-1)^{\mu} \frac{\langle S M_S | \, \mathbf{S}_{\mu} \, | S M'_S \rangle}{2S} \int\limits_{\mathbf{r}'=\mathbf{r}} \mathrm{d}\mathbf{r} \, O_{-\mu}(\mathbf{r}') \, (\rho^{\alpha}(\mathbf{B}|\mathbf{r},\mathbf{r}') - \rho^{\beta}(\mathbf{B}|\mathbf{r},\mathbf{r}')) \\
&= \sum_{y} \frac{\langle S M_S | \, \mathbf{S}_{y} \, | S M'_S \rangle}{2S} \int\limits_{\mathbf{r}'=\mathbf{r}} \mathrm{d}\mathbf{r} \, O_{y}(\mathbf{r}') \, (\rho^{\alpha}(\mathbf{B}|\mathbf{r},\mathbf{r}') - \rho^{\beta}(\mathbf{B}|\mathbf{r},\mathbf{r}')) \, . \qquad \text{(A.170)}
\end{aligned}$$

Hieruit volgt dat G_{xy} gelijk is aan:

$$G_{xy} = \left[\frac{\partial}{\partial B_x} \frac{1}{2S} \int\limits_{\mathbf{r}'=\mathbf{r}} \mathrm{d}\mathbf{r} \left(h_y^{01} + \sum_{s=1}^{3} B_s h_{sy}^{11} \right) (\rho^{\alpha}(\mathbf{B}|\mathbf{r},\mathbf{r}') - \rho^{\beta}(\mathbf{B}|\mathbf{r},\mathbf{r}')) \right] \Bigg|_{\mathbf{B}=0} . \qquad \text{(A.171)}$$

De bovenstaande uitwerking laat toe (A.145) te schrijven als:[44]

$$g_{xy} = \frac{2}{\alpha} \left[\frac{\partial}{\partial B_x} \int\limits_{\mathbf{r}'=\mathbf{r}} \mathrm{d}\mathbf{r} \left(h_y^{01} + \sum_{s=1}^{3} B_s h_{sy}^{11} \right) (\rho^{\alpha}(\mathbf{B}|\mathbf{r},\mathbf{r}') - \rho^{\beta}(\mathbf{B}|\mathbf{r},\mathbf{r}')) \right] \Bigg|_{\mathbf{B}=0} , \qquad \text{(A.172)}$$

met h_y^{01} en h_{sy}^{11} gegeven door:

$$\begin{aligned}
h_y^{01} &= h_{\mathrm{SO},y} + h_{\mathrm{SOO},y} \\
&= \frac{\alpha^2 g'}{4} \left((\nabla_{\mathbf{r}'} V_{\mathrm{KS}}) \times \mathbf{p}_{\mathbf{r}'} \right)_y + h_{\mathrm{SOO},y} \, , \qquad \text{(A.173)} \\
h_{sy}^{11} &= h_{\mathrm{Z},sy} + h_{\mathrm{ZKE},sy} + h_{\mathrm{SO},sy}^{\mathrm{dia}} + h_{\mathrm{SOO},sy}^{\mathrm{dia}} \\
&= \frac{\alpha}{2} g_e \delta_{sy} - g_e \frac{\alpha^3}{4} p'^2 \delta_{sy} \\
&+ \frac{\alpha^3 g'}{8} \left((\nabla_{\mathbf{r}'} V_{\mathrm{KS}}) . \mathbf{r}' \delta_{sy} - (\nabla_{\mathbf{r}'} V_{\mathrm{KS}})_s r'_y \right) + h_{\mathrm{SOO},sy}^{\mathrm{dia}} \, , \qquad \text{(A.174)}
\end{aligned}$$

[44] Merk op: we gaan uit van een netto elektronenspin gelijk aan $\frac{1}{2}$.

met $p'^2 = -\nabla^2_{\mathbf{r}'}$. Door de gestoorde elektronendichtheden $\rho(\mathbf{B}|\mathbf{r},\mathbf{r}')$ te ontwikkelen tot op eerste orde in B_x, kunnen we de afleiding naar het magnetische veld uitvoeren, en na het stellen van $\mathbf{B} = \mathbf{0}$, krijgen we voor de verschillende contributies tot de g-tensor (SOO-termen uitgezonderd):

$$g^{\mathrm{Z}}_{xy} = g_e \delta_{xy} \,, \tag{A.175}$$

$$\Delta g^{\mathrm{ZKE}}_{xy} = -\frac{\alpha^2 g_e}{2} \int\limits_{\mathbf{r}'=\mathbf{r}} \mathrm{d}\mathbf{r}\; p^2 \left[\rho^{\alpha}(\mathbf{r},\mathbf{r}') - \rho^{\beta}(\mathbf{r},\mathbf{r}'))\right] \delta_{xy} \,, \tag{A.176}$$

$$\Delta g^{\mathrm{SO}}_{xy} = \frac{\alpha g'}{2} \left[\int \mathrm{d}\mathbf{r}\; [\mathbf{j}^{\alpha}_{\mathrm{P},\mathbf{B}_x}(\mathbf{r}) - \mathbf{j}^{\beta}_{\mathrm{P},\mathbf{B}_x}(\mathbf{r})] \times \nabla V_{\mathrm{KS}}(\mathbf{r}) \right]_y \,, \tag{A.177}$$

$$\Delta g^{\mathrm{SO,dia}}_{xy} = \frac{\alpha g'}{2} \left[\int \mathrm{d}\mathbf{r}\; [\mathbf{j}^{\alpha}_{\mathrm{D},\mathbf{B}_x}(\mathbf{r}) - \mathbf{j}^{\beta}_{\mathrm{D},\mathbf{B}_x}(\mathbf{r})] \times \nabla V_{\mathrm{KS}}(\mathbf{r}) \right]_y \,, \tag{A.178}$$

met $\mathbf{j}^{\tau}_{\mathrm{D},\mathbf{B}_x}$ en $\mathbf{j}^{\tau}_{\mathrm{P},\mathbf{B}_x}$ respectievelijk de diamagnetische (D) en de paramagnetische (P) component van $\mathbf{j}^{\tau}_{\mathbf{B}_x}$, de totale geïnduceerde stroomdichtheid in één spin-kanaal tot op eerste orde in het uitwendig magnetisch veld $\mathbf{B}_x$. Dit wordt aangetoond in paragraaf A.4.5. De totale SO-component kunnen we dan schrijven als:

$$\Delta g^{\mathrm{SO}}_{xy} = \frac{\alpha g'}{2} \left[\int \mathrm{d}\mathbf{r}\; [\mathbf{j}^{\alpha}_{\mathbf{B}_x}(\mathbf{r}) - \mathbf{j}^{\beta}_{\mathbf{B}_x}(\mathbf{r})] \times \nabla V_{\mathrm{KS}}(\mathbf{r}) \right]_y \,. \tag{A.179}$$

Aangezien in de spingepolariseerde variant van Kohn-Sham-DFT V_{KS} verschillend is voor α- en β-elektronen, kunnen we de bovenstaande afleiding overdoen met inachtname van dit onderscheid, om te komen tot:

$$\Delta g^{\mathrm{SO}}_{xy} = \frac{\alpha g'}{2} \left[\int \mathrm{d}\mathbf{r}\; \mathbf{j}^{\alpha}_{\mathbf{B}_x}(\mathbf{r}) \times \nabla V^{\alpha}_{\mathrm{KS}}(\mathbf{r}) - \mathbf{j}^{\beta}_{\mathbf{B}_x}(\mathbf{r}) \times \nabla V^{\beta}_{\mathrm{KS}}(\mathbf{r}) \right]_y \,. \tag{A.180}$$

Tot nu hebben we de H_{SOO}- en $H^{\mathrm{dia}}_{\mathrm{SOO}}$-termen nog niet behandeld. De spin-andere-baankoppelingsterm beschrijft de afscherming van het externe veld $\mathbf{B}$ door de geïnduceerde elektronische stroomdichtheden, zoals gevoeld door het ongepaarde elektron. Een benadering voor de SOO-bijdrage werd opgesteld door Pickard en Mauri:[6]

$$\Delta g_{xy}^{\mathrm{SOO}} = 2\int \mathrm{d}\mathbf{r}\, B_{\mathbf{B}_x,y}(\mathbf{r})[\rho^{\alpha}(\mathbf{r}) - \rho^{\beta}(\mathbf{r})]\,, \tag{A.181}$$

waar $\mathbf{B}_{\mathbf{B}_x}$ het magnetische veld voorstelt afkomstig van de geïnduceerde stroomdichtheid, die onstaat bij het aanleggen van een homogeen eenheids magnetisch veld samenvallend met de x-as:

$$\mathbf{B}_{\mathbf{B}_x}(\mathbf{r}) = \alpha \int \mathrm{d}\mathbf{r}'\, \frac{\mathbf{r}' - \mathbf{r}}{|\mathbf{r}' - \mathbf{r}|^3} \times \left[\left(\mathbf{j}^{\alpha}_{\mathbf{B}_x}(\mathbf{r}') + \mathbf{j}^{\beta}_{\mathbf{B}_x}(\mathbf{r}')\right) - \left(\mathbf{j}^{\alpha}_{\mathbf{B}_x}(\mathbf{r}') - \mathbf{j}^{\beta}_{\mathbf{B}_x}(\mathbf{r}')\right)\right]\,. \tag{A.182}$$

De totale geïnduceerde stroomdichtheid werd gecorrigeerd voor zelfinteractie door aftrekken van $\mathbf{j}^{\alpha}_{\mathbf{B}_x} - \mathbf{j}^{\beta}_{\mathbf{B}_x}$, nagenoeg de bijdrage tot de stroomdichtheid van het ongepaarde elektron.

Uiteindelijk bekomen we de volgende expliciete uitdrukking voor de g-tensor:

$$g_{xy} = g_{xy}^{\mathrm{Z}} + \Delta g_{xy}^{\mathrm{ZKE}} + \Delta g_{xy}^{\mathrm{SO}} + \Delta g_{xy}^{\mathrm{SOO}}\,, \tag{A.183}$$

$$g_{xy}^{\mathrm{Z}} = g_e \delta_{xy}\,, \tag{A.184}$$

$$\Delta g_{xy}^{\mathrm{ZKE}} = -\alpha^2 g_e (T^{\alpha} - T^{\beta})\delta_{xy}\,, \tag{A.185}$$

$$\Delta g_{xy}^{\mathrm{SO}} = \frac{\alpha g'}{2} \int \mathrm{d}\mathbf{r} \left[\mathbf{j}^{\alpha}_{\mathbf{B}_x}(\mathbf{r}) \times \nabla V^{\alpha}_{\mathrm{KS}}(\mathbf{r}) - \mathbf{j}^{\beta}_{\mathbf{B}_x}(\mathbf{r}) \times \nabla V^{\beta}_{\mathrm{KS}}(\mathbf{r})\right]_y\,, \tag{A.186}$$

$$\Delta g_{xy}^{\mathrm{SOO}} = 2\int \mathrm{d}\mathbf{r}\, B_{\mathbf{B}_x,y}(\mathbf{r})[\rho^{\alpha}(\mathbf{r}) - \rho^{\beta}(\mathbf{r})]\,, \tag{A.187}$$

waarbij T^{τ} de totale ongeperturbeerde kinetische energie aanduidt van de τ-elektronen:

$$T^{\tau} = -\frac{1}{2}\int_{\mathbf{r}'=\mathbf{r}} \mathrm{d}\mathbf{r} \nabla^2_{\mathbf{r}'} \rho^{\tau}(\mathbf{r}, \mathbf{r}')\,. \tag{A.188}$$

T^{τ}, $\nabla V^{\tau}_{\mathrm{KS}}$ en ρ^{τ} zijn reeds gekend (of kunnen vrij eenvoudig worden berekend) na het doorlopen van de zelfconsistente procedure van het Kohn-Sham-DFT-schema. De geïnduceerde stroomdichtheden $\mathbf{j}^{\tau}_{\mathbf{B}_x}$ en de magnetische velden $\mathbf{B}_{\mathbf{B}_x}$ die er uit volgen, vormen een groter probleem. Een ingenieuze manier om deze termen te evalueren werd opgesteld door Sebastiani *et al*,[39, 40] en vereist kennis van de volgende begrippen:

- Dichtheidsfunctionaal-storingstheorie, een techniek voor de bepaling van de eerste-ordecorrecties als gevolg van een uitwendig magnetisch veld op een set van ééndeeltjesorbitalen (paragrafen A.4.2 en A.4.3).
- Wannier-functies, een alternatieve voorstelling van de oplossingen van een ééndeeltje-Schrödingervergelijking in een periodieke potentiaal (paragraaf A.4.4).

Het belang van deze begrippen wordt duidelijk in paragraaf A.4.5, waar de methode van Sebastiani *et al.* voor de berekening van de geïnduceerde stroomdichtheden wordt belicht.

A.4.2 Dichtheidsfunctionaal-storingstheorie

Voor de bepaling van de geïnduceerde stroomdichtheden $\mathbf{j}^{\tau}_{\mathbf{B}_x}$ en het geïnduceerde magnetische veld $\mathbf{B}_{\mathbf{B}_x}$ is het noodzakelijk de eerste-ordecorrecties als gevolg van een uitwendig magnetisch veld op een set van ééndeeltjesorbitalen te kennen. De KS-orbitalen zullen voor onze doeleinden niet geschikt blijken, zodat de (standaard) storingstheorie geen uitweg biedt. Een flexibele variationele techniek die dit wel toelaat heet dichtheidsfunctionaal-storingstheorie (*density functional perturbation theory*, DFPT),[41–43] in zijn algemene vorm opgesteld door Putrino *et al*.[44]

Om een externe perturbatie in rekening te brengen wordt aan E_{tot} (A.32) op adiabatische wijze een extra storingsfunctionaal E_{p} toegevoegd. Uitgedrukt als functie van een orthonormaal set van ééndeeltjesorbitalen ψ_i geeft dit:

$$E_{\text{tot+p}}\left[\{\psi_i\}\right] = E_{\text{tot}}\left[\{\psi_i\}\right] + \lambda E_{\text{p}}\left[\{\psi_i\}\right] \ . \tag{A.189}$$

Hier is λ een kleine ($0 \leq \lambda \leq 1$) storingsparameter die de sterkte van de interactie met het statische externe veld E_{p} weergeeft. De nieuwe energiefunctionaal $E_{\text{tot+p}}$ zal nu een minimale waarde E hebben die we kunnen ontwikkelen in machttermen van λ rond de ongestoorde minimale waarde $E^{(0)}$:

$$E = E^{(0)} + \lambda E^{(1)} + \lambda^2 E^{(2)} + \ldots \ . \tag{A.190}$$

De orbitalen die $E_{\text{tot+p}}$ minimaliseren, worden analoog ontwikkeld rond de ongestoorde set $\psi_i^{(0)}$:

$$\psi_i(\mathbf{r}) = \psi_i^{(0)}(\mathbf{r}) + \lambda\psi_i^{(1)}(\mathbf{r}) + \lambda^2\psi_i^{(2)}(\mathbf{r}) + \dots . \tag{A.191}$$

Tot op eerste orde wordt de ladingsdichtheid dan:

$$\rho(\mathbf{r}) = \rho^{(0)}(\mathbf{r}) + \lambda\rho^{(1)}(\mathbf{r}) + \dots , \tag{A.192}$$

met:

$$\rho^{(1)}(\mathbf{r}) = \sum_i \psi_i^{(0)*}(\mathbf{r})\psi_i^{(1)}(\mathbf{r}) + \psi_i^{(1)*}(\mathbf{r})\psi_i^{(0)}(\mathbf{r}) . \tag{A.193}$$

We formuleren nu het variatonele principe uit het **$(2n+1)$-theorema**:[42]

> Wanneer in het algemeen storingstheorie wordt toegepast op een grootheid waarvoor een variationeel principe geldt, dan geldt eveneens een variationeel principe voor de even ordes van die grootheid ontwikkeld in machten van de storingsparameter λ.
>
> **Bewijs**
>
> Voor een minimaal variationeel principe geldt dat de functionaal $X[\Phi]$ bij een testgolffunctie Φ die verschilt van de minimale golffunctie Φ_0 steeds een waarde zal geven hoger of gelijk aan X_0, de waarde van de functionaal voor Φ_0. Bovendien is het verschil, onder voldoende voorwaarde voor differentieerbaarheid, steeds kwadratisch in het verschil tussen de golffuncties, i.e. er bestaat een vast reëel getal K zodat:
>
> $$\forall\Phi,\ \ 0 \leq X[\Phi] - X_0 \leq K\,\|\Phi - \Phi_0\|^2 . \tag{A.194}$$
>
> Veronderstel nu dat de functionaal $X_{(\lambda)}$ ook afhankelijk is van een parameter λ. De golffuncties die deze functionaal minimaliseren zullen dan natuurlijk ook afhangen van deze parameter:

$$\forall\Phi,\ \ 0 \leq X_{(\lambda)}[\Phi] - X_0(\lambda) \leq K \left\|\Phi - \Phi_0(\lambda)\right\|^2 \ . \tag{A.195}$$

We ontwikkelen $\Phi_0(\lambda)$ nu in een oneindige machtreeks in λ rond Φ_0:

$$\Phi_0(\lambda) = \sum_{i=0}^{\infty} \lambda^i \Phi_0^{(i)} \ , \tag{A.196}$$

en kiezen de volgende testgolffunctie Φ, die reeds gelijk is aan $\Phi_0(\lambda)$ tot op orde λ^n,

$$\begin{aligned} \Phi(\lambda) &= \sum_{i=0}^{n} \lambda^i \Phi_0^{(i)} + \lambda^{n+1}\delta\Phi \\ &= \Phi_0(\lambda) - \lambda^{n+1}\left(\sum_{i=n+1}^{\infty} \lambda^{i-n-1}\Phi_0^{(i)} - \delta\Phi\right) \ . \end{aligned} \tag{A.197}$$

Introduceren we de ontwikkelingen van $\Phi_0(\lambda)$ en $\Phi(\lambda)$ in (A.195), dan krijgen we:

$$\begin{aligned} 0 &\leq X_{(\lambda)}\left[\sum_{i=0}^{n} \lambda^i \Phi_0^{(i)} + \lambda^{n+1}\delta\Phi\right] - X_0(\lambda) \\ &\leq K\lambda^{2n+2}\left\|\sum_{i=n+1}^{\infty} \lambda^{i-n-1}\Phi_0^{(i)} - \delta\Phi\right\|^2 \ , \end{aligned} \tag{A.198}$$

een uitdrukking die geldig is voor alle $\delta\Phi$. Als we $\delta\Phi$ nul stellen, dan vereenvoudigt voorgaande tot:

$$\begin{aligned} 0 &\leq X_{(\lambda)}\left[\sum_{i=0}^{n} \lambda^i \Phi_0^{(i)}\right] - X_0(\lambda) \\ &\leq K\lambda^{2n+2}\left\|\sum_{i=0}^{\infty} \lambda^{i}\Phi_0^{(i+n+1)}\right\|^2 \ . \end{aligned} \tag{A.199}$$

We zien dus dat de kennis van de ontwikkeling in machttermen van $\Phi_0(\lambda)$ tot op orde λ^n een fout geeft in de evaluatie van de functionaal van de orde λ^{2n+2}.

Keren we terug naar (A.198), maar nu enkel met de termen in de orde λ^{2n+2}, omdat we uit voorgaande weten dat de expansietermen tot en met orde λ^{2n+1} toch verdwijnen. We houden over:

$$\begin{aligned} 0 &\leq \left\{ X_{(\lambda)} \left[\sum_{i=0}^{n} \lambda^i \Phi_0^{(i)} + \lambda^{n+1} \delta\Phi \right] \right\}^{2n+2} - X_0^{2n+2}(\lambda) \\ &\leq K \left\| \Phi_0^{(n+1)} - \delta\Phi \right\|^2 . \end{aligned} \tag{A.200}$$

Dit is het variationele principe voor de $(2n+2)$de-ordeterm van de functionaal in λ wanneer de golffunctie al gekend is tot op orde λ^n. Kenden we de exacte golffunctie al tot op orde λ^{n-1}, dan kunnen we schrijven:

$$\begin{aligned} 0 &\leq \left\{ X_{(\lambda)} \left[\sum_{i=0}^{n-1} \lambda^i \Phi_0^{(i)} + \lambda^{n} \delta\Phi \right] \right\}^{(2n)} - X_0^{(2n)}(\lambda) \\ &\leq K \left\| \Phi_0^{(n)} - \delta\Phi \right\|^2 . \end{aligned} \tag{A.201}$$

Dus, op het minimum $\{...\}^{(2n)} \rightarrow X_0^{(2n)}$, is de $n$de-orde testgolffunctie gelijk aan $\Phi_0^{(n)}$.

Wanneer we een energie functionaal $X[\Phi]$ dienen te minimaliseren onder een bindingsvoorwaarde $C[\Phi]$ (gebonden extremum vraagstuk), wordt de te extremeren Lagrangiaan:

$$Z[\Phi] = X[\Phi] - \Lambda C[\Phi] . \tag{A.202}$$

Via éénzelfde redenering komen we tot:

$$\begin{aligned} 0 &\leq \left\{ Z_{(\lambda)} \left[\sum_{i=0}^{n-1} \lambda^i \Phi_0^{(i)} + \lambda^n \delta\Phi \right] \right\}^{(2n)} - Z_0^{(2n)}(\lambda) \\ &\leq K \left\| \Phi_0^{(n)} - \delta\Phi \right\|^2 . \end{aligned} \tag{A.203}$$

Passen we het variationele principe van het $(2n+1)$-theorema toe op energiefunctionaal $E_{\text{tot+p}}$ uit (A.189), dan kunnen we de eerste-ordecorrecties $\psi_i^{(1)}$ op de ongestoorde orbitalen berekenen door minimalisatie van de tweede-ordecomponent van $E_{\text{tot+p}}$ in λ:[45]

$$\begin{aligned} E_{\text{tot+p}}^{(2)} &= \frac{1}{2} \int \mathrm{d}\mathbf{r}\mathrm{d}\mathbf{r}' \rho^{(1)}(\mathbf{r}) \frac{\partial (V_{\text{H}}(\mathbf{r}) + V_{\text{xc}}(\mathbf{r}))}{\partial \rho(\mathbf{r}')} \rho^{(1)}(\mathbf{r}') \\ &+ \sum_{i,j} \int \mathrm{d}\mathbf{r} \psi_j^{(1)*}(\mathbf{r}) \left(H_{\text{KS}}(\mathbf{r}) \delta_{ij} - \int \mathrm{d}\mathbf{r}' \psi_i^{(0)*}(\mathbf{r}') H_{\text{KS}}(\mathbf{r}') \psi_j^{(0)}(\mathbf{r}') \right) \psi_i^{(1)}(\mathbf{r}) \\ &+ \sum_j \int \mathrm{d}\mathbf{r} \psi_j^{(1)*}(\mathbf{r}) \frac{\partial E_{\text{p}}}{\partial \psi_j^{(0)*}(\mathbf{r})} + \frac{\partial E_{\text{p}}}{\partial \psi_j^{(0)}(\mathbf{r})} \psi_j^{(1)}(\mathbf{r}) , \end{aligned} \tag{A.204}$$

waarbij rekening werd gehouden met:[46]

$$\frac{\partial \left[E_{\text{tot}} - \sum_i \epsilon_i \left(\int \mathrm{d}\mathbf{r} \psi_i^{(0)*}(\mathbf{r}) \psi_i^{(0)}(\mathbf{r}) - 1 \right) \right]}{\partial \psi_i^{(0)*}(\mathbf{r})} = 0 , \qquad \forall i . \tag{A.205}$$

De orthonormaliteitsvoorwaardes voor de orbitalen (A.191) leiden in eerste orde in λ tot:

$$\int \mathrm{d}\mathbf{r} \left(\psi_i^{(0)*}(\mathbf{r}) \psi_j^{(1)}(\mathbf{r}) + \psi_i^{(1)*}(\mathbf{r}) \psi_j^{(0)}(\mathbf{r}) \right) = 0 , \qquad \forall i, j . \tag{A.206}$$

Deze voorwaarden worden in de praktijk vervangen door strengere voorwaarden:

[45] Merk op dat we uitgaan van een lokale KS-Hamiltoniaan H_{KS}. Wanneer H_{KS} een niet-lokale operator bevat, zoals bijvoorbeeld bij pseudopotentialen van het type besproken in (A.2.5), worden de vergelijkingen – althans in de coördinatenrepresentatie – iets ingewikkelder.

[46] Zie (2.34).

$$\int \mathrm{d}\mathbf{r}\psi_i^{(0)*}(\mathbf{r})\psi_j^{(1)}(\mathbf{r}) = 0, \qquad \forall i,j\,, \tag{A.207}$$

wat ook automatisch inhoudt dat de totale lading q van het systeem behouden blijft, door het verdwijnen van de eerste-ordebijdrage $q^{(1)}$:

$$q^{(1)} = \int \mathrm{d}\mathbf{r}\rho^{(1)} = 0\,. \tag{A.208}$$

De voorwaarden (A.207) kunnen worden opgelegd door middel van een Lagrange multiplicator, en de te extremeren Lagrangiaan $\mathcal{L}$ wordt:

$$\mathcal{L} = E^{(2)}_{\mathrm{tot+p}} - \sum_{i,j}\Lambda_{ij}\int \mathrm{d}\mathbf{r}\psi_i^{(0)*}(\mathbf{r})\psi_j^{(1)}(\mathbf{r})\,. \tag{A.209}$$

A.4.3 Magnetische DFPT

Een magnetisch veld wordt in de Hamiltoniaan van een systeem geïntroduceerd via het principe van de minimale koppeling (zie paragraaf A.3.1). Voor een elektron is dit:

$$\mathbf{p} \to \boldsymbol{\pi} = \mathbf{p} + \alpha\mathbf{A}(\mathbf{r})\,, \tag{A.210}$$

met $\mathbf{A}$ de vectorpotentiaal van het magnetische veld. Zo kan de één-elektron-Hamiltoniaan in een potentiaal V geschreven worden als:

$$H = \frac{1}{2}\left(\mathbf{p} + \alpha\mathbf{A}(\mathbf{r})\right)^2 + V(\mathbf{r})\,. \tag{A.211}$$

Aangezien $\mathbf{A}$ voor een constant magnetisch veld $\mathbf{B}$ lineair is in $\mathbf{B}$,

$$\mathbf{A}(\mathbf{r}) = -\frac{1}{2}(\mathbf{r} - \mathbf{R}_\mathrm{g}) \times \mathbf{B}\,, \tag{A.212}$$

met $\mathbf{R}_\mathrm{g}$ de ijk-oorsprong (zie verder in hoofdstuk A.4.5), bevat de bovenstaande Hamiltoniaan operatoren van eerste en tweede orde in het magnetisch veld:

$$H^{(1)} = \frac{\alpha}{2}(\mathbf{p}.\mathbf{A}(\mathbf{r}) + \mathbf{A}(\mathbf{r}).\mathbf{p}) \,, \tag{A.213}$$

$$H^{(2)} = \frac{\alpha^2}{2}\mathbf{A}(\mathbf{r}).\mathbf{A}(\mathbf{r}) \,. \tag{A.214}$$

De tweede-ordeterm $H^{(2)}$ is voor de berekening van de g-tensor van geen tel (zie de bespreking in paragraaf A.3.4). Bovendien stellen we vast dat de matrixelementen van $H^{(1)}$ in de coördinatenrepresentatie,

$$\langle \mathbf{r}| \, H^{(1)} \, |\mathbf{r}'\rangle = \frac{i\alpha}{2}\delta^3(\mathbf{r}-\mathbf{r}') \left((\mathbf{r}-\mathbf{R}_\mathrm{g}) \times \mathbf{B}\right).\nabla \,, \tag{A.215}$$

strikt imaginair zijn, zodat uit i) de (noodzakelijk) reële energiefunctionaal $E^{(2)}_{\mathrm{tot+p}}$ (A.204) en ii) de keuze van reële ongestoorde orbitalen[47] volgt dat de eerste-ordecorrecties $\psi_i^{(1)}$ ook strikt imaginair moeten zijn:

$$\Re\psi_i^{(1)}(\mathbf{r}) = 0 \,, \tag{A.216}$$

waarbij $\Re$ het reële deel van $\psi_i^{(1)}$ selecteert. Hieruit volgt dat de eerste-ordedichtheid $\rho^{(1)}$ uit (A.193) exact verdwijnt, net als de bindingsvoorwaarden uit (A.209), zodat de te extremeren Lagrangiaan $\mathcal{L}$ sterk vereenvoudigt tot:[48]

$$\begin{aligned}\mathcal{L} &= \sum_{i,j}\int \mathrm{d}\mathbf{r}\psi_j^{(1)*}(\mathbf{r})\left(H_\mathrm{KS}(\mathbf{r})\delta_{ij} - \int \mathrm{d}\mathbf{r}'\psi_i^{(0)*}(\mathbf{r}')H_\mathrm{KS}(\mathbf{r}')\psi_j^{(0)}(\mathbf{r}')\right)\psi_i^{(1)}(\mathbf{r}) \\ &+ \sum_j\int \mathrm{d}\mathbf{r}\psi_j^{(1)*}(\mathbf{r})H^{(1)}(\mathbf{r})\psi_j^{(0)}(\mathbf{r}') + \sum_j\int \mathrm{d}\mathbf{r}\psi_j^{(0)*}H^{(1)}(\mathbf{r})\psi_j^{(1)}(\mathbf{r}) \,,\end{aligned} \tag{A.217}$$

[47] Deze keuze is toegestaan in afwezigheid van een extern magnetisch veld en in de Γ-puntbenadering.

[48] Merk op dat $\psi_i^{(0)}$ niet (noodzakelijk) de KS-orbitalen voorstellen (zie bijvoorbeeld de volgende paragraaf), zodat bijgevolg de matrix A met matrixelementen $A_{ij} = \int \mathrm{d}\mathbf{r}'\psi_i^{(0)*}(\mathbf{r}')H_\mathrm{KS}(\mathbf{r}')\psi_j^{(0)}(\mathbf{r}')$ niet (noodzakelijk) diagonaal is.

met $H^{(1)}$ gelijk aan:

$$H^{(1)}(\mathbf{r}) = \frac{i\alpha}{2}\left((\mathbf{r}-\mathbf{R}_\mathrm{g})\times\mathbf{B}\right).\nabla\ . \tag{A.218}$$

Uit het opleggen van de stationariteitsvoorwaarden,

$$\frac{\partial\mathcal{L}}{\partial\psi_j^{(1)*}(\mathbf{r})} = 0\ , \qquad \forall i\ , \tag{A.219}$$

volgt dan een inhomogeen set van gekoppelde vergelijkingen voor $\psi_i^{(1)}$:

$$-\sum_i\left(H_\mathrm{KS}(\mathbf{r})\delta_{ij} - \int \mathrm{d}\mathbf{r}'\psi_i^{(0)*}(\mathbf{r}')H_\mathrm{KS}(\mathbf{r}')\psi_j^{(0)}(\mathbf{r}')\right)\psi_i^{(1)}(\mathbf{r}) = H^{(1)}(\mathbf{r})\psi_j^{(0)}(\mathbf{r})\ . \tag{A.220}$$

Deze vergelijkingen kunnen worden opgelost via Greense-functietechnieken of direct via minimalisatie van de gradiënten.

A.4.4 Wannier-functies

De oplossingen van een ééndeeltje-Schrödingervergelijking in een periodieke potentiaal kunnen worden geschreven (A.2.3) in termen van Bloch-functies vermenigvuldigd met de golffunctie van een vrij elektron. Deze Bloch-functies hebben dezelfde periodiciteit als de potentiaal, en zijn dus oneindig uitgebreid. Een alternatieve voorstelling van deze oplossingen in termen van gelokaliseerde functies, de *Wannier-functies*, werd in 1937 opgesteld door de Zwiterse natuurkundige Gregory Wannier.[45]

De Wannier-functie $\psi_{m,\mathbf{R}}$ behorend bij de bandindex m en de roostercel bepaald door de roostervector $\mathbf{R}$, wordt uitgaande van de oplossingen $\psi_{m,\mathbf{k}}$ (A.53) gedefinieerd als:

$$\psi_{m,\mathbf{R}}(\mathbf{r}) = \frac{V}{(2\pi)^3}\int_\mathrm{BZ}\mathrm{d}\mathbf{k}\mathrm{e}^{-i\mathbf{k}.\mathbf{R}}\psi_{m,\mathbf{k}}(\mathbf{r})\ . \tag{A.221}$$

Het is eenvoudig om aan te tonen dat de Wannier-functies een orthonormaal set vormen, en dat twee Wannier-functies $\psi_{m,\mathbf{R}}$ en $\psi_{m,\mathbf{R}'}$ in elkaar overgaan via

een translatie over een roostervector $\mathbf{R} - \mathbf{R}'$.

Wannier-functies zijn niet uniek bepaald door (A.221). In geval van één enkele band is dit het gevolg van een onbepaaldheid van de oplossingen $\psi_{m,\mathbf{k}}$ tot op een arbitraire fase $\vartheta_m(\mathbf{k})$, periodiek in de reciproque ruimte, die niet wordt vastgelegd door de Schrödingervergelijking:

$$\psi_{m,\mathbf{k}}(\mathbf{r}) \rightarrow \mathrm{e}^{i\vartheta_m(\mathbf{k})}\psi_{m,\mathbf{k}}(\mathbf{r}) \ . \tag{A.222}$$

Deze onbepaaldheid propageert verder in de Wannier-functie.

De onbepaaldheid is zelfs nog algemener als gevolg van de invariantie van de energiefunctionaal E_{tot} (A.32) onder een unitaire transformatie in de subruimte van de n bezette oplossingen $\psi_{m,\mathbf{k}}$ behorend bij een golfvector $\mathbf{k}$, waardoor we kunnen schrijven dat:

$$\psi_{m',\mathbf{k}}(\mathbf{r}) \rightarrow \sum_m U^{(\mathbf{k})}_{m'm}\psi_{m,\mathbf{k}}(\mathbf{r}) \ , \tag{A.223}$$

met $U^{(\mathbf{k})}$ een unitaire $(n \times n)$-matrix.

We zullen nu van de onbepaaldheid (A.223) gebruik maken om maximaal gelokaliseerde Wannier-functies (*maximally localized Wannier functions*, MLWF) te definiëren. MLWFs hebben in het geval van een niet-geleidend materiaal een exponentieel dalend verloop,[46] een eigenschap die in de volgende paragraaf zal worden gebruikt voor de behandeling van het probleem van de positie-operator. De lokalisatie van een functie kan gekwantificeerd worden aan de hand van een spreidingsfunctionaal $\Delta^{(2)}$:

$$\Delta^{(2)} = \langle\psi|\, r^2\, |\psi\rangle - \langle\psi|\, r\, |\psi\rangle^2 = \left\langle r^2 \right\rangle - \langle r\rangle^2 \ . \tag{A.224}$$

De lokalisatieprocedure die de MLWFs oplevert moet dan de spreidingsfunctionaal van het volledige systeem minimaliseren:

$$\Delta^{(2)}_{\text{tot}} = \sum_i \left\langle r^2 \right\rangle_i - \langle r\rangle_i^2 \ . \tag{A.225}$$

In de Γ-puntbenadering (zie A.2.3) is de overgang op Wannier-functies eigenlijk niets anders dan een unitaire transformatie binnen de subruimte van orbitalen $\psi_{m,\mathbf{k}}$.

A.4.5 Berekening van de geïnduceerde stroomdichtheid

Om verwarring te vermijden, zullen we in deze paragraaf een positie-operator als $\mathbf{r}$ aanduiden, en een positie-variabele als $\tilde{\mathbf{r}}$.

Algemeen wordt de stroomdichtheid verkregen als de verwachtingswaarde van de stroomoperator in de totale elektronische toestand:

$$\mathbf{j}(\tilde{\mathbf{r}}) = -\frac{1}{2} \langle \Psi | \left[\boldsymbol{\pi} | \tilde{\mathbf{r}} \rangle \langle \tilde{\mathbf{r}} | + | \tilde{\mathbf{r}} \rangle \langle \tilde{\mathbf{r}} | \boldsymbol{\pi} \right] | \Psi \rangle \ . \tag{A.226}$$

De stroomdichtheid afkomstig van n niet-interagerende elektronen (bijvoorbeeld de KS-orbitalen) is gelijk aan de som van de stroomdichtheden afkomstig van elk elektron afzonderlijk:

$$\mathbf{j}(\tilde{\mathbf{r}}) = -\frac{1}{2} \sum_i \langle \psi_i | \left[\boldsymbol{\pi} | \tilde{\mathbf{r}} \rangle \langle \tilde{\mathbf{r}} | + | \tilde{\mathbf{r}} \rangle \langle \tilde{\mathbf{r}} | \boldsymbol{\pi} \right] | \psi_i \rangle \ . \tag{A.227}$$

De aanname is nu dat (A.227) een goede benadering vormt voor (A.226). Als we de stroomdichtheid ontwikkelen in machten van het magnetische veld, dan vinden we in nulde orde:

$$\begin{aligned} \mathbf{j}^{(0)}(\tilde{\mathbf{r}}) &= -\frac{1}{2} \sum_i \left\langle \psi_i^{(0)} \right| \left[\mathbf{p} | \tilde{\mathbf{r}} \rangle \langle \tilde{\mathbf{r}} | + | \tilde{\mathbf{r}} \rangle \langle \tilde{\mathbf{r}} | \mathbf{p} \right] \left| \psi_i^{(0)} \right\rangle \\ &= -\frac{1}{2} \sum_i \left[\left(i \nabla \psi_i^{(0)*}(\tilde{\mathbf{r}}) \right) \psi_i^{(0)}(\tilde{\mathbf{r}}) + \psi_i^{(0)*}(\tilde{\mathbf{r}}) \left(-i \nabla \psi_i^{(0)}(\tilde{\mathbf{r}}) \right) \right] \\ &= 0 \, . \end{aligned} \tag{A.228}$$

De laatste gelijkheid steunt op het feit dat we de ongestoorde orbitalen $\psi^{(0)}$ reëel hebben gekozen (zie paragraaf A.4.3). In dat geval is de som in (A.228) nul.

De eerste-ordecomponent van de stroomdichtheid bestaat uit een diamagnetische en een paramagnetische component:

$$\mathbf{j}^{(1)}(\tilde{\mathbf{r}}) = \mathbf{j}_{\mathrm{D}}^{(1)}(\tilde{\mathbf{r}}) + \mathbf{j}_{\mathrm{P}}^{(1)}(\tilde{\mathbf{r}}) \,, \tag{A.229}$$

met:

$$\mathbf{j}_{\mathrm{D}}^{(1)}(\tilde{\mathbf{r}}) = -\alpha \mathbf{A}(\tilde{\mathbf{r}}) \sum_i \left| \psi_i^{(0)}(\tilde{\mathbf{r}}) \right|^2 \,, \tag{A.230}$$

$$\begin{aligned} \mathbf{j}_{\mathrm{P}}^{(1)}(\tilde{\mathbf{r}}) &= -\frac{i}{2} \sum_i \Big[\left(\nabla \psi_i^{(0)*}(\tilde{\mathbf{r}}) \right) \psi_i^{(1)}(\tilde{\mathbf{r}}) - \psi_i^{(0)*}(\tilde{\mathbf{r}}) \left(\nabla \psi_i^{(1)}(\tilde{\mathbf{r}}) \right) \\ &+ \left(\nabla \psi_i^{(1)*}(\tilde{\mathbf{r}}) \right) \psi_i^{(0)}(\tilde{\mathbf{r}}) - \psi_i^{(1)*}(\tilde{\mathbf{r}}) \left(\nabla \psi_i^{(0)}(\tilde{\mathbf{r}}) \right) \Big] \,. \end{aligned} \tag{A.231}$$

Bij reële $\psi_i^{(0)}$ en imaginaire $\psi_i^{(1)}$ vereenvoudigt $\mathbf{j}^{(1)}$ verder tot:

$$\begin{aligned} \mathbf{j}^{(1)}(\tilde{\mathbf{r}}) &= -\alpha \mathbf{A}(\tilde{\mathbf{r}}) \sum_i \left| \psi_i^{(0)}(\tilde{\mathbf{r}}) \right|^2 \\ &- i \sum_i \Big[\left(\nabla \psi_i^{(0)}(\tilde{\mathbf{r}}) \right) \psi_i^{(1)}(\tilde{\mathbf{r}}) - \psi_i^{(0)}(\tilde{\mathbf{r}}) \left(\nabla \psi_i^{(1)}(\tilde{\mathbf{r}}) \right) \Big] \,. \end{aligned} \tag{A.232}$$

Deze stroom, die wegens (A.228) eveneens de totale stroom tot op eerste orde in het magnetisch veld voorstelt, kunnen we ook berekenen voor elk spinkanaal afzonderlijk. De definitie van deze *spinstroomdichtheden* (A.232) komt exact overeen met de overgang op $\mathbf{j}_{\mathbf{B}_x}^{\tau} = \mathbf{j}_{\mathrm{D},\mathbf{B}_x}^{\tau} + \mathbf{j}_{\mathrm{P},\mathbf{B}_x}^{\tau}$ die in (A.177) en (A.178) werd gemaakt.

Continue set van ijk-transformaties

De vectorpotentiaal $\mathbf{A}$ behorend bij een magnetisch veld is slechts een hulpgrootheid, zonder een directe fysische betekenis. Een typische keuze voor de vectorpotentiaal $\mathbf{A}$ in het geval van een homogeen magnetisch veld $\mathbf{B}$ is:

$$\mathbf{A}(\mathbf{r}) = -\frac{1}{2} \mathbf{r} \times \mathbf{B} \,. \tag{A.233}$$

Maar ook een vectorpotentiaal van het type:

$$\mathbf{A}(\mathbf{r}) = -\frac{1}{2}(\mathbf{r} - \mathbf{R}_\mathrm{g}) \times \mathbf{B} \,, \tag{A.234}$$

is een geldige vectorpotentiaal, aangezien nog steeds voldaan is aan:

$$\mathbf{B}(\mathbf{r}) = \nabla \times \mathbf{A}(\mathbf{r}) \,. \tag{A.235}$$

We zien dat in (A.234) de oorsprong van het coördinatenstelsel wijzigt in $\mathbf{R}_\mathrm{g}$. Daarom noemt men $\mathbf{R}_\mathrm{g}$ ook wel de **ijk-oorsprong** van de vectorpotentiaal. Het is een cyclische variabele, waarmee we willen zeggen dat deze geen invloed heeft op de fysische observabelen. Hieruit volgt dat de berekening van de stroomdichtheid (A.232) onafhankelijk is van de keuze van de ijk-oorsprong. In de praktijk kan de keuze van de ijk-oorsprong in dit geval toch een vrij belangrijk effect hebben. De reden hiervoor is van numerieke aard: $\mathbf{j}_\mathrm{D}^{(1)}$ en $\mathbf{j}_\mathrm{P}^{(1)}$ zijn elk afzonderlijk afhankelijk van de ijk, terwijl de totale stroomdichtheid $\mathbf{j}^{(1)}$ ijk-onafhankelijk moet zijn. Aangezien $\mathbf{A}$ lineair toeneemt in de ijk-oorsprong $\mathbf{R}_\mathrm{g}$, neemt ook de diamagnetische stroomdichtheid $\mathbf{j}_\mathrm{D}^{(1)}$ (A.230) lineair toe in $\mathbf{R}_\mathrm{g}$, en moet $\mathbf{j}_\mathrm{P}^{(1)}$ hiervoor compenseren zodat de invariantie voldaan is voor de totale stroomdichtheid. Voor grote afstanden $\left|\tilde{\mathbf{r}} - \mathbf{R}_\mathrm{g}\right|$ wordt de totale stroomdichtheid $\mathbf{j}^{(1)}$ dan berekend uit het verschil van twee grote weinig verschillende termen. In een computersimulatie met een (noodzakelijk) eindige basisset krijgen beide termen foutenvlaggen die substantieel zijn in vergelijking met de totale stroomdichtheid, waardoor de invariantie numeriek niet langer opgaat.

Om dit probleem te minimaliseren, werden verschillende methodes voorgesteld. In dit werk maken we voornamelijk gebruik van de continue set van ijk-transformaties (*continuous set of gauge transformations*, CSGT),[47] waarin de ijk-oorsprong afhangt van de positie waarvoor de stroomdichtheid moet worden berekend. Voor elk punt $\tilde{\mathbf{r}}$ in de coördinatenruimte, wordt de stroomdichtheid berekend met de ijk-oorsprong $\mathbf{R}_\mathrm{g}$ gelijk aan $\tilde{\mathbf{r}}$. Deze aanpak zorgt ervoor dat de diamagnetische component van de stroomdichtheid exact verdwijnt:

$$\mathbf{j}_\mathrm{D}^{(1)}(\tilde{\mathbf{r}}) = 0 \,, \tag{A.236}$$

waardoor de numerieke problemen niet langer voorkomen.

Translatievrijheid van de oorsprong voor elke individuele orbitaal

We kunnen formeel aantonen dat de stroomdichtheid uit (A.232), die enkel uit een paramagnetische component bestaat in de CSGT-methode, invariant blijft onder willekeurige orbitaalspecifieke translaties van de oorsprong. Om dit te bewijzen voeren we de Greense functie in van het inhomogeen set van gekoppelde vergelijkingen voor $\psi_i^{(1)}$ (A.220):

$$G_{ij}(\tilde{\mathbf{r}},\tilde{\mathbf{r}}') = -\left(H_{\mathrm{KS}}(\mathbf{r})\delta_{ij} - \int \mathrm{d}\tilde{\mathbf{r}}''\psi_i^{(0)*}(\tilde{\mathbf{r}}'')H_{\mathrm{KS}}(\mathbf{r}'')\psi_j^{(0)}(\tilde{\mathbf{r}}'')\right)^{-1} . \quad \text{(A.237)}$$

Voor een willekeurige storingsoperator O kunnen we de oplossingen van (A.220) dan formeel schrijven als:

$$\psi_i^{(O)}(\tilde{\mathbf{r}}) = \sum_j \int \mathrm{d}\tilde{\mathbf{r}}' G_{ij}(\tilde{\mathbf{r}},\tilde{\mathbf{r}}')O(\mathbf{r}')\psi_j^{(0)}(\tilde{\mathbf{r}}') \; . \quad \text{(A.238)}$$

Een dergelijke formulering laat ten eerste toe vast te stellen dat de oplossingen van (A.220) voor de storingsoperator gedefinieerd in (A.218), die voor een constant magnetisch veld gelijk is aan:

$$H^{(1)} = -\frac{\alpha}{2}\left((\mathbf{r}-\mathbf{R}_{\mathrm{g}})\times\mathbf{p}\right).\mathbf{B} \; , \quad \text{(A.239)}$$

wegens lineariteit kunnen worden berekend als de som van de oplossingen (A.238) bij storingsoperatoren $O_1 = -\frac{\alpha}{2}\left(\mathbf{r}\times\mathbf{p}\right).\mathbf{B}$ en $O_2 = -\frac{\alpha}{2}\left(\mathbf{R}_{\mathrm{g}}\times\mathbf{p}\right).\mathbf{B}$:

$$\begin{aligned}\psi_i^{(1)}(\tilde{\mathbf{r}}) &= -\frac{\alpha}{2}\sum_j \left(\int \mathrm{d}\tilde{\mathbf{r}}' G_{ij}(\tilde{\mathbf{r}},\tilde{\mathbf{r}}')\left(\mathbf{r}'\times\mathbf{p}'\right)\psi_j^{(0)}(\tilde{\mathbf{r}}')\right. \\ &- \left.\int \mathrm{d}\tilde{\mathbf{r}}' G_{ij}(\tilde{\mathbf{r}},\tilde{\mathbf{r}}')\left(\mathbf{R}_{\mathrm{g}}\times\mathbf{p}'\right)\psi_j^{(0)}(\tilde{\mathbf{r}}')\right).\mathbf{B} \; . \quad \text{(A.240)}\end{aligned}$$

Daarnaast wordt het ook duidelijk dat de stroomdichtheid invariant blijft onder willekeurige orbitaalspecifieke translaties $\mathbf{d}_j$ van de oorsprong van de positie-operator $\mathbf{r}$ en de ijk-oorsprong $\mathbf{R}_{\mathrm{g}} = \tilde{\mathbf{r}}$:

$$\begin{aligned}\psi_i^{(1)}(\tilde{\mathbf{r}}) &= -\frac{\alpha}{2}\sum_j \Bigg(\int \mathrm{d}\tilde{\mathbf{r}}' G_{ij}(\tilde{\mathbf{r}},\tilde{\mathbf{r}}') \left((\mathbf{r}'-\mathbf{d}_j)\times\mathbf{p}'\right) \psi_j^{(0)}(\tilde{\mathbf{r}}') \\ &- \int \mathrm{d}\tilde{\mathbf{r}}' G_{ij}(\tilde{\mathbf{r}},\tilde{\mathbf{r}}') \left((\tilde{\mathbf{r}}-\mathbf{d}_j)\times\mathbf{p}'\right) \psi_j^{(0)}(\tilde{\mathbf{r}}') \Bigg) .\mathbf{B} \,. \end{aligned} \tag{A.241}$$

De eerste storingsoperator in (A.241) vereist één berekening van (A.220).[49] De tweede storingsoperator hangt af van de positie in de coördinatenruimte waarvoor de stroomdichtheid moet worden berekend, zodat voor elke positie (A.220) opnieuw moet worden opgelost. De computationele kost van één dergelijke berekening is van dezelfde grootte-orde als de zelfconsistente procedure van het Kohn-Sham-DFT-schema (zie paragraaf A.2.2), en is dus beter te vermijden. Daarom wordt het tweede deel van (A.241) verder uitgewerkt tot:

$$\begin{aligned} &\frac{\alpha}{2}\sum_j \Bigg(\int \mathrm{d}\tilde{\mathbf{r}}' G_{ij}(\tilde{\mathbf{r}},\tilde{\mathbf{r}}') \left((\tilde{\mathbf{r}}-\mathbf{d}_j)\times\mathbf{p}'\right) \psi_j^{(0)}(\tilde{\mathbf{r}}') \Bigg) .\mathbf{B} \\ = \;& \frac{\alpha}{2}\sum_j \Bigg((\tilde{\mathbf{r}}-\mathbf{d}_i)\times \int \mathrm{d}\tilde{\mathbf{r}}' G_{ij}(\tilde{\mathbf{r}},\tilde{\mathbf{r}}') \mathbf{p}' \psi_j^{(0)}(\tilde{\mathbf{r}}') \\ + \;& \int \mathrm{d}\tilde{\mathbf{r}}' G_{ij}(\tilde{\mathbf{r}},\tilde{\mathbf{r}}') \left((\mathbf{d}_i-\mathbf{d}_j)\times\mathbf{p}'\right) \psi_j^{(0)}(\tilde{\mathbf{r}}') \Bigg) .\mathbf{B} \,. \end{aligned} \tag{A.242}$$

De eerste en tweede storingsoperator in (A.242) vereisen respectievelijk 1 en n berekeningen van (A.220), met n het aantal elektronen. Bovendien is het mogelijk om vanuit de bijdrage tot $\psi_i^{(1)}$ van het tweede deel van (A.242) heel snel de bijdrage tot $\psi_j^{(1)}$ te berekenen, op voorwaarde dat $\mathbf{d}_i \approx \mathbf{d}_j$.[48, 49] In het geval $\mathbf{d}_i = \mathbf{d}_j$ kan de bijdrage tot $\psi_j^{(1)}$ zelfs rechtstreeks uit deze tot $\psi_i^{(1)}$ worden afgeleid, dus zonder een bijkomende berekening van (A.220).

Het probleem van de positie-operator in PBC

De positie-operator $\mathbf{r}$ inwerkend op een (ééndeeltjes)golffunctie in de coördinatenrepresentatie $\psi(\tilde{\mathbf{r}})$ vermenigvuldigt die golffunctie met de positie-variabele $\tilde{\mathbf{r}}$. Wanneer periodieke randvoorwaarden worden opgelegd, wordt de Hilbertruimte van de ééndeeltjesgolffuncties $\psi(\tilde{\mathbf{r}})$ bepaald door de voorwaarde $\psi(\tilde{\mathbf{r}}+$

[49] Merk op dat in (A.220) meteen de correcties voor alle i worden berekend.

$\mathbf{L}) = \psi(\tilde{\mathbf{r}})$. Een geldige operator transformeert elke vector (in casu: de golffunctie) van een gegeven Hilbert-ruimte in een vector behorend tot diezelfde Hilbert-ruimte. De vermenigvuldigende positie-operator is dan duidelijk geen geldige operator, aangezien de cartesiaanse componenten van $\tilde{\mathbf{r}}\psi(\tilde{\mathbf{r}})$ duidelijk niet langer periodiek zijn. Dit vormt duidelijk een probleem, aangezien de storingsoperator $(\mathbf{r} - \mathbf{d}_j) \times \mathbf{p}$ uit (A.241) de positie-operator bevat.

De oplossing voor dit probleem bestaat uit een aaneenschakeling van procedures, waarvan sommige reeds in de voorgaande paragrafen werden besproken.

Ten eerste worden de KS-orbitalen getransformeerd tot MLWFs. Voor een niet-geleidend materiaal nemen deze functies exponentieel af. Wanneer de simulatiecel dan zo gekozen wordt dat de dimensies groter blijven dan de vervallengte, volgt hieruit dat (de dichtheid van) elke MLWF slechts verschilt van nul in een beperkt gebied van de simulatiecel, en daarbuiten praktisch verdwijnt. Deze eigenschap blijft evengoed geldig na inwerking van de semilokale operator $\mathbf{p} = -i\nabla$.

De volgende stap bestaat erin om aan elke MLWF een individuele virtuele cel toe te kennen met dezelfde dimensies $L_x \times L_y \times L_z$ als de simulatiecel. Deze virtuele cel wordt zodanig gekozen dat het geometrisch centrum ervan samenvalt met het Wannier-centrum, dit is het ladingscentrum van de corresperende MLWF. Daarna herdefiniëren we de positie-operator $\mathbf{r}$ zodanig dat zijn verwachtingswaarde $\tilde{\mathbf{r}}$ binnenin elke virtuele cel in elke cartesische component lineair van $-L_i/2$ tot $+L_i/2$ ($i = x, y, z$) loopt. Met andere woorden, we gebruiken de translatievrijheid (zie vorige paragraaf) om de oorsprong $\mathbf{d}_j$ van het coördinatenstelsel voor elke individuele MLWF j uit (A.241) gelijk te stellen aan het corresponderende Wannier-centrum. Aan de grenzen van de virtuele cel loopt de verwachtingswaarde terug van $+L_i/2$ naar $-L_i/2$, zodat (in elke cartesische component) een zaagtandprofiel ontstaat. Op die manier voldoet de positie-operator aan de periodieke randvoorwaarden, en wordt deze dus een geldige operator. Het gedrag aan de grenzen van de virtuele cel is van geen tel, aangezien de dimensies van de simulatiecel zo werden gekozen dat de MLFW daar toch verdwenen is. Deze definitie van de positie-operator wordt geïllustreerd in Figuur A.3.

Hierin schuilt meteen ook een belangrijke praktische beperking voor de besproken techniek: in sommige materialen, zoals metalen en andere geleiders, is de vervallengte van de MLWFs zodanig groot, dat de dimensies van de

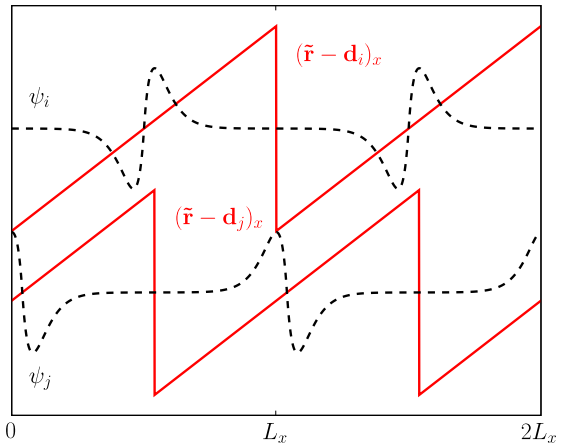

Figuur A.3: Twee MLWFs ψ_i en ψ_j met hun bijhorende verwachtingswaarden van de positie-operator (in één dimensie).

simulatiecel het computationeel haalbare ver overstijgen.

Wanneer de simulatiecellen veel groter zijn dan de dimensies van de MLWFs, kan men de oorsprong (van het coördinatenstelsel) van MLWFs met nabijgelegen Wannier-centra aan elkaar gelijk stellen ($\mathbf{d}_i = \mathbf{d}_j$), wat computationeel voordelig is (zie vorige paragraaf). Wanneer de dimensies van de MLWFs niet groter zijn dan $L_x/2 \times L_y/2 \times L_z/2$,[50] kan men eenvoudig aantonen dat voor een willekeurige distributie van de MLWFs maximaal slechts 8 berekeningen van (A.220) nodig zijn om de storingen als gevolg van de tweede storingsoperator uit (A.242) volledig te kennen. Het schalingsgedrag daalt in dit geval met één orde.

Het probleem van de definitie van afstanden in PBC

Bijkomende aandacht moet worden besteed aan de definitie van $(\mathbf{d}_i - \mathbf{d}_j)$ in (A.242). In een PBC-simulatie is deze afstand slechts gedefinieerd tot op een willekeurige roostervector $\mathbf{L_a} = a\mathbf{L}_x + b\mathbf{L}_y + c\mathbf{L}_z$ na, $(\mathbf{d}_i - \mathbf{d}_j + \mathbf{L_a})$, met $\mathbf{a}$ de vector van gehele getallen a, b, c. Omdat $(\mathbf{d}_i - \mathbf{d}_j)$ en $\mathbf{p}$ (semi-)lokale operatoren zijn, en omdat de Greense functie $G_{ij}(\tilde{\mathbf{r}}, \tilde{\mathbf{r}}')$ enkel beduidend is voor punten $\tilde{\mathbf{r}}$

[50] Of anders gesteld: wanneer de simulatiecel zo gekozen wordt dat de dimensies van de MLWFs niet groter zijn dan $L_x/2 \times L_y/2 \times L_z/2$.

en $\tilde{\mathbf{r}}'$ die in de ruimte *dicht* bij elkaar liggen, terwijl elke MLWF bij constructie sterk gelokaliseerd is rond zijn corresponderende Wannier-centrum, kiezen we enkel de roostervector $\mathbf{L_a}$ die de afstand $\left|\mathbf{d}_i - \mathbf{d}_j + \mathbf{L_a}\right|$ minimaliseert (*minimal image convention*).

A.4.6 De g-tensor in CPMD: implementatie en implicaties

CPMD maakt gebruik van een PW-basisset, en vereist dus het gebruik van de PSP-benadering om de grootte van de basisset binnen de grenzen van de computationele haalbaarheid te houden. In de PSP-benadering maken de kern-elektronen niet langer expliciet deel uit van het veeldeeltjesprobleem, en hebben de golffuncties van de valentie-elektronen in de buurt van de atoomkernen niet de correcte vorm. Het eerste gevolg heeft slects een ondergeschikt effect op de berekening van de g-tensor, aangezien in (A.185)-(A.187) spin-op- en spin-neer-componenten van elkaar worden afgetrokken, zodat – bij verwaarlozing van de polarisatie van de kernelektronen – de bijdragen van de kern-elektronen grotendeels verdwijnen. V_{KS}^{τ} is in de PSP-benadering een niet-lokale operator, we zullen deze benaderen tot de lokale component. Ook zal het geïnduceerde magnetische veld $\mathbf{B}_{\mathbf{B}_x}$ dan geen bijdragen van de kernelektronen bevatten, maar gelukkig is $\Delta g_{xy}^{\mathrm{SOO}}$ vaak veruit ondergeschikt aan $\Delta g_{xy}^{\mathrm{SO}}$ en (in mindere mate) $\Delta g_{xy}^{\mathrm{ZKE}}$. De belangrijkste fouten volgen dan uit de foutieve vorm van de golffuncties van de valentie-elektronen, maar zoals wordt geïllustreerd in Ref. [Art. 1/2], hebben de meest energetische valentie-elektronen (waarin de spinpolarisatie het duidelijkst optreedt) bij lichte elementen zelfs in de PSP-benadering toch een benaderend correcte vorm.

De implementatie van de berekening van $\mathbf{j}_{\mathbf{B}_x}^{\tau}$ en $\mathbf{B}_{\mathbf{B}_x}$ in CPMD is grotendeels het werk van Sebastiani *et al.*[39, 40]

De berekening van $\Delta g_{xy}^{\mathrm{ZKE}}$ (A.185) in CPMD

$\Delta g_{xy}^{\mathrm{ZKE}}$ wordt in een spingepolariseerde DFT-berekening berekend uitgaande van de kinetische energie van de KS-orbitalen in de PW-basisset. In de reciproque ruimte wordt de berekening van de kinetische energie tot een eenvoudige som over de vlakke golven van de basisset (A.58) gereduceerd.

De berekening van $\Delta g_{xy}^{\mathrm{SO}}$ (A.186) in CPMD

De geïnduceerde stroomdichtheden $\mathbf{j}^{\tau}_{\mathbf{B}_x}$ worden onder meer berekend uit de oplossingen van het inhomogeen set van gekoppelde vergelijkingen (A.220) in de reciproque ruimte voor respectievelijk $(\mathbf{r}-\mathbf{d}_j)\times\mathbf{p}$ (de *baanimpulsmoment*-operator, notatie: $\mathbf{L}$), $\mathbf{p}$ (de *impuls*-operator, notatie: $\mathbf{p}$) en $(\mathbf{d}_i-\mathbf{d}_j)\times\mathbf{p}$ (de *volledige-correctie*-operator, notatie: $\boldsymbol{\Delta i}$). De inwerking van de impuls-operator (alsook de ∇-operator) gebeurt in de reciproque ruimte, de inwerking van de positie-operator in de reële ruimte (zie de discussie over de positie-operator in paragraaf A.4.5), zodat via opeenvolgende FFT's de functie waarop moet worden ingewerkt in de correcte representatie wordt verkregen. Voor de positie-operator is het belangrijk dat de overgang aan de randen van de virtuele cel zacht gebeurt om ongewenste hoogfrequente componenten in de positie-operator te vermijden. De eerste-ordecorrecties $\psi^{(1)}_{\mathbf{B}_\alpha,i}$ op de MLWFs zijn dan gelijk aan:

$$\psi^{(1)}_{\mathbf{B}_\alpha,i}(\mathbf{r}) = -\frac{i\alpha}{2}\left(\psi_i^{L_\alpha}(\mathbf{r}) - \epsilon_{\alpha\beta\gamma}(\mathbf{r}-\mathbf{d}_i)_\beta\psi_i^{p_\gamma}(\mathbf{r}) - \psi_i^{\Delta i_\alpha}(\mathbf{r})\right) . \qquad \text{(A.243)}$$

Het vectorieel produkt werd bondig genoteerd met behulp van de totale antisymmetrische tensor $\epsilon_{\alpha\beta\gamma}$, het Levi-Cività-symbool. De indices β en γ volgen de Einstein-sommatieregels.[51] Merk ook op dat we in de bovenstaande vergelijking het imagaire karakter van $\psi^{(1)}_{\mathbf{B}_\alpha,i}$ expliciet hebben geschreven, zodat we steeds met reële functies $\psi_i^{L_\alpha}$, $\psi_i^{p_\gamma}$ en $\psi_i^{\Delta i_\alpha}$ kunnen werken. Hieruit berekenen we dan de spinafhankelijke stroomdichtheid volgens (A.232):[52]

$$\begin{aligned}
\mathbf{j}^{\tau}_{\mathbf{B}_\alpha}(\mathbf{r}) &= \sum_i^{n_\tau}\mathbf{j}_{\mathbf{B}_\alpha,i}(\mathbf{r}) \\
&= -i\sum_i^{n_\tau}\left[\left(\nabla\psi_i^{(0)}(\mathbf{r})\right)\psi^{(1)}_{\mathbf{B}_\alpha,i}(\mathbf{r}) - \psi_i^{(0)}(\mathbf{r})\left(\nabla\psi^{(1)}_{\mathbf{B}_\alpha,i}(\mathbf{r})\right)\right] \\
&= -\frac{\alpha}{2}\sum_i^{n_\tau}\left[\left(\nabla\psi_i^{(0)}(\mathbf{r})\right)\psi_i^{L_\alpha}(\mathbf{r}) - \epsilon_{\alpha\beta\gamma}(\mathbf{r}-\mathbf{d}_i)_\beta\left(\nabla\psi_i^{(0)}(\mathbf{r})\right)\psi_i^{p_\gamma}(\mathbf{r})\right. \\
&- \left(\nabla\psi_i^{(0)}(\mathbf{r})\right)\psi_i^{\Delta i_\alpha}(\mathbf{r}) - \psi_i^{(0)}(\mathbf{r})\left(\nabla\psi_i^{L_\alpha}(\mathbf{r})\right) \\
&+ \left.\epsilon_{\alpha\beta\gamma}(\mathbf{r}-\mathbf{d}_i)_\beta\psi_i^{(0)}(\mathbf{r})\left(\nabla\psi_i^{p_\gamma}(\mathbf{r})\right) + \psi_i^{(0)}(\mathbf{r})\left(\nabla\psi_i^{\Delta i_\alpha}(\mathbf{r})\right)\right] . \qquad \text{(A.244)}
\end{aligned}$$

[51] Dit betekent dat over alle mogelijke waarden (x, y, z) van β en γ wordt gesommeerd.
[52] Ter herinnering: we berekenen de stroomdichtheid in de CSGT-methode.

V_{KS}^{τ}, de tweede relevante component van $\Delta g_{xy}^{\mathrm{SO}}$, wordt in de reciproque ruimte berekend als de som van het lokale deel van de pseudopotentialen, de Hartree-potentiaal $v_{\mathrm{H},\mathbf{G}\neq\mathbf{0}} = 2\pi\Omega\sum_{\mathbf{G}\neq\mathbf{0}}\frac{|\rho(\mathbf{G})|^2}{G^2}$,[53] en dezelfde uitwisselings-correlatiepotentiaal als deze die werd gebruikt in de zelfconsistente procedure van het Kohn-Sham-DFT-schema. De ruimtelijke afgeleiden van V_{KS}^{τ} worden nadien berekend in de reciproque ruimte. De gebruikte uitwisselings-correlatiepotentiaal is steeds dezelfde als deze die werd gebruikt in de zelfconsistente procedure van het Kohn-Sham-DFT-schema.

De berekening van $\Delta g_{xy}^{\mathrm{SO}}$ is dan uiteindelijk niet meer dan de uitwerking van:

$$\Delta g_{xy}^{\mathrm{SO}} = \frac{\alpha g'}{2}\int_{\mathrm{FFT}} \mathrm{d}\mathbf{r}\left[\mathbf{j}_{\mathbf{B}_x}^{\alpha}(\mathbf{r})\times\nabla V_{\mathrm{KS}}^{\alpha}(\mathbf{r}) - \mathbf{j}_{\mathbf{B}_x}^{\beta}(\mathbf{r})\times\nabla V_{\mathrm{KS}}^{\beta}(\mathbf{r})\right]_y , \qquad \text{(A.245)}$$

waarbij het subscript *FFT* uitdrukt dat de integratie gebeurt op de discrete punten van het FFT-raster.

De berekening van $\Delta g_{xy}^{\mathrm{SOO}}$ (A.187) in CPMD

Het magnetisch veld $\mathbf{B}_{\mathbf{B}_x}$ afkomstig van de geïnduceerde en voor zelfinteractie gecorrigeerde stroomdichtheid $\mathbf{j}_{\mathbf{B}_x}^{\mathrm{corr}} = \left(\mathbf{j}_{\mathbf{B}_x}^{\alpha} + \mathbf{j}_{\mathbf{B}_x}^{\beta}\right) - \left(\mathbf{j}_{\mathbf{B}_x}^{\alpha} - \mathbf{j}_{\mathbf{B}_x}^{\beta}\right)$ wordt berekend volgens (A.182):

$$\begin{aligned} B_{\mathbf{B}_x,\alpha}(\mathbf{r}) &= \alpha\left[\int_{\Omega_{\mathrm{S}}}\mathrm{d}\mathbf{r}'\frac{\mathbf{r}'-\mathbf{r}}{|\mathbf{r}'-\mathbf{r}|^3}\times\mathbf{j}_{\mathbf{B}_x}^{\mathrm{corr}}(\mathbf{r}')\right]_{\alpha} \\ &= \alpha\left[\int_{\Omega_{\mathrm{S}}}\mathrm{d}\mathbf{r}'\left(\frac{\partial}{\partial\mathbf{r}}\frac{1}{|\mathbf{r}'-\mathbf{r}|}\right)\times\mathbf{j}_{\mathbf{B}_x}^{\mathrm{corr}}(\mathbf{r}')\right]_{\alpha} \\ &= \alpha\epsilon_{\alpha\beta\gamma}\frac{\partial}{\partial r_\beta}\int_{\Omega_{\mathrm{S}}}\mathrm{d}\mathbf{r}'\frac{1}{|\mathbf{r}'-\mathbf{r}|}j_{\mathbf{B}_x,\gamma}^{\mathrm{corr}}(\mathbf{r}') . \end{aligned} \qquad \text{(A.246)}$$

In de bovenstaande vergelijkingen beslaat het integratiedomein de volledige ruimte (Ω_{S}), en dus niet enkel de simulatiecel (Ω). Met de vector $\mathbf{e}_\alpha$ duiden we de eenheidsvector in de cartesiaanse richting α aan. De stroomdichtheid $j_{\mathbf{B}_x,\gamma}^{\mathrm{corr}}$ herhaalt zich met de periodiciteit van de simulatiecel, terwijl de functies $\frac{\mathbf{r}'-\mathbf{r}}{|\mathbf{r}'-\mathbf{r}|^3}$ en $\frac{1}{|\mathbf{r}'-\mathbf{r}|}$ dat juist niet doen. Bovendien geldt voor de integraal over de simulatiecel van de stroomdichtheden van elk elektron i afzonderlijk dat:

[53] de component ($\mathbf{G} = \mathbf{0}$) laten we achterwege, omdat we uiteindelijk toch de ruimtelijke afgeleide nodig hebben

$$\int_{\Omega} \mathrm{d}\mathbf{r} \mathbf{j}_{\mathbf{B}_x,i}(\mathbf{r}) = \mathbf{0} \,, \tag{A.247}$$

en bijgevolg ook dat:

$$\int_{\Omega} \mathrm{d}\mathbf{r} \mathbf{j}^{\mathrm{corr}}_{\mathbf{B}_x}(\mathbf{r}) = \mathbf{0} \,. \tag{A.248}$$

Om de uiteenzetting overzichtelijk te houden, zullen we slechts één cartesiaanse component van de stroomdichtheid $\mathbf{j}^{\mathrm{corr}}_{\mathbf{B}_x}(\mathbf{r})$ uit de integraal in (A.246) behandelen:

$$I^{\mathrm{corr}}_{\mathbf{B}_x,\gamma}(\mathbf{r}) = \int_{\Omega_\mathrm{S}} \mathrm{d}\mathbf{r}' \frac{1}{|\mathbf{r}' - \mathbf{r}|} j^{\mathrm{corr}}_{\mathbf{B}_x,\gamma}(\mathbf{r}') \,. \tag{A.249}$$

De eigenschap (A.248) geldt voor alle cartesiaanse componenten, en uitgedrukt in de reciproque ruimte komt deze overeen met:

$$j^{\mathrm{corr}}_{\mathbf{B}_x,\gamma}(\mathbf{G} = \mathbf{0}) = 0 \,. \tag{A.250}$$

We vervangen nu $j^{\mathrm{corr}}_{\mathbf{B}_x,\gamma}$ in (A.249) door zijn reciproque uitdrukking:

$$\begin{aligned} I^{\mathrm{corr}}_{\mathbf{B}_x,\gamma}(\mathbf{r}) &= \int_{\Omega_\mathrm{S}} \mathrm{d}\mathbf{r}' \frac{1}{|\mathbf{r}' - \mathbf{r}|} \frac{1}{N_G} \sum_{\mathbf{G}\neq\mathbf{0}} e^{i\mathbf{G}.\mathbf{r}'} j^{\mathrm{corr}}_{\mathbf{B}_x,\gamma}(\mathbf{G}) \\ &= \frac{1}{N_G} \sum_{\mathbf{G}\neq\mathbf{0}} e^{i\mathbf{G}.\mathbf{r}} j^{\mathrm{corr}}_{\mathbf{B}_x,\gamma}(\mathbf{G}) \int_{\Omega_\mathrm{S}} \mathrm{d}\mathbf{r}' \frac{1}{|\mathbf{r}' - \mathbf{r}|} e^{i\mathbf{G}.(\mathbf{r}'-\mathbf{r})} \\ &= \frac{1}{N_G} \sum_{\mathbf{G}\neq\mathbf{0}} e^{i\mathbf{G}.\mathbf{r}} j^{\mathrm{corr}}_{\mathbf{B}_x,\gamma}(\mathbf{G}) \int_{\Omega_\mathrm{S}} \mathrm{d}\mathbf{s} \frac{1}{s} e^{i\mathbf{G}.\mathbf{s}} \,, \end{aligned} \tag{A.251}$$

waarbij $N_\mathbf{G}$ het aantal reciproque roostervectoren aanduidt. De integraal uit de bovenstaande vergelijking wordt verder uitgewerkt via:

$$\begin{aligned} \lim_{a\to 0} \int_{\Omega_\mathrm{S}} \mathrm{d}\mathbf{s} \frac{1}{s} e^{-as} e^{i\mathbf{G}\cdot\mathbf{s}} &= \lim_{a\to 0} \int_{\Omega_\mathrm{S}} \mathrm{d}\varphi \mathrm{d}(\cos\theta_s) \mathrm{d}s s^2 \frac{1}{s} e^{-as} e^{iGs\cos\theta_s} \\ &= \lim_{a\to 0} \frac{4\pi}{a^2 + G^2} \\ &= \frac{4\pi}{G^2} \,. \end{aligned} \tag{A.252}$$

Merk op dat deze integraal divergeert voor $\mathbf{G} = \mathbf{0}$. Via (A.251) kunnen we (A.246) herwerken tot, de $(\mathbf{G} = \mathbf{0})$-component niet meegerekend:

$$\begin{aligned} B_{\mathbf{B}_x,\mathbf{G}\neq\mathbf{0},\alpha}(\mathbf{r}) &= \alpha\epsilon_{\alpha\beta\gamma}\frac{\partial}{\partial r_\beta} I^{\text{corr}}_{\mathbf{B}_x,\gamma}(\mathbf{r}) \\ &= \frac{1}{N_G}\sum_{\mathbf{G}\neq\mathbf{0}} e^{i\mathbf{G}\cdot\mathbf{r}}\left[i\alpha\epsilon_{\alpha\beta\gamma}G_\beta\frac{4\pi}{G^2} j^{\text{corr}}_{\mathbf{B}_x,\gamma}(\mathbf{G})\right] . \end{aligned} \tag{A.253}$$

Hieruit zien we dat het magnetische veld in de reciproque ruimte, voor het geval $\mathbf{G} \neq \mathbf{0}$, gelijk is aan de volgende eenvoudige uitdrukking:

$$\begin{aligned} B_{\mathbf{B}_x,\alpha}(\mathbf{G}) &= i\alpha\epsilon_{\alpha\beta\gamma}G_\beta\frac{4\pi}{G^2} j^{\text{corr}}_{\mathbf{B}_x,\gamma}(\mathbf{G}) \\ &= i\alpha\frac{4\pi}{G^2}\left[\mathbf{G}\times\mathbf{j}^{\text{corr}}_{\mathbf{B}_x}(\mathbf{G})\right]_\alpha . \end{aligned} \tag{A.254}$$

De $(\mathbf{G} = \mathbf{0})$-component van het geïnduceerde magnetische veld kan niet worden berekend uitgaande van periodieke randvoorwaarden. Een benaderende waarde voor de bijdrage van deze component tot het geïnduceerde magnetische veld in de reële ruimte kan worden berekend via:[39]

$$\mathbf{B}_{\mathbf{B}_x,\mathbf{G}=\mathbf{0}} = \kappa\frac{2\pi\alpha}{\Omega}\int_\Omega \mathrm{d}\mathbf{r}\,\mathbf{r}\times\mathbf{j}^{\text{corr}}_{\mathbf{B}_x}(\mathbf{r}) . \tag{A.255}$$

Deze uitdrukking hangt af van de macroscopische vorm van het bestudeerde materiaal via een dimensieloze vormfactor κ. Voor een sferische vorm is de bovenstaande vergelijking exact, en is $\kappa = \frac{2}{3}$ (dit is meteen ook de standaardwaarde voor κ).[54]

De uitdrukking $\mathbf{B}_{\mathbf{B}_x,\mathbf{G}=\mathbf{0}}$ bevat opnieuw de positie-variabele, waarvan we reeds eerder opmerkten dat we die met de nodige aandacht moeten behandelen. We

[54] Aangezien $\Delta g^{\text{SOO}}_{xy}$ in haast alle gevallen een relatief kleine term is ten opzichte van $\Delta g^{\text{ZKE}}_{xy}$ en $\Delta g^{\text{SO}}_{xy}$, wordt de mathematische afleiding van (A.255) hier achterwege gelaten. De nauwkeurige berekening van het geïnduceerde magnetische veld is van groter belang bij NMR-parameters zoals de susceptibiliteit en de chemische verschuiving. Een nauwkeurige uitwerking is te vinden in Ref. [40].

nemen aan dat de lokalisatie van elke MLWF i transfereerbaar is naar de corresponderende stroomdichtheid. Dan kunnen we met dezelfde definitie van de positie-variabele als in paragraaf A.4.5 (zaagtandprofiel + oorsprong gelijk aan het Wannier-centrum van de corresponderende MLWF) de vermenigvuldiging met de positie-variabele voor elke stroomdichtheid i afzonderlijk uitvoeren:

$$\begin{aligned} \mathbf{B}_{\mathbf{B}_x,\mathbf{G}=\mathbf{0}} &= \kappa\frac{2\pi\alpha}{\Omega}\sum_i\left(\int_\Omega \mathrm{d}\mathbf{r}(\mathbf{r}-\mathbf{d}_i)\times\mathbf{j}^{\mathrm{corr}}_{\mathbf{B}_x,i}(\mathbf{r})\right. \\ &- \left.\int_\Omega \mathrm{d}\mathbf{r}\mathbf{d}_i\times\mathbf{j}^{\mathrm{corr}}_{\mathbf{B}_x,i}(\mathbf{r})\right) . \end{aligned} \tag{A.256}$$

Omwille van (A.247), wordt in de bovenstaande vergelijking de correctieterm voor elke i vermenigvuldigd met nul.

$\mathbf{B}_{\mathbf{B}_x}(\mathbf{r}) = \mathbf{B}_{\mathbf{B}_x,\mathbf{G}\neq\mathbf{0}}(\mathbf{r}) + \mathbf{B}_{\mathbf{B}_x,\mathbf{G}=\mathbf{0}}$ wordt daarna vermenigvuldigd met de spindichtheid $\rho_\mathrm{s} = \rho^\alpha - \rho^\beta$ om de verschillende componenten van $\Delta g^{\mathrm{SOO}}_{xy}$ te bepalen:[55]

$$\begin{aligned} \Delta g^{\mathrm{SOO}}_{xy} &= 2\int \mathrm{d}\mathbf{r}\; B_{\mathbf{B}_x,y}(\mathbf{r})\rho_\mathrm{s}(\mathbf{r}) \\ &= 2\int_{\mathrm{FFT}} \mathrm{d}\mathbf{r}\left(B_{\mathbf{B}_x,\mathbf{G}\neq\mathbf{0},y}(\mathbf{r}) + B_{\mathbf{B}_x,\mathbf{G}=\mathbf{0},y}\right)\rho_\mathrm{s}(\mathbf{r}) . \end{aligned} \tag{A.257}$$

Gebruik van een pure PW-methode voor de g-tensor

Op basis van berekeningen op enkele geïsoleerde moleculen in Ref. [Art. 1/2] kwamen we tot de vaststelling dat de PSP-benadering voor radicalen (in de gasfase) met elementen uit de eerste en tweede rij van de periodieke tabel der elementen voorspellingen voor de g-tensor oplevert van hetzelfde niveau als alle-elektronenberekeningsmethodes voor de gasfase. Voor zwaardere elementen moeten ofwel meer kern-elektronen expliciet in de berekening worden opgenomen dan normaal nodig voor een structuuroptimalisatie, wat door het gebruik van een PW-basisset een zeer grote bijkomende computationele kost creëert, ofwel moeten reconstructietechnieken worden gehanteerd, zoals bijvoorbeeld de (GI)PAW-methode beschreven in Ref. [6] en ook – weliswaar

[55] Merk op dat x de richting van het externe magnetische veld aanduidt, en y de cartesische componenten van $\mathbf{B}_{\mathbf{B}_x}$.

voor de A-tensor – in paragraaf A.5.2. Hoewel de (GI)PAW-methode de voornoemde tekortkomingen grotendeels wegneemt, zal deze toch nooit de effecten van de polarisatie van de kernelektronen kunnen weergeven. Bovendien, zoals werd opgemerkt in Ref. [50], lost de (GI)PAW-methode evenmin de problemen op gerelateerd aan de spinafhankelijke uitwisselings-correlatiepotentiaal v_{XC}^{τ} in de PSP-benadering, nodig voor een correcte beschrijving van de polarisatie van de valentie-elektronen.

A.4.7 De g-tensor in CP2K: implementatie en implicaties

De tekortkomingen bij de berekening van de g-tensor in de PSP-benadering illustreren duidelijk de nood aan een hybride methode die – met een zo klein mogelijke computationele kost – een AE-beschrijving[56] van het radicaal centrum en eventueel zijn directe omgeving mogelijk maakt, terwijl daarnaast een PSP-beschrijving van de overige atomen mogelijk blijft. Een dergelijke benadering zal hoogstwaarschijnlijk geen invloed hebben op de g-tensor, aangezien deze hoofdzakelijk wordt bepaald door de elektronische structuur in een beperkt gebied rond het radicaal centrum. De GAPW-methode (zie paragraaf A.2.6) is voor deze doeleinden uitermate geschikt: de methode bestaat in zowel een PSP- als een AE-variant, en beide kunnen eenvoudig worden gecombineerd binnen één simulatie. Bovendien vereist een GAPW-simulatie met een AE-beschrijving voor de interessante atomen slechts een relatief kleine bijkomende computationele kost, dankzij het gebruik van Gaussische functies[57]. In een pure PW-basisset bijvoorbeeld is de bijkomende computationele kost veel groter.[58]

De berekening van $\Delta g_{xy}^{\mathrm{ZKE}}$ (A.185) in CP2K

$\Delta g_{xy}^{\mathrm{ZKE}}$ wordt in een spingepolariseerde DFT-berekening berekend uitgaande van de kinetische energie van de KS-orbitalen in de basisset van CPGF. De matrixelementen van de kinetische-energie-operator $-\frac{\nabla^2}{2}$ ten opzichte van willekeurige primitieve cartesische Gaussische functies kunnen analytisch worden uitgewerkt.[20]

[56] Dus gebruik makend van de nucleaire Coulomb-potentiaal.

[57] preciezer nog: gecontraheerde periodieke Gaussische functies.

[58] Omdat een basisset met *heel* veel vlakke golven noodzakelijk is voor de correcte beschrijving van de Coulomb-potentiaal en de snelle oscillaties in de golffuncties in de buurt van de atoomkernen.

De berekening van $\Delta g_{xy}^{\mathrm{SO}}$ (A.186) in CP2K

De geïnduceerde stroomdichtheden $\mathbf{j}_{\mathbf{B}_x}^{\tau}$ worden volledig analytisch afgeleid in een Gaussische voorstelling. In de basisset van CPGF zijn de MLWFs gedefinieerd zoals in (A.48):

$$\psi_i^{(0)}(\mathbf{r}) \quad = \quad \sum_k C_{ki}^{(0)} \psi_k^{\mathrm{AO,P}}(\mathbf{r}) \; . \tag{A.258}$$

De matrixelementen van het inhomogeen set van gekoppelde vergelijkingen (A.220) worden gelijk aan:[59]

$$-\sum_{il}\left(H_{\mathrm{KS},kl}\delta_{ij} - S_{kl}\int \mathrm{d}\mathbf{r}\psi_i^{(0)}(\mathbf{r})H_{\mathrm{KS}}(\mathbf{r})\psi_j^{(0)}(\mathbf{r})\right) iC_{li}^{(1)} = \sum_l H_{kl(j)}^{(1)} C_{lj}^{(0)} \; , \quad \forall k,j \; , \tag{A.259}$$

met S_{kl} de elementen van de overlapmatrix en $H_{kl}^{(1)}$ de matrixelementen van de baanimpulsmoment-operator $\mathbf{L}$, de impuls-operator $\mathbf{p}$ en de volledige-correctie-operator $\boldsymbol{\Delta i}$. Merk ook op dat we in (A.259) het imagaire karakter van $\psi_i^{(1)}$ expliciet hebben geschreven, zodat we steeds met reële expansiecoëfficiënten $C_{li}^{(1)}$ kunnen werken.

De positie-operator uit de baanimpulsmoment-operator inwerkend op MLWF j wordt gerefereerd ten opzichte van de positie van de atoomkern $\mathbf{R}_l$ waartoe de atomaire orbitaal $\psi_l^{\mathrm{AO,P}}$ behoort:

$$\begin{aligned} H_{klj}^{L_\alpha} &= -i\epsilon_{\alpha\beta\gamma}\int \mathrm{d}\mathbf{r}\psi_k^{\mathrm{AO,P}}(\mathbf{r})\left((\mathbf{r}-\mathbf{d}_j)_\beta\nabla_\gamma\right)\psi_l^{\mathrm{AO,P}}(\mathbf{r}) \\ &= -i\epsilon_{\alpha\beta\gamma}\left(\int \mathrm{d}\mathbf{r}\psi_k^{\mathrm{AO,P}}(\mathbf{r})\left((\mathbf{r}-\mathbf{R}_l)_\beta\nabla_\gamma\right)\psi_l^{\mathrm{AO,P}}(\mathbf{r})\right. \\ &+ \left.(\mathbf{R}_l-\mathbf{d}_j)_\beta\int \mathrm{d}\mathbf{r}\psi_k^{\mathrm{AO,P}}(\mathbf{r})\left(\nabla_\gamma\right)\psi_l^{\mathrm{AO,P}}(\mathbf{r})\right) \; . \end{aligned} \tag{A.260}$$

Hierdoor zijn de matrixelementen herleid tot gekende integralen over cartesische Gaussische functies.[20] Een bijkomend voordeel is dat deze matrixelementen ook maar één keer moeten worden berekend, in plaats van voor

[59] Ter herinnering (zie paragraaf A.4.5): $\psi_i^{(0)}$ zijn respectievelijk reële en $\psi_i^{(1)}$ imaginaire golffuncties.

elke MLWF afzonderlijk. De matrixelementen van de impuls-operator en de volledige-correctie-operator zijn ook functie van gekende integralen:

$$H_{kl}^{p_\alpha} = -i \int \mathrm{d}\mathbf{r} \psi_k^{\mathrm{AO,P}}(\mathbf{r}) \left(\nabla_\alpha\right) \psi_l^{\mathrm{AO,P}}(\mathbf{r}) \,, \tag{A.261}$$

$$\begin{aligned} H_{klj}^{\Delta i_\alpha} &= -i\epsilon_{\alpha\beta\gamma} \int \mathrm{d}\mathbf{r} \psi_k^{\mathrm{AO,P}}(\mathbf{r}) \left((\mathbf{d}_i - \mathbf{d}_j)_\beta \nabla_\gamma\right) \psi_l^{\mathrm{AO,P}}(\mathbf{r}) \\ &= -i\epsilon_{\alpha\beta\gamma} (\mathbf{d}_i - \mathbf{d}_j)_\beta \int \mathrm{d}\mathbf{r} \psi_k^{\mathrm{AO,P}}(\mathbf{r}) \left(\nabla_\gamma\right) \psi_l^{\mathrm{AO,P}}(\mathbf{r}) \,. \end{aligned} \tag{A.262}$$

Uit de oplossingen van (A.259) voor de storingsoperatoren met matrixelementen gegeven door respectievelijk (A.260), (A.261) en (A.262), halen we de expansiecoëfficiëntenmatrices C^{L_α}, C^{p_γ} en $C^{\Delta i_\alpha}$. Hiermee kunnen we de eerste-ordecorrecties $\psi^{(1)}_{\mathbf{B}_\alpha,i}$ berekenen, alsook hun ruimtelijke afgeleiden $\nabla\psi^{(1)}_{\mathbf{B}_\alpha,i}$:

$$\psi^{(1)}_{\mathbf{B}_\alpha,i}(\mathbf{r}) = -\frac{i\alpha}{2} \sum_k \left(C_{ki}^{L_\alpha} - \epsilon_{\alpha\beta\gamma} (\mathbf{r} - \mathbf{d}_i)_\beta C_{ki}^{p_\gamma} - C_{ki}^{\Delta i_\alpha} \right) \psi_k^{\mathrm{AO,P}}(\mathbf{r}) \,, \tag{A.263}$$

$$\nabla\psi^{(1)}_{\mathbf{B}_\alpha,i}(\mathbf{r}) = -\frac{i\alpha}{2} \sum_k \left(C_{ki}^{L_\alpha} - \epsilon_{\alpha\beta\gamma} (\mathbf{r} - \mathbf{d}_i)_\beta C_{ki}^{p_\gamma} - C_{ki}^{\Delta i_\alpha} \right) \nabla\psi_k^{\mathrm{AO,P}}(\mathbf{r}) \,. \tag{A.264}$$

In een volgende stap worden de stroomdichtheidsmatrices opgebouwd. Wanneer we één stroomdichtheidsmatrix zouden willen maken voor elke richting van het extern magnetisch veld, zou de aanwezigheid van de term $(\mathbf{r} - \mathbf{d}_i)$ in (A.263) en (A.264) ervoor zorgen dat we voor elk punt in de ruimte waar we de stroomdichtheid willen kennen een nieuwe stroomdichtheidsmatrix moeten aanmaken. We zullen dus meerdere stroomdichtheidsmatrices moeten construeren behorend bij verschillende sets van functies van $\mathbf{r}$. Door een bijkomende substitutie $(\mathbf{r} - \mathbf{d}_i) = (\mathbf{r} - \mathbf{R}_l) + (\mathbf{R}_l - \mathbf{d}_i)$ gebeurt dit op de meest efficiënte manier, aangezien de positie-variabele op die manier wordt gescheiden van de MLWF-afhankelijke Wannier-centra. Na substitutie zien (A.263) en (A.264) er als volgt uit:

$$
\begin{aligned}
\psi^{(1)}_{\mathbf{B}_\alpha,i}(\mathbf{r}) &= -\frac{i\alpha}{2}\sum_k \left(C^{L_\alpha}_{ki} - \epsilon_{\alpha\beta\gamma}(\mathbf{R}_k - \mathbf{d}_i)_\beta C^{p_\gamma}_{ki} - C^{\Delta i_\alpha}_{ki}\right)\psi^{\mathrm{AO,P}}_k(\mathbf{r}) \\
&+ \frac{i\alpha}{2}\sum_k \epsilon_{\alpha\beta\gamma} C^{p_\gamma}_{ki}\left((\mathbf{r}-\mathbf{R}_k)_\beta \psi^{\mathrm{AO,P}}_k(\mathbf{r})\right) \\
&= -\frac{i\alpha}{2}\sum_k C^{a_\alpha}_{ki}\psi^{\mathrm{AO,P}}_k(\mathbf{r}) \\
&+ \frac{i\alpha}{2}\sum_k \epsilon_{\alpha\beta\gamma} C^{p_\gamma}_{ki}\left((\mathbf{r}-\mathbf{R}_k)_\beta \psi^{\mathrm{AO,P}}_k(\mathbf{r})\right)\ , \qquad \text{(A.265)} \\
\nabla\psi^{(1)}_{\mathbf{B}_\alpha,i}(\mathbf{r}) &= -\frac{i\alpha}{2}\sum_k C^{a_\alpha}_{ki}\nabla\psi^{\mathrm{AO,P}}_k(\mathbf{r}) \\
&+ \frac{i\alpha}{2}\sum_k \epsilon_{\alpha\beta\gamma} C^{p_\gamma}_{ki}\left((\mathbf{r}-\mathbf{R}_k)_\beta \nabla\psi^{\mathrm{AO,P}}_k(\mathbf{r})\right)\ . \qquad \text{(A.266)}
\end{aligned}
$$

Hieruit berekenen we dan de spinafhankelijke stroomdichtheid volgens (A.232):[60]

$$
\begin{aligned}
\mathbf{j}^\tau_{\mathbf{B}_\alpha}(\mathbf{r}) &= \sum_i^{n_\tau} \mathbf{j}_{\mathbf{B}_\alpha,i}(\mathbf{r}) \\
&= -i\sum_i^{n_\tau}\left[\left(\nabla\psi^{(0)}_i(\mathbf{r})\right)\psi^{(1)}_{\mathbf{B}_\alpha,i}(\mathbf{r}) - \psi^{(0)}_i(\mathbf{r})\left(\nabla\psi^{(1)}_{\mathbf{B}_\alpha,i}(\mathbf{r})\right)\right] \\
&= -\frac{\alpha}{2}\sum_i^{n_\tau}\left[\sum_{kl}\left(C^{(0)}_{ki}C^{a_\alpha}_{li}\right)\left\{\nabla\psi^{\mathrm{AO,P}}_k(\mathbf{r})\psi^{\mathrm{AO,P}}_l(\mathbf{r}) - \psi^{\mathrm{AO,P}}_k(\mathbf{r})\nabla\psi^{\mathrm{AO,P}}_l(\mathbf{r})\right\}\right. \\
&- \epsilon_{\alpha\beta\gamma}\sum_{kl}\left(C^{(0)}_{ki}C^{p_\gamma}_{li}\right)\left\{\nabla\psi^{\mathrm{AO,P}}_k(\mathbf{r})(\mathbf{r}-\mathbf{R}_l)_\beta\psi^{\mathrm{AO,P}}_l(\mathbf{r})\right. \\
&- \left.\left.\psi^{\mathrm{AO,P}}_k(\mathbf{r})(\mathbf{r}-\mathbf{R}_l)_\beta\nabla\psi^{\mathrm{AO,P}}_l(\mathbf{r})\right\}\right]\ . \qquad \text{(A.267)}
\end{aligned}
$$

Twaalf stroomdichtheidsmatrices, te weten:

$$
J^{a_\alpha,\tau}_{kl} = \sum_i^{n_\tau} C^{(0)}_{ki}C^{a_\alpha}_{li}\ , \qquad J^{p_\alpha,\tau}_{kl} = \sum_i^{n_\tau} C^{(0)}_{ki}C^{p_\alpha}_{li} \qquad (\alpha = x,y,z;\tau = \alpha,\beta)\ , \text{(A.268)}
$$

[60] Ter herinnering: we berekenen de stroomdichtheid in de CSGT-methode.

zijn dus nodig om de spinafhankelijke stroomdichtheden als gevolg van een extern magnetisch veld in de 3 cartesische richtingen te beschrijven, omdat deze stroomdichtheidsmatrices voorkomen in combinatie met verschillende functies van CPGFs [benadrukt via haakjes $\{\}$ in (A.267)].

Voor de berekening van $\Delta g_{xy}^{\mathrm{SO}}$ worden deze stroomdichtheden vervolgens op de hulpbasisset (vlakke golven bij de GPW-methode, een combinatie van vlakke golven en primitieve periodieke Gaussische functies bij de GAPW-methode) geprojecteerd.

In de GAPW-methode wordt net zoals bij de elektronendichtheid een GAPW-voorstelling van de stroomdichtheid geconstrueerd, dit is een opsplitsing in globale en lokale componenten die voldoet aan de voorwaarden (A.87)-(A.90).

De zachte globale component ontstaat terug door in $\psi_i^{(0)}$ en $\psi_i^{(1)}$ de coëfficiënten behorend bij de sterkst gelokaliseerde primitieve Gaussische functies op nul te stellen, zodat in (A.267) effectief slechts functies van een beperkte set $\tilde{\chi}^{\mathrm{P}}$ worden gebruikt. Deze functies worden, na vermenigvuldiging met de corresponderende coëfficiënt, geëvalueerd op de discrete punten van het FFT-raster in de reële ruimte, en nadien passend opgeteld.

Voor de lokale componenten wordt via een bijkomende substitutie $(\mathbf{r}-\mathbf{R}_k) = (\mathbf{r}-\mathbf{R}_I)+(\mathbf{R}_I-\mathbf{R}_k)$ in (A.265) en (A.266) de positie-variabele gerefereerd ten opzicht van de positie van de atoomkern I:

$$\begin{aligned}
\psi^{(1)}_{\mathbf{B}_\alpha,i}(\mathbf{r}) &= -\frac{i\alpha}{2}\sum_k C_{ki}^{a_\alpha}\psi_k^{\mathrm{AO,P}}(\mathbf{r}) \\
&+ \frac{i\alpha}{2}\sum_k \epsilon_{\alpha\beta\gamma} C_{ki}^{p_\gamma}\left((\mathbf{r}-\mathbf{R}_k)_\beta \psi_k^{\mathrm{AO,P}}(\mathbf{r})\right) \\
&= -\frac{i\alpha}{2}\sum_k C_{ki}^{a_\alpha}\psi_k^{\mathrm{AO,P}}(\mathbf{r}) \\
&+ \frac{i\alpha}{2}\sum_k \epsilon_{\alpha\beta\gamma} C_{ki}^{p_\gamma}\left((\mathbf{R}_I-\mathbf{R}_k)_\beta \psi_k^{\mathrm{AO,P}}(\mathbf{r})\right) \\
&+ \frac{i\alpha}{2}\sum_k \epsilon_{\alpha\beta\gamma} C_{ki}^{p_\gamma}\left((\mathbf{r}-\mathbf{R}_I)_\beta \psi_k^{\mathrm{AO,P}}(\mathbf{r})\right) \\
&= -\frac{i\alpha}{2}\sum_k C_{ki}^{a'_\alpha}\psi_k^{\mathrm{AO,P}}(\mathbf{r}) \\
&+ \frac{i\alpha}{2}\sum_k \epsilon_{\alpha\beta\gamma} C_{ki}^{p_\gamma}\left((\mathbf{r}-\mathbf{R}_I)_\beta \psi_k^{\mathrm{AO,P}}(\mathbf{r})\right) . \qquad \text{(A.269)}
\end{aligned}$$

Aangezien de CPGF worden ontwikkeld in de primitieve Gaussische functies χ_I^{P} en $\tilde{\chi}_I^{\mathrm{P}}$ behorend bij de atoomkern I, kunnen we dankzij deze substitutie de lokale stroomdichtheid uitschrijven met een beperkt aantal stroomdichtheidsmatrices behorend bij verschillende sets van functies van primitieve Gaussische functies met centrum in $\mathbf{R}_I$:

$$\begin{aligned}
\mathbf{j}^{1,\tau}_{\mathbf{B}_\alpha,I}(\mathbf{r}) &= -\frac{\alpha}{2}\left[\sum_{vw}\sum_{kl} Q^I_{vk} J^{a'_\alpha,\tau}_{kl} Q^I_{wl}\left\{\nabla\chi^{\mathrm{P}}_{I,v}(\mathbf{r})\chi^{\mathrm{P}}_{I,w}(\mathbf{r}) - \chi^{\mathrm{P}}_{I,v}(\mathbf{r})\nabla\chi^{\mathrm{P}}_{I,w}(\mathbf{r})\right\}\right. \\
&- \epsilon_{\alpha\beta\gamma}\sum_{vw}\sum_{kl} Q^I_{vk} J^{p_\alpha,\tau}_{kl} Q^I_{wl}\left\{\nabla\chi^{\mathrm{P}}_{I,v}(\mathbf{r})(\mathbf{r}-\mathbf{R}_I)_\beta\chi^{\mathrm{P}}_{I,w}(\mathbf{r})\right. \\
&- \left.\left.\chi^{\mathrm{P}}_{I,v}(\mathbf{r})(\mathbf{r}-\mathbf{R}_I)_\beta\nabla\chi^{\mathrm{P}}_{I,w}(\mathbf{r})\right\}\right] , \qquad \text{(A.270)} \\
\tilde{\mathbf{j}}^{1,\tau}_{\mathbf{B}_\alpha,I}(\mathbf{r}) &= -\frac{\alpha}{2}\left[\sum_{vw}\sum_{kl} \tilde{Q}^I_{vk} J^{a'_\alpha,\tau}_{kl} \tilde{Q}^I_{wl}\left\{\nabla\tilde{\chi}^{\mathrm{P}}_{I,v}(\mathbf{r})\tilde{\chi}^{\mathrm{P}}_{I,w}(\mathbf{r}) - \tilde{\chi}^{\mathrm{P}}_{I,v}(\mathbf{r})\nabla\tilde{\chi}^{\mathrm{P}}_{I,w}(\mathbf{r})\right\}\right. \\
&- \epsilon_{\alpha\beta\gamma}\sum_{vw}\sum_{kl} \tilde{Q}^I_{vk} J^{p_\alpha,\tau}_{kl} \tilde{Q}^I_{wl}\left\{\nabla\tilde{\chi}^{\mathrm{P}}_{I,v}(\mathbf{r})(\mathbf{r}-\mathbf{R}_I)_\beta\tilde{\chi}^{\mathrm{P}}_{I,w}(\mathbf{r})\right. \\
&- \left.\left.\tilde{\chi}^{\mathrm{P}}_{I,v}(\mathbf{r})(\mathbf{r}-\mathbf{R}_I)_\beta\nabla\tilde{\chi}^{\mathrm{P}}_{I,w}(\mathbf{r})\right\}\right] . \qquad \text{(A.271)}
\end{aligned}$$

De matrix Q^I bevat de expansiecoëfficiënten van de CPGF in de primitieve Gaussische functies behorend tot atoomkern I.[61]

De GAPW-representatie van de stroomdichtheid berekend op deze manier convergeert echter zeer traag met de grootte van de Gaussische basisset. Enerzijds wordt dit veroorzaakt door het gebruik van de CSGT-methode in de buurt van de atoomkernen. Als oplossing werd voor $\mathbf{j}^{1,\tau}_{\mathbf{B}_\alpha,I}$ binnen U_I de ijkoorsprong vast gekozen op de positie van de atoomkern I, i.e. $\mathbf{R}_\mathrm{g} = \mathbf{R}_I$. Hierdoor is de diagmagnetische component van de stroomdichtheid (A.232) in dit gebied niet langer gelijk aan nul. Buiten U_I geldt nog steeds dat $\mathbf{R}_\mathrm{g} = \mathbf{r}$,[62] zodat zeker aan (A.88) wordt voldaan. $\mathbf{j}^{1,\tau}_{\mathbf{B}_\alpha,I}$ blijft buiten U_I gelijk aan (A.270), binnen U_I is deze dan gelijk aan:

[61] Voor een CPGF behorend tot de atoomkern I is de expansie natuurlijk gelijk aan (A.52).
[62] De overgang aan de grens van U_I kan (desgewenst) zachter worden gemaakt.

$$\begin{aligned}\mathbf{j}^{1,\tau}_{\mathbf{B}_\alpha,I}(\mathbf{r}) &= -\frac{\alpha}{2}\left[\sum_{vw}\sum_{kl} Q^I_{vk} J^{a'_\alpha,\tau}_{kl} Q^I_{wl}\left\{\nabla\chi^{\mathrm{P}}_{I,v}(\mathbf{r})\chi^{\mathrm{P}}_{I,w}(\mathbf{r}) - \chi^{\mathrm{P}}_{I,v}(\mathbf{r})\nabla\chi^{\mathrm{P}}_{I,w}(\mathbf{r})\right\}\right. \\ &+ \left.\sum_{vw}\sum_{kl} Q^I_{vk} P_{kl} Q^I_{wl}\left\{(\mathbf{B}_\alpha\times\mathbf{r})\,\chi^{\mathrm{P}}_{I,v}(\mathbf{r})\chi^{\mathrm{P}}_{I,w}(\mathbf{r})\right\}\right] \\ &\quad \text{voor } \mathbf{r}\in U_I\ . \end{aligned} \tag{A.272}$$

Een tweede oorzaak voor de trage convergentie betreft het gebruik van de expansiecoëfficiënten Q^I_{vk} voor de ruimtelijke afgeleiden van de CPGF in de primitieve Gaussische functies behorend tot de atoomkern I:

$$\nabla\psi^{\mathrm{AO,P}}_k(\mathbf{r}) = \sum_v Q^I_{vk}\nabla\chi^{\mathrm{P}}_{I,v}(\mathbf{r})\ , \tag{A.273}$$

wat zeker voor kleinere Gaussische basissets een vrij ruwe benadering blijkt. Als oplossing worden nieuwe expansiecoëfficiënten berekend voor elke ruimtelijke afgeleide van $\psi^{\mathrm{AO,P}}_k$ in diezelfde afgeleide van elke primitieve Gaussische functie behorend tot de atoomkern I:

$$\mathbf{Q}^I_{vk} = \int \mathrm{d}\mathbf{r} p_{\nabla\chi^{\mathrm{P}}_{I,v}}(\mathbf{r})\nabla\psi^{\mathrm{AO,P}}_k(\mathbf{r})\ , \tag{A.274}$$

met $\mathbf{Q}^I_{vk} = (Q^I_{vk,x}, Q^I_{vk,y}, Q^I_{vk,z})$ en $p_{\nabla\chi^{\mathrm{P}}_{I,v}}$ de projector corresponderend met $\nabla\chi^{\mathrm{P}}_{I,v}$.

Vervolgens bespreken we de berekeningswijze van $\nabla V^\tau_{\mathrm{KS}}$, de tweede component van $\Delta g^{\mathrm{SO}}_{xy}$.

We maken voor de berekening van $\nabla V^\tau_{\mathrm{KS}}$ een vaste keuze voor de uitwisselings-correlatiepotentiaal, de X_α-potentiaal:[51][63]

$$v^\tau_{\mathrm{X}_\alpha}[\rho(\mathbf{r})] = -\frac{3}{2}\left(\frac{6}{\pi}\right)^{1/3}\alpha\rho^\tau(\mathbf{r})^{1/3}\ , \tag{A.275}$$

een keuze ingegeven door het werk van Schreckenbach en Ziegler.[1] De variabele α is een in te stellen reële parameter, die standaard gelijk is aan 2/3.

[63] Deze potentiaal wordt ook wel de Dirac/Slater-uitwisselingspotentiaal genoemd.

In de GPW-methode is V_{KS}^{τ} zacht, door het verplichte gebruik van pseudopotentialen. We evalueren deze term in de reciproque ruimte en berekenen vervolgens de ruimtelijke afgeleiden, op dezelfde manier als in CPMD. We maken daarbij bovendien handig gebruik van de analytische uitdrukking voor Goedecker-pseudopotentialen in de reciproque ruimte.

In de GAPW-methode proberen we de aanwezigheid van zowel vlakke golven als atoomgecentreerde rasters te benutten. Een GAPW-voorstelling van $\nabla V_{\mathrm{KS}}^{\tau}$ is helaas niet mogelijk: net zoals de elektrostatische energie (zie paragraaf A.2.6) kunnen we weliswaar een opsplitsing maken in onafhankelijke globale en lokale, rond de atoomkern gecentreerde componenten, maar er gelden in het algemeen geen verbanden (A.87-A.90) tussen deze componenten. Wel is het zo dat de lokale componenten beperkt blijven tot een geringe zone rond de atoomkernen. $\nabla V_{\mathrm{KS}}^{\tau}$ wordt opgesplitst in een zachte globale component $\nabla \tilde{V}_{\mathrm{KS}}^{\tau,\mathrm{PSP}}$ of $\nabla \tilde{V}_{\mathrm{KS}}^{\tau,\mathrm{AE}}$ en lokale componenten $\nabla V_{\mathrm{KS},I}^{\tau,1,\mathrm{PSP}}$ of $\nabla V_{\mathrm{KS},I}^{\tau,1,\mathrm{AE}}$ (naargelang een pseudopotentiaal of een nucleaire Coulombpotentiaal wordt gebruikt), gedefinieerd als:

$$\begin{aligned}
\nabla \tilde{V}_{\mathrm{KS}}^{\tau,\mathrm{PSP}}(\mathbf{r}) &= \nabla \left(\sum_{I \in \mathrm{PSP}} V_{\mathrm{loc,sr},I}^{\mathrm{PSP}} H(\alpha_{\mathrm{c}} - \frac{1}{2r_{\mathrm{loc},I}^2}) + v_{\mathrm{H}}[\tilde{\rho}(\mathbf{r}) + \rho^0(\mathbf{r})] \right. \\
&+ \left. v_{X_\alpha}^{\tau}[\tilde{\rho}(\mathbf{r})] \right) , \qquad \text{(A.276)} \\
\nabla \tilde{V}_{\mathrm{KS}}^{\tau,\mathrm{AE}}(\mathbf{r}) &= \nabla \left(v_{\mathrm{H}}[\tilde{\rho}(\mathbf{r}) + \rho^0(\mathbf{r})] + v_{X_\alpha}^{\tau}[\tilde{\rho}(\mathbf{r})] \right) , \qquad \text{(A.277)} \\
\nabla V_{\mathrm{KS},I}^{\tau,1,\mathrm{PSP}}(\mathbf{r}) &= \nabla \left(V_{\mathrm{loc,sr},I}^{\mathrm{PSP}}(\mathbf{r}) H'(\alpha_{\mathrm{c}} - \frac{1}{2r_{\mathrm{loc},I}^2}) + v_{\mathrm{H}}[\rho_I^1(\mathbf{r}) + \rho_I^{\mathrm{c}}(\mathbf{r})] \right. \\
&- \left. v_{\mathrm{H}}[\tilde{\rho}_I^1(\mathbf{r}) + \rho_I^0(\mathbf{r})] + v_{X_\alpha}^{\tau}[\rho_I^1(\mathbf{r})] - v_{X_\alpha}^{\tau}[\tilde{\rho}_I^1(\mathbf{r})] \right) , \qquad \text{(A.278)} \\
\nabla V_{\mathrm{KS},I}^{\tau,1,\mathrm{AE}}(\mathbf{r}) &= \nabla \left(\frac{Q_I}{r} \mathrm{erfc} \left(\frac{r}{\sqrt{2} r_{\mathrm{loc},I}} \right) + v_{\mathrm{H}}[\rho_I^1(\mathbf{r}) + \rho_I^{\mathrm{c}}(\mathbf{r})] \right. \\
&- \left. v_{\mathrm{H}}[\tilde{\rho}_I^1(\mathbf{r}) + \rho_I^0(\mathbf{r})] + v_{X_\alpha}^{\tau}[\rho_I^1(\mathbf{r})] - v_{X_\alpha}^{\tau}[\tilde{\rho}_I^1(\mathbf{r})] \right) . \qquad \text{(A.279)}
\end{aligned}$$

H is de Heaviside-functie, en $H' = -(H-1)$, wat ervoor zorgt dat $V_{\mathrm{loc,sr},I}^{\mathrm{PSP}}$ in de globale respectievelijk bijpassende lokale component wordt opgenomen, al naargelang de exponentiële functie in (A.77) trager of sneller afvalt dan $e^{-\alpha_{\mathrm{c}} r^2}$, met α_{c} een zelf in te stellen limietwaarde. We verwaarlozen dus de niet-lokale component van de pseudopotentialen, die toch enkel invloed heeft in de nabije omgeving van de betreffende atoomkern. Het lange-drachtsgedrag

van de pseudopotentiaal blijft dus gevrijwaard, zodat we ons in die regio van de simulatiecel waar een AE-beschrijving nodig is geen zorgen moeten maken over het gebruik van pseudopotentialen voor de overige atomen in de simulatiecel. De zachte $\tilde{V}_{\mathrm{KS}}^{\tau}$ wordt in de reciproque ruimte opgebouwd, en vervolgens worden de ruimtelijke afgeleiden berekend, opnieuw op dezelfde manier als in CPMD. $V_{\mathrm{KS},I}^{\tau,1,\mathrm{PSP}}$ en $V_{\mathrm{KS},I}^{\tau,1,\mathrm{AE}}$ gaan snel naar nul voor groter wordende $r = |\mathbf{r}|$, een effect dat nog wordt versterkt voor hun ruimtelijke afgeleiden. Wij zullen steeds veronderstellen dat $\nabla V_{\mathrm{KS},I}^{\tau,1,\mathrm{PSP}}$ en $\nabla V_{\mathrm{KS},I}^{\tau,1,\mathrm{AE}}$ enkel beduidend zijn binnen U_I.

We hebben nu alle termen van $\Delta g_{xy}^{\mathrm{SO}}$ in hun globale en lokale componenten uitgewerkt. De effectieve berekening van $\Delta g_{xy}^{\mathrm{SO}}$ is dan de volgende uitdrukking:

$$\begin{aligned}
\Delta g_{xy}^{\mathrm{SO}} = \quad & \frac{\alpha g'}{2} \Bigg\{ \int \mathrm{d}\mathbf{r} \left[\tilde{\mathbf{j}}_{\mathbf{B}_x}^{\alpha}(\mathbf{r}) \times \nabla \tilde{V}_{\mathrm{KS}}^{\alpha}(\mathbf{r}) - \tilde{\mathbf{j}}_{\mathbf{B}_x}^{\beta}(\mathbf{r}) \times \nabla \tilde{V}_{\mathrm{KS}}^{\beta}(\mathbf{r}) \right]_y \\
& + \sum_I \int \mathrm{d}\mathbf{r} \left[\tilde{\mathbf{j}}_{\mathbf{B}_x,I}^{\alpha,1}(\mathbf{r}) \times \nabla V_{\mathrm{KS},I}^{\alpha,1}(\mathbf{r}) \right]_y \\
& - \sum_I \int \mathrm{d}\mathbf{r} \left[\tilde{\mathbf{j}}_{\mathbf{B}_x,I}^{\beta,1}(\mathbf{r}) \times \nabla V_{\mathrm{KS},I}^{\beta,1}(\mathbf{r}) \right]_y \\
& + \sum_I \int \mathrm{d}\mathbf{r} \left[\left(\mathbf{j}_{\mathbf{B}_x,I}^{\alpha,1}(\mathbf{r}) - \tilde{\mathbf{j}}_{\mathbf{B}_x,I}^{\alpha,1}(\mathbf{r}) \right) \times \nabla \tilde{V}_{\mathrm{KS}}^{\alpha}(\mathbf{r}) \right]_y \\
& - \sum_I \int \mathrm{d}\mathbf{r} \left[\left(\mathbf{j}_{\mathbf{B}_x,I}^{\beta,1}(\mathbf{r}) - \tilde{\mathbf{j}}_{\mathbf{B}_x,I}^{\beta,1}(\mathbf{r}) \right) \times \nabla \tilde{V}_{\mathrm{KS}}^{\beta}(\mathbf{r}) \right]_y \\
& + \sum_I \int \mathrm{d}\mathbf{r} \left[\left(\mathbf{j}_{\mathbf{B}_x,I}^{\alpha,1}(\mathbf{r}) - \tilde{\mathbf{j}}_{\mathbf{B}_x,I}^{\alpha,1}(\mathbf{r}) \right) \times \nabla V_{\mathrm{KS},I}^{\alpha,1}(\mathbf{r}) \right]_y \\
& - \sum_I \int \mathrm{d}\mathbf{r} \left[\left(\mathbf{j}_{\mathbf{B}_x,I}^{\beta,1}(\mathbf{r}) - \tilde{\mathbf{j}}_{\mathbf{B}_x,I}^{\beta,1}(\mathbf{r}) \right) \times \nabla V_{\mathrm{KS},I}^{\beta,1}(\mathbf{r}) \right]_y \Bigg\} \ , \qquad \text{(A.280)}
\end{aligned}$$

wat vereenvoudigt tot:

$$\begin{aligned}\Delta g_{xy}^{\mathrm{SO}} = \quad & \frac{\alpha g'}{2}\left\{\int_{\mathrm{FFT}} \mathrm{d}\mathbf{r}\left[\tilde{\mathbf{j}}_{\mathbf{B}_x}^{\alpha}(\mathbf{r}) \times \nabla \tilde{V}_{\mathrm{KS}}^{\alpha}(\mathbf{r}) - \tilde{\mathbf{j}}_{\mathbf{B}_x}^{\beta}(\mathbf{r}) \times \nabla \tilde{V}_{\mathrm{KS}}^{\beta}(\mathbf{r})\right]_y\right. \\ & + \sum_I \int_{\mathrm{LL},U_I} \mathrm{d}\mathbf{r}\left[\left(\mathbf{j}_{\mathbf{B}_x,I}^{\alpha,1}(\mathbf{r}) - \tilde{\mathbf{j}}_{\mathbf{B}_x,I}^{\alpha,1}(\mathbf{r})\right) \times \nabla \tilde{V}_{\mathrm{KS}}^{\alpha}(\mathbf{r})\right]_y \\ & - \sum_I \int_{\mathrm{LL},U_I} \mathrm{d}\mathbf{r}\left[\left(\mathbf{j}_{\mathbf{B}_x,I}^{\beta,1}(\mathbf{r}) - \tilde{\mathbf{j}}_{\mathbf{B}_x,I}^{\beta,1}(\mathbf{r})\right) \times \nabla \tilde{V}_{\mathrm{KS}}^{\beta}(\mathbf{r})\right]_y \\ & + \sum_I \int_{\mathrm{LL},U_I} \mathrm{d}\mathbf{r}\left[\mathbf{j}_{\mathbf{B}_x,I}^{\alpha,1}(\mathbf{r}) \times \nabla V_{\mathrm{KS},I}^{\alpha,1}(\mathbf{r})\right]_y \\ & \left. - \sum_I \int_{\mathrm{LL},U_I} \mathrm{d}\mathbf{r}\left[\mathbf{j}_{\mathbf{B}_x,I}^{\beta,1}(\mathbf{r}) \times \nabla V_{\mathrm{KS},I}^{\beta,1}(\mathbf{r})\right]_y\right\} . \end{aligned} \tag{A.281}$$

Het onderschrift LL betekent dat de integratie uitgevoerd wordt op een sferisch raster gecentreerd op de positie van de atoomkern, logaritmisch in de radiale component en met een hoekafhankelijke verdeling van het Lebedev-type.[52–54] U_I duidt erop dat het integratiedomein mag worden beperkt tot de sferische regio rond atoomkern I. De tweede en derde term van de bovenstaande vergelijking bevatten de zachte componenten $\nabla \tilde{V}_{\mathrm{KS}}^{\tau}$. Deze zijn enkel beschikbaar op het FFT-raster, maar moeten worden vermenigvuldigd met spinstroomdichtheden gedefinieerd op de LL-rasters rond elke atoomkern I. Dit probleem wordt opgelost via lineaire interpolatie van de waarden van $\nabla \tilde{V}_{\mathrm{KS}}^{\tau}$ van de FFT-rasterpunten naar de LL-rasterpunten.

De berekening van $\Delta g_{xy}^{\mathrm{SOO}}$ (A.187) in CP2K

Het geïnduceerde magnetische veld (A.182) wordt berekend uitgaande van een niet-lokale operator inwerkend op de stroomdichtheid. Hierdoor is het moeilijk om uit de GAPW-voorstelling van de stroomdichtheid een GAPW-voorstelling van het geïnduceerde magnetische veld te ontwikkelen. Ook een analytische afleiding via de Gaussische voorstelling van de stroomdichtheid ligt niet voor de hand. Daartegenover staat de (reeds eerder vermelde) vaststelling dat $\Delta g_{xy}^{\mathrm{SOO}}$ in haast alle gevallen een relatief kleine term is ten opzichte van $\Delta g_{xy}^{\mathrm{ZKE}}$ en $\Delta g_{xy}^{\mathrm{SO}}$. Daarom zullen we de moeilijk te berekenen bijdragen van de atoomgecentreerde stroomdichtheden $\mathbf{j}_{\mathbf{B}_x}^{\mathrm{corr},1} - \tilde{\mathbf{j}}_{\mathbf{B}_x}^{\mathrm{corr},1}$ tot de $(\mathbf{G} \neq \mathbf{0})$-componenten van het magnetisch veld verwaarlozen. $\tilde{\mathbf{B}}_{\mathbf{B}_x,\mathbf{G}\neq\mathbf{0}}$ (let op de tilde) is dus enkel afkomstig van de zachte stroomdichtheid $\tilde{\mathbf{j}}_{\mathbf{B}_x}^{\mathrm{corr}}$, en wordt berekend via (A.253). $\mathbf{B}_{\mathbf{B}_x,\mathbf{G}=\mathbf{0}}$ wordt berekend via (A.256) op analytische

wijze via de Gaussische voorstelling van de stroomdichtheid (zie verderop). In formulevorm samenvattend wordt $\Delta g_{xy}^{\mathrm{SOO}}$ dus als volgt berekend:[64]

$$\begin{aligned}
\Delta g_{xy}^{\mathrm{SOO}} &= 2\int \mathrm{d}\mathbf{r}\; B_{\mathbf{B}_x,y}(\mathbf{r})\rho_{\mathrm{s}}(\mathbf{r}) \\
&\approx 2\int \mathrm{d}\mathbf{r}\left(\tilde{B}_{\mathbf{B}_x,\mathbf{G}\neq\mathbf{0},y}(\mathbf{r}) + B_{\mathbf{B}_x,\mathbf{G}=\mathbf{0},y}\right)\left(\tilde{\rho}_{\mathrm{s}}(\mathbf{r}) + \rho_{\mathrm{s}}^1(\mathbf{r}) - \tilde{\rho}_{\mathrm{s}}^1(\mathbf{r})\right) \\
&= 2\int_{\mathrm{FFT}} \mathrm{d}\mathbf{r}\tilde{B}_{\mathbf{B}_x,\mathbf{G}\neq\mathbf{0},y}(\mathbf{r})\tilde{\rho}_{\mathrm{s}}(\mathbf{r}) \\
&+ 2\sum_I \int_{U_I} \mathrm{d}\mathbf{r}\tilde{B}_{\mathbf{B}_x,\mathbf{G}\neq\mathbf{0},y}(\mathbf{r})\left(\rho_{\mathrm{s},I}^1(\mathbf{r}) - \tilde{\rho}_{\mathrm{s},I}^1(\mathbf{r})\right) \\
&+ 2B_{\mathbf{B}_x,\mathbf{G}=\mathbf{0},y}\;. \qquad \text{(A.282)}
\end{aligned}$$

$\mathbf{B}_{\mathbf{B}_x,\mathbf{G}=\mathbf{0}}$ wordt, zoals reeds gezegd, berekend via (A.256). De stroomdichtheid afkomstig van elk elektron – zonder de bijkomende substituties die tot doel hadden de stroomdichtheid met een beperkt aantal dichtheidsmatrices te beschrijven – is gelijk aan:

$$\begin{aligned}
\mathbf{j}_{\mathbf{B}_\alpha,i}(\mathbf{r}) &= -\frac{\alpha}{2}\sum_{kl} C_{ki}^{(0)}\left(C_{li}^{L_\alpha} - \epsilon_{\alpha\beta\gamma}(\mathbf{r}-\mathbf{d}_i)_\beta C_{li}^{p_\gamma} - C_{li}^{\Delta i_\alpha}\right) \\
&\quad \left\{\nabla\psi_k^{\mathrm{AO,P}}(\mathbf{r})\psi_l^{\mathrm{AO,P}}(\mathbf{r}) - \psi_k^{\mathrm{AO,P}}(\mathbf{r})\nabla\psi_l^{\mathrm{AO,P}}(\mathbf{r})\right\}\;. \qquad \text{(A.283)}
\end{aligned}$$

Invullen van deze stroomdichtheid in (A.256), en rekening houdend met de volgende eigenschappen voor $\beta' \neq \gamma'$:

$$\begin{aligned}
&\int \mathrm{d}\mathbf{r}\left(\frac{\partial}{\partial\gamma'}\psi_k^{\mathrm{AO,P}}(\mathbf{r})\right)(\mathbf{r}-\mathbf{d}_i)_{\beta'}\psi_l^{\mathrm{AO,P}}(\mathbf{r}) \\
&= -\int \mathrm{d}\mathbf{r}\psi_k^{\mathrm{AO,P}}(\mathbf{r})(\mathbf{r}-\mathbf{d}_i)_{\beta'}\left(\frac{\partial}{\partial\gamma'}\psi_l^{\mathrm{AO,P}}(\mathbf{r})\right)\;, \qquad \text{(A.284)} \\
&\int \mathrm{d}\mathbf{r}\left(\frac{\partial}{\partial\gamma'}\psi_k^{\mathrm{AO,P}}(\mathbf{r})\right)(\mathbf{r}-\mathbf{d}_i)_{\beta'}(\mathbf{r}-\mathbf{d}_i)_\alpha\psi_l^{\mathrm{AO,P}}(\mathbf{r}) \\
&= -\int \mathrm{d}\mathbf{r}\psi_k^{\mathrm{AO,P}}(\mathbf{r})(\mathbf{r}-\mathbf{d}_i)_{\beta'}(\mathbf{r}-\mathbf{d}_i)_\alpha\left(\frac{\partial}{\partial\gamma'}\psi_l^{\mathrm{AO,P}}(\mathbf{r})\right) \\
&-\delta_{\alpha,\gamma'}\int \mathrm{d}\mathbf{r}\psi_k^{\mathrm{AO,P}}(\mathbf{r})(\mathbf{r}-\mathbf{d}_i)_{\beta'}(\mathbf{r}-\mathbf{d}_i)_\alpha\psi_l^{\mathrm{AO,P}}(\mathbf{r})\;, \qquad \text{(A.285)}
\end{aligned}$$

[64] Ter herinnering: we gaan (zie de inleiding) steeds uit van een elektronisch systeem met netto elektronische spin gelijk aan $\frac{1}{2}$, de integraal van de spindichtheid over de simulatiecel is dan exact gelijk aan 1, waardoor de constante term $\mathbf{B}_{\mathbf{B}_x,\mathbf{G}=\mathbf{0}}$ in (A.282) overblijft.

krijgen we voor de α'-component van $\mathbf{B}_{\mathbf{B}_\alpha,\mathbf{G}=\mathbf{0}}$, met n_β het aantal spin-neer-elektronen:

$$
\begin{aligned}
B_{\mathbf{B}_\alpha,\mathbf{G}=\mathbf{0},\alpha'} &= \kappa\frac{\pi\alpha^2}{\Omega}\sum_i^{n_\beta}\Bigg\{\sum_{kl}C_{ki}^{(0)}\left(C_{li}^{L_\alpha}-C_{li}^{\Delta i_\alpha}\right)\times \\
&\quad\Bigg[2\int \mathrm{d}\mathbf{r}\psi_k^{\mathrm{AO,P}}(\mathbf{r})(\mathbf{r}-\mathbf{d}_i)_{\beta'}\left(\frac{\partial}{\partial\gamma'}\psi_l^{\mathrm{AO,P}}(\mathbf{r})\right) \\
&\quad -2\int \mathrm{d}\mathbf{r}\psi_k^{\mathrm{AO,P}}(\mathbf{r})(\mathbf{r}-\mathbf{d}_i)_{\gamma'}\left(\frac{\partial}{\partial\beta'}\psi_l^{\mathrm{AO,P}}(\mathbf{r})\right) \\
&\quad +2d_{i,\beta'}\int \mathrm{d}\mathbf{r}\psi_k^{\mathrm{AO,P}}(\mathbf{r})\left(\frac{\partial}{\partial\gamma'}\psi_l^{\mathrm{AO,P}}(\mathbf{r})\right) \\
&\quad -2d_{i,\gamma'}\int \mathrm{d}\mathbf{r}\psi_k^{\mathrm{AO,P}}(\mathbf{r})\left(\frac{\partial}{\partial\beta'}\psi_l^{\mathrm{AO,P}}(\mathbf{r})\right)\Bigg] \\
&- \epsilon_{\alpha\beta\gamma}\sum_{kl}C_{ki}^{(0)}C_{li}^{p_\gamma}\times \\
&\quad\Bigg[2\int \mathrm{d}\mathbf{r}\psi_k^{\mathrm{AO,P}}(\mathbf{r})(\mathbf{r}-\mathbf{d}_i)_{\beta'}(\mathbf{r}-\mathbf{d}_i)_{\beta}\left(\frac{\partial}{\partial\gamma'}\psi_l^{\mathrm{AO,P}}(\mathbf{r})\right) \\
&\quad +\delta_{\beta\gamma'}\int \mathrm{d}\mathbf{r}\psi_k^{\mathrm{AO,P}}(\mathbf{r})(\mathbf{r}-\mathbf{d}_i)_{\beta'}\left(\frac{\partial}{\partial\gamma'}\psi_l^{\mathrm{AO,P}}(\mathbf{r})\right) \\
&\quad -2\int \mathrm{d}\mathbf{r}\psi_k^{\mathrm{AO,P}}(\mathbf{r})(\mathbf{r}-\mathbf{d}_i)_{\gamma'}(\mathbf{r}-\mathbf{d}_i)_{\beta}\left(\frac{\partial}{\partial\beta'}\psi_l^{\mathrm{AO,P}}(\mathbf{r})\right) \\
&\quad -\delta_{\beta\beta'}\int \mathrm{d}\mathbf{r}\psi_k^{\mathrm{AO,P}}(\mathbf{r})(\mathbf{r}-\mathbf{d}_i)_{\gamma'}\left(\frac{\partial}{\partial\beta'}\psi_l^{\mathrm{AO,P}}(\mathbf{r})\right) \\
&\quad +2d_{i,\beta'}\int \mathrm{d}\mathbf{r}\psi_k^{\mathrm{AO,P}}(\mathbf{r})(\mathbf{r}-\mathbf{d}_i)_{\beta}\left(\frac{\partial}{\partial\gamma'}\psi_l^{\mathrm{AO,P}}(\mathbf{r})\right) \\
&\quad -2d_{i,\gamma'}\int \mathrm{d}\mathbf{r}\psi_k^{\mathrm{AO,P}}(\mathbf{r})(\mathbf{r}-\mathbf{d}_i)_{\beta}\left(\frac{\partial}{\partial\beta'}\psi_l^{\mathrm{AO,P}}(\mathbf{r})\right)\Bigg]\Bigg\}\ .
\end{aligned}
\tag{A.286}
$$

Gebruik van de GPW-methode voor de g-tensor

De GPW-methode voor de g-tensor heeft dezelfde tekortkomingen als de implementatie in CPMD (en werd eigenlijk hoofdzakelijk geïmplementeerd ter verificatie van diverse onderdelen van de CP2K-implementatie, vooraleer deze uit te breiden naar de GAPW-methode).

Gebruik van de GAPW-methode voor de g-tensor

In Ref. [Art. 9] wordt de GAPW-methode voor de g-tensor uitgebreid getest. De g-tensoren van een uitgebreide selectie van kleine molecules in de gasfase, berekend met de AE-variant van de GAPW-methode, stemmen uitstekend overeen met deze geproduceerd door ADF,[55] een simulatiepakket (uitsluitend) voor berekeningen in de gasfase, dat eveneens de LCAO-benadering aanneemt maar de atomaire orbitalen uitdrukt als Slater-type-functies (zie daarvoor Ref. [55]). Daarnaast heeft het hybride gebruik van de AE-variant voor het radicalair centrum en de PSP-variant voor de omgeving geen significante invloed op de berekende g-tensoren. We kunnen dus stellen dat we een accurate en tegelijkertijd relatief goedkope methode (in termen van computationele kost) hebben afgeleid voor de berekening van g-tensoren in PBC-simulaties. Toch wensen we op te merken dat de GAPW-methode (net zoals de GPW-methode) voorlopig enkel in de Γ-puntbenadering beschikbaar is, wat de keuzemogelijkheden voor de dimensies van de simulatiecel van een te bestuderen materiaal beïnvloedt, en op die manier ook bepaalt of dit materiaal in deze benadering wel aan een redelijke computationele kost kan worden gesimuleerd.

A.5 Berekening van de A-tensor in PBC-simulaties

A.5.1 De A-tensor in DFT

Voor de berekening van de A-tensor van atoomkern I, A_I, gedefinieerd volgens (A.158),

$$A_{I,xy} = \langle \Psi | \left. \frac{\partial^2 H^{\mathrm{A}_I}}{\partial I_{I,x} \partial S_y} \right|_{\mathbf{I}_I = \mathbf{S} = \mathbf{0}} | \Psi \rangle \ , \tag{A.287}$$

maken we opnieuw gebruik van spinveldreductie en het Wigner-Eckhart-theorema (zie hoofdstuk A.4.1) op de termen $H_{\mathrm{FC},I}$ (A.156) en $H_{\mathrm{DC},I}$ (A.157). Dit geeft:

$$A_{I,xy} = \int\limits_{\mathbf{r}'=\mathbf{r}} \mathrm{d}\mathbf{r} \left[\frac{\partial}{\partial I_{I,x}} \left(h_{\mathrm{FC},I,y} + h_{\mathrm{DC},I,y} \right) \right]_{\mathbf{I}_I = \mathbf{0}} \left(\rho^{\alpha}(\mathbf{r}, \mathbf{r}') - \rho^{\beta}(\mathbf{r}, \mathbf{r}') \right) , \tag{A.288}$$

met $h_{\mathrm{FC},I,y}$ en $h_{\mathrm{DC},I,y}$ in een elektronisch systeem met netto elektronische spin gelijk $\frac{1}{2}$ gegeven door:

$$h_{\mathrm{FC},I,y} = \frac{2}{3}\mu_0 g_e \mu_e g_I \mu_I \delta\left(\mathbf{r}' - \mathbf{R}_I\right) I_{I,y} \,, \tag{A.289}$$

$$h_{\mathrm{DC},I,y} = \frac{1}{4\pi}\mu_0 g_e \mu_e g_I \mu_I \left[\frac{3\left(\mathbf{r}' - \mathbf{R}_I\right)^{\mathrm{T}}\left(\mathbf{r}' - \mathbf{R}_I\right) - \mathbf{1}\left|\mathbf{r}' - \mathbf{R}_I\right|^2}{\left|\mathbf{r}' - \mathbf{R}_I\right|^5} \cdot \mathbf{I}_I\right]_y \,. \tag{A.290}$$

Gerefereerd ten opzichte van een coördinatenstelsel met de oorsprong gelijk aan de positie van de atoomkern I, en na invoering van de spindichtheid $\rho_{\mathrm{s}} = \rho^{\alpha} - \rho^{\beta}$, vereenvoudigt (A.288) tot:

$$A_{I,xy} = A^{\mathrm{iso}}_{I,xy}\delta_{xy} + A^{\mathrm{ani}}_{I,xy} \,, \tag{A.291}$$

$$A^{\mathrm{iso}}_{I,xy} = \frac{2}{3}\mu_0 g_e \mu_e g_I \mu_I \rho_{\mathrm{s}}(\mathbf{0}) \,, \tag{A.292}$$

$$A^{\mathrm{ani}}_{I,xy} = \frac{1}{4\pi}\mu_0 g_e \mu_e g_I \mu_I \int \mathrm{d}\mathbf{r}\rho_{\mathrm{s}}(\mathbf{r})\frac{3r_x r_y - \delta_{xy}r^2}{r^5} \,. \tag{A.293}$$

A.5.2 De A-tensor in CPMD: implementatie en implicaties

In (A.291)-(A.293) is de elektronische spindichtheid ρ_{s} de enige variabele die volgt uit het elektronisch veeldeeltjesprobleem. Daarnaast zien we dat de tensor A_I voornamelijk de spindichtheid aftast in een beperkt gebied rond de positie van de atoomkern I. Het is dus van belang de spindichtheid daar zo goed mogelijk te kennen.

Het vrijwel noodzakelijke gebruik van pseudopotentialen in de CPMD-code (zie paragraaf A.4.6) impliceert echter (zie paragraaf A.2.4) dat i) de PSP-KS-orbitalen binnen vooraf gedefinieerde regio's rond de atoomkernen verschillen van de AE-KS-orbitalen die (zouden) volgen uit een alle-elektronenberekening, en ii) de bijdragen van de eventuele polarisatie van de kernelektronen niet worden meegeteld. Een vaakgebruikte oplossing voor het eerstgenoemde probleem is een reconstructie van de AE-KS-orbitalen uitgaande van de PSP-KS-orbitalen op basis van enkele aannames over de samenstellende componenten van de AE/PSP-KS-orbitalen in de nabije omgeving van de atoomkernen

(*projector augmented wave*, PAW).[56] De CPMD-implementatie is een *ex-post*-toepassing van de PAW-methode,[7] aangezien de reconstructie gebeurt na voltooiing van een PSP-Kohn-Sham-DFT-schema.[65]

De PAW-methode: het basisconcept

Essentieel stelt de PAW-methode dat een PSP-KS-orbitaal ψ_i^{PSP} uit een simulatie van een moleculaire configuratie in de buurt van een atoomkern I atomair is (atoomachtig), en aldus daar lokaal kan worden ontwikkeld in een lineaire combinatie van de atomaire PSP-golffuncties ϕ_I^{PSP} van dit atoom in zijn referentieconfiguratie (zie paragraaf A.2.4). Hetzelfde geldt voor het corresponderende KS-orbitaal uit een alle-elektronenberekening (hier steeds aangeduid met het superscript *AE*), met dien verstande dat het set van atomaire AE-golffuncties beperkt is tot het subset van AE-golffuncties waarvoor een corresponderende PSP-golffunctie beschikbaar is (zie opnieuw paragraaf A.2.4). Daarenboven stellen we de expansiecoëfficiënten behorend bij elk paar atomaire AE- en PSP-golffuncties aan elkaar gelijk.

Wanneer we via gepaste projectoren p_I de gewichten van elke ϕ_I^{PSP} in ψ_i^{PSP} berekenen, laat dit toe elke PSP-component uit ψ_i^{PSP} te vervangen door een overeenkomstige AE-component, zodat effectief de AE-KS-orbitaal wordt gereconstrueerd. In formulevorm luidt dit als volgt:[66]

$$\psi_i^{\mathrm{AE}}(\mathbf{r}) = \psi_i^{\mathrm{PSP}}(\mathbf{r}) + \sum_{I\in\mathrm{PSP},nlm} \left(\phi_{I,nlm}^{\mathrm{AE}}(\mathbf{r}) - \phi_{I,nlm}^{\mathrm{PSP}}(\mathbf{r})\right) \int \mathrm{d}\mathbf{r}' p_{I,nlm}^{*}(\mathbf{r}')\psi_i^{\mathrm{PSP}}(\mathbf{r}') \;, \tag{A.294}$$

waarbij de som in nlm alle atomaire PSP-golffuncties (en dus ook de corresponderende AE-golffuncties) uit de referentieconfiguratie van atoom I bestrijkt. Deze som zullen we omwille van de bondigheid met slechts één indexgetal $k \in \{nlm\}$ aanduiden.

[65] De PAW-methode is beter bekend in de variant waarin de reconstructie *tijdens* de zelfconsistente procedure van het Kohn-Sham-DFT-schema gebeurt. Op die manier ontstaat effectief een alle-elektronenschema voor de valentie-elektronen (de kernelektronen worden nog steeds vast verondersteld). Ook voor deze variant bestaat een procedure voor de berekening van de A-tensor.[8]

[66] Merk op dat we voor elke functie behorend bij een specifiek atoom impliciet veronderstellen dat $\mathbf{r}$ is gerefereerd ten opzichte van de positie van de atoomkern I.

De vorm van de projectoren p_I wordt bepaald door de volgende voorwaarden: i) de projectie gebeurt enkel in een beperkt gebied rond de atoomkern I, waar de golffunctie atoomachtig wordt verondersteld, en ii) de overlapintegralen met de atomaire PSP-golffuncties ϕ_I^{PSP} voldoen aan:

$$\int \mathrm{d}\mathbf{r} p_{I,k'}^*(\mathbf{r}) \phi_{I,k}^{\mathrm{PSP}}(\mathbf{r}) = \delta_{k'k} \; . \tag{A.295}$$

Aan de eerste voorwaarde wordt voldaan door een (sferisch symmetrische) afsnijfunctie d_I rond de atoomkern I voorop te stellen:

$$p_I(\mathbf{r}) = d_I(r) \tilde{p}_I(\mathbf{r}) \; . \tag{A.296}$$

Onder de bijkomende aanname van compleetheid van de atomaire PSP-golffuncties in het atoomachtig gebied, waardoor:

$$\tilde{p}_{I,k'}(\mathbf{r}) = \sum_{k''} \alpha_{k''k'} \phi_{I,k''}^{\mathrm{PSP}}(\mathbf{r}) \; , \tag{A.297}$$

kunnen we (A.295) schrijven als:

$$\int \mathrm{d}\mathbf{r} p_{I,k'}^*(\mathbf{r}) \phi_{I,k}^{\mathrm{PSP}}(\mathbf{r}) = \sum_{k''} \alpha_{k''k}^* \int \mathrm{d}\mathbf{r} d_I^*(r) \phi_{I,k''}^{*,\mathrm{PSP}}(\mathbf{r}) \phi_{I,k}^{\mathrm{PSP}}(\mathbf{r}) = \delta_{k'k} \; . \tag{A.298}$$

Hieruit kunnen we de expansiecoëfficiënten $\alpha_{k''k}$ bepalen.

Via (A.294) kunnen we de matrixelementen van een (semi-)lokale ééndeeltjes-operator $O(\mathbf{r})$ in de AE-KS-orbitalen berekenen:

$$\begin{aligned} \int \mathrm{d}\mathbf{r} \psi_j^{*,\mathrm{AE}}(\mathbf{r}) O(\mathbf{r}) \psi_i^{\mathrm{AE}}(\mathbf{r}) &= \int \mathrm{d}\mathbf{r} \psi_j^{*,\mathrm{PSP}}(\mathbf{r}) O(\mathbf{r}) \psi_i^{\mathrm{PSP}}(\mathbf{r}) \\ &+ \sum_{I \in \mathrm{PSP}} \sum_{k'k} \int \mathrm{d}\mathbf{r} \psi_j^{*,\mathrm{PSP}}(\mathbf{r}) p_{I,k'}(\mathbf{r}) \left(\int \mathrm{d}\mathbf{r} \phi_{I,k'}^{*,\mathrm{AE}}(\mathbf{r}) O(\mathbf{r}) \phi_{I,k}^{\mathrm{AE}}(\mathbf{r}) \right. \\ &\left. - \int \mathrm{d}\mathbf{r} \phi_{I,k'}^{*,\mathrm{PSP}}(\mathbf{r}) O(\mathbf{r}) \phi_{I,k}^{\mathrm{PSP}}(\mathbf{r}) \right) \int \mathrm{d}\mathbf{r} p_{I,k}^*(\mathbf{r}) \psi_i^{\mathrm{PSP}}(\mathbf{r}) \; . \end{aligned} \tag{A.299}$$

Nu voeren we nog de volgende drastische benaderingen in: in de atomaire regio's zijn de PSP-KS-orbitalen slechts opgebouwd uit één atomaire PSP-golffuncties van het s-type en drie van het p-type (wegens de multipliciteit

$2l+1$ in de energieniveaus van het baanimpulsmoment). $d_I(r) = 1$ in de atomaire regio van de atoomkern I en gelijk aan nul daarbuiten. Daarnaast herdefiniëren we de atomaire golffuncties: buiten de betreffende atomaire regio worden ze gelijk aan nul gesteld, en het gedeelte binnen de atomaire regio wordt op 1 genormaliseerd. Uit (A.298) volgt dan ten eerste dat de projectoren gelijk zijn aan:

$$p_{I,s}(\mathbf{r}) = \phi_{I,s}^{\mathrm{PSP}}(r) Y_{00}(\Omega) \,, \qquad p_{I,p_m}(\mathbf{r}) = \phi_{I,p}^{\mathrm{PSP}}(r) Y_{1m}(\Omega) \,, \tag{A.300}$$

met Y de sferische harmonieken en Ω de ruimtehoek. Zo komen we tot een vereenvoudigde PAW-methode voor de A-tensor, zoals die werd voorgesteld in Ref. [7].

De anisotrope component A^{ani} van de A-tensor in de vereenvoudigde PAW-methode

$A_{I,xy}^{\mathrm{ani}}$ kan worden herschreven als een lineaire combinatie van matrixelementen van het type:

$$\int \mathrm{d}\mathbf{r} \psi_i^{*,\mathrm{AE}}(\mathbf{r}) \frac{3r_x r_y - \delta_{xy} r^2}{r^5} \psi_i^{\mathrm{AE}}(\mathbf{r}) \,, \tag{A.301}$$

met – zoals steeds – de oorsprong van $\mathbf{r}$ gelijk is aan de positie van de atoomkern I. Op deze matrixelementen kunnen we de PAW-methode (A.299) toepassen. Daarbij nemen we aan dat de operator $\frac{3r_x r_y - \delta_{xy} r^2}{r^5}$ dermate gelokaliseerd is, dat de reconstructie enkel op de atomaire regio van de eigen atoomkern I moet worden uitgevoerd. Daarnaast stellen we vast dat, na opsplitsing van de operator in radiale en hoekafhankelijke componenten,[67] het hoekafhankelijk deel van de integralen $\int \mathrm{d}\mathbf{r} \phi_{I,k'}^{*,\mathrm{AE}}(\mathbf{r}) \frac{3r_x r_y - \delta_{xy} r^2}{r^5} \phi_{I,k}^{\mathrm{AE}}(\mathbf{r})$ en $\int \mathrm{d}\mathbf{r} \phi_{I,k'}^{*,\mathrm{PSP}}(\mathbf{r}) \frac{3r_x r_y - \delta_{xy} r^2}{r^5} \phi_{I,k}^{\mathrm{PSP}}(\mathbf{r})$ gelijk aan nul is, tenzij de atomaire golffuncties in de integralen allebei van van het p-type zijn voor de hoekafhankelijke component. Uit (A.299) volgt dan dat:

[67] Dit is via:

$$\begin{aligned}
r_x r_x &= r^2 \sin^2(\theta) \cos^2(\phi) \\
r_y r_y &= r^2 \sin^2(\theta) \sin^2(\phi) \\
r_z r_z &= r^2 \cos^2(\theta) \\
r_x r_y = r_y r_x &= r^2 \sin^2(\theta) \cos(\phi) \sin(\phi) \\
r_x r_z = r_z r_x &= r^2 \sin(\theta) \cos(\theta) \cos(\phi) \\
r_y r_z = r_z r_y &= r^2 \sin(\theta) \cos(\theta) \sin(\phi)
\end{aligned}$$

$$\int \mathrm{d}\mathbf{r}\psi_i^{*,\mathrm{AE}}(\mathbf{r})\frac{3r_xr_y-\delta_{xy}r^2}{r^5}\psi_i^{\mathrm{AE}}(\mathbf{r}) = \int \mathrm{d}\mathbf{r}\psi_i^{*,\mathrm{PSP}}(\mathbf{r})\frac{3r_xr_y-\delta_{xy}r^2}{r^5}\psi_i^{\mathrm{PSP}}(\mathbf{r})$$
$$+\int r^2\mathrm{d}r\frac{r^2}{r^5}\left(|\phi_{I,p}^{\mathrm{AE}}(r)|^2-|\phi_{I,p}^{\mathrm{PSP}}(r)|^2\right)$$
$$\times\sum_{p_{m'},p_m}\mathcal{C}_{p_{m'},p_m,x,y}\int \mathrm{d}\mathbf{r}\psi_i^{*,\mathrm{PSP}}(\mathbf{r})\phi_{I,p_{m'}}^{\mathrm{PSP}}(\mathbf{r})\int \mathrm{d}\mathbf{r}\phi_{I,p_m}^{*,\mathrm{PSP}}(\mathbf{r})\psi_i^{\mathrm{PSP}}(\mathbf{r})\,. \quad \text{(A.302)}$$

Hierin is $\mathcal{C}_{p_{m'},p_m,x,y}$ de integraal over de ruimtehoek van het product van twee sferische harmonieken $Y_{1m'}^*(\Omega)$ en $Y_{1m}(\Omega)$ en het hoekafhankelijke deel van $\frac{3r_xr_y-\delta_{xy}r^2}{r^5}$.

Gelukkig kunnen we het berekenen van $(\sum_{p_{m'},p_m}...)$ in (A.302) vermijden,[68] door gebruik te maken van de compleetheid van de atomaire PSP-golffuncties voor de beschrijving van de PSP-KS-orbitalen in de atomaire omgeving van de kern. Om deze omgeving aan te duiden, voeren we opnieuw de afsnijfunctie $d_I(r)$ in. Het matrixelement van de operator $d_I(r)\frac{3r_xr_y-\delta_{xy}r^2}{r^5}$ in de PSP-KS-orbitalen kunnen we dan schrijven als:

$$\int \mathrm{d}\mathbf{r}\psi_i^{*,\mathrm{PSP}}(\mathbf{r})d_I(r)\frac{3r_xr_y-\delta_{xy}r^2}{r^5}\psi_i^{\mathrm{PSP}}(\mathbf{r}) = \int r^2\mathrm{d}r d_I(r)\frac{r^2}{r^5}|\phi_{I,p}^{\mathrm{PSP}}(r)|^2$$
$$\times\sum_{p_{m'},p_m}\mathcal{C}_{p_{m'},p_m,x,y}\int \mathrm{d}\mathbf{r}\psi_i^{*,\mathrm{PSP}}(\mathbf{r})\phi_{I,p_{m'}}^{\mathrm{PSP}}(\mathbf{r})\int \mathrm{d}\mathbf{r}\phi_{I,p_m}^{*,\mathrm{PSP}}(\mathbf{r})\psi_i^{\mathrm{PSP}}(\mathbf{r})\,. \quad \text{(A.303)}$$

Gebruik makend van (A.303) kunnen we de som $\sum_{p_i,p_j}$ in (A.302) elimineren. Tenslotte verkrijgen we via een gepaste sommatie over spin-op- en spin-neer-KS-orbitalen volgende uitdrukking voor de anisotrope component A^{ani} van de A-tensor:[69]

[68] De berekening van de integralen $\int \mathrm{d}\mathbf{r}\psi_i^{*,\mathrm{PSP}}(\mathbf{r})\phi_{I,p_{m'}}^{\mathrm{PSP}}(\mathbf{r})$ en $\int \mathrm{d}\mathbf{r}\phi_{I,p_m}^{*,\mathrm{PSP}}(\mathbf{r})\psi_i^{\mathrm{PSP}}(\mathbf{r})$ is computationeel onaantrekkelijk: ψ_i^{PSP} is gedefinieerd op een raster bepaald door de simulatiecel, $\phi_{I,p_m}^{\mathrm{PSP}}$ op een sferisch raster.

[69] Zonder de voorfactor, zie daarvoor (A.293).

$$\int \mathrm{d}\mathbf{r}\rho_{\mathrm{s}}^{\mathrm{AE}}(\mathbf{r})\frac{3r_xr_y-\delta_{xy}r^2}{r^5} = \int \mathrm{d}\mathbf{r}\rho_{\mathrm{s}}^{\mathrm{PSP}}(\mathbf{r})\frac{3r_xr_y-\delta_{xy}r^2}{r^5}$$
$$+\frac{\int \mathrm{d}\mathbf{r}d_I(r)\rho_{\mathrm{s}}^{\mathrm{PSP}}(\mathbf{r})\frac{3r_xr_y-\delta_{xy}r^2}{r^5}}{\int r^2\mathrm{d}r d_I(r)\frac{r^2}{r^5}|\phi_{I,p}^{\mathrm{PSP}}(r)|^2}\int r^2\mathrm{d}r\frac{r^2}{r^5}\left(|\phi_{I,p}^{\mathrm{AE}}(r)|^2-|\phi_{I,p}^{\mathrm{PSP}}(r)|^2\right) . \tag{A.304}$$

In de praktijk worden de integralen die de spindichtheid bevatten uitgewerkt in de reciproque ruimte, aangezien er voor een willekeurige periodieke functie $f(\mathbf{r})$ geldt dat:

$$\int \mathrm{d}\mathbf{r}f(\mathbf{r})\frac{3(r_x-R_{I,x})(r_y-R_{I,y})-\delta_{xy}\left|\mathbf{r}-\mathbf{R}_I\right|^2}{\left|\mathbf{r}-\mathbf{R}_I\right|^5}$$
$$= -4\pi\sum_{\mathbf{G}\neq\mathbf{0}}\frac{G_xG_y-\frac{1}{3}G^2\delta_{xy}}{G^2}f(\mathbf{G})\mathrm{e}^{i\mathbf{G}.\mathbf{R}_I} , \tag{A.305}$$

met $\mathbf{R}_I$ de positie van de atoomkern I. De integralen die de atomaire golffuncties bevatten worden via numerieke integratietechnieken in de reële ruimte geëvalueerd. Deze golffuncties zijn beschikbaar bij de creatie van de pseudopotentiaal.

De isotrope component A^{iso} van de A-tensor in de vereenvoudigde PAW-methode

We kunnen eenzelfde techniek toepassen bij de berekening van de isotrope hyperfijn-parameter $A_{I,xy}^{\mathrm{iso}}$ (A.292). Hier is de operator $O(\mathbf{r})$ uit (A.299) gelijk aan $\delta(\mathbf{r})$. Deze operator is vanzelfsprekend sterk gelokaliseerd, zodat de reconstructie opnieuw enkel op de atomaire regio van de eigen atoomkern I moet worden uitgevoerd. Aangezien de radiale componenten van de atomaire golffuncties van het p-type verdwijnen op de positie van de atoomkern, terwijl deze van het s-type dat niet doen, volgt uit (A.299) dat:

$$\int \mathrm{d}\mathbf{r}\psi_i^{*,\mathrm{AE}}(\mathbf{r})\delta(\mathbf{r})\psi_i^{\mathrm{AE}}(\mathbf{r}) = \int \mathrm{d}\mathbf{r}\psi_i^{*,\mathrm{PSP}}(\mathbf{r})\delta(\mathbf{r})\psi_i^{\mathrm{PSP}}(\mathbf{r})$$
$$+\left(|\phi_{I,s}^{\mathrm{AE}}(\mathbf{0})|^2-|\phi_{I,s}^{\mathrm{PSP}}(\mathbf{0})|^2\right)$$
$$\times\int \mathrm{d}\mathbf{r}\psi_i^{*,\mathrm{PSP}}(\mathbf{r})\phi_{I,s}^{\mathrm{PSP}}(\mathbf{r})\int \mathrm{d}\mathbf{r}\phi_{I,s}^{*,\mathrm{PSP}}(\mathbf{r})\psi_i^{\mathrm{PSP}}(\mathbf{r}) . \tag{A.306}$$

Opnieuw kunnen we het berekenen van de overlapintegralen tussen golffuncties op incompatibele rasters vermijden, door gebruik te maken van de compleetheid van de atomaire PSP-golffuncties voor de beschrijving van de PSP-KS-orbitalen in de atomaire omgeving van de kern, waardoor:

$$\begin{aligned}&\int \mathrm{d}\mathbf{r}\psi_i^{*,\mathrm{PSP}}(\mathbf{r})\delta(\mathbf{r})\psi_i^{\mathrm{PSP}}(\mathbf{r}) = |\phi_{I,s}^{\mathrm{PSP}}(\mathbf{0})|^2 \\ &\times \int \mathrm{d}\mathbf{r}\psi_i^{*,\mathrm{PSP}}(\mathbf{r})\phi_{I,s}^{\mathrm{PSP}}(\mathbf{r}) \int \mathrm{d}\mathbf{r}\phi_{I,s}^{*,\mathrm{PSP}}(\mathbf{r})\psi_i^{\mathrm{PSP}}(\mathbf{r}) \,. \end{aligned} \tag{A.307}$$

Na eliminatie van de overlapintegralen uit (A.306) met behulp van (A.307), en een gepaste sommatie over spin-op- en spin-neer-KS-orbitalen verkrijgen we de volgende uitdrukking voor de isotrope component A^{iso} van de A-tensor:[70]

$$\begin{aligned}\rho_{\mathrm{s}}^{\mathrm{AE}}(\mathbf{0}) &= \rho_{\mathrm{s}}^{\mathrm{PSP}}(\mathbf{0}) + \left(|\phi_{I,s}^{\mathrm{AE}}(\mathbf{0})|^2 - |\phi_{I,s}^{\mathrm{PSP}}(\mathbf{0})|^2\right) \frac{\rho_{\mathrm{s}}^{\mathrm{PSP}}(\mathbf{0})}{|\phi_{I,s}^{\mathrm{PSP}}(\mathbf{0})|^2} \,, \\ &= \rho_{\mathrm{s}}^{\mathrm{PSP}}(\mathbf{0}) \frac{|\phi_{I,s}^{\mathrm{AE}}(\mathbf{0})|^2}{|\phi_{I,s}^{\mathrm{PSP}}(\mathbf{0})|^2} \,. \end{aligned} \tag{A.308}$$

Gebruik van de vereenvoudigde variant van de PAW-methode voor de A-tensor

De vereenvoudigde variant van de PAW-methode voor de A-tensor is gebaseerd op verschillende aannames, waaronder de drastische benadering dat in de atomaire regio's één s-type en drie p-type atomaire golffuncties een compleet set vormen voor de beschrijving van een willekeurige PSP-KS-orbitaal. Dit beperkt het gebruik van de vereenvoudigde PAW-methode tot lichte elementen, omdat de PSP-KS-orbitalen in de atomaire regio's van deze atomen geen significante componenten met een hoger baankwantumgetal hebben. Voor deze lichte elementen levert de vereenvoudigde PAW-methode goede resultaten: de isotrope component voor de A-tensor kan weliswaar enigzins afwijken, maar de anisotrope component wordt meestal nauwkeurig voorspeld.[Art. 1-3][50] De algemene PAW-methode kan natuurlijk worden toegepast voor hogere baankwantumgetallen, maar zal op die manier toch nooit de effecten van de polarisatie van de kernelektronen kunnen weergeven. Bovendien, zoals werd opgemerkt in Ref. [50], lost de PAW-methode

[70] Zonder de voorfactor, zie daarvoor (A.292).

evenmin de problemen op gerelateerd aan de spinafhankelijke uitwisselings-correlatiepotentiaal v_{XC}^{τ} in de PSP-benadering, nodig voor een correcte beschrijving van de polarisatie van de valentie-elektronen.

A.5.3 De A-tensor in CP2K: implementatie en implicaties

De bovengenoemde tekortkomingen bij de berekening van de A-tensor in de PSP-benadering illustreren duidelijk de nood aan een hybride methode die – met een zo klein mogelijke computationele kost – een AE-beschrijving[71] van de *interessante* atoomkernen mogelijk maakt (dit is gewoonlijk het radicaal centrum en eventueel zijn directe omgeving), terwijl daarnaast een PSP-beschrijving van de overige atomen mogelijk blijft. Een dergelijke benadering zal hoogstwaarschijnlijk geen invloed hebben op de gewenste A-tensoren, aangezien deze hoofdzakelijk worden bepaald door de elektronische spindichtheid in een beperkt gebied rond de positie van de respectievelijke atoomkern. De GAPW-methode (zie paragraaf A.2.6) is voor deze doeleinden uitermate geschikt: de methode bestaat in zowel een PSP- als een AE-variant, en beide kunnen eenvoudig worden gecombineerd binnen één simulatie. Bovendien vereist een GAPW-simulatie met een AE-beschrijving voor de interessante atomen slechts een relatief kleine bijkomende computationele kost, dankzij het gebruik van Gaussische functies[72]. In een pure PW-basisset bijvoorbeeld is de bijkomende computationele kost veel groter.[73]

De anisotrope component A^{ani} van de A-tensor in de GAPW-methode

Voor de berekening van $A_{I,xy}^{\mathrm{ani}}$ wordt de GAPW-voorstelling van de spindichtheid (A.84) herordend:

$$\rho_s = \tilde{\rho}_s + \rho_{s,I}^1 - \tilde{\rho}_{s,I}^1 + \sum_{J(J\neq I)} \left(\rho_{s,J}^1 - \tilde{\rho}_{s,J}^1\right) \ . \tag{A.309}$$

Wanneer we deze uitdrukking invoeren in (A.293), en rekening houden met (A.305) voor de zachte spindichtheid $\tilde{\rho}_s$, kunnen we $A_{I,xy}^{\mathrm{ani}}$ als volgt berekenen:

[71] Dus gebruik makend van de nucleaire Coulomb-potentiaal.

[72] preciezer nog: gecontraheerde periodieke Gaussische functies.

[73] Omdat een basisset met *heel* veel vlakke golven noodzakelijk is voor de correcte beschrijving van de Coulomb-potentiaal en de snelle oscillaties in de golffuncties in de buurt van de atoomkernen.

$$
\begin{aligned}
A^{\text{ani}}_{I,xy} &= \frac{1}{4\pi}\mu_0 g_e \mu_e g_I \mu_I \Bigg(\\
&- 4\pi \sum_{\frac{1}{2}|\mathbf{G}|<E_c, \mathbf{G}\neq\mathbf{0}} \frac{\left(G_x G_y - \frac{1}{3}G^2\delta_{xy}\right)}{G^2} \tilde{\rho}_s(\mathbf{G}) \mathrm{e}^{i\mathbf{G}\cdot\mathbf{R}_I} \\
&+ \int_{U_I} \mathrm{d}\mathbf{r} \left(\rho^1_{s,I}(\mathbf{r}) - \tilde{\rho}^1_{s,I}(\mathbf{r})\right) \frac{3r_x r_y - \delta_{xy} r^2}{r^5} \Bigg) \\
&+ \Delta A^{\text{ani}}_{I,xy} \, .
\end{aligned} \tag{A.310}
$$

De integratie over de atoomgecentreerde spindichtheden kan beperkt worden tot U_I wegens (A.88). $\Delta A^{\text{ani}}_{I,xy}$ duidt de kleine bijdragen aan afkomstig van het verschil tussen de echte en de zachte spindichtheden $\rho^1_{s,J} - \tilde{\rho}^1_{s,J}$ in nabijgelegen atomaire regio's U_J:

$$
\begin{aligned}
\Delta A^{\text{ani}}_{I,xy} &= \frac{1}{4\pi}\mu_0 g_e \mu_e g_I \mu_I \\
&\times \sum_{J(J\neq I, R_{IJ}<R_c)} \int_{U_J} \mathrm{d}\mathbf{r} \left(\rho^1_{s,J}(\mathbf{r}) - \tilde{\rho}^1_{s,J}(\mathbf{r})\right) \\
&\times \frac{3\left(r_x + R_{JI,x}\right)\left(r_y + R_{JI,y}\right) - \delta_{xy}\left|\mathbf{r} + \mathbf{R}_{JI}\right|^2}{\left|\mathbf{r} + \mathbf{R}_{JI}\right|^5} \, .
\end{aligned} \tag{A.311}
$$

In de bovenstaande vergelijking is de oorsprong van $\mathbf{r}$ steeds gelijk aan de positie van de atoomkern J, en is $\mathbf{R}_{JI} = \mathbf{R}_J - \mathbf{R}_I$ de vector die atoomkernen J en I verbindt. Enkel de meest nabijgelegen atomaire regio's moeten in de som worden opgenomen. Dit kan door een maximumwaarde R_c te kiezen voor $R_{JI} = \left|\mathbf{R}_{JI}\right|$. De invloed van $\Delta A^{\text{ani}}_{I,xy}$ op de totale A tensor werd bestudeerd in Ref. [Art. 3].

De isotrope component A^{iso} van de A-tensor in de GAPW-methode

$A^{\text{iso}}_{I,xy}$ wordt berekend uitgaande van de atoomgecentreerde spindichtheid $\rho^1_{s,I}$, die gelijk is aan ρ_s in het gebied U_I (A.89):

$$
A^{\text{iso}}_{I,xy} = \frac{2}{3}\mu_0 g_e \mu_e g_I \mu_I \rho^1_{s,I}(\mathbf{0}) \, . \tag{A.312}
$$

Daarnaast is er ook een scalair-relativistische variant van (A.292) geïmplementeerd. Deze is gedefinieerd als:[8, 57][74]

$$A^{\text{iso}}_{I,xy} = \frac{2}{3}\mu_0 g_e \mu_e g_I \mu_I \int_{U_I} \mathrm{d}\mathbf{r}\rho_{\text{s}}(\mathbf{r})\delta_{\text{T},I}(\mathbf{r}) \; . \tag{A.313}$$

$\delta_{\text{T},I}$ is een uitgesmeerde δ-functie die afhangt van het atoomnummer Z behorend bij atoomkern I:

$$\delta_{\text{T},I}(\mathbf{r}) \cong \frac{1}{4\pi r^2}\frac{2}{Z_I\alpha^2}\frac{1}{\left(1+\frac{2r}{Z_I\alpha^2}\right)^2} \; . \tag{A.314}$$

In de niet-relativistische limiet vereenvoudigt $\delta_{\text{T},I}$ tot de Diracdelta.

Dankzij deze δ-functie kunnen we de integratie in (A.313) zonder problemen beperken tot U_I, en opnieuw de atoomgecentreerde spindichtheid $\rho^1_{s,I}$ gebruiken.

Gebruik van de GAPW-methode voor de A-tensor

Zeer gelijkaardige uitspraken als bij de g-tensor kunnen worden gedaan over de A-tensor. In Ref. [Art. 3] werd de GAPW-methode voor de A-tensor uitgebreid getest. De A-tensoren van een uitgebreide selectie van atomen en kleine molecules in de gasfase, berekend met de AE-variant van de GAPW-methode, stemmen uitstekend overeen met deze geproduceerd door GAUSSIAN 03,[58] een simulatiepakket (uitsluitend) voor berekeningen in de gasfase, dat eveneens de LCAO-benadering aanneemt en de atomaire orbitalen uitdrukt als CGF's (zie paragraaf A.2.3). Daarnaast heeft het hybride gebruik van de AE-variant voor het radicalair centrum en de PSP-variant voor de omgeving in de diverse bestudeerde kristallen (zie [Art. 3] en [Art. 4]) geen merkbare invloed op de berekende A-tensoren. We kunnen dus stellen dat we een accurate en tegelijkertijd relatief goedkope methode (in termen van computationele kost) hebben afgeleid voor de berekening van A-tensoren in PBC-simulaties. Toch wensen we (opnieuw) op te merken dat de GAPW-methode (net zoals de GPW-methode) voorlopig enkel in de Γ-puntbenadering beschikbaar is, wat de keuzemogelijkheden voor de dimensies

[74] De theoretische afleiding zal hier niet aan bod komen. De geïnteresseerde lezer wordt doorverwezen naar de genoemde referenties.

van de simulatiecel van een te bestuderen materiaal beïnvloedt, en op die manier ook bepaalt of dit materiaal in deze benadering wel aan een redelijke computationele kost kan worden gesimuleerd.

A.6 Conclusies

Dit doctoraatsonderzoek richtte zich op de ontwikkeling, implementatie, validatie en toepassing van DFT-methodes voor de snelle en nauwkeurige berekening van de g- en A-tensoren in PBC-simulaties. Daartoe werden een aantal nieuw-ontwikkelde theoretische methodes geïmplementeerd in CPMD en CP2K, twee populaire simulatiepakketten die gebruik maken van periodieke randvoorwaarden. Vervolgens werden de ontwikkelde theoretische methodes gevalideerd, door de EPR-parameters van een uitgebreide selectie van atomen en kleine molecules in de gasfase te vergelijken met reeds bestaande berekeningsmethodes voor de gasfase (zowel CPMD als CP2K kunnen via speciale technieken ook met de gasfase overweg). Daarna werden met de nieuwe methode de EPR-parameters van enkele periodieke structuren berekend, en grondig vergeleken met de beschikbare experimentele gegevens en resultaten verkregen met onder andere cluster-in-vacuomodellen. Verschillende ideeën voor de versnelling van de methodes, zoals bijvoorbeeld het gebruik van een gelaagde hybride AE/PSP/MM-aanpak, werden zorgvuldig getest.

Waarschijnlijk zal blijken dat de CP2K-methodes, omdat zij breder inzetbaar zijn, beter tegen de tijd bestand zijn dan hun CPMD-tegenhangers. Via de GAPW-voorstelling en de gelaagde aanpak, bieden de CP2K-methodes een zeer aantrekkelijk compromis tussen nauwkeurigheid en computationele kost in vergelijking met het beperkte aantal concurrerende methodes voor PBC-simulaties, aangezien ze een volledig AE-behandeling (zonder het verplichte gebruik van reconstructietechnieken zoals PAW die, zoals bekend, niet alle problemen gerelateerd aan de PSP-benadering verhelpen) van het radicalaire centrum mogelijk maken tegen een relatief kleine bijkomende computationele kost, terwijl daarnaast een relatief goedkope PSP-benadering of MM-technieken voor de rest van de simulatiecel mogelijk blijven.

Een aantal interessante toepassingen zijn reeds uitgevoerd, zoals bijvoorbeeld de studie van de afhankelijkheid van de moleculaire omgeving van A-tensoren in een reeks van suikerkristalradicalen [Art. 7], de berekening van de A-tensoren van het R2-centrum in β-D-fructose langsheen een compleet moleculaire-dynamicatraject op eindige temperatuur [Art. 7], en de berekening van de g-tensor voor het E_1'-centrum in α-kwarts met behulp van een simulatiecel bestaande uit 15551 atomen en de gelaagde hybride AE/PSP/MM-aanpak [Art. 8]. Nieuwe toepassingen worden volop onderzocht.

Er bestaan uiteraard nog een aantal mogelijkheden voor verbetering. Toekomstig onderzoekswerk zou zich in eerste instantie op de volgende drie pistes moeten concentreren: i) De verbetering van de schaalbaarheid bij de berekening van de eerste-ordegolffuncties $\psi_i^{(1)}$, zoals besproken in paragraaf A.4.5, ii) de mogelijkheid om hybride functionalen te gebruiken, en iii) het implementeren van (bijkomende) relativistische effecten, die (onder meer) moeten toelaten de EPR-parameters voor zware elementen nauwkeuriger te berekenen.

Bibliography

[1] G. Schreckenbach and T. Ziegler. *J. Phys. Chem. A*, 101:3388–3399, 1997.

[2] O. L. Malkina, J. Vaara, B. Schimmelpfennig, M. Munzarová, V. G. Malkin, and M. Kaupp. *J. Am. Chem. Soc.*, 122:9206–9218, 2000.

[3] F. Neese. *J. Chem. Phys.*, 115:11080–11096, 2001.

[4] E. van Lenthe, P. E. S. Wormer, and A. van der Avoird. *J. Chem. Phys.*, 107:2488–2498, 1997.

[5] K. M. Neyman, D. I. Ganyushin, A. V. Matveev, and V. A. Nasluzov. *J. Phys. Chem. A*, 106:5022–5030, 2002.

[6] C. J. Pickard and F. Mauri. *Phys. Rev. Lett.*, 88:086403, 2002.

[7] C. G. Van de Walle and P. E. Blöchl. *Phys. Rev. B*, 47:4244–4255, 1993.

[8] P. E. Blöchl. *Phys. Rev. B*, 62:6158–6179, 2000.

[9] G. Csányi and T. A. Arias. *Chem. Phys. Lett.*, 360:552–556, 2002.

[10] R. G. Parr and W. Yang. *Density functional theory of atoms and molecules*. Oxford University Press, New York, 1989.

[11] N. W. Ashcroft and N. D. Mermin. *Solid state physics*. Brooks/Cole, Philadelphia, 1976.

[12] P. Hohenberg and W. Kohn. *Phys. Rev.*, 136:B864, 1964.

[13] M. Levy. *Phys. Rev. A*, 26:1200–1208, 1982.

[14] T. L. Gilbert. *Phys. Rev. B*, 12:2111–2120, 1975.

[15] W. Kohn and L. J. Sham. *Phys. Rev.*, 140:A1133, 1965.

[16] U. von Barth and L. Hedin. *J. Phys. C: Solid State Phys.*, 5:1629–1642, 1972.

[17] M. M. Pant and A. K. Rajagopal. *Solid State Commun.*, 5:1157–1160, 1972.

[18] R. Stowasser and R. Hoffmann. *J. Am. Chem. Soc.*, 121:3414–3420, 1999.

[19] A. D. Becke. *J. Chem. Phys.*, 98:1372–1377, 1993.

[20] S. Obara and A. Saika. *J. Chem. Phys.*, 84:3963–3974, 1986.

[21] F. Bloch. *Z. Phys.*, 52:555–600, 1928.

[22] X. Gonze, P. Käckell, and M. Scheffler. *Phys. Rev. B*, 41:12264–12267, 1990.

[23] D. R. Hamann, M. Schlüter, and C. Chiang. *Phys. Rev. Lett.*, 43:1494–1497, 1979.

[24] S. G. Louie, S. Froyen, and M. L. Cohen. *Phys. Rev. B*, 26:1738–1742, 1982.

[25] G. Lippert, J. Hutter, and M. Parrinello. *Mol. Phys.*, 92:477–488, 1997.

[26] S. Goedecker, M. Teter, and J. Hutter. *Phys. Rev. B*, 54:1703–1710, 1996.

[27] C. Hartwigsen, S. Goedecker, and J. Hutter. *Phys. Rev. B*, 58:3641–3662, 1998.

[28] G. Lippert, J. Hutter, and M. Parrinello. *Theor. Chem. Acc.*, 103:124–140, 1999.

[29] P. E. Blöchl. *Phys. Rev. B*, 50:17953–17979, 1994.

[30] M. Krack and M. Parrinello. *Phys. Chem. Chem. Phys.*, 2:2105–2112, 2000.

[31] P. A. M. Dirac. *Proc. Roy. Soc.*, A117:610–624, 1928.

[32] P. A. M. Dirac. *Proc. Roy. Soc.*, A118:351–361, 1928.

[33] C. D. Anderson. *Phys. Rev.*, 43:491–494, 1933.

[34] G. Breit. *Phys. Rev.*, 34:553–573, 1929.

[35] L. L. Foldy and S. A. Wouthuysen. *Phys. Rev.*, 78:29–36, 1950.

[36] Z. V. Chraplyvy. *Phys. Rev.*, 91:388–391, 1953.

[37] Z. V. Chraplyvy. *Phys. Rev.*, 92:1310–1315, 1953.

[38] Codata recommended values of the fundamental physical constants: 2006.

[39] D. Sebastiani and M. Parrinello. *J. Phys. Chem. A*, 105:1951–1958, 2001.

[40] D. Sebastiani. Development of a new ab initio approach for NMR chemical shifts in periodic systems (Doctoral thesis).

[41] S. Baroni, P. Giannozzi, and A. Testa. *Phys. Rev. Lett.*, 58:1861–1864, 1987.

[42] X. Gonze. *Phys. Rev. A*, 52:1086–1095, 1995.

[43] X. Gonze. *Phys. Rev. A*, 52:1096–1114, 1995.

[44] A. Putrino, D. Sebastiani, and M. Parrinello. *J. Chem. Phys.*, 113:7102–7109, 2000.

[45] G. H. Wannier. *Phys. Rev.*, 52:191–197, 1937.

[46] W. Kohn. *Phys. Rev.*, 115:809–821, 1959.

[47] T. A. Keith and R. F. W. Bader. *Chem. Phys. Lett.*, 210:223–231, 1993.

[48] D. Sebastiani, G. Goward, I. Schnell, and M. Parrinello. *Comput. Phys. Commun.*, 147:707, 2002.

[49] D. Sebastiani, G. Goward, I. Schnell, and H. W. Spiess. *J. Mol. Struct.*, 625:283–288, 2003.

[50] O. V. Yazyev, I. Tavernelli, L. Helm, and U. Röthlisberger. *Phys. Rev. B*, 71:115110, 2005.

[51] J. C. Slater. *Phys. Rev. 81*, 81:385–390, 1951.

[52] Lebedev VI (1975) Zh Vychisl Mat Mat Fiz 15: 48.

[53] Lebedev VI (1976) Zh Vychisl Mat Mat Fiz 16: 293.

[54] Lebedev VI (1977) Sib Math 15: 48.

[55] ADF2007.01, SCM, Theoretical Chemistry, Vrije Universiteit, Amsterdam, The Netherlands, http://www.scm.com.

[56] P. E. Blöchl. *Phys. Rev. B*, 50:17953–17979, 1994.

[57] S. Blügel, H. Akai, R. Zeller, and P. H. Dederichs. *Phys. Rev. B*, 35:3271–3283, 1987.

[58] J. M. Frisch *et al.*, Gaussian 03, Revision D.01. Gaussian, Inc., Wallingford, CT, 2004.